

MAY 24 1991

0830-H-10  
0309

NAS 1.55:3113

*NASA Conference Publication 3113*

# 25th Aerospace Mechanisms Symposium

*Proceedings of a symposium held at  
the Jet Propulsion Laboratory  
Pasadena, California  
May 8-10, 1991*

---

---

NASA

HGW

*NASA Conference Publication 3113*

# 25th Aerospace Mechanisms Symposium



*Jet Propulsion Laboratory  
Pasadena, California*

Proceedings of a symposium sponsored by  
the National Aeronautics and Space Administration,  
the California Institute of Technology, and the  
Lockheed Missiles & Space Company, Inc., and held at  
the Jet Propulsion Laboratory  
Pasadena, California  
May 8-10, 1991

**NASA**

National Aeronautics and  
Space Administration

Office of Management

Scientific and Technical  
Information Division

1991

**BLANK PAGE**

## PREFACE

The proceedings of the 25th Aerospace Mechanisms Symposium held at the Jet Propulsion Laboratory in Pasadena, California, on May 8-10, 1991, are in this NASA Conference Publication. The symposium was sponsored by the National Aeronautics and Space Administration, the California Institute of Technology, and Lockheed Missiles and Space Company, Inc.

The purpose of the symposium was to provide a forum for the interchange of information among those active in the field of mechanisms technology. To that end, 25 papers were presented on aeronautics and space flight hardware, with special emphasis on actuators, latches, cryogenic mechanisms, vacuum tribology, bearings, robotics, ground support for aerospace applications and other mechanisms for large space structures. The papers were prepared by engineers from a broad aerospace background, including the U.S. aerospace industry, NASA, and European and Asian participants.

The efforts of the review committee, session chairmen, and speakers contributing to the technical excellence and professional character of the conference are especially appreciated.

The use of trade names or names of manufacturers in this publication does not constitute an official endorsement of such products or manufacturers, either expressed or implied, by the National Aeronautics and Space Administration.

**BLANK PAGE**

## CONTENTS

Preface .....	iii
THE ORGANIZING COMMITTEE .....	vii
PROGRAM .....	ix
CETA TRUCK AND EVA RESTRAINT SYSTEM .....	1
David C. Beals and Wayne R. Merson	
SYSTEM REQUIREMENTS AND DESIGN FEATURES OF SPACE STATION REMOTE MANIPULATOR SYSTEM MECHANISMS .....	15
Rajnish Kumar and Robert Hayes	
"DEAD-BLOW" HAMMER DESIGN APPLIED TO A CALIBRATION TARGET MECHANISM TO DAMPEN EXCESSIVE REBOUND .....	31
Brian Y. Lim	
DESIGN AND DEVELOPMENT OF THE REDUNDANT LAUNCHER STABILIZATION SYSTEM FOR THE ATLAS II LAUNCH VEHICLE .....	45
M. Nakamura	
BRAKE LOCK MECHANISM FOR THE TWO AXIS POINTING SYSTEM .....	61
Alan Posey, Mike Clark, and Larry Mignosa	
AN ANTENNA-POINTING MECHANISM FOR THE ETS-VI K-BAND SINGLE ACCESS (KSA) ANTENNA .....	77
Noboru Takada, Takahiro Amano, Toshiro Ohhashi, and Shigeo Wachi	
POINTING/ROLL MECHANISM FOR THE ULTRAVIOLET CORONAGRAPH SPECTROMETER .....	93
Miroslaw A. Ostaszewski and Larry J. Guy	
SIRTF/IRS CRYOGENIC GRATING DRIVE MECHANISM (ARC SECOND POSITIONING AT 4 K) .....	107
Michael J. Kubitschek	
DEVELOPMENT OF A RELATCHABLE COVER MECHANISM FOR A CRYOGENIC IR-SENSOR .....	125
R. Birner, G. Lange, M. Roth, and A. Voit	
A SYNCHRONOUS CHOPPER MECHANISM FOR USE AT CRYOGENIC TEMPERATURE .....	135
Claef Hakun, Allen Tyler, and Cornelis de Kramer	
CRYOGENIC MECHANISMS FOR SCANNING AND INTERCHANGE OF THE FABRY- PEROT INTERFEROMETERS IN THE ISO LONG WAVELENGTH SPECTROMETER .....	151
G. R. Davis, I. Furniss, T. J. Patrick, R. C. Sidey, and W. A. Towlson	
SPIN BEARING RETAINER DESIGN OPTIMIZATION .....	161
Edward A. Boesiger and Mark H. Warner	

WEAR CHARACTERISTICS OF BONDED SOLID FILM LUBRICANT UNDER HIGH LOAD CONDITION .....	179
Naofumi Hiraoka, Akira Sasaki, Noritsugu Kawashima, and Toshio Honda	
DEVELOPMENT OF SOLID-LUBRICATED BALL-SCREWS FOR USE IN SPACE .....	195
Masatoshi Chiba, Toru Gyougi, Makoto Nishimura, and Katsuni Seki	
TOPEX HIGH-GAIN ANTENNA SYSTEM DEPLOYMENT ACTUATOR MECHANISM.....	205
Stephen R. Jones	
RESETTABLE BINARY LATCH MECHANISM FOR USE WITH PARAFFIN LINEAR MOTORS .....	221
Daryl Maus and Scott Tibbitts	
HARMONIC DRIVE GEAR ERROR: CHARACTERIZATION AND COMPENSATION FOR PRECISION POINTING AND TRACKING.....	237
Ted W. Nye and Robert P. Kraml	
PAYOUT SPIN ASSEMBLY FOR THE COMMERCIAL TITAN LAUNCH VEHICLE.....	253
Wilf Robinson and Greg Pech	
SMA APPLICATIONS IN AN INNOVATIVE MULTISHOT DEPLOYMENT MECHANISM .....	275
D. Stella, G. Pedrazzoli, G. Secci, and C. Portelli	
SPACE SHUTTLE HOLDDOWN POST BLAST SHIELD .....	291
F. B. Larracas	
THE DYNAMIC TORQUE CALIBRATION UNIT: AN INSTRUMENT FOR THE CHARACTERIZATION OF BEARINGS USED IN GIMBAL APPLICATIONS.....	307
Louise Jandura	
A NEW ACTIVE VIRTUAL PIVOT SIX-DEGREE-OF-FREEDOM HAND CONTROLLER FOR AEROSPACE APPLICATIONS.....	323
William C. Marshall, Kathleen M. Radke, Robert E. DeMers, David J. Lowry, and Lee Levitan	

## THE ORGANIZING COMMITTEE

The papers presented at the Symposium were selected and reviewed by the Organizing Committee. Authors are responsible for the content and the technical accuracy of their respective papers.

Donald Sevilla	Host Chairman	JPL
Pat McLane	Symposium Coordinator	JPL
Charles W. Coale	General Chairman	LMSC
Joel Burdick	Administrative Chairman	CIT
Stuart H. Loewenthal	Operations Chairman	LMSC
Obie H. Bradley	NASA LaRC	
Charles S. Cornelius	NASA MSFC	
Michael Eiden	ESTeC	
David F. Engelbert	NASA ARC	
Harvey H. Horiuchi	JPL	
Ronald E. Mancini	NASA ARC	
Jerry E. McCullough	NASA JSC	
James D. Phillips	NASA KSC	
John W. Redmon, Sr.	NASA MSFC	
John F. Rogers	NASA LaRC	
Douglas A. Rohn	NASA LaRC	
Gordon Rysavy	NASA JSC	
William C. Schneider	NASA JSC	
Jesse D. Timmons	NASA HQ	
Sterling W. Walker	KSC	
Bowden W. Ward	NASA GSFC	
SYMPOSIUM ADVISORY COMMITTEE		
Paul W. Bomke	JPL	
Aleck C. Bond	NASA JSC (Ret)	
Thomas F. Bonner	Space Industries	
H. Mervyn Briscoe	ESTeC (Ret)	
Kenneth C. Curry	JPL(Ret)	
Otto H. Fedor	LSOC (Ret)	
Frank T. Martin	NASA GSFC (Ret)	
James H. Parks	NASA LaRC	
Alfred L. Rinaldo	LMSC (Ret)	
Nathan D. Watson	NASA LaRC (Ret)	
Joseph F. Wilson	LMSC	

**BLANK PAGE**

## PROGRAM

### TUESDAY, 7 MAY 1991

7:00-9:30 pm                      Early Registration and Social  
    (Room 1221, Pasadena Hilton)

### WEDNESDAY, 8 MAY 1991

8:00        Wednesday Authors' Breakfast  
    (Executive Dining Room, JPL Cafeteria)

8:00        REGISTRATION AND COFFEE  
    (von Karman Auditorium, JPL)

9:30        INTRODUCTORY REMARKS  
    Mr. Donald R. Sevilla, Host Chairman  
    Jet Propulsion Laboratory  
    Mr. Stuart Loewenthal, Operations Chairman  
    Lockheed Missiles & Space Co., Sunnyvale, CA

CENTER WELCOME  
Dr. Edward Stone, Director  
Jet Propulsion Laboratory

10:00      SESSION I  
    Ms. Virginia Ford, Session Chairman  
    Jet Propulsion Laboratory  
    - *CETA Truck and EVA Restraint System*  
    David C. Beals  
    NASA Langley Research Center, Hampton, VA  
    Wayne R. Merson  
    Lockheed Engineering & Science Co., Hampton, VA  
    - *System Requirements and Design Features of Space Station Remote Manipulator System Mechanisms*  
    Rajnish Kumar and Robert Hayes  
    Spar Aerospace Ltd., Toronto, Canada  
    - *"Dead-Blow" Hammer Design Applied to a Calibration Target Mechanism to Dampen Excessive Rebound*  
    Brian Y. Lim  
    Jet Propulsion Laboratory, Pasadena, CA

- *Design and Development of the Redundant Launcher Stabilization System for the Atlas II Launch Vehicle*  
Mark Nakamura  
General Dynamics Space Systems Division, San Diego, CA

12:00 LUNCH

1:30 SESSION II

- Mr. Michael D. Menning, Session Chairman  
Lockheed Missiles & Space Co., Sunnyvale, CA
- *Brake Lock Mechanism for the Two Axis Pointing System*  
Alan Posey and Mike Clark  
NASA Goddard Space Flight Center, Greenbelt, MD
- Larry Mignosa  
Swales and Associates, Beltsville, MD
- *An Antenna-Pointing Mechanism for the ETS-VI K-Band Single Access (KSA) Antenna*  
N. Takada  
National Space Development Agency of Japan, Ibaraki, Japan
- T. Amano, T. Ohhashi, and S. Wachi  
Toshiba Corporation, Kanagawa, Japan
- *Pointing/Roll Mechanism for the Ultraviolet Coronagraph Spectrometer*  
Miroslaw A. Ostaszewski and Larry J. Guy  
Ball Corporation, Boulder, CO

3:00 COFFEE BREAK

3:15 SPECIAL PRESENTATION

- JPL Image Processing*  
Dr. Denis Elliott, Presenter  
Jet Propulsion Laboratory

5:30 WELCOMING RECEPTION

- Descanso Botanical Gardens  
La Canada/Flintridge, CA (near JPL)
- 5:30 Buses depart from the Hilton Hotel
- 6:00 Reception
- 9:00 Buses return to the Hilton Hotel

**THURSDAY, 9 May 1991**

- 7:15 Thursday Authors' Breakfast  
(Executive Dining Room, JPL Cafeteria)
- 8:30 SESSION III  
Mr. Gerald W. Lilienthal, Session Chairman  
Jet Propulsion Laboratory  
- *SIRTF/IRS Cryogenic Grating Drive Mechanism (Arc Second Positioning at 4K)*  
Michael J. Kubitschek  
Ball Aerospace Systems Group, Boulder, CO.  
- *Development of a Relatchable Cover Mechanism for a Cryogenic IR-Sensor*  
R. Birner, G. Lange, M. Roth, and A. Voit  
MBB GmbH, Munich, Germany  
- *A Synchronous Chopper Mechanism for Use at Cryogenic Temperature*  
Claef Hakun, Allen Tyler, and Cornelis de Kramer  
NASA Goddard Space Flight Center, Greenbelt, MD  
- *Cryogenic Mechanisms for Scanning and Interchange of the Fabry-Perot*  
*Interferometers in the ISO Long Wavelength Spectrometer*  
G.R. Davis, I. Furniss, T.J. Patrick, and W.A. Towlson  
University College London, London, and Dorking, Surrey, England  
R.C. Sidey  
Custom Development Ltd., Kew, Surrey, England
- 10:30 COFFEE BREAK
- 10:45 SESSION IV  
Mr. Jerry E. McCullough, Session Chairman  
NASA Johnson Space Center, Houston, TX  
- *Spin Bearing Retainer Design Optimization*  
Edward A. Boesiger  
Lockheed Missiles & Space Co., Sunnyvale, CA  
Mark H. Warner  
Honeywell Corp., Glendale, AZ  
- *Wear Characteristics of Bonded Solid Film Lubricant Under High Load Condition*  
N. Hiraoka, A. Sasaki, N. Kawashima, and T. Honda  
Toshiba Corp., Kawasaki, Japan

- *Development of Solid-Lubricated Ball-Screws for Use in Space*  
M. Chiba, T. Gyougi  
Nissan Motor Co., Ltd., Tokyo, Japan  
M. Nishimura and K. Seki  
National Aerospace Laboratory, Tokyo, Japan

12:15 LUNCH

1:30 SESSION V

- Mr. Robert M. Warden, Session Chairman  
AEC-Able Engineering Co., Goleta, CA
- *TOPEX High-Gain Antenna System Deployment Actuator Mechanism*  
Stephen R. Jones  
Honeywell Inc., Glendale, AZ
- *Resettable Binary Latch Mechanism for Use With Paraffin Linear Motors*  
Daryl Maus and Scott Tibbitts  
Starsys Research Corp., Boulder, CO
- *Harmonic Drive Gear Error: Characterization and Compensation for Precision Pointing and Tracking*  
Ted W. Nye and Robert P. Kraml  
TRW, Redondo Beach, CA
- *Payload Spin Assembly for the Commercial Titan Launch Vehicle*  
Wilf Robinson  
Honeywell, Inc., Glendale, AZ  
Greg Pech  
Martin Marietta Corp., Denver, CO

5:30 EVENING SOCIAL ACTIVITIES

- 5:30 Buses depart from the Hilton Hotel for Lawry's California Center
- 6:30 Social Hour and Entertainment
- 7:30 Dinner
- 10:00 Buses return to the Hilton Hotel

**FRIDAY, 10 MAY 1991**

- 7:30 Friday Authors' Breakfast  
(Executive Dining Room, JPL Cafeteria)
- 8:30 SESSION VI  
Mr. Michael L. Agronin, Session Chairman  
Jet Propulsion Laboratory  
- *SMA Applications in an Innovative Multishot Deployment Mechanism*  
D. Stella, G. Pedrazzoli, and G. Secci  
Contraves Italiana, SpA, Rome, Italy  
C. Portelli  
Agenzia Spaziale Italiana, Rome, Italy  
- *Space Shuttle Holdown Post Blast Shield*  
Francisco B. Larracas  
Lockheed Space Operations Co., Titusville, FL  
- *The Dynamic Torque Calibration Unit: An Instrument for the Characterization of Bearings Used in Gimbal Applications*  
Louise Jandura  
Jet Propulsion Laboratory, Pasadena, CA  
- *A New Active Virtual Pivot Six-Degree-of-Freedom Hand Controller for Aerospace Applications*  
W.C. Marshall, K.M. Radke, R.E. DeMers, D.J. Lowry, and L. Levitan  
Honeywell, Inc., Minneapolis, MN
- 10:30 COFFEE BREAK
- 10:45 JET PROPULSION LABORATORY OVERVIEW  
*Multimedia Presentation*
- 11:15 25TH ANNIVERSARY CEREMONY  
PRESENTATION OF COMMEMORATIVE PLAQUE  
Presenter: Dr. Charles W. Coale, General Chairman  
Lockheed Missiles & Space Co., Sunnyvale, CA
- Accepting for JPL: Dr. Peter Lyman  
Jet Propulsion Laboratory

**PRESENTATION OF THE HERZL AWARD**

**Mr. Nathan D. Watson**

**NASA Langley Research Center (Retired)**

**CLOSING REMARKS**

**Mr. Donald R. Sevilla, Host Chairman**

**Jet Propulsion Laboratory**

**12:00 LUNCH**

**1:15 TOUR OF JET PROPULSION LABORATORY FACILITIES**

**Mr. Anthony Agajanian, Tour Director**

**Jet Propulsion Laboratory**

**(Tour will be from 1:15-3:00 pm)**

# CETA Truck and EVA Restraint System

25th Aerospace Mechanisms Symposium

David C. Beals, NASA Langley Research Center

Wayne R. Merson, Lockheed Engineering & Science Company

## Executive Summary

The Crew Equipment Translation Aid (*CETA*) experiment is an extra-vehicular activity (*EVA*) Space Transportation System (*STS*) based flight experiment which will explore various modes of transporting astronauts and light equipment for Space Station *Freedom* (SSF - Fig. 1). The basic elements of *CETA* are: (1) - Two 25 foot long sections of monorail, which will be *EVA* assembled in the *STS* cargo bay to become a single 50 ft. rail called the "track"; (2) - A wheeled baseplate called the "truck" which rolls along the track and can accept three cart concepts; (3) - The three carts (Figs. 2 and 3) are designated "manual", "electric", and "mechanical". The three carts serve as the astronaut restraint and locomotive interfaces with the track. The manual cart is powered by the astronaut grasping the track's handrail and pulling himself along. The electric cart is operated by an astronaut turning a generator which powers the electric motor and drives the cart. The mechanical cart is driven by a Bendix type transmission and is similar in concept to a man-propelled railroad cart. During launch and landing, the truck is attached to the deployable track by means of *EVA* removable "restraint bolts" and held in position by a system of retractable shims. These shims are positioned on the exterior of the rail for launch and landing (when the truck is bolted down) and rotate out of the way for the duration of the experiment. The shims are held in position by strips of Velcro nap, which rub against the sides of the shim and exert a tailored force. The amount of force required to rotate the shims was a major *EVA* concern, along with operational repeatability and extreme temperature effects. The restraint system has been tested in a thermal-vac and vibration environment and has been shown to meet all of the

initial design requirements. Using design inputs from the astronauts who will perform the EVA, CETA evolved through an iterative design process and represented a cooperative effort between two NASA centers and contractors.

#### CETA Flight Experiment Overview

The CETA concept grew from a SSF requirement for a small and quick transportation system to move astronauts along the length of the SSF 15M cubic erectable trusswork. Additionally, the requirement calls for a system concept that can be operated by a single astronaut, propelled at rates up to normal walking speeds (faster in the event of an emergency), and fitted to carry small hand tools and small replacement parts. The CETA would have the capability to travel in both directions along the length of the truss and to park anywhere along the track. The CETA is required to have an extended lifetime and be easily serviced or replaced on orbit.

A typical use of the CETA could involve a maintenance function for the photovoltaic arrays which are located at the extreme ends of the trusswork. The transporter would be used to carry the larger replacement units, tools and remote power supplies to the work site. However, as is common in any repair job, a tool or part could be left behind at the habitation module. It would be extremely time consuming for the transporter, designed for stability rather than speed, to inch its way back to pick up a tool. The CETA would allow an astronaut to quickly return to the habitation module, pick up the tool, and return to the work site using a minimum amount of valuable EVA time.

Another use of the CETA could be as an emergency return to the habitation module in the event of an injury or space suit malfunction. In this case the CETA would have to be powered by one astronaut and have the capability to carry a disabled crewman.

The CETA flight experiment was conceived to test the basic concept of a CETA system and three candidate carts. In addition, the CETA will gather data on operational loads, attainable velocities and flight temperature using sensors located on the truck.

A design team, with members from NASA's Langley Research Center (*LaRC*), Johnson Space Center (*JSC*), McDonnell Douglas, Lockheed Engineering and Science Co., Rockwell International, ILC Space Systems Corp. and others, was assembled at JSC in June of 1989 to design an experiment which could be built and flown the following summer (June 1990) with the Gamma Ray Observatory (*GRO*) experiment. This mission was chosen because once GRO is deployed the cargo bay will be clear for its entire length, allowing a sufficient run to test the candidate carts. Due to delays in the *Atlantis* STS-37 launch schedule, the GRO and CETA mission is set for April 1991. Astronauts Jerry Ross and Jay Apt, who were both very active in all phases of the CETA development, are the crewmen scheduled to perform the EVA.

The experiment is formed of three basic categories: (1) A track that could be stowed in two sections along the sidewall of the orbiter and assembled on orbit to form a continuous track approximately 50 feet in length, (2) a wheeled platform called the "truck" which would provide a standard interface to the carts and would ride along the track, (3) three concept carts to evaluate the most efficient way for an astronaut to propel a CETA for SSF. LaRC was responsible for the development of the tracks and the truck. McDonnell Douglas and Lockheed were responsible for the development of the manual cart, and JSC developed the mechanical and electrical carts. The ILC Corporation was responsible for the flight support equipment (*FSE*) that adapts the track to the STS.

The three cart concepts are the manual cart, the mechanical cart, the electrical cart (Figs. 2 and 3). The manual cart is powered solely by an astronaut pulling the CETA along the track by a handrail mounted to the track. The manual cart has a handbrake and parking brake integrated into the cart. The mechanical cart is similar to a man-powered railway cart. The astronaut will pump a handle which is connected to a Bendix type transmission. In order to stop the cart the handle is pushed past a certain set limit, which engages a brake internal to the transmission. The electric cart uses a hand cranked generator to supply electric current to a motor located at the base of the cart which propels the cart. Braking is accomplished by turning the generator backwards to develop back-EMF in the motor. The three carts will be interchangeable on the truck, which serves as the common interface.

The truck (Fig. 4) consists of five main sub-assemblies.

(1) Baseplate - a 20 inch square mounting surface and the main structural frame;

(2) Latches - mounted to the baseplate and secure the carts to the truck;

(3) Wheel Clusters - capture the rail and provide a rolling interface to the track. The wheel clusters are EVA removable, in the event of a jam or need to jettison the cart;

(4) Restraint System - secures the truck to the track for launch and landing;

(5) Arrestors - emergency stopping devices that impact a pair of aluminum honeycomb columns in the event of a brake failure during the experiment.

### Truck Restraint System

The truck is restrained to the deployable track for launch and landing by means of the launch restraint system (Fig. 5) and consists of four main sub-assemblies;

(1.) Restraint Bracket

(2.) Restraint Bolt

(3.) Compression Spring

(4.) Shim

Adequate storage space is not available along the sidewall of the cargo bay to stow all three carts and the truck. Therefore it is required upon launch and landing that the truck, with the manual cart attached, be secured to the deployable track. An additional requirement is that during the experiment, the track surface must be free of protrusions to avoid the possibility of a crewmember being caught. This brought forward the concept of the truck restraint system which consists of track mounted retractable shims and EVA compatible restraint bolts which are captured in the truck. The shims hold the wheels away from the surface of the track so that launch and landing vibration will not overstress and damage the wheels. The restraint bolts screw into locking inserts in the track bulkheads, which secure the truck to the track. For the experiment, the restraint bolts are loosened (and held captured in the truck), the truck is moved away from the shims, and the shims are rotated into pockets within the track leaving the top surface of the track free from protrusions.

The shims are held in the pockets by strips of the nap side of Velcro tape. The truck is reinstalled on the shims for landing.

The truck launch restraint system posed a number of unique challenges for EVA design. The first was the development of the four (4) launch restraint bolts and brackets which are an integral part of the truck. The restraint bolts had to be retracted and captured during truck usage, meet EVA requirements, and be strong enough to restrain the truck (with the manual cart attached) during STS launch and landing. The four restraint bolts were designed to satisfy the 15g limit load factor that acts independently in three axis when the truck is restrained on the track during launch. The installation torque requirement of 25 ft-lbs came from astronaut inputs concerning the amount of torque they could exert on a bolt in the weightless environment. The restraint bolts have a 7/16 hex head, and the truck has 1.00 inch diameter tool clearance holes to satisfy EVA tool requirements.

A redundant method of retracting the restraint bolt has been incorporated in the restraint bolt design. A manual retract hole is located in the head of the restraint bolt with a hole drilled transversely through the head. The astronaut inserts a pip Pin in the hole and rotates it so that the handle aligns with the line on the head of the restraint bolt, locating the pip pin ball detents into the transverse hole. With the detents extended into the holes the astronaut can now pull up on the restraint bolt and allow the spring to secure it in the retracted position.

The bolts are captured by the restraint bracket and the truck as shown in Fig. 6. During truck usage, the compression spring forces the bolt up into the restraint bracket while the bottom surface of the truck acts as a stop. The spring was designed to exert enough force on the bolt to hold it in the retracted position during the experiment; yet without exerting so much force that the crewmember would have difficulty engaging the bolt for landing restraint. The spring design also has built in redundancy. If the spring were to break in the middle, either half would still have enough spring force to secure the bolt in the retracted position.

Another challenge for the shim design was the requirement that the top surface of the track remain free from protrusions during the experiment so that the astronaut could not inadvertently catch a gloved hand on anything. This required a shim that had to be removed from the surface of the track. The original concept was to have the

removable shims placed on the track during launch and landing and during the experiment they would be removed and either stowed away or tethered nearby. This proved to be unacceptable because to tether the shims would introduce a safety problem. Stowing a removable shim would require space and time, both of which are in limited supply. A pivoting shim concept was therefore designed to be an integral part of the track itself. The shims rest on the surface of the track (Fig. 6) during launch and landing and rotate on a fixed pin into the track during the experiment.

When retracted, the shims must be held firmly in place so that they will not rotate out of position, yet the rotating force must be low enough so that an astronaut can easily manipulate the shim. The solution was to line the shim housing with the nap portion of Velcro strip. The advantage of this solution lies in its reliability and simplicity, and it works over a wide range of temperatures. During launch and landing, the shims are secured to the track by means of the truck and restraint bolts. During operation, it is necessary to ensure that the shims stay down below the track surface otherwise the truck would run into them. The Velcro acts as a brush that presses against the shim and thus holds it in place (Fig. 7). Testing determined the amount of Velcro needed to apply a particular force at a particular temperature. The astronauts rotated the shims and determined that a 12-15 lb force was optimum. For the projected flight environment low temperature of -80 degrees Fahrenheit, the corresponding surface area of Velcro required was installed in the track.

As the truck rolls along the track, it has the ability to "touch and go" at any wheel surface due to a 0.25 inch gap between the track and the horizontal wheels and a 0.125 inch gap between the track and the vertical wheels (Fig. 4). This tolerance, along with visual interference from the truck, make aligning the four bolt holes very difficult. The shims were therefore also designed to serve as an alignment ramp and stop for restowing the truck (Fig. 5), with the shims positioned on the track surface the astronaut simply pushes the truck until it slides up on the shims and is self-aligned. When the truck hits the stops at the ends of the shims, it is in position to secure the restraint bolts.

There exists a possibility of the shims bouncing off the track surface due to vibration while the astronaut pushes the truck into position for restraint. Once again, Velcro was used to eliminate this situation. A strip of Velcro nap (loop portion) was bonded to the track surface with a space grade epoxy and a strip of Velcro (hook portion)

was bonded to a pocket in the shim (Fig. 7). The amount of Velcro used was a function of the force desired and the experiment's operational temperature.

#### LESSONS LEARNED

The Velcro method of retaining the shims in position was developed after the failure of a previous method. The original design incorporated the use of spring loaded ball detents located in the shims. Grooves were machined into the walls of the shim housings to retain the ball detents as the shim rotated into position. The force required to dislodge the shim from the grooves was easily controlled through the selection of ball detents with a specific spring force.

A problem in that design developed as the shims were repeatedly rotated back and forth between stowed position and launch/landing position. The harder stainless steel ball detents began to wear the softer anodized aluminum housing walls. Small pieces of aluminum became wedged in between the ball and the ball casing. The obstruction of aluminum became lodged between the casing and the ball bearing due to the inherent "self locking taper" in the design of the ball detent assembly. The shims therefore became stuck in either the stowed position or launch/landing position.

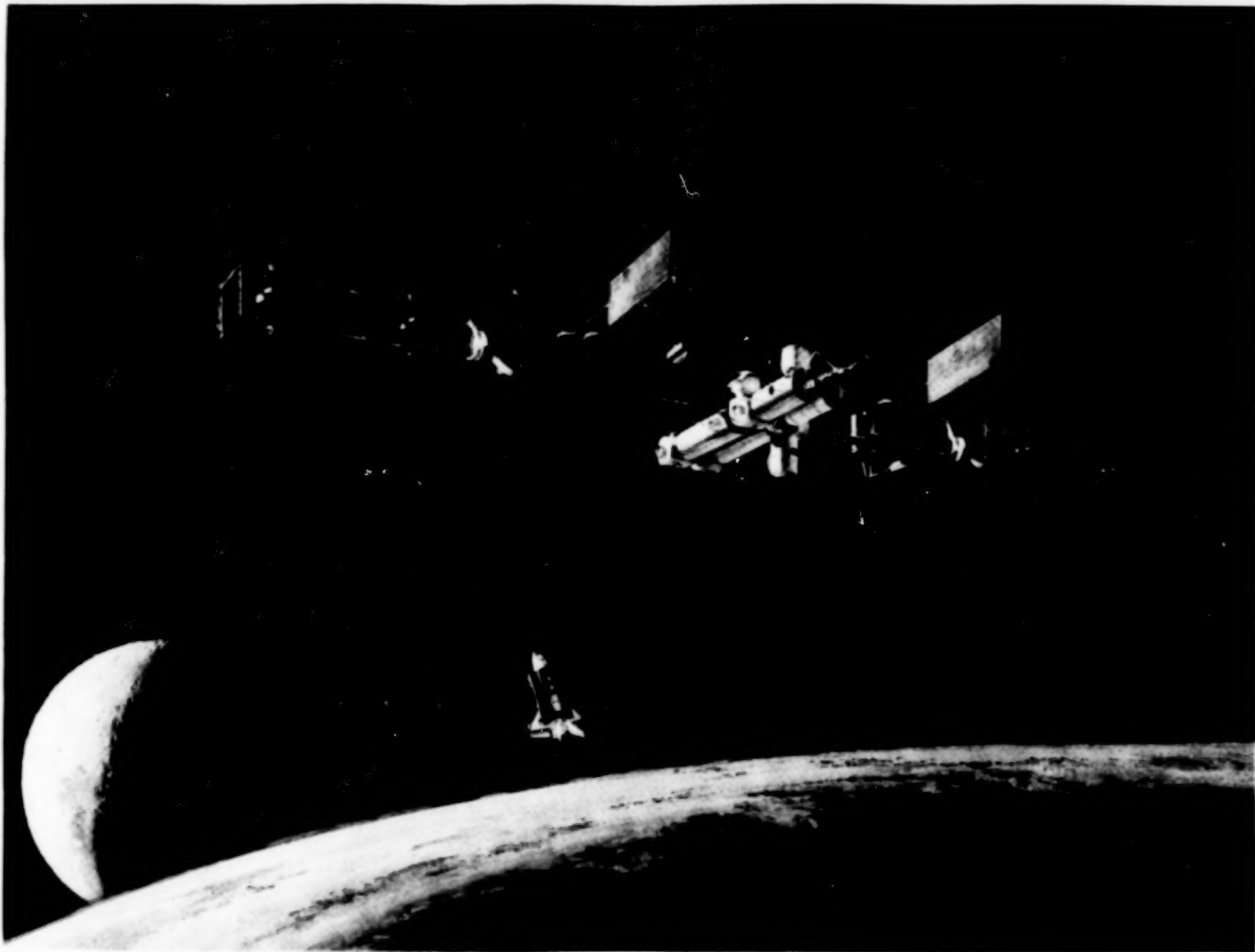
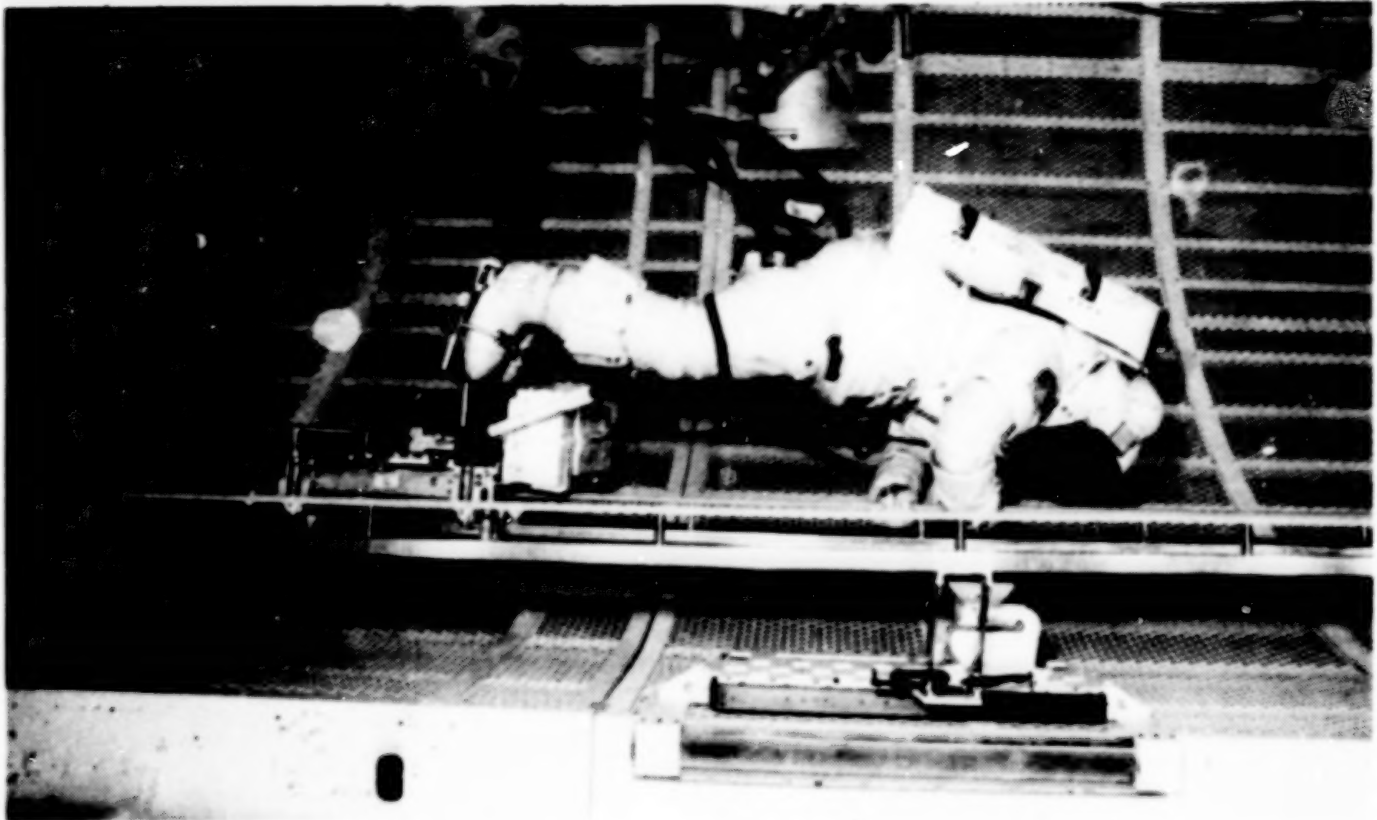
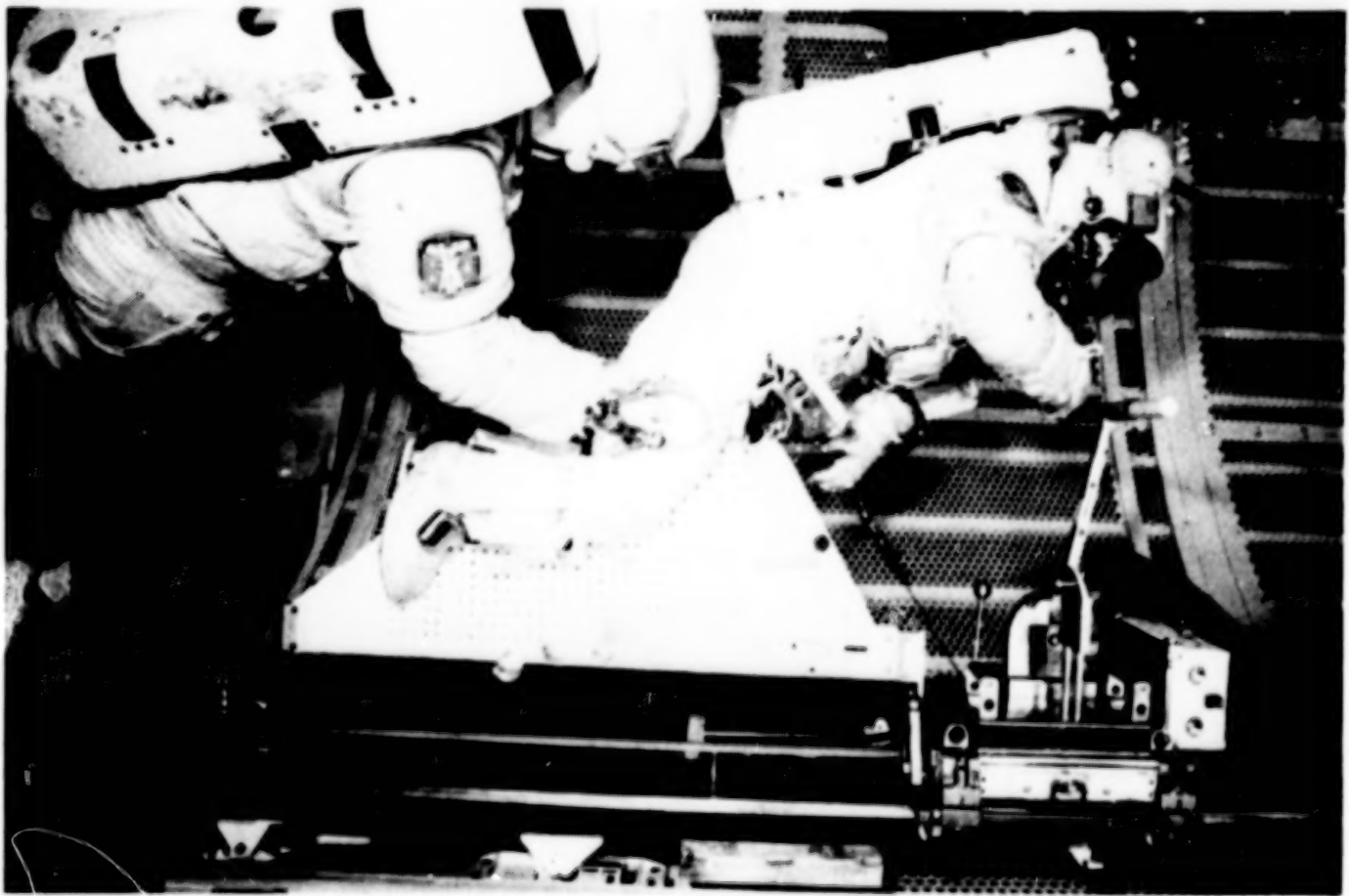


Fig. 1 Space Station Freedom

8

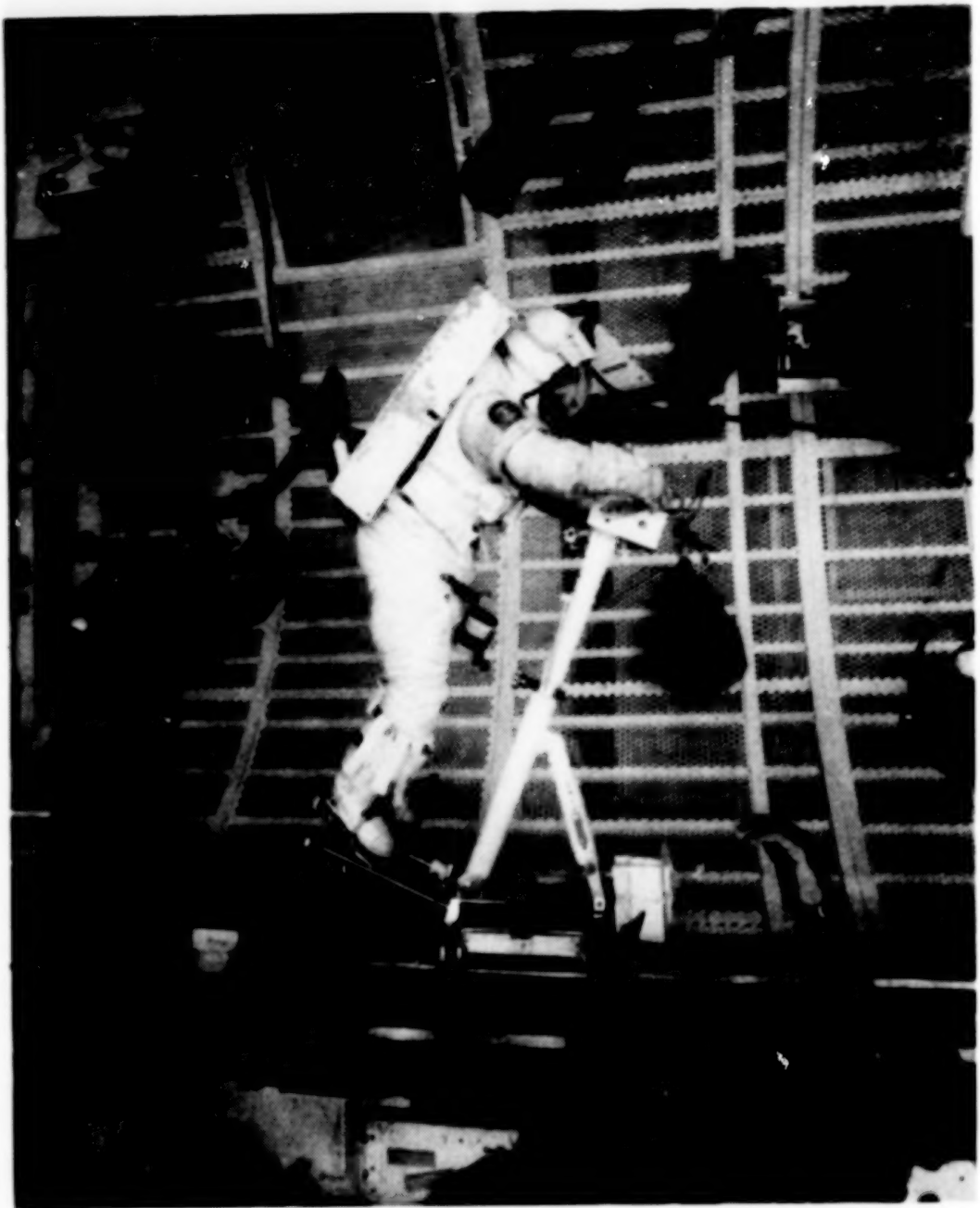


Manual Cart Mock-up in WETF Testing at JSC



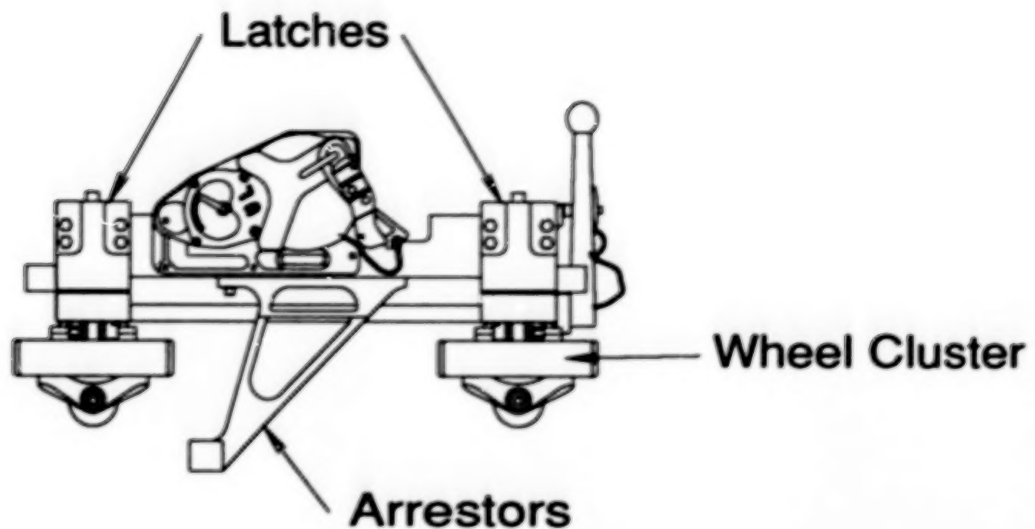
Mechanical Cart Mock-up in WETF Testing at JSC

Fig. 2



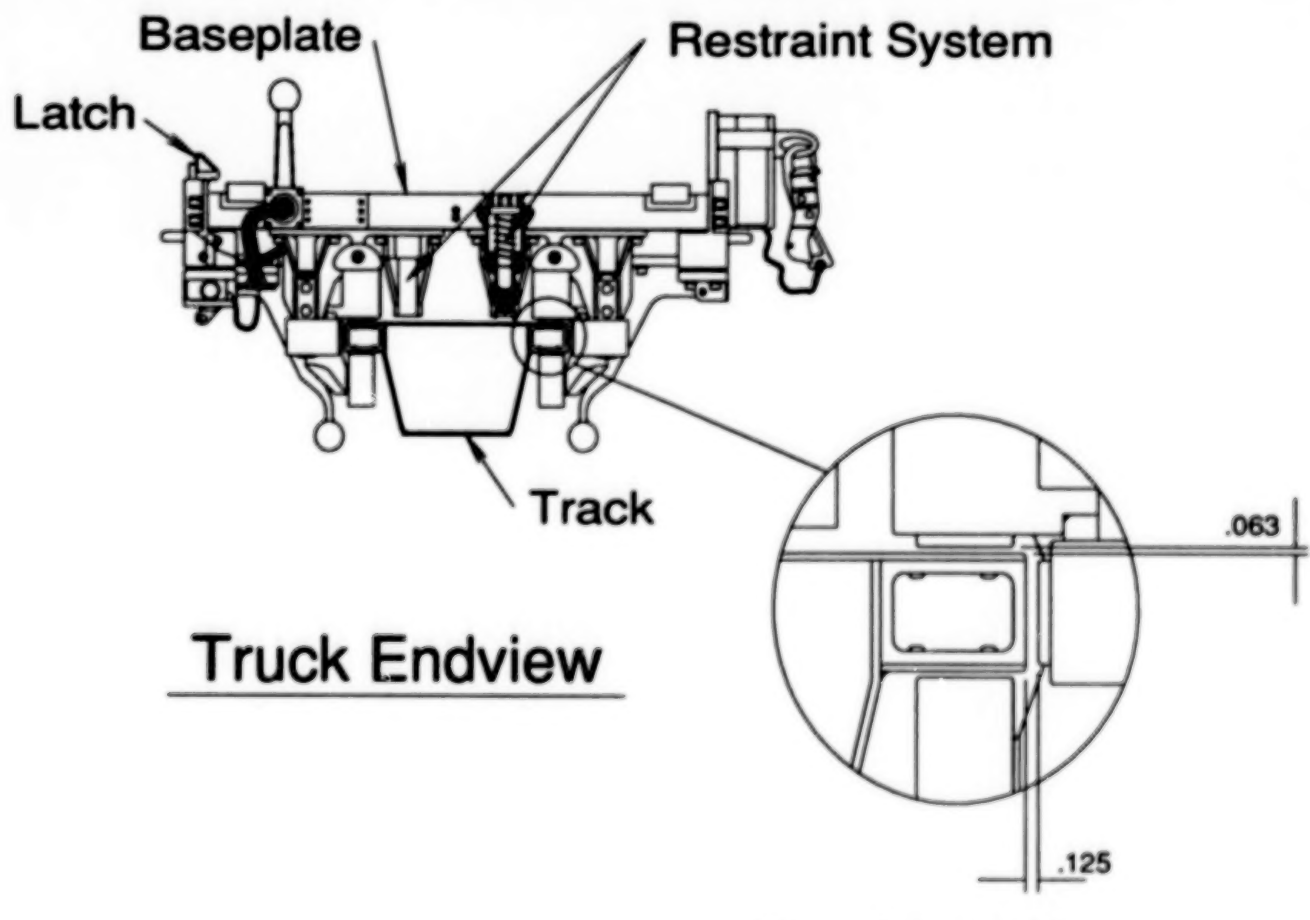
Electric Cart Mock up in WETF Testing at JSC

Fig. 3



## Truck Sideview

---



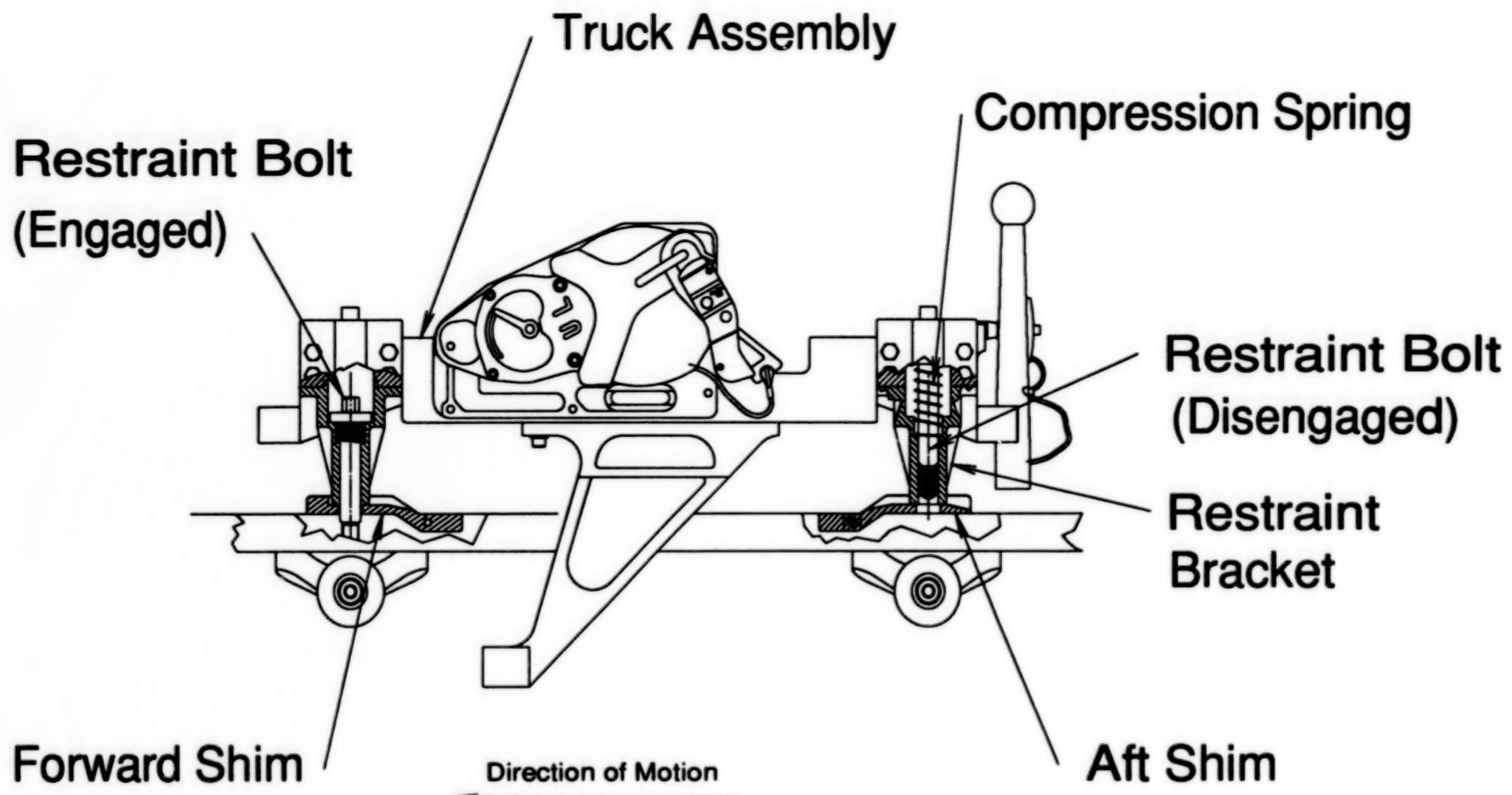
## Truck Endview

### Wheel/Track Gap

Fig. 4

**BLANK**

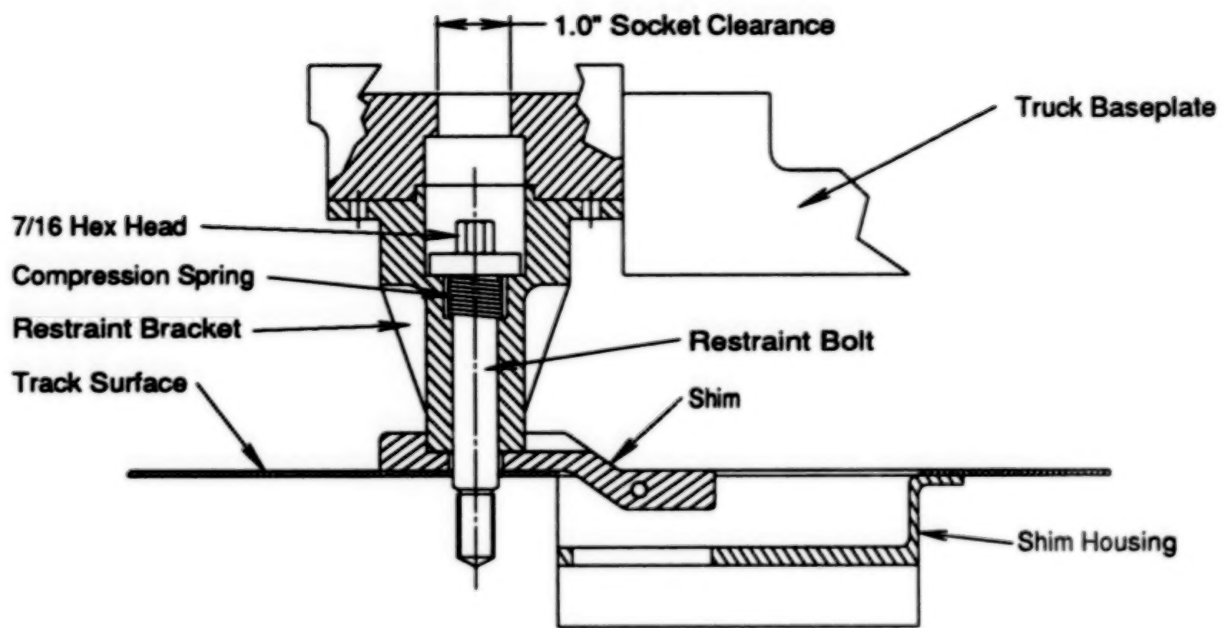
**PAGE**



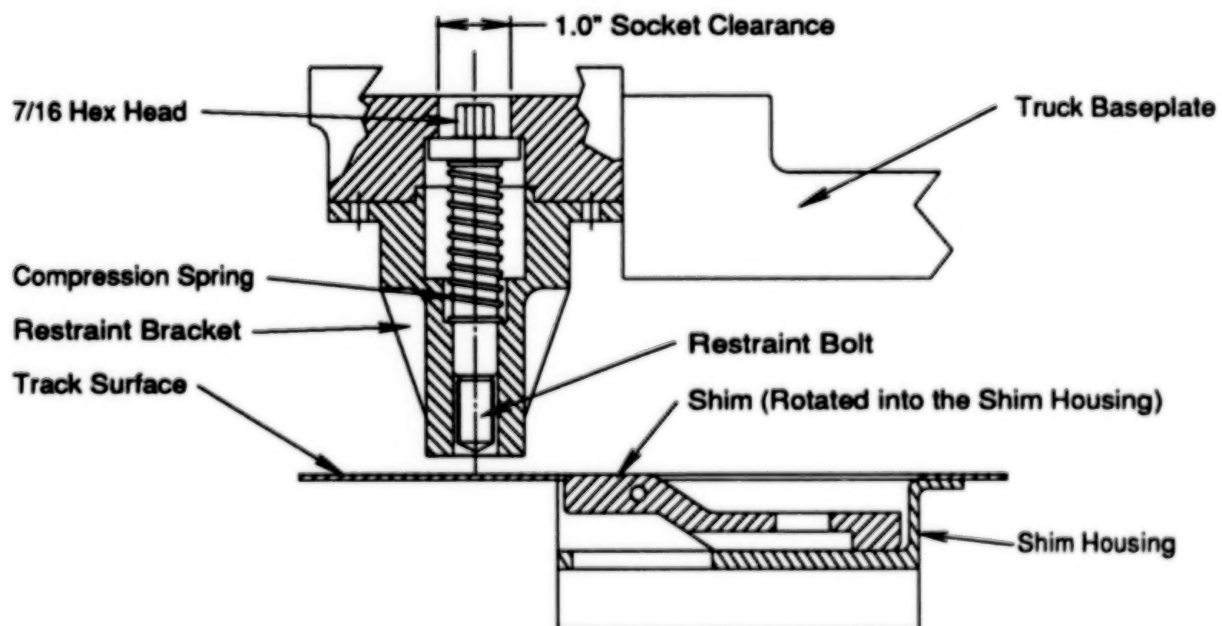
Truck In Launch/Landing Configuration

Fig. 5

12



Truck Forward End  
Restraint Engaged



Truck Forward End  
Restraint Disengaged with the Shim stowed.

Fig. 6

**BLANK**

**PAGE**

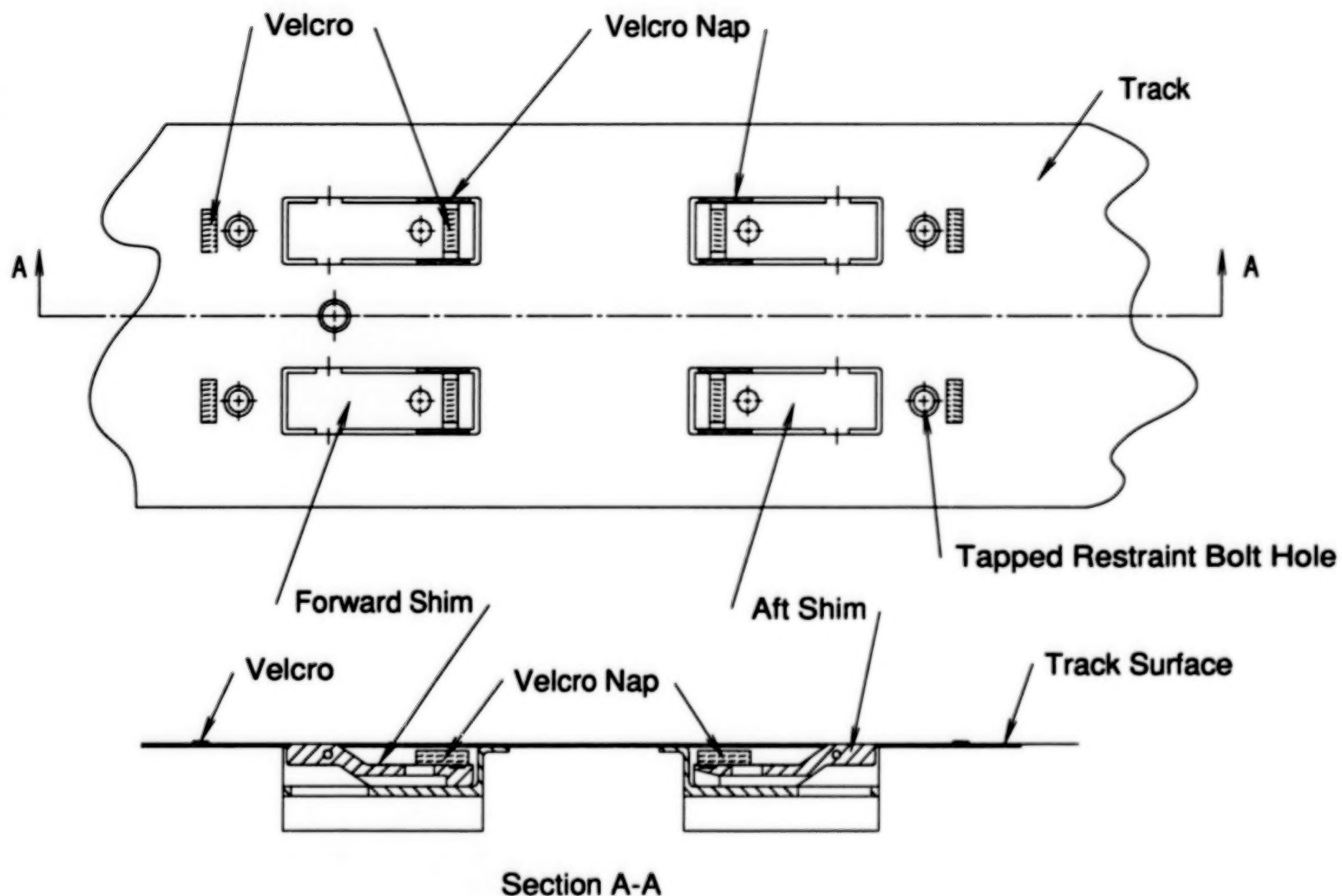


Fig. 7

**SYSTEM REQUIREMENTS AND DESIGN FEATURES OF  
SPACE STATION REMOTE MANIPULATOR SYSTEM MECHANISMS**

By

Rajnish Kumar  
and  
Robert Hayes

Advanced Technology Systems Group  
Spar Aerospace Limited, Toronto, Canada

**ABSTRACT**

The Space Station Remote Manipulator System (SSRMS) is a long robotic arm for handling large objects/payloads on the International Space Station "Freedom." The mechanical components of the SSRMS include seven joints, two latching end effectors (LEEs) and two boom assemblies. The joints and LEEs are complex aerospace mechanisms. This paper presents the system requirements and design features of these mechanisms.

All seven joints of the SSRMS have identical functional performance. The two LEEs are identical. This feature allows either end of the SSRMS to be used as tip or base. As compared to the end effector of the Shuttle Remote Manipulator System, the LEE has a latch and umbilical mechanism in addition to the snare and rigidize mechanisms. The latches increase the interface preload and allow large payloads (up to 116,000 Kg) to be handled. The umbilical connectors provide power, data and video signal transfer capability to/from the SSRMS.

**INTRODUCTION**

The Space Station Program "Freedom" is a joint venture of the United States, Canada, Japan and the European Space Agency. Canada's contribution to this Program is to provide the Mobile Servicing System (MSS). The Space Station Remote Manipulator System is a key system of the MSS (Ref. 1). Spar Aerospace Limited is the prime contractor for the development of the MSS for the Canadian Space Agency.

The SSRMS is a 17.6 m (57.3 ft.) long robotic arm to be used for handling large objects on the Space Station. It consists of seven joints, two latching end effectors (LEEs), two boom assemblies, two arm computer units (ACUs), video cameras and associated equipment. The physical configuration of the SSRMS is

shown in Figure 1. Each boom assembly has a hinge mechanism for compact stowage of the SSRMS during launch. These hinges are locked in the straight position of the boom assemblies for operation on the Space Station. The joints and the LEEs are complex aerospace mechanisms. The seven joints, each representing a rotational degree of freedom, provide maneuvering and positioning capabilities to the arm. The LEE at the base provides structural and electrical (power, data and video) connections to the Space Station. The tip LEE is used for payload capture and release. The design of the base and the tip LEEs are identical. This provides operational flexibility using either end as the tip or base. Also, the SSRMS can relocate itself on the Space Station.

This paper presents the system requirements and design features of the SSRMS joints and LEE mechanisms. Several trade studies were carried out prior to establishing the requirements and design concepts. Many breadboard tests were conducted to demonstrate the functionality of the mechanisms. The results of such studies and tests have been utilized for the design of the LEEs and the joints. The data and the experience gathered over a decade of the Shuttle Remote Manipulator System (SRMS) operation and during testing and refurbishing of its components have been of great significance in conceiving enhanced features for the SSRMS mechanisms.

The design data and numerical values presented in this paper represent the current state of the development and should be considered preliminary at this stage as the detail design work is in process.

#### SYSTEM REQUIREMENTS

A summary of the SSRMS system requirements considered for the design of the joints and LEEs are as follows:

- o The SSRMS is required to operate in the extravehicular environment of the Space Station. As shown in Figure 2, the Mobile Remote Servicer Base System (Ref.3) is the base for SSRMS operations. However, the SSRMS can also operate in a stand-alone configuration from a Power and Data Grapple Fixture (PDGF) located on the Space Station. Figure 3 shows a physical configuration of the PDGF. The joints and LEE mechanisms assist in performing the following tasks of the SSRMS:
  - (a) Space Station construction, assembly and maintenance
  - (b) Payload handling and servicing ( The design case payloads are defined in Table 1)
  - (c) Capture and handling of free flyers ( Figure 4 shows the use of the LEE for holding the Shuttle Orbiter)
  - (d) Support to extravehicular activities and Space Station safe haven.

**Table 1: SSRMS Payloads, Maximum Tip Velocity and Stopping Distance Requirements**

Payload Size			Translational & Rotational Velocity		Translational and rotational stopping distance	
Mass	Length	Diameter	m/sec.	deg./sec	m	Deg.
Kg.	m	m				
0 (Unloaded Arm)	-	-	0.37	4.0	0.61	3.0
20900	4.5	17.0	0.022	0.24	0.61	3.8
116000	24.1	34.3	0.012	0.04	1.09	5.7

- o The tip end effector has to be compatible with the SRMS-type Grapple Fixtures defined in Reference 2.
- o The capture operation of the SSRMS shall accommodate the following misalignment of the grapple probe:
  - Linear misalignment = 0 to 0.1 m axial direction,  
 ± 0.1 m radial direction
  - Angular misalignment = ± 10 Deg. roll,  
 ± 15 Deg pitch and yaw
- o The specified performance in terms of the tip velocity and worst case stopping distances with respect to the base of the SSRMS are given in Table 1.
- o The SSRMS is required to transfer electrical power, data and video resources to and from the attached payload. The required power transfer capability is 1800 watts average and 2500 watts peak. The data transfer requires two 1553B data buses. The video capability requires transfer of up to three simultaneous composite NTSC video channels.
- o Thermal Requirements
 

Thermal control is to be independent of other MSS and Space Station items. The specified temperature limits for the components of the SSRMS are given in Table 2.
- o Structural Requirements
  - (a) Yield safety factor = 1.1 (minimum value)
  - (b) Ultimate safety factor = 1.5 (minimum value)
  - (c) Scatter factor for fatigue = 4
  - (d) Stiffness and Strength are to be maximized within the constraint of the mass.

Table 2: Component Temperature Limits (Deg., C)

Component	Operational		Acceptance		Qualification		Survival	
	Max.	Min.	Max.	Min.	Max.	Min.	Max.	Min.
Gears, Bearings	135	-25	140	-30	151	-41	155	-50
Motor Windings	180	-25	185	-30	196	-41	200	-50
Brakes	99	-25	104	-30	115	-41	120	-50
Cables & Connectors	135	-70	140	-75	151	-86	155	-90
Electronics	65	-20	70	-25	81	-36	85	-50

o Reliability and Failure Tolerance Requirements

- (a) Single failure tolerant design
- (b) Automatic safing following any failure

o System Lifetime

The SSRMS is required to operate on orbit for 30 years with periodic maintenance and refurbishment.

#### JOINT MECHANISM DESIGN

The physical configuration of the SSRMS joints is given in Figure 5. A block diagram representing the joint components and their interfaces is given in Figure 7. Each joint has two major assemblies, viz. joint drive module (JDM) and the housing assembly, as shown in Figure 6.

The JDM constitutes the mechanism part of the joint. The JDM is housed in the housing assembly. The joint electronic units mounted on the joint housing control the operation of the joint. All the seven joints have the identical JDM. The three pitch joints (shoulder pitch, elbow pitch and wrist pitch joints) have identical housing assemblies. The remaining four joints (two roll and two yaw joints) also have identical housing assemblies. The housing assembly for the pitch joints differs slightly from the housing assembly of the roll/yaw joints.

The main components for the JDM are as follows:

- (a) Two identical Joint Motor Modules (JMM1 and JMM2)
- (b) G1/G2 Gear Box
- (c) Joint Angle Resolver (JAR) Assembly
- (d) Extra Vehicular Activity (EVA) Drive

A brief design description of the JDM components is as follows:

#### Joint Motor Module (JMM)

Each JMM consists of:

- (i) Brushless permanent magnet DC motor
- (ii) Motor Resolver for motor rate sensing and commutation
- (iii) Redundantly wound electromechanical brake.

Each JMM is capable of driving, stopping and holding the joint in the desired position. Only one JMM is operational at any time. Normally the backdriving torque of the motor is used for stopping the joint. The brakes are used under emergency conditions (e.g., joint runaway). The brakes of both the JMMs engage and disengage simultaneously. Also the brakes engage automatically when the power to the joint is turned off or lost due to a power failure.

#### G1/G2 Gear Box

The G1/G2 Gear Box is a two-stage speed reducer. The overall speed reduction achieved is 1845:1 from the motor shaft to the joint output. The design of the gear box is based on the proven design of the SRMS joints.

#### JAR Assembly

The JAR assembly consists of two identical JARs (JAR1 and JAR2) mounted on a common shaft. The function of the JAR is to measure angular position of the joint. This measurement is used for close loop control of the joint and establishing the SSRMS tip position.

#### EVA Drive

An EVA drive has been provided for manual operation of the joints. This drive bypasses the JMMs and the joint can be driven in case of a jammed JMM.

#### Joint Thermal Protection and Thermal Control

Passive means supplemented by film heaters have been used for thermal protection of the joints. The hardware for thermal protection consists of the following items:

- (i) Multilayer insulation (MLI) blankets
- (ii) White paint for radiator surfaces
- (iii) Film heaters
- (iv) Thermistors for temperature sensing and electronic thermostats for heater control.

#### Joint Performance Data

Each of the SSRMS joints has the following performance

##### (a) Joint Travel Range:

- (i) With software stops =  $\pm 270$  deg.
- (ii) position of hard stops =  $\pm 281$  deg.

(b) Joint Output Torque

- |  |                      |
|--|----------------------|
| (i) Servo controlled torque                                | = 1044 N-m (Minimum) |
| (ii) Brake torque of both JMMs                             | = 1630 N-m (Minimum) |
| (Brakes of both JMMs engage &<br>Disengage simultaneously) |                      |
| (c) Maximum joint angular velocity                         | = 5.0 deg./sec       |

LEE MECHANISM DESIGN

Figure 9 illustrates the configuration of the LEE. A block diagram representing the LEE components and interfaces is shown in Figure 8. The LEE consists of the following mechanisms:

- (a) Snare mechanism
- (b) Rigidize mechanism
- (c) Latch and Umbilical mechanism
- (d) EVA drive
- (e) Force moment sensor (FMS).

All these mechanisms are housed in a shell structure which also supports two LEE electronic units (LEU1 and LEU2) and a video camera. The FMS is to be used for measuring and limiting the force at the SSRMS tip. The concept and the requirements of FMS are under investigation. A brief description of the other mechanisms is as follows:

**Snare and Rigidize Mechanisms**

The concept and the functions of these mechanisms are similar to SRMS snare and rigidize mechanism. As illustrated in Figure 8, the snare and rigidize mechanisms are driven by independent motor modules, i.e., MS1 and MR1 or MS2 and MR2.

**Latch and Umbilical Mechanism**

This mechanism provides a stiff structural link and electrical connection at the end of the SSRMS. Figure 10 illustrates the concept of a latch with an umbilical connector in its center. There are four such latches mounted externally to the LEE shell. These latches are driven by an internally mounted motor module (ML1 or ML2). The operation of this mechanism is carried out in two stages. In the first stage, only the latches are connected to the PDGF. The second stage operation consists of mating the electrical connectors with the PDGF. The latching operation can be performed only after completion of the snare and rigidize operations.

A payload can be captured by using any one of the following combinations of the LEE operations:

- (i) snare and rigidize
- (ii) snare, rigidize and latch
- (iii) snare, rigidize, latch and mate electrical connectors.

## EVA Drive for Latch Mechanism

The LEE design includes an EVA drive for EVA operation of the Latch and Umbilical mechanism.

## Thermal Protection and Thermal Control Provisions

The passive/semipassive means are provided for the thermal protection of the LEE. The hardware used for thermal protection is similar to the joint thermal hardware. The operation of the heaters is controlled by one of the two LEUs.

## LEE Performance Data

- (a) The LEE snare and rigidize mechanisms are similar to the SRMS snare and rigidize mechanism. These mechanisms meet the specified requirements for misalignment.
- (b) The normal time for completion of the snare, rigidize, latch and umbilical mate operations is as follows:

Snare	= 3 sec.
Rigidize	= 25 sec.
Latch	= 60 sec.
Mate	= 60 sec.

A fast capture mode has also been provided in which the snare, rigidize and latch operations are completed within 30 sec. This fast mode is useful for the capture of free flyers.

- (c) The load transfer capability of the LEE is as follows:

- (i) 950 N-m Torque and 1220 N-m Bending Moment when snared and rigidized, allowing 3 deg. separation at the interface.
- (ii) 3120 N-m Moment about any axis and 1110 N axial/shear force when snared, rigidized and latched and no separation at the interface.

## SUMMARY OF KEY DESIGN FEATURES OF JOINT & LEE MECHANISMS

- o After snaring and rigidization of the LEE, the engagement of latches provides a stiff structural interface for the payloads. This makes the SSRMS capable of handling high inertia payloads, as given in Table 1.
- o The umbilical connectors provide the power, data and video links between the payload and the Space Station.
- o The LEE snare and rigidize mechanisms are similar to the SRMS End Effector design. This permits the use of SSRMS to capture and maneuver payloads fitted with SRMS-type grapple fixtures.
- o EVA drives for joints and LEE latch mechanisms have been provided for emergency EVA operation of the SSRMS.
- o The Joint Drive Module (JDM) is a commonality item for all the seven joints and it is on-orbit replaceable. The joints and LEE are also on-orbit replaceable.

## ACKNOWLEDGEMENT

The authors are thankful to the Canadian Space Agency and Spar Aerospace Limited for permitting the presentation and publication of this paper.

## REFERENCES

1. D.A. Bassett et al., "Mobile Servicing System Flight Operations and Support", Presented at 39th International Aeronautical Congress of the IAF, Bangalore, India, October 8-15, 1988.
2. NSTS 07700, Vol. xiv, Appendix 8, "System Description and Design Data for Payload Deployment and Retrieval System", Rev. J, 1988.
3. Kumar, R. et al., "Concept and Design Considerations for Mobile Servicer Base System of MSS for the Space Station" CASI Symposium on Space Station, Ottawa, Canada, November 1989.

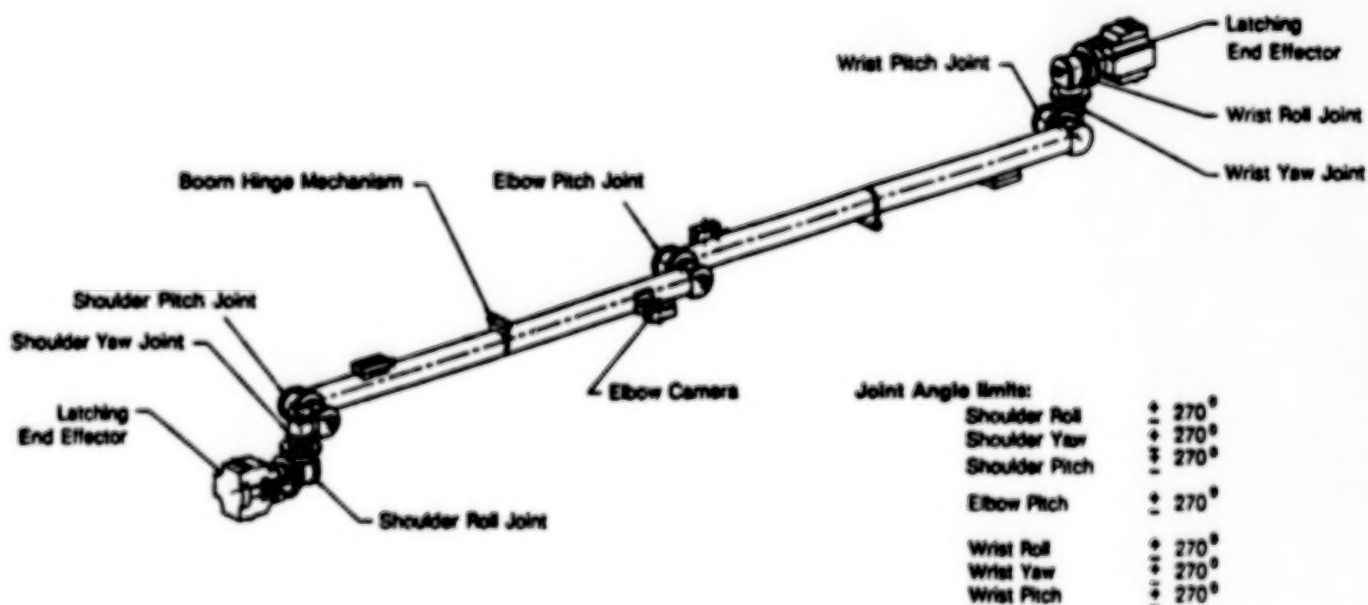
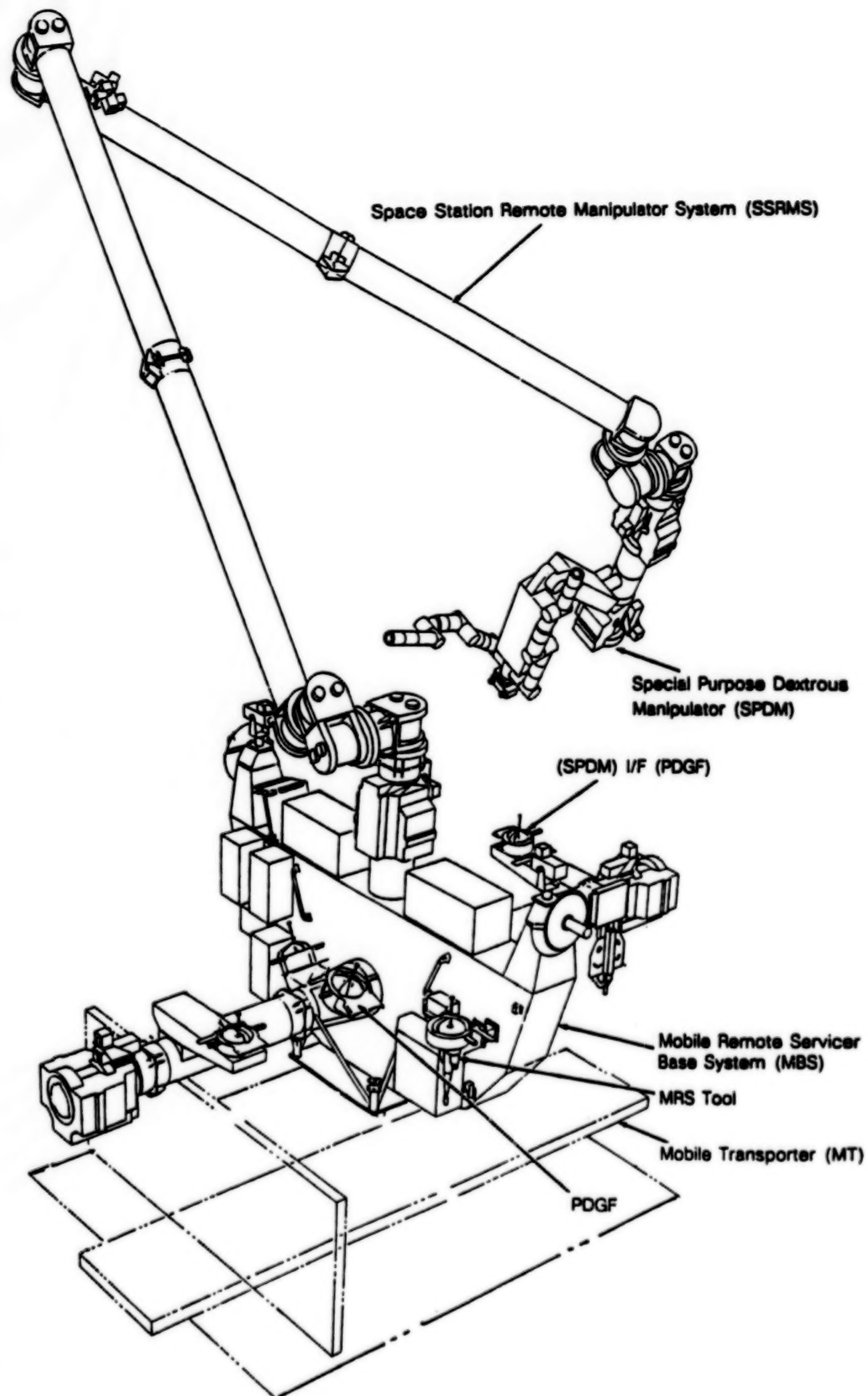


FIGURE 1: PHYSICAL CONFIGURATION OF THE SPACE STATION REMOTE MANIPULATOR SYSTEM (SSRMS)



**FIGURE 2: SSRMS OPERATION ON THE SPACE STATION FROM THE MOBILE REMOTE SERVICER BASE SYSTEM**

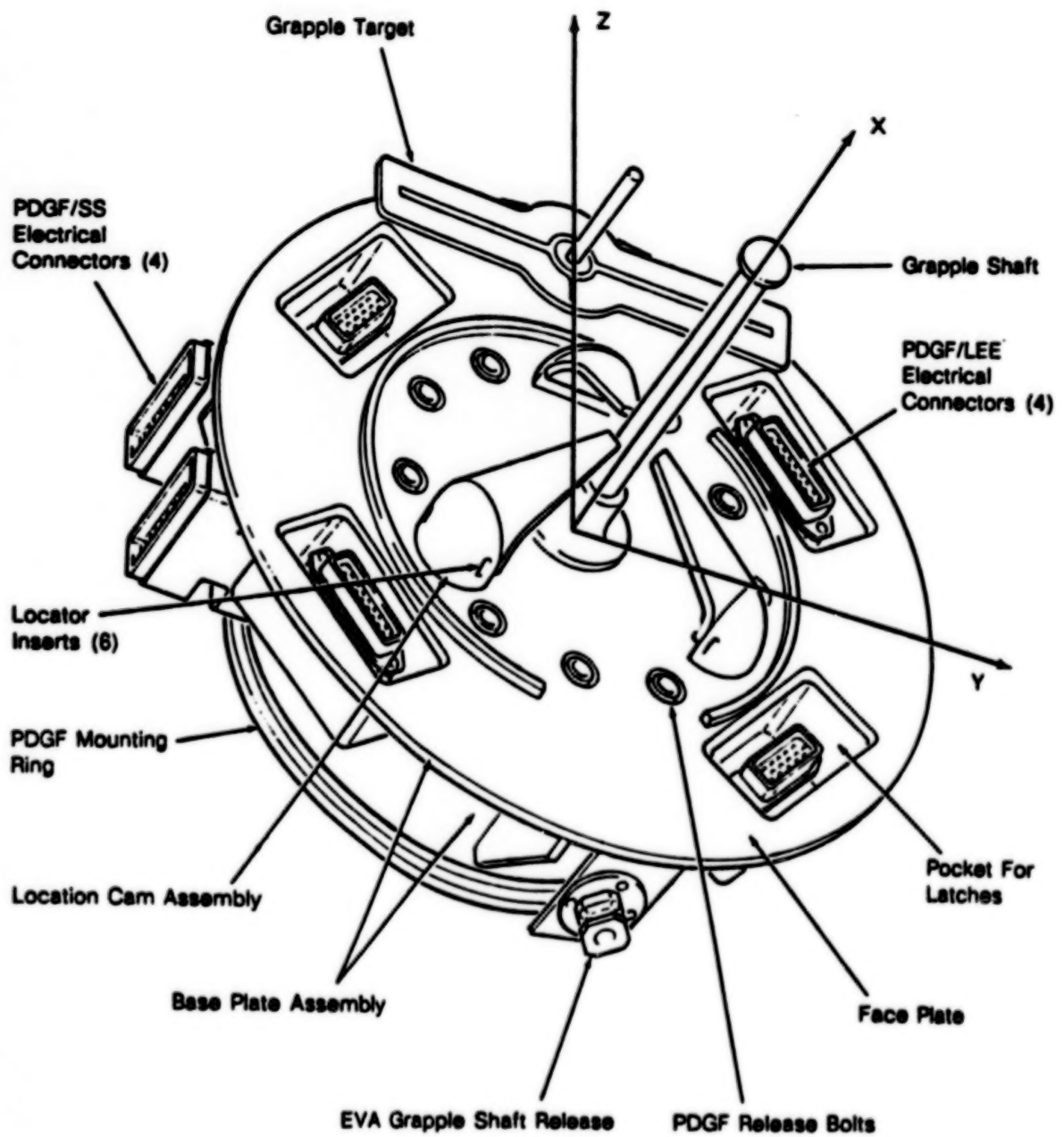


FIGURE 3: CONCEPT OF POWER AND DATA GRAPPLE FIXTURE (PDGF)

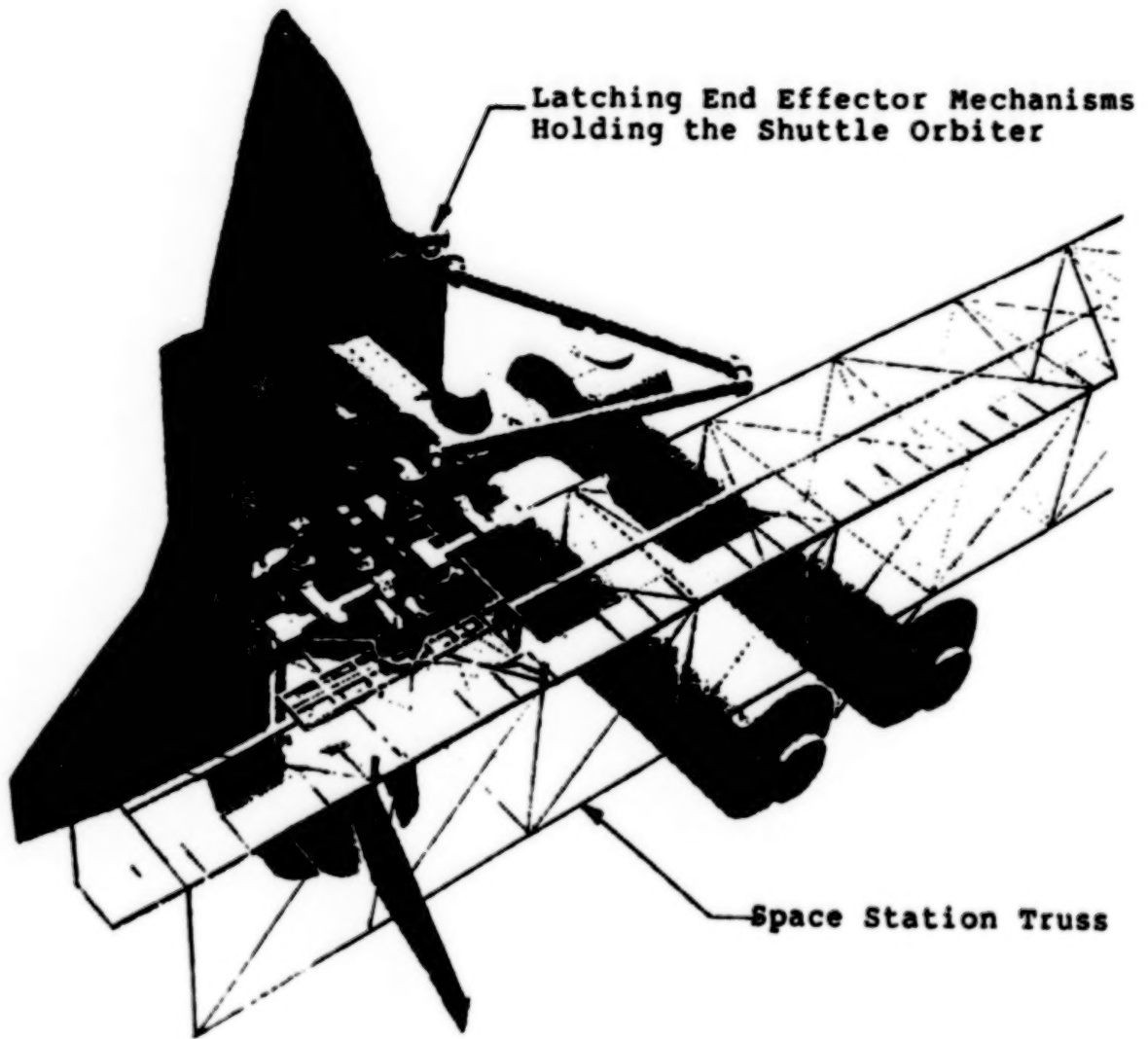


FIGURE 4: USE OF THE LEE FOR HOLDING THE SHUTTLE ORBITER

**BLANK**

**PAGE**

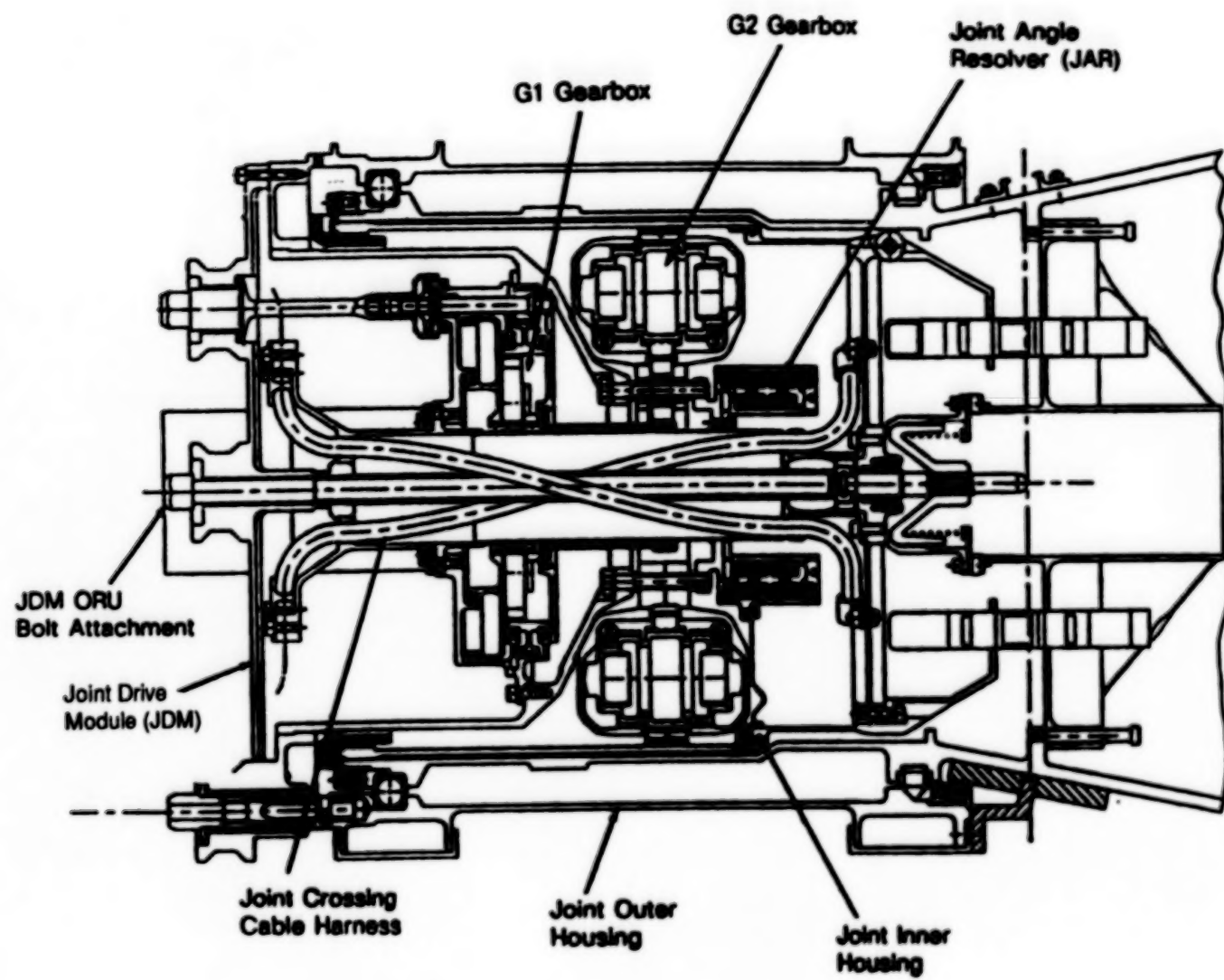


FIGURE 5: Joint Cross Section

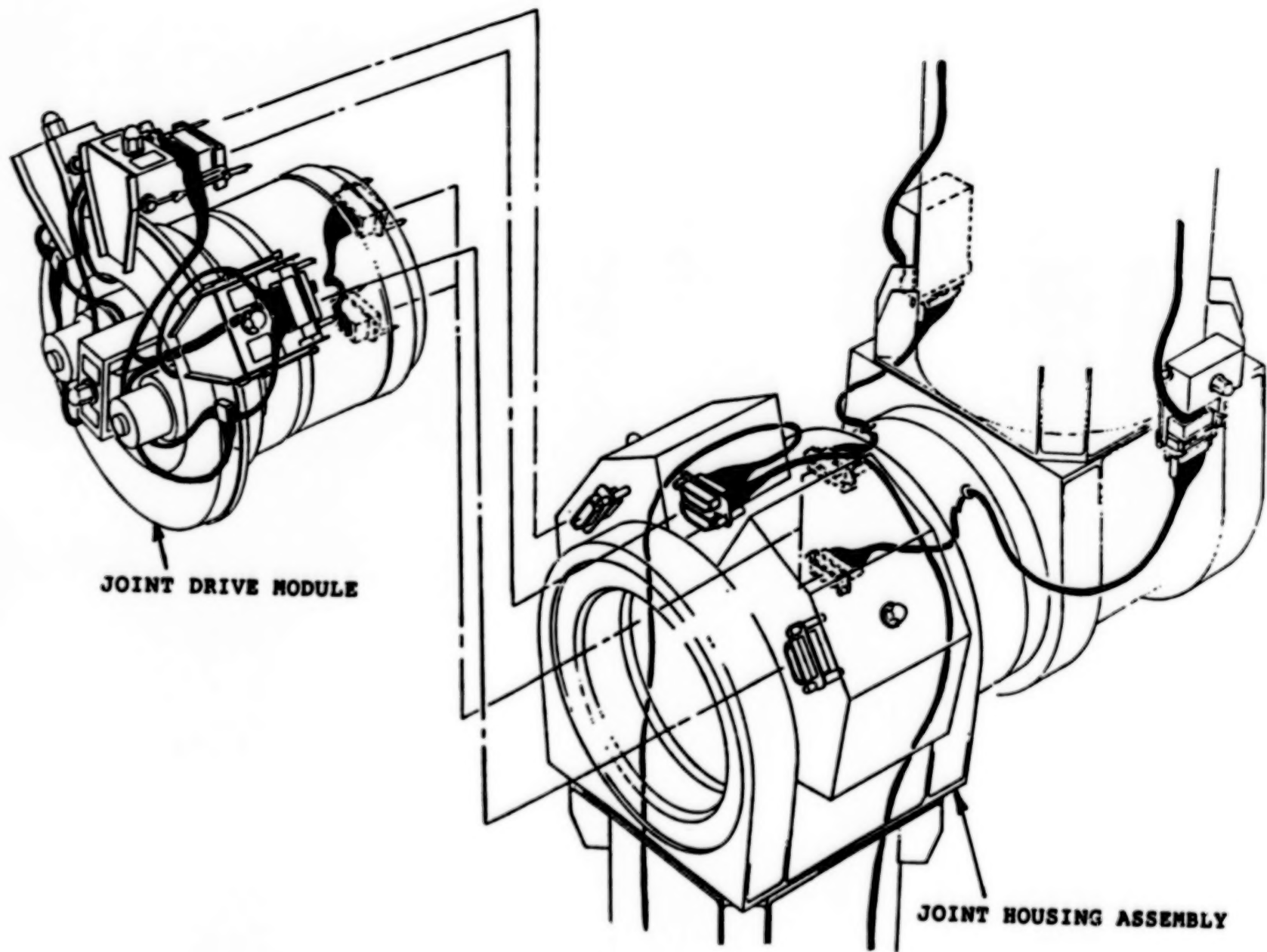
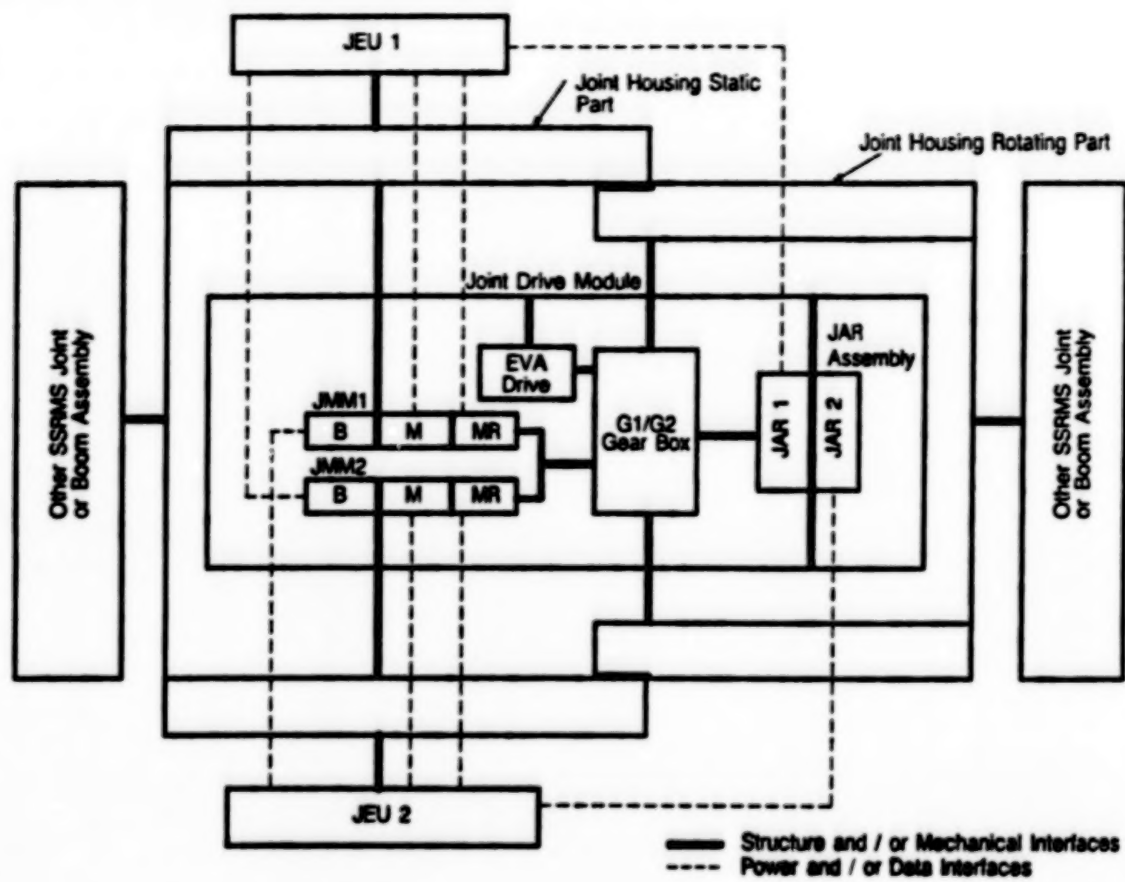
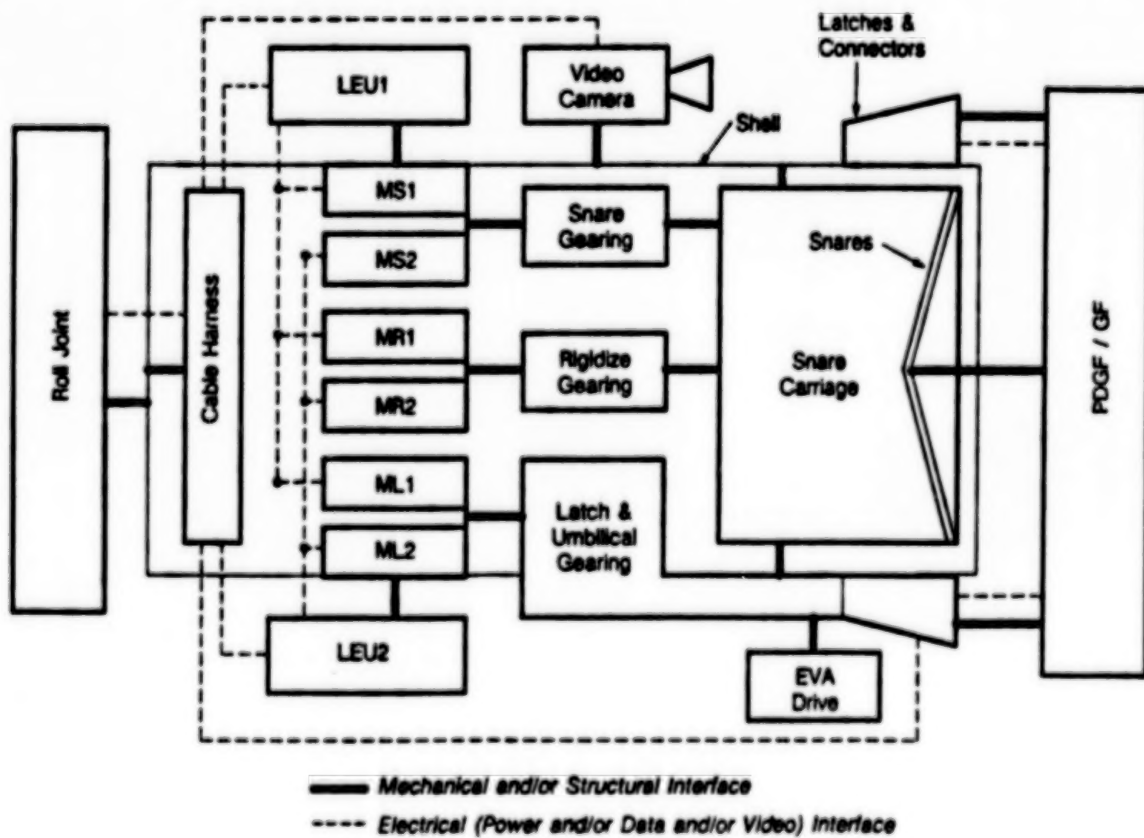


FIGURE 6: JOINT DRIVE MODULE AND JOINT HOUSING



**FIGURE 7: BLOCK DIAGRAM REPRESENTING JOINT COMPONENTS AND INTERFACES**



**FIGURE 8: BLOCK DIAGRAM REPRESENTING THE LEE COMPONENTS AND INTERFACES**

**BLANK**

**PAGE**

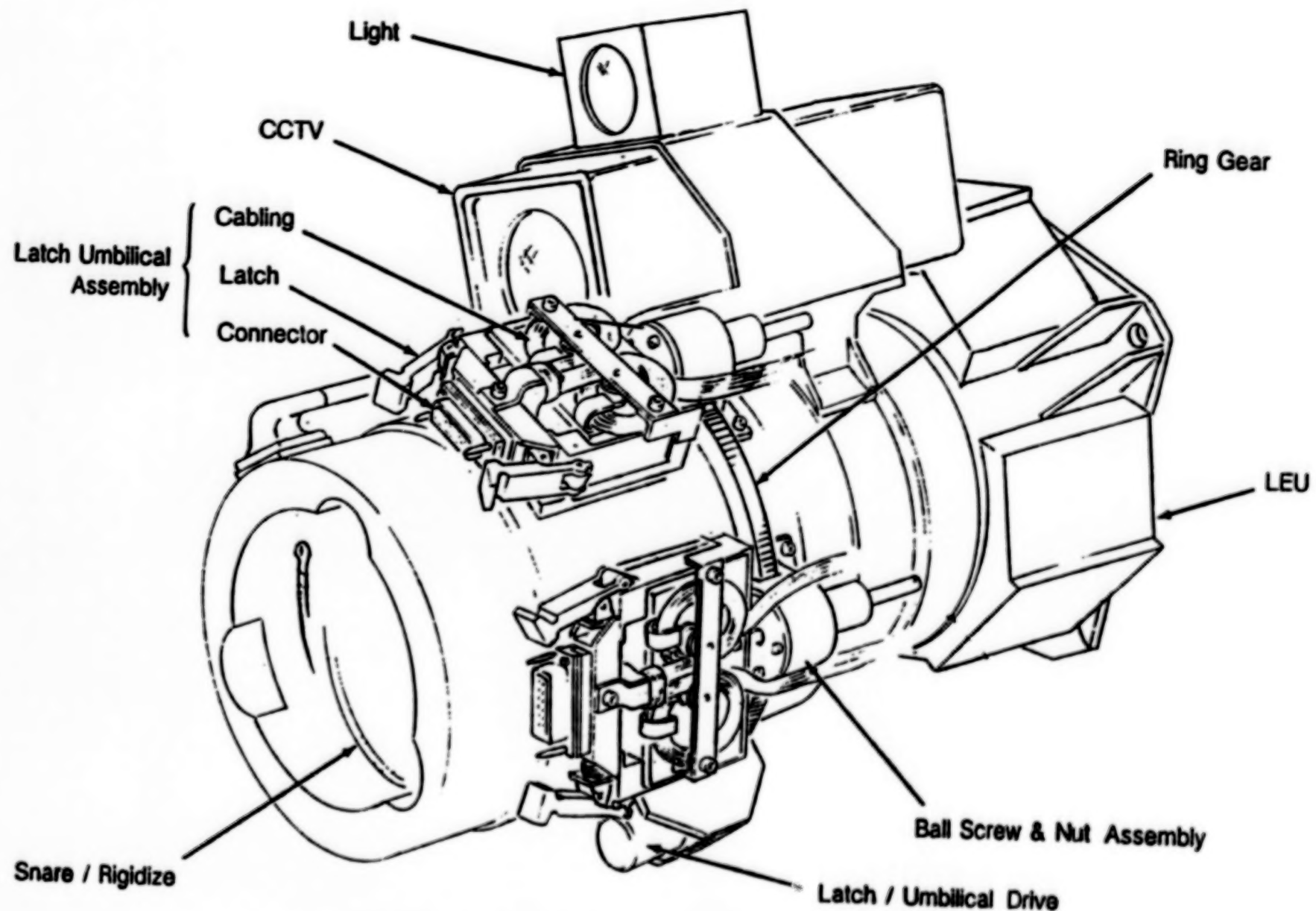
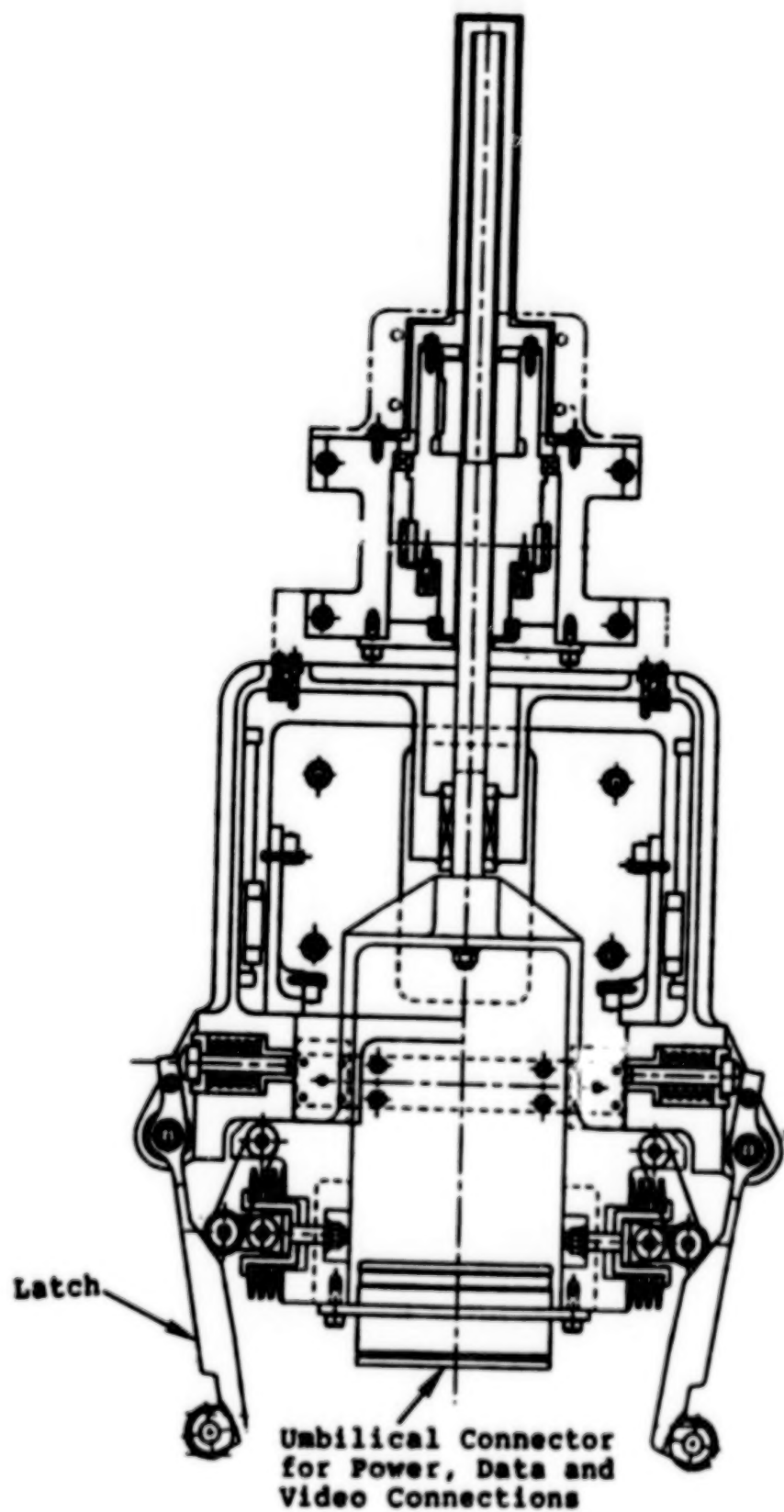


FIGURE 9: LATCHING END EFFECTOR CONCEPT



Note: Four such Latches are mounted on  
LEE Shell for mating with Payload PDGF.

FIGURE 10. CONCEPT OF LATCH AND UMBILICAL CONNECTORS FOR THE LEE

# **"DEAD-BLOW" HAMMER DESIGN APPLIED TO A CALIBRATION TARGET MECHANISM TO DAMPEN EXCESSIVE REBOUND**

Brian Y. Lim\*

## **ABSTRACT**

An existing rotary electromagnetic driver was specified to be used to deploy and restow a Blackbody Calibration Target inside of a spacecraft infrared science instrument. However, this target was much more massive than any other previously "inherited" design applications. The target experienced unacceptable bounce when reaching its stops. Without any design modification, the momentum generated by the driver caused the target to bounce back to its starting position. Initially, elastomeric dampers were used between the driver and the target. However, this design could not prevent the bounce, and it compromised the positional accuracy of the calibration target. A design that successfully met all the requirements incorporated a sealed pocket 85 percent full of 0.76-mm diameter stainless steel balls in the back of the target to provide the effect of a "dead-blow" hammer. The energy dissipation resulting from the collision of balls in the pocket successfully damped the excess momentum generated during the target deployment. This paper describes the disastrous effects of new requirements on a design with a successful flight history, the modifications that were necessary to make the device work, and the tests performed to verify its functionality.

## **INTRODUCTION**

The Pressure Modulator Infrared Radiometer (PMIRR) is a nine-channel limb and nadir scanning instrument on the Mars Observer Spacecraft, designed to study the geosciences and climatology of Mars. It achieves high radiometric precision by means of a two-point calibration cycle. The first calibration source is an external, flat aluminum target disk that views cold space. The second source is a 300-degree Kelvin blackbody target internal to the instrument. This

---

\*Jet Propulsion Laboratory, California Institute of Technology,  
4800 Oak Grove Drive, Pasadena, California 91109

target's surface has a high emissivity coating (Martin Marietta Optical Black) on a 6061-T651 aluminum alloy substrate with concentric V-groove rings for a predicted emissivity greater than 0.97 in the wavelength range of 6 to 50 microns. The target is driven into the optical path of the detectors in front of the prime focus of the telescope every 20 minutes for 8 seconds during the mapping phase of the spacecraft mission.

In an effort to minimize the development cost and time, the drive mechanism of the Focal Plane Shutter (FPS) (Figure 1) was specified to be used for driving the Blackbody Calibration Target. The principles of this drive mechanism are illustrated in Figure 2. A capacitor discharge into a wound bobbin generates a magnetic field that repels the detents of a permanent magnet about its pivot from the starting position until they are attracted to, and then held in the actuated position. A second winding when energized reverses the direction of rotation. The mechanism is a bistable magnetically latching device with a long history of successful flight applications on the Mariner, Viking, Voyager, and Galileo Missions. However, the drivers were originally designed to actuate thin aluminum shutter blades with a mass of no more than 0.5 grams. The mass of the Blackbody Calibration Target had to be greater than 1.97 grams to satisfy a temperature stability requirement of 0.02 degree Kelvin or less change in 64 seconds. Because thermal stability is a critical parameter in calibration, a temperature sensor was required to be placed on the back side of the Blackbody Target, which increased the mass of the target. Also, the cabling for the temperature sensor placed an additional torque load on the driver.

## DESIGN CONSTRAINTS

The constraints imposed by the project were as follows. The power supply for the coils had to be supplied from a discharging capacitor because the spacecraft cannot tolerate a sudden current drain. The drive mechanism of the FPS had to be used to actuate the device with an existing mounting interface, since the optical bench had already been fabricated. Any modifications to the existing mechanism had to fit within an extremely tight envelope (Figure 3). The Blackbody Calibration Target required a Platinum Resistance Temperature (PRT) sensor with four wire leads shielded from electromagnetic interference. The mechanism had to operate for a minimum life of 50,000 cycles during a two-year mission period. The target had to completely cover the field of the

view of all detectors during calibration cycles and retract completely away from the optical paths when stowed. The target had to have a positional repeatability tolerance of fewer than 0.7 mm. No chance of a bounce back could be permitted, since failure of the Blackbody Target to retract from the optical path is a catastrophic failure for the entire instrument. By choosing an existing mechanism for this task, no fail-safe features could be incorporated. Additionally, the hardware delivery date for integration to the instrument left no schedule margin for development of an entirely new mechanism.

## DRIVE MARGIN TESTS

Margin tests were conducted by using a drive mechanism identical to the flight design. The Drive Arm, Blackbody Target, and the cabling from the temperature sensor were simulated. Tests were conducted on the drive mechanism by using a setup similar to one shown in Figure 4. Three photoelectric sensors were positioned to indicate the two ends of travel and the midpoint of travel. A thin flag was attached to the Drive Arm, which triggered the position sensors as the arm moved. A sample of the typical test result is shown in Figure 5. The bottom trace shows the capacitor voltage discharging into the coils. The top trace shows the photoelectric sensors indicating the position of the target. When the flag attached to the Drive Arm triggered a photoelectric sensor, the voltage output from the sensor jumped from 0 to 5 volts. The magnitude and the number of bounces were deduced from the number of peaks and the distance separating them.

Extensive tests were conducted using this setup for targets of various masses. The results of these tests show that the Drive Arm bounced when the mass of the target was greater than 1 gram. The bounce problem occurs when the momentum generated by the arm and the target during actuation overcomes the latching force of the magnet. In addition to generating greater momentum, driving a larger mass has the compounded effect of lengthening the actuation time. Because the voltage from the capacitor decays quickly after a slow actuation, the coil provides little holding force to assist the magnet in overcoming the arm/target rebound at the end of travel. With a target mass less than 1.5 grams, the bounce merely lengthened the settling time; the Drive Arm always ended up where it was supposed to go. However, with a target mass greater than 1.5 grams, the drive arm would bounce overcenter to its starting position.

The torque effects of the magnetic field on the Drive Arm were characterized using a force transducer (Figure 6). While running a constant voltage from a power supply through the coil, the torque on the Drive Arm was measured at different arm positions. The effects of the cabling were characterized using the same method without the magnet at the Drive Arm pivot point. It was found that, for coil voltages less than or equal to 5 volts, the magnitude of the torque from the cabling is greater than the torque generated by the coil.

## DESIGN MODIFICATIONS

### More Powerful Drive Electronics

The initial drive electronics initially provided a 33-millisecond discharge from a 660-microfarad capacitor charged to 50 volts. With this drive source, it took 30 milliseconds for the Drive Arm with a 2-gram target to reach the actuated position. Since the 2-gram mass caused bounce, the magnetic field generated by the coil had dissipated even though the Drive Arm was still moving. Thus, a bounce greater than 50 percent of total travel would cause the Drive Arm to settle at the position from which it initially started.

The first modification to the design was to the electronic driver. The pulse length was increased from 33 to 100 milliseconds and the capacitance was doubled from 660 to 1320 microfarads. By increasing the length of the pulse, there would still be a significant magnetic field directing the Drive Arm to the correct orientation during the bounce. Although doubling the capacitance increases the momentum that must be dissipated, it also reduces the rate of time decay, so that the magnetic field generated by the higher voltage helps to attract the magnet detents to the right position during settling. The electronic chassis that houses the capacitors physically limited any additional increase in power.

### Flex Print Cabling

In order to minimize the torque effects of the PRT cables across the Drive Arm pivot, a dynamic flex print circuit was designed at Jet Propulsion Laboratory and fabricated at Tayco Engineering in Long Beach, CA. The leads from the PRT and the twisted quad shielded and jacketed (TQSJ) cable were

integrated into a Flex Print Assembly (Figure 7). The flexible part of the cable was made of four 0.07- x 0.25-mm copper conductors laminated with FEP Teflon in between two pieces of 0.03-mm thick Kapton film. The leads from the PRT and the TQSJ cable were welded to the conductors internal to the Kapton laminate. This design uses the same fabrication techniques used for manufacturing film heaters. The flex print design minimizes the torque loading on the drive system because the cable acts as a weak spring; the spring is oriented so that it assists the drive mechanism when restowing out of the optical path. Flex print cables have demonstrated high reliability and long life in many military and commercial applications.

To meet the requirements for shielding the conductors, the flex print was vacuum deposited with gold. Since the flex print has to withstand dynamic flexing throughout the mission, there is a risk of gold flaking off. In order to be certain that there is no potential for particulate contamination, the vacuum deposited gold had to undergo a tape pull test without any residue on the tape. The only method attempted that left no residue on the tape test involved exposing the Kapton to an ion beam and vacuum depositing it with titanium prior to vacuum depositing it with gold. The shield on the flex print was electrically bonded to the shield on the TQSJ cable through a hole in the Kapton which exposed the shield of the TQSJ cable. Although the vacuum deposited gold connects the shield on the TQSJ cable to the surface of the Kapton, an electrically conductive adhesive was also used to ensure continuity.

### Eliminating Excessive Rebound

The bounce problem was addressed by experimenting with different methods of damping. Initially, the drive margin tests were conducted with a stiff arm to minimize the bending (stored energy) and to increase the natural frequency. When the bounce became a serious reliability concern, a two-piece arm coupled with an elastomeric damper was tested in place of the stiff arm. It was hoped that the elastic deformation of the rubber would absorb and dissipate the kinetic energy. Although this design reduced the bounce, it did not eliminate it or prevent bounce-back of heavier targets. More important, the positional accuracy of the target was significantly compromised.

In other designs using a drive mechanism similar to the FPS, end of travel bumpers were used to dampen out the excessive momentum. However, the

envelope restrictions of the Blackbody Target Mechanism precluded incorporation of useful bumpers.

Another momentum dampening method investigated was inspired by the dead-blow hammer (Figure 8). This damper involved filling an enclosed cavity with 0.76-mm diameter stainless steel balls. The smallest readily available balls were used since they could contour to the cavity for higher packing density. Although balls made of materials of low coefficient of restitution, such as lead, would have improved damping characteristics, the advantages in easy procurement of ball bearing parts with certification for spacecraft application and the success of stainless steel balls during prototype testing discouraged a lengthy investigation on material choice. Individually, each ball would have very little momentum so that the effects of the random motions at the latched positions in a microgravity environment would be minimized. Collectively, the balls had enough counter momentum to dissipate the excessive kinetic energy in the Drive Arm before it bounced out of the designated position. On the prototype setup, this method damped the bounce more effectively than other methods. More importantly, the bounce-back was completely eliminated.

The allowable envelope for the calibration target mechanism restricted the volume of the cavity for the dead-blow balls. With the given cavity, the quantity of the balls for the optimal dead-blow effect was determined empirically by using the drive margin test setup. Because the dead-blow effect worked so effectively, the capacitance of the test drive electronics had to be decreased to create bounce that could be analyzed. By iterating the test with the cavity full of different amounts of balls, and comparing the bounce that each produced, the optimum amount was found. For the application in the Blackbody Target Mechanism, this optimum amount occupied 85 percent of the volume in the cavity.

## CONCLUSION

Despite the long history of successful flight applications, retrofitting the Focal Plane Shutter Drive Mechanism for use on a new instrument with a different set of requirements demanded much more effort than was originally anticipated. The modifications necessary to reliably operate the Blackbody Calibration Target Mechanism by the use of existing inherited hardware required design changes in the drive electronics, incorporation of flexible

cabling, and incorporation of a damping method. The constraints imposed by the instrument were met by using a dynamic flex print cable for the PRT sensor and by using a dead-blow damper on the back side of the Blackbody Target. The dead-blow damper uses the momentum of the free-floating balls inside a cavity to counter and dissipate the momentum stored in the Drive Arm and the target when actuated. The drive margin tests using the dead-blow damper demonstrated consistant results with minimal rebound and no bounce-back.

The work described in this paper was carried out by the Jet Propulsion Laboratory, California Institute of Technology, under a contract with the National Aeronautics and Space Administration.

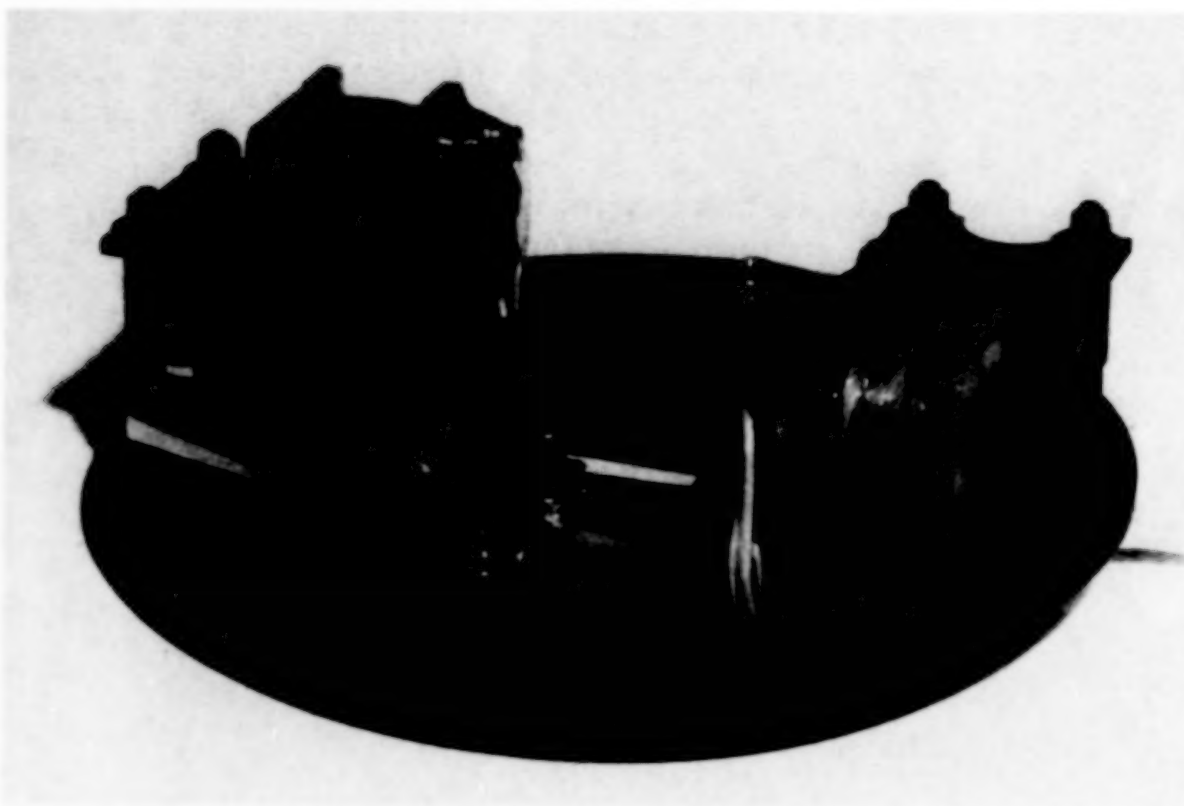
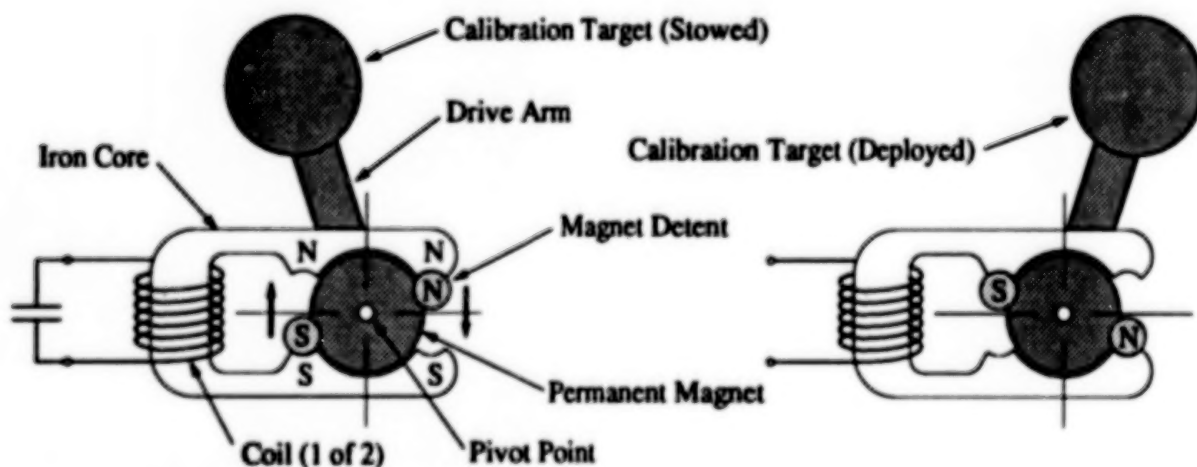


Figure 1: Focal Plane Shutter Mechanism. The mass of each aluminum blade is less than 0.5 gram.



The Detents are repelled from their initial position when the current flowing through the coil generates a magnetic field in the iron core.

The magnetic force causes the calibration target to rotate about the pivot point until the detents have settled. Detents are magnetically latched to the iron core until the next actuation command.

Figure 2: Drive mechanism principle of operation.

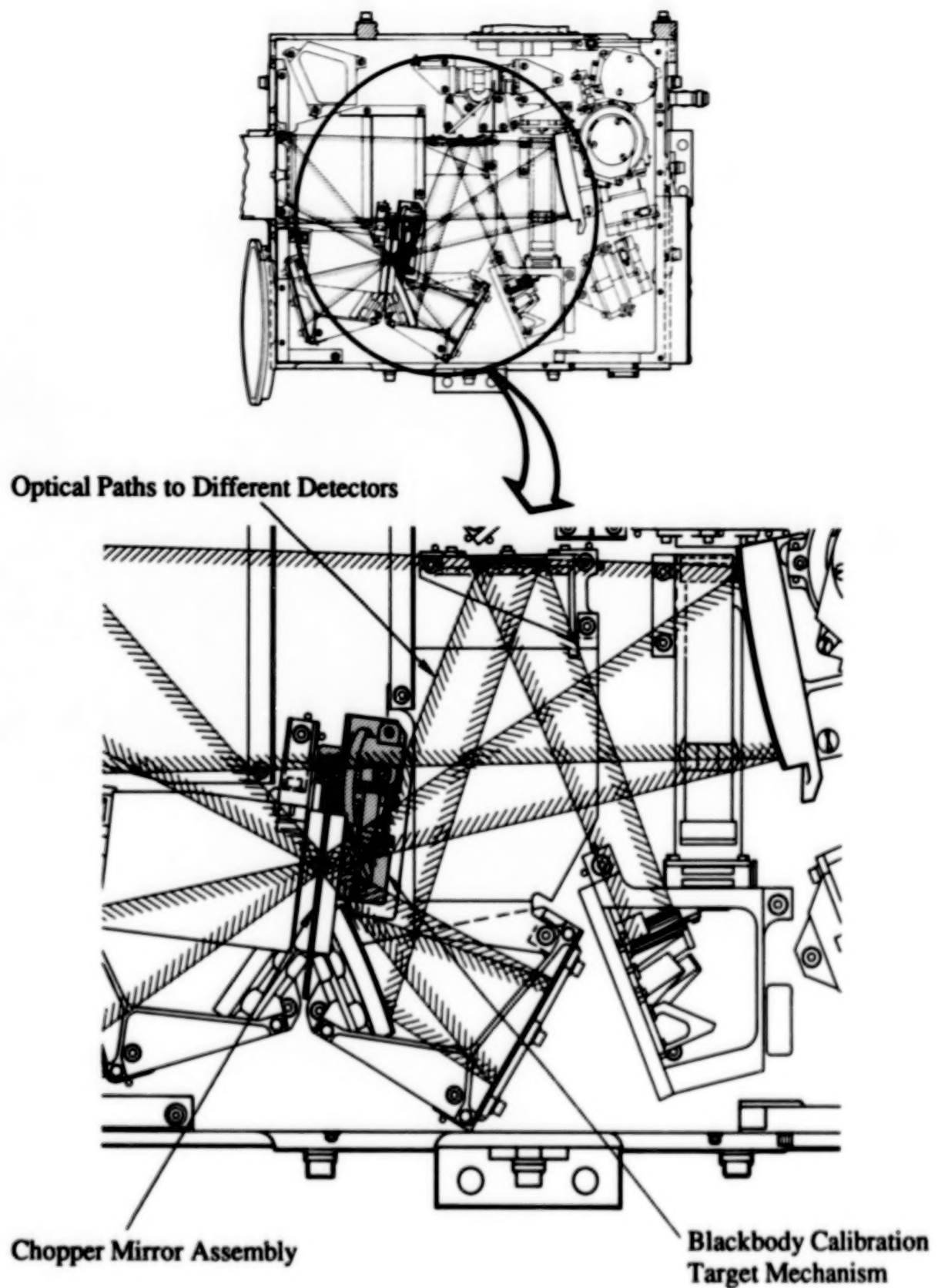
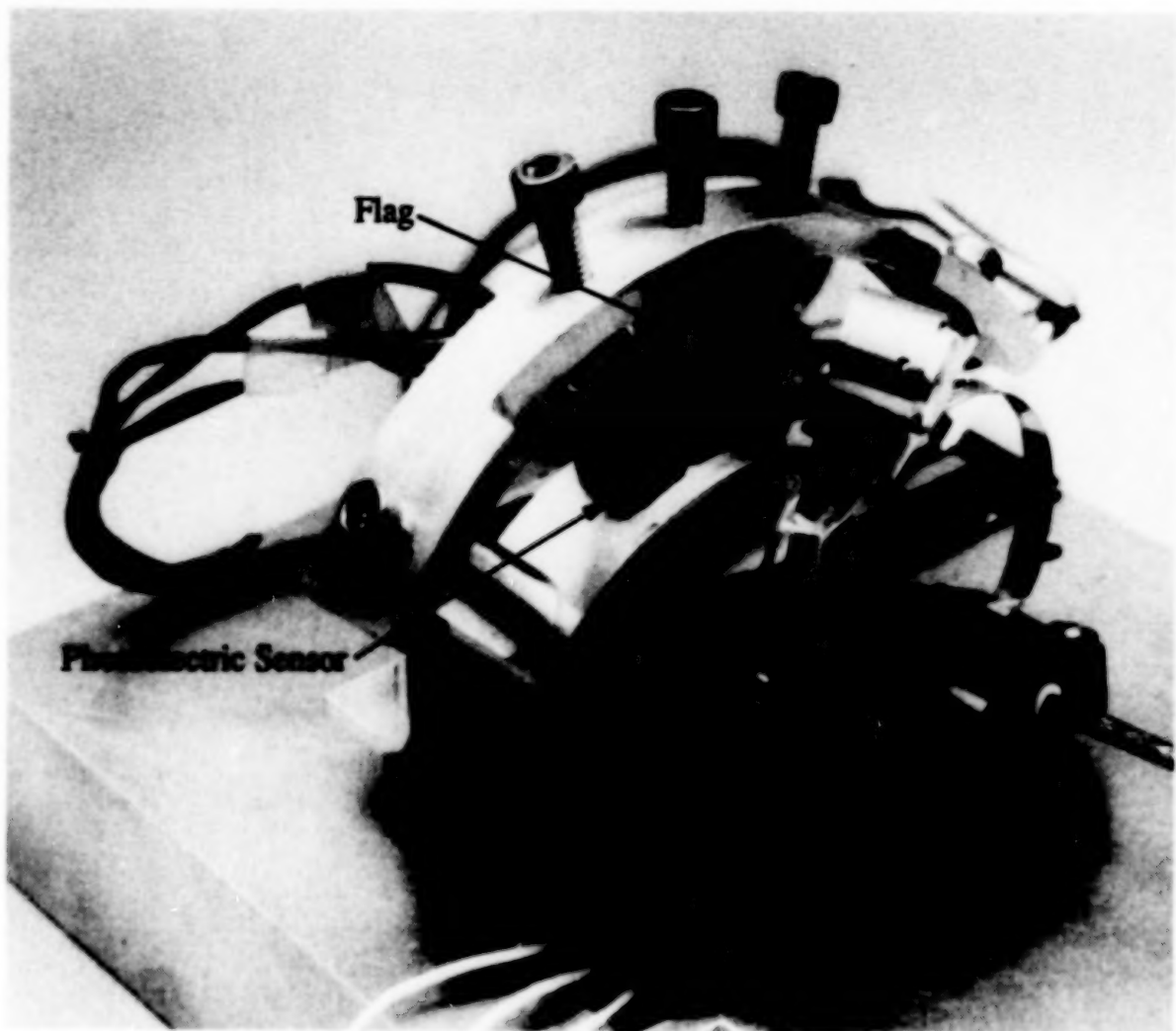
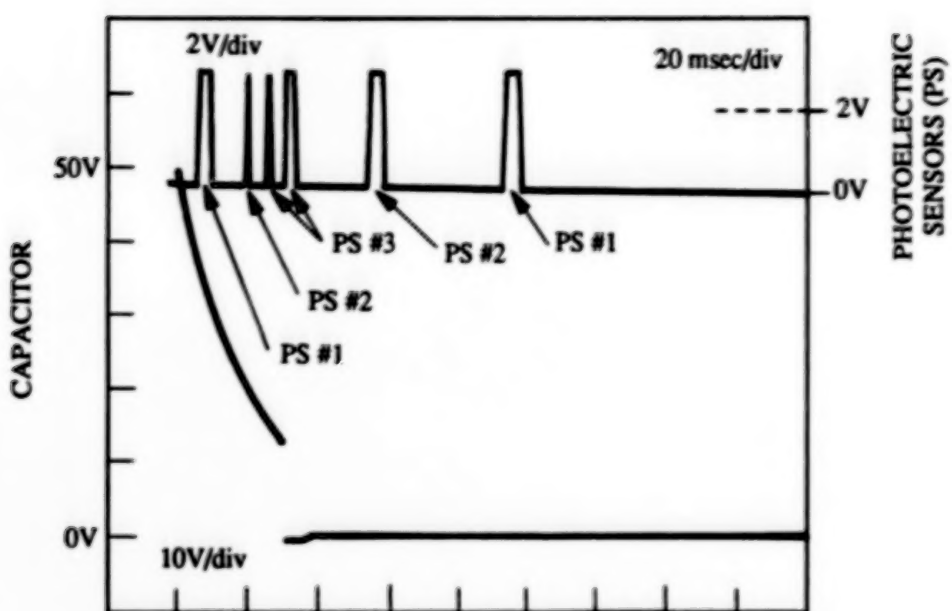


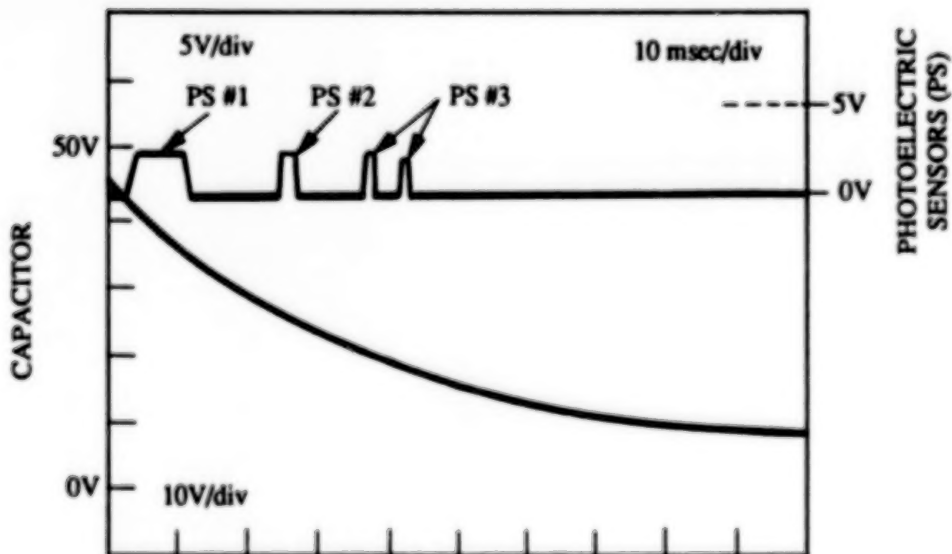
Figure 3: Envelope restrictions on Blackbody Target Mechanism.



**Figure 4: Drive Margin Test Setup.**



Without any modifications, the momentum generated by a target mass of 2 grams caused it to bounce back to the position from which it started.



With all the modifications incorporated, rebound was minimized and bounce-back was eliminated.

Figure 5: Sample of Typical Drive Margin Test Results.

**Drive Mechanism Profile**  
**Energized Toward the Deployed Position**

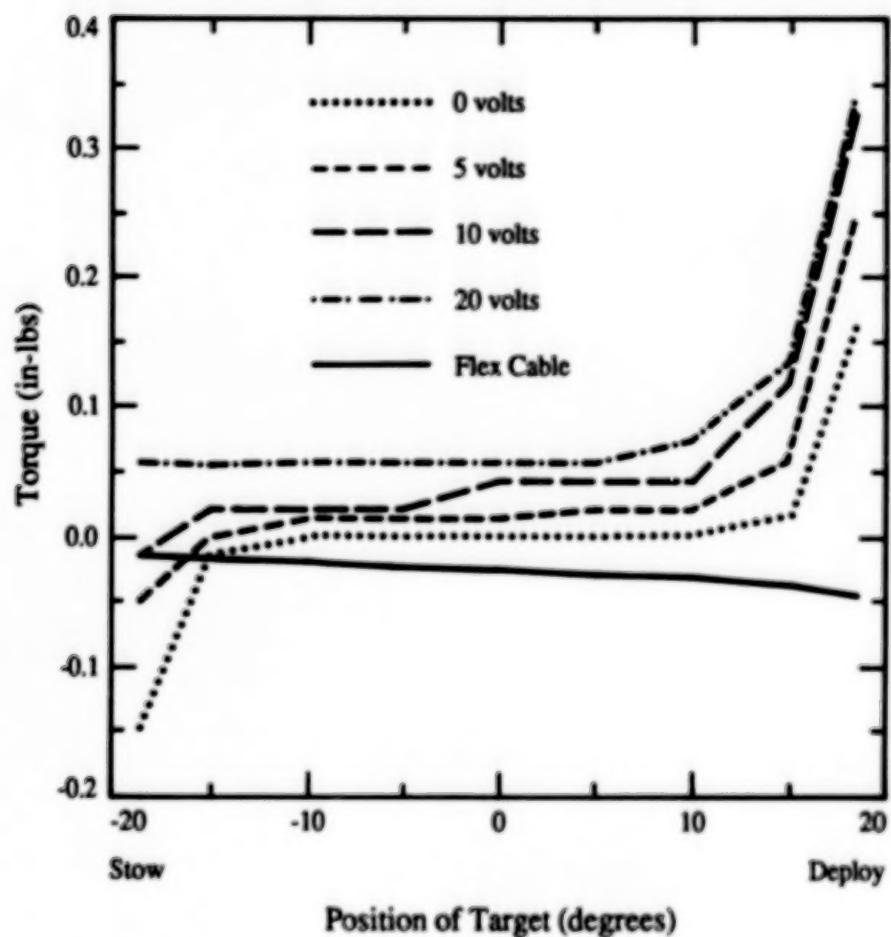
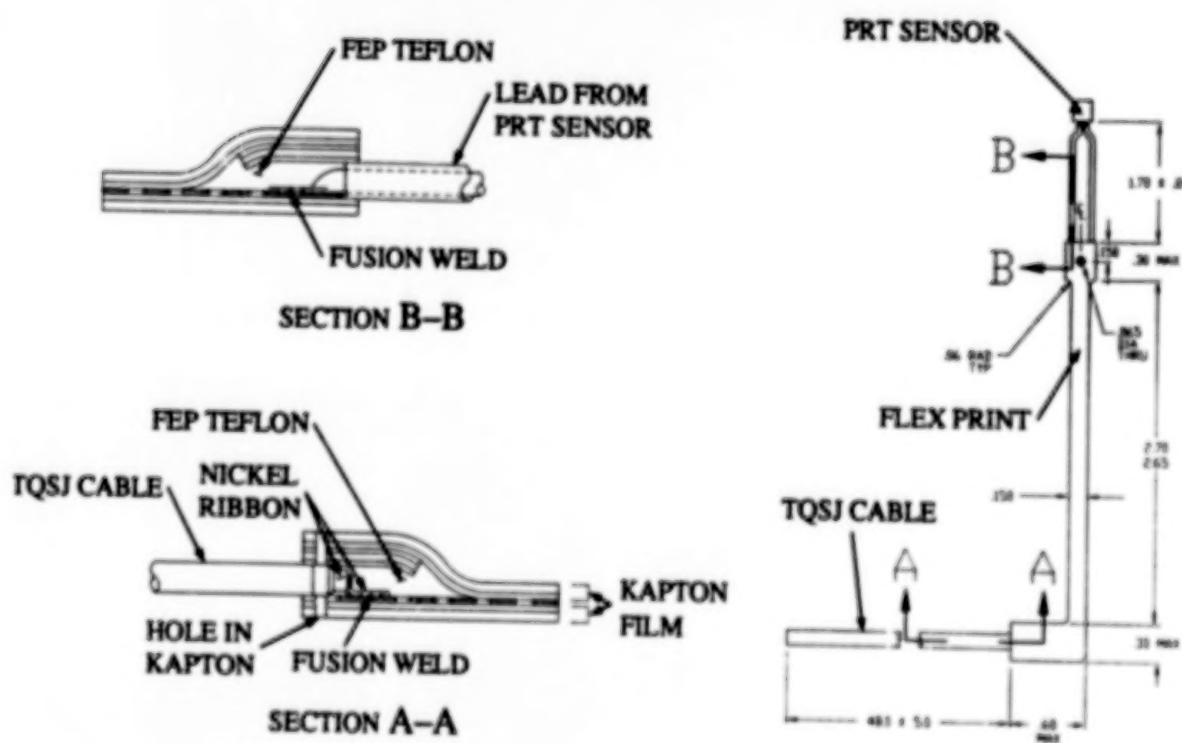
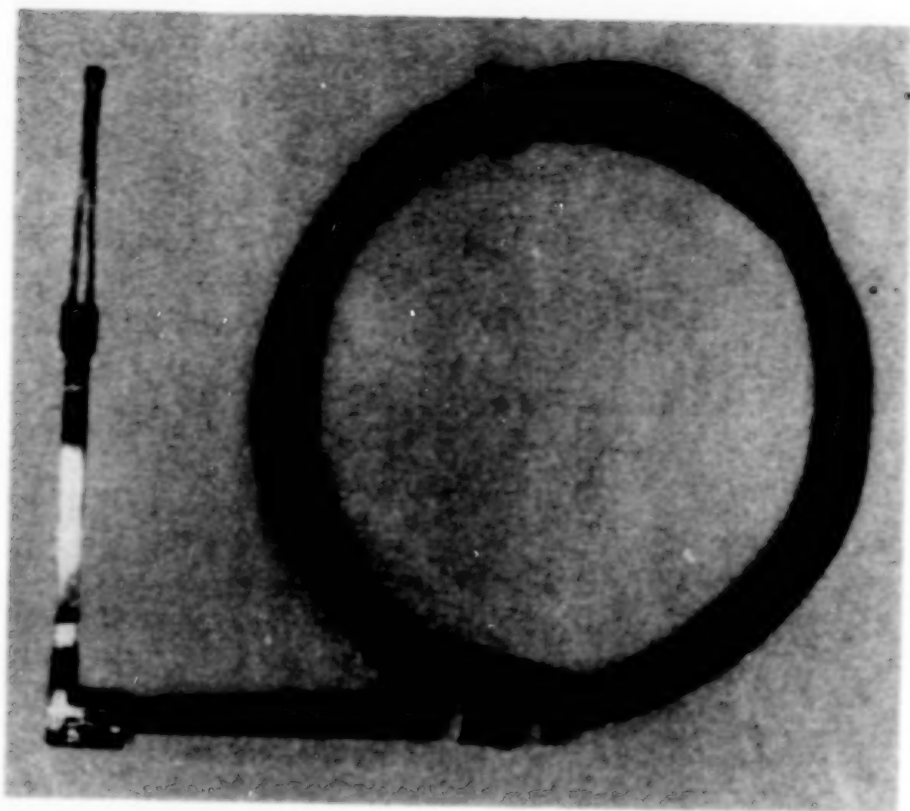


Figure 6: Characterization of magnetic forces on Drive Arm.



**Units are presented in inches.**

**Figure 7: Flex Print Cable Assembly.**

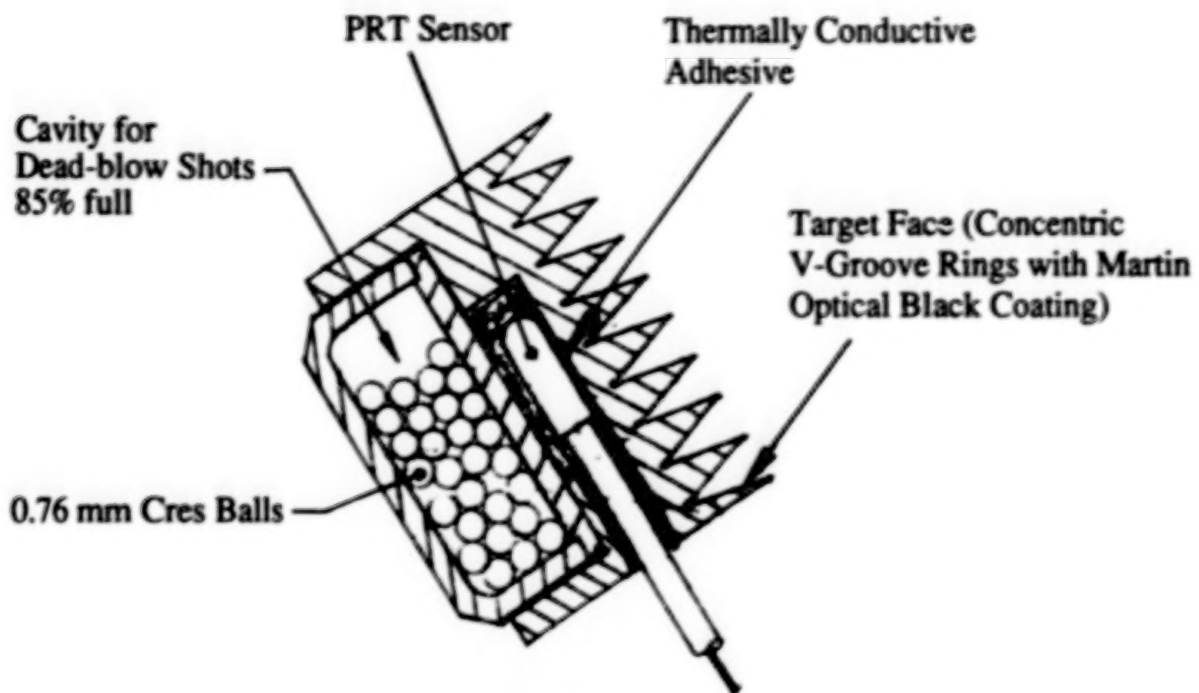


Figure 8: Dead-blow damper incorporated into the target.

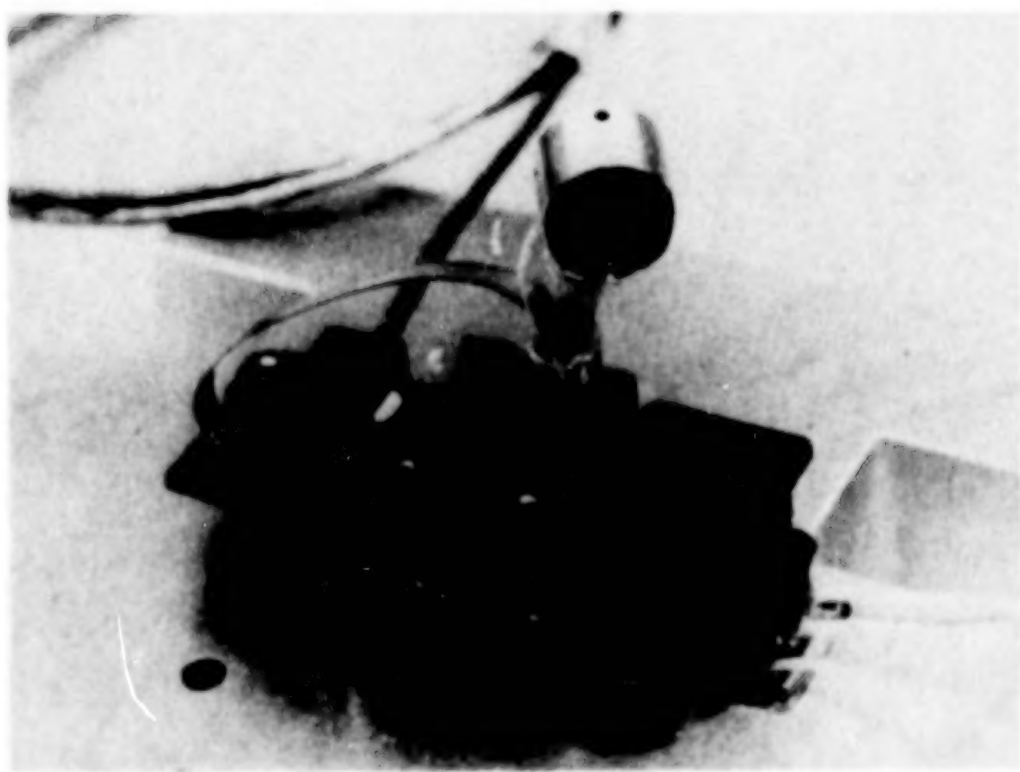


Figure 9: Front view of Black body Calibration Target Mechanism prototype unit without Martin Optical Black coating on target surface.

**DESIGN AND DEVELOPMENT  
OF THE  
REDUNDANT LAUNCHER STABILIZATION SYSTEM  
FOR THE  
ATLAS II LAUNCH VEHICLE**

**M. Nakamura\***

**ABSTRACT**

The Launcher Stabilization System (LSS) is a pneumatic/hydraulic ground system used to support an Atlas launch vehicle prior to launch. This paper describes the redesign and development activity undertaken to achieve an LSS with increased load capability and a redundant hydraulic system for the Atlas II launch vehicle.

**INTRODUCTION**

General Dynamics started design of the original Atlas rocket in 1955. Since then, General Dynamics has refined and expanded the capabilities of this launch vehicle, which has proven itself to be a reliable and effective contributor to the United States space effort. However, without the support of the LSS, which is the subject of this paper, the Atlas would not have flown into history.

The Atlas vehicle has historically employed a controlled release launch system. During a launch sequence, the vehicle engines are ignited on the ground and verified for proper operation before the vehicle is released. The ground launcher system must support the vehicle in the prelaunch condition and release the vehicle at liftoff.

The Atlas ground launcher system (see Figure 1) consists of a large, welded steel structure that is firmly anchored to the launchpad along with pneumatic and hydraulic systems. The holdown and release (HD/R) system serves the primary role of supporting the vehicle prior to launch and releasing the vehicle when commanded. The vehicle is restrained from flight by two holdown pins mounted on the launcher structure acting in the Y-Y plane. The vehicle can freely rotate about this axis. At liftoff, the HD/R system retracts these pins and rotates the

---

\* Senior Engineer, General Dynamics Space Systems Division, 5001 Kearny Villa Road, San Diego, California 92123

entire assembly away from the vehicle. The LSS is also part of the ground launcher system and provides an upward, balancing force called preload in the X-X plane to the outside structure of the vehicle to preclude it from toppling over. The LSS provides this force to the vehicle from the uppermost portion of the launcher structure called the A-frame.

The latest upgrade to the Atlas vehicle is the Atlas II. This new vehicle has the capability to launch heavier payloads but unfortunately not without an increase to vehicle weight and size. As a result, the previous design LSS could not provide a sufficient amount of preload nor counter the increased wind effects. Therefore, in order to retain the proven, controlled release method of launch, a redesign of the ground launcher system was necessary. The LSS was included as part of the overall ground launcher redesign. In addition, a design improvement to incorporate a redundant hydraulic system was implemented.

## SYSTEM DESCRIPTION

The LSS is primarily required to support the vehicle from wind loads acting on the vehicle structure. It accomplishes this by sensing and adjusting the preload to apply more or less force on each side. The hydraulic system of the existing LSS did not use any pumps, valves, or complex control circuits and yet could precisely balance the vehicle in an upright position. However, if a leak were to develop, the LSS would malfunction and the vehicle would tilt unacceptably.

During ground checkout and prelaunch servicing, a mobile service tower (MST) is positioned to surround the vehicle on three sides and physically blocks any wind loads to the vehicle. With the MST in place, the LSS is backed up with adjustable shims that limit vehicle tilt and thereby provide an additional safety feature against tipping. Therefore, the time of critical need for the LSS is during the conditions of simulated and actual launches. In these situations, the MST is rolled away, the safety shims have been removed and the LSS must now counter the full effect of the wind loads. The response frequency of the LSS must react quicker than the vehicle tilt frequency.

During the launch sequence, there are several conditions that affect the LSS. They are thrust buildup (TBU), liftoff (LO), and thrust cutoff (TCO):

TBU = A condition in which the vehicle engines have been ignited but the release command has not been given, usually lasting about 2 seconds. There is a slight rise in vehicle position, resulting from the flexure of the vehicle and launcher mechanical structures, but the HD/R system is restraining the vehicle from flight. During TBU, the LSS must follow the rising vehicle and continue to exert a preload force to the vehicle while still maintaining balance.

LO = A condition following TBU, where the vehicle is released from the ground launcher system and allowed to lift off. As the vehicle rises off the launch pad, the LSS must follow the vehicle, and gradually reduce the preload to zero. The preload must be reduced before the vehicle physically separates from the LSS. This is necessary in order to avoid a sudden load transient being imparted to the vehicle or the payload (spacecraft).

TCO = A condition in which the launch has been aborted. This could occur at any time during the launch sequence, up to and including after the engines are ignited and the TBU condition exists. A TCO will result in a sudden, downward movement of the vehicle from a TBU condition. During a TCO, the LSS must follow the vehicle and stroke downward. The preload being applied to the vehicle should not change, and the LSS must still maintain vehicle balance against wind effects. After the initial downward movement, a series of diminishing rebound oscillations must be accommodated by the LSS.

## GOALS/REQUIREMENTS

The primary goal of the LSS redesign was to develop a new system that could support the Atlas II vehicle. This support was necessary from the time of vehicle erection until liftoff and all intervening conditions, such as TBU, LO, and TCO. If possible, this new LSS was to be designed with growth capability in order to accommodate heavier payloads or launch vehicle weight increases as the Atlas program developed.

The secondary goal was to incorporate the redundancy feature into the hydraulic system of the new LSS. The redundancy feature must

provide a means to support the vehicle in the event of a hydraulic system failure, making the LSS single-failure-tolerant.

The LSS was designed to meet the following requirements:

Nominal preload (total)	462,600 N (104,000 lb)
Nominal preload (per side)	231,300 N (52,000 lb)
Wind moment capability	542,400 Nm ( $4.8 \times 10^6$ in.-lb)
Allowable vehicle tilt	$\pm 0.00349$ Rad max ( $\pm 0.2$ deg)
TBU vehicle rise rate	152 mm/sec (6 in./sec)
LO vehicle rise rate	280 mm/sec (11 in./sec)
TCO vehicle descent rate	216 mm/sec (8.5 in./sec)
Response frequency	4 Hz minimum

## DESIGN SELECTION/OPERATION

The previous design of the LSS used a passive hydraulic system that was pressurized with gaseous nitrogen (GN<sub>2</sub>) but did not have a redundancy feature (see Figure 2A). An increase of the component sizes in this configuration would only meet the primary goal of supporting the vehicle. Therefore, the first task was to determine a system configuration with a redundancy feature that would support the vehicle. A series of trade studies were performed to evaluate several system configurations (see Figures 2B, 2C, and 2D). Each system was evaluated for basic capability, redundancy, simplicity, and cost. After the configurations were analytically modeled through computer simulation and static analysis, the proposed schematic of Figure 2D was selected.

The detailed designs of the cylinder and compensator were originally proposed as identical components. A common, tandem cylinder was chosen to minimize design efforts and costs. A tandem cylinder would be installed at each A-frame and two tandem cylinders joined together at their shafts would constitute a compensator. This enhanced by placing the compensator cylinders adjacent to each other with a tilt beam to couple the shafts together (see Fig. D). This resulted in a reduced size envelope for the compensator. The design was eventually discarded due to one major flaw. However, this compensator required many mechanical joints to enable the cylinders to be interconnected. These joints were a source of free play to the system and would have effectively degraded the performance of the LSS to the

point where it could not properly respond to vehicle motions. In addition, the cylinders required many flexible hoses to connect the system together. These hoses would have expanded with pressure, which would also have reduced system performance as well as provide potential failure points. As a result, the configuration was refined to a tandem cylinder and four-piston, common shaft compensator design (see Figure 3).

The operation of this new system is simple but elegant. GN2 is used to pressurize all four pistons of the compensator. This pneumatic force acts on these pistons, which are, in turn, hydraulically connected to the tandem cylinders. Two separate hydraulic circuits are routed to each cylinder and the resultant forces from each hydraulic circuit are then joined to apply the balancing force to the vehicle. When a wind gust acts on the vehicle structure, the LSS responds immediately by countering the vehicle force with an increase in the LSS hydraulic system pressure on that side. This pressure increase is possible as the compensator simply shifts the amount of "effective" pneumatic force to the piston/circuits that demand it. This transfer of force also results in a reduction in the preload on the opposite side—a subtle feature that aids the LSS balancing efforts by minimizing the preload on the side that is actually aiding the wind in trying to tip the vehicle.

The redundancy of the LSS is possible through the use of the two individual hydraulic circuits on each side of the vehicle. If one of the circuits develops a leak, the remaining circuit pressure will essentially double to maintain support of the vehicle. The increase in hydraulic pressure is possible as the compensator pneumatic force shifts to the remaining circuit.

## DESIGN DEVELOPMENT

A preliminary analysis showed that the oil volumes of the cylinder and the compensator circuits had to be virtually identical in order to function properly. This also meant that the tubing lines connecting the cylinders and compensator had to be exactly the same length. Furthermore, any amount of leakage would result in a volumetric imbalance and was undesirable, as the system would start to shift to the remaining circuit. To this end, all tubing pressure connections were either welded or were of the lipseal design to ensure leak-free reliability. In addition, the seals within the cylinder and compensator

had to be virtually zero leakage in order to eliminate them as a source of problems. However, in the event of leakage, an indicating device was desired to show when a circuit had failed. Several elaborate indicator designs were evaluated, but after development testing it was determined that monitoring the system circuit pressures was sufficient to evaluate the health of the system. If one circuit loses oil, the pressure drops off, and the adjoining circuit has a pressure increase.

A prototype test setup was constructed and preliminary development testing was conducted. This mock-up LSS was tested to verify the preliminary design assumptions of flow and pressure effects. Testing proved that the response time for the LSS would be in the order of 25 Hz. This is significantly faster than the predicted vehicle frequency of 4 Hz. The response capability of the LSS is comparable to an automotive brake system, where response is virtually immediate.

Component sizing was performed based upon the system load requirements. The LSS was required to provide a total preload of 462,600 N (104,000 lb) of force to the vehicle, 231,300 N (52,000 lb) per side. In order to provide this amount of force, each individual hydraulic circuit had to provide 115,650 N (26,000 lb). However, should one circuit fail, the remaining circuit then had to provide the full 231,300 N (52,000 lb) of force to maintain vehicle support. For this reason, each circuit had to be sized to permit a full load to be supported on only one cylinder. In effect, the system would be functioning only at half capacity at all times, but capable of switching to full capacity whenever necessary.

Preliminary sizing of the circuit was based upon a 31,000-kPa (4,500-lb/in.<sup>2</sup>) operating system during a failed circuit condition. At normal operating pressures, the individual circuit pressures would have been 15,500 kPa (2,250 lb/in.<sup>2</sup>). In order to achieve 115,650 N (26,000 lb) of force, the piston area had to be 74.59 cm<sup>2</sup> (11.56 in.<sup>2</sup>). This would have necessitated a 97.54-mm (3.84-in.) diameter piston with an estimated cylinder external housing diameter of 178 mm (7 in.). This size would have readily fit into the installation; unfortunately, these design values did not offer any provision for growth capability. Thus, it was apparent that the system could be sized much larger.

The final sizing of the system was based upon a minimum piston area of 298 cm<sup>2</sup> (46.18 in.<sup>2</sup>), operating at a circuit pressure of 3,875

kPa (563 lb/in.<sup>2</sup>). This would provide the necessary preload of 462,600 N (104,000 lb):

$$298 \text{ cm}^2 \times 3875 \text{ kPa} \times 2 \text{ circuits} = 231,300 \text{ N per side}$$
$$(46.18 \text{ in.}^2 \times 563 \text{ lb/in.}^2 \times 2 \text{ circuits} = 52,000 \text{ lb per side})$$

In the event that a hydraulic circuit should fail, the circuit pressure would double to 7,750 kPa (1,125 lb/in.<sup>2</sup>). However, the system was purposely designed to handle an operating pressure of 7,750 kPa (1,125 lb/in.<sup>2</sup>) and a failed circuit pressure of 15,500 kPa (2,250 lb/in.<sup>2</sup>). Essentially, the system was designed to support twice the loads anticipated, thus satisfying the growth capability feature. The piston area required a large external housing diameter of 356 mm (14 in.). Concurrent with the LSS redesign effort, the A-frame was being redesigned to accommodate greater loads. Once the cylinder size was determined, the A-frame was designed to fit the new cylinder parameters. In order to expedite the installation of the LSS components, full-scale wooden mock-ups of the cylinders and compensators were fabricated.

The system was not complete without the tubing to connect the cylinders and compensator. The tube size was determined by the oil flow rate (during TBU, LO, and TCO) and the maximum system pressure anticipated. The highest flow rate for the vehicle movement was LO, at 280 mm/sec (11 in./sec). For a piston area of 298 cm<sup>2</sup> (46.18 in.<sup>2</sup>), the equivalent flow rate of oil was calculated to be approximately 492 liters/min (130 gal/min). Furthermore, the maximum system pressure anticipated for the LSS was 31,000 kPa (4,500 lb/in.<sup>2</sup>), based upon a failed circuit pressure of 15,500 kPa (2,250 lb/in.<sup>2</sup>) and the wind moment of 542,400 Nm ( $4.8 \times 10^6$  in.-lb) added to it. In order to support these flow rate and pressure values, a line size of 31.75 mm (1.25 in.) diameter, with a wall thickness of 3.05 mm (0.120 in.) was selected. The final line lengths of each circuit were approximately 12,190 mm (480 in.) between the cylinders and the compensator.

## PROBLEMS ENCOUNTERED

This new LSS was a marked departure from the previous design and required further analysis and evaluation to qualify the concept before the design could be finalized. During the course of this evaluation,

several problems surfaced and were resolved. Problems concerning heat expansion effects, TCO effects, handling difficulties, volumetric imbalance effects, and tilt effects were addressed.

The LSS would be subjected to the effects of solar heating and rocket engine blast. The heat from these sources would heat the oil and cause a volumetric imbalance resulting in a vehicle tilt. The launchpad installation results in half of the LSS being exposed to direct sunlight, while the other half is in the shadow of other structures. An oil temperature gradient of as much as 37.78°C (100°F) was anticipated between the two sides of the vehicle, and the resultant expansion of oil on one side would have resulted in a slight (and undesired) tipping of the vehicle. As the vehicle lifts off, the entire launcher is exposed to temperatures as high as 2,760°C (5,000°F) for approximately 12 seconds. In certain cases, direct rocket blast impingement could occur. These conditions would affect the operation of the LSS or its longevity. In both cases, the problem was solved by shielding the system from exposure, thus eliminating any heating problem. The selected method was an ablative, silicone coating. This room temperature vulcanizing (RTV) coating provides shade from the sun as well as an insulating barrier from rocket blast temperatures.

If a TCO were to occur, the LSS would stroke downward with the vehicle. This motion would displace system fluid from the cylinder to the compensator and compression of the GN<sub>2</sub> within the compensator would result. This compression would result in a significant pressure rise in the pneumatic chambers of the compensator and would rebound back into the hydraulic circuit and raise pressures uncontrollably. To alleviate this problem, storage bottles (pressure vessels) were connected to the pneumatic chambers of the compensator (see Figure 3). The GN<sub>2</sub> would flow into these bottles, thereby avoiding any undue pressure. An additional benefit of these storage bottles was to provide an additional supply of GN<sub>2</sub> should the primary supply be shut off or fail.

The operation of the LSS requires preload drop-off prior to vehicle separation. A flow-rate analysis showed a need for an orifice to control the oil flow during a LO condition. At the same time, this orifice must not constrict the flow so that separation occurs during TBU. Further, the orifice would restrict oil flow in the event of a TCO and result in an over-pressurization of the hydraulic system. Therefore, the orifice must

"free flow" during the TCO event. In order to achieve this, an orifice check valve was added to each hydraulic circuit. The orifice was sized to control the flow of oil for LO (yet not permit vehicle separation during TBU) and the free-flowing feature of the check valve would allow TCO to occur without incurring the unwanted pressure rise.

During fabrication of the LSS components, the size and weight of the units made machining or even simply moving items very difficult. A fully assembled cylinder weighs about 2,225 N (500 lb) and a compensator weighs approximately 8,900 N (2,000 lb) (See Figures 4 and 5). Aside from the weight, the size and shape of the items also contributed to the difficulty. Specialized tooling was required to hold, lift, move, or even turn items. This was accomplished by using portable gantry-type cranes, special lifting adapters, and wheeled dollies.

The LSS compensator piston assembly consists of four individual pistons stacked together (see Figure 5). They are held together by a nut and bolt assembly on a central shaft. The entire assembly had to be mechanically preloaded to ensure there was no free play that would degrade system performance. Unfortunately, there was no way to physically apply the load and still torque the nut. The problem was solved by initially assembling the pistons, then pneumatically pressurizing the entire assembly. The nut was tightened, and when the pneumatic pressure was removed, the assembly was automatically preloaded and the four individual pistons acted as a single unit.

Volumetric imbalance of the LSS hydraulic system was evaluated. The imbalance could result from improper fill and bleed, where excess air is not removed from the system or if the chambers do not contain the same amount of oil, as in the case of a leak. During system testing, the LSS performance was evaluated with a fully bled system and with calibrated, increasing amounts of air (of as much as 3% of the total system) within the system. Test results indicated the volumetric imbalance with air in the system did not affect the system operation significantly. The reason for this was twofold. First, the air volume within the hydraulic system would compress when the system was pressurized, resulting in a very small volume, thus minimizing its effect to vertical displacement. Second, the relatively large piston area requires a large imbalance to cause any significant vertical displacement. Therefore, a minor imbalance can be readily accommodated. The vertical displacement is directly related to vehicle tilt, which is automatically minimized by the small effect of these imbalances. In all cases, the

+/-0.00349 Rad (+/-0.2 deg) of vehicle tilt was not exceeded.

During testing, a method of fill and bleed was employed that consisted of flowing pressurized oil through the LSS. After filling and bleeding, due to the length and complexity of bends and connections, there was no way to determine when the fill and bleed was complete and all the air had been removed. System-level tests did not indicate any presence of air within the system due to the previously mentioned large piston area. It was therefore necessary to accurately determine the amount of air within each circuit, and a method of verification was developed. The method employed was to connect a small test cylinder to the hydraulic system, fill the entire system with oil, and pressurize the opposite side of the piston within the small cylinder (see Figure 3). In this way, the air within the hydraulic system would compress and the test cylinder's piston would stroke the same amount as the air would compress. This method was tested and proved to be a very simple yet accurate means of checking the condition of the system.

## LESSONS LEARNED

### Design/Analysis Aspects

1. Discretely separate analysis activity was conducted to cross-check the overall design. One method was through computer simulation modeling, and the other was static analysis of the system operation.
2. Computer simulation modeling was performed to predict the performance of various system configurations without having to build physical prototypes of these systems to test their performance.
3. A single-component design was not the best option, despite the relative simplicity and cost savings, as the free play in the mechanical joints and expansion of the hoses results in system response degradation.
4. Maximization of performance was obtained through deliberate oversizing of the components while staying within fixed interface requirements.
5. Simple effects, such as solar heating, can have a dramatic effect on system operation and should not be overlooked.
6. System-level evaluation of the entire design must be conducted to preclude such problems as the TCO pneumatic system pressure rise and handling difficulties.

### **Test/Installation Aspects**

1. System performance could be monitored through the use of pressure gauges rather than elaborate indicating devices.
2. The effects of volumetric imbalance and temperature effects were minimized by the large piston area, which resulted in a minimal vertical displacement.
3. After deciding on a system configuration, building a prototype test setup was beneficial in that crucial design assumptions of flow and pressure effects could be laboratory-tested to verify computer predictions.
4. An auxiliary cylinder can be used to verify the quality of a hydraulic system fill and bleed.
5. Fabrication of a full-scale wooden mock-up ensured a perfect fit of the components prior to the deliverable hardware arrival at the site installation.

### **CONCLUSION**

The redesign project of the LSS was successfully completed in a very short period of time. The LSS was conceived in January 1989. The design/fabrication contract was awarded in June 1989, and fully fabricated and tested hardware was delivered by August 1990. In short, a program that should have taken two to three years to design and develop was conducted successfully in just over a year and a half.

At this time, four LSS units have been fabricated. Two units have been acceptance tested and delivered to Cape Canaveral Launch Complex 36A and 36B to support upcoming Atlas II launches. A third system is intended as a spare unit and the remaining system is currently undergoing extensive qualification testing.

### **ACKNOWLEDGEMENTS**

The LSS was developed for the Air Force, Atlas II, Medium Launch Vehicle II (MLV II) contract. The prime contractor was General Dynamics Space Systems Division (GDSS) with a subcontract to Hydraulic Research-Textron Corporation (HRT). The bulk of the design, development, and test effort was performed by HRT under close supervision by GDSS. The author wishes to express his appreciation for the design contributions and assistance provided by all the personnel associated with the LSS redesign project at both GDSS and HRT, especially J.G. Bodle and N.C. Burns of GDSS and N.T. Jenkins of HRT.

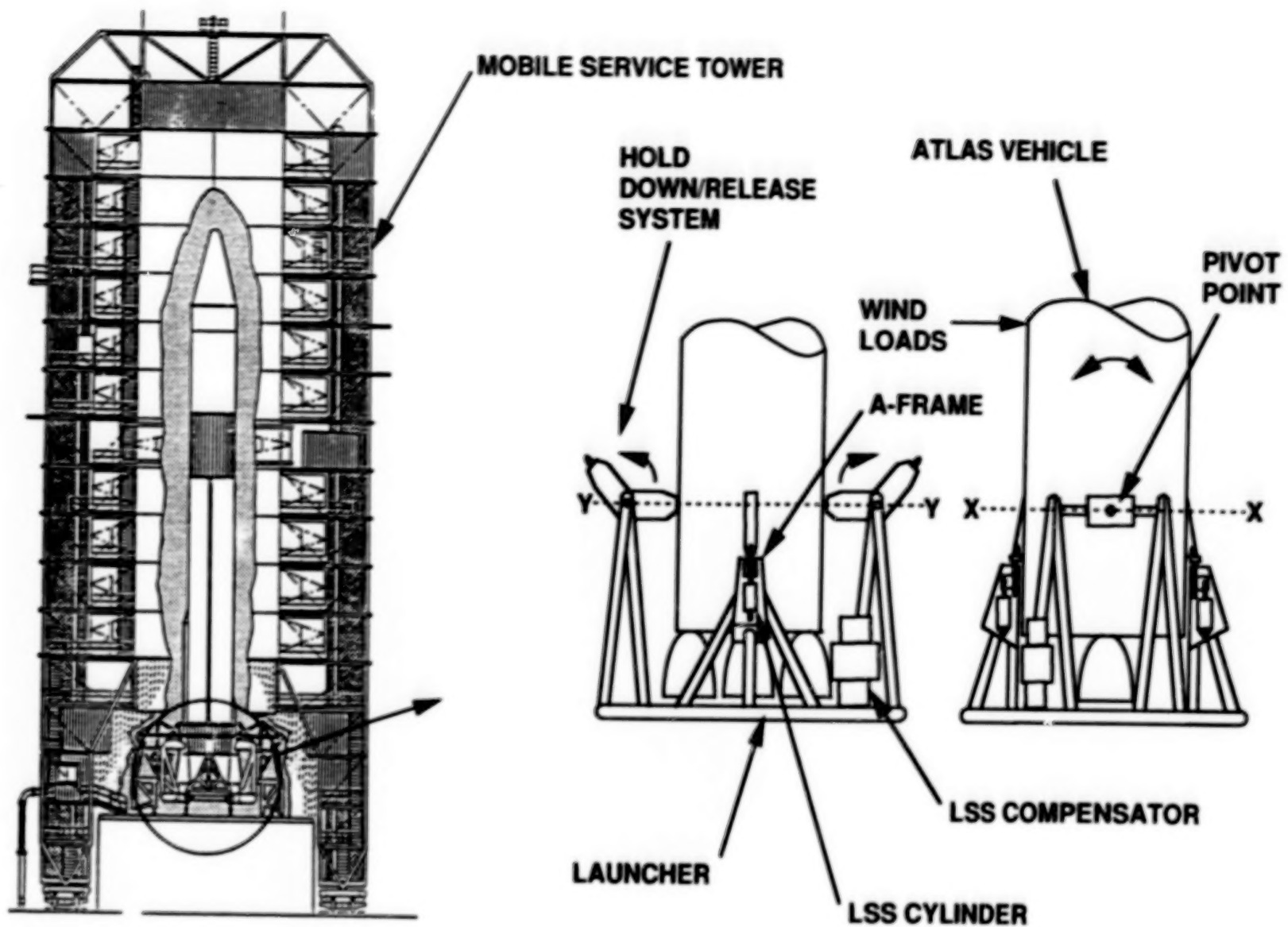


Figure 1. Atlas Ground Launcher System

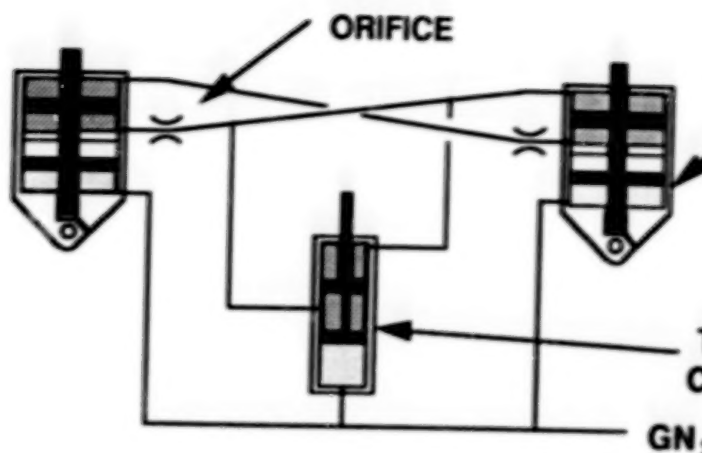


Figure 2A. Previous LSS Schematic

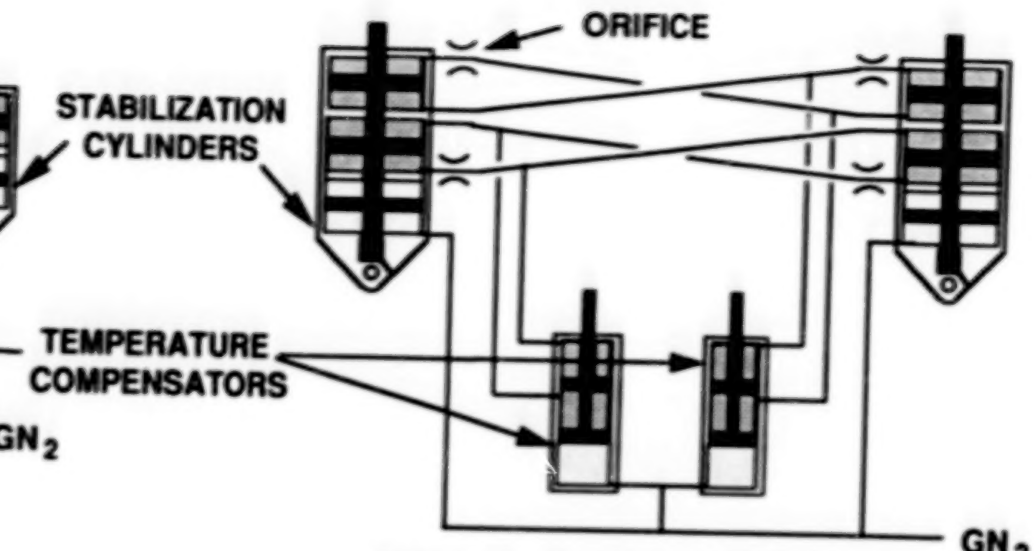


Figure 2B. Proposed LSS Schematic

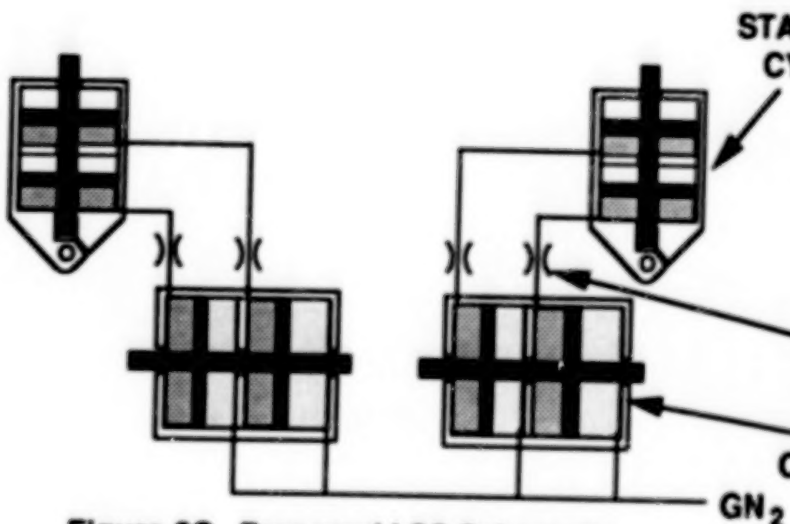


Figure 2C. Proposed LSS Schematic

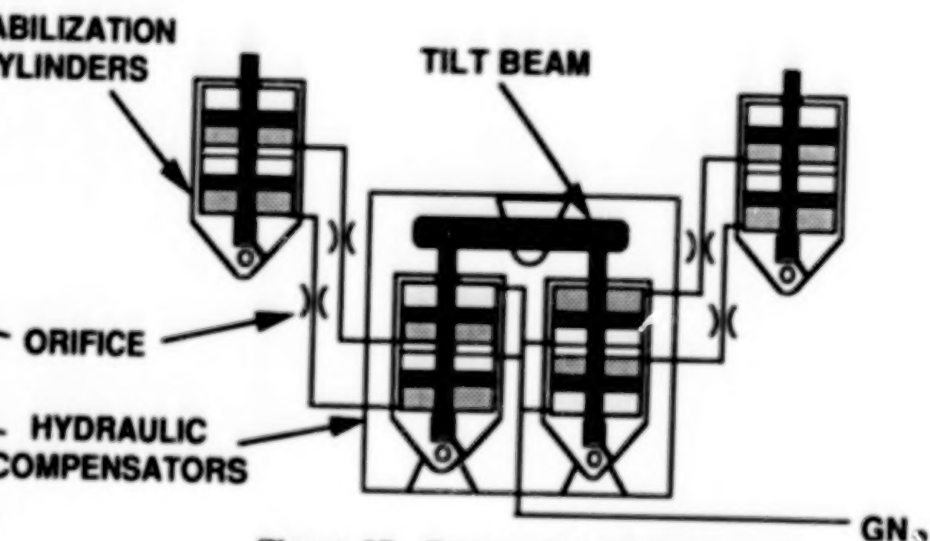
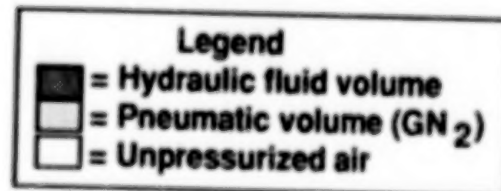


Figure 2D. Proposed LSS Schematic



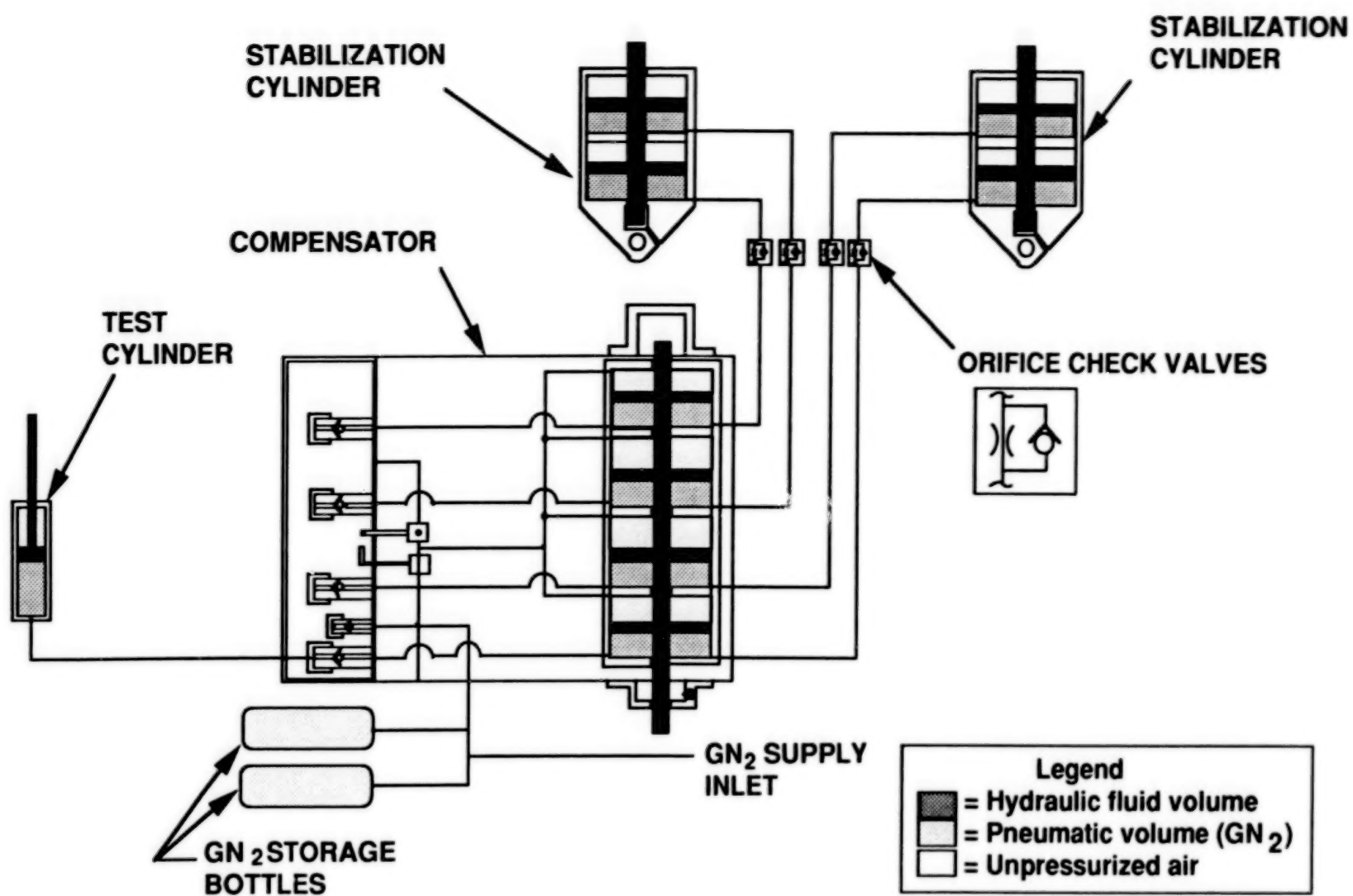


Figure 3. New LSS schematic

37

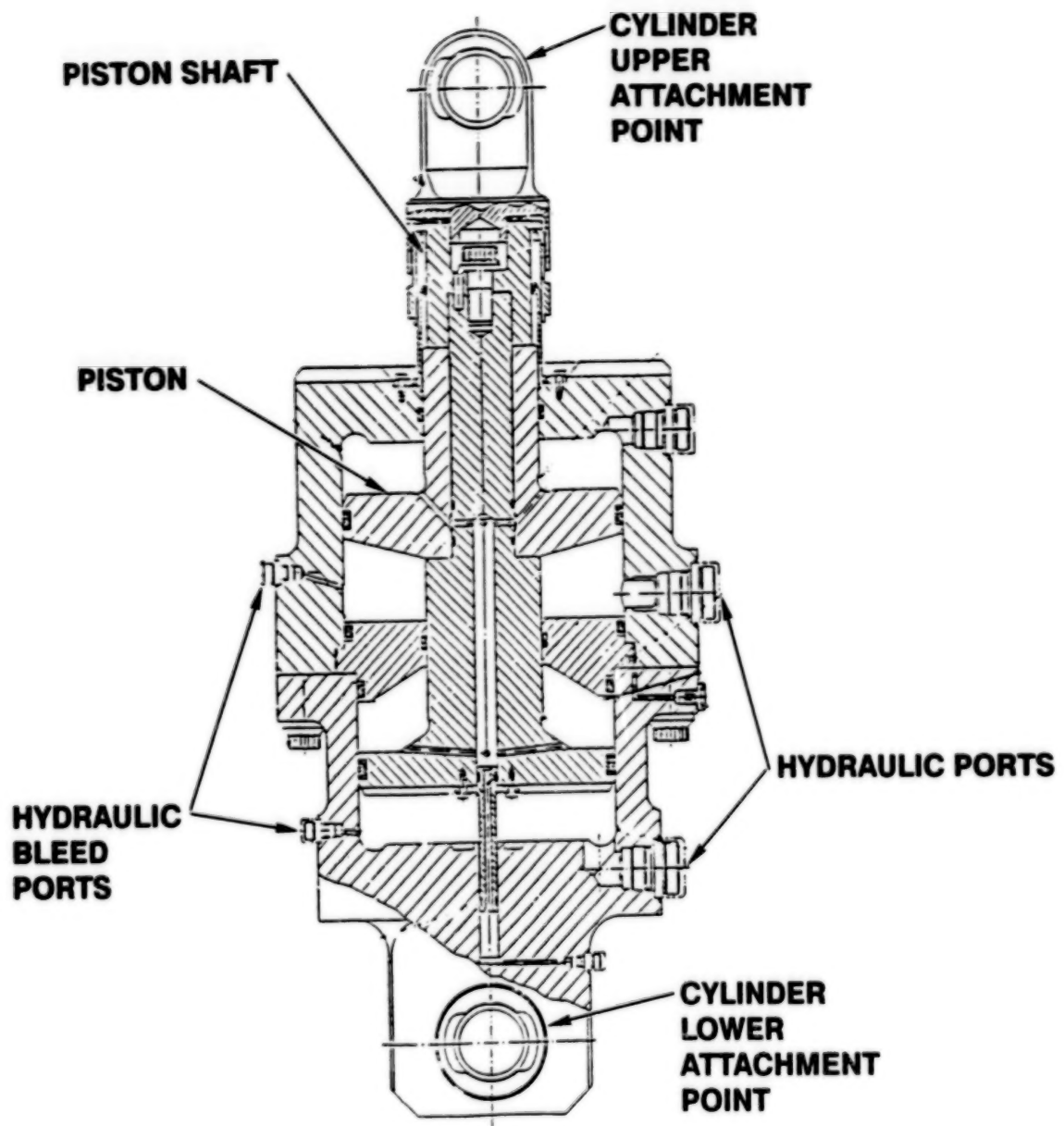
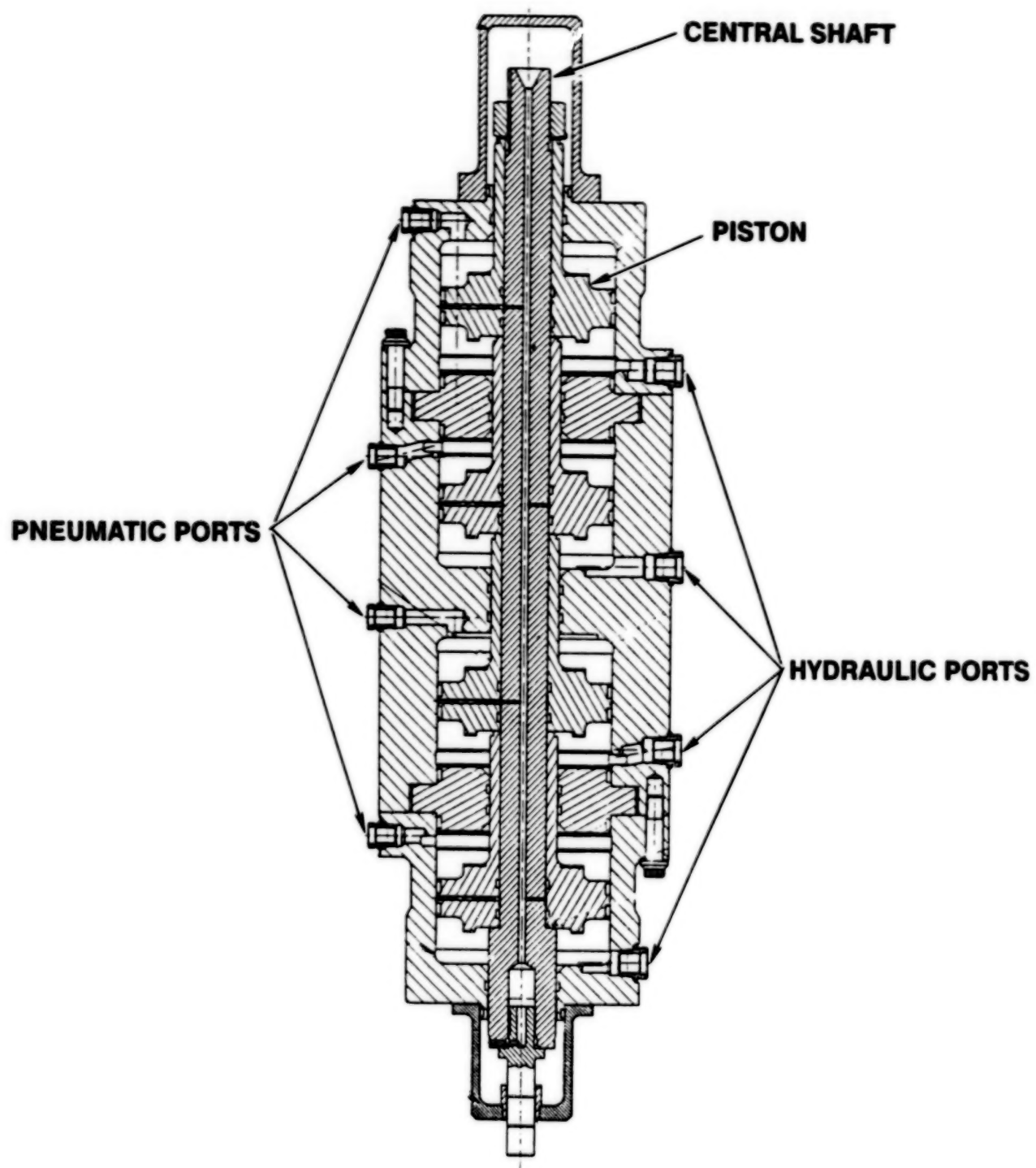


Figure 4. LSS cylinder assembly



**Figure 5. LSS compensator assembly**

## Brake Lock Mechanism for the Two Axis Pointing System

Alan Posey\*, Mike Clark\*, and Larry Mignosa\*\*

### ABSTRACT

Six months prior to shipment of the Broad Band X-Ray Telescope to the Kennedy Space Center for flight aboard the space shuttle Columbia, a major system failure occurred. During modal survey testing of the telescope's gimbal pointing system, the roll axis brake unexpectedly released. Low-level vibration and static preloads present during the modal survey were within the expected flight environment. Brake release during shuttle liftoff or ascent was an unacceptable risk to mission success; thus, a Brake Lock Mechanism (BLM) was developed.

### INTRODUCTION

The BLM was developed to correct a design problem identified during ground testing of a space shuttle payload. The Broadband X-Ray Telescope (BBXRT) is a Goddard Space Flight Center (GSFC) attached shuttle payload that is part of the National Space Transportation System STS-35 ASTRO-1 Mission, which flew successfully on board the shuttle Columbia in December 1990 (Figure 1). Six months prior to shipment of the payload to the launch site at the Kennedy Space Center, a major system failure occurred. This failure would have resulted in significant loss of BBXRT science if it had occurred during shuttle liftoff or ascent.

The BBXRT payload is composed of three major subsystems: the Two Axis Pointing System (TAPS), the TAPS Support Structure (TSS), and the BBXRT instrument (Figure 2). The TSS is an across-the-bay carrier that supports the TAPS and provides the payload mechanical interface to the shuttle cargo bay. The TAPS supports the BBXRT instrument and provides two axis (roll and pitch) arc minute class pointing capability. The TAPS was built by Space Data Corporation, while the TSS and the BBXRT were built in-house at GSFC.

The TAPS' primary structure consists of an outer gimbal frame, an inner gimbal frame, and two Drive Brake Modules (DBM) as shown in Figure 3. The outer gimbal frame houses the pitch DBM and idler module. The inner gimbal frame

---

\* NASA/Goddard Space Flight Center, Greenbelt, MD  
\*\* Swales and Associates, Inc., Beltsville, MD

houses the roll DBM and idler module and attaches to the outer frame at the pitch DBM and idler module. The roll axis DBM and idler module are the mechanical interfaces to the BBXRT instrument.

The DBMs restrain the system during shuttle liftoff/ascent and descent/landing events and control system rotation for on-orbit instrument pointing operations. The braking function is accomplished with a rotating gear plate attached to the drive shaft and a translating gear plate restrained in rotation by its tangs and the DBM housing (Figure 4). Each gear plate has 45 teeth that engage every 8 degrees over the normal operating slew range of + / - 20 degrees (Figure 5). The gear teeth have 8 degree sloped sides and a nominal engagement of 2 mm (0.080 in). The translating gear plate is preloaded with four springs to provide positive engagement with the rotating gear plate, thus preventing system rotation. To release the gear plates, power is supplied to a solenoid that retracts the translating gear plate from the rotating plate and holds it there against the force of the springs.

If a TAPS brake were to fail during flight, a Backup Landing Lock (BULL) would safely capture and dissipate the kinetic energy of the freely rotating system. This system failure presents no safety hazards to vehicle or crew. The BULL, however, cannot be released on-orbit and engagement of this backup system would result in significant loss of BBXRT science.

Ground testing at GSFC included a modal survey on the TAPS flight spare unit using low-level mechanical vibration to measure and record its structural dynamic characteristics. A static torsional preload was applied to each DBM to remove nonlinear system responses generated by backlash in the translating gear plate. Under the combined torsional static preload and low-level axial vibration loads, the inner frame brake unexpectedly disengaged and the freely rotating system was captured in the BULL. Since these applied loads were similar in nature to the Space Transportation System (STS) flight environment, it was evident that this failure could occur during shuttle liftoff or ascent.

A TAPS brake failure during shuttle liftoff or ascent was an unacceptable risk to mission success and a hardware change was required. Payload development and launch schedule constraints would not allow DBM disassembly. The design fix had to be accomplished on the TAPS flight unit with the payload in the full-up flight configuration and without disruption to payload Integration and Test activities.

A multi-phase recovery plan was implemented to investigate and determine the cause of the brake failure, to design a mechanism that would preclude unintentional brake release, and to qualify the mechanism for STS flight. The DBM is a large mechanism located in the primary structural load path. Tests and analyses performed to understand the failure demonstrated the sensitivity of DBM gear plate motion to simultaneously applied static and dynamic loading conditions. This implied that flight level static and dynamic loads had to be applied

simultaneously to properly qualify the mechanism.

## INVESTIGATION OF BRAKE RELEASE

A Phase 1 test program was developed and executed to determine the cause of the brake release. Phase 1 tests were performed with TAPS in the modal survey facility using a range of flight-like static torques between 339 N-m (3000 in-lb) and 2260 N-m (20,000 in-lb) applied to both the inner and outer frame DBMs. Low-level dynamic axial loads were applied as a sinusoidal sweep. Motion of the translating gear plates was monitored throughout the test. Results for the inner frame DBM indicated incremental axial displacement of the translating gear plate relative to the rotating gear plate at static torques greater than 339 N-m (3000 in-lb). This gear plate "walking" behavior consistently led to complete disengagement at a static torque of 2260 N-m (20,000 in-lb). It was noted that these static torque values were well within the expected range of liftoff and ascent values. The translating gear plate for the outer frame DBM showed no significant motion and never released for the range of applied static torques. The translating gear plate for the inner frame DBM consistently moved when the frequency of the sine sweep reached the fundamental modes of the inner frame structure. The fundamental mode of the outer frame structure was much higher, resulting in a lower force transmitted to the DBM. Therefore, the brake release phenomenon appeared to be a function of displacement caused by an applied axial force and not resonances internal to the DBM.

Phase 1 testing confirmed that static torques and dynamic axial loads are critical to the gear plate "walking" phenomenon. It was apparent that the 8 degree sloped sides of the gear teeth allow the two plates to move in unison when friction at the translating gear plate tangs is overcome. When the applied axial force is reversed, the translating gear plate remains in its displaced position. Figure 6 shows the free body diagram of the translating gear plate and Equation 1 solves for the axial force required to displace this plate. For the translating plate to walk

$$A = T\mu/R2 + S \quad (1)$$

Where:  
A = axial force  
T = static torque  
S = spring force  
 $\mu$  = coefficient of friction  
R2 = radius at tangs

back, the applied axial force must overcome both the friction force at the tangs, due to static torque, and the preload spring force. If at any time during the dynamic cycle the force along the tooth surface exceeds the friction force, the teeth

slip and motion of the translating gear plate is stopped. Equation 2 can be solved for A to determine the axial force required for the gear teeth to slip. Figure 7 shows the region of brake release as a function of static torque and axial force. The upper line in Figure 7, defined by Equation 1, represents the axial force required to displace the translating gear plate. The lower line, defined by Equation 2, represents the axial force required for the gear teeth to slip.

$$A\mu \sin\alpha + (T\mu/R1) \cos\alpha = A \cos\alpha - (T/R1) \sin\alpha \quad (2)$$

Where:  $\alpha$  = tooth angle  
R1 = radius at teeth

Measurements were performed to define the axial and torsional stiffness of the inner and outer frame DBMs for both the flight and flight spare units. The axial loads were cycled twice from + to - 17800 N (4000 lb) and the torsional loads were cycled twice from + to - 3390 N-m (30,000 in-lb). The axial load was approximately 70% and the torsional load approximately 20% of the maximum expected flight loads. Stiffness test results showed wide variation of axial and torsional stiffness for each DBM as shown in Figure 8. Note that the critical direction for gear plate disengagement is the negative axial force direction indicated on the plots. These wide variations were caused by a lack of adequate preload on the DBM bearings. It was noted that the DBM which consistently released during Phase 1 testing was also the most flexible in the axial direction. This flexibility allowed the translating gear plate to displace a greater amount during each dynamic load cycle. Axial and torsional dead bands were also measured. The axial dead band was negligible and the torsional dead band or backlash was as expected.

#### BRAKE LOCK MECHANISM DESIGN

Investigation of the DBM design identified a simple and reliable concept that would increase the preload spring forces in Equation 1. The BLM design incorporates very few moving parts and extremely reliable pyrotechnic pin pullers (Figure 9).

Various options were investigated before settling on the final design. Motor/gear-driven mechanisms, redesigned gear plates and on-orbit relatch capabilities were considered. Motor/gear-driven mechanisms were avoided because of their added complexity and reduced reliability. Gear plate redesigns would require deintegration of the flight-configured payload and disassembly of the flight DBMs. This was considered a noncredible option due to launch schedule constraints. Phase 1 testing identified the magnitude of applied static torque as a determining factor for brake disengagement. It was thought that low static

decelerations during STS descent and landing would not generate the magnitude of static torque necessary to cause brake release. Therefore, an on-orbit relatch capability was not included in the baseline design. This conclusion would be verified during Phase 2 qualification testing.

The original DBM design employed four equally spaced compression springs to preload the translating gear plate against the rotating plate. Both plates had 2.0 mm (0.080 in) deep gear teeth which meshed every 8 degrees. Externally accessible set screws were used to adjust the spring forces to 98 N (22 lb) each for a total preload of 392 N (88 lb). Once on orbit, the solenoid would pull the translating gear plate against the preload springs, releasing the gimbal to rotate. When power was removed, the solenoid was deenergized, and the preload springs reengaged the translating gear plate with the rotating plate.

The BLM design took advantage of the set screw holes to gain access to the translating gear plate without disassembly of the DBM. Two of the four set screws (located 180 degrees apart) were replaced with two phosphor bronze push rod guides having a 3/8-24 external thread and a 4.8 mm (0.188 in) diameter bore through the center. A stainless steel push rod, burnished with a solid film lubricant, was installed in the push rod guide prior to the guide being threaded into the DBM aft housing. The push rods were held in place by pyrotechnic pin pullers which in turn were held in position by an aluminum pin puller bracket that was bolted to the DBM aft housing. Each pin puller bracket was individually shimmed into position so that, when the pin pullers were installed, the push rods compressed the preload springs to about .25 mm (0.010 in) above their solid height.

The solidly compressed springs restrained the translating gear plate and prevented the "walking" action previously observed. Once on orbit, the pin pullers would be fired to release the push rods. The push rod guides were shimmed and set so that after the push rods were released the preload springs would retract to their originally designed positions (392 N preload). When the preload springs were released, the solenoid could be activated, thus retracting the translating gear plate and allowing the gimbal to operate.

For added redundancy, the BLM was made compatible for an Extra Vehicular Activity. If a pin puller failed to fire on orbit, an STS crewmember could release the push rods by loosening three bolts and rotating the bracket until the pin puller no longer contacted the push rod.

#### FLIGHT LOAD DETERMINATION

Phase 1 testing showed that the brake release phenomenon is sensitive to static torque and dynamic axial loading conditions. Dynamic torques were also included due to their uncertain effect on brake motion. Expected flight loads were

derived for the Phase 2 qualification test program using actual flight data measured on STS-26 and coupled loads analysis data for STS-35. The STS steady state thrust acceleration profile for liftoff and ascent is shown in Figure 10. The steady state thrust reaches a maximum of 1.5 G's during the high dynamic transient liftoff event and approximately 3 G's during main engine cutoff (MECO). The center of gravity of the BBXRT instrument shifts as the argon in the cryogenic coolers at the bottom of the instrument boils off, and can range 12.7 cm (5.0 in) on either side of the instrument center of rotation. This offset center of gravity and steady state thrust acceleration provide a static torque, to the outer frame DBM, during the liftoff and ascent stages of flight. As the static torque increases during ascent, the expected dynamic axial force is reduced. The dynamic axial load is 17800 N (4000 lb) during liftoff with a 1220 N-m (10800 in-lb) static torque. When the steady state thrust load and static torque reach a maximum, the expected dynamic axial load is only 2980 N (670 lb). The inner frame DBM is oriented in the shuttle thrust direction and is subject to high axial loads but insignificant static torques.

STS descent and landing also provide a steady state load environment in the shuttle thrust direction. The maximum steady state deceleration during STS-26 descent and landing was approximately .4 G and occurred after reentry, approximately five minutes before main gear touchdown. The resulting static torque for descent and landing was much lower than the static torque developed during liftoff and ascent; however, it was still high enough at 339 N-m (3000 in-lb) to be a concern. Phase 1 tests showed gear plate motion for this same static torque. A summary of flight load data for the entire flight sequence is shown in Table 1.

#### BLM QUALIFICATION TESTING

Qualification testing of the BLM was performed at the environmental test facilities of GSFC during August 1989. The purpose of the testing program was to qualify the prototypical BLM units for flight by subjecting the units to the expected flight environment while installed on the flight spare DBMs.

#### Test Set-up

Physical size limitations of the 1361 kg (3000 lb) flight spare TAPS prevented system-level testing as a complete unit. As a result, each DBM was removed and installed in a test fixture. The test fixture and test set-up are shown in Figure 11. The DBM and test fixture were mounted to the primary (155,700 N/35,000 lb) electrodynamic shaker slip table and a 907 kg (2000 lb) mass simulator was bolted to the DBM drive shaft. The center of gravity of the mass was centered on the drive shaft. A bracket was mounted at one end of the mass to which a bungee

cord was attached. In-line with the bungee, a turnbuckle and crane scale were installed to apply and monitor the static torque. A square tube was welded to the other end of the mass simulator and a 1.8 m (6.0 ft) long shaker stinger was attached. The stinger was attached at the opposite end to an auxiliary (1100 N/250 lb) electrodynamic shaker. The long stinger provided isolation between slip table movement and the auxiliary shaker.

The test fixture was skewed 30 degrees to the primary shaker axis so that sinusoidal acceleration of the 907 kg (2000 lb) mass produced both dynamic axial and shear loads. Static and dynamic torques were applied with the bungee cord and auxiliary shaker, respectively. High levels of dynamic torque were possible by dwelling at the torsional resonance of the DBM drive shaft. Various combinations of dynamic axial loads and dynamic and static torques were simultaneously applied to the DBMs. The test levels were derived from actual flight load data for the entire flight sequence as shown in Table 1. The actual test levels included a 1.25 test factor on all the maximum expected flight levels. The test load cases are presented in Table 2.

Three Linear Variable Differential Transformers (LVDT) were mounted to the DBM aft housing with probes penetrating through the housing and contacting the translating gear plate. The LVDTs measured movement of the translating gear plate relative to the aft housing so that translating gear plate motion could be monitored during the test.

Each BLM push rod was instrumented with two back-to-back uniaxial strain gages. Prior to qualification testing, the push rod/strain gage assemblies were calibrated in compression to indicate load as a function of average strain. During the qualification testing, each back-to-back strain gage pair was averaged and the output force displayed. The push rod loads were monitored very carefully during the test to determine if the induced side loads on the pin pullers would exceed their allowable design limit loads. Seven accelerometers monitored the acceleration of the mass simulator by which the dynamically induced loads could be controlled.

#### Test Sequence

Prior to installation of the BLM, the DBMs were subjected to the liftoff and ascent load cases shown in Table 2 to demonstrate that at least one of these load cases would cause the brake plates to disengage. After the brake disengaged, it was reset, the BLM was installed and the tests were repeated. Following completion of the liftoff and ascent load cases, a prototypical level random vibration test was performed. The load case causing the most gear plate displacement without the BLM in place was then re-run to obtain a worst case side load on the pin puller. The pin pullers were then fired and the descent/landing load cases run with the preload springs in their as-designed positions. Post-test functional checks were performed to demonstrate that DBM performance requirements were

maintained.

The actual test start-up sequence for each load case began by applying the required static torque. The auxiliary shaker excitation frequency was then manually adjusted from below the DBM drive shaft torsional resonance upward until the excitation frequency was identical to the DBM torsional resonance. Once at resonance, the auxiliary shaker drive current was increased until the desired dynamic torque was attained. High levels of dynamic torque were difficult to attain due to the nonlinearities of the system. When the torsional resonance was dwelled at, and the input level increased, the system would sometimes detune and fall off the resonance, resulting in a drop in the dynamic torque. When the dynamic torque reached an acceptable level, the primary (155,700 N/35,000 lb) electrodynamic shaker was energized. The primary shaker profile was a below resonance sine dwell at 15 hz for 30 seconds and at an appropriate level to achieve the desired dynamic axial force induced by acceleration of the mass simulator.

### Test Results

Prior to installing the BLM, high static torque load cases 1A2 and 1A3 resulted in gear plate disengagement on both inner and outer frame DBMs. Typical LVDT responses for this event are shown in Figure 12. With the BLM in place, the translating gear plate was successfully restrained for all liftoff and ascent load cases. Load cases 1A2 and 1A3 caused only 0.5 mm displacement of the translating plate with respect to the rotating plate before the BLM stopped further motion (see Figure 13). Low static torque load case 1A1 caused insignificant displacement of the translating gear plate.

Push rod strain gage data indicated that the maximum side load in the pin puller was only 355 N (80 lb), which is well below the allowable side load of 4000 N (900 lb). After this maximum side load was attained, the pyrotechnic pin pullers were fired, releasing the preload springs to their on-orbit operational position. This completed qualification of the BLM for shuttle liftoff and ascent.

Descent and landing load cases caused insignificant motion of the translating gear plate. Typical LVDT data for these load cases is shown in Figure 14. Since the brake did not disengage during any of the descent and landing load cases, a mechanism to re-lock the gear plates was not required.

Some of the higher levels of dynamic torque were not attainable with the test setup due to the lower than expected amplification factor. The highest target dynamic torque was 20,340 N-m (180,000 in-lb) and the highest level attained was 13,000 N-m (115,000 in-lb). This was acceptable because test results indicated that dynamic torque tended to reseat the translating gear plate.

## CONCLUSION AND SUMMARY

Unexpected release of the roll axis brake during the TAPS modal survey testing dictated the need for a design change. A multi-phase recovery plan began with a series of tests to understand the brake failure. Magnitude of static torque and dynamic axial force was identified as a key factor. Simultaneous application of static torque and axial forces to the DBM drive shaft caused the translating gear plate to incrementally displace, or "walk," with respect to the rotating gear plate. Loading conditions that caused the gear plates to separate were representative of the expected flight environment. In parallel with these tests, the BLM was developed to ensure positive gear plate engagement during shuttle liftoff and ascent. Mechanism qualification tests reflected a complex set of simultaneously applied static and dynamic forces to accurately represent the expected flight environment. Without the BLM, the tests consistently demonstrated gear plate walking and eventual disengagement for the high static torque liftoff and ascent load cases. With the BLM in place, the tests conclusively demonstrated that gear plate release was prevented. The translating gear plate showed no significant motion for descent and landing load cases; therefore, a mechanism to re-lock the gear plates was not required.

Analyses and tests performed during execution of the recovery plan resulted in the following lessons learned for future payload and mechanism designs. The wide variation of DBM stiffness measurements was due to inadequate preload on the bearings. Proper bearing preload would not prevent the "walking" phenomenon; however, the displacement of the translating gear plate during each dynamic load cycle would be reduced, which in turn would delay the brake release process. The DBM is a large mechanism located in the primary structural load path. Carrying structural loads through a mechanism that, by definition, is designed to move is not recommended. An improved design would incorporate a true structural load path that could be disabled on orbit to allow normal system operations. Structures are often tested with an equivalent set of loads to represent the combined action of static and dynamic forces. When mechanisms are located in the primary structural load path, verification testing must account for the proper combinations of simultaneously applied static and dynamic loads.

## ACKNOWLEDGEMENT

The authors wish to acknowledge and express their appreciation to Ed Devine and Joe O'Connor of Swales and Associates, Inc. for their support and guidance during the design and development of the RLM. Without their invaluable support, it is unlikely that the severe schedule constraint for shipment of the BBXRT payload to the launch site would have been met.

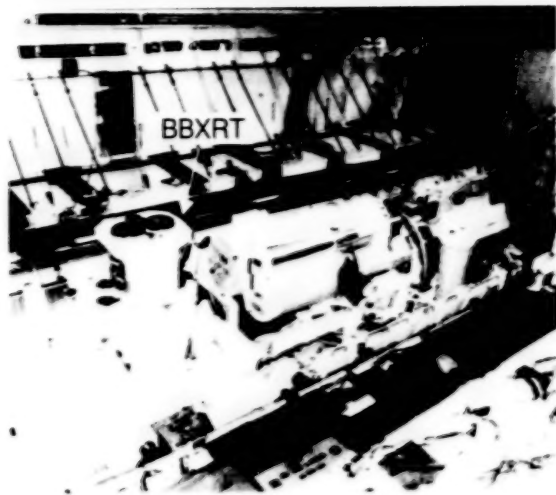
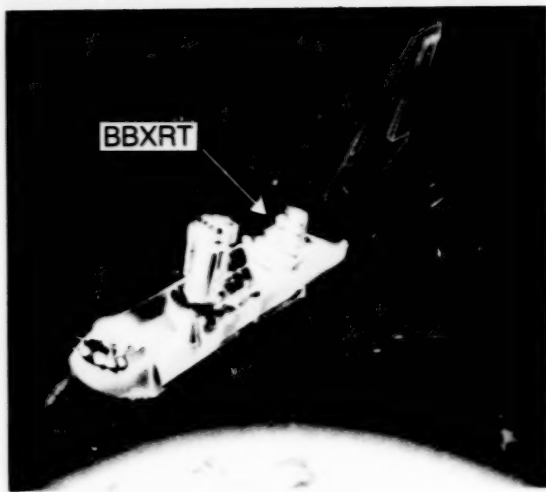


**Figure 1 - STS-35 ASTRO-1 Mission**

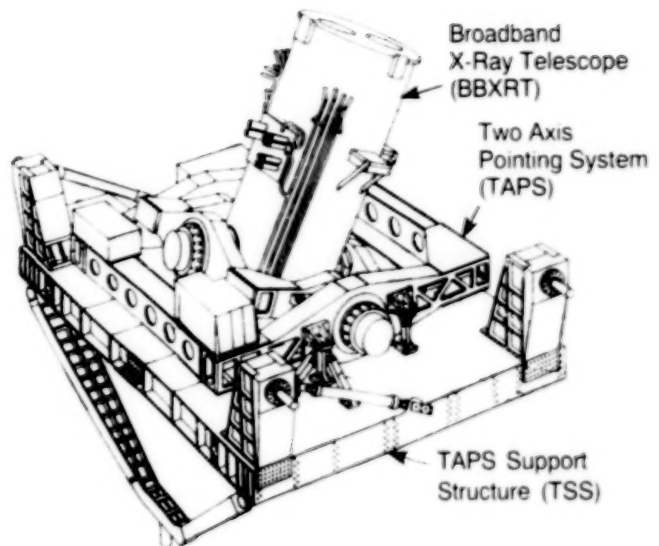
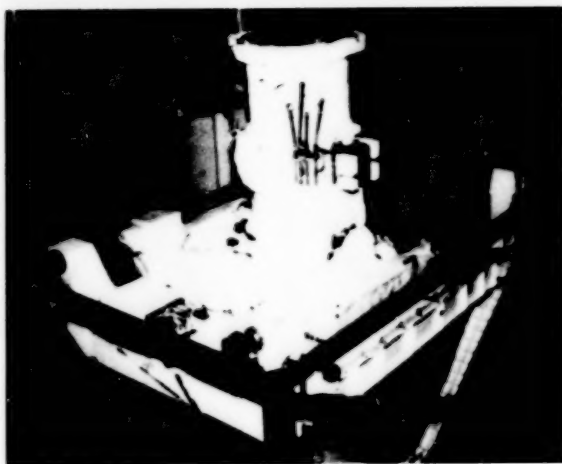


**Figure 2 - BBXRT Payload Flight Configuration**

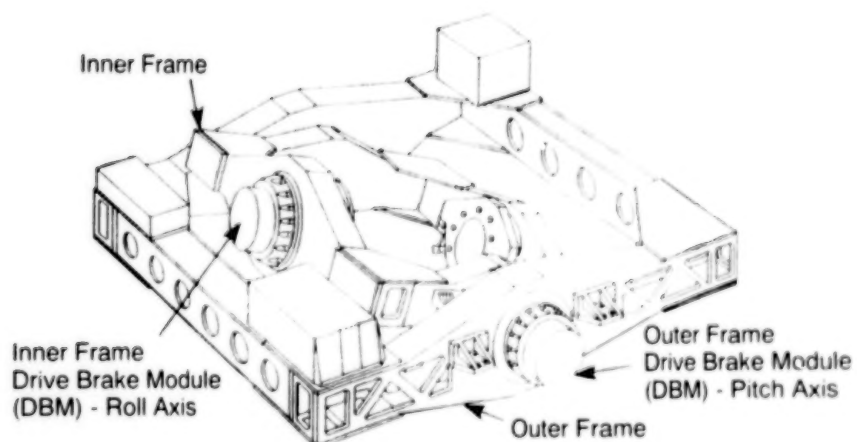


**Figure 3 - Two Axis Pointing System (TAPS)**

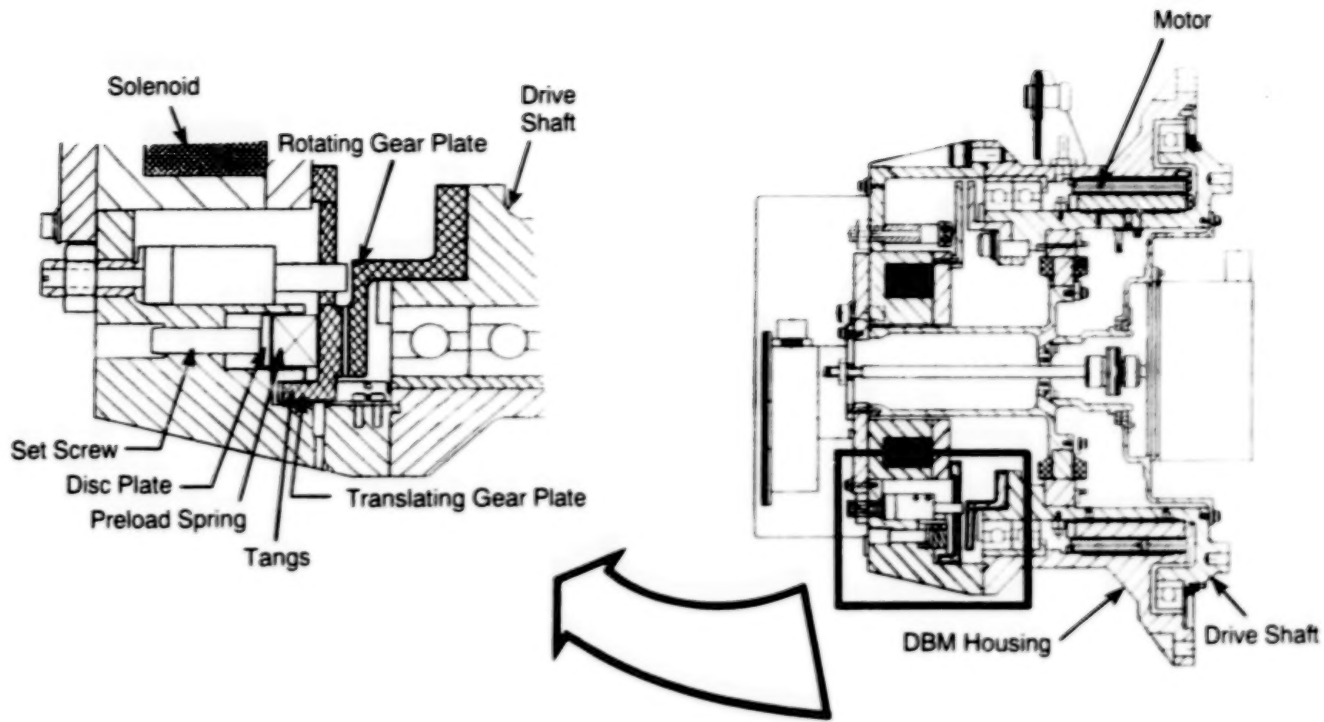


**Figure 4 - Drive Brake Module (DBM) Cross Section**



**Figure 5 - DBM Translating and Rotating Gear Plates**

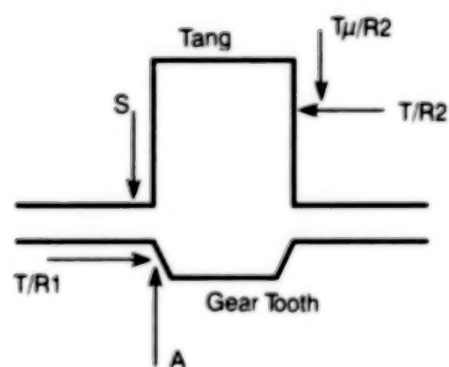


**Figure 6 - Free Body Diagram of Translating Gear Plate**



**Figure 7 - Gear Plate Release as a Function of Static Torque and Axial Force**

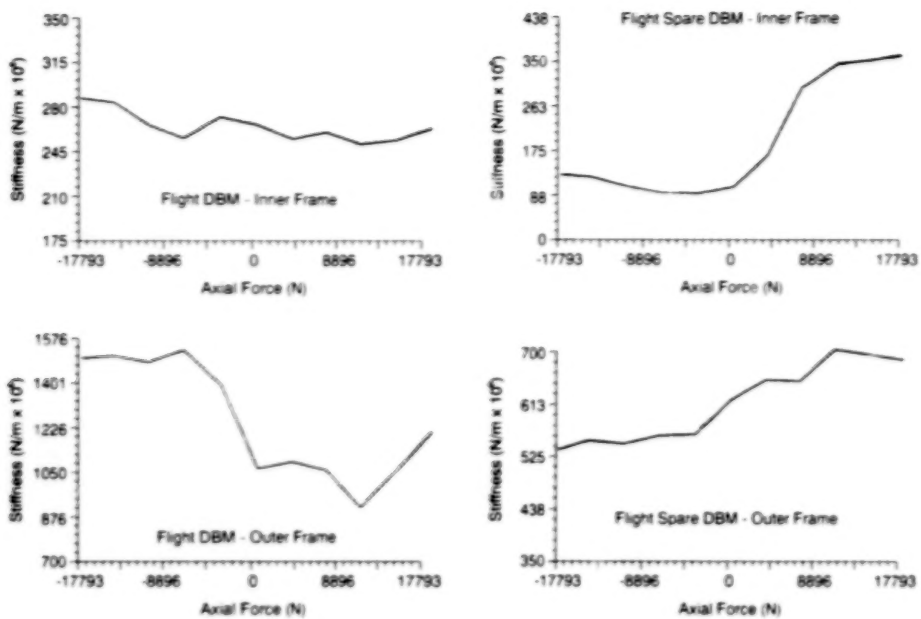


**Figure 8 - Results of Drive Brake Module (DBM) Axial Stiffness Measurements**

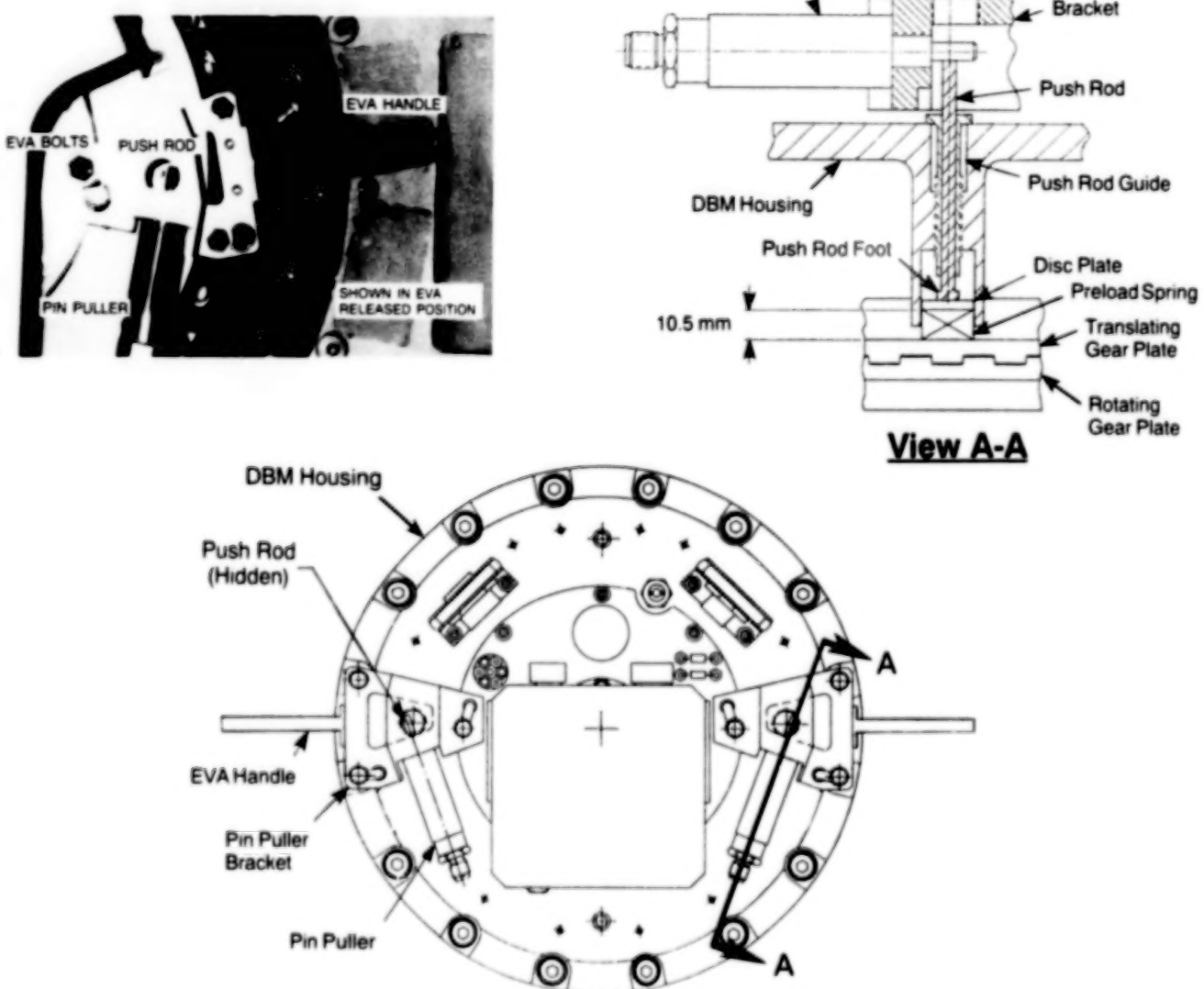


**Figure 9 - Brake Lock Mechanism (BLM)**

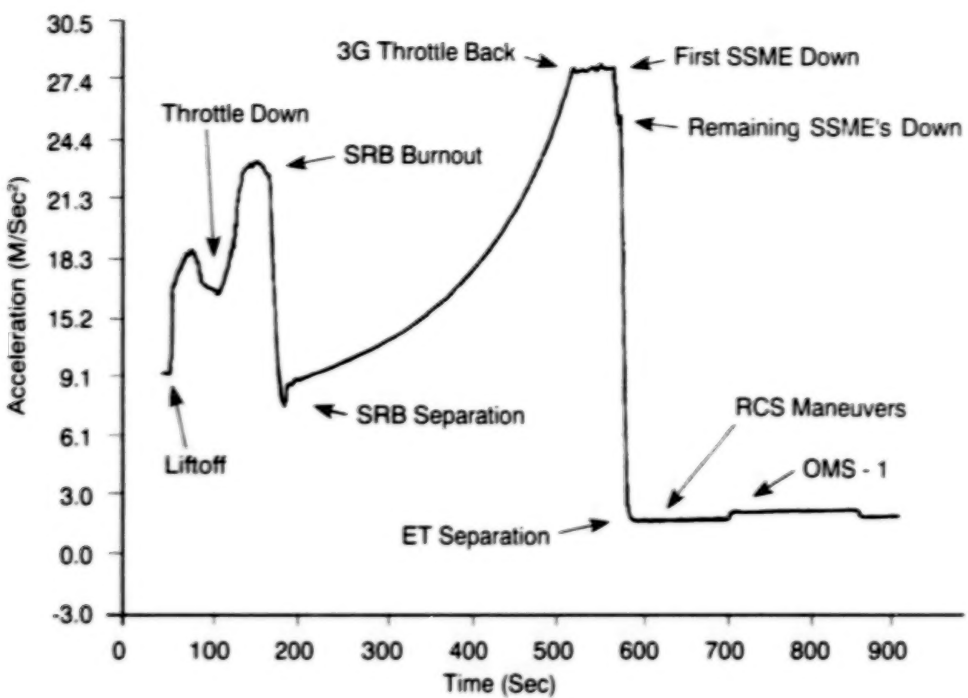


**Figure 10 - Steady State Thrust Acceleration Profile for STS Liftoff and Ascent**

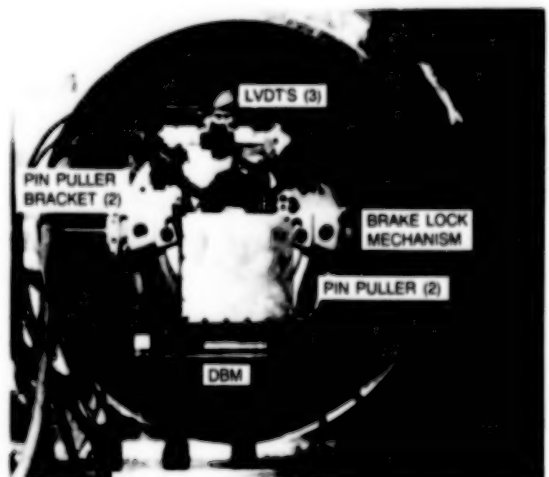
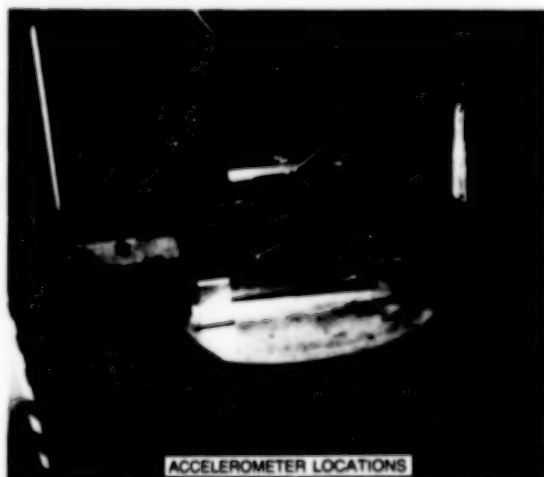
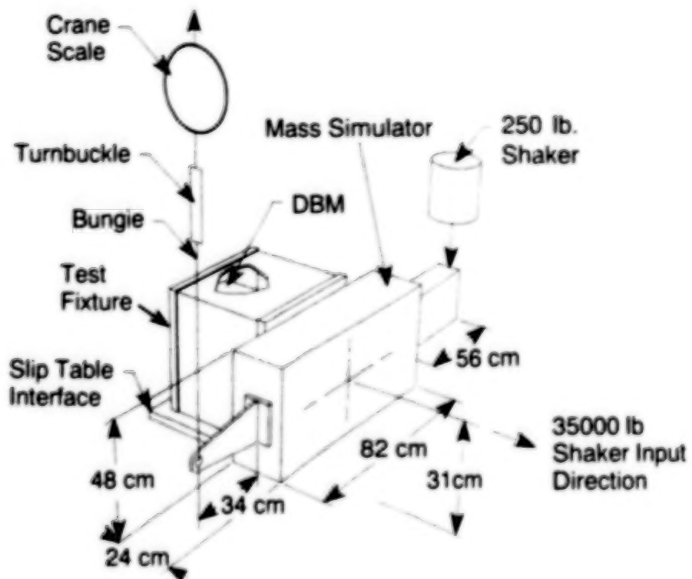


**Figure 11 - Phase 2 BLM Qualification Test Configuration**

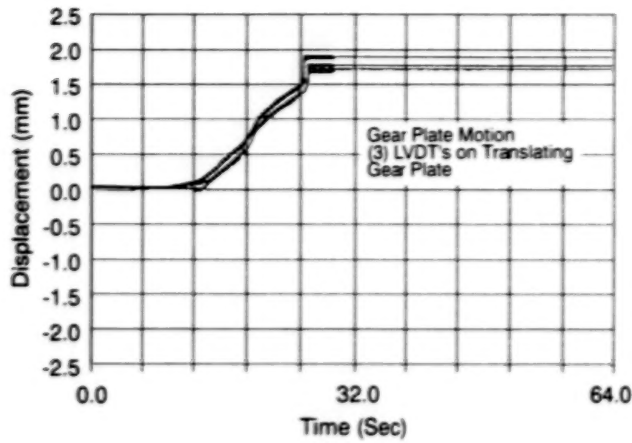


**Figure 12 - Translating Gear Plate Displacement for Liftoff and Ascent Load Case 1A3 - Without Brake Lock Mechanism**

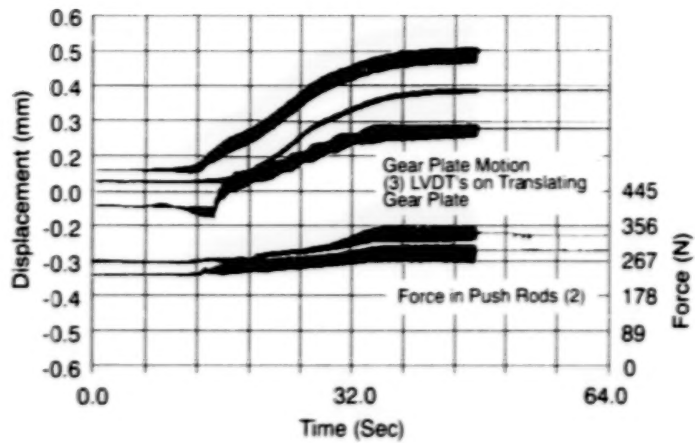


**Figure 13 - Translating Gear Plate Displacement and Forces in the Push Rods for Liftoff and Ascent Load Case 1A3 - With Brake Lock Mechanism**

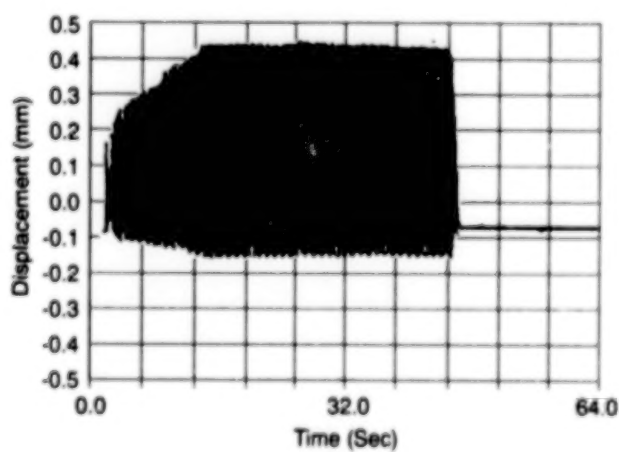
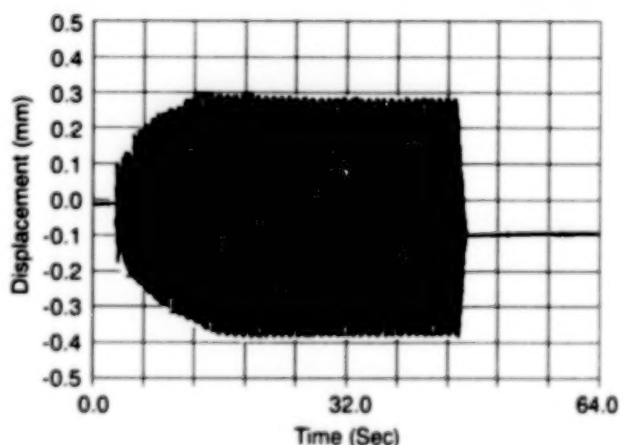
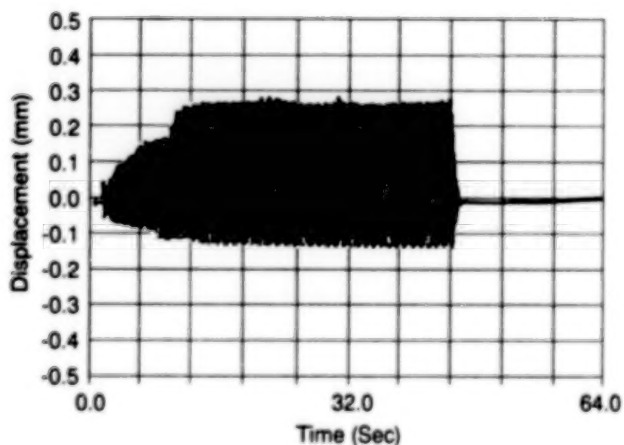


**Figure 14 - Translating Gear Plate Displacement for a Typical Descent and Landing Load Case - Without Brake Lock Mechanism**

**TABLE 1. PREDICTED FLIGHT LOADS FOR TAPS DRIVE BRAKE MODULES (DBM)**

EVENT	DBM	STATIC AXIAL (N)	DYNAMIC AXIAL (N)	STATIC TORQUE (N-m)	DYNAMIC TORQUE (N-m)
LIFTOFF	INNER	11565	20905	-	10168
	OUTER	-	17792	1220	14687
MAX. AERO PRESS.	INNER	15123	4893	-	5084
	OUTER	-	8896	1627	3445
MECO	INNER	24464	1423	-	1694
	OUTER	-	2980	2598	870
DECENT	INNER	1868	5782	124	13490
	OUTER	2224	23708	170	3389
LANDING	INNER	3558	38163	-	12428
	OUTER	-	33716	339	12880

**TABLE 2. PHASE 2 BLM QUALIFICATION TEST LOAD CASES<sup>1</sup>**

LOAD CASE NO.	DYNAMIC AXIAL (N)	STATIC TORQUE (N-m)	DYNAMIC TORQUE (N-m)
<b>LIFTOFF/ASCENT</b>			
1A1	22241	825	0
1A2	22241	1649	0
1A3	22241	2062	0
1B1	22241	825	9185
1B2	22241	1649	9185
1B3	22241	2062	9185
1C1	22241	825	17965
1C2	22241	1649	17965
1C3	22241	2062	17965
2A1	3736	1300	0
2A2	3736	2598	0
2A3	3736	3248	0
2B1	3736	1300	1059
2B2	3736	2598	1059
2B3	3736	3248	1059
<b>DECENT/LANDING</b>			
3A	47596	0	0
3B	47596	0	7773
3C	47596	0	15535
4A	42169	410	0
4B	42169	410	10168
4C	42169	410	20337

<sup>1</sup> These levels include a 1.25 test factor

**BLANK PAGE**

# AN ANTENNA-POINTING MECHANISM FOR THE ETS-VI K-BAND SINGLE ACCESS (KSA) ANTENNA

Noboru TAKADA\*

Takahiro AMANO\*\*, Toshiro OHHASHI\*\* and Shigeo WACHI\*\*

## Abstract

This paper describes both the design philosophy for the Antenna Pointing Mechanism (APM) to be used for the K-band Single Access (KSA) antenna system and experimental results of the APM's Engineering Model (EM) tests. The KSA antenna system will be flown on the Engineering Test Satellite VI (ETS-VI).

## I. Introduction

Recently, the requirements of data-relay satellite systems have been increasing. The Data Relay Tracking Satellite (DRTS) and some user satellites will be launched in the 1990s in Japan. The DRTS system will provide data-relay services between low-earth-orbit satellites and ground stations. A high bit-rate communications link is required to transmit the enormous amount of data (including image data), so pointing requirements for an antenna are becoming more stringent. The technology of acquiring and tracking low-earth-orbit satellites is also becoming more important. The KSA antenna system of ETS-VI is currently under development to establish the essential technology of DRTS for acquiring and tracking satellites. The mechanism to position the antenna in a desired direction forms one of the essential components of this technology. The engineering model of the APM for the ETS-VI KSA antenna has been designed, developed, integrated and tested.

The configuration of ETS-VI is shown in Figure 1. The KSA antenna is attached to the earth panel of the main body. The APM of the KSA positions the antenna about 2 axes to acquire the user satellite and the ground terminal, while providing the antenna position signal and physical support for the antenna.

The results of design trade-offs are shown in Table 1. For the APM, speed can be controlled by pulse rates; the antenna position can be determined by counting input pulses without the need for a fine angular displacement sensor; the antenna position can be held by the holding torque of a stepping motor without the need for a brake; and

\* Tsukuba Space Center, National Space Development Agency of Japan, 2-1-1, Sengen Tsukuba-shi, Ibaraki, 305 Japan

\*\* Toshiba Corporation, Komukai Works, 1, Toshiba-cho, Komukai, Saiwai-ku, Kawasaki-shi, Kanagawa, 210 Japan

the driving electronic circuit can be simple. So an APM using a stepping motor, a harmonic drive, and a position indicator was selected.

The APM consists of a two-axis gimbal. Only one axis of the Engineering Model of the APM (APM-EM) was planned to be manufactured to evaluate functionality. The mechanical configuration of the APM EM is shown in Figure 2.

The APM EM consists of

- A stepping motor, whose function is to rotate the antenna according to input pulses.
- A harmonic drive, whose function is to reduce the rotation angle and to increase the rotation torque of the stepping motor.
- A position indicator, whose function is to provide a position signal for the antenna.
- Bearings, which support the structure assembly.
- An electrical limit switch, whose function is to provide a stop signal in the case of exceeding the permitted limit for the rotation.
- Mechanical stoppers, whose function is to stop the rotation.
- A structure assembly, which supports the antenna and the above elements.

## 2. System Requirements for the APM

The system requirements for the APM are shown in Table 2. The maximum slew rate is the one required to acquire the low-orbit user satellite. The pointing range is determined by the need to cover the orbit of the user satellites. The step size is driven by the range of the Radio Frequency (RF) sensor and by other factors. The holding torque is necessary to prevent rotation of the KSA antenna at the time of the deployment and the firing of thrusters for the main body during attitude or orbit control. Maximum mass and electric power are also determined as a part of identifying system requirements.

## 3. Design of the APM

### 3.1 Design philosophy

The system requirements for a small step size is one of the most important specifications allowing the APM to achieve high pointing accuracy. To accomplish high pointing accuracy, the need to prevent alignment errors becomes very strict. Two sources of alignment errors are mentioned. One is static error and the other is dynamic error. The static error is almost negligible in rotating the APM about 2 axes. However, dynamic errors cannot be neglected. So the dynamic errors are considered in the design.

The alignment is influenced by the thermal environment. The clearance between the outer race of the bearing and the housing causes the alignment error. It is a result of the temperature range and the difference between the thermal expansion coefficient of the material of the bearing outer race and that of the housing material. The relation between temperature range and alignment error is shown in Figure 3. By using a titanium alloy housing, the alignment error is lessened even if the temperature range is wide. Also, the weight of the APM is reduced.

The torsional stiffness of the APM also influences the dynamic error. The stiffness of the APM was dominated by the stiffness of the harmonic drive. Therefore, the torsional stiffness of the harmonic drive was measured during performance testing.

### 3.2 Design of elements

The design of each element of the APM is described in the following section.

#### Harmonic drive

The harmonic drive is well known as a lightweight gear with a high reduction ratio. The configuration of the harmonic drive is shown in Figure 4. A good characteristic is that it has no backlash. This characteristic is suitable for the APM-required high pointing accuracy.

The design of the harmonic drive starts from a determination of required size. After considering the output torque of the APM, a CS-32-SP-type harmonic drive was selected. Though a high reduction ratio decreases the motor torque required, it also increases the pulse rate of the motor. A high reduction ratio also requires that the teeth of the gears be smaller, so manufacturing becomes difficult. The reduction ratio of the harmonic drive is 1/157. The lubricants used for the harmonic drive are shown in Table 3.

#### Stepping motor

In determining the specifications of the stepping motor, one must take into consideration the electrical power, the step angle, the output torque, the pulse rate, and the size. The specification for the motor is shown in Table 4. The electrical power is determined by the requirements of the APM. Both the step angle of the motor and the reduction ratio of the harmonic drive meet the pointing accuracy requirement. The output torque has two aspects. The first is the torque needed to rotate the moment of inertia of both the harmonic drive and the KSA antenna at the maximum slew rate. The second is the torque needed to bend the cable between the KSA RF platform and the ETS-VI main body by rotating the APM. The step angle of the motor is 0.45 degree,

and the motor can respond to a pulse rate of 110 pulses per second (pps) to perform the maximum slew rate of the APM. Generally, the torque of a stepping motor is proportional both to the square of the diameter and to the axial length. Therefore, the weight of the motor is mainly determined by the output torque. The diameter of the motor is equal to that of the harmonic drive.

#### Position indicator

During signal acquisition, the KSA antenna direction is positioned by closed-loop control using the output of the position indicator. So the position indicator is required to provide the correct position of the antenna. The potentiometer was chosen because of its heritage in space, simplicity of the electric circuit, and light weight. The specifications of the potentiometer are shown in Table 5.

#### Bearings

Radial and axial load capacity are the most important requirements for the bearings. Light weight and protection from the harmonic drive's wear debris are also required for the bearings. Therefore, the shielding-type, single deep-groove ball bearings (6008ZZZ) were selected. The solid lubricant and the material of a retainer for the bearings are described in Table 6.

### 4. Results of design

The results of the design are shown in Table 7. The APM EM satisfies every requirement. The developed APM EM is shown in Figure 5.

### 5. Test of the APM

#### 5.1 Sequence of the test

The APM EM was subjected to a functional test, a thermal-vacuum test and a vibration test. After these tests, the requirement of a 3-year orbital life was shown to be met by performing the life test in a thermal-vacuum environment. The sequence of these tests is shown in Figure 6.

#### 5.2 Method of test

The test configuration for the functional test is shown in Figure 7. A dummy inertial mass simulating the moment of inertia of the KSA antenna and RF compartment was connected to the APM through couplings and a vacuum feed-through element. The dummy inertial mass, consisting of four masses, was rotated in a horizontal plane so imbalance of the masses gave no torque to the APM. Therefore, this configuration was

suitable for measuring a small step angle with heavy inertia. An accurate rotary encoder was set at the top of the functional-test apparatus. The small step size of the APM was measured by the rotary encoder. The environment around the APM was gaseous nitrogen at the time of operation.

For the thermal-vacuum test, the functional-test apparatus was used again. The APM and the hardware below the flange were in a vacuum chamber. The configuration for the thermal-vacuum test is shown in Figure 8. The temperature of the APM was controlled by the base plate temperature. The vacuum level was less than  $10^{-5}$  torr. The life-test configuration was the same as the one for the thermal-vacuum test, except that the torque for the APM to bend the cable between the KSA RF platform and the ETS-VI main body is simulated.

For the functional test and the thermal-vacuum test, the following functions and performance parameters of the APM were measured:

- electric power
- maximum slew rate
- step size
- holding torque

The temperature conditions of the thermal-vacuum test are shown in Figure 9. The functions and the performances of the APM were measured at  $-15^{\circ}\text{C}$  and  $+55^{\circ}\text{C}$  in the thermal-vacuum test. The vibration test was performed to confirm that the APM would survive the launch environment.

To demonstrate the capability of a 3-year orbital life, the life test was performed in the thermal-vacuum environment for about 5 months. For the life test, the APM rotated the dummy inertial mass against the torque required to bend the RF cables for over a  $\pm 10$ -degree range. The driving pattern was determined for the assumed case of a user satellite for 3 years. Functions and performance were measured about every 2 weeks.

## 6. Test results

Performance data from the functional test, thermal-vacuum test and the life test are shown in Table 8. The APM EM accomplished the required functions and performance both at atmospheric pressure and in thermal-vacuum conditions. Its performance did degrade after the vibration test. Also, after the life test, the APM satisfied all of its requirements.

## 7. Conclusion

The design of the APM for the KSA antenna of ETS-VI satellite was completed, and capability of the design to meet all performance requirements was established by test.

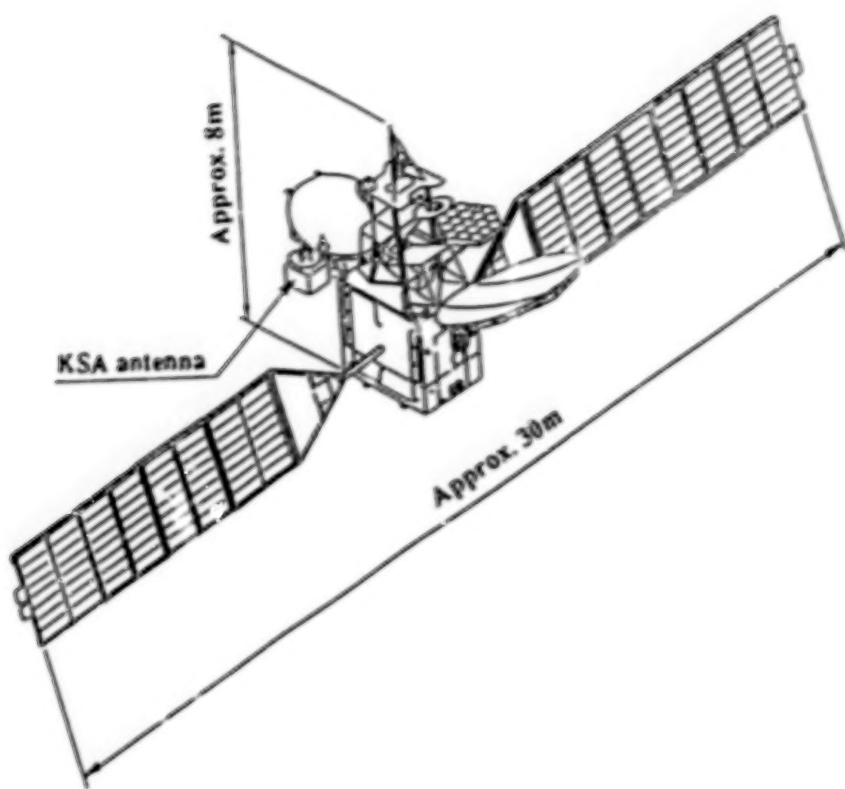


Figure 1. Configuration of the ETS-VI

Table 1. Trade-offs in Designing the Antenna-Pointing Mechanism

	Stepping Motor +Reduction Gear	DC Servo Motor +Reduction Gear	Direct Drive
<b>Control Law</b>	Open Loop	Closed Loop	Closed Loop
<b>Positioning Sensor</b>	Fine Null-Position Sensor	Fine Angular Displacement Sensor	Fine Angular Displacement Sensor
<b>Angular Velocity Sensor</b>	None	Necessary	Necessary
<b>Speed</b>	Low	Necessary	High
<b>Holding Torque</b>	High	Low (used with Brake)	Low (used with Brake)
<b>Output Torque</b>	High	High	Low
<b>Volume, Mass</b>	Small	Small	Large
<b>Drive Electronics</b>	Simple	Complex	Complex
<b>Past Development</b>	PDM (Paddle Drive Mechanism) developed	JEMRMS (JEM's Remote Manipulator System ongoing)	None

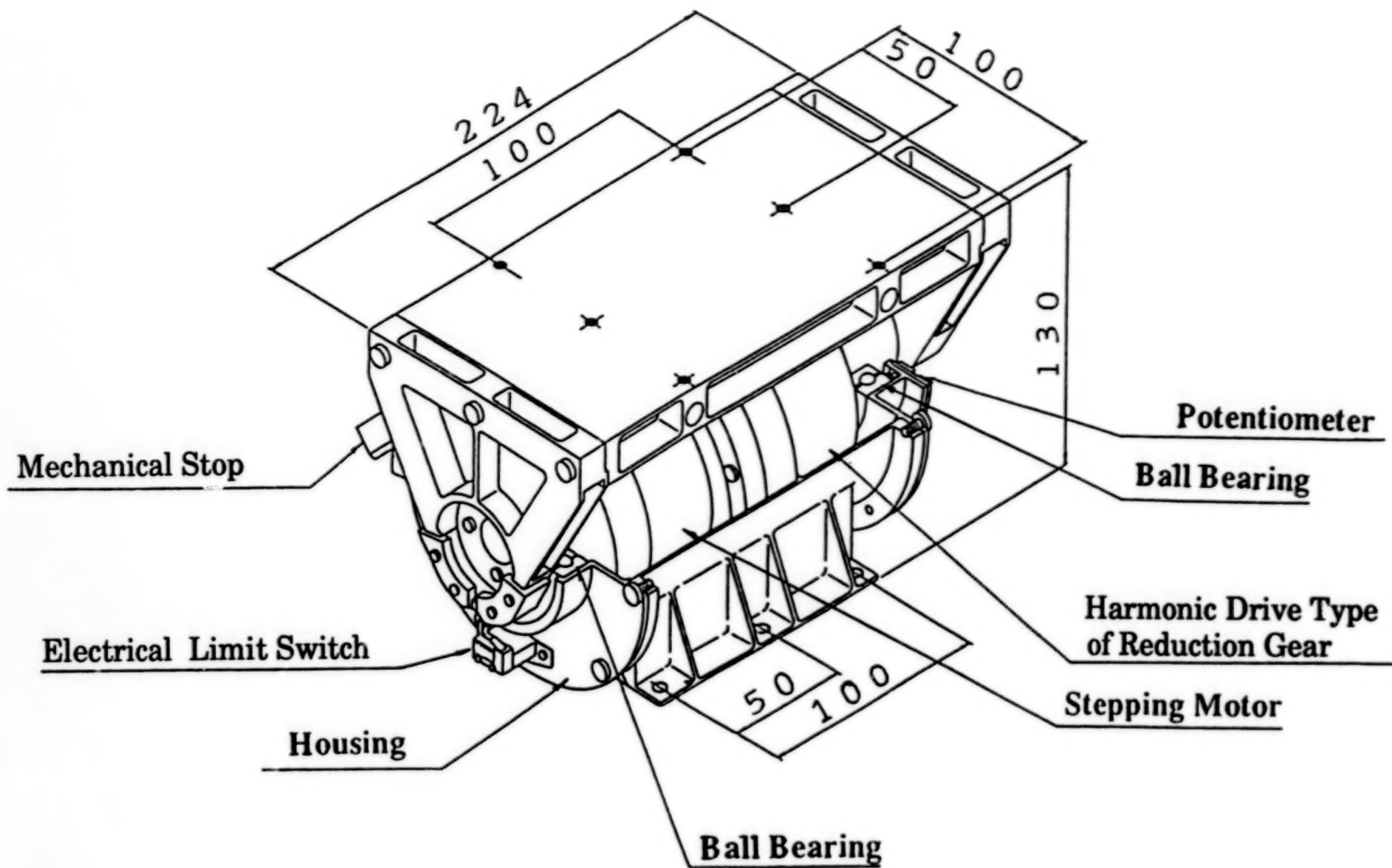
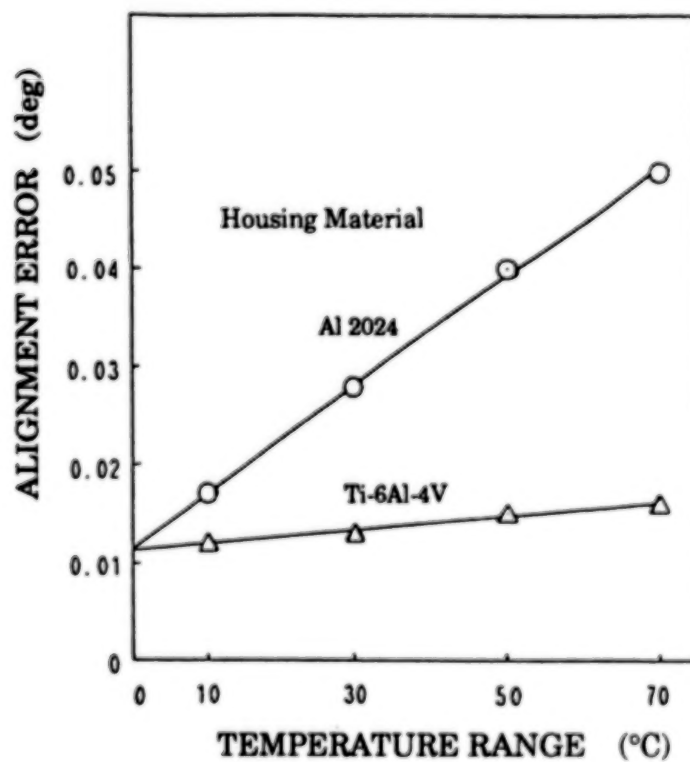


Figure 2. Configuration of the APM EM

54

**Table 2. Requirements for the APM**

ITEM	REQUIREMENT
MASS	10 kg (max)
ELECTRIC POWER	39 W (max) SLEWING MODE 4.5 W (max) TRACKING MODE
POINTING RANGE	0.3 deg/sec
MAXIMUM SLEW RATE	$\pm 10$ deg
STEP SIZE	0.005 deg (max)
HOLDING TORQUE	10.3 Nm (min)
PAYLOAD INERTIA	13 kgm <sup>2</sup> (max)
REQUIRED LIFE	3 YEARS



**Figure 3. Temperature Range and Alignment Error**

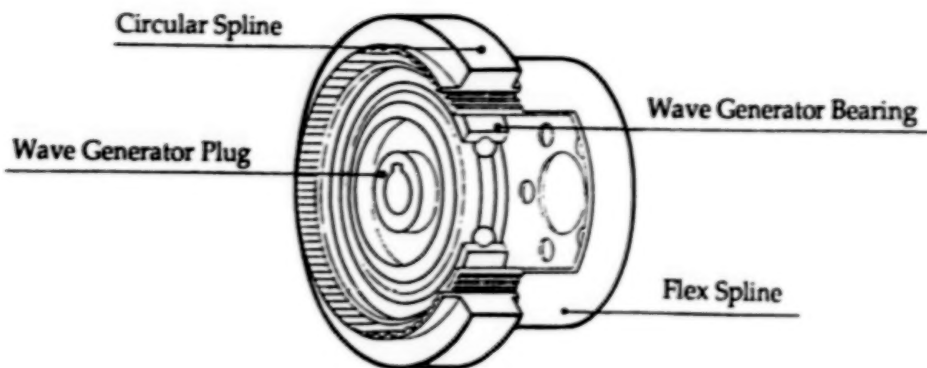


Figure 4. Configuration of Harmonic Drive®

Table 3. Lubricant of the Harmonic Drive®

PARTS		LUBRICANT
BEARING	OUTER RACE	
	INNER RACE	SILVER ION PLATING
	BALL	
RETAINER		GOLD PLATING
	FLEX SPLINE	GOLD PLATING

**Table 4. Specifications of the Stepping Motor**

ITEM	SPECIFICATION
ELECTRIC POWER	15 W
VOLTAGE	26 ± 2V
STEP ANGLE	0.45 deg
OUTPUT TORQUE	0.45 Nm
PULSE RATE	0 ~ 110 pps
MASS	1760 g

**Table 5. Specifications of the Potentiometer**

ITEM	SPECIFICATION
TEMPERATURE	-30 ~ +70 °C (Operation) -60 ~ +100 °C (Non-Operation)
RANGE OF MOVEMENT	360 deg
EFFECTIVE ANGLE	± 18 deg
LINEARITY	± 0.08 deg ± 0.016 deg (null point)
INPUT VOLTAGE	± 15 V (max)

**Table 6. Lubrication of Bearings**

PARTS	LUBRICANT
OUTER RACE	$\text{MoS}_2$ Sputtering
INNER RACE	
BALL	
RETAINER	PTFE + glass fiber + Mo

**Table 7. Results of Design\***

ITEM	REQUIREMENT	DESIGN*
MASS	5 kg (max)	4.9 kg (max)
ELECTRIC POWER	19.5 W (max) Slewing Mode 2.25 W (max) Tracking Mode	19.5 W (max) Slewing Mode 2.25 W (max) Tracking Mode
MAXIMUM SLEW RATE	0.3 deg/sec	0.31 deg/sec
POINTING RANGE	$\pm 10$ deg	$\pm 13.0$ deg $\pm 0.5$ deg (Mechanical Stopper) $\pm 11.5$ deg $\pm 0.5$ deg (Electrical Limit)
STEP SIZE	0.005 deg (max)	0.00287 deg (Nominal)
HOLDING TORQUE	10.3 Nm (min)	10.3 Nm (min)
PAYOUT LOAD INERTIA	$13 \text{ kgm}^2$ (max)	$13 \text{ kgm}^2$ (max)
REQUIRED LIFE	3 YEARS	3 YEARS (15624 cycles)

\*(For One Axis)

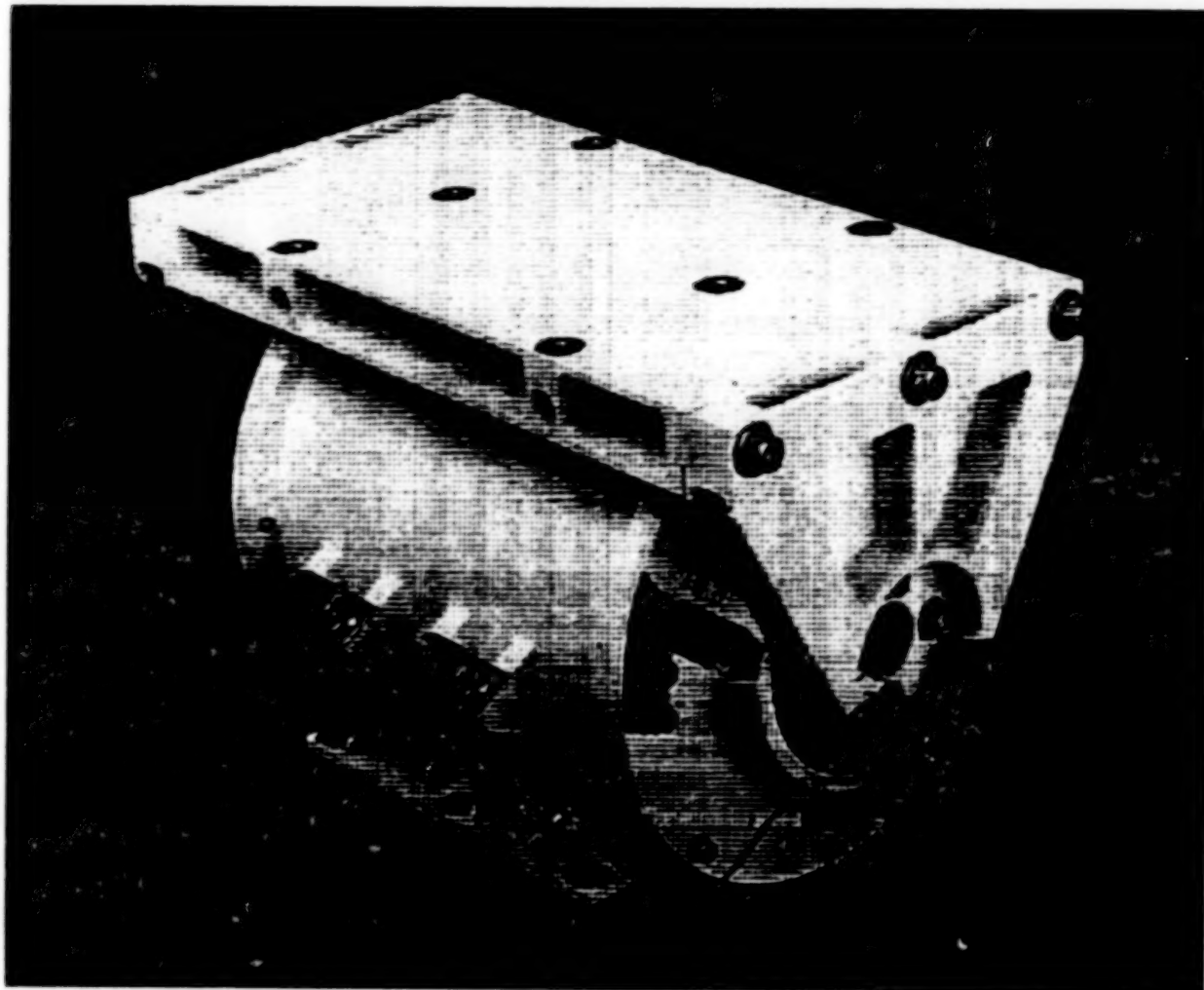
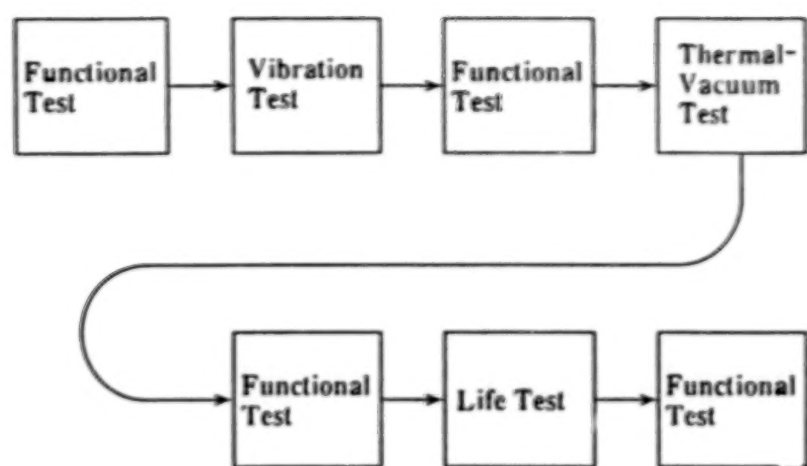
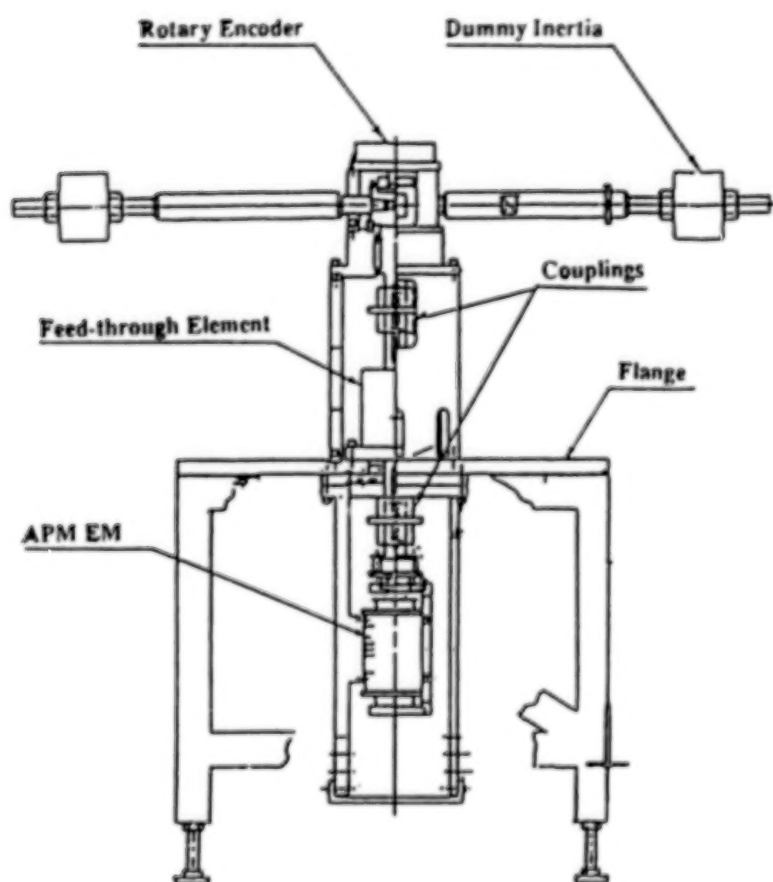


Figure 5. The APM EM

89



**Figure 6. The Sequence of the Tests**



**Figure 7. Configuration of the Functional Test**

**BLANK**

**PAGE**

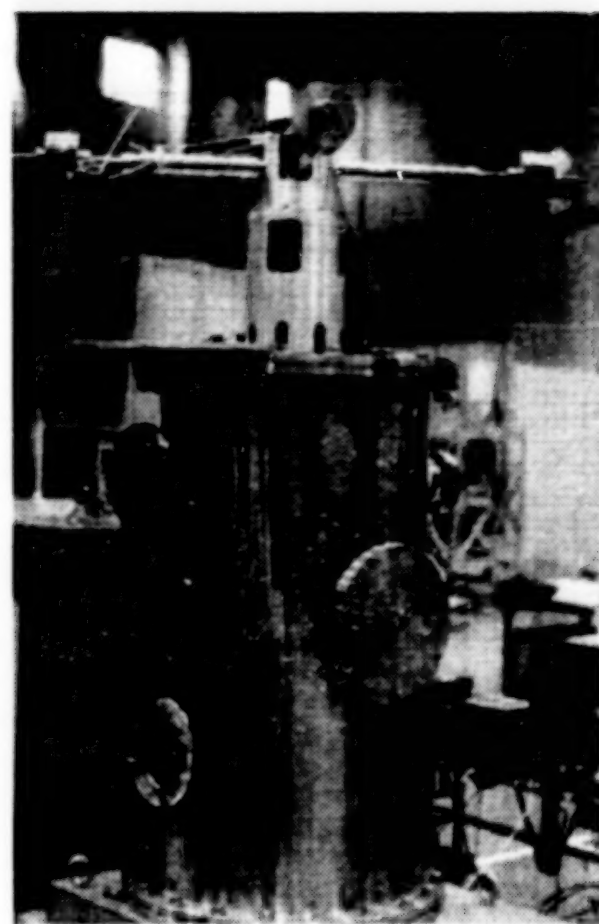


**Figure 8. Configuration of the Thermal-Vacuum Test**

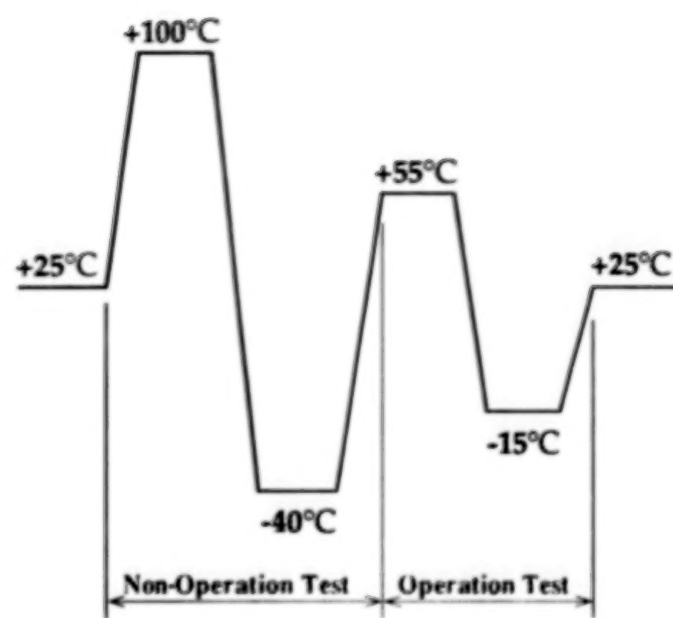


**Figure 9. Temperature Conditions**

Table 8. Test Results of the APM

ITEM	REQUIREMENT	FUNCTION TEST	FUNCTION TEST (after vibration test)	THERMAL-VACUUM TEST		FUNCTION TEST (after thermal vacuum test)	LIFE TEST		FUNCTION TEST (after life test)
				+55°C	-15°C		+55°C	-15°C	
ELECTRIC POWER	19.5 W (max)	8.9 W	8.6 W	8.9 W	10.3 W	9.2 W	8.6 ~ 8.9 W	9.8 ~ 10.5 W	9.8 W
MAXIMUM SLEW RATE	0.3 deg/sec	0.57 deg/sec	0.41 deg/sec	0.57 deg/sec	0.48 deg/sec	0.48 deg/sec	0.57 deg/sec	0.57 deg/sec	0.57 deg/sec
POINTING RANGE	±11.5 ± 0.5 deg (Electrical Limit)	+11.215 ~ +11.259 deg -11.711 ~ -11.816 deg	—	—	—	—	—	—	—
STEP SIZE	0.00257 deg cw (Nominal) ccw	0.00257 deg 0.00268 deg	0.00291 deg 0.00285 deg	0.00285 deg 0.00285 deg	0.00294 deg 0.00252 deg	0.00274 deg 0.00264 deg	0.00253 deg ~0.00273 deg	0.00284 deg ~0.00287 deg	0.00276 deg 0.00277 deg
HOLDING TORQUE	10.3 Nm (min)	10.3 Nm (min)	10.3 Nm (min)	10.3 Nm (min)	10.3 Nm (min)	10.3 Nm (min)	10.3 Nm (min)	10.3 Nm (min)	10.3 Nm (min)

92

POINTING/ROLL MECHANISM  
FOR THE  
ULTRAVIOLET CORONAGRAPH SPECTROMETER

Miroslaw A. Ostaszewski\* and Larry J. Guy\*

ABSTRACT

A pointing/roll mechanism for the Ultraviolet Coronagraph Spectrometer (UVCS) is presented along with a description of the mechanism control algorithm. The mechanism, operating in space, will position the 2.1 meter long, 0.7 meter diameter UVCS instrument in pitch and yaw, within a 54 arc-minute half angle cone, and will also allow it to rotate  $\pm 179.75$  degrees. After considerable design effort, an optimum mechanical solution was achieved, which meets all scientific requirements as well as weight, volume, and power budgets. Evolution of the mechanism is presented along with the design status.

INTRODUCTION

Background

The Ultraviolet Coronagraph Spectrometer (UVCS) is a scientific instrument that will be used to observe the solar corona aboard the Solar and Heliospheric Observatory (SOHO) spacecraft. SOHO is a mission to study the sun, sponsored by European Space Agency (ESA) along with National Aeronautics and Space Administration (NASA). SOHO will be launched into a halo orbit about the L1 Lagrangian point where a gravitational null exists in the sun-earth system. L1 is an ideal location for continuous and unobstructed observation of the sun. During the two-year mission, the UVCS will aid in the study of such phenomena as solar wind acceleration in the extended solar corona. Figure 1 shows the UVCS instrument located on the SOHO spacecraft.

Scientific Goals

The UVCS instrument will provide ultraviolet spectroscopic measurements of the entire solar coronal region from near the solar horizon out to 10 solar radii ( $R_\odot$ ). The telescope, pointed at the sun-center, receives coronal radiation from the primary field of view (FOV) as shown in Figure 2. Internal mirrors focus a thin strip of this radiation onto entrance slits of a spectrometer. A mechanism tilts the mirrors to scan coronal images across the entrance slits. By rotating the telescope, different radial regions of the corona can be viewed. The extended FOV can be accessed by offset pointing the telescope axis to observe direct solar radiation.

---

\*Ball Corporation, Ball Electro-Optics/Cryogenics Division  
Boulder, Colorado

## UVCS Operation

Once in orbit, the SOHO spacecraft will closely maintain its longitudinal axis pointed at the sun-center. This provides a stable platform from which the UVCS instrument can perform coronal or solar observations. Prior to a typical observation, the UVCS telescope will be rolled about its longitudinal axis followed by a pointing adjustment in pitch and yaw (see Fig. 3., which shows the pitch, yaw and roll axes). The pointing adjustment will be necessary to re-align the telescope to required accuracy.

## UVCS System

The UVCS system consists of the telescope and the forward and rear support assemblies (see Fig. 3). The telescope is a long tubular structure consisting of a seven-sided graphite fiber reinforced epoxy (GFRE) trussed framework to which is attached a cylindrical end-cap. The aperture cover/door mechanism is mounted to the end-cap while all the other optical components (mirror mechanism, sunlight trap and spectrometer) are housed inside the the telescope (see Fig 4).

The forward and rear support assemblies provide the pointing and roll capability to the UVCS instrument and are presented in detail in this paper.

## UVCS POINTING/ROLL REQUIREMENTS

During operation, the UVCS is required to pitch and yaw within a pointing envelope defined by a 54 arc-minute half angle cone. The pointing accuracy throughout this envelope is 60 arc-seconds with the exception of the central 32 arc-minute cone, where, the instrument must be capable of fine pointing corrections with a precision of 2 arc-seconds. The mechanism is also required to rotate the telescope  $\pm 179.75$  degrees with an accuracy of 6 arc-minutes.

The mechanism, which cannot exceed 20 kg mass, must be designed to operate 60,000 pointing cycles and 23,000 rotation cycles, providing a factor of safety of 4 over the actual mission requirements. To insure reliability, redundant position sensors and motor windings are required.

## UVCS POINTING/ROLL MECHANISM DESCRIPTION

### Pointing Mechanism

The pointing portion of the mechanism consists of three primary subassemblies: the pointing ring, aft support assembly and the pointing roller assemblies. A titanium pointing ring is attached to the GFRE telescope structure by filling the radial gap between the ring and the structure with polyurethane bonding material. The gap is sized to minimize thermally induced stresses due to the coefficient of thermal expansion (CTE) difference between the ring and the essentially zero CTE structure. The ring surfaces which contact the pointing and retention rollers are hard coated and dry film lubricated to minimize wear.

The aft structure assembly (see Fig. 5) provides telescope support and two axis rotational freedom. The structure incorporates four GFRE tubular legs which mount between the spacecraft and a GFRE roll drive interface plate. Each leg end has a spherical bearing at the mounting interface. The legs are oriented such that they form perpendicular 4-bar linkages. The geometry of the 4-bar link systems is such that they have coincident instantaneous centers of rotation, emulating the functions of a two axis gimbal. They are also positioned such that the telescope mounting is stiff in the radial directions. Axial stiffness is tailored to meet minimum operational requirements and to minimize stresses caused by thermal mismatch between the telescope structure and the aluminum spacecraft mounting plate when the telescope is launch locked.

The two pointing roller assemblies each consist of a linear translation stage, a crowned pointing roller, a spring loaded retention roller and a roller support (see Fig. 6). Pointing is accomplished by independently positioning the pointing rollers using the linear stages causing the telescope to pivot on the aft support. Essentially, moving the rollers towards or away from each other for pitch and together in the same direction to adjust yaw.

The pointing rollers are 52 mm diameter double row ball type cam follower bearings with a 500 mm radius crown. The linear translation stages are stepper motor driven crossed roller type with lapped leadscrew/nut assemblies for minimum backlash. The 2.5 mm lead pitch combined with a 1.8 degree/step motor provides .02 mm of linear travel per step. This corresponds to about 1.5 arc seconds of telescope motion per step. A lapped nut was selected over a ball nut because of a requirement that the mechanism not back drive when subjected to telescope weight during ground operations with motor power off. The lapped nut meets the requirement without the necessity of adding a gear reducer to the motor, which would increase size, weight and backlash. A linear potentiometer is incorporated into each stage to monitor position. The linearity of the potentiometer is sufficient to meet the 60 arc-second pointing accuracy requirement (sun sensors provide fine position feedback to meet the 2 arc-second accuracy requirement within the central portion of the pointing envelope). The crowned rollers permit the required telescope motion while minimizing contact stresses at the pointing ring interface. Each roller assembly includes a retention roller which rides on an inner surface of the pointing ring. These rollers are also crowned and are spring loaded to 49 N each. The rollers are mounted with a pivoting link system that insures the ring maintains contact with the pointing rollers during operation. The pointing rollers and the retention rollers are finished with a zirconium nitride coating for wear resistance.

### Roll Mechanism

The roll mechanism (see Fig. 7) consists primarily of a pre-loaded duplex bearing pair, a resolver, a harmonic drive gear reducer, a stepper motor, a rotation shaft and a rotation housing. The rotation shaft and housing are silicon-carbide reinforced aluminum for high stiffness and to match CTE characteristics of the

bearings and resolver. A size 11, 90 degree stepper motor drives the telescope through a gearhead and Harmonic Drive reducer which yields a 5000:1 overall gear reduction. This provides approximately 1 arc-minute of telescope rotation per step. The Harmonic Drive was selected for efficient packaging and high torsional stiffness. The resolver is a redundant pancake type with 2 arc-minute accuracy. The rotating shaft mounts to the telescope and the housing mounts to the interface plate on the aft support (see Figs 5 and 7). A mechanical stop is incorporated to limit rotation.

### Launch Lock Configuration

The pointing mechanism is not capable of withstanding the severe vibrational loading caused during launch. Therefore, an auxiliary launch lock system is engaged. The telescope is lowered by the pointing mechanism until pins on the telescope engage specific locations on the forward support. The pointing rollers continue to move outward and are separated from the telescope pointing ring. Afterwards, pawls are deployed which hook around the pins locking the telescope in place. This system provides restraint in three axes and transfers loads directly to the spacecraft through the interfaces. To disengage the launch lock, the pawls are rotated, which allows the telescope be lifted by the pointing mechanism from the launch lock restraints.

## EVOLUTION OF THE UVCS POINTING/ROLL MECHANISM

The telescope pointing/roll mechanism went through a number of evolutionary iterations and many different design approaches were considered. It is worthwhile to review the main development stages.

From the mechanical point of view, the UVCS telescope is essentially a 91 kg cylinder, 2.1 meters long and 0.7 meter in diameter, with the center of gravity located approximately 0.9 meters along the roll axis behind the front aperture. To be able to fit within the allowed volume and not obstruct the front aperture, the mechanism was constrained to occupy volume available to the rear of the telescope and some space between the telescope and the spacecraft mounting panel.

The first consideration was to place a unified pointing/roll mechanism in the available volume at the rear of the telescope. With the center of mass located near the front of the telescope, the mechanism was required to accurately position and stabilize the large cantilevered inertial load. Early analysis indicated that the mechanism could not meet pointing, stability and launch requirements within volume, weight and power restrictions.

It was decided next to consider placing a 2-axis gimbal at the aft end and mount a separate mechanism as far forward as possible to do the actual pointing. This maximizes pointing "leverage" and allows larger mechanism step size. The concept at the proposal stage included a single mechanism located up front with rollers that would pinch a ring mounted around the telescope and a 2-axis linear

motion device that would move the telescope up and down and side to side for pointing. The pinch rollers would double as a traction drive system for rolling the telescope.

At the preliminary design phase, the pinch roller concept was investigated in detail. It was determined that there was not sufficient space to install a single mechanism which met the stiffness and pointing requirements. There was also a concern about possible slippage of the traction roll drive system. Another issue concerned the fact that the contact point between the rollers and the pointing ring moves along an arc during telescope pointing. This required some compliance in the mechanism to allow for angular and distance variations.

This led to a mechanism where the telescope would rest on a pair of crowned rollers, each attached to a linear translation stage. With this arrangement, pointing was accomplished by independently moving the rollers together or apart to point the telescope for pitch motion or in the same direction for yaw motion. Roll was accomplished via a cable drive system where a cable is wrapped radially around the telescope near the pointing ring and around an idler pulley and a motorized pulley. The pulleys were attached to each of the translation stages near the crowned pointing rollers. The cable also acted to hold the telescope down onto the rollers.

This design was determined to have contamination drawbacks due to the use of stranded cable which was required for its flexibility. There was a concern that the cable would be impossible to thoroughly clean and that particulates would continually work out of the braid during operation. It was also not desirable from a reliability standpoint. Redundant cables required a considerable amount of room and if a cable were to break, the loose end stood a good chance of getting tangled. The cable drive also was sensitive to the telescope angular motion.

At this point, a mechanism trade study was performed and it was decided to abandon the cable drive system. The crowned roller scheme, however, was determined to be a very good approach and it was decided to retain the pointing system, but incorporate a direct drive roll mechanism into the gimbal where it is immune to telescope angular motion. Retention rollers were added to the pointing mechanism to insure contact of the telescope ring with the pointing rollers.

The next major design change was driven by weight. A detailed weight analysis disclosed that the instrument was exceeding the overall mass allocation. It was recognized that a large percentage of the weight of the pointing/roll mechanism was the gimbal assembly. Launch loads and a 70 Hz axial stiffness requirement had driven up the weight of the gimbal and aft support structure to provide adequate stiffness. Clarification of the specification revealed that the 70 Hz resonant frequency was only a launch requirement. This allowed us to include a simple axial launch lock at the front support to meet the 70 Hz requirement and re-evaluate the telescope pivoting method in order to reduce weight.

The design, presented earlier, precipitated out of this evolutionary process.

## MECHANISM CONTROL ALGORITHM

Successful operation of the UVCS pointing mechanism requires a simple control algorithm that will position the pointing rollers to proper locations, orienting the UVCS telescope to a desired angular orientation. A suitable algorithm, in the form of mathematical equations, relates  $\theta$  and  $\phi$  (pitch and yaw angles of the telescope) to  $\Delta_1$  and  $\Delta_2$  (positions of the pointing rollers). In order to develop such an algorithm, it was necessary to first mathematically describe the pointing geometry which yielded a set of simultaneous nonlinear equations. Since the complex equations were not suitable to be used directly, simplified polynomials were developed which approximate the solution to a desired accuracy throughout the pointing envelope.

### Description of Geometry

The general configuration of the UVCS pointing system is shown in Figure 8. For a given orientation of the telescope (mathematically described by angles  $\theta$  and  $\phi$ ), there is a unique position for each pointing roller. Also, the aft support legs assume specific orientations to accommodate the telescope. This logic is the basis for the analysis, since the mathematical description of the system must also be unique. Vector equations describe the contact point between the pointing rollers and the pointing ring as well as positions of the aft legs. Additional equations are included to constrain the system. The total number of equations developed is 28 with 28 unknowns.

### Solution of Simultaneous Equations

From the preceding discussion, the description of the pointing geometry yielded a system of equations which are applicable to a particular orientation of the instrument. For a pointing envelope of  $\pm 54$  arc-minute in both pitch and yaw, the system of equations was solved every 2 arc-minutes. The resulting data is represented as two surfaces, each describing the position of one roller versus telescope pitch and yaw.

### Curve Fit of Pointing Surfaces

A curve fit approximation of the pointing surfaces was performed using polynomials in two variables. It was found that fourth power polynomials were required to achieve the desired 2 arc-second accuracy. The left pointing surface and corresponding polynomial is shown in Figure 9.

### Design Optimization

In order to minimize the amount of sliding of the pointing roller on the roll ring, the pointing stages were placed on a angle of 6 degrees as shown in Figure 5.

This angle was mathematically optimized to account for relative motion between the pointing ring and the pointing rollers due to the arc motion of the telescope.

## CONCLUSION

To date, the mechanical layout and analysis of the mechanism is complete as well as 95% of the mechanical drawings. Wear testing has been done to select finishes for the pointing ring and rollers and bearing lubrication analysis has been performed. Fabrication is under way on items for an engineering model and units to be life-tested. Computer simulation models have been developed to verify the motor sizes and control electronics, and also to determine the mechanisms' momentum and torque disturbance inputs to the spacecraft. These models include all of the mechanical characteristics of the system such as friction, spring rate and inertia. The models have been run at the minimum and maximum values (including safety margins) of the constituents to prove the mechanisms will operate correctly under any condition. Finite element modeling has been done on critical items such as the rotation shaft and the pointing ring. The pointing ring bond was also modeled to check for deflection of the ring during 1-g loading and thermally induced stresses of the bond material. The mechanism control algorithm is being implemented in the system software.

## ACKNOWLEDGMENTS

UVCS is a scientific experiment of the Smithsonian Astrophysical Observatory (SAO) with Dr. John L. Kohl as the Principal Investigator. The project is also in collaboration with a group of scientists and engineers from Italy and with participation from Switzerland, Norway and Germany as well as several American institutions. Ball Electro-Optics/Cryogenics Division will provide the telescope assembly and electronics unit, Aeritalia and Officine Galileo will provide the spectrometer assembly and Contraves Corporation will provide the diffraction gratings and cells used in the spectrometer.

The authors wish to thank SAO for permission to publish this paper and all the UVCS participants for their support.

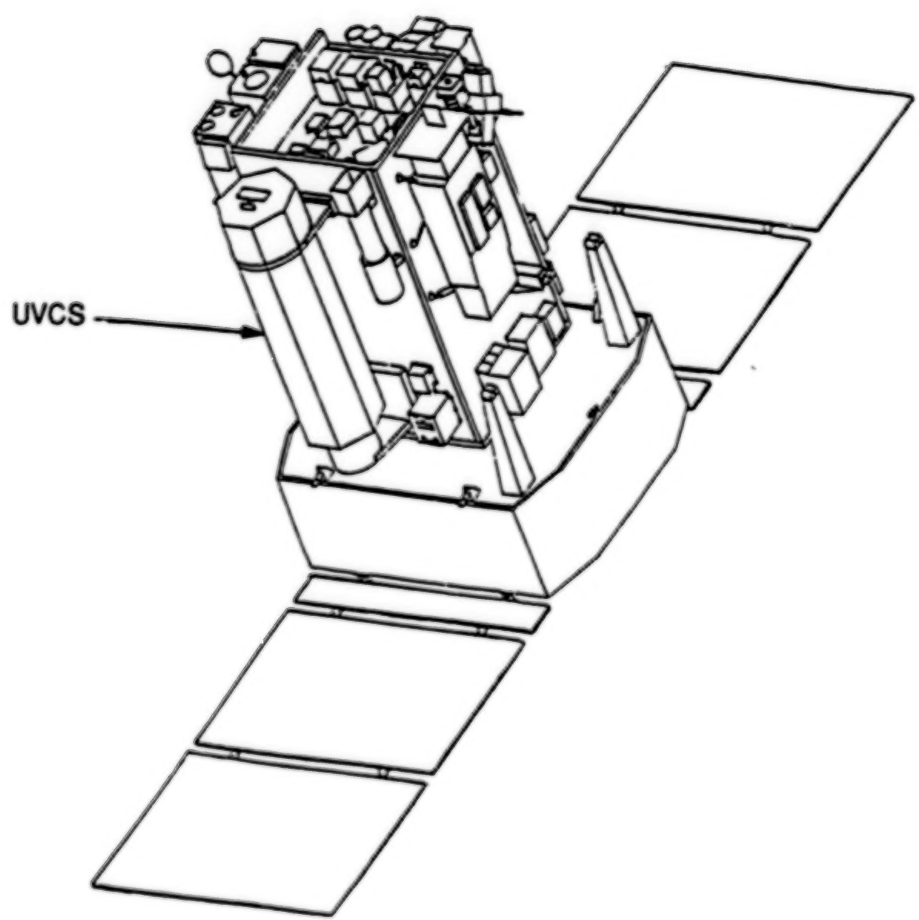
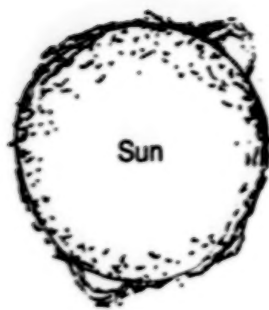


Figure 1. SOHO spacecraft with the UVCS instrument.

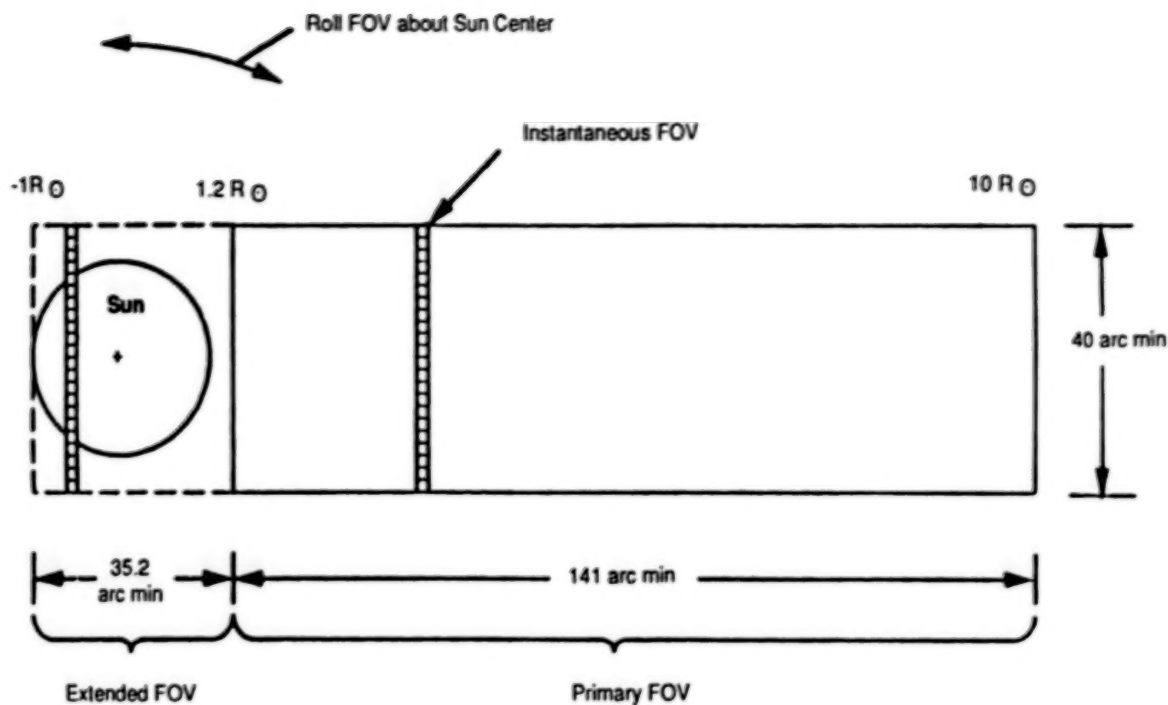


Figure 2. The UVCS instrument field of view (FOV).

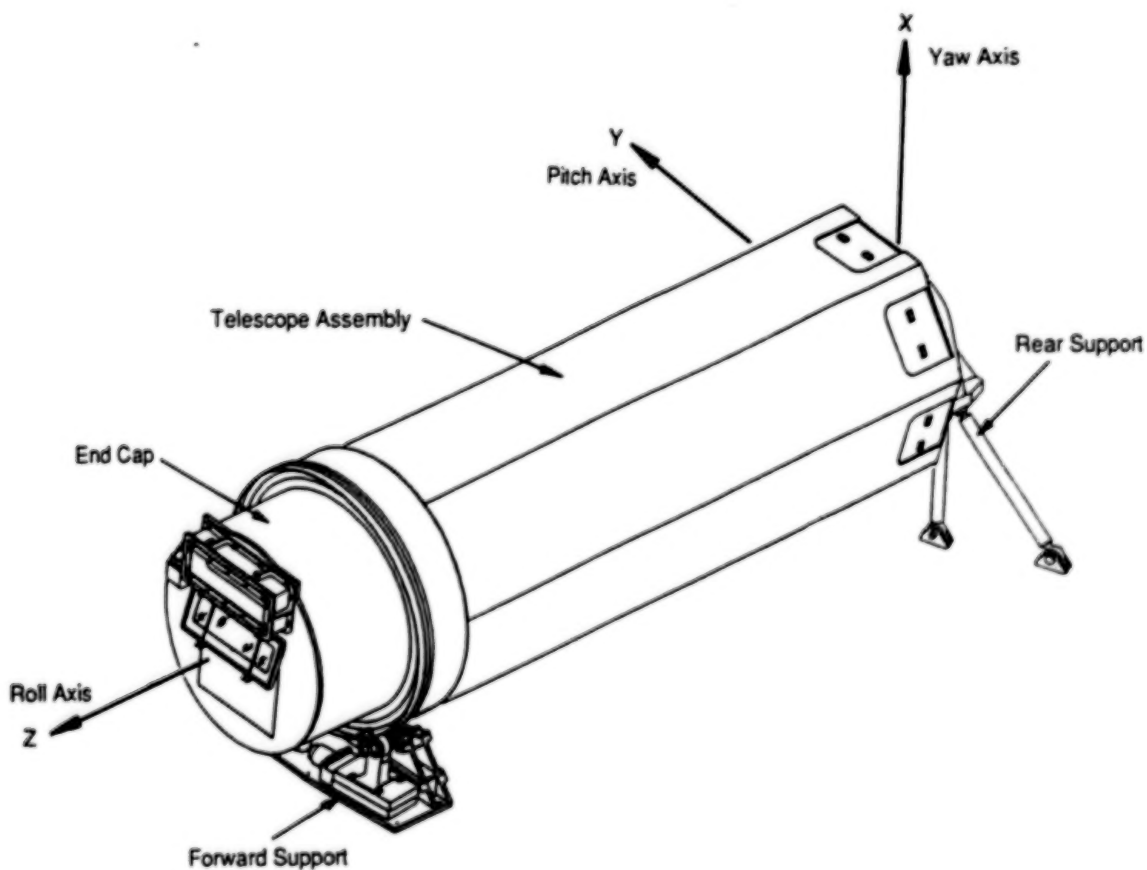


Figure 3. The UVCS instrument .

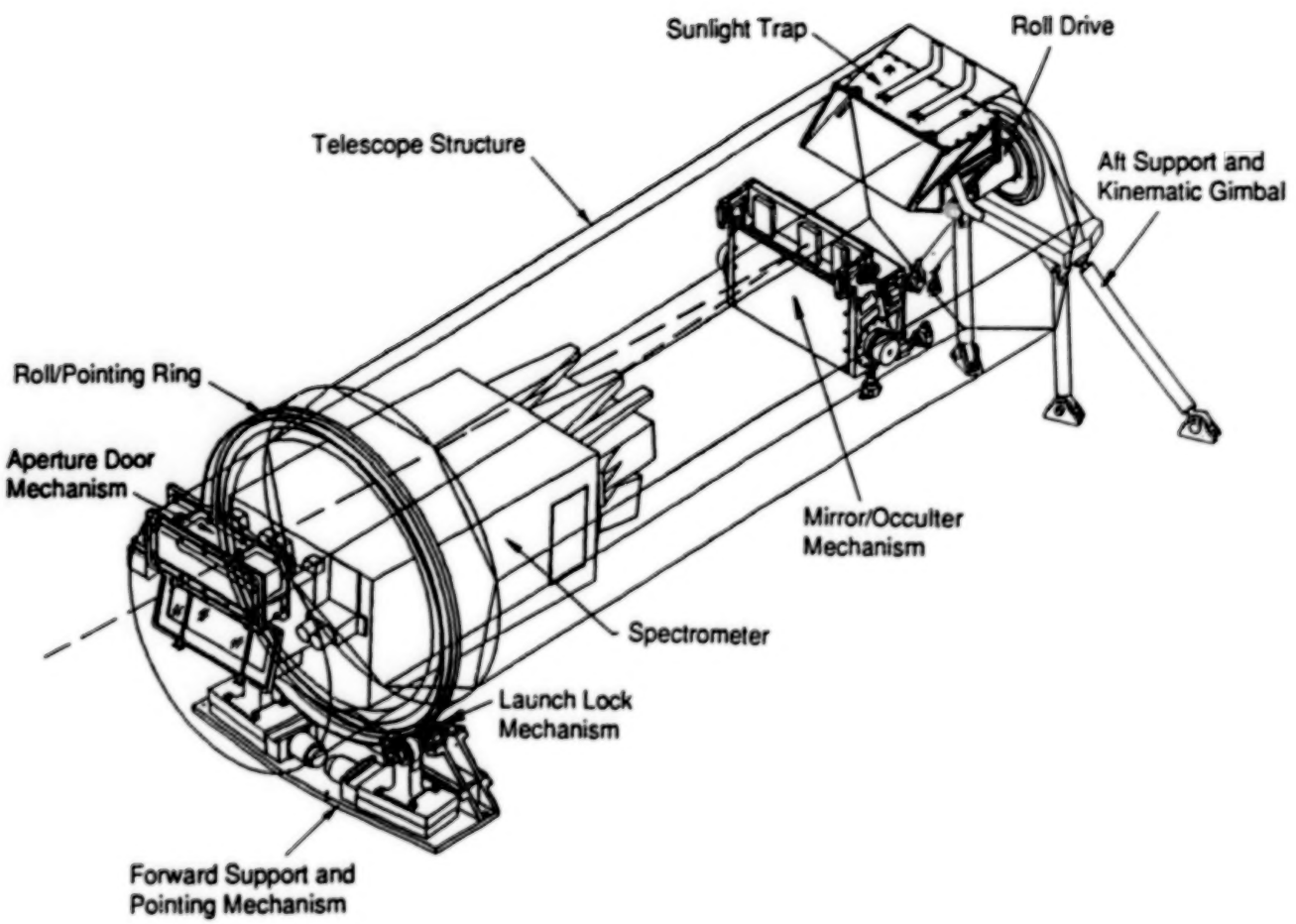


Figure 4. UVCS instrument system overview.

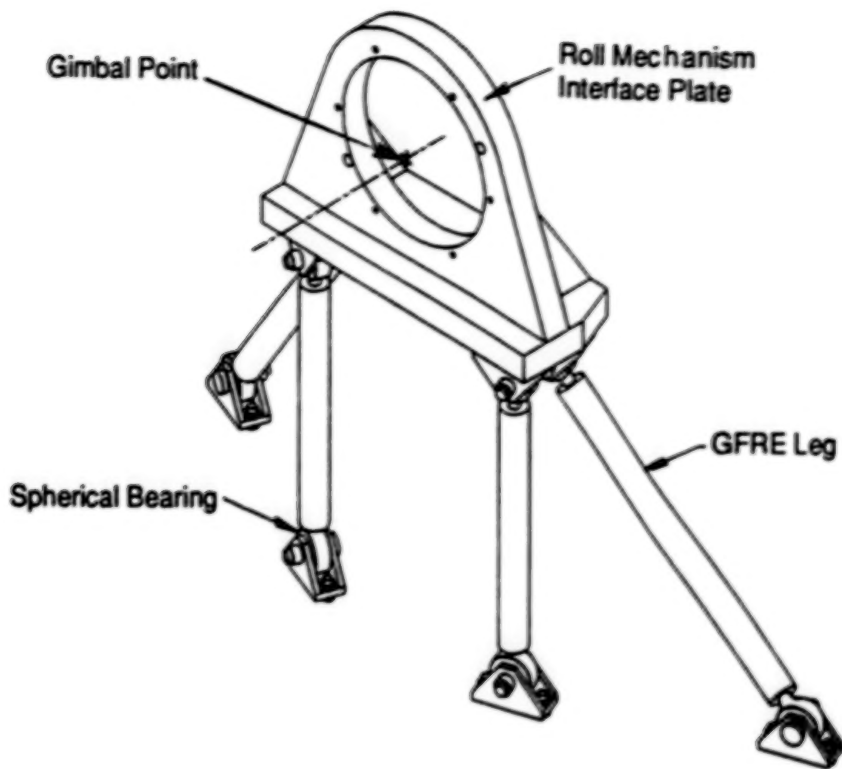


Figure 5. Aft support and kinematic gimbal.

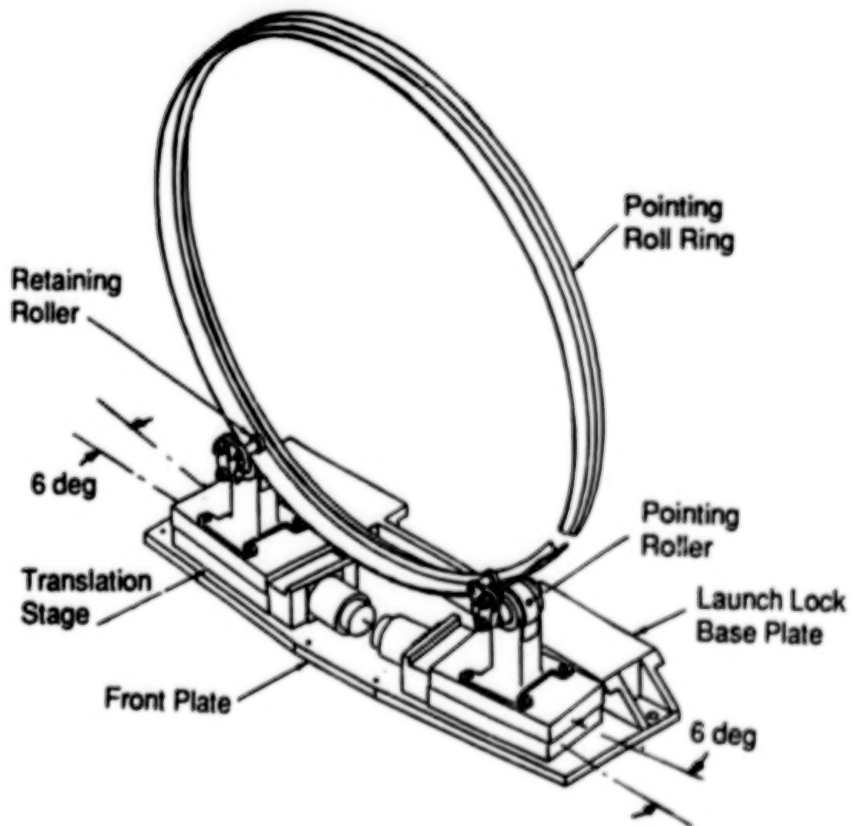


Figure 6. Pointing mechanism.

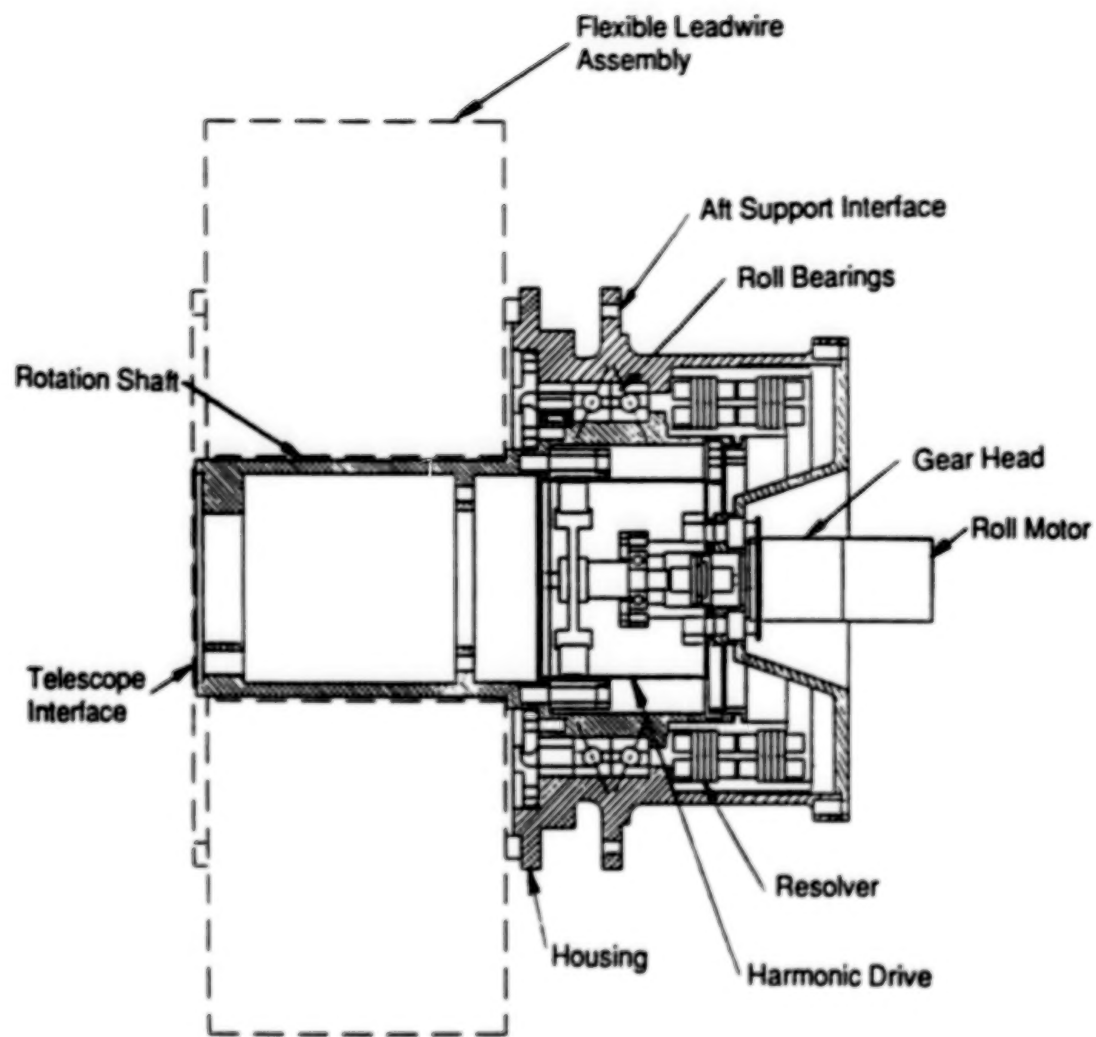


Figure 7. Aft roll drive.

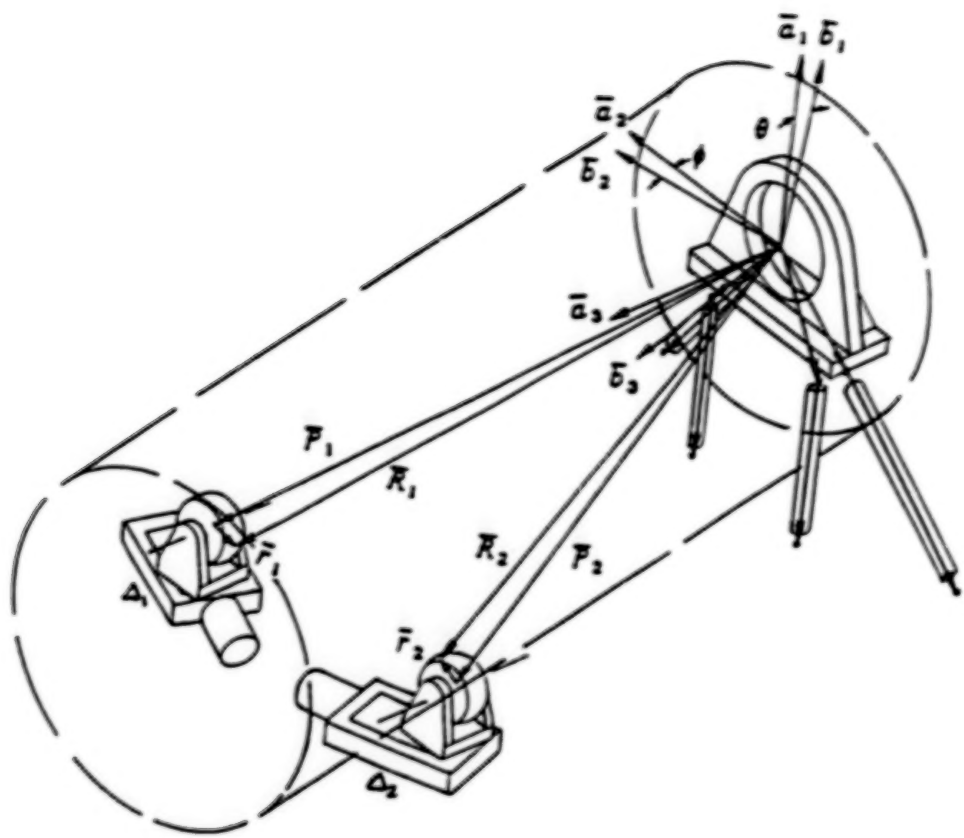


Figure 8. Vector description of the pointing geometry.

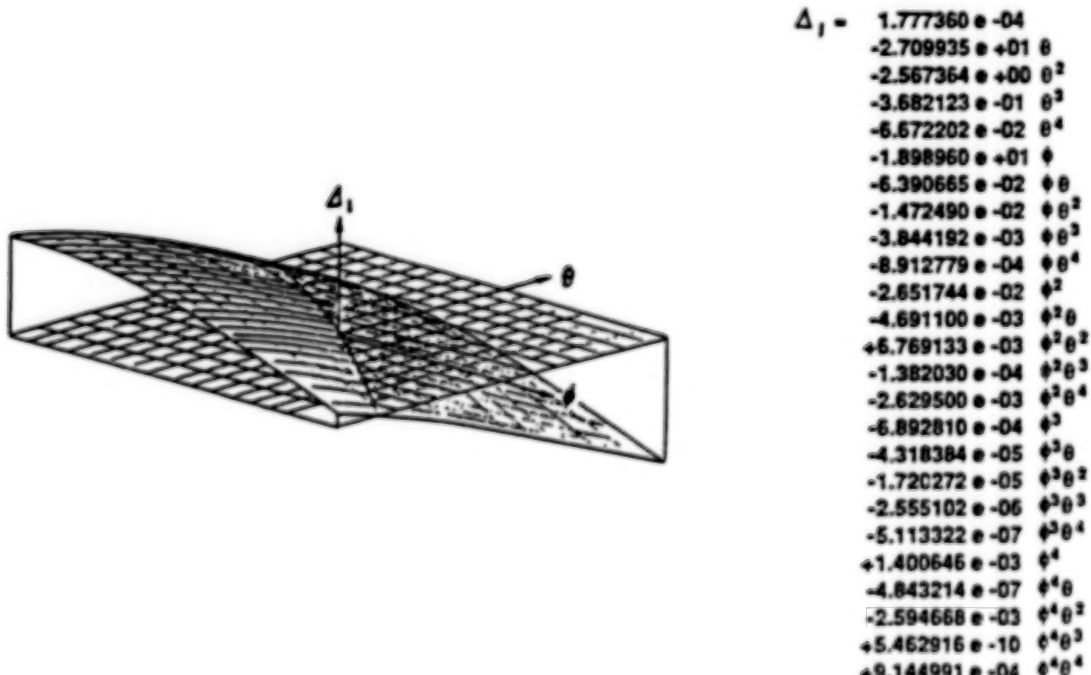


Figure 9. Left pointing surface and corresponding pointing algorithm in the form of a fourth degree polynomial.

**BLANK PAGE**

# SIRTF/IRS CRYOGENIC GRATING DRIVE MECHANISM (ARC SECOND POSITIONING AT 4 K)

Michael J. Kubitschek\*

## ABSTRACT

This paper describes the requirements, design, and test results of a grating drive mechanism for the Infrared Spectrograph (IRS) science instrument on the proposed superfluid helium-cooled Space Infrared Telescope Facility (SIRTF). The IRS grating drive mechanism, tested in fall 1989, satisfied all performance requirements in vacuum at 4 Kelvin. Measured mechanism performance included: 1.5 arc second (arc sec) root-mean-squared (rms) error positioning resolution, 2.2 arc sec rms position repeatability error, less than 10 milli-joules/degree dissipated power, and  $\pm 170$  degree (deg) angular range of travel. Mechanisms that precisely position optical elements at very low cryogenic temperatures (at/below 4 Kelvin) are vital to the operating success of a number of proposed infrared scientific instruments, like those in SIRTF.

## INTRODUCTION

The SIRTF telescope shown in Figure 1(a), is considered part of NASA's Great Observatories Program along with the Hubble Space Telescope (HST), the Gamma-Ray Observatory (GRO), and the Advanced X-Ray Astrophysics Facility (AXAF). SIRTF will be the first true infrared observatory in space, with >1000 times greater sensitivity and a broader wavelength coverage (1.8-700  $\mu\text{m}$ ) than the earlier, successful Infrared Astronomical Satellite (IRAS).<sup>1</sup> The performance gains will result from the use of extremely sensitive, cryogenically-cooled infrared detectors. The size, weight, power, and spatial constraints of a space-borne telescope necessitate positioning optical elements and related mechanisms in the same vicinity, near the 'cold' detectors, and demand proper function of these mechanisms at liquid helium (LHe) temperature; 4 Kelvin (4 K) and below.

Four mechanisms have been identified as necessary to obtain the desired scientific configuration of the IRS instrument shown in Figures 1(b) and 1(c), consistent with the SIRTF application: (1) filter wheel, (2) slit wheel, (3) grating wheel, (4) echelle.<sup>2</sup> The object of the IRS cryogenic mechanism development effort was to demonstrate, with a single mechanism, the technology to meet the most stringent performance requirements of all the proposed mechanisms. The IRS grating drive mechanism was therefore designed, built, and tested to meet the following requirements in a vacuum environment at 4 K:  $\pm 4$  arc sec positioning resolution for 8 separate equally spaced  $\pm 3$  deg ranges of grating motion,  $\pm 2$  arc sec command position repeatability, <1 milli-watt average power dissipation,  $\pm 170$  deg rotational travel, in a maximum package size of 6-in. diameter by 6-in. length.

\*Ball Corporation, Aerospace Systems Group,  
Electro-Optics/Cryogenics Division, Boulder, Colorado

The IRS demonstration mechanism was designed to specifically address the tight positional accuracy and 4 K functional requirements. The design uses structural materials selected for their desirable properties at cryogenic temperatures, such as low relative brittleness and close matching of coefficients of thermal expansion (CTE) for dissimilar materials between room temperature (300 K) and LHe temperature (4 K). Critical mechanism drive, position sensing components, and required processes were identified, while extensive vendor searches were performed with the cryogenic environment in mind. Survival qualification tests followed for a D.C. brushless torque motor. An arc sec rotary transducer configuration was selected and developed for position sensing. Dry lubrication was specified for the mechanism ball bearings. These components and processes were all reviewed and evaluated for their capability to meet all system performance requirements for operation in vacuum at 4 K, before final selections were made for incorporation into the IRS mechanism design.

### MECHANISM DESCRIPTION

Figure 2 shows an isometric cut-away view of the IRS grating drive mechanism. The unit is a simple drive mechanism that consists of a hollow rotating shaft which is simply supported by a single pair of angular contact ball bearings. An 8-faceted grating drum is used to mount test mirrors to the near end of the shaft. The mirrors were later used to verify the angular motion of shaft and drum. The bearings are mounted into the stationary housing and preloaded axially by means of a diaphragm. The physical envelope of the unit is approximately 6 inches in diameter by 6 inches in length.

The rotating assembly is driven by a brushless D.C. torque motor. The permanent magnet rotor is mounted integral to the mechanism shaft, and the stator with armature windings, is mounted into a stationary ring on the housing. The radial and axial spacing of the rotating components is accomplished by individual spacers that fit over the shaft and are shimmed at assembly to coincide with the respective stationary part (stator, housing, etc.) axial locations. The rotating assembly is axially loaded and retained by a jam nut screwed onto threads provided at the far end of the mechanism drive shaft.

The mechanism employs two position sensor configurations which indicate the coarse ( $\pm 10$  arc min) and fine position ( $\pm 1$  arc sec) of the rotating assembly. The coarse sensor is located at the far end of the unit near the torque motor and consists of a rotating, 'Nautilus shell'-shaped cam sensor wheel and a stationary sensor reading head coil. The fine position sensor assembly is located at the near end of the unit, adjacent to the grating drum, and is comprised of a rotating 8-toothed sensor wheel (corresponding to the 8 facets of the grating drum) and two stationary fine sensor reading cores. These sensors will be discussed in more detail later in this paper.

The stationary portion of the mechanism is comprised of the main bearing housing, diaphragm, and separate mounting rings for the torque motor stator and fine sensor assemblies. The radial location and axial spacing of the mounting

rings and housing is handled with three separate, 3-piece sets of mounting flexures that physically link the stationary components together. The cold plate flexure set also serves as a tripod base that mounts the entire mechanism assembly to the dewar cold plate.

## BEARINGS AND LUBRICATION

The IRS mechanism design approach focused on two main objectives: arc sec position accuracy at 4 K and  $\pm 170$  deg of rotational travel. The large range of travel dictated the use of ball bearings to support the mechanism shaft. Operation at cryogenic temperatures necessitated dry lubrication in order to maintain bearing torques at uniform, acceptable levels during operation at 4 K. The ball bearings also required a compliant preload scheme to avoid brinelling during cool-down and required precise control of the preload, in order to meet the position accuracy requirements for operation at both 300 and 4 K.

The bearings used for this application were 440C stainless steel, precision (ABEC-7), angular contact ball bearings (bore diameters 0.875 and 0.750 in., respectively), with 440C stainless steel ball separators, manufactured by Miniature Precision Bearing (MPB) Corp. The bearing balls, separators, and races were lubricated with a sputtered, 800 Angstroms-thick coating of Molybdenum disulphide ( $\text{MoS}_2$ ). This particular combination of bearing and lubrication was chosen for a number of reasons,<sup>8,9</sup> based on meeting the most severe position/design-driving requirements at 4 K. Angular contact ball bearings in particular were selected so that the internal radial clearance of the bearing could be eliminated with sufficient preload. The thin, hard-sputtered  $\text{MoS}_2$  lubrication coating was selected to insure smooth rotational motion, minimize torque non-uniformities due to lubrication 'pile-up', and maintain absolute minimum contamination levels at 300 and 4 K.<sup>9</sup>

Bearing friction torque is nominally a function of the bearing geometry (pitch diameter), the bearing preload, and the ball lubricant. To achieve the required positional accuracy in a cryogenic environment, a single pair of reasonably sized ball bearings consistent with the mechanism package were chosen. The larger diameter bearing (0.875 in. bore) was positioned just beneath the grating drum in order to provide the most stable shaft restraint as close to the grating drum and critical mirror surfaces as possible. The other bearing (0.750 in. bore diameter) was mounted into an axially compliant diaphragm. The compliant diaphragm ensures that the preload level is closely maintained at both 300 and 4 K, without over-stressing the bearings throughout the temperature transition. Snubbers were designed and would be used to carry the axial loads on the diaphragm for a launch environment.

The amount of preload necessary to maximize mechanism positional performance characteristics in the arc sec regime involves a trade-off between maximizing system response stiffness in all extraneous degrees of freedom, yet minimizing resistive, and most important, nonlinear or discontinuous resistive torques (stiction, Dahl effects, etc.) opposing pure rotation. As the axial preload on a bearing increases, the system response stiffness to undesired motions increases,

but so do the unwanted resistive and non-uniform torques (both are functions of preload and lubrication). The approach adopted was to apply 5 pounds (lb) of preload to the bearings via a diaphragm deflection, which corresponds to approximately a 60,000 psi Hertzian contact stress between the bearing balls and races, and yields an empirical torque minimum for a particular bearing.<sup>3</sup>

## MATERIALS CHOICES

A selection of 'flight-like' materials and careful specification of dimensional tolerances were performed in the detailed design to closely match material CTEs and account for the differential thermal contraction of dissimilar materials from room temperature (300 K) to 4 K. The most critical mechanical component required to achieve the mechanism accuracy and travel requirements was undoubtedly the angular contact ball bearings. As previously mentioned, the bearing material chosen was 440C stainless steel, a common ball bearing material. Structural material selections for the mechanism piece part fabrication then, was based primarily on their respective CTE match with the 440C bearings. Figure 3 shows published values for the percent of thermal contraction between 300 and 4 K of some candidate structure materials considered.<sup>4</sup>

The thermal contraction of 6Al-4V titanium (6Al-4V Ti) most closely matches that of 440C while avoiding the extremely brittle properties of the 400-series stainless steels at low temperatures (see Figure 4), and was therefore chosen for the mechanism shaft, housing, diaphragm, and flexure/motor mounting ring materials. The decision was made to fabricate the bearing spacers and mounting plate flexures out of 416S stainless steel (ss). At the same time, this choice was accounted for by increasing slightly the bearing preload (by approximately 2 lb) at room temperature to offset the anticipated decrease in bearing preload at 4 K, due to the differential thermal contraction between the titanium housing and the 416S ss bearing spacers. Test results show that the bearing preload did decrease somewhat between 300 and 4 K as predicted, but the diaphragm was compliant while maintaining a preload on the bearings as designed.

There is however, an unavoidable disadvantage of using either 440C stainless steel or titanium seen in Figure 5, which shows the low thermal conductivity of both materials. Low thermal conductivity slows the overall mechanism cool-down, increases temperature gradients, and could possibly limit the mechanism moves or available scientific observation time, due to inefficient removal of local dissipative heat inputs during flight operation. Temperature gradients of more than 100 K between rotating and stationary assemblies were analytically estimated to occur, if uncontrolled during mechanism cool-down. This is due to the small contact area and poor thermal conduction across the interface between the 440C bearing balls and races. There was serious and immediate concern, since temperature gradients of this size were certain to cause brinelling of the outer bearing races. Flexible copper thermal strapping (multiple strands of 44 AWG 'Litz-wire') was therefore added to both rotating and stationary portions of the mechanism to speed

cool-down, efficiently remove dissipative heat inputs, and minimize the undesirable temperature gradients.

## ADDITIONAL MECHANICAL DESIGN FEATURES

Several features were incorporated into the IRS grating drive mechanism design, shown in Figure 6, to meet the tight system level position performance requirements and achieve these at 4 K. For instance, different bearing sizes were chosen so that the shaft diameters corresponding to these bearing bores could be machined from the same machine set up and the bearings could be assembled from the same end of the shaft. This allows tighter machining tolerances to be held and the most accurate bearing bore-to-bore locational press-fits to be achieved so that shaft fits and possible tilt within the bearings are minimized. The axial span of the bearings was also maximized in order to mitigate the cyclic tilt effect that runout in the 0.750 in. bore diameter bearing will have on the shaft and grating drum. Runout in the 0.875 in. bore diameter bearing would be seen more as a lateral, cyclic shaft wobble at the grating drum and was evaluated to be slight, less than 50 millionths of an inch, but unavoidable. This wobble motion due to bearing runout is dealt with and rejected by the specific configuration of the fine sensors that will be discussed later in the description of the fine sensors.

The construction of the mechanism also features the three separate sets of 3-piece flexures which were mentioned previously and which are used to locate the stationary mounting rings for the torque motor, fine sensors, and mechanism housing. Each flexure in a set is equally spaced around the circumference of the respective mounting rings (see Figures 7 and 8) to serve dual functions. The flexures provide accurate radial and axial location of the mounting rings, and they compensate for the differential thermal contraction between the dissimilar ring materials that they physically join. The individual flexures within each set were match-machined for identical registration of mounting surfaces, designed with sufficient stiffness to maintain mechanism torsion mode resonant frequencies outside the servo control bandwidth, and designed to carry lateral launch loads. Yet the flexures are flexible enough radially to handle the differential thermal contraction between rings with a minimum of induced stresses. Once accurately located during the initial assembly at 300 K, these flexures were match-drilled and pinned in order to negate any flexure base movement during cool-down and insure disassembly and subsequent assembly repeatability.

## DRIVE COMPONENTS SELECTION AND DEVELOPMENT

The motor selection for the IRS demonstration mechanism focused on a commercial vendor search based in part on previously reported experience of motor testing at cryogenic temperatures.<sup>6,7</sup> The search centered primarily on materials and configuration options for motor magnets, epoxies, laminations, armature windings, encapsulants, and their behavior down to 4 K. A torque motor was chosen to drive the mechanism because it provides an 'infinitely precise' positioning drive without gear reduction or associated backlash; it met the low

power dissipation requirements; and a configuration was available that had survived multiple excursions to 4 K without degradation.

The particular torque motor selected for the IRS grating mechanism is a 'pancake-type', 8-pole, 3-phase, D.C. brushless torque motor manufactured by Magnetic technologies, Inc. (P/N 2374H-050P-1750). The physical package of the motor unit is 0.5 in. thick by a 2.375 in. outside diameter. The stationary portion of the motor (stator) has three armature windings wound in a wye configuration around a stack of M-19 silicon steel laminations that are encapsulated with Epoxylite CF682A epoxy resin. Samarium-Cobalt (SmCo) permanent magnets are retained on the rotating portion of the unit (rotor) using 3M-EC-2214 adhesive. To date, the motor and spares have experienced approximately 15 thermal excursions to 4 K without a measured or visible degradation in performance or mechanical integrity.<sup>5</sup>

Accurate and precise angular position sensing at 4 K posed the single most significant component challenge to the operational success of the IRS mechanism design, as no previously published experience at cryogenic temperatures had been found. The rotational position sensing of the IRS drive mechanism was accomplished with an angular transducer technology developed specifically for this mechanism demonstration and more generally for precise angular shaft motions at cryogenic temperatures. The mechanism grating position is indicated by two different magnetically inductive, rotary transducer configurations. The coarse sensor and cam plate shown in Figure 7 provide absolute position feedback ( $\pm 10$  arc min) for large grating moves (between facets) in the  $\pm 170$  deg range of mechanism travel.

The fine sensor configuration shown in Figure 8 uses two sensor reading cores and an 8-toothed wheel to provide arc sec position resolution feedback over the 8 separate  $\pm 3$  deg ranges of shaft rotation that correspond to the 8-facets available on the grating drum for mounting mirrors. The sensor cores are placed on opposite sides of the toothed wheel center to simultaneously detect the position of the shaft within each of the 8 grating drum facets. In this configuration, sensitivity to axial and radial motion, such as bearing runout, are rejected by the differential nature of the two sensors spaced on opposite sides of the wheel.

The IRS control system to drive the mechanism had to be capable of performing 3 major functions: commutating the torque motor, providing control for velocity feedback from the coarse sensor channel for large grating moves (between facets), and providing control for arc sec position feedback from the fine sensor channel for small grating moves ( $\pm 3$  deg within a facet). Figure 9 shows the block diagram of the overall servo control system implemented. The logic gate determines the selection of the individual control loop to be employed. The mechanism control is passed between three separate servo loops during the functional operation of selecting a location and then moving to that exact position within the appropriate facet. The three loops are the velocity loop (trajectory generator), the coarse position loop, and the fine position loop, as well as the torque motor commutation to carry these out. The trajectory generator is utilized in order to optimize

dissipative power consumption for grating moves between facets, as a way to conserve dewar cryogen.

A more detailed discussion of the torque motor selection, sensor technology development, and control system design and implementation for this application is presented in reference 5. It should be mentioned here, however, that the fine position servo loop has an integral compensation feature which accounts and compensates for difficulties controlling the ball bearing suspended hardware in the arc sec positioning regime. The servo loop compensation adequately handles any potential control system difficulties experienced as a result of an increase in the torsional spring constant of the ball bearings for very small angular movements. This torsional stiffening or "Dahl" behavior of ball bearing systems (i.e., ball bearings acting like springs over very small angular excursions) has been quite well documented for room temperature applications,<sup>8,11</sup> and was not found here, to differ drastically at 4 K. The fine position servo loop, along with this associated compensation and arc sec position feedback supplied by the fine sensors, are the functional blocks in the architecture of the control system that afford the mechanism the capability of arc sec positioning resolution and repeatability performance within the required  $\pm 3$  deg angular range of each grating facet.

#### APPARATUS AND TEST SET-UP

Figure 10 shows a schematic layout of the mechanism performance test set-up. All mechanism performance tests were completed in a vacuum environment at LHe temperature (4 K) inside a bench-top dewar manufactured by Precision Cryogenics, Inc. The dewar has a 40 hour hold time and a working volume adjacent to the aluminum cold plate that is approximately 8-in. in diameter by 8-in. in length. The mechanism housing support flexures were attached directly to the dewar cold plate via threaded fasteners and holes tapped into the cold plate (see Figure 2).

Polished mirror surfaces were attached to the rotating, grating drum surfaces and viewed from outside the dewar by means of a 1/4 wave flat, BK-7 glass window. The window was placed in the side of the dewar, insulated and 'stopped-down' with reflective material to minimize parasitic/radiative thermal load to the dewar cryogen. The mirror surfaces themselves were diamond turned blanks of 6061 aluminum, polished to 1/2 wave flat, and mounted to three of the grating drum facet surfaces by using simple 3-point mounts. In order to expedite testing at 4 K, only three grating facets were chosen to verify the mechanism positioning capability and performance accuracy. The facets employed were not uniquely selected in any predetermined manner other than by the desire to choose two adjacent facets, as well as a facet more than 90 deg (2 facets) away from these, in order to vary the test movement range between facets. All actual grating position verification tests were performed optically using a Wild-Heerbrugg T-2000 digital theodolite positioned external and adjacent to the dewar on an optical bench in the lab. An additional mirror was mounted on the mechanism housing in view of the window to serve as a stationary reference.

## MEASURED PERFORMANCE 5

The main objective of the mechanism performance tests was to determine the stepping precision and repeatability of the IRS grating drive mechanism at 4 K. All results reported here were performed in a vacuum at 4 K inside the dewar described. The unit achieved the cool-down from 300 to 4 K in approximately 12 hours, and the expected temperature gradients between the mechanism shaft and housing were significantly reduced as a result of the thermal strapping. Stepping resolution was determined by advancing the mechanism grating with a sequence of steps ranging from 2 to 200 arc sec and optically measuring angular deviation (error) from the commanded step size. In this manner, the rms error for small steps ( $2 < \theta < 200$  arc sec) within a single facet was measured to be 1.5 arc sec.

The performance capability of the mechanism to accurately repeat large angle steps was also measured. For 3 deg steps within a single facet, the rms error for repeatability was measured to be 2.2 arc sec. The same rms error was observed for larger angle steps from facet-to-facet, ranging in step size from 45 deg to 135 deg. Tests were also done to measure the time it took the mechanism to settle within 2 arc sec of the command step position for three separate angular displacements. The step and settling times for 330 arc sec, 7.9 deg, and 263 deg moves of the instrument grating were 130 msec, 180 msec, and 1.7 sec, respectively.

Since the spectrometer will be operated at 4 K, the power consumption of its cryogenic components directly impacts the SIRTF helium consumption, and hence the mission lifetime. Total power dissipation at 4 K for both coarse and fine position sensors was measured to be 60 microwatts. Under normal operational conditions the grating mechanism is moved intermittently, and its impact on the consumption is best expressed as the energy required to step and settle to a new angular position. Figure 11 shows this relationship for angular displacements up to about 2 deg. For larger angular displacements, considerable reduction in the slope of this curve is possible by employing the principles of the optimum velocity trajectory mentioned earlier.<sup>5</sup>

In the process of testing and optimizing the precision and repeatability of the IRS unit, significant effort was also directed towards characterizing the Dahl behavior of the mechanism ball bearings. Figure 12 shows a graph of the measured torsional spring constant of the mechanism for various step angle sizes at 300 and 4 K.<sup>10</sup> This data was generated by analyzing the open loop frequency response of the mechanism to position commands of the angular step sizes shown, computing the torsional stiffness (spring constant) of the mechanism, and characterizing the appropriate control compensation required to account for the changes, at both 300 and 4 K. The author believes that the difference in the overall magnitudes of the two curves (between 300 K and 4 K curves) may be attributed primarily to the reduction in bearing preload (approximately 2 lb) of the system between room temperature and 4 K that results from differential thermal contraction between the bearing spacer (416S ss) and housing (6Al-4V Ti).

## CONCLUSIONS

The IRS demonstration mechanism met all system performance requirements at 4 K and successfully demonstrated this grating drive positioning technology at cryogenic temperatures. In addition, the behavior of the ball bearings used in this mechanism was characterized by measuring the torsional flexure constant at both 300 and 4 K for various ranges of motion precision in the arc sec regime. The test data revealed only a slight change in the mechanism stiffness and position resolution performance between 300 and 4 K. The reduction in preload was, in all probability, significant enough to account for the decrease in position resolution by reducing mechanical hardware stiffness and frequency response to the point of introducing nonlinearities that were not as tightly controllable. It is believed that the performance of the mechanism at 4 K could be made to match that measured at 300 K by using a bearing spacer fabricated out of the identical material as the housing (6Al-4V Ti), thus insuring that the bearing preload remains unchanged over the temperature excursion.

In addition to changing the material for the bearing spacer, future work and improvements to the mechanism design and configuration include: overall reduction in the mechanism package size and weight, further test and characterization of Dahl friction effects for varying values of bearing preload in order to optimize mechanism performance with this parameter, 4 K vibration survival and subsequent performance data acquisition to simulate the environmental condition to which the mechanism will be subjected for flight, as well as extended mechanism life-test data acquisition. Present plans for reduction in package size entail: eliminating the flexure mounting ring and fastening the cold plate base flexures directly to the mechanism housing, moving the axial location of the torque motor inboard of the bearings to mount it within the mechanism housing, and refining the position sensor technology as a means of further reducing the necessary mechanism envelope diameter. These modifications are expected to reduce the mechanism to a 5-in. diameter by 5-in. length maximum package size.

The schedule for further characterization of the mechanism performance under varying bearing preloads and vibration qualification testing is uncertain at the time of this publication. However, the current mechanism hardware is to be life-tested and incorporated into a cryogenic, infrared, spectrographic instrument built by Cornell University, which is scheduled for operation with the ground-based telescope facility at Palomar Observatory in California, sometime late in 1991.

The IRS mechanism development program success has established baselines for mechanism design at cryogenic temperatures in a number of key areas: motor selection and design, angular transducer design and development, ball bearing behavior, and lubrication use. The IRS grating drive mechanism test results have demonstrated the technical and functional viability of all these technologies together in a cryogenic environment (4 K) that successfully meets required optical grating accuracies approaching 1 arc sec for the Infrared Spectrograph (IRS) instrument for SIRTF.

## ACKNOWLEDGEMENTS

The author would like to acknowledge contributions made to the IRS grating drive mechanism design, fabrication, test, and support activities without which the writing of this paper would not have been realized. Dr. James R. Houck of Cornell University and Principal Investigator for the IRS instrument on SIRTF. At Ball Aerospace Systems Group (BASG), Dr. Harold Reitsema; program manager-IRS mechanism technology development, for editorial comments and support. Dick Maxwell; functional management, for funding to write this paper. Charles Downey for system engineering direction, performance tests data, and editorial suggestions. Bob Loomis for his conceptual design and resource throughout the detailed design. Kent Roller for his bearing and lubrication expertise and recommendations. Jim Tucker for the machining and assembly craftsmanship with the mechanism hardware. Rich Tarde for the electrical engineering and servo-control system design. Damon Phinney, Walter Roll, and Cliff Highman for their editorial comments and suggestions. Peggy Irwin and Joellen Domenico for their word processing and graphical presentation support. Bob Unger for his support, encouragement , and guidance throughout the whole labor-intensive process these past two years.

## REFERENCES

1. Lee, J. H. Thermal Performance of a Five-Year Lifetime Superfluid Helium Dewar for SIRTF. *Cryogenics*. vol 30. March 1990. pgs 166-172.
2. Ramos, R., Hing, S. M., Leidich, C. A., Fazio, G., Houck, J.R., and Riche, G. Space Infrared Telescope Facility (SIRTF) Science Instruments. *Proc SPIE* (1988) 973 2.
3. Phinney, D. D. A Simple Way To Predict Drag Torque In Preloaded Angular Contact Ball Bearings Running At Very Low Speed. Report No. SER DDP-14. Ball Aerospace Systems Division. Aug 1987. and Friction Torque in Lightly Loaded Ball Bearings With Vac Kote Lubrication. Report No. TN66-162. Ball Brothers Research Corp. 30 Nov 1966.
4. Handbook on Materials for Superconducting Machinery. Cryogenics Division, National Bureau of Standards. Boulder, CO USA. Jan 1977.
5. Downey, C. H., Tarde, R. W., Kubitschek, M. J., and Houck, J.R. An Arc second Grating Drive Mechanism for Operation at 4 Kelvin. Submitted for publication to *Cryogenics*. Feb 1991.
6. Pompea, S. M., Bartko, F., and Houck, J. R. Cryogenic Testing of Stepper Motors. *Proc SPIE, Instrumentation in Astronomy IV*. Vol 331. 1982. pgs 35-43.
7. Luciano, G. Cryogenic Mechanism of ISO Camera. *Proc 3<sup>rd</sup> European Space Mechanisms and Tribology Symposium*. Dec 1987. pgs 233-236.

8. Todd, M. J. Models for Steady and Non-steady Coulomb Torque in Ball Bearings. Proc 3rd European Space Mechanisms and Tribology Symposium. Dec 1987. pgs 137-148.
9. Gould, S. G., and Roberts, E. W. The In-Vacuo Torque Performance of Dry-Lubricated Ball Bearings at Cryogenic Temperatures. Proc 23<sup>rd</sup> Aerospace Mechanisms Symposium. 1989. pgs 319-333.
10. Tarde, R. W. SIRTF-IRS Control System Design and Analysis Final Report. Report No. 2562.89.040. Ball Aerospace Electro-Optics/Cryogenics Division. Boulder, CO USA. 18 Dec 1989.
11. Dahl, P. R. Solid Friction Damping of Mechanical Vibrations. AAIA Journal. 14(12). Dec 1976. pgs 1675-1682.

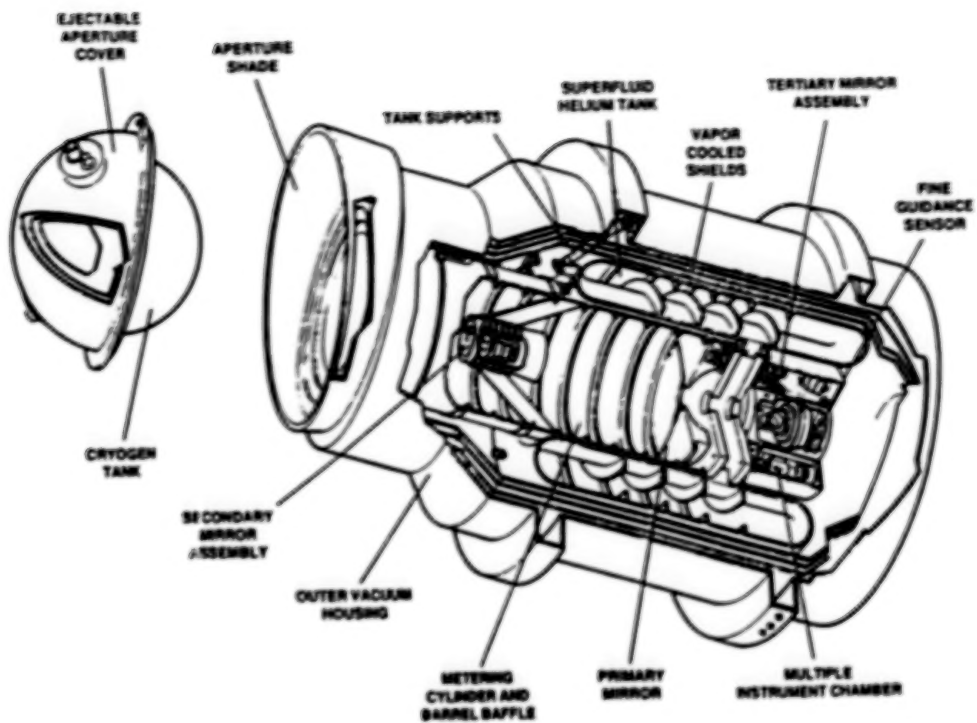


Figure 1(a). Cut-away view of SIRTF telescope assembly<sup>1</sup>.

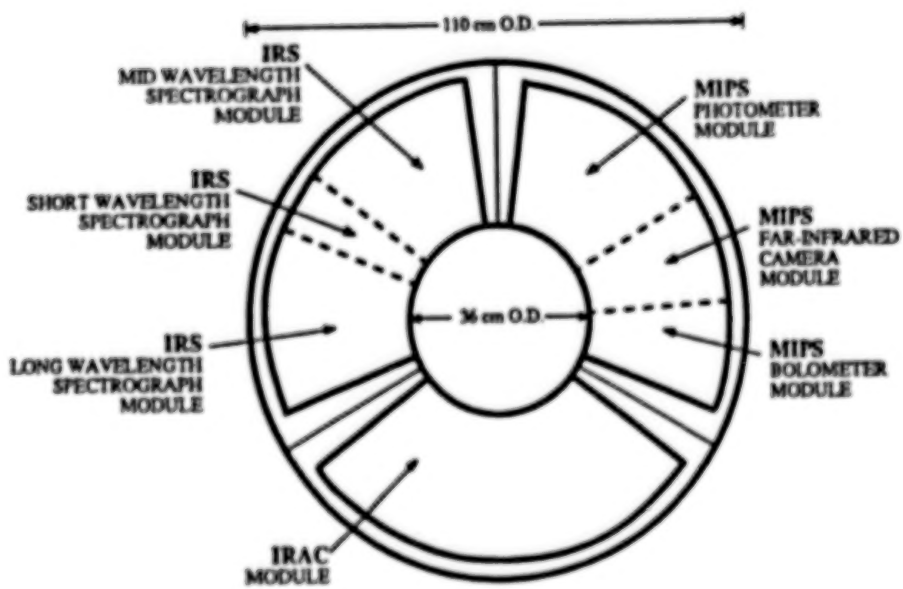


Figure 1(b). SIRTF multiple instrument chamber (MIC)<sup>2</sup>.

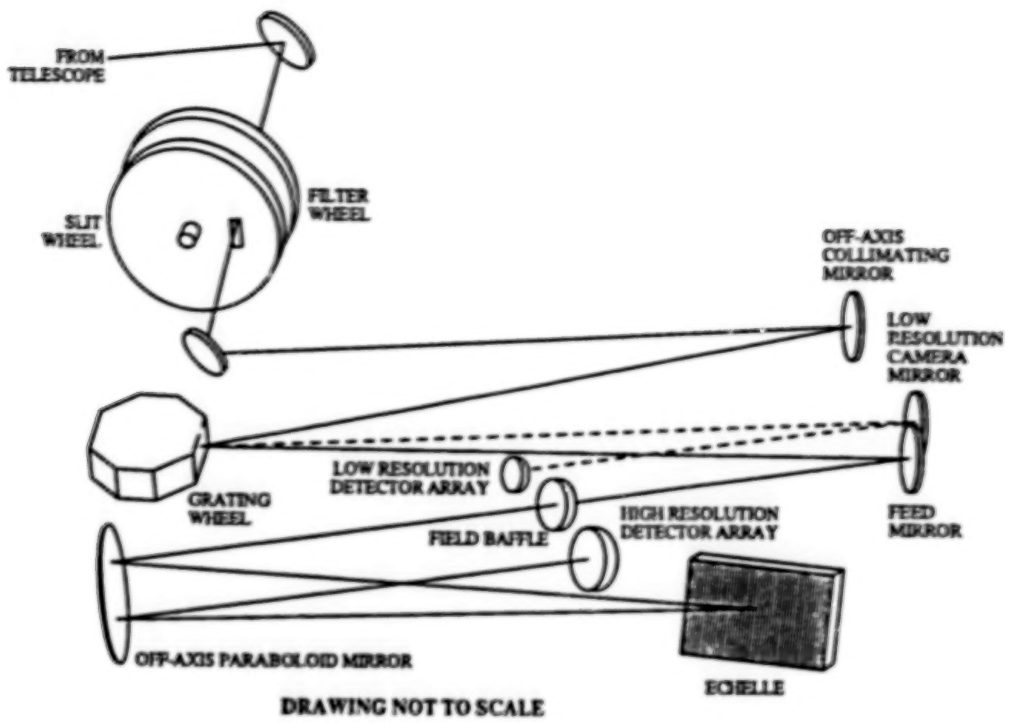


Figure 1(c). IRS mid wavelength module baseline optical system schematic<sup>2</sup>.

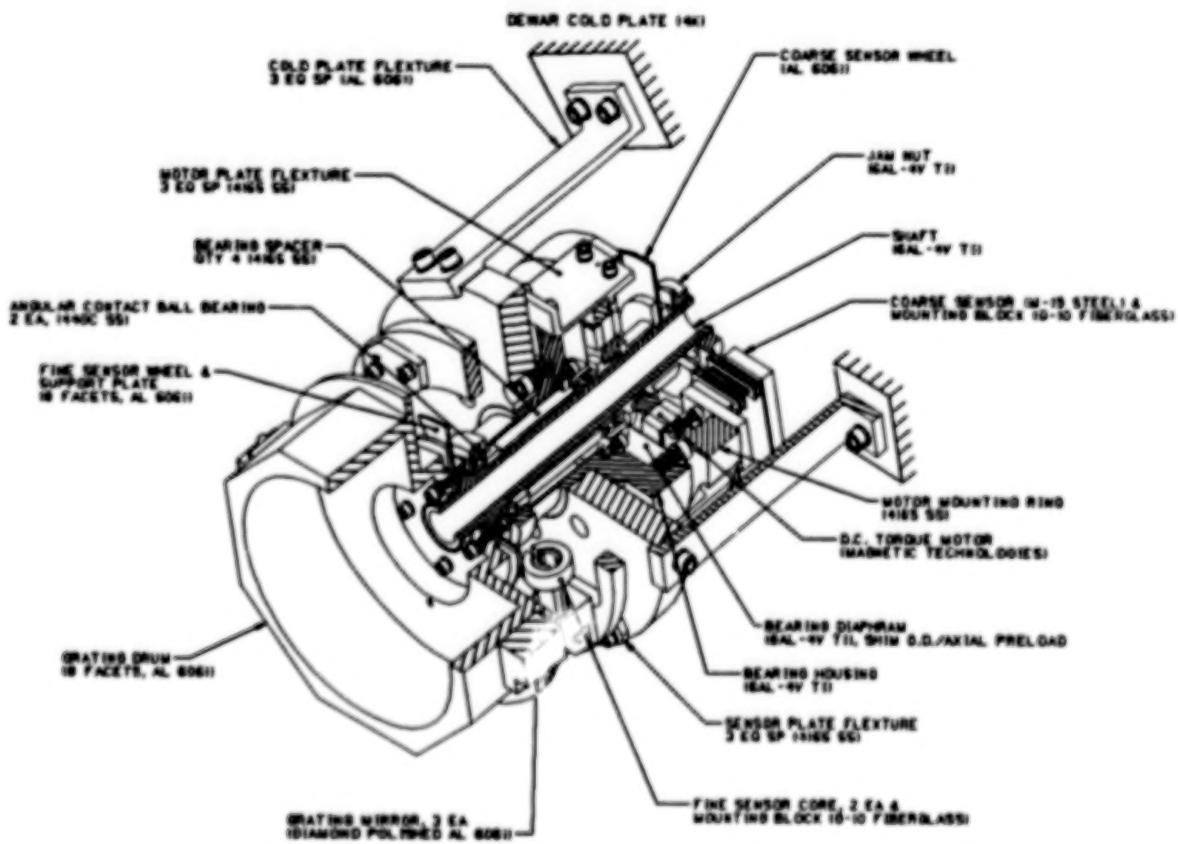


Figure 2. Isometric cut-away view of the IRS grating drive mechanism.

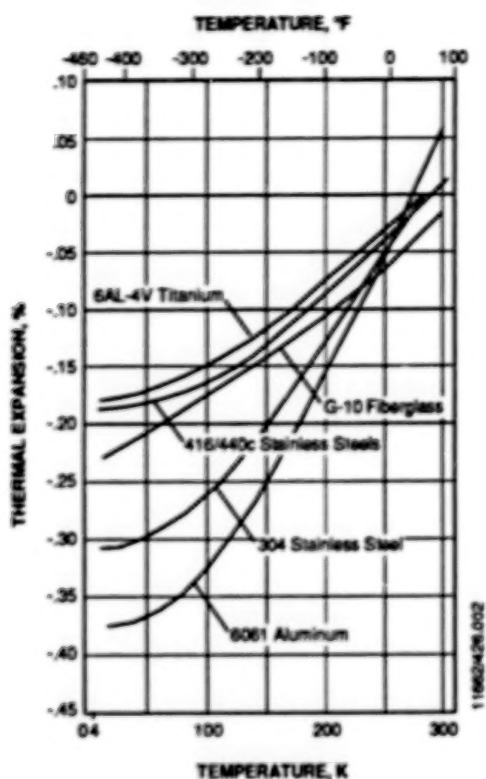


Figure 3. Published values of thermal expansion of candidate structure materials vs. temperature<sup>4</sup>.

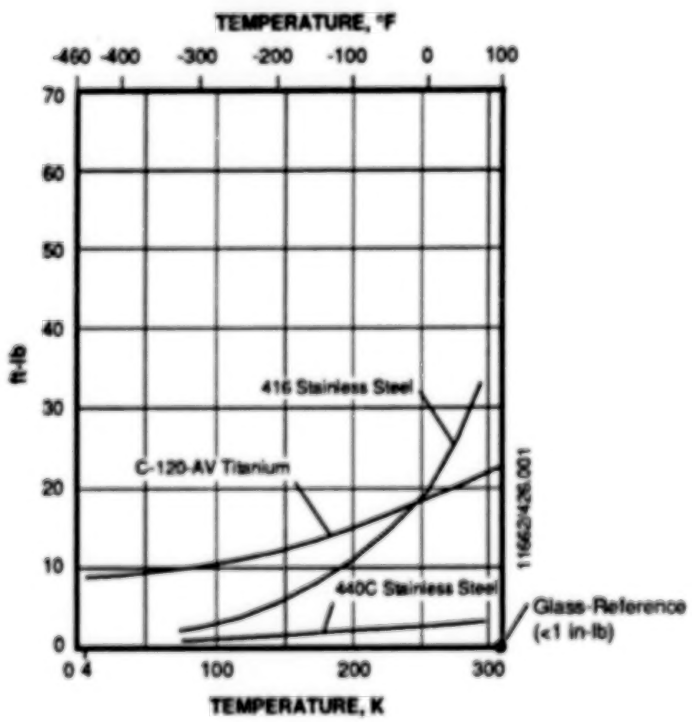


Figure 4. Published values of impact energy of engineering materials vs. temperature<sup>4</sup>.

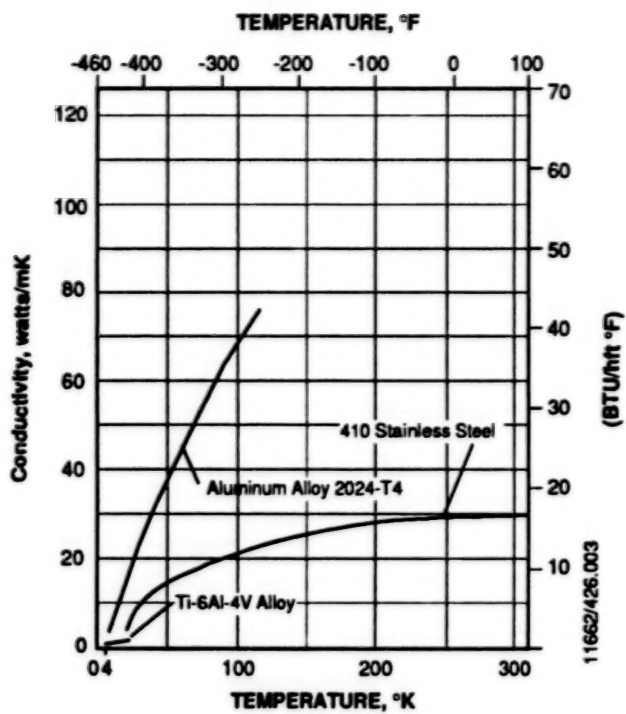


Figure 5. Published values of thermal conductivity of engineering materials vs. temperature<sup>4</sup>.

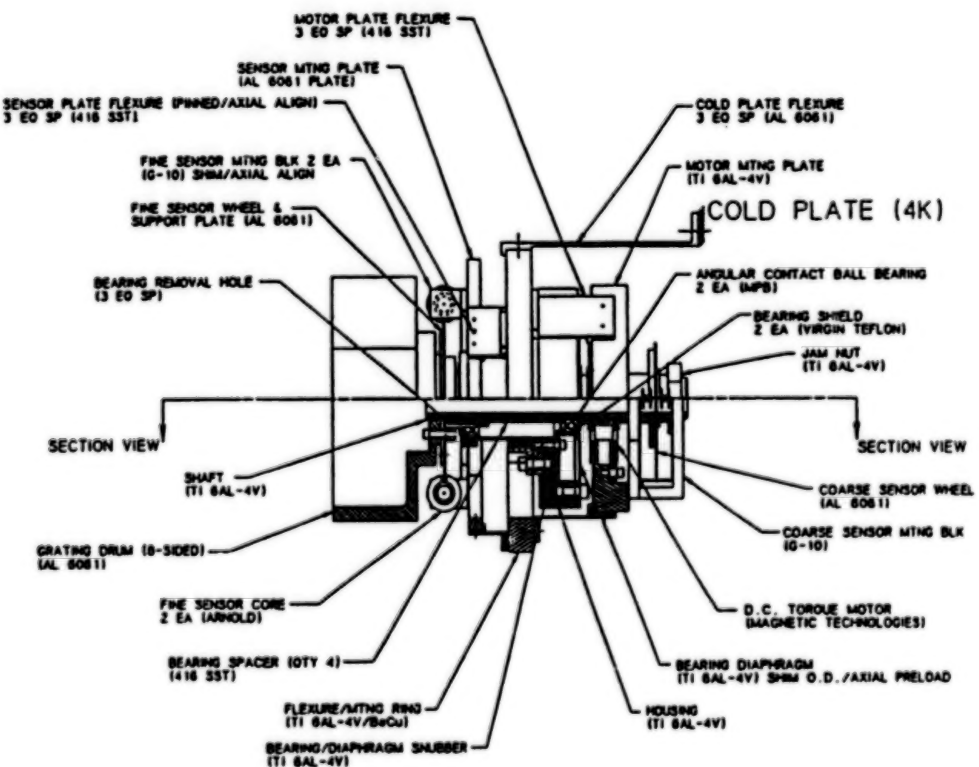


Figure 6. Orthogonal cross-section view of the IRS grating drive mechanism.

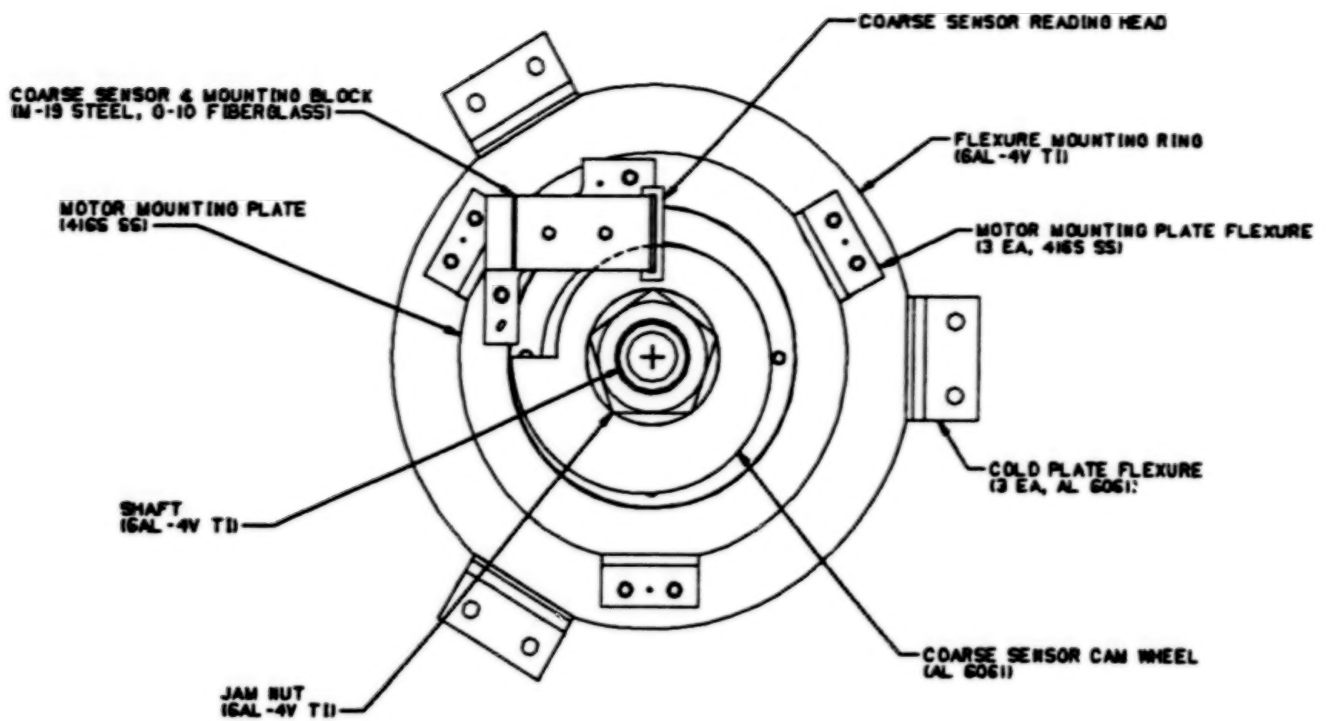


Figure 7. Bottom-end view of the IRS mechanism coarse sensor configuration .

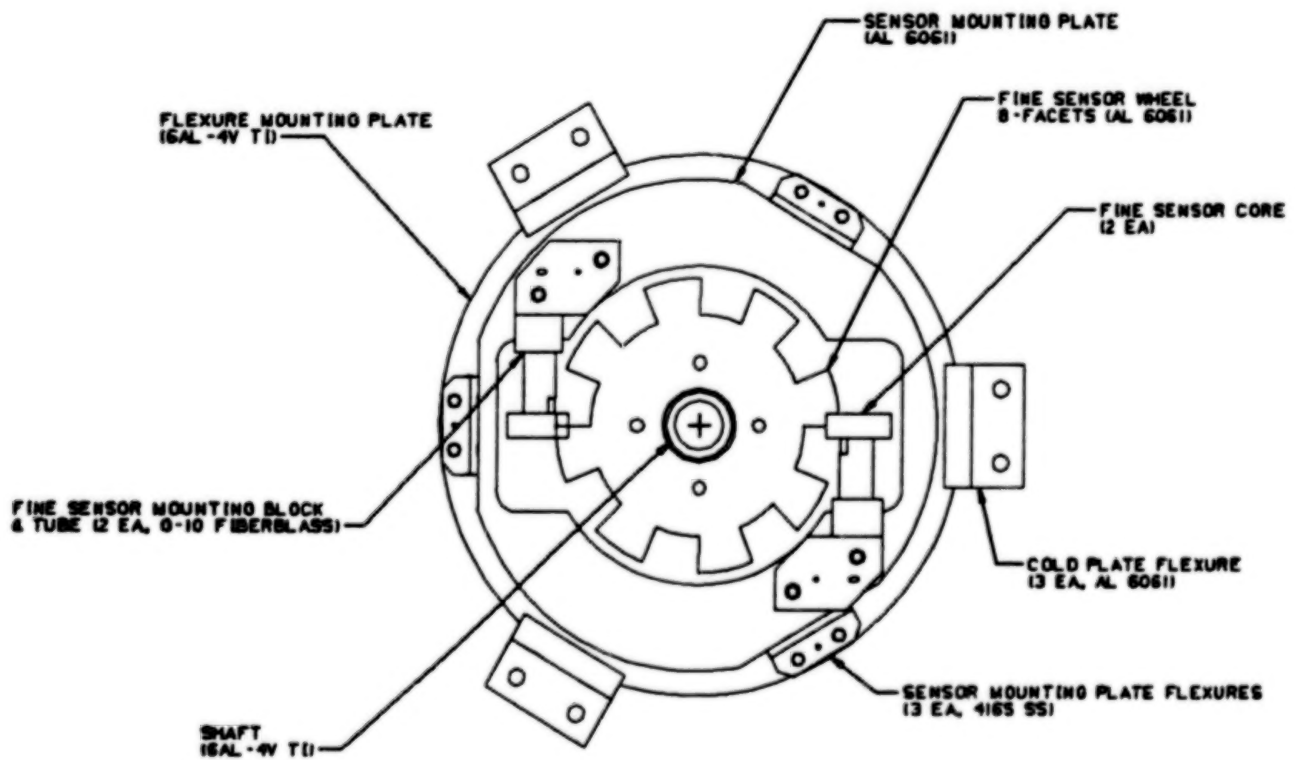
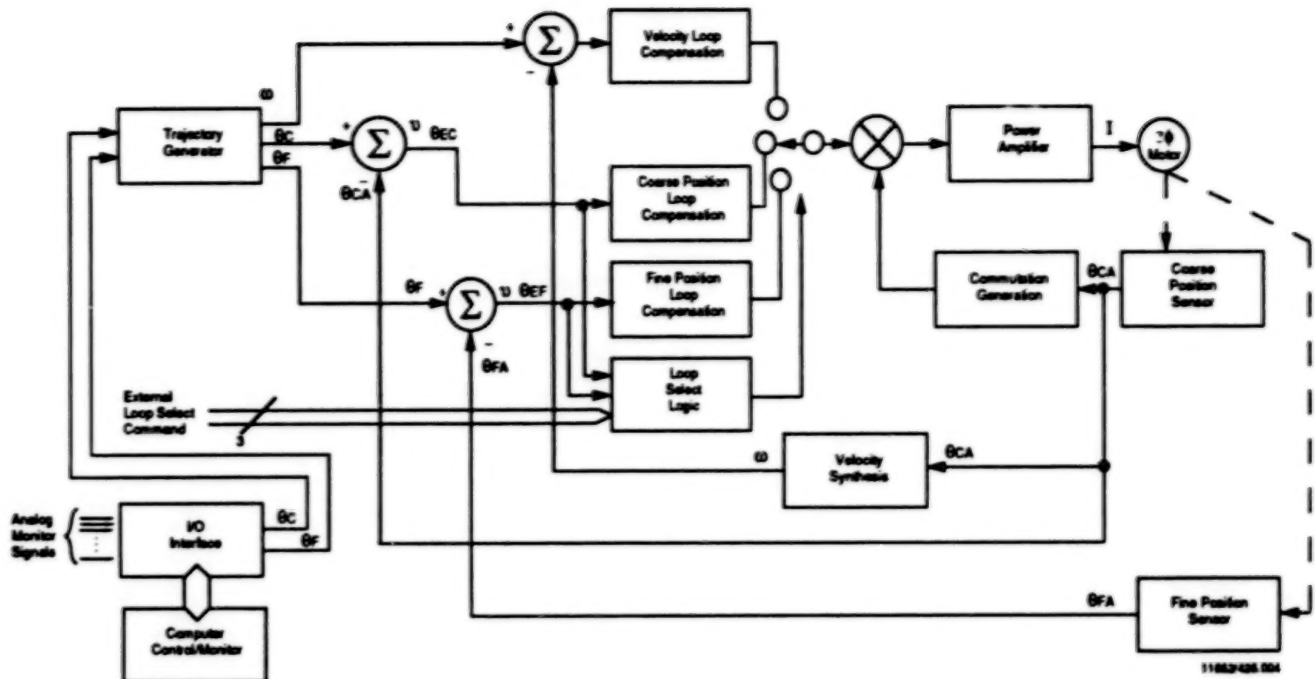


Figure 8. Top-end view of the IRS mechanism fine position configuration (grating drum not shown).



WHERE:

- $\ominus$  - Velocity Command
- $\theta_C$  - Coarse Position Command
- $\theta_F$  - Fine Position Command
- $\theta_{CA}$  - Actual Coarse Position
- $\theta_{FA}$  - Actual Fine Position
- $v$  - Command/Actual Error

Figure 9. IRS grating mechanism servo system block diagram<sup>10</sup>.

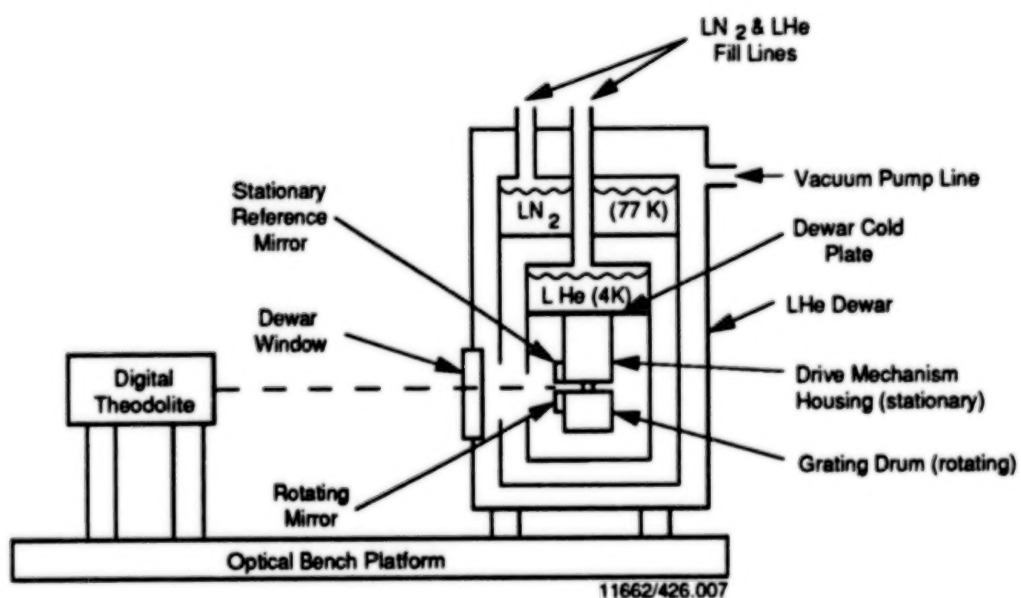


Figure 10. Schematic layout of the IRS grating drive mechanism cryogenic performance test setup<sup>5</sup>.

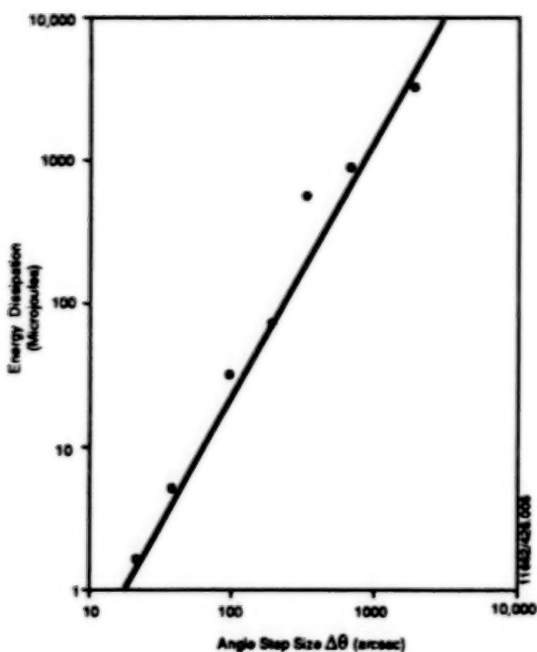


Figure 11. Energy per commanded grating step size at 4 kelvin<sup>5</sup>.

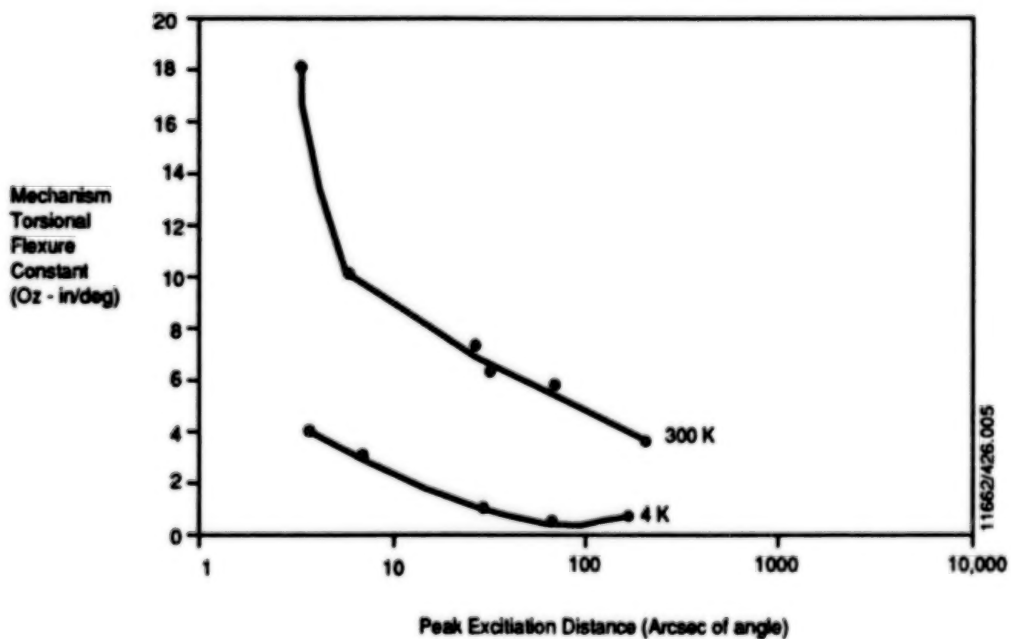


Figure 12. IRS grating drive mechanism torsional constant vs. sweep distance<sup>10</sup> (Random plant test – 6.9 V facet about fine transfer function center).

## **Development of a Relatchable Cover Mechanism for a Cryogenic IR-Sensor**

R. Birner, G. Lange, M. Roth, and A. Voit \*

### **ABSTRACT**

A Cover Mechanism for use on the Infrared Background Signature Survey (IBSS) Cryostat has been developed. The IBSS IR-Instrument is scheduled for STS launch in early 1991 as a payload of the SPAS II satellite.

The cover is hinged, with a motorized rope drive. During ground processing, launch, entry and landing, the cryostat, which houses the IR-Instrument, is required to be a sealed vacuum tight container for cooling purposes and contamination prevention. When on orbit, the cover is opened to provide an unobstructed field of view for the IR-Instrument. A positive seal is accomplished through the use of a latch mechanism. The cover and the latch are driven by a common redundant actuator consisting of DC motors, spur gears and a differential gear. Hall probe limit switches and position sensors (rotary variable transformers) are used to determine the position of the cover and the latch. The Cover Mechanism has been successfully qualified for thermal vacuum (-25 to 35 °C), acoustic noise, vibration (6 G's sine, 9.7 G RMS) and life cycles.

This paper describes constricting requirements, mechanical and electronic control design, specific design details, test results of functional performance, environmental and life tests.

### **I. INTRODUCTION**

The Infrared Background Signature Survey (IBSS) is an SDIO-sponsored program with the purpose of obtaining scientific data for use in the development of defense sensor systems. The IBSS payload will be carried by the Shuttle Payload Satellite (SPAS) II, an advanced version of the SPAS-01 spacecraft, which flew on space shuttle flights STS-7 and STS-11. Figure 1 illustrates the SPAS II spacecraft. The IBSS instrument (Figure 2) consists of four major functional units, which are the cryogenically cooled telescope, baffle, spectrometer and imaging radiometer. The instrument is mounted inside a cryostat equipped with a supercritical He cooling subsystem [1]. The cover mechanism described below is a constituent of the cryostat vessel and acts as an aperture door for the telescope. During ground operations, launch and landing, the cover must be closed and sealed to maintain the isolation vacuum essential for the cryostat.

---

\* Messerschmitt-Bölkow-Blohm GmbH (FRG), P.O.Box 801169, D-8000 München 80

## 2. REQUIREMENTS

Key requirements for the cover mechanism are listed in Table 1. In addition, a design for low mass, power consumption and minimum contamination was required.

Opening angle .....	Nominal 110° Minimum 103°
Travel time (both motors)	
Without latching .....	Nominal 55 sec
With latching .....	Nominal 130 sec
Number of closing/opening operations	
Without latching .....	100
Number of latching operations .....	40
Motor drive	
Current limit .....	300 mA ± 30 %
Voltage .....	23 to 31.5 V dc
Cover position accuracy .....	± 1.5°
Cover limit switch accuracy .....	± 0.5°
Vacuum Tightness (GHe) .....	≤ 10 <sup>-7</sup> mbar*l/sec
Diameter of cover .....	270 mm
Mass .....	≤ 6 kg

TABLE 1: COVER MECHANISM REQUIREMENTS

## 3. DESIGN DESCRIPTION

The principal functional scheme of the cover mechanism is shown in Figure 3. The Cover Mechanism comprises the following constituents:

- Cover with rope drive
- Latch
- Rotary Actuator
- Instrumentation
- Cover Drive Electronics

The principle adopted to actuate the cover provides the following major features:

- Only one actuator drives both cover and latch mechanism
- The sequencing of latch and cover motion is achieved by mechanical means
- The actuator is located close to the latch. Therefore the load path of highly loaded mechanism elements is kept as short as possible
- Cover lift-off is assisted by a cam
- Temperature excursion tolerant design by use of flexible bellows couplings, spherical bearings and appropriate tolerancing of bearing gaps

### **3.1 Cover**

The cover as shown in Figure 4 is hinged, with a motorized rope drive. When required, a positive seal is accomplished through the use of a latch mechanism. The cover houses a light source to facilitate inflight check of IR sensor alignment. The cover is attached to the hinged yoke by a ball joint. This arrangement assures self aligning seating of the cover on the cryostat o-ring seal. The hinge design heritage is a space qualified solar panel hinge. Each of the two hinges (Figure 5) has a spherical bearing for self aligning of the cover tilting axis. The cover is actuated by redundant rope drives via the latch drive shaft. Two small pulleys connect the ropes from the large pulleys to the cover hinges. Spiral flat springs connect to the cryostat vessel and to the small pulleys. The springs apply tension in a direction which tends to close the cover. The springs take up slack in the rope pulleys.

### **3.2 Latch**

The latch mechanism shown in Figure 6 is connected directly to the axle shaft between the large rope pulleys. The latch mechanism uses an overcenter link to obtain a high mechanical advantage and to hold down the cover in a selflocking manner. The latch provides a nominal hold down force of 4700 N. A cam attached to the latch drive shaft is implemented to provide a lift assist for the potential critical phase, when the cover takes off from the seal. The cam performs a direct levering beneath a shoulder rigidly attached to the cover with a force capacity greater than 950 N. If this force had to be applied via the hinge shafts, an actuator torque in excess of 700 Nm would be required. This would have resulted in a much larger and heavier actuator and obviously considerably higher peak power demands. For on-orbit operations the cover can be closed but left unlatched to shorten the opening and closing times and to avoid unnecessary use of the latch mechanism.

### **3.3 Rotary Actuator**

The rotary actuator is composed of redundant dc-motor/spur gear trains, a differential, and a worm gear drive with a built-in overrunning clutch. The clutch provides adjustable limiting of output shaft travel. The mounting plate of the actuator is equipped with heaters and thermostats. The heaters keep the actuator temperature above 0 °C in a cold temperature environment. The stall torque of the actuator is 22 Nm. The static load capability without damage is 41 Nm.

### **3.4 Instrumentation**

The cover is equipped with limit switches, position indicators, temperature sensors and strain gauges. The position indicators are of the rotary variable transformer type. The strain gauges are used for force adjustment and testing only. Miniature hall probes are used to sense the end positions of cover and latch. The cover qualification model was equipped with an additional torque transducer to allow for measurement of the actuation torque.

### **3.5 Lubrication**

All bearings of cover and latch are MoS<sub>2</sub> dry lubricated. The actuator uses a grease lubrication. The bearings are equipped with dust covers to prevent contamination of the IR telescope.

### **3.6 Materials**

The cover is made from aluminum 6061 T4 (same material as used for the cryostat vessel). The design aimed for minimum usage of plastic materials to minimize contamination. Highly loaded parts of the latch and cover hinges are made from titanium or corrosion resistant steel. A steel/bronze material pairing is being used on the spherical bearing of cover hinges and latch.

### **3.7 Cover Drive Electronics**

The cover drive electronics comprises two separate power and logic switching units for redundant cover operation and latching. Each system has its own set of commands. Logic switching unit no. 1 uses the four hall probe limit switches to determine the position of the cover and latch while logic switching unit 2 uses the two position indicators. An override command is built-in to overcome a failure of limit switches, position indicators or logic unit. In the override mode the motors are activated directly by manual power on/off commands. Each motor current is limited in order to prevent a high current draw in the event of a short, jam, or motor stall.

The cover drive electronics are housed in the cryostat electronic box and includes telemetry signal conditioning of limit switches, position indicators, motor currents, and temperatures.

Power to the electronics is supplied by orbiter fuel cells in the attached mode or by two batteries in the detached mode. Redundant converters supply regulated power for the logic switching units.

#### 4. TESTING

The Cover Mechanism Qualification model has been successfully qualified for thermal vacuum (-25 to 35 °C), acoustic noise (OASPL 138 dB), vibration (6 G's sine, 9.7 G RMS), vacuum tightness ( $GHe 2 \times 10^{-8}$  mbar\*L/sec) and life cycles. The thermal vacuum testing included a simulation of worst case thermal gradients of 35°C between yoke and cover hinge baseplate by means of heaters attached to the yoke. The life cycle testing covered more than 200 operating cycles in different modes including cover closing without latching and single motor operation. The cover also passed EMC testing performed together with the cover drive electronics.

In order to allow for functional cover tests on the integrated evacuated cryostat at cold conditions, a vacuum tight test bulkhead was used.

Typical records of cover and latch position angles versus time obtained during opening and closing operation are shown in Figure 6. Figure 7 presents the cover holdown force and actuator torque versus latch drive angle. The measured total power consumption of the motors was less than 6 watts.

#### 5. CONCLUSION

A reusable cover and latch mechanism compatible for use on space borne telescopes has been developed and successfully qualified. The design features vacuum tight sealing, high holdown force, redundancy, low mass and power. The instrumentation and electronics allow for appropriate redundant control and monitoring.

#### ACKNOWLEDGMENT

This work has been funded by a SDIO contract and MBB funds. The authors wish to express their thanks to all MBB personnel who contributed to the program. In particular, we wish to thank F. Diewald for his contribution to the electronics design.

#### REFERENCE

1. G. Lange, H. Pulkert  
"A Supercritical Helium Dewar for the Infrared Background Signature Survey Experiment"  
SPIE Technical Symposium, San Diego, CA., July 9-13

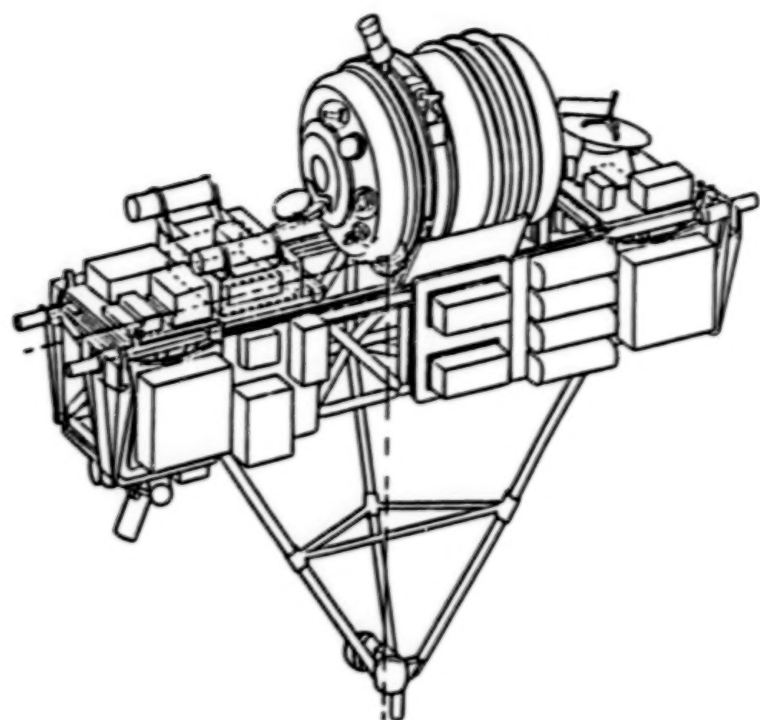


**Figure 1: SPAS II Satellite**

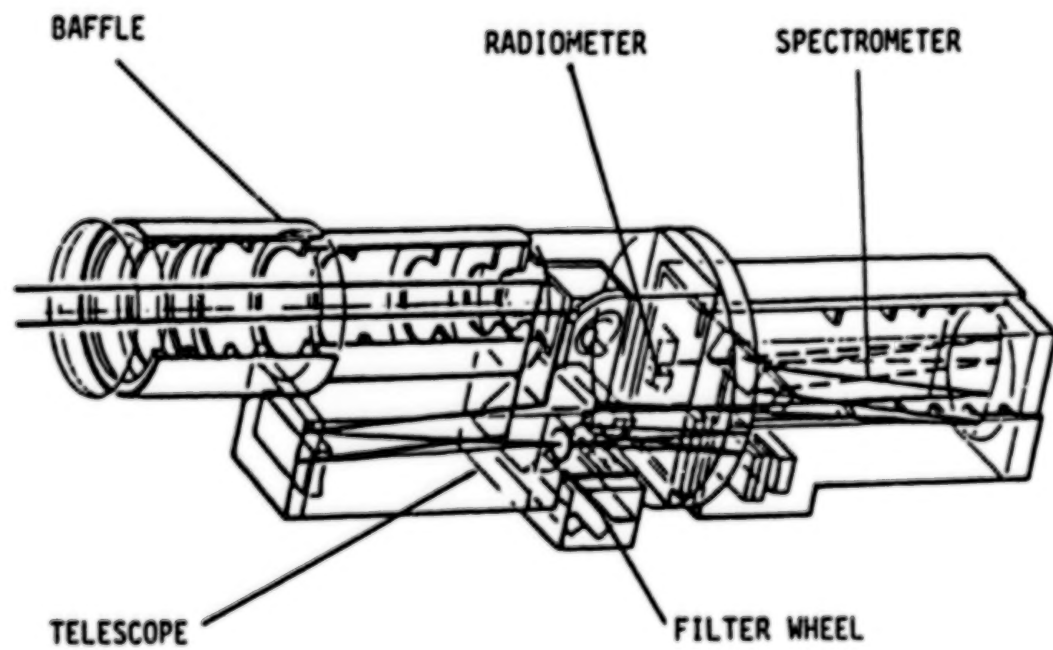


**Figure 2: IBSS IR Instrument**

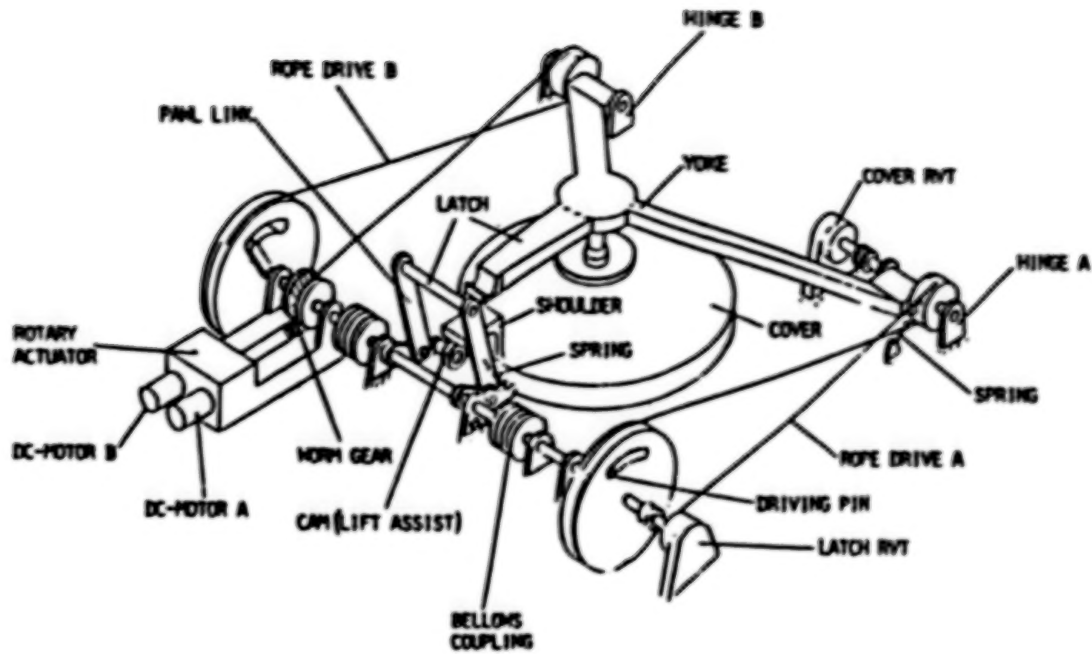


Figure 3: Actuation Scheme of Cover

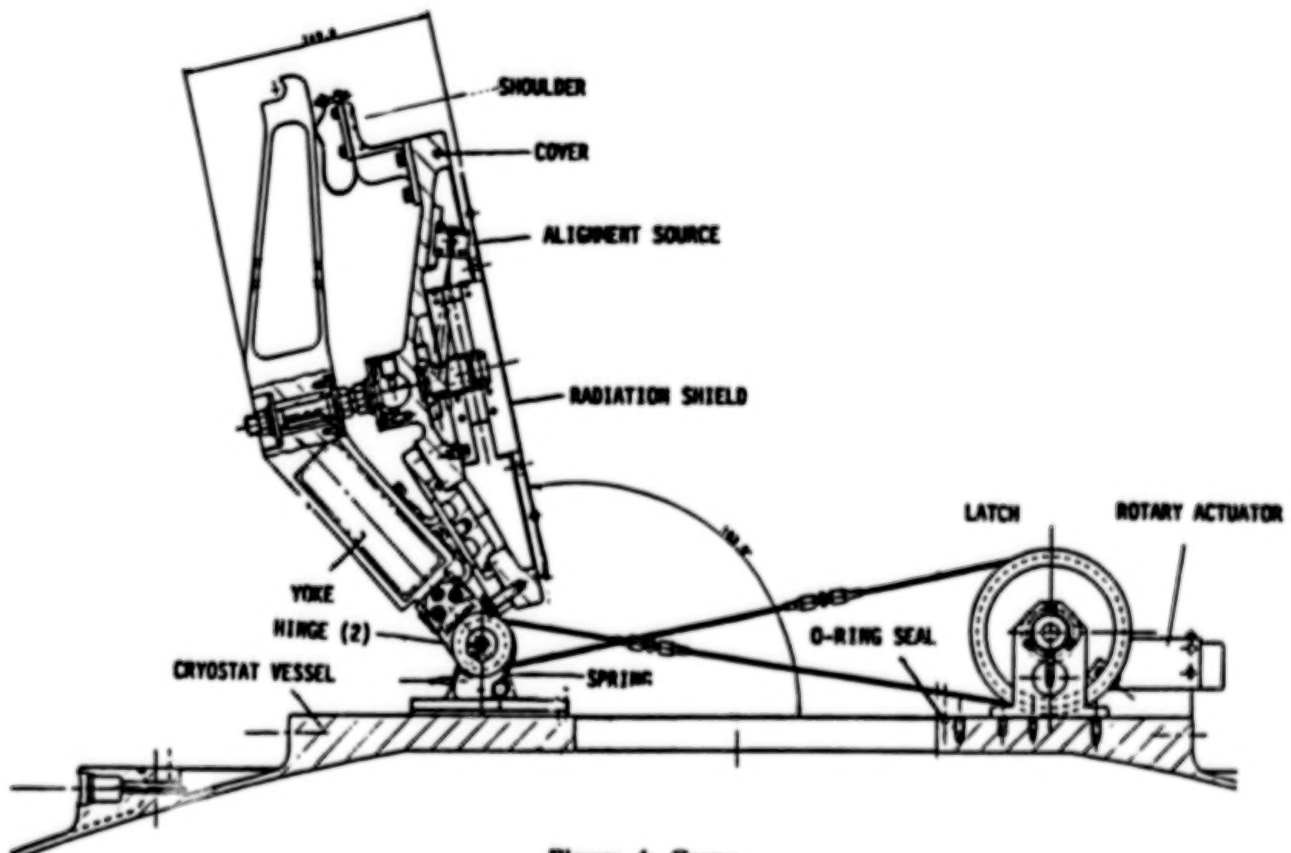
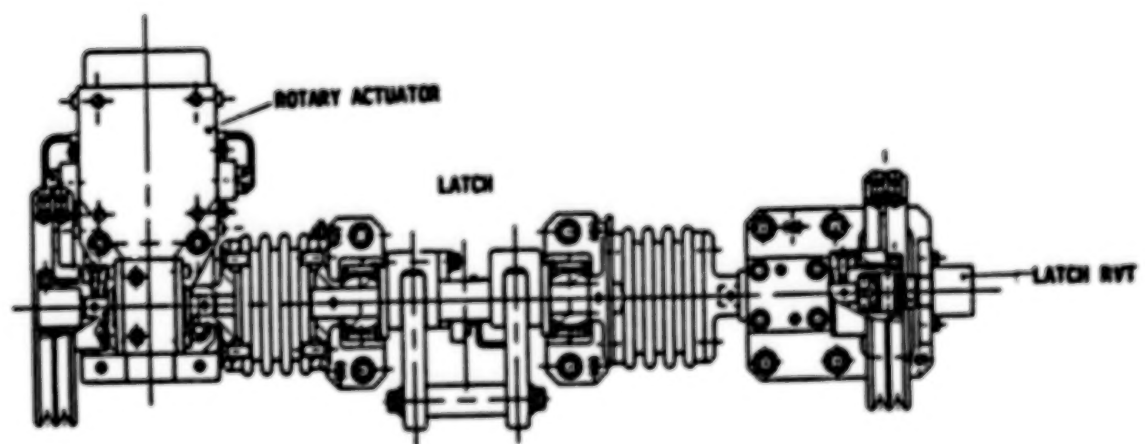
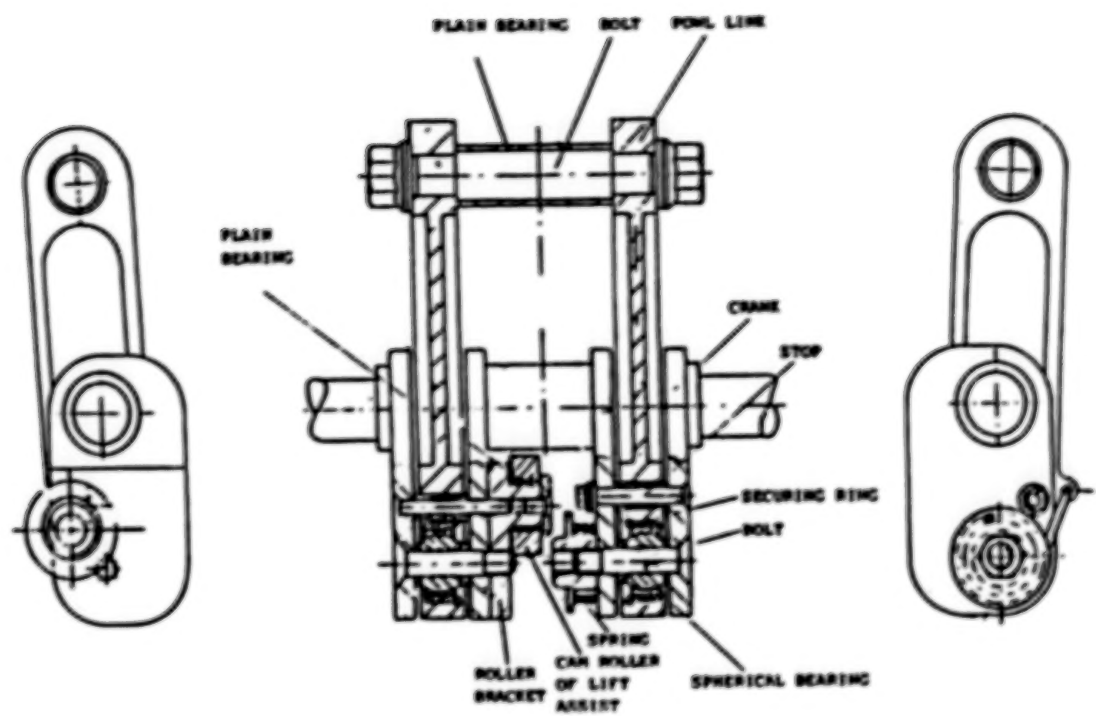


Figure 4: Cover



**Figure 5: Latch Mechanism**

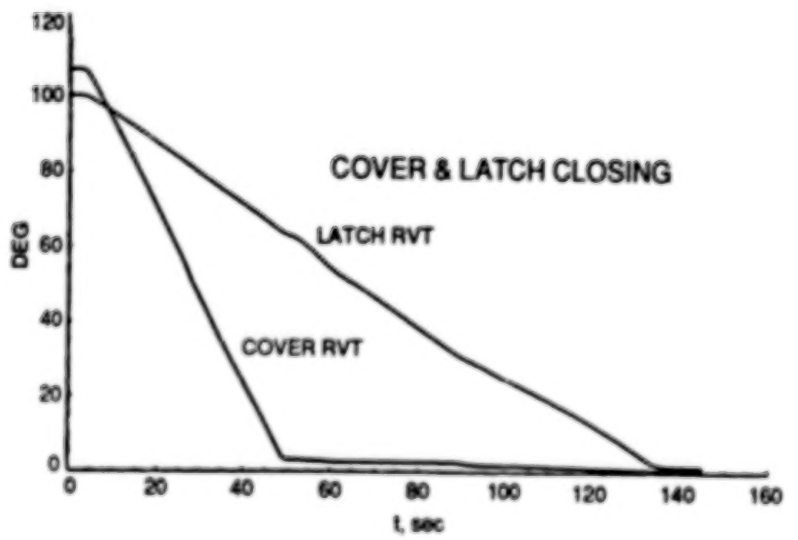
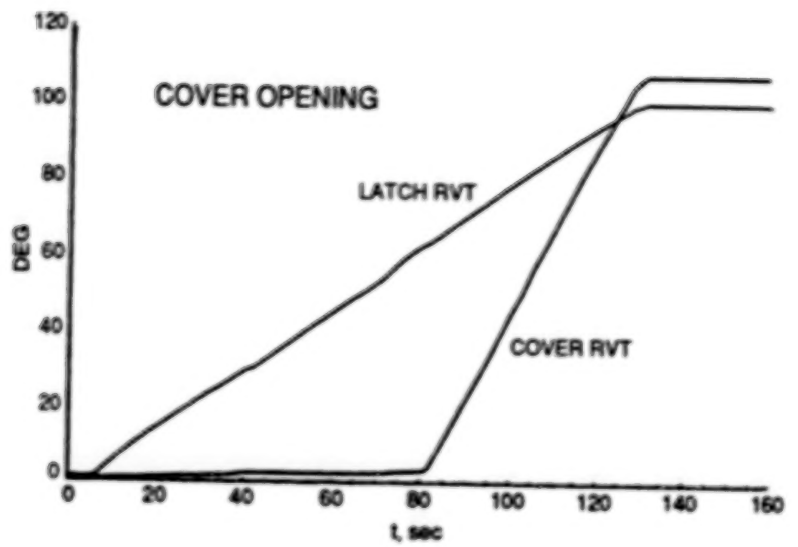


Figure 6: Record of Cover and Latch Angle vs. Time

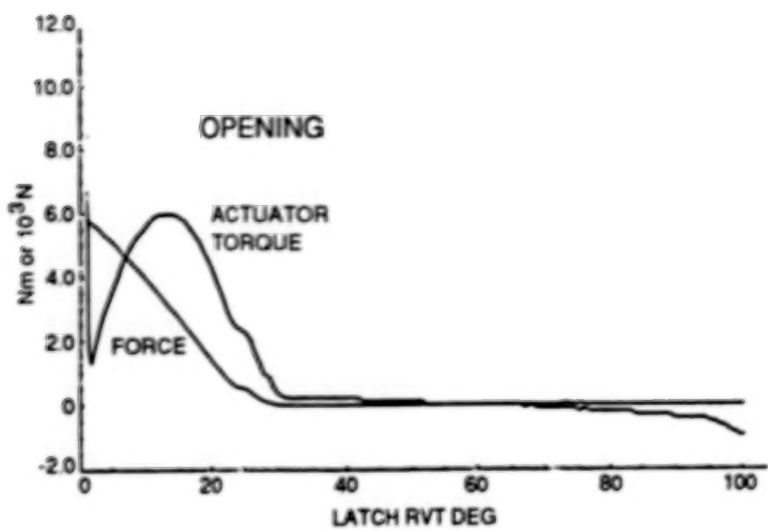


Figure 7: Record of Actuation Torque and Holddown Force vs. Latch Angle

# A SYNCHRONOUS CHOPPER MECHANISM FOR USE AT CRYOGENIC TEMPERATURE

by Claef Hakun, Allen Tyler and Cornelis de Kramer  
NASA Goddard Space Flight Center  
Greenbelt, Maryland

## ABSTRACT

This paper describes a mechanically resonant synchronous chopper mechanism for use at cryogenic temperatures. The mechanism is a critical optical component of the Diffuse Infrared Background Experiment (DIRBE) and has been operating on orbit without incident since November, 1989. The requirements, electromechanical design, and testing of the mechanism are described. A description of the problems encountered and solutions implemented during the development of the mechanism is provided. Finally, a modified chopper design, which incorporated lessons learned and that has several advantages over the flight chopper design, is offered.

## INTRODUCTION

### DIRBE Overview

The DIRBE is one of three instruments on the Cosmic Background Explorer spacecraft (COBE). Designed, fabricated, and tested at the Goddard Space Flight Center (GSFC), the COBE spacecraft was launched into a polar orbit on November 18, 1989. Originally designed to be launched on the shuttle, the spacecraft was redesigned to be launched on a Delta.

The three instruments of the COBE spacecraft have mapped the electromagnetic spectrum of the entire universe in the region between infrared and microwave wavelengths. The DIRBE instrument detectors operate over the range from 1-300 micrometers. The detectors and the instrument are cooled to approximately 2 Kelvin (K) and are located in the Cryogenic Optical Assembly. DIRBE was designed to search for the light of primordial galaxies and other celestial objects that formed after the big bang. The DIRBE instrument has successfully completed its primary scientific mission.

### Functional Description

A critical optical component of the DIRBE instrument, the synchronous chopper mechanism, operates at less than 2 Kelvin at a frequency synchronized with the spacecraft data rate of 32 Hz. The chopper mechanism modulates the incoming light beam from the sky to allow continuous comparison of sky brightness to the cold reference source. The entire DIRBE instrument is located in a liquid helium (LHe) cooled dewar. The location of the chopper mechanism within the DIRBE optical system is shown in Figure 1 (Ref. 1). When the chopper is open, the incoming beam is transmitted to detector assembly 2, and the cold reference source is viewed by detector assemblies 1 and 3. When the chopper is closed, the

incoming beam is reflected to detector assembly 1 and to detector assembly 3 via a beam splitter, and the cold reference source is viewed by detector assembly 2.

The mechanism consists of a vibrating tuning fork with mirror vanes mounted on the end of the tines (Figure 2). The tines are electromagnetically excited near their resonant frequency by the drive coil. Feedback for the closed-loop control system is provided by the sensing coils.

### **History/Trade-off Studies**

The basic chopper mechanism configuration was designed and fabricated through a contract with Frequency Control Products Inc. Programmatic problems were encountered, so the task of completing the design, fabrication and test of the chopper mechanism was reassigned to the Electromechanical Branch (Code 716) at the GSFC. Several chopper units were developed; a test unit, a spare unit, the flight unit, and a modified design unit.

A mechanism trade-off study was completed during the conceptual design of the instrument. A rotating disc with cut-outs and other alternative mechanism concepts were investigated. However, because of the large number of cycles required (over one billion) and the thermal environment (~2 K), mechanisms which utilized ball bearings were considered likely to fail. Therefore, the vibrating tuning fork concept which exhibited no wear was the baseline for further development. Similar chopper mechanisms have been flown on other spacecraft such as Mariner (Ref. 2). To our knowledge, a mechanism meeting the optical and thermal requirements of the DIRBE chopper has not been previously developed.

## **MECHANISM OVERVIEW**

The requirements, electromechanical design and operation, balancing procedure, nonlinear characteristics, and mechanism testing are described.

### **Requirements**

The environmental and performance requirements listed below were developed at the DIRBE system engineering level.

- 1) Continuous operation for 1 year on orbit at less than 2 K (1.0 billion cycles)
- 2) Average power dissipation less than 1.0 milliwatt
- 3) Survive launch loads
- 4) Vanes to chop a 10-millimeter diameter pupil
- 5) Vanes to act as a high-quality infrared mirror
  - Optical vane flatness -  $\lambda/4$  at  $\lambda = .6$  micrometers
  - Vane reflectance  $\geq .9$  for  $\lambda > .9$  micrometers
- 6) Vane temperature less than 5 K
- 7) Chopper frequency synchronous with spacecraft data rate (32.0 Hz)
- 8) Withstand thermal cycling between room temperature and 2 K
- 9) Dual windings and electronics for redundancy

It should be noted that as the development of the chopper mechanism proceeded, some of the requirements changed. A major impact to the design of the chopper was the change in launch vehicles from the shuttle to the Delta. This resulted in increased vibration loads on the mechanism. The Delta launch vehicle vibration environment transmits significant vibration input to the payload in the frequency region between 27 and 32 Hz. The increased vibration loading resulted in the redesign of the chopper mirror vanes.

During initial testing, as the DIRBE instrument became better characterized, some of the optical requirements placed on the chopper mechanism were relaxed. It was determined by means of system level testing that the chopper mechanism operated quite satisfactorily. Power dissipation of less than 1.0 milliwatt (mW) was not achieved. The actual power dissipation of 4.8 mW shortened the mission lifetime by approximately 2 weeks due to the slight increase in cryogen boil-off rate.

Perhaps one of the most important lessons learned should be mentioned here. The system design of the chopper required that the mechanism must operate synchronously with the spacecraft data rate of 32 Hz. It is a difficult task to fabricate, control, and test a mechanism which exhibits nonlinear behavior, is sensitive to its orientation to gravity, and operates at 2 K. It would be a less difficult task if requirements allowed for asynchronous operation, although the command and data handling electronics would become slightly more complex.

### **Electromechanical Design and Operation**

The chopper mechanism was designed to modulate a 9.80-mm (0.3858-in.) diameter light beam on approximately a 50 percent open/50 percent closed duty cycle. Light is transmitted half the time and light is reflected off the mirror vanes half the time. The amplitude of vibration (apex diameter or largest opening) of the vanes is approximately 13.15 mm (0.518 in.). The vanes move in opposite directions from the apex diameter to a closed position where the offset vanes act as a continuous mirror and overlap by a minimum of 0.12 mm (0.005 in.). The gap between the vanes in a direction perpendicular to the mirrored surfaces is 0.30 mm (0.012 in.). The chopper was balanced to operate at the desired amplitude and frequency with minimal power output at LHe temperature. The mechanical amplification factor ( $q$ ) of the chopper was measured to be approximately 138.

The chopper is a mechanically resonant assembly driven by the drive coil in two modes; free running and synchronized. The control system of the chopper mechanism utilizes positive feedback from the sensing coils which are connected in series. A phase lock loop (PLL) technique is used to drive the chopper slightly above its resonant frequency. The amplitude of vibration is controlled. A pseudo sine wave current input is applied to the drive coil. If the amplitude starts to increase above desired levels, the drive current is decreased. The control circuitry is connected to the dual wound drive and sensing coils so that the A or B side can fully operate the chopper.

The following chopper mechanism telemetry is available: power on/off status bit, free run override switch, and chopper in phase and out of phase components. From this telemetry and science data the following characteristics of the chopper operation can be determined: safe operating ranges, the relative phase of the vanes, and the absolute phase.

Figure 3 is a photograph of the flight chopper. A detailed description of the primary components of the chopper is presented below. The dimensions of the chopper are shown in Figure 4.

The chopper mechanism consists of the following primary components:

- **Vanes** - Two gold-plated copper mirror vanes were machined by a diamond turning process. Several mirror vane sets were fabricated by Aero Research Associates, Inc. The vanes were gold plated to meet the optical reflectivity requirement. They were aligned, bonded with epoxy (Stycast), and pinned to the end of the tines of the tuning fork. The shape of the vanes was an optimized compromise to allow the most uniform modulation of the three detector assemblies. The flight vane design dramatically changed from the original vane design for reasons which are described in the problems/solutions section.
- **Tuning Fork** - A one-piece tuning fork made of Ni-Span C was machined using a wire electron discharge machining (EDM) process. Ni-Span C was picked as the tine material because of its stable material properties over a large temperature range, magnetic properties, and fatigue properties. The tuning fork was bolted to an aluminum baseplate. Several forks were made and the spring constant of the tines was determined. Forks with the most closely matched spring constants for both tines were selected for balanced operation.
- **Baseplate** - An aluminum baseplate was bolted and pinned to the flat mirror number 2 mirror mount. The baseplate supports the fork, coils, and thermal strapping. The leads from the coils were bonded (Uralane) to the plate. The chopper was aligned to the optical system through this interface.
- **Coils** - The drive and sensing coils were wrapped on round bobbins. Each coil has independent redundant windings and is encapsulated with "Scotchcast #3 3M." Permanent magnets are bonded with epoxy inside both the drive and sensing coils. The magnets supply a D.C. bias magnetic flux. When current is applied to the drive coil, the D.C. bias flux is modulated, thus creating the driving force. As the tines vibrate, the magnetic flux through the sensing coils is modulated, and a current is generated which is proportional to the tine velocity. A fixture was made to align the 3 coils and magnets with each other and the tines. The polarities are indicated in Figure 4. Several coil/permanent magnet core configurations were investigated; alnico magnet cores, samarium cobalt magnet wafers bonded with epoxy to both sides of an iron rod, and neodymium iron wafers bonded with epoxy to an iron core. The coils with alnico magnets were installed on the flight chopper.

- **Bumpers** - Bumpers are required to assure that the tines do not hit the pole faces of the coils. The bumpers were made of aluminum and were bolted and epoxied to the base. To obtain maximum attainable clearance between the bumper and tine, the bumper alignment is critical.
- **Straps** - Thermal strapping is required to heat sink the chopper to the DIRBE optic plate. Indium foil was placed between thermal interfaces to assure good thermal contact. The thermal strapping of the chopper was essential to the optical performance of the mirror vanes because they reflect signals at infrared wavelengths and very low intensity.

### Balancing Procedure

The balancing of the flight chopper was done in 3 iterations. Balance weights made of tungsten were clamped and eventually bonded with epoxy to the end of the tuning fork tines. They were made heavier than required and then filed to tune the free running frequency of the chopper. Frequency, apex diameter, and power measurements were made at both room temperature and 4 K. These parameters were also measured with the chopper in the horizontal (zero g for tines) and vertical orientations and in the free running and synchronized drive modes at both temperatures. The free running frequency would shift as the chopper was cooled down to LHe temperature. The final balancing iteration resulted in a room temperature free running frequency of 32.9 Hz and a LHe free running frequency of 31.8 Hz. It should be noted that the orientation of the chopper and the electronic component values also affected the free running fundamental frequency. Apex and power measurements in both free running and synchronized drive modes were taken to verify a satisfactory balanced condition.

### Nonlinear Characteristics

The tuning fork material is used as a primary magnetic flux path for the drive coil magnetic circuit. As the tines vibrate, the gaps between the tines and the permanent magnets change. The attractive force applied to the tines by the permanent magnets is proportional to the flux density squared. The flux density is inversely proportional to the gap. Therefore, as the gap changes in the magnetic circuit, nonlinear characteristics result.

Magnetic flux measurements were made on individual coils and on the chopper as a whole system. The coils which exhibited the most uniform magnetic characteristics were selected. Approximately 1.45 kilogauss was measured on both the left and right side of the drive coil. To give an indication of the magnetic field and circuit of the chopper mechanism, a piece of paper with iron filings was placed just above the chopper. The iron filings line up in the direction of the field lines. Figure 5 shows the magnetic field lines of the magnet configuration used on the flight chopper. Several other magnetic configurations were also investigated.

The spring constants of the tines of the chopper mechanism were measured with and without the magnets in place. Figure 6 shows the force versus displacement curves for the two tines as they were moved in both directions: toward the drive

coils and toward the sensing coils. As the tines move closer to the coils, the attractive magnetic force of the permanent magnets in the coils acts to decrease the spring constant of the system. Therefore, the resonant frequency of the system is amplitude dependant. This results in nonlinear behavior and the system is said to have a negative spring. This is undesirable because performance is affected by the mechanism's orientation to gravity.

Due to the dependence of the system spring constant on amplitude of vibration of the tines, different amplitude versus frequency plots result when the drive coil input frequency is swept in an increasing or decreasing manner through the mechanical resonance of the system. Figure 7 is a plot of the output of the sensing coil versus the frequency of the drive input in the vicinity of the mechanical resonance of the tuning fork. Sweeping up in frequency yields a higher system resonance than when sweeping down in frequency. The nonlinear characteristic of the system is apparent between the frequencies of the sweep-up resonance and the sweep-down resonance, since two stable vibration amplitudes exist for a given frequency. To assure that the chopper mechanism operates in a stable manner (with margin), the chopper was designed such that the sweep-down resonance is below the desired synchronized frequency. Therefore, the chopper mechanism operating in the synchronized mode operates slightly less efficiently than if the mechanism operated directly at the sweep-down resonance where little margin for stable operation exists.

In addition, because of this behavior, a start-up circuit is required in the control system. The system is allowed to free run until a particular amplitude is achieved. Once the amplitude threshold is reached, the control system activates the phase lock loop control and the chopper synchronizes with the spacecraft data rate of 32 Hz. If, during start-up of the mechanism, the amplitude becomes too large and the tine hits a bumper, a windshield wiper mode can develop. In the wiper mode, the two vanes move in the same direction instead of opposite directions as desired. This phenomenon has only occurred twice in ground testing. To halt this mode of operation, turn off the chopper, wait several minutes, and then turn the chopper back on. This mode has not occurred on orbit.

### Mechanism Testing

**Optical -** Extensive measurements were made of mirror orientation, optical figure, and vane motion. The above parameters were measured at both room and LHe temperature. The amplitude of vibration (apex diameter) is a critical factor in the performance of the chopper. Apex diameter of the vane motion was measured with a stroboscope and a traveling microscope. The chopper was balanced and the control system component values were selected at the required apex diameter. A stroboscopic auto-collimating theodolite developed at GSFC was used to measure mirror orientation (twists and tilt) both statically and dynamically. A Zygo interferometer was used to perform metrology measurements on the mirror vane flatness.

**Life Test** - A life test of the mechanism was not conducted. However, throughout the testing of the flight chopper and the DIRBE instrument, the chopper operated at cryogenic temperature for approximately 2.5 months. It was shown through analysis that the maximum stress in the tines was below the fatigue limit of Ni-Span C. The maximum calculated stress in the tine was 207 MPa (30 ksi). The fatigue limit of Ni-Span C is approximately 414 MPa (60 ksi). A determining factor in not performing a life test was that it would take a year. As the chopper design evolved, no two of the choppers were exactly the same. The schedule did not allow a year to evaluate a particular design. There was no clear way to perform an accelerated test. The chopper has been successfully operating on orbit for over a year.

**Vibration** - Sine burst, random, and sine sweep vibration tests were conducted on the chopper mechanism at both room and cryogenic temperatures. Figure 8 gives the levels, frequencies, and duration of the vibration tests. The chopper mechanism resonates in the windshield wiper mode as the input vibration frequency approaches the tuning fork resonance. Due to the relatively high  $q$  of the mechanism, launch vibration levels cause the tines to impact the bumpers with significant forces. The bumpers limit the amplitude of vibration and dissipate energy during these impacts. The nonlinear characteristics of the mechanism were observed during the tests. The second mode of the individual tines was verified to be approximately 370 Hz.

Two problems became apparent during the tests. The first problem was that the surfaces on the mirror vanes were compromised due to vane clashing during vibration. The second problem was concern that the increased vibration input of the Delta launch environment would make the integrity of the epoxy joint which connected the vane to the vane holder marginal. These two problems led to the redesign of the mirror vanes, which is described below.

**Thermal Vacuum** - The chopper was cycled from room temperature to less than 4 K seven times. Several dewars were used during the testing of the mechanism. Both optical and vibration tests were performed at LHe temperature. One dewar was equipped with a window so that optical measurements could be made, another dewar was used for vibration testing, and a third larger dewar was used to vibrate the entire DIRBE test unit.

## Problems/Solutions

Three major problems were encountered in the development of the chopper.

- 1) The mirrored surface of the vane was scratched during vibration testing. As vibration input frequencies approach the resonance of the chopper, the tines start to hit the bumpers. This impact loading on the tines causes the vanes to clash against each other.

2) There was concern that the original mirror/vane holder epoxied interface would not survive launch loads and the fatigue cycling over the lifetime of the mechanism.

3) During an instrument-level test of the optical system and detectors at LHe temperature, it was determined that the vanes of the chopper were heating up to an unacceptable level. It was later determined that the temperature of the vanes was approximately 18 K. Vane heating was due to eddy current losses in the tines and molecular friction created by vibration of the tines.

The solutions to these problems which are incorporated in the flight chopper are described below. In addition, the modified chopper design is described. The modified design could eliminate heating of the vanes and other problems which were encountered due to the nonlinear characteristics of the flight chopper design.

The first two problems were solved by changing the mirror vane design. The original design of the mirror vane consisted of two parts: a polished mirror and a separate vane holder. The mirror was bonded with epoxy to the vane holder and the vane holder was then bonded with epoxy and pinned to the end of a tine. The orientation of the mirror/vane holder joint was in the direction of the tine motion (see Figure 9). This joint would therefore be subjected to significant launch loads and continuous fatigue loads during operation.

The redesign of the mirror vanes resulted in an integral mirror vane (vane and vane holder machined as one piece) with an additional 0.038 mm (0.0015 in.) plating of gold on the top edge of the vanes. The integral vane eliminated the need for a vane holder, minimized mounting stresses in the mirror, and elimination of the mirror/vane holder joint relieved concern that the epoxied joint would fail under launch loads and fatigue cycling. The thin plating of gold on the top of the vanes (outside of the useable area) solved the problem of scratching of the mirror surfaces under vibration loading by assuring that any contact between the two mirrors would be limited to the area of increased gold plating. Figure 9 shows the comparison of the original and flight vane designs. The mirror vanes were made by a diamond turning machining process which allowed overhang of the mirror mount. An overhang of this type is difficult to accommodate when conventional mirror polishing techniques are employed. Other solutions to these problems were developed, however the integral vane with a gold plated strip was the simplest and most reliable solution.

The third problem, heating of the chopper vanes, turned out to be a very challenging one. It was cleverly solved by modifying the tine design to allow 0.25-mm (0.010-in.) diameter copper wires to be incorporated into a keyhole slot along the length of the tine. The copper wires are captured in the keyhole and silver epoxied to the end of the tine and to the vane. A wire EDM was used to cut out a key hole on both edges of each tine. The copper wires came out of the aft end of the tine and were looped and then soldered to a copper T-bar which was installed at the base of the tuning fork. The copper T-bar was then heat strapped to the side of the

aluminum base plate. Figure 9 shows a cutaway of the aft end of the chopper, the T-bar and the thermal strap. The heat from the vane and tine was conducted away via the copper wires to the optic plate. The wires are redundant. Only one wire for each tine is required to cool the vanes. Analysis on the fatigue of the wires shows that the maximum stresses developed in the wires are below the fatigue limit of copper.

A test was conducted in which the chopper was driven in the synchronized mode at LHe temperature. One side of the chopper had copper wires installed and the other side did not. The side which did not have the wires reached an equilibrium temperature of approximately 18 K. The side with the wires installed reached a temperature of less than 3 K.

### The Modified Chopper Design

A modified chopper mechanism incorporating lessons learned was designed and fabricated toward the end of the DIRBE/COBE program. Figure 10 is a drawing of the modified chopper design. This design employs a magnetic circuit that is common to commercially available choppers. A magnet is bonded with epoxy to each tine. The magnets are centered in coils mounted on each side of the tuning fork. One coil is used as the drive while the other is used as a sensing coil. A magnetic configuration of this type was considered in the early development of the DIRBE chopper, however, problems were encountered when the mechanism was cooled to LHe temperature. Since the magnets were directly mounted to the tines, the tines were deformed in the regions of the magnets because of the differential thermal strains of the magnet and tine materials. The modified design provides mounting tabs which isolate the strain to the tab and leaves the tine undeformed.

There are several advantages to using a chopper of this design. The chopper operates in a linear manner because the motion of the magnets through the coils does not affect the magnetic flux flow through the mechanism. Sensing coil output amplitude vs. drive coil excitation frequency in the region of the mechanical resonance of this design is shown in Figure 11. The traces of the sweep up and the sweep down are essentially the same. The second peak is the desired operating mode (out of phase) while the first peak is the undesirable windshield wiper mode (in phase). The geometry of the chopper mechanism can be optimized to decrease the  $q$  of the undesirable mode. This clear definition between the two modes and the linear characteristics of the mechanism greatly simplify control of the mechanism. The mechanism can be driven with stability at the resonance of the fork. Power dissipation is greatly reduced. Milliamps are required to drive the flight chopper. In this design, only microamps are required. Balancing, testing and calculation of system margins are also simpler because the mechanism is less sensitive to its orientation to gravity. Unlike the flight chopper, eddy currents are virtually nonexistent. The fact that the eddy currents are minimized in the modified design may eliminate the need for thermal wires to be incorporated into the tines to conduct heat away from the mirror vanes as in the flight chopper.

A test is currently pending in which the modified chopper design will be cooled to LHe temperature and driven at the free running frequency. The temperature of the vanes will be measured without the thermal wire attached. Therefore, the heat generated by the molecular friction of the mechanical motion and the eddy currents in the tines will not be conducted away. It is expected that the temperature of the vanes will be well below the 18 K measured in the test performed on the flight mechanism. One indication that a lower temperature should result is that the  $q$  of the modified chopper is approximately an order of magnitude greater than that of the flight chopper. It is hoped that the heat generated by the mechanism motion of the vibrating tines and the eddy currents can be separated and quantified.

## Conclusion

The flight chopper operates with an apex diameter of 13.15 mm (0.518 in.) and was tuned to have a free running frequency of 31.8 Hz at LHe temperature. The power dissipated at this temperature is approximately 4.8 milliwatts. The vane temperature during operation is less than 3 K. The optical performance of the chopper is highly satisfactory.

An integral vane with gold plating on the top edge was incorporated to eliminate an epoxy joint and prevent the vanes from rubbing under vibration loads. Thermal wires were incorporated into the tines to conduct heat away from the mirror vanes. In addition, a modified design chopper is offered as a potential solution to several of the problems encountered in the buildup and test of the DIRBE chopper.

The DIRBE synchronous chopper has been continuously operating on orbit without incident since the COBE spacecraft was launched on November 18, 1989. The DIRBE has fulfilled its primary mission requirement to map the electromagnetic spectrum of the entire universe between the wavelengths of 1 to 300 micrometers. Although the dewar liquid helium coolant was expended on schedule as expected, several of the detectors are still providing valuable scientific data. It is anticipated that the DIRBE instrument will continue to produce world-class scientific data.

## References

- 1) Magner, T., "Diffuse Infrared Background Experiment (DIRBE) Optics Module Breadboard Alignment Methods and Results," Optical Engineering, March 1987, Vol 26. No. 3, Pg. 264-269.
- 2) Reich, S. M., Brill, H. L., "An Unconventional Chopper For Infrared Applications," Proc. of 21<sup>st</sup> International Technical Symposium of the Society of Photo-Optical Instrumentation Engineers.

## Acknowledgements

Some of the many people who played major roles in the development, fabrication, and test of the chopper mechanism at the GSFC are Jim Poland, Dwight Roberts, Pat Humphrey, Phil Studer, Tom French, John Wood, Tom Magner, Mark Wilson, John Hui, Art Serlimetsos, Dan McHugh, Regis Brekosky, John Zahniser, Ed Lewis, and John Bowerman.

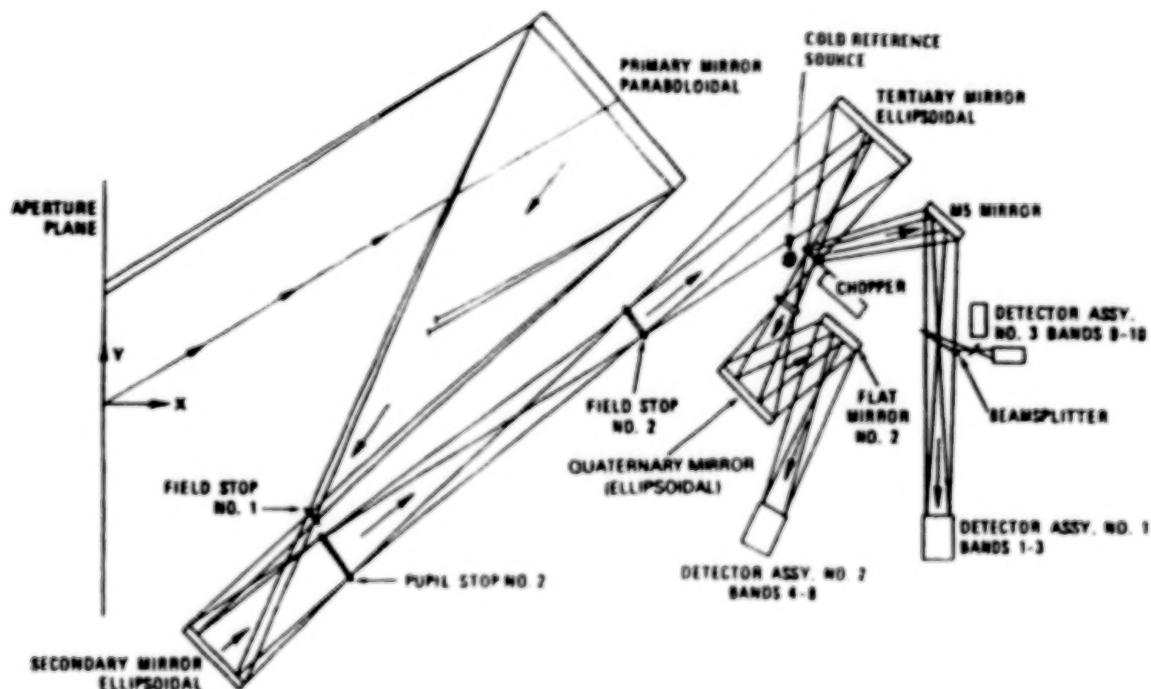


Figure 1 - The DIRBE Optical System

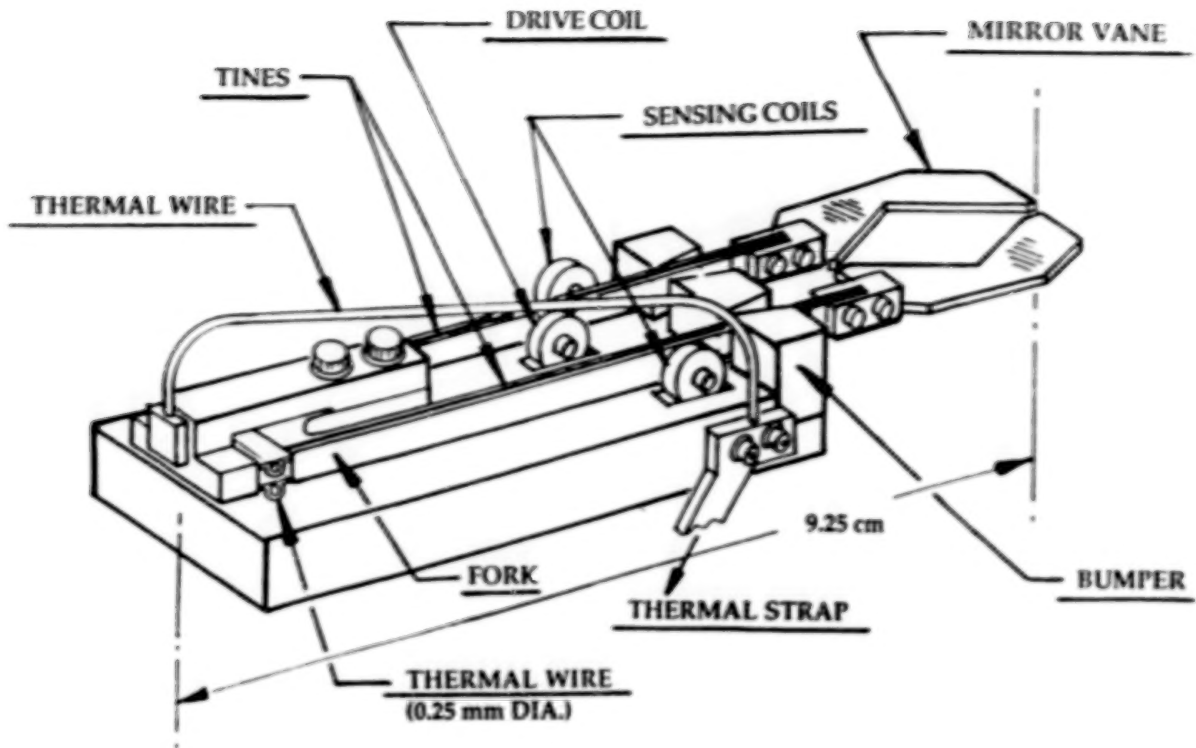


Figure 2 - The DIRBE Chopper Mechanism



Figure 3 - The DIRBE Chopper Mechanism

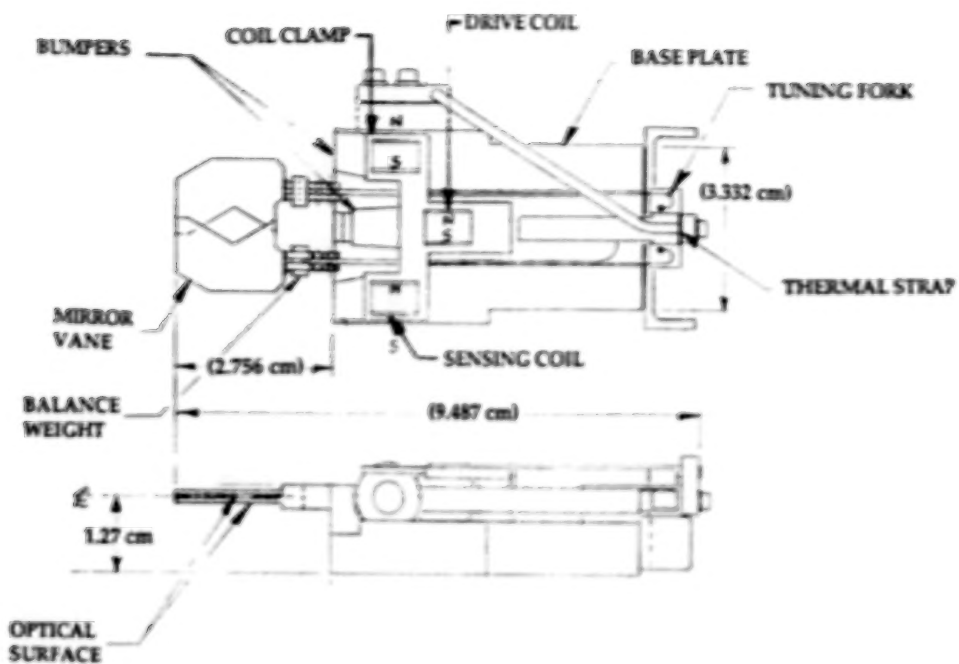
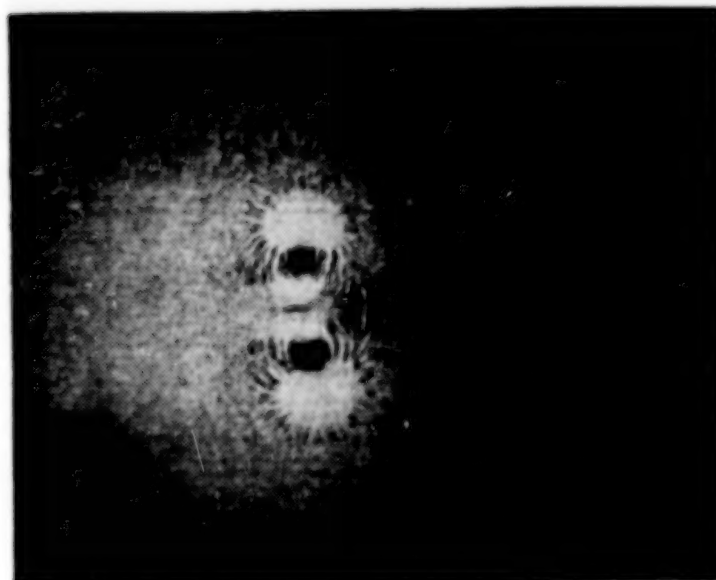
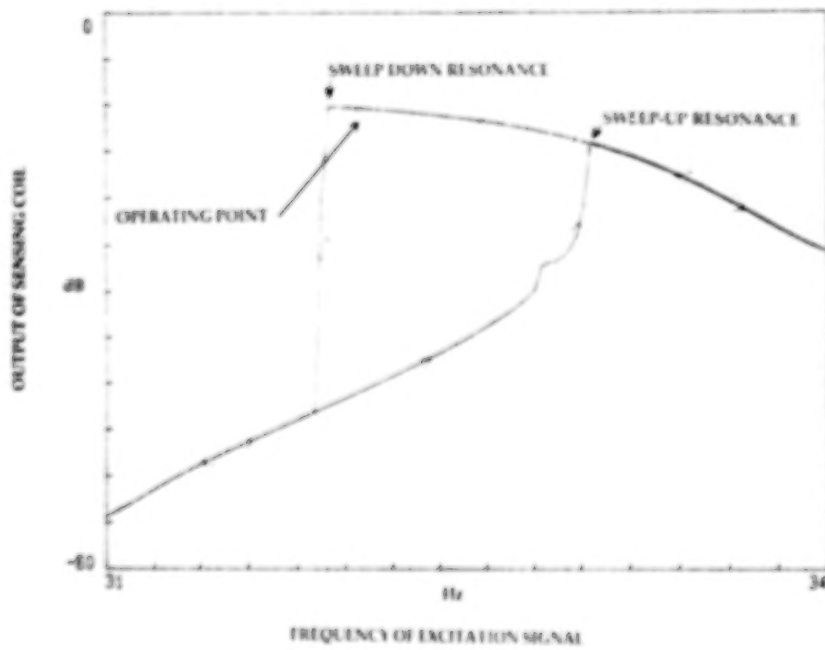
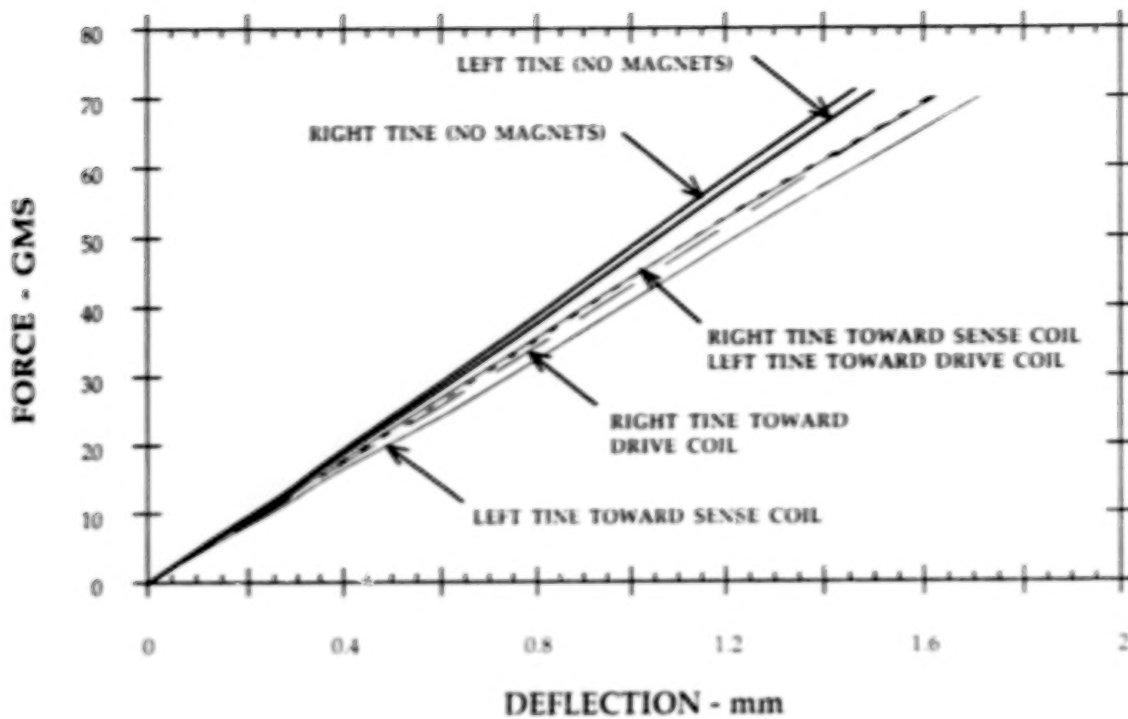


Figure 4 - The DIRBE Chopper Mechanism



CHOPPER ORIENTED AS SHOWN IN FIGURE 4  
(TOP VIEW)

Figure 5 - The Chopper Magnetic Field



<u>AXES</u>			
	X	Y	Z
<u>SINE BURST</u> (G's)	±14.0	±5.9	±5.9
<u>RANDOM</u>			
<u>X-AXIS</u>		<u>FREQ RANGE (Hz)</u>	
		<u>Level</u>	
20		.0001 g <sup>2</sup> /Hz	
20-125		+11.0 dB/oct	
125-300		08 g <sup>2</sup> /Hz	
300-2000		-10.6 dB/oct	
2000		.0001 g <sup>2</sup> /Hz	

Overall Level = 5.1 grms  
Test Duration = 30 seconds

<u>SINE SWEEP</u>			
<u>AXIS</u>	<u>FREQUENCY (Hz)</u>	<u>LEVEL</u>	<u>SWEEP RATE</u>
X	15-21	±6.5g	
	21-30	±4.0g	2 oct./min.
	30-40	±1.0g	
Y & Z	15-21	±1.4g	
	21-30	±.6g	2 oct./min
	30-40	±1.4g	

Figure 8 - The DIRBE Chopper Vibration Specification

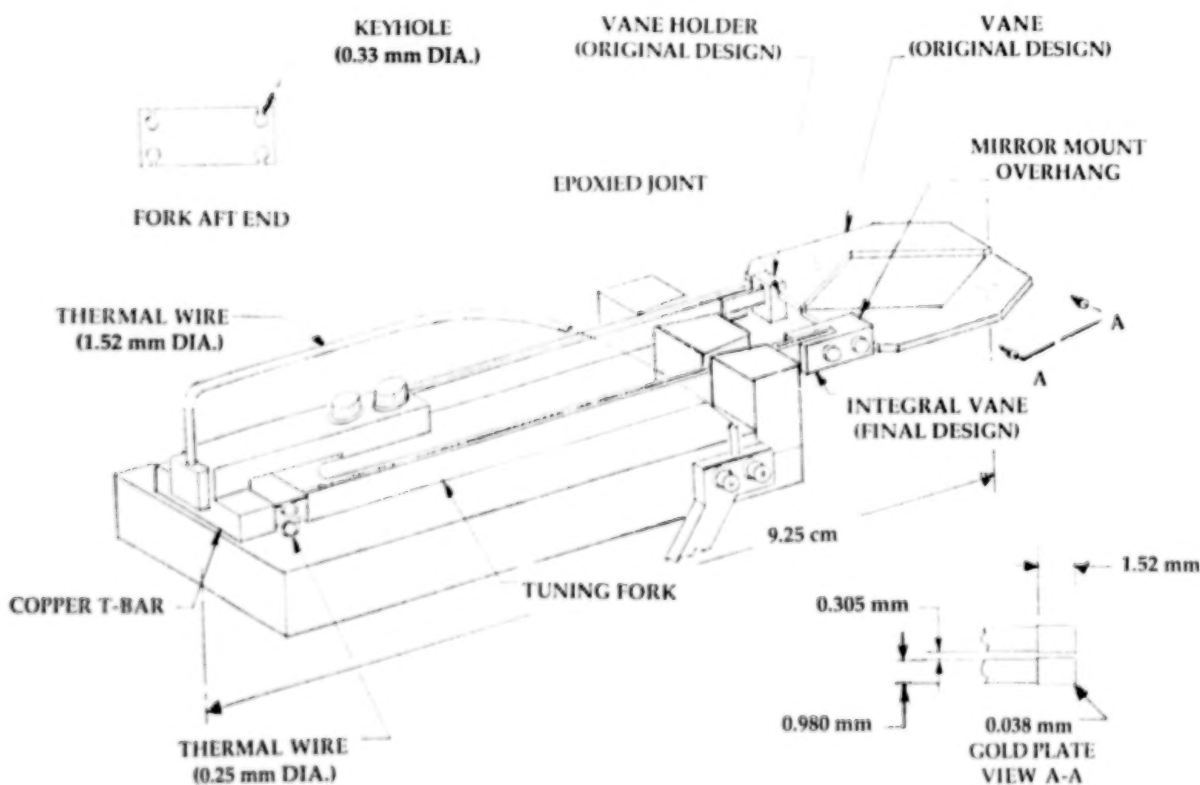


Figure 9 - Chopper Mechanism Solution Summary

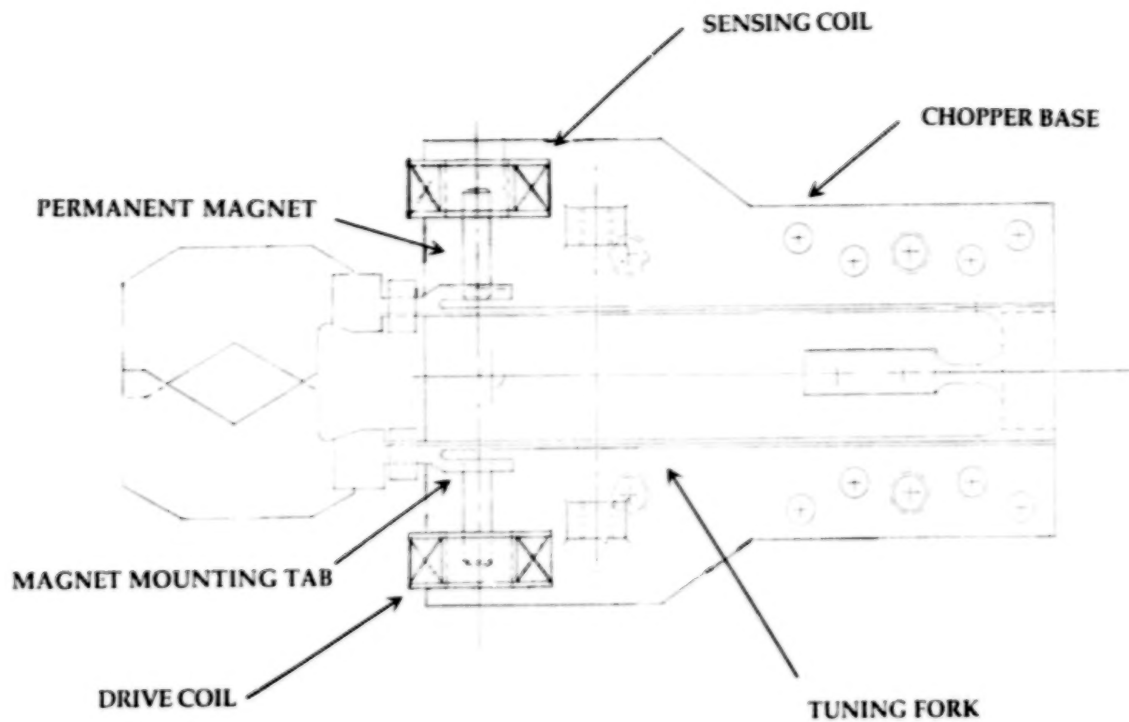


Figure 10 - Modified Chopper Mechanism Design

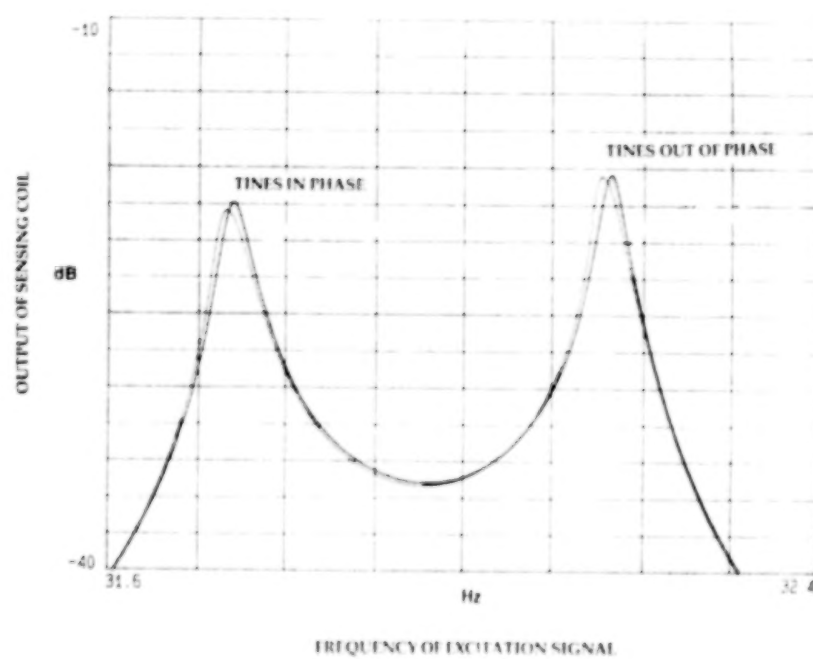


Figure 11 - Modified Chopper Frequency Response

# **CRYOGENIC MECHANISMS FOR SCANNING AND INTERCHANGE OF THE FABRY-PEROT INTERFEROMETERS IN THE ISO LONG WAVELENGTH SPECTROMETER**

G.R. Davis<sup>1</sup>, I. Furniss<sup>2</sup>, T.J. Patrick<sup>1</sup>, R.C. Sidey<sup>3</sup>, W.A. Towlson<sup>2</sup>

## **1. Introduction.**

The Infrared Space Observatory (ISO) is an ESA cornerstone mission for infrared astronomy. Scheduled for launch in 1993, its four scientific instruments will provide unprecedented sensitivity and spectral resolution at wavelengths which are inaccessible using ground-based techniques. One of these, the Long Wavelength Spectrometer (LWS), will operate in the 45–180  $\mu\text{m}$  region (Emery *et al.*, 1985) and features two Fabry-Perot interferometers mounted on an interchange mechanism. The entire payload module of the spacecraft, comprising the 60-cm telescope and the four focal plane instruments, is maintained at 2–4 K by an onboard supply of liquid helium. The mechanical design and testing of the cryogenic interferometer and interchange mechanisms are described in this paper.

## **2. Fabry-Perot Interferometers.**

The LWS features two scanning interferometers, one each for the wavelength ranges 45–90  $\mu\text{m}$  and 90–180  $\mu\text{m}$ . These differ only in the spacing and characteristics of the reflectors. An exploded isometric view (fig. 1) shows the compact construction, mostly of Al 6061 alloy.

The interferometers consist of two metal mesh reflectors built into three plates, the middle of which is sandwiched between the outer two and suspended by three BeCu leaf springs. The springs are profiled to a sector of an annulus, anchored with a small screw and pin to the back plate, and fixed again with a screw to the moving plate. This arrangement is highly compliant in the direction of motion, but very stiff in the perpendicular direction.

---

<sup>1</sup> *Mullard Space Science Laboratory, University College London, Holmbury St. Mary, nr. Dorking, Surrey, England RH5 6NT.*

<sup>2</sup> *Dept. of Physics & Astronomy, University College London, Gower St., London, England WC1E 6BT.*

<sup>3</sup> *Custom Development Ltd., Cambridge Mews, Cambridge Road, Kew, Surrey, England TW9 3JB.*

The plate motion is generated by three moving coil actuators, equispaced around the circumference to enable active control of the mesh parallelism. The coils, comprising 800 turns of 44 swg (0.081 mm) copper wire, are mounted on the moving plate and engage with shielded SaCo magnets which are fixed to the back plate. This arrangement minimises the moving mass.

The separation of the fixed and moving plates, which carry the two reflectors, is monitored by three capacitance micrometers, also equispaced around the circumference. A closed loop electronic circuit provides servo control of the plate position and operates as follows. The micrometers are excited at 10 kHz and the current through each is compared with that through a 100 pF reference capacitor (fig. 2). The micrometer excitation voltage can be controlled by digital command. At the balance point of the servo, we have:

$$KC_M = C_R, \quad (1)$$

where  $K$  is the digital multiplier,  $C_M$  is the capacitance of the micrometer, and  $C_R$  is the reference capacitance. Since the micrometer capacitance is simply related to the plate separation  $d$ , we have:

$$d = K \frac{\epsilon_0 A}{C_R} \quad (2)$$

(ignoring edge effects), where  $A$  is the area of the micrometer pads. The plate separation is linearly related to the digital command  $K$  and is independent of the amplitude and frequency of the driving voltage. In practice, the relationship is slightly nonlinear due to edge effects. This control system provides for plate motion over a range of  $\sim 100 \mu\text{m}$ , with a step size of  $\sim 25 \text{ nm}$ .

A block diagram of the complete servo control system is shown in fig. 3. One 12-bit command is applied to each channel to control the plate motion, while two 8-bit commands are applied to channels 2 and 3 to provide independent control of the parallelism. This adjustment has a range of  $\pm 10 \mu\text{m}$ .

The coil current is limited to  $\pm 15 \text{ mA}$  by the resistance of the harness which connects the analogue electronics unit to the focal plane instrument. The power dissipation in each coil is typically  $250 \mu\text{W}$ . This heat is efficiently conducted to the LHe reservoir through the leaf springs; tests have not revealed any significant heating effects due to dissipation in the drive coils.

The reflectors are precision nickel meshes, of thickness  $3 \mu\text{m}$ , bar width  $6 \mu\text{m}$  and pitch  $15\text{--}19 \mu\text{m}$ . Each mesh is initially stretched over a titanium alloy ring and bonded to it by gold thermocompression. The rings are then attached,

by 0-80 screws, to the aluminium alloy plates which feature rims for additional stretching. Such use of dissimilar materials demands prior characterisation of the mesh elasticity, enabling the tension in the meshes to be controlled such that they remain intact and taut at 4 K.

The stretching rims define the operating position of the meshes, and must be flat to  $\sim 0.1 \mu\text{m}$  rms to avoid degradation of the interferometer performance. This is achieved by precision diamond turning of the rims, the micrometer pads and associated reference surfaces. Finally, cleanliness is of paramount importance at the assembly stage, since particulate contamination can also degrade the mesh flatness.

### 3. Interchange Mechanism.

The LWS requirement for two interferometers, and also for a lower resolution operating mode with no interferometer in the beam, led to the development of an interchange mechanism. In the absence of suitable commercial devices for this application, we decided to develop a low power, long life mechanism for the cryogenic space environment (Patrick *et al.*, 1989). A brief summary of the mechanical and thermal design of the mechanism and its performance in vibration and life tests is given here.

The interchange mechanism is driven by a cryogenic stepping motor, which features a two-phase drive technique and is characterised by its rugged and simple construction. Magnetic materials were selected following evaluation of prospective materials under cryogenic conditions. In practice, two pairs of drive coils, eight wires and two drive circuits are employed for end-to-end redundancy, since the mechanism represents a critical single point failure for the LWS. The 440C stainless steel bearings and pinion are sputter coated with MoS<sub>2</sub> for lubrication.

The interferometers are attached to an aluminium alloy (6061) wheel using a three-point fixing, which allows for the introduction of shims as necessary to bring the alignment of the meshes with respect to the LWS beam within the 4 arc min tolerance. The wheel features a rim gear which engages the motor pinion with a gear ratio of 29. The form of the gear teeth was to the conventional involute ( $20^\circ$  pressure angle) standard, and backlash was set to 0.1 mm at room temperature. The gear teeth were hard anodised for mechanical protection and sputter coated with MoS<sub>2</sub> to a nominal thickness of  $0.2 \mu\text{m}$ . The angular contact ball bearings on which the wheel shaft was mounted were pre-loaded through a compressed Belleville washer to eliminate play up to  $\sim 100\text{g}$  vibration. The rings

and balls were sputter coated with MoS<sub>2</sub> (Gould and Anderson, 1990) and fitted with a duroid ball cage.

A thermal model of the subsystem reveals that the interferometer springs and the wheel bearings represent the largest thermal impedances. In the former case, no action was taken since the power dissipation level was so small; in the latter case, however, initial cooldowns were unacceptably protracted. A clock-spring thermal strap was therefore introduced, consisting of high purity copper sheet coiled into a spiral, the inner end rotating with the shaft and the outer end anchored. The elasticity of this strap is one of the major sources of resistance in the interchange mechanism.

The other source of torsional resistance is the wiring bundle to the interferometers. The harness consists of a mixture of 24 stainless steel and copper wires, all coated with PTFE insulation, and is passed through the hollow shaft of the wheel en route from the interferometers to the fixed connectors on the LWS wall. To minimise wind-up in the harness, a guide tube is included which provides 20 cm of free length; nevertheless, the power requirement is substantially higher at the extremes of the wheel motion due to the stiffness of the PTFE insulation at 4 K.

The wheel has four operating positions: the two interferometers, an open aperture, and a blanking plate for reference measurements. The wheel position is detected by an inductive sensor, consisting of three fixed coils on one support bracket and magnetic markers at each of the four operating positions. The response is sharply peaked and of either polarity, enabling the wheel position to be set with an accuracy of  $\pm 0.7^\circ$ ; the 2-fold degeneracy is decoded by the drive software. Spring stops limit the rotation to  $5^\circ$  beyond the extreme positions.

The interchange mechanism is controlled by a 3-bit counter from the on-board computer. In a normal interchange, the motor is ramped up over the first 127 steps, driven at the slew speed of 250 Hz, and ramped down over the final 127 steps. The wheel is brought to a stop 7 steps before the intended position, and is then single stepped until the peak response from the position sensor is detected. A  $90^\circ$  interchange requires  $\sim 2$  s and dissipates only 150 mW, thereby minimising the boil-off of stored cryogen on the spacecraft.

A development model of the interchange mechanism was subjected to room temperature vibration to ISO qualification levels, on the basis of which the bearing pre-load and the thermal strap design were both revised. Cryogenic vibration of the LWS Engineering Qualification Model resulted in two broken wires at the interferometers; these led to small design changes, which were later proven by further cryogenic vibration in the convenient facility at F.U. Berlin.

The interchange mechanism is expected to undergo 10,000 operations during the ISO mission, depending on the scientific observations programme. Following vibration of the development model, an accelerated life test was undertaken at 4 K. The test was terminated after 40,000 interchanges, at which point the motor had begun to drop steps. The motor current (fig. 4), which is the indicator of bearing friction, was within operational limits throughout. No wear debris was found in the cryostat, and subsequent dismantling produced no evidence of end-of-life wear.

#### 4. Conclusions.

The development of cryogenic mechanisms for the scanning and interchange of two Fabry-Perot interferometers has recently reached a successful conclusion. Following five years of design and test effort, the Flight Model instrument has been manufactured, tested and integrated into the LWS for launch by ESA in 1993.

#### Acknowledgements.

The authors wish to thank the following for their invaluable contributions to the design and development of the mechanisms described here: Dr. D.A. Naylor, University of Lethbridge (Canada); the European Space Tribology Laboratory; C. dela Nougerede, A.J. Barsby and the staffs of the design office and mechanical workshop at MSSL.

#### References.

1. Emery, R.J., P.A.R. Ade, I. Furniss, M. Joubert and P. Saraceno (1985): SPIE 589, 194.
2. Patrick, T.J., G.R. Davis, I. Furniss, W.A. Towson and R.C. Sidey (1989): "Further Development of the Cryogenic Fabry-Perot Interchange Mechanism for ISO LWS", Fourth European Space Mechanisms Conference, Cannes (ESA SP-299).
3. Gould, S.G. and M.J. Anderson (1990): "Ball Bearing Lubricants for use in Cryogenically Cooled Infrared Telescopes", Proc. Low Temperature Engineering and Cryogenics Conf., University of Southampton.

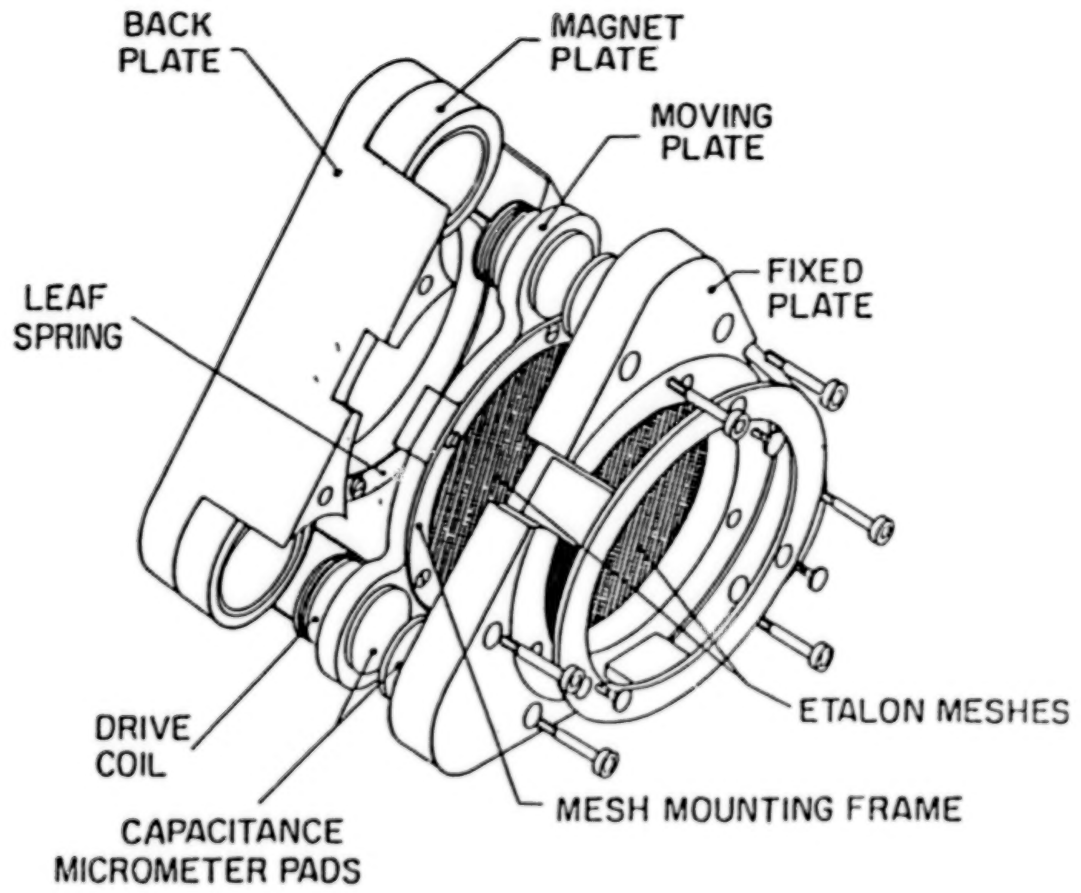
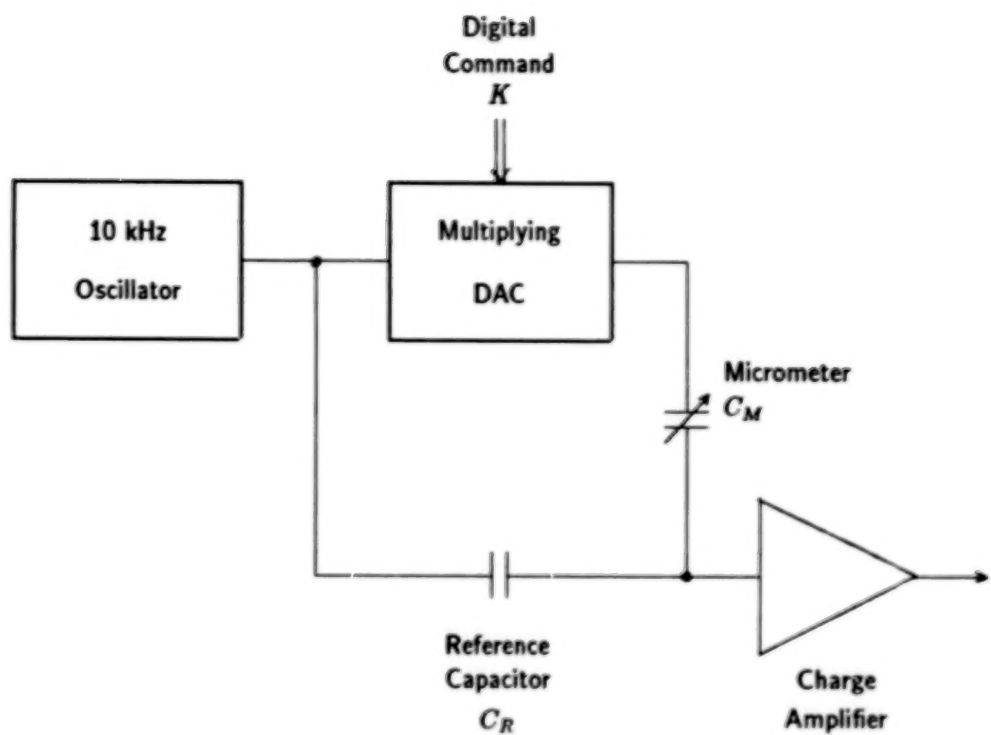


FIGURE 1

*Exploded Isometric View of the Fabry-Perot Interferometer*



**FIGURE 2**  
*Schematic Representation of the Capacitance Micrometer*

**BLANK**

**PAGE**

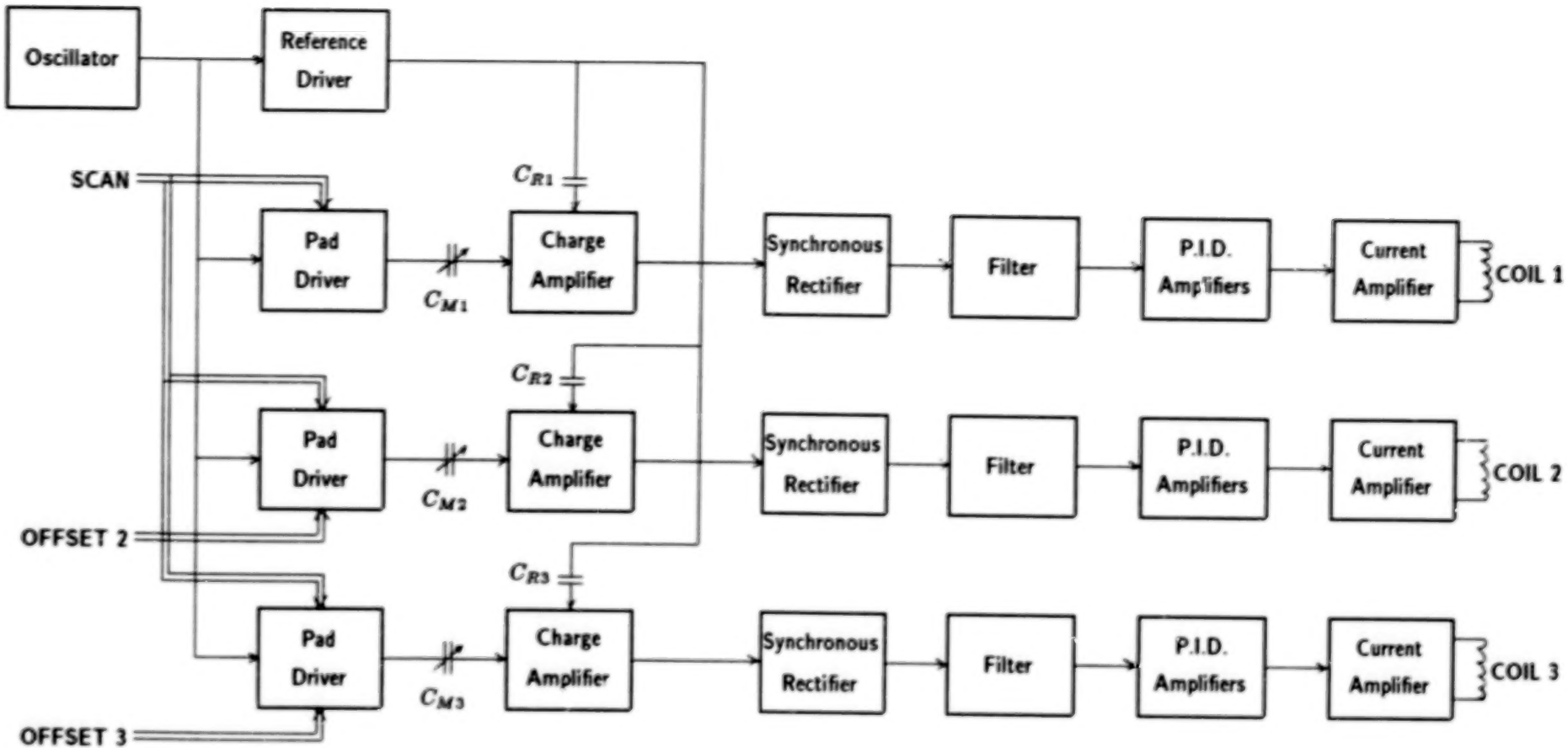


**FIGURE 3**

*Block Diagram of Interferometer Servo Circuit*

13F

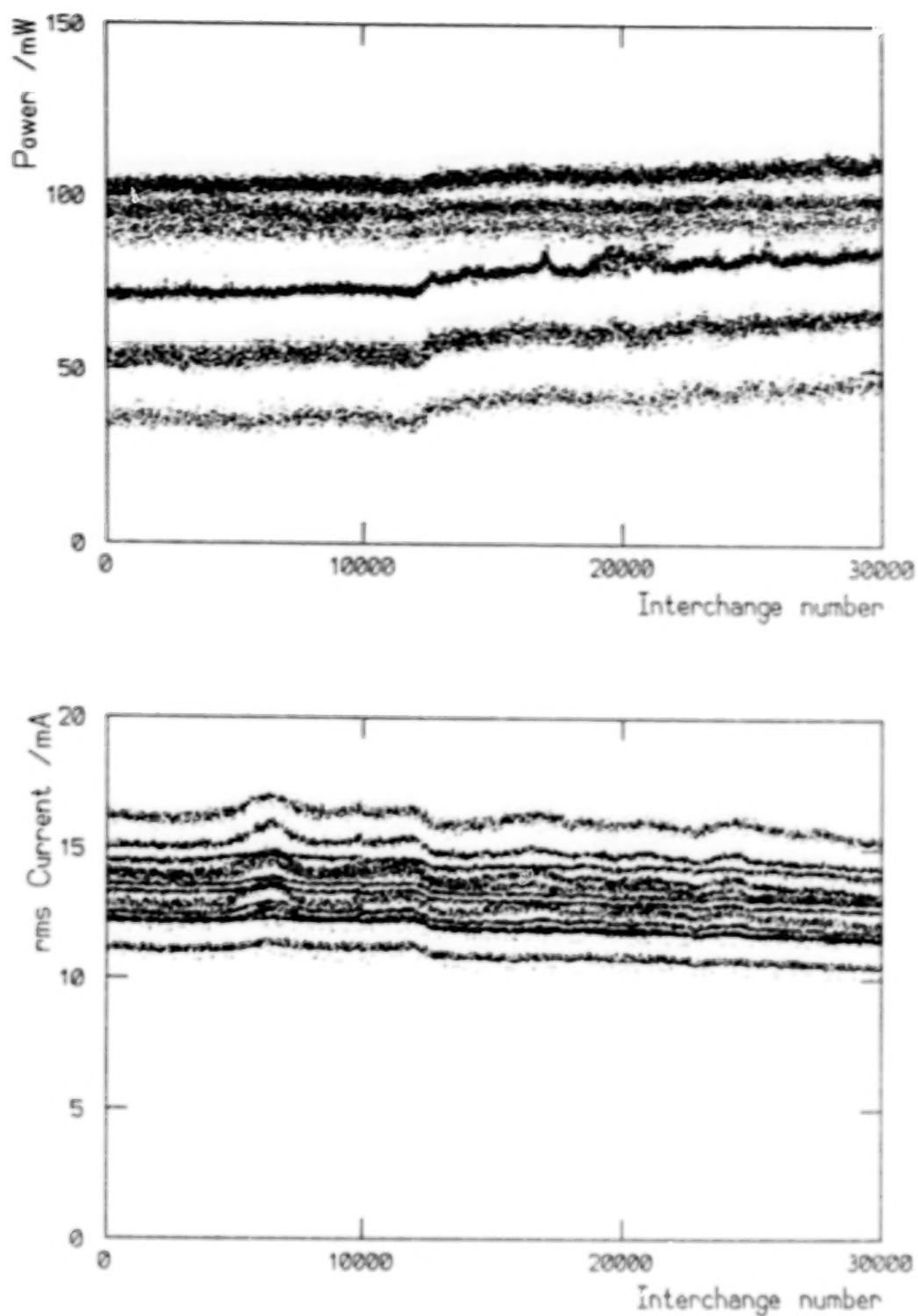


**FIGURE 4**

*Measured power consumption and rms current (both per phase) during the cryogenic life test of a development model of the interchange mechanism. Each point represents one interchange. The bands correspond to interchanges between different combinations of the four wheel positions.*

**BLANK PAGE**

# SPIN BEARING RETAINER DESIGN OPTIMIZATION

Edward A. Boesiger\* and Mark H. Warner\*\*

## ABSTRACT

The dynamic behavior of spin bearings for momentum wheels (control-moment gyroscope, reaction wheel assembly) is critical to satellite stability and life. Repeated bearing retainer instabilities hasten lubricant deterioration and can lead to premature bearing failure and/or unacceptable vibration. These instabilities are typically distinguished by increases in torque, temperature, audible noise, and vibration induced into the bearing cartridge. Ball retainer design can be optimized to minimize these occurrences. A retainer was designed using a previously successful smaller retainer as an example. Analytical methods were then employed to predict its behavior and optimize its configuration.

## INTRODUCTION

Ball retainer instability, usually characterized by a squealing noise, is not uncommon with bearings operating at certain speeds and conditions. It has been observed in gyroscope bearings ("chatter") [1], momentum wheel bearings [2], and main shaft turbine engine thrust bearings [3], but is by no means limited to these types. Momentary periods of instability are normally non-destructive, such as noise heard during run-up. However, prolonged operation with instability can eventually lead to cage failure.

At the onset of retainer instability, ball-retainer collisions in a bearing occur with progressively increasing force, and the motion of the retainer departs from simple rotation (for more information about retainer instability see [4, 5]). These retainer motions can include random motions as well as repeating whirling-type behavior. The energy to drive the retainer unstable is believed to come from friction or viscous drag of the lubricant. Retainer instability is therefore aggravated by lubricant degradation or migration. When the instability begins, increased forces and friction in the bearing cause the power dissipation to increase, the ball slip along the races to increase, and thus the temperatures in the bearing increase. These increased

\* Lockheed Missiles and Space Company, Inc., Sunnyvale, California

\*\* Honeywell Corporation, Satellite Systems Operations, Glendale, Arizona

temperatures further the degradation of the lubricant, which propagates this instability cycle.

A life test of a control-moment gyroscope (CMG) spin bearing system was conducted under a relatively strenuous duty cycle. The bearings developed excessive drag torque prior to the end of their design life. Subsequent inspection of the test article revealed that a retainer had broken and that the lubricant had degraded. This failure prompted an investigation for an improved system.

Practice indicates that adequate lubrication reduces the risk of instability. A retainer can be designed to make it less susceptible to friction-induced instabilities. Therefore, a design effort was undertaken to optimize the retainer design for an existing bearing. To increase retainer strength, the land diameters of this bearing were set to their limits based on stress and spill-over in order to allow the use of the thickest practical retainer. Then, an "optimal" retainer was designed based on stability using a commercial dynamic bearing code in conjunction with other empirical tests. Predicted results generally correlated with bearing test data. The final configuration of the retainer is presently being manufactured and will be thoroughly tested.

## ANALYSIS

### Bearing Analysis Code

The modeling of the spin bearing was primarily accomplished using the commercially available ADORE (Advanced Dynamics of Rolling Elements) computer program [6]. This program simulates the dynamics (time and position dependent) of the bearing components, in contrast to other bearing computer programs that only calculate quasi-static (position dependent) conditions. A dynamic model is required to simulate retainer instability. Several dynamic bearing codes are available [5, 7]; however, ADORE was thought to be the most comprehensive and best suited for this application, although it is the most computer resource intensive.

To use ADORE for this design effort, pre- and post-processing code development was required. The retainer designs analyzed required accurate mass properties information. A pre-processor program was written to calculate the mass properties and transform them into ADORE format. A post-processor program was also written to assimilate the large amount of ADORE output data into a form where comparisons

among designs could be made. The many lessons learned about using the ADORE program were incorporated in a comprehensive user manual. Considerable training was found necessary to use ADORE effectively.

In addition, the ADORE program required modification to incorporate a retainer with a full inertia tensor and general mass center location. The retainer is a patented Honeywell design that incorporates a 'force' and 'moment' bias. The bias is achieved by offsetting the retainer mass center from the rotation center. A full inertia matrix (moments and products of inertia) is also required to characterize the retainer dynamics. Figure 1 shows an exaggerated schematic of a retainer with force and moment bias. The coupling of the products of inertia and the angular velocity of the retainer produce a 'moment bias' torque that tends to rotate the retainer out of the plane of the ball centers. The radial offset of the retainer mass center produces a force bias due to the centrifugal acceleration of the mass center. The force bias is thus proportional to the square of the instantaneous retainer rotational speed.

It was found that when modeling this retainer, ADORE was sensitive to small changes in input parameters, such as lubricant traction values, retainer stiffness, friction, and damping. Numerous tests and analyses were performed to identify accurate values for the system being modeled. These included ball-race lubricant traction parameter tests and retainer rub-block friction testing with the actual materials, surface finishes, and retainer dimensions. In addition, finite element modeling and tests for stiffness and modulus of the retainer material were conducted. Tests to determine damping coefficients, weight, and density were also performed. A thermal analysis was conducted for accurate temperature inputs into ADORE.

### **Design Evaluation**

The primary question asked of the analyst at every parameter change is, "Is the bearing now stable or unstable?" To obtain an optimal design, a refinement to this question is whether or not a particular change to the design is an improvement toward being more stable. A performance ranking method was needed to quantify small differences in the many indicators of stability (forces, wear, motion, etc.) between two cases that have similar, but not exactly the same, results. Two such methods were developed: using the critical friction threshold and combining stability indicators into a performance number. Both give

the same results, but the performance number is more efficient for optimization of the retainer.

### Critical Friction Threshold

The hypothesis for the onset of instability (insufficient or degraded lubrication) led to an investigation of the friction level that causes instability. It was found that a critical level of friction exists at which a dramatic deterioration in motion stability and force magnitude is observed. This friction level is defined here as the critical friction coefficient. It was found that different retainer designs had different critical friction coefficients, and thus the retainer with a higher coefficient has more resistance to the effects of lubricant degradation.

In order to evaluate the critical friction coefficient of a particular design, as many as ten to fifteen computer runs were required. While this method of using the critical friction coefficient to compare designs appeared to work well, there were occasional inconsistencies in the results. The transition between the stable and unstable regions was usually a distinct friction coefficient value. However, there were instances where this transition occurred over such a large range that no meaningful comparisons to other designs could be made. In this range, increases in friction caused an unstable motion to become stable again. For example, a retainer design was stable with a friction coefficient less than 0.15, unstable with a friction level of 0.16, stable again for a friction coefficient of 0.17, and then unstable for coefficients greater than 0.19. The large number of simulations required and the inconsistencies observed led to the development of an alternate method that could be used for the optimization.

### Performance Number

In order to rank the stability of bearing designs quickly and quantitatively, a method using a 'Performance Number' (PN) was developed. The Performance Number permits direct comparison of stability for those cases where a clear distinction is not obtained by observation of the results.

The PN defined here answers the question "Is it now more or less stable than the nominal or previous case?" After running many parameter variation cases, it was realized that a definitive stable or unstable label was difficult to assign to each case. There are many requirements for a bearing; if the motion is not perfectly stable but the forces, torques, and wear are low, the bearing may be acceptable.

Although instabilities with irregular retainer motions may produce noise and torque variation, they may not result in mechanical failure of the retainer. Excessive forces, however, may produce structural failure. Generally, the more stable in both motion and forces, the better the bearing is for meeting requirements for full bearing life.

The Performance Number is intended as a comparison of the relative stability of designs, on the basis of both the motion and forces in the bearing. Two values used for the PN are calculated from the computer model output: the Stability Performance Number (SPN), based on retainer motion, and the Wear/Power Performance Number (WPPN), based on the forces in the bearing. The SPN and WPPN are combined to form the PN. Increased values of all three numbers relate to an increasingly stable bearing.

The PN provides a comparison relative to the nominal case. Thus, the PN does not measure absolute stability, only relative stability. If the nominal case is assigned a PN of 1, a case with a PN of 0.5 may or may not be "unstable," but is less stable than the nominal case. However, if the second case's PN is greater than 1 and if neither the WPPN nor SPN decreases significantly, the second case is considered more stable than the nominal case. This method is also applicable in optimization work where a modified case is compared with a previous case. The PN simply compares both to the nominal case, and the one with the higher PN is regarded as the most stable.

The SPN comprises the following indicators of retainer motion stability: retainer whirl ratio, retainer omega ratio, retainer mass center orbit shape, and the integration run time. Whirl and omega ratios give an indication of how the retainer is moving relative to the race rotation, and are constant when the retainer motion is stable [1]. A small, steady ball-retainer contact force produces a circular mass center orbit, while random or whirling retainer mass center motion results when the contact forces are large and have no defined pattern, as is the case during instability. Figure 2 illustrates the ADORE whirl ratio and orbit plots for a stable and unstable condition. Integration run time, though not an obvious stability indicator, is included because stable retainers have fewer and less severe contacts, and the integration proceeds more easily than if the retainer is unstable.

The WPPN is a measure of wear and power stability based on the forces, torques, and power losses in the bearing. Experience has shown

that stable bearings have lower drive torque, less power loss, and lower retainer contact forces than unstable ones. The WPPN is calculated by combining the values of drive torque, power loss, retainer wear rate, ball-retainer forces, and retainer-race forces. Torque, power, and forces in the bearing are somewhat obvious indicators of bearing stability. The slope and value of the retainer wear rate is also an indicator of retainer stability. If the forces and sliding velocities are increasing, the wear rate increases, and this generally indicates instability.

### Optimization Methods

After developing a performance criteria for evaluating retainer designs, an efficient method of iterating to an improved overall design was required. Common methods, such as Monte Carlo, and a full matrix of possibilities were rejected due to the large number of simulations needed. The ADORE simulations were run on a Cray computer and required approximately 1500 CPU seconds to run. The man-hours and computer time needed to make the hundreds or thousands of simulations for these methods was time and cost prohibitive. Another common method is to vary each parameter separately to the end of its tolerance range and, after observing its effect on the stability, combine all the parameters in a 'best-on-best' fashion. This method would have had limited success with this bearing dynamics problem, as it was found that the parameters have a significant amount of coupling among them. It was not possible to predict the effect of changing the value of one parameter when other parameters were also changed.

The optimization technique of steepest descent avoids the problems of these other methods. In this method, several variables are changed a small amount for each computer run rather than varying one parameter at a time. A systematic approach was desired, especially when the interactions of the parameters were unknown. Steepest descent is based on the premise that limiting the changes in variables to small fractions of their initial value tends to keep the effect on the output monotonic. This means that an optimal design can be found by iterating, using small increments of the variables in the direction of increased stability for each. Based on having the PN to determine relative stability among cases and the smaller number of runs required, the steepest descent method was chosen to do the retainer design optimization.

### Optimization Results

The strategy for this study was to find an improved design that

took into account the interactions of the various parameters. The optimization was based on changing only the retainer design. Changing the ball size or further changes to the races would have too great an impact on the system design (shaft, cartridge, housing, etc.). Thus, the following five primary characteristics of the retainer were chosen as variables:

- 1) retainer pocket-ball diametral clearance
- 2) retainer-race diametral clearance
- 3) number of balls
- 4) force bias
- 5) moment bias

The optimization study was carried out while operating under the nominal operating conditions, which included gravity, a small radial load, a shaft speed of 6000 RPM, and retainer-race and ball-retainer friction coefficients of 0.12.

The nominal condition was run to establish a baseline. This nominal case has a PN of 1.0. Each of the five parameters was then varied either positively or negatively in separate runs. For each parameter, it was then determined whether the change had improved or degraded the retainer dynamic stability (i.e., by the PN). It should be noted that the steepest descent method was initially tested using a simpler bearing dynamic analysis program with good results [8]. However, when using ADORE, the steepest descent method with the PN required too fine a change in the parameters for the PN to accurately predict the direction to change the variables for increasing stability.

A parameter study and experimental data indicated the primary parameters that influenced the retainer stability. Of the five parameters listed previously for the steepest descent study, all except the moment bias had a significant effect on stability. Figure 3 illustrates the effect of two of these parameters (land and pocket clearance) on the retainer stability. The land clearance, pocket clearance, number of balls, and force bias parameters were then used in a 'partial matrix' optimization. The realistic range that these parameters could be varied was divided into three possibilities and all the combinations of these parameters were simulated (54 cases). The simulations were run with a high friction value to help distinguish between stable and unstable.

The high friction level eliminated a large number of the cases, and

there were only a few noticeably superior designs. This was confirmed with the PN of the cases. These few designs were then rerun with various operating conditions seen by the spin bearing system, including zero gravity, high radial loads, degraded lubricant, different speeds, and various press fits between the bearing and the shaft and housing. The results of these runs were more important than initially expected. It became obvious that one particular design was the best performer throughout the range of operating conditions. This design included smaller retainer pockets, larger retainer-land clearance, one less ball, and larger force bias.

## TESTING

The bearing dynamics problem (and simulation) is complicated, and there is considerable uncertainty associated with these types of calculations and model assumptions. As a result, it was believed that testing for confirmation and confidence in the model was essential. The optimized retainer design also had to be verified. Two bearing test fixtures were used to observe stability. An existing fixture, Universal Bearing Test System (UBTS), was considered a retainer screening tool. The Bearing Stability Tester (BeST) tests an end-item duplex bearing pair and was developed in parallel to complement the testing on the UBTS. Since the UBTS tests were done with one of the bearings from the duplex pair, the BeST more closely simulates the actual bearing system configuration.

### UBTS Fixture

The UBTS is a fixture that was developed to perform ball bearing dynamics research. The fixture was designed primarily as a single bearing screening device, but it can also be configured to accept a preloaded pair. Figure 4 shows the UBTS, along with its support equipment. The spindle is suspended on an air bearing, and the axial preload on the bearing can be varied by adjusting the gas pressure. Radial and axial induced vibration forces are measured using two piezoelectric load cells. In addition, two linear variable differential transformer deflectometers measure bearing drag torque. The amplitude variation of the induced vibration radial component at the retainer frequency, as well as audible noise and an increase in drag torque, give indications of retainer instability.

The UBTS was used in conjunction with a "rub block" fixture that measured the coefficient of friction in both the ball pocket and land

regions of the retainer. By accurately measuring these friction values and then evaluating the retainer's performance on the UBTS, a retainer's stability characteristics as a function of friction could be established. The retainer's friction coefficient could be increased by either cleaning with a solvent (Freon) or by vacuum baking the retainer. In this manner, a critical friction coefficient for a given retainer design was found. For friction levels above this value, the retainer exhibited unstable characteristics, and when below the critical value, the retainer appeared stable.

Figure 5 shows a plot of the Performance Number versus friction coefficient for both the old retainer and the new design optimized by the computer modeling. This friction coefficient is input in the model at both the ball/pocket and retainer/land interfaces. Superimposed on the graph are the actual UBTS-measured values for critical friction coefficients for the two retainers. While the actual values for measured and analytical critical coefficients are not exactly equal, the model did correctly predict that the new retainer would be less susceptible to increasing friction (i.e., the new retainer would have a higher critical friction coefficient). This empirical correlation is very important because as the lubricant degrades, friction forces on the retainer increase. The model-optimized design allows the retainer to remain stable for approximately 50% larger values of friction than the original design.

UBTS was also used to verify the model's prediction that the retainer stability was more sensitive to increasing friction in the ball pocket region than in the land region. Two retainers were completely cleaned using Freon TF and then run on UBTS. Both exhibited unstable behavior (audible noise, large variation in radial induced vibration, etc.). The friction coefficients at the ball-pocket and land-retainer interfaces were measured and found to be 0.36 and 0.44, respectively, on both retainers. The inner land of one of the retainers was then swabbed with a very light coat of lubricant, while the pockets of the other were lubricated in a similar manner. Both retainers were then rerun on UBTS. The retainer with its pockets lubricated did not exhibit any unstable behavior, while the retainer with the inner land lubricated behaved exactly as it did when it was unlubricated. The coefficients of friction of both retainers were then measured again. The retainer with its pockets lubricated had a friction coefficient of 0.23 in its pockets, and 0.44 in its land region. The retainer with its land region lubricated had a friction coefficient of 0.36 in its pockets, and 0.28 in its land

region. This verification of the model's prediction that the ball/pocket interface is the driver of retainer instability gave confidence in the output of the model.

### BeST Fixture

The BeST fixture was developed to simulate the end-item configuration while being able to measure the forces, motor current, accelerations, bearing temperatures, speed, and retainer motions. The bearings were rotated by a DC servo motor through a flexible coupling. The fixture was also designed to be compatible with mounting onto a shaker table. Figure 6 shows the BeST fixture and the associated wiring for the instrumentation.

A servo motor controlled the rotating speed of the bearing pair. The drive motor current is an indirect measure of the torque required to turn the bearings. A three-axis accelerometer was mounted on the side of the housing to measure radial and axial accelerations. Thermocouples measure the outer race temperature at two places on each bearing. An infrared pyrometer measured the temperature of the inner race. Two three-axis piezoelectric load cells were intended to measure the forces and torques in the bearing. However, the poor quasi-static performance and high thermal sensitivity of the cells on the BeST fixture made it difficult to obtain useful steady state information.

The BeST fixture was used to test the bearings with the old retainer design by running up the bearings from 0 to 6000 RPM. The bearings did exhibit unstable behavior at some speeds during the run-up, which is consistent with the results observed during the bearing life tests. The instabilities were confirmed by audible noise, an increase in bearing temperature, an increase in motor current, and a sharp rise in acceleration. Figure 7 is a spectral waterfall-style plot for the axial direction during a run-up. The acceleration is plotted versus frequency for every 100 RPM. It can be seen that during certain speed ranges, a rise in acceleration at about 1500 Hz occurs. The same frequency peaks at instability are also seen in the other two accelerometer directions. This instability frequency has not been positively associated with a physical bearing characteristic, although it does correspond to the natural frequency of the ball-retainer collisions. At one of these speeds, 3400 RPM, the ADORE program was run at a high friction level to simulate the instability. The post-processing code was then used to produce retainer acceleration spectral plots for the radial, orbital and axial directions. The analysis found the predominant frequency during

instability to be 1500 Hz in the orbital and radial directions and 1700 Hz in the axial direction. These frequency values show general correlation between test and analytical results.

An important output of the computer simulations is the motion of the retainer mass center. It was desired to observe this retainer motion for both a stable and unstable condition on the BeST fixture. Cage motions were measured using non-contact proximity probes. A 0.008-inch thick aluminum ring was pressed onto the outer diameter of the inner-race guided retainer. Two proximity probes were mounted in the housing 90° apart, and were placed so that they could read the radial motion of the retainer. The bearings were rotated, and when no audible noise was heard, the proximity probe information was recorded. The proximity probe information was converted to mass center position and plotted as an orbit plot. The comparison of the ADORE prediction and the BeST test for this stable condition is shown in Figure 8.

The addition of the aluminum ring did change the retainer's dynamic characteristics. The ring was attached on the one side of the retainer not preloaded against the other bearing in the pair, and since the inner and outer retainer diameters are not concentric, the weight, force bias, and moment bias of the retainer were increased. These changes had the effect of stabilizing the retainer. The bearings had to be ultrasonically cleaned to remove any lubricant in order for the bearings to become unstable. Figure 9 shows the comparison between the ADORE prediction and the test result. Both mass center orbit plots show the whirling loops characteristic of the unstable retainer motion and there is good correlation between the two.

## CONCLUSION

An existing CMG bearing retainer design was optimized for stability using a bearing dynamics code in conjunction with experimental data. Bearing instabilities were observed during tests with proximity probes, accelerometers, and audible noise. Preliminary testing of retainer motion, instability frequency, and friction threshold have correlated with the computer modeling predictions. This design is being refined and fabricated and will be thoroughly tested in an end-item configuration. From this optimization effort, a number of important "lessons learned" became apparent:

- There is a critical friction level associated with each retainer design beyond which the retainer is unstable.

- Ball pocket friction is more critical to stability than retainer land friction for the bearing investigated.
- The nature of the bearing dynamics problem makes retainer optimization a very difficult task for the following reasons:
  - the parameters are coupled
  - the high accuracy of input data required
  - the specific operating conditions are important
- It is difficult to discern the effects of small changes on the indicators of stability from the bearing dynamics program.
- The steepest descent optimization method appears to be the most promising, but is hard to implement accurately for bearing dynamics.

### ACKNOWLEDGMENTS

The authors wish to thank Pradeep Gupta for his consultations concerning ADORE, and Sean McCully for his help in running multitudes of cases. We also wish to thank Allan Donley and Mark Heller for their invaluable experimental work, and Stuart Loewenthal for his guidance on the analysis and the BeST fixture.

### REFERENCES

1. Kingsbury, Edward P. "Torque Variations in Instrument Ball Bearings." *ASLE Transactions*, 8 (1965), 435-441.
2. Stevens, K. T. "Experimental Observations on Torque Variation Caused by Bearing Cage Instabilities." *Proceedings of the Second Space Tribology Workshop*, (October 1980), pp. 101-110.
3. Gupta, Pradeep K., J. F. Dill and H. E. Bandow. "Dynamics of Rolling Element Bearings - Experimental Validation of the DREB and RAPIDREB Computer Programs." *ASME Journal of Tribology*, 107 (January 1985), 132-137.
4. Kannel, J. W., and D. Snediker. "Hidden Cause of Bearing Failure." *Machine Design* (7 April 1977), pp. 78-82.
5. Kannel, J. W. "A Simplified Model of Cage Motion in Angular Contact Bearings Operating in the EHD Lubrication Regime." *ASME Journal of Lubrication Technology*, 100, no. 3 (July 1978), 395-403.
6. Gupta, Pradeep K. *Advanced Dynamics of Rolling Elements*. Berlin: Springer-Verlag, ©1984.
7. Meeks, Crawford R., and Karen O. Ng. "The Dynamics of Ball Separators in Ball Bearings - Part 1: Analysis." *ASLE Transactions*, 28, no. 3, 277-287.

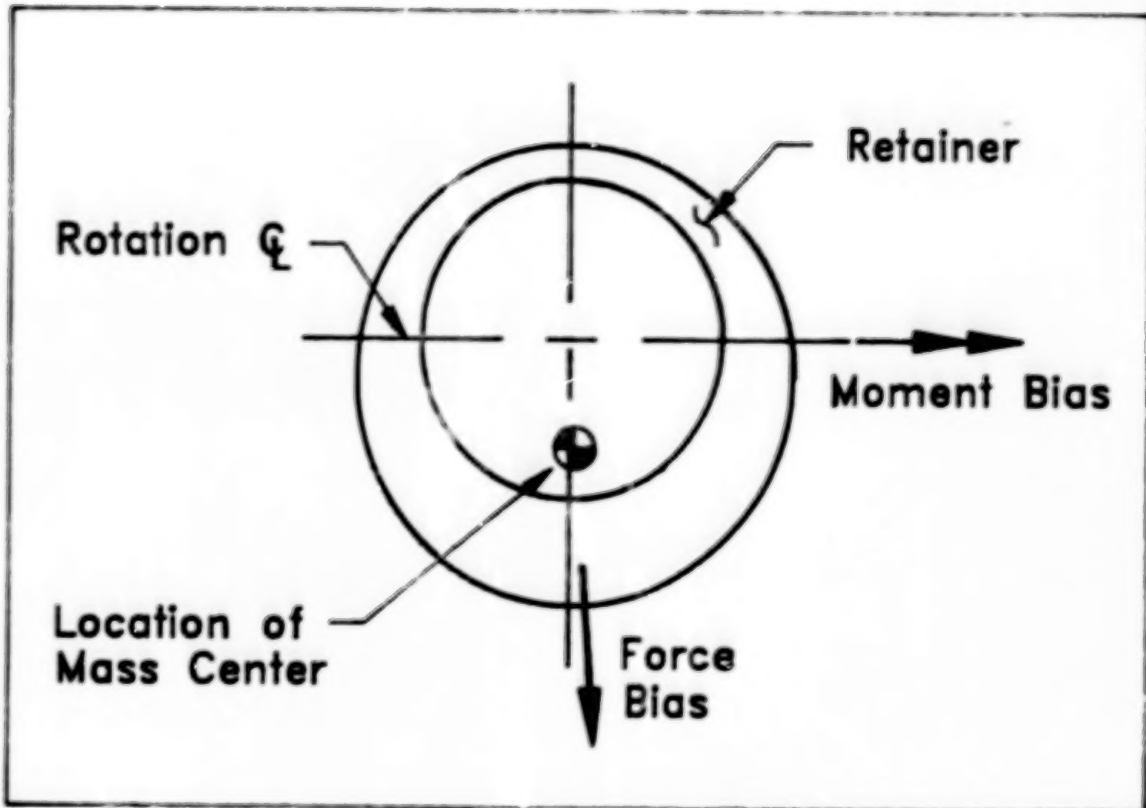


**Figure 1: Cage Force and Moment Bias**

Cage design offsets the mass center from the rotation center. At speed, the design induces forces and moments on the retainer.

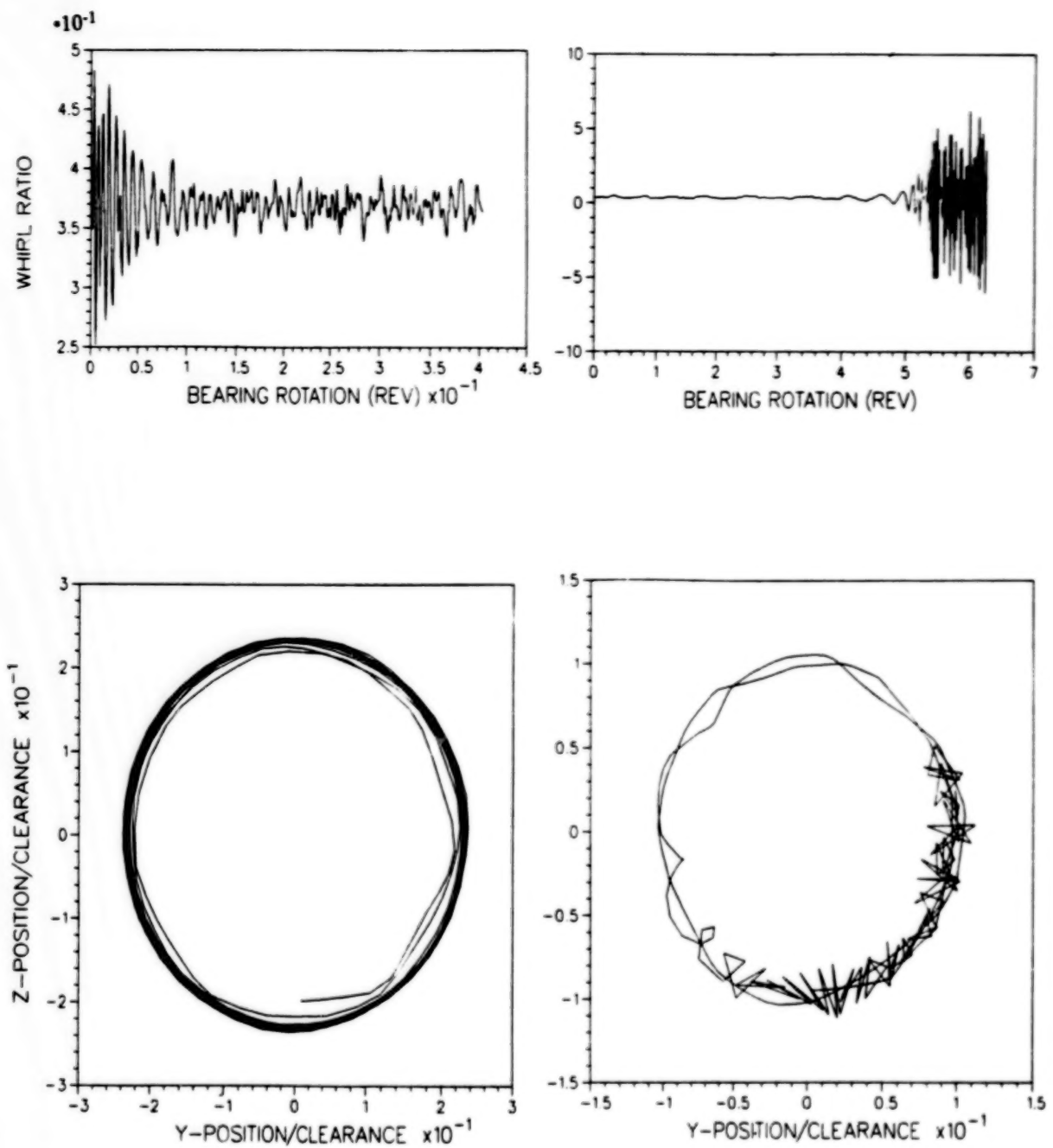


**Figure 2: Typical ADORE Output**

Shown are two indicators of retainer stability for runs where the retainer was stable (left column) and unstable (right column). The retainer whirl ratio is the ratio of the retainer mass center speed to the race speed. The orbit plots are the position of the retainer mass center relative to the bearing center.

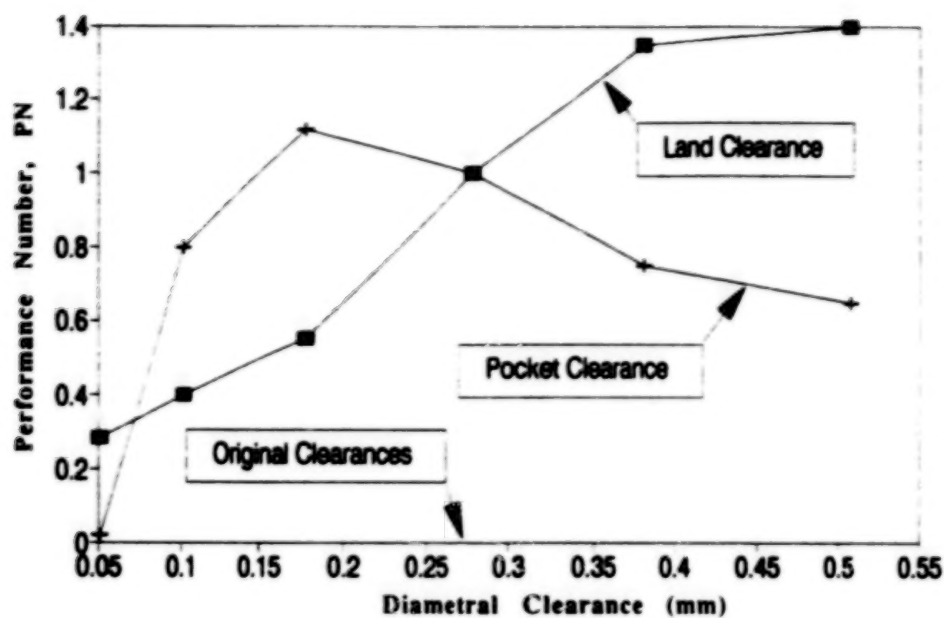


**Figure 3: Parameter Study Results**

Perturbations from the original design were studied to determine the sensitivity of the land and pocket clearance. Nominal land and pocket clearances of the original design were both 0.28 mm.



**Figure 4: UBTS Fixture**

Pictured is the UBTS fixture used for friction threshold bearing tests.

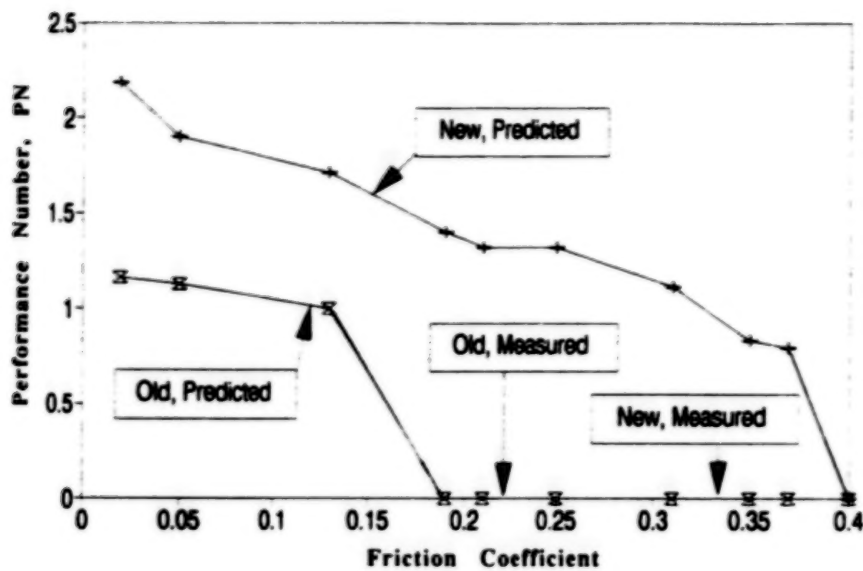


**Figure 5: Optimization Results**

The optimal ("new") retainer is shown to be superior to the original ("old") design by the Performance Number, and by both the analytical and tested critical friction threshold.



**Figure 6: BeST Fixture**

Pictured is the BeST fixture used for retainer acceleration and motion tests.

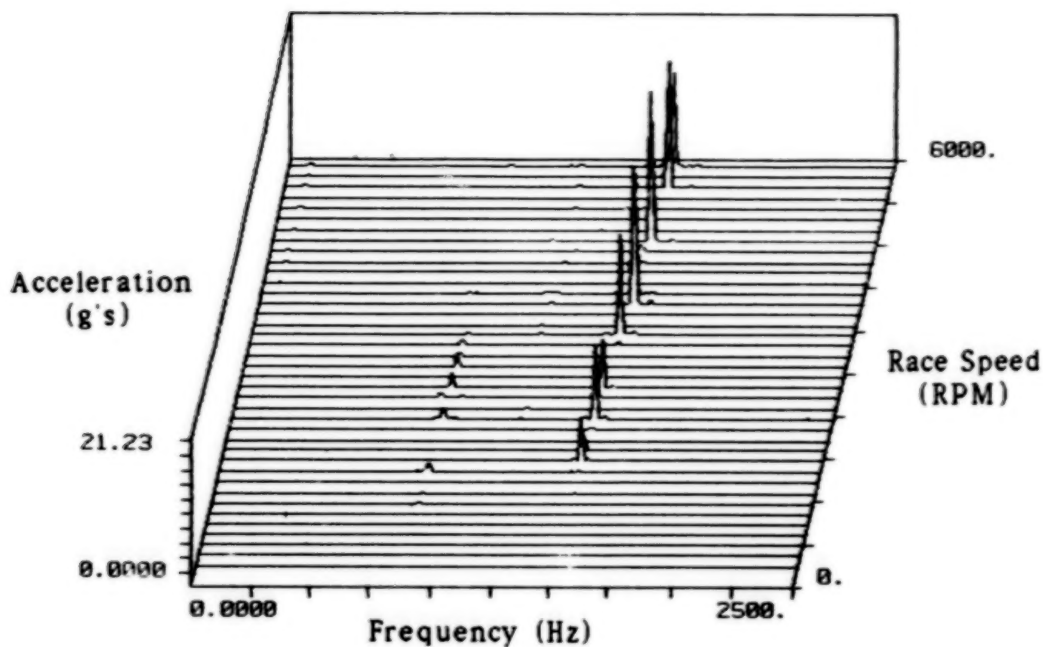


**Figure 7: Typical Accelerometer Spectral Plot**

A spectral plot of the axial direction is shown. Acceleration in g's is plotted versus frequency in Hertz for every 100 RPM from 0 to 6000 RPM. Note periods of instability distinguished by the high accelerations.

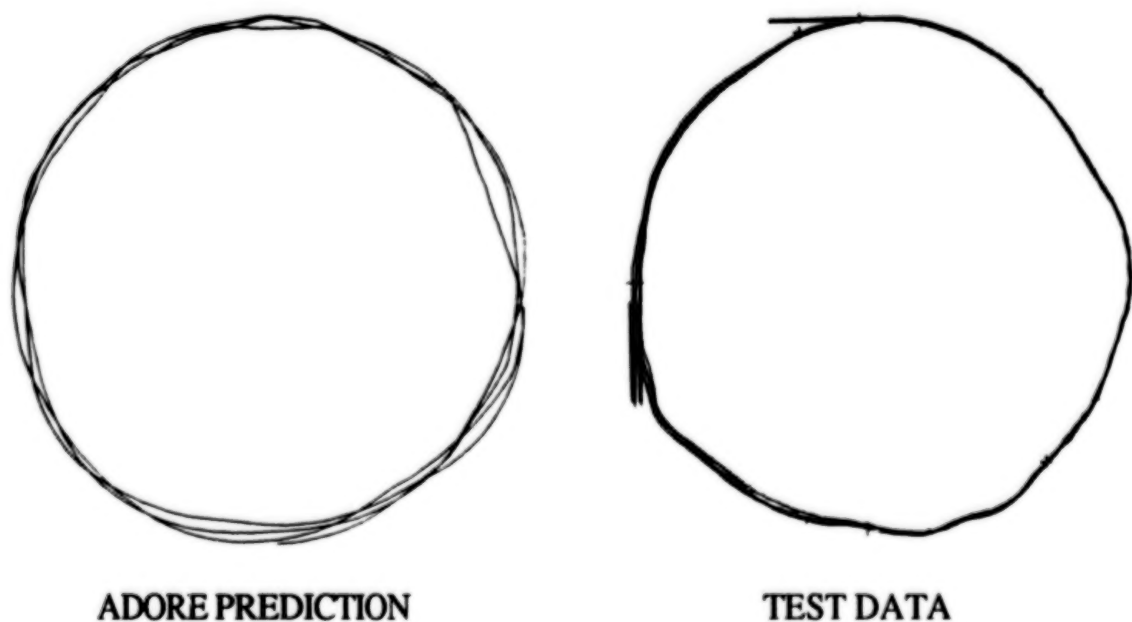


**Figure 8: Stable Cage Mass Center Orbit Plots**

Mass center orbit plots from the analysis and test data for a stable retainer condition at 1750 RPM show a qualitative correlation.



ADORE PREDICTION



TEST DATA

**Figure 9: Unstable Cage Mass Center Orbit Plots**

Mass center orbit plots from the analysis and test data for an unstable retainer condition at 1780 RPM show a qualitative correlation.

## WEAR CHARACTERISTICS OF BONDED SOLID FILM LUBRICANT UNDER HIGH LOAD CONDITION

Naofumi Hiraoka, Akira Sasaki, Noritsugu Kawashima\* and Toshio Honda\*\*

### ABSTRACT

Wear properties of phenolic resin bonded molybdenum disulfide film lubricant were studied. In-vacuo journal bearing tests were carried out to evaluate the wear-life of this film lubricant. The wear-life depends on substrate materials and on sliding velocity. Pretreated substrate surfaces were examined to reveal the reasons for these results. Additionally, investigations on film wear mechanism were made.

### INTRODUCTION

Bonded solid film lubricants are favorable candidates for lubricating gears, cams, sliding bearings or other sliding elements in mechanisms used in outer space(1)(2)(3). They are, in general, useful in high load and low speed conditions(4). They have a lower coefficient of friction, compared to soft metal films, higher allowable contact pressures, compared to bulk plastics, longer lives in pure sliding conditions, compared to sputter-deposited molybdenum disulfide films(5) and they are less sensitive to temperature change, compared to oils or greases.

Resin bonded molybdenum disulfide films probably have been the most widely examined of these kinds of lubricants. The authors have studied these films, especially from the viewpoint of application to the gears(6) and the journal bearings for the use of manipulator mechanisms for the Japanese Experiment Module (JEM) in space station "FREEDOM". Experimental results of durability tests, which were carried out for the application of the film lubricant to journal bearings, are described in this paper. In addition, a discussion on film wear mechanism is also included.

### EXPERIMENTAL EQUIPMENT AND PROCEDURES

In order to evaluate the friction and wear-life for plain journal bearings lubricated by the bonded solid film lubricant, an in-vacuo journal bearing tester was used. Figure 1 shows the tester configuration. The bearings used for the tests had a 10 mm bore and 7 mm width. The lubricant used in the tests was commercially available phenolic resin bonded molybdenum disulfide film. The films were spray-coated on both mating surfaces of bearings and shafts, then they were heat-cured. The film thickness was controlled between 7 to 13 microns. Material and pretreatments of shaft and bearing substrates are shown in Table 1.

Pretreatment is a very important factor to determine the film performance(7)(8). The sand-blasting is made mainly in order to roughen the surface to strengthen the mechanical bonding of the film to the substrate. Passivating is made mainly to give chemical stability to the surface.

---

\* Toshiba Corporation, R&D Center, Kawasaki, Japan

\*\* Toshiba Corporation, Komukai Works, Kawasaki, Japan

Substrate material combinations and bearing clearances with films applied are shown in Table 2. Only the 304 stainless steel bearings took the form of a bushing press-fitted into aluminum alloy holders. Other bearings were made directly on the holders.

The tester was set in a laboratory air environment and specimen temperature was not controlled. In all cases, the tester chamber was evacuated by a rotary and turbo-molecular pump system up to the  $10^{-5}$ Pa mark first, then the test started. As soon as the test started, the vacuum went down to the  $10^{-4}$ Pa mark, because of released gases from the lubricant. After a few minutes, the vacuum got back to the  $10^{-5}$ Pa mark, which continued to the end of the test.

The shaft was oscillated by an AC servo motor through a reduction gear and feedthrough with an oscillational angle of 50 deg. The standard angular velocity examined was 10 deg./s, which was 0.87 mm/s in sliding velocity. Also some other velocities were examined. The loads were 1470 N (150 kg) and 1960 N (200 kg), which yielded 21 MPa and 28 MPa in projected area contact pressure, respectively.

## EXPERIMENTAL RESULTS

Figure 2 shows a typical measured frictional torque trend for the bearings. The torque was large in the beginning and decreased to a steady level (Fig. 2-a). At the end of the test duration, the torque increased suddenly. This point was regarded as the wear-life for the bearing (Fig. 2-b). All the life-ended bearings had scoring damages and the damages positioned on the motor side end of the bearings, as shown in Fig. 3. That was probably caused by a peculiar misalignment of the tester.

Figure 4 shows the wear-life and coefficient of friction (steady state torque / bearing radius / load) for three kinds of shaft and bearing-substrate materials combinations. The coefficient of friction values were similar, but wear-life was very different between combinations, and there was considerable scatter in life for a given combination. The wear-life decreased in the order of SET 3, SET 2, SET 1 in Table 2.

Figure 5 shows the film wear-life and the coefficient of friction at several angular velocities. Although the wear-life seems to decrease at lower angular velocity, more experiments are required to confirm this trend because of the large data scatter. The coefficient of friction increases with the decrease in angular velocity.

## DISCUSSION

### Substrate Materials for Shafts and Bearings

It was reported that the wear-life generally increases with the increase in hardness for the substrate (7). However, such was not the case with these tests, i.e., the SET 3 wear-life exceeded that for SET 2. In order to reveal the reasons for these results, pretreated surfaces of materials used in the tests were investigated. Specimens with a flat surface of these materials were prepared for this investigation. Figure 6 shows the shape of the specimen. These flat surfaces were partially pretreated, and film was bonded to half of the pretreated area.

Figure 7 shows surface profiles for the specimens measured with TALYSURF. Corresponding numerical data are shown in Table 3. The aluminum alloy pretreated surface (Fig. 7-a) indicates a large degree of roughness, owing to sand-blasting. Heights of some peaks are comparable to lubricant film thickness, which means that films on such peaks had only a slight thickness, or even that there was no film on them. This is probably the most important reason for the short wear-life for the aluminum substrate bearing, besides low mechanical toughness of

aluminum alloy. The sand-blasting of the aluminum was the same as that for stainless steel, but this observation suggests that lower pressure or finer particles would be recommendable for sand-blasting aluminum alloy.

The pretreated surface of 440C stainless steel (martensitic stainless steel) in Fig. 7-b exhibits lower roughness height, on the average, than non-pretreated surface. This is because material was removed from the surface by sand-blasting. On the other hand, the pretreated surface of 304 stainless steel (austenitic stainless steel) in Fig. 7-c retained about the same height, on the average, as that for a non-pretreated surface. This is because plastic deformation was predominant, compared to material removal in sand-blasting on 440C stainless steel.

Table 3 indicates that 304 stainless steel had a greater roughness and wavelength than 440C stainless steel had, but the differences were small. Figure 8 shows cross sections of the pretreated area of the specimens. The difference in surface topography is more easily discernible. Finer irregularities are found on the surface of 304 stainless steel, which were never detected by TALYSURF, because of its poor resolution in the horizontal direction, compared to that in the vertical direction. These fine irregularities are assumed to be more helpful for mechanical bonding of the film to the substrate than the greater scale of roughness mentioned above. Consequently the 304 stainless steel bearing had longer wear-life.

Another possible reason for the longer wear-life for the 304 stainless steel bearing is that the 304 steel bushing, which was press-fitted into soft aluminum alloy holder moderated contact pressure, because it more easily deforms than the bulk steel. This is now under examination, using a 304 stainless steel holder as a bearing.

### Angular Velocity

The decrease in wear-life, with the decrease in velocity, could be accounted for by film fatigue, which will be discussed again in the next section. The reason for the increase in the friction with the decrease in velocity is not clear, but it is assumed that the decrease in the release of absorbed gases in the film by the frictional heat, with decrease in velocity, would increase the friction(9).

The temperature measured at the outside wall of the holder (see Fig. 1) increased by only five or less at under 50 deg./s in angular velocity at the beginning of the tests, when the friction was higher than in the test when the friction was steady. Later in the test, temperature change by frictional heating was insignificant compared to room temperature changes. The frictional heat, generated under 50 deg./s angular velocity, was small and would not significantly affect the film wear-life (but would affect the friction). At 100 deg./s angular velocity, temperature increased more than 15 degrees. The decrease in the wear-life at 100 deg./s was therefore attributed to the frictional heat increase. In a larger velocity range, the decrease in the wear-life with the increase in the sliding velocity was previously reported(10). This would also be due to the frictional heat increase.

### Wear Mechanism

Figures 9 and 10 show the worn film surface on a 304 stainless steel shaft and its profile. Figure 9 indicates many pits around flat surface. The width scale for these pits is on the order of a hundred microns and corresponds to that for profile's valleys of the corresponding area shown in Fig. 10a. Pits several microns in depth appear in the figure. In pertinent literature(10)(11)(12), 'blisters' were observed under much larger velocity conditions, but it is not clear whether the pits have anything in common with the blisters mentioned in the literature or not.

The pits are not considered to originate from the inherently existing voids in the film, according to the observation of the film cross section, which is shown in Fig. 11. They were also not considered to be the blisters produced by frictional heat, because higher angular velocity did not decrease the wear-life under 50 deg./s, as mentioned above. This means frictional heat did not increase the film damage, such as the pits, in this sliding velocity range. Thus, the pits were estimated to be traces of partial debonding of the film materials from the film caused by fatigue entailed during the sliding process.

Figure 10-b shows the worn film surface profile for the shaft at approximately a half of the number of oscillations for the life-ended bearings. A wide, deep groove is observed on the motor side end of the worn surface. Figure 12 shows a microscopic image of this groove. The groove appears not to be the trace of abrasion, but to be an aggregation of pits or a trace of flaking in Fig. 12. Thus, the pitting or flaking wear is considered to dominate the film decrement.

If it is true that the film wear-life decreases with the decrease of sliding velocity, one reason is the increase in friction with the decrease in velocity, as mentioned above, and another is the increase in time in contacting area with the decrease in sliding velocity, both of which are the cause of the decrease in fatigue life.

Film-debonding, which is the direct cause of bearing failure, occurs at the interface between the lubricant film and substrate. Film-debonding from the substrate surface would strongly depend on the pretreated surface topography of the substrate, as compared with that from film itself. When the film-debonded points on the shaft and the bearing meet, the bearing life ends. However, even if film on one side, probably on the shaft, remains, failure could occur.

The debonded particles from the film consisted of molybdenum disulfide, bonding resin, additives and impurities. They, including molybdenum disulfide, could be abrasives to the metal substrate(12), but probably not so abrasive to the film itself, because of its embeddability. Once the film debonded from the substrate, it would act as an abrasive on the metal substrate.

Figure 13 shows a cross section of the film coated ring specimen, which was used in the block-on-ring wear test in nitrogen gas in another study(13). A deep wear groove was observed, including ring material between thick remaining films. This could be considered the trace of abrasion of the film wear particles to the ring material, as stated above.

Although friction still indicated a low value (coefficient of friction was 0.03) in the block-on-ring test, the metal wear particles from metal substrate, produced by the abrasion of the film wear particles, could cause a sudden increase in friction in the journal bearing, where it is much more difficult to exclude the particles from between the contacting surfaces than in the case of the block-on-ring test.

From the mechanism mentioned above, it is reasonable that a harder substrate has a longer film wear-life, because the harder substrate generally has greater resistance against abrasives. However, this is not always true, because the film wear-life also depends on the film bonding capacity for the pretreated substrate surface.

## CONCLUSIONS

Wear properties for bonded molybdenum disulfide film were studied especially from the viewpoint of the application to journal bearings used in outer space. The following results were obtained.

1. The longest film wear-life ranked in the order of 304 stainless steel, 440C stainless steel and aluminum alloy material substrate.
2. The film wear-life seems to decrease with a decrease in sliding velocity in the low velocity range, though more experiments are needed to confirm this concept.
3. 440C and 304 stainless steel, which were processed with the same pretreatment, had different surface topographies. Probably, this difference gave longer life to the 304 stainless steel bearing.
4. The film lost its thickness mainly by pitting wear. Once the film debonded from the substrate, the dedonding particles could abrade the metal substrate, and the bearing life ended, even if the film on either the shaft or the bearing remained.

In this study, 304 stainless steel bearing, lubricated by this film, was proved to have a life over a hundred times as long as that required for the JEM remote manipulator system mission, though the film's resistance to radiation and atomic oxygen must be investigated in the future. Suggestions for producing tougher bearings were also found from this study.

#### REFERENCES

- (1) Matthey, R.A., "Lubrication of Space Systems", ASLE Preprint, 76-AM-5C-1.
- (2) Taylor, H.J., "A Large-Scale Manipulator for Space Shuttle Payload Handling—the Shuttle Remote Manipulator System," Proc. of 26th Conf. on Remote Systems Technology, 1978, 90.
- (3) Harp, J.A., "An Evaluation of Dry Film Lubricants and Substrate Materials for Use on SSME Gimbal Bearings, NASA TM X-64989, Jan. 1976.
- (4) Itoh, K., "Typical Properties of Bonded Lubricants", Solid Lubrication Symposium, Tokyo, Japan, 6-7 Sep. 1990, 46 (in Japanese).
- (5) Miyagawa, I., Fushimi, H., and Nakayama, K., "Friction and Wear Properties of MoS<sub>2</sub> Films under Rolling-sliding Condition", Proc. of 32nd JSLE Conf., Osaka, Japan, Nov. 1987, 149 (in Japanese).
- (6) Sasaki, A. et al., "Lubrication Method and Durability of Gears for Space Application", J. of Japanese Society of Tribologists, 34, 4, 1989, 265 (in Japanese).
- (7) Horwedel, L.C., "Bonded Solid Lubricants", SAMPE J., Jan./Feb. 1976, 1.
- (8) Neale, M.J., editor, Tribology Handbook, Newnes-Butterworths, London, B5.
- (9) Tsuya, Y., editor, Solid Lubrication Handbook, Saiwai Shobo, Tokyo, 1978, 53 (in Japanese).
- (10) Bartz, W.J., Holinski, R., and Xu, J., "Wear Life and Frictional Behavior of Bonded Solid Lubricants", Lubr. Eng., 42, 12, Dec. 1986, 762.

- (11) Bartz, W.J. and Xu, J., "Wear Behavior and Failure Mechanism of Bonded Solid Lubricants", *Lubr. Eng.*, 43, 7, Jul. 1987, 514.
- (12) Lancaster, J.K., "Anisotropy in the Mechanical Properties of Lamellar Solids and its Effect on Wear and Transfer", *Wear*, 9, 1966, 169.
- (13) Hiraoka, N., Kawashima, N., and Honda, T., "Wear-life Property of Bonded Solid Film Lubricant", Proc. of 34th Space Sciences and Technology Conference, Oct. 1990, 252 (in Japanese).

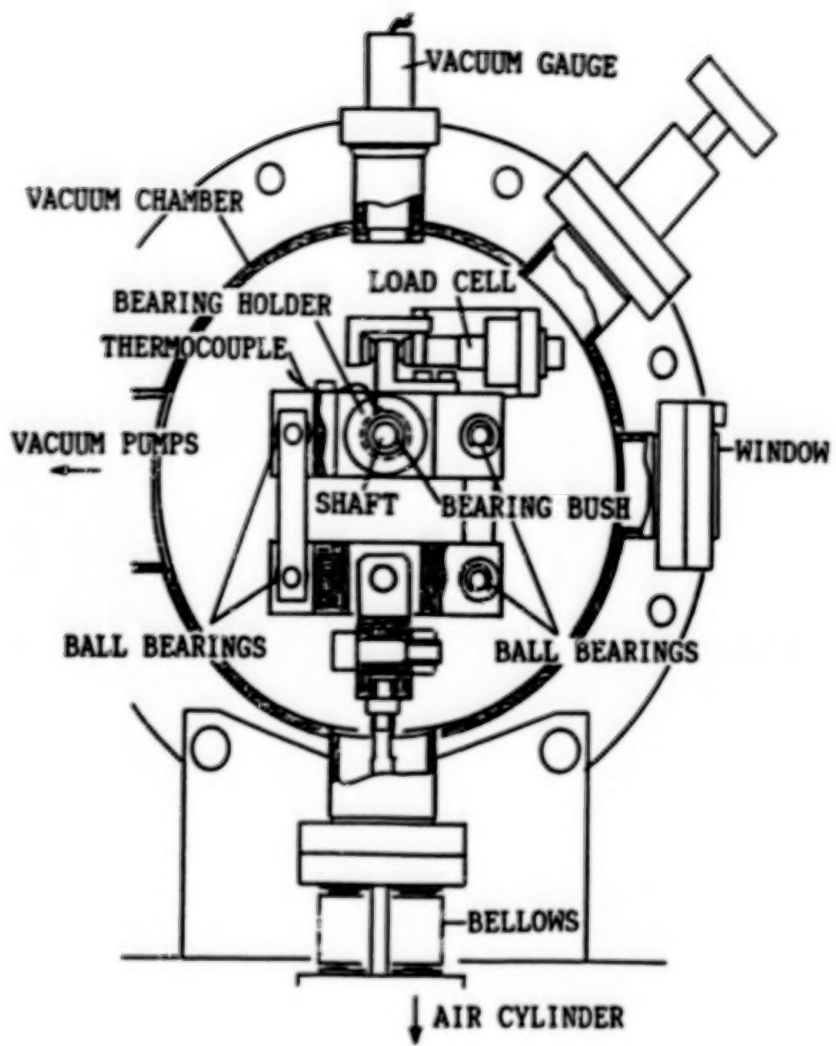


Figure 1. In-vacuo Journal Bearing Tester

Table 1. Substrate Materials

No.	MATERIAL	HEAT-TREATMENT	HARDNESS Hv.	PRETREATMENT
①	2017 ALUMINUM ALLOY	T4	120~130	SAND-BLASTING
②	440C STAINLESS STEEL	QUENCH HARDENING AND TEMPERING	570~590	SAND-BLASTING AND PASSIVATING
③	304 STAINLESS STEEL	-	220~250	SAND-BLASTING AND PASSIVATING

Table 2. Substrate Material Combinations

SET No.	SUBSTRATE MATERIAL		DESIGNED BEARING CLEARANCE ( $\mu\text{m}$ )
	BEARING	SHAFT	
1	①	②	40
2	②	②	10
3	③	③	20

\*①, ② and ③ are Corresponding to Those in Tab. 1

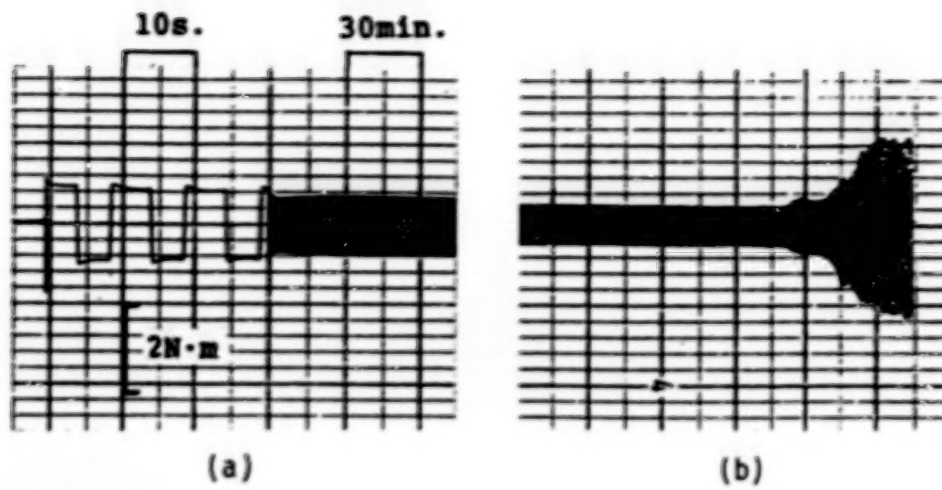


**Figure 2. Typical Frictional Torque Trend**

Specimen: SET 1, Angular Velocity: 10 deg./s, Load: 1470N  
 (a): at the Beginning of the Test,  
 (b): at the End of the Test

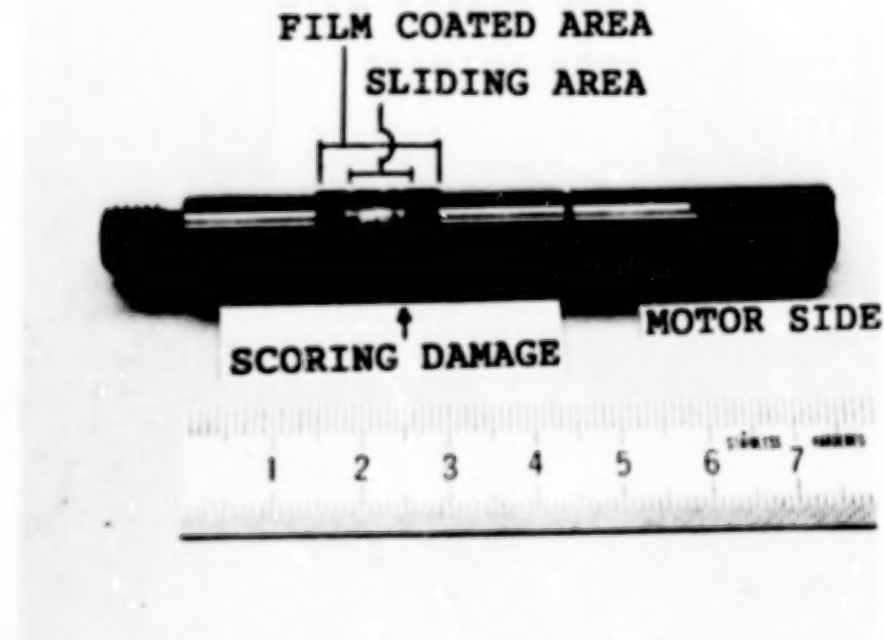


**Figure 3. No Longer Usable Bearing Shaft**

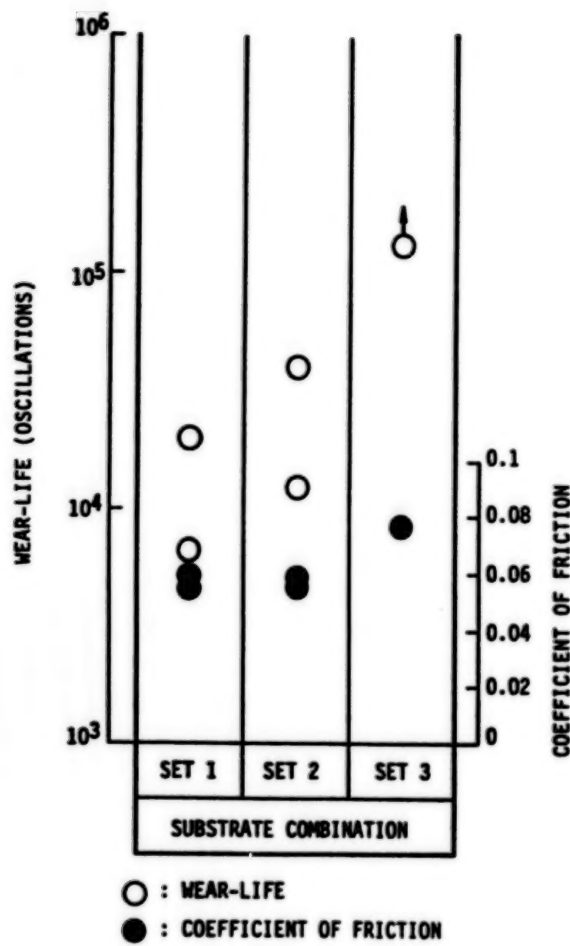


Figure 4. Wear Life and Coefficient of Friction for Three Substrate Combinations  
 Angular Velocity: 10 deg./s  
 Load: 1470N

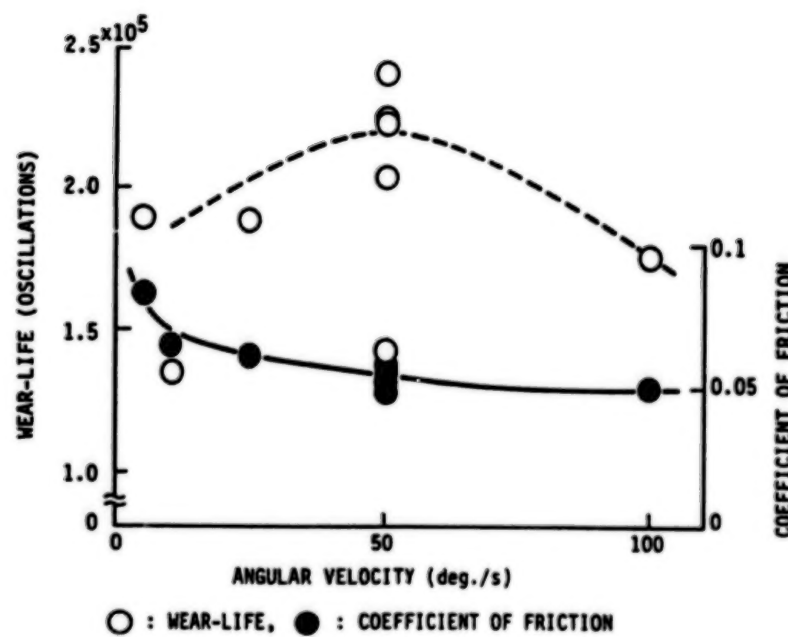


Figure 5. Wear-life and Coefficient of Friction at Several Angular Velocities  
 Specimen: SET 3, Load: 1960N

188

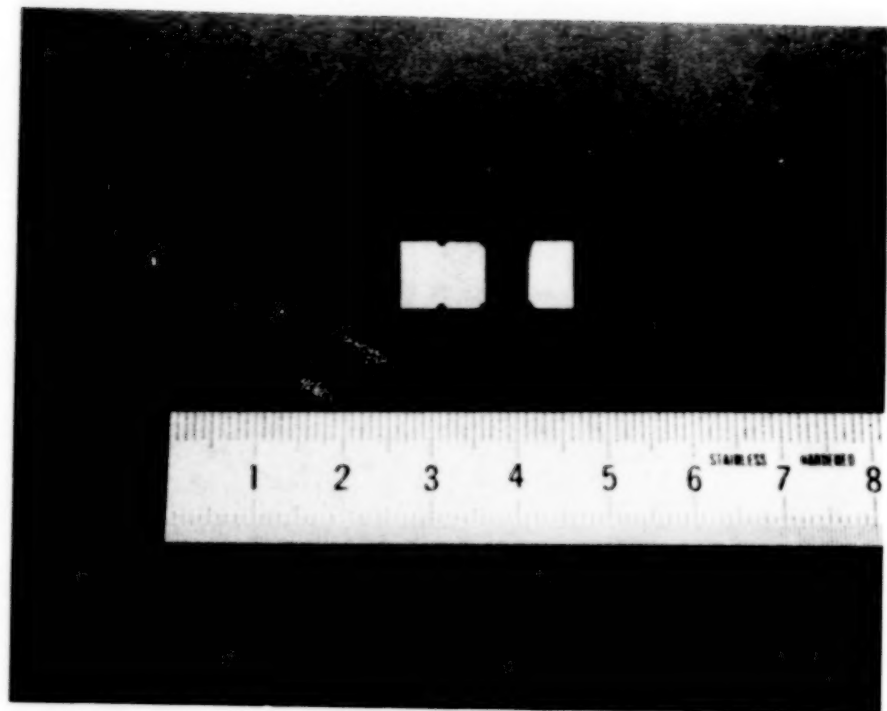


Figure 6. Pretreatment Surface Specimen



Figure 9. Typical Worn Film Surface

**BLANK**

**PAGE**

Table 3. Numerical Data for Pretreated Surface Topography

MATERIAL	R <sub>a</sub> ( $\mu\text{m}$ )	R <sub>max</sub> ( $\mu\text{m}$ )	SKEWNESS	WAVELENGTH (rms $\mu\text{m}$ )
2017 ALUMINUM ALLOY	1.9	15.5	-0.20	40.1
440C STAINLESS STEEL	1.1	7.5	-0.42	23.8
304 STAINLESS STEEL	1.2	8.8	-0.42	27.9

190

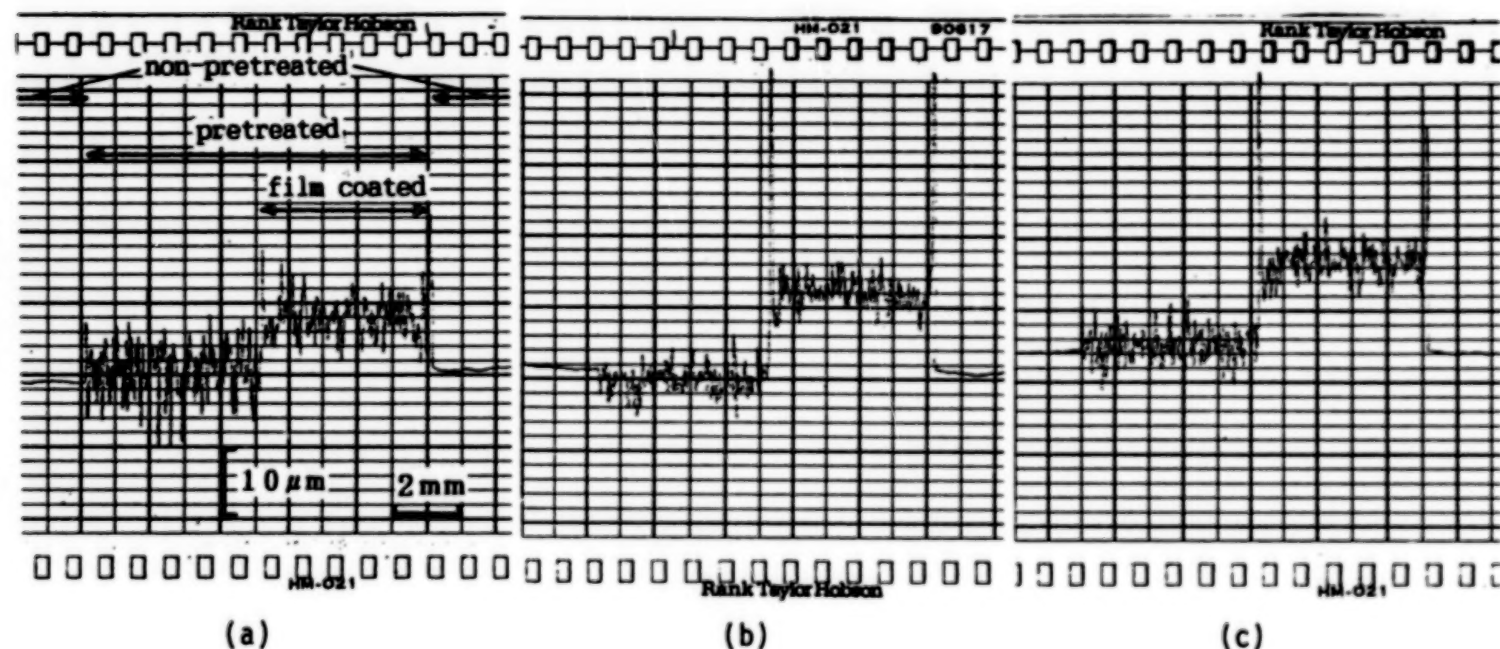
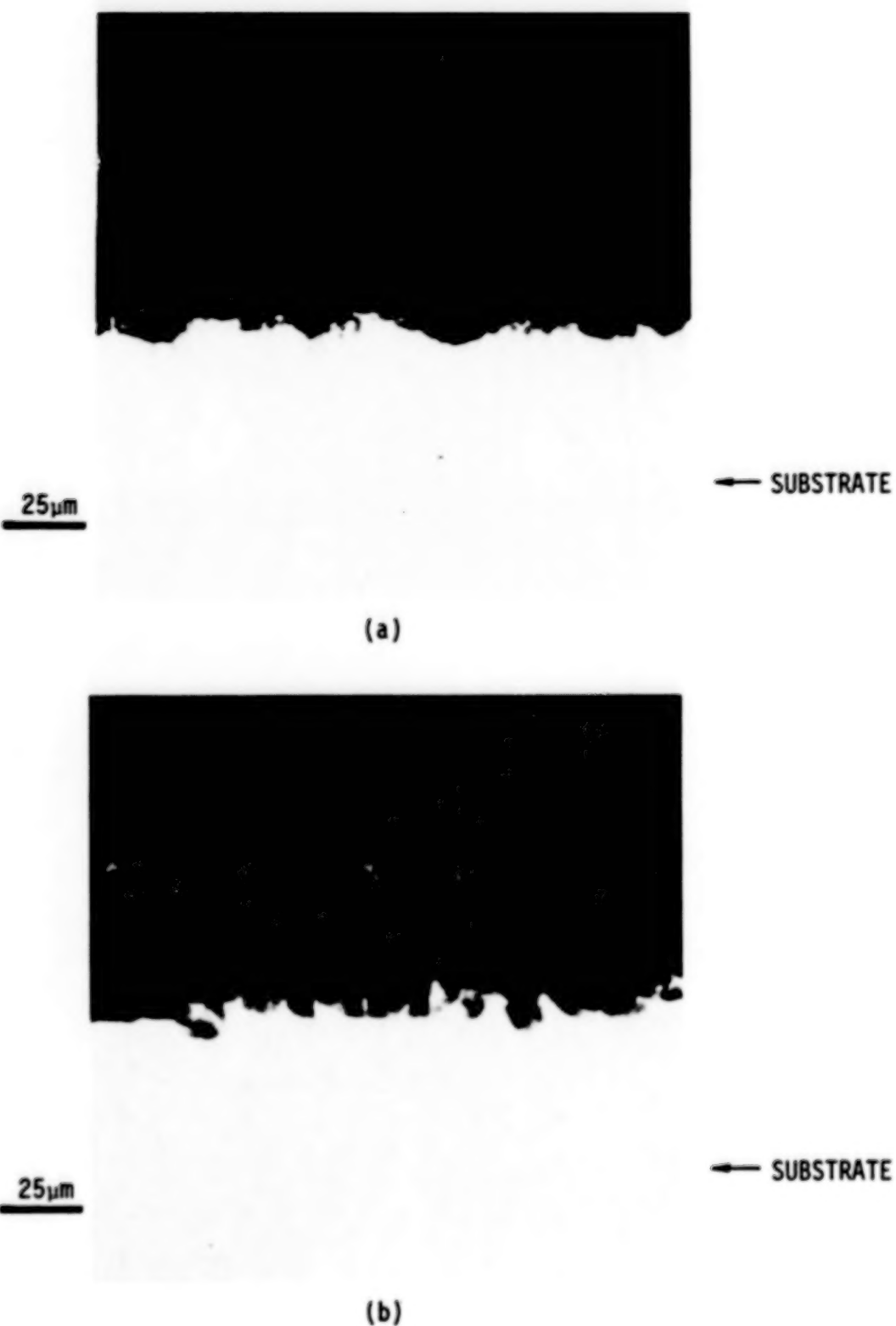


Figure 7. Surface Profiles for Pretreated Surface Specimens  
(a): 2017 Aluminum Alloy, (b): 440C Stainless Steel, (c): 304 Stainless Steel

19d



**Figure 8. Cross Sections of Pretreated Surface Specimens**  
**(a): 440C Stainless Steel (b): 304 Stainless Steel**

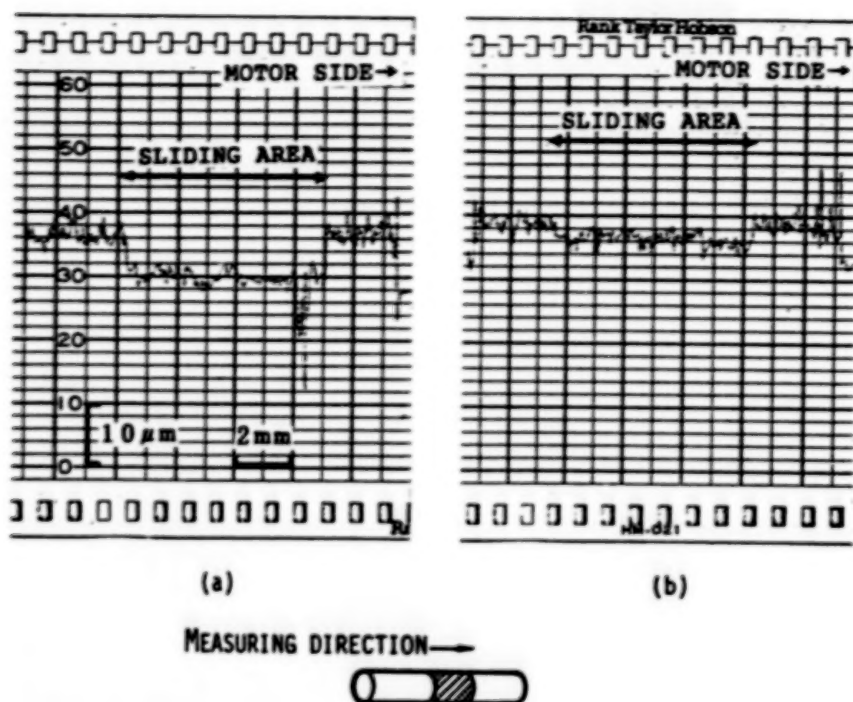


Figure 10. Surface Profiles for Worn Film on 304 Stainless Steel Shaft  
 (a): No Longer Usable (b): After  $1.27 \times 10^5$  Oscillations



Figure 11. Cross Section View, Film Coated Surface for 304 Stainless Steel Pretreated Surface Specimen. Cut at  $10^\circ$  Inclination.



Figure 12. Large Groove in Fig. 10(b)

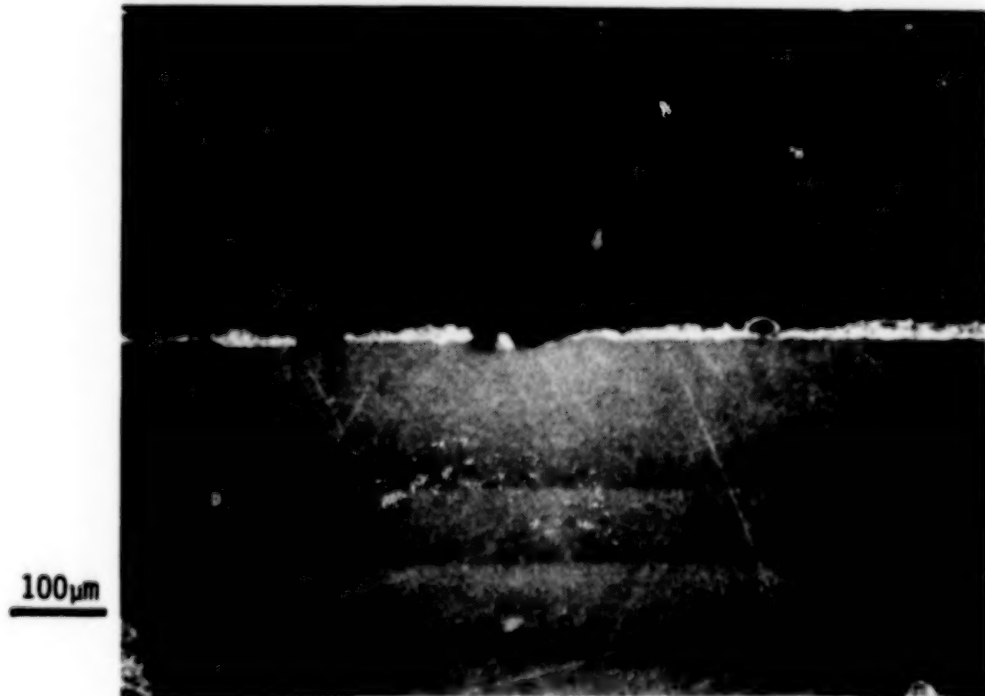


Figure 13. Cross Section of Ring Specimen

**BLANK PAGE**

# Development of Solid-Lubricated Ball-Screws for Use in Space

Masatoshi CHIBA\*, Toru GYOUGI\*, Makoto NISHIMURA\*\* and Katsumi SEKI\*\*

## Abstract

The purpose of this study is to develop ball-screws lubricated by solid lubricant films containing molybdenum disulphide. The ball-screws (shaft diameter:  $\phi 25\text{mm}$ , length:  $667\text{mm}$ ) were operated under a load of 40 to 120N at a speed of 1.5 to 200 rpm at  $10^{-6}\text{ Pa}$ . First, ball-screws made of stainless steel SUS 440C were studied using test equipment originally designed for this study. To reduce weight, the next step taken was to develop a ball-screw made of 6Al-4V-Titanium.

Long wear-life of more than  $1 \times 10^7$  revolutions was achieved with solid lubricated ball-screws made of SUS440C and 6Al-4V-Titanium in a hard vacuum. According to the surface profile of the shaft measured after  $1 \times 10^7$  revolutions, more solid lubricant remained on the surface of 6Al-4V-titanium than that of stainless-steel. Auger and EPMA analysis confirmed lubrication was maintained by solid lubricant on nuts and screws after the lubricant films on the balls were worn off.

## Introduction

Rotating parts of space mechanisms are supported by sliding and rolling bearings. Among them a ball-screw provides a unique function: changing linear motion to rotation or vice versa with high energy efficiency. The need for a ball-screw for space use has been increasing, as space structures become larger and more complicated. For instance, a deployable test bed<sup>1</sup> will be realized only when a solid-lubricated ball-screw is employed. However, the friction and wear mechanism for a ball-screw for space use, when lubricated by a solid lubricant, remains unsolved. A limited number of papers referred to this unique machine element for space use<sup>2, 3</sup>.

Tribological behavior of a ball screw is of particular interest because it operates under a rolling-sliding frictional condition which is somewhat different from rolling or sliding friction.

This paper describes research and development of ball-screws

---

\* Nissan Motor Co., Ltd., Aerospace Division  
3-5-1, Momoi, Suginami-ku, Tokyo, 167 Japan

\*\* National Aerospace Laboratory  
7-44-1, Jindaijihigashi-machi, Chofu, Tokyo, 182 Japan

lubricated by inorganic-bonded molybdenum disulphide films.

### Experimental Procedures

#### 1) Test Equipment

Fig. 1 shows the schematic diagram of the apparatus originally designed for this experiment. A shaft is set up vertically in the vacuum chamber and load is put on a nut by a dead weight. Lubrication characteristics of a ball-screw were studied by measuring frictional torque variation using strain-gages bonded on a plate spring which was set between a magnetic feedthrough and a ball-screw rotating shaft. Accordingly, the measured friction torque represents that of a ball screw and supporting bearings.

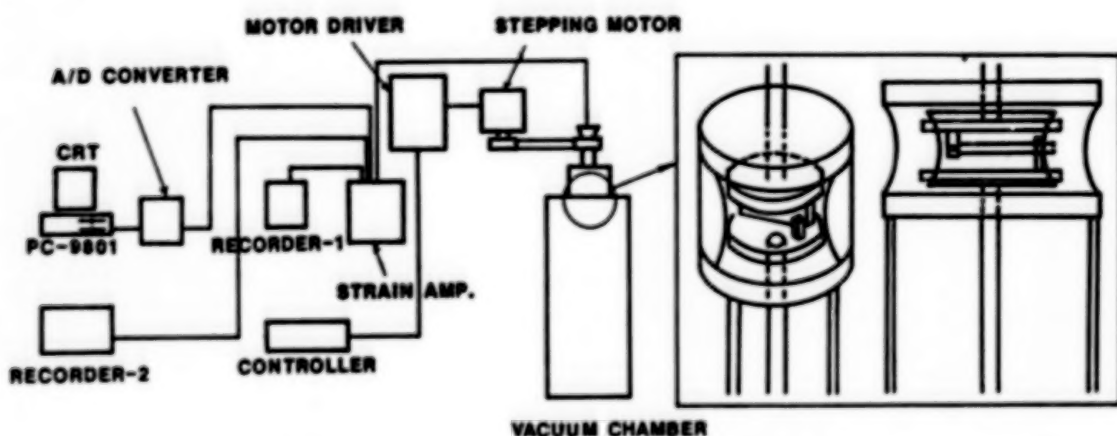


Figure 1 Schematic diagram of Apparatus

#### 2) Test Specimens

The shape and size of ball-screw specimens used in this study are presented in Table 1 and Fig. 2. A ball-screw consists of three components: a screw shaft, 25mm in diameter and 667mm length with 6mm pitch, balls, and a nut with circulation parts. We selected two materials for a shaft and a nut. One is stainless steel, the other is 6Al-4V-titanium. Balls were made of stainless steel SUS 440C (equivalent to AISI 440C) and have diameter of  $\phi$  5/32" ( $\phi$  3.969mm). All parts were coated with an inorganic-bonded molybdenum disulphide film.

Table 1 Specification of Testpiece

Shaft Diameter	$\phi$ 25
Lead	6mm
Ball Diameter	5/32"(3.969mm)
Material	Stainless Steel Ti alloy
Lubricant	MoS <sub>2</sub> , Solid Lubricant

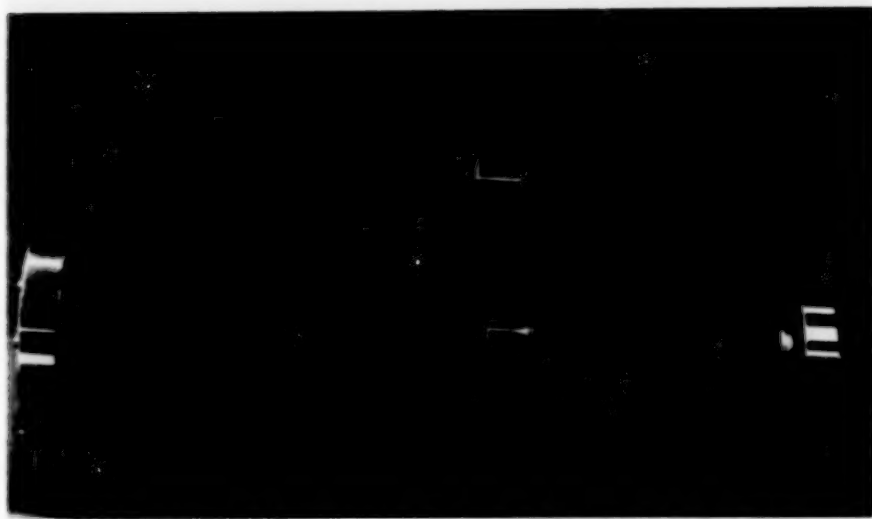


Figure 2 Ball Screw and Dead Weight

### 3) Test Condition

Test conditions are given in Table 2. Pressure in the test chamber was kept less than  $10^{-6}$  Pa during testing. Tests were carried out at room temperature under an axial load of 40(Hertzian Contact Pressure: 95.6 MPa) to 120 N(157.7 MPa). The rotational speed of a shaft was typically 200 rpm but in some cases it was varied from 1.5 to 200 rpm in order to know the effect of rotational speed. Tests were terminated either when the frictional torque exceeded 2.5 N·m, or when the total number of rotations was over  $1 \times 10^7$  revolutions.

Table 2 Test Conditions

Pressure	$10^{-6}$ Pa
Load	40N~120N
Temperature	Room Temperature
Rotational Speed	1.5~200rpm

### Results and Discussion

#### Stainless Steel Ball-Screws

Table 3 summarizes all test results obtained with stainless steel ball-screws. Three specimens used were designated as 001, 002 and 003.

Testpiece 001 was run under a load of 95.6, 109.3, 137.7, and 157.7 MPa(Hertzian contact pressure). The operating stroke of the nut was shortened whenever the load was increased. This made the comparison of shaft surfaces

under different load conditions possible. Changes of friction torque with increase of load are presented in Fig. 3. Surface roughness and surface profiles of the shaft after the test are given in Table 3 and Fig. 4, respectively.

Table 3 Test Results of 440C Ball Screws

T/P No.	Hertzian Contact Pressure (MPa)	Total Number of Spins (rev.)	Surface Roughness ( $\mu\text{m}$ )		Film Thickness ( $\mu\text{m}$ )
			R <sub>a</sub>	Pk.to Valley	
001	(a) 95.6	$6.74 \times 10^6$	1.36	10.28	1.0
	(b) 109.3	$1.34 \times 10^6$	1.40	14.51	1.0
	(c) 137.7	$0.79 \times 10^6$	2.13	17.89	1.0
	(d) 157.7	$0.70 \times 10^6$	3.37	25.76	1.0
002	157.7	$1.00 \times 10^6$	1.42	12.78	1.0
003	157.7	$1.40 \times 10^6$	0.08	1.51	3.0

Friction torque exceeded the upper limit of  $2.5 \text{ N}\cdot\text{m}$  when the specimen performed  $6.74 \times 10^6$  revolutions. The specimen was disassembled and inspected with the naked eye. No damage was found except accumulation of wear debris. Therefore, debris was taken away and the operation was restarted under a higher load of 109.3 MPa for  $1.34 \times 10^6$  revolutions. Since the friction torque remained stable, the load was increased to 137.7 MPa for  $0.79 \times 10^6$  revolutions and then to 157.7 MPa for  $0.7 \times 10^6$  revolutions when the friction torque finally reached the limit of  $2.5 \text{ N}\cdot\text{m}$ .

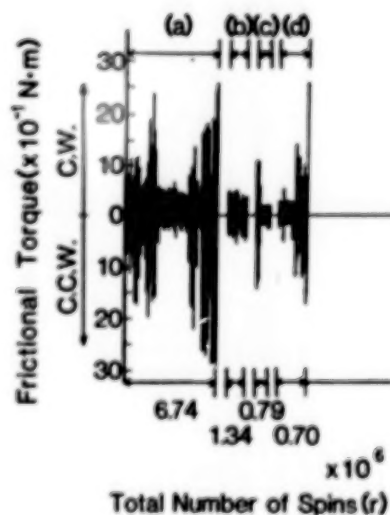
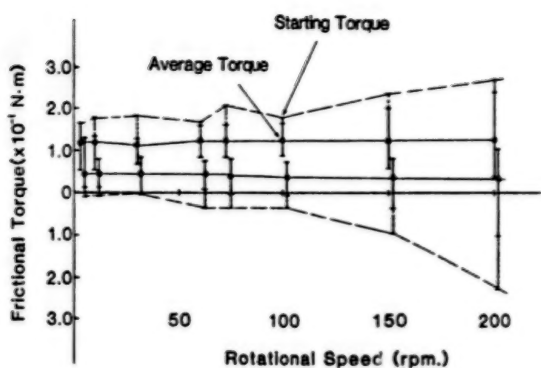


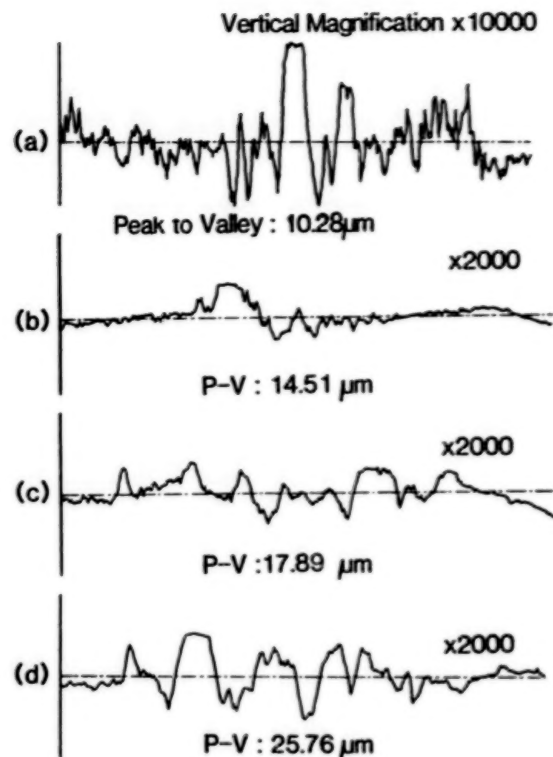
Figure 3 Variation of friction torque

Figure 5 illustrates variations of maximum and average friction torque at different speeds; these variations were measured



↑ Figure 5 Effect of rotational speed on friction torque of specimen 001

→ Figure 4 Surface profile of specimen 001



under a load of 95.6 MPa after the ball-screw was run about  $4 \times 10^6$  revolutions.

At 100 rpm, both maximum and average torque are independent of rotational speed. They increased gradually as rotational speed exceeded 100 rpm.

When the frictional torque was stable, the calculated mechanical efficiency of the ball-screw was 0.95. This efficiency is almost as high as that of a conventional grease-lubricated ball-screw.

To know the wear life under the heaviest load(157.7 MPa), the specimen 002 was operated successively until the film was worn off. Variation of friction torque is presented in Fig. 6. Friction torque exceeded 2.5 N·m at  $1 \times 10^6$  revolutions.

In general, torque behavior is divided into three stages as seen

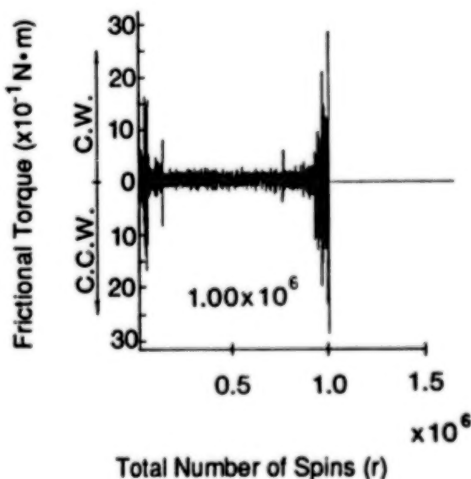


Figure 6 Variation of friction torque of specimen 002

in the Figure. The first stage represents an initial running-in process and is characterized by relatively high and unstable friction torque. In the second stage, friction torque becomes stable and good lubrication is maintained. In the third stage, friction becomes irregular.

Under a load of 157.7 MPa, the film lost lubricating ability after only  $1 \times 10^6$  revolutions. Therefore, thicker film(thickness:3  $\mu$ m) was tested with the specimen 003. To avoid blocking of operation caused by wear particles, which was observed in the specimen 001, wear particle reservoirs were prepared in the nut. The result is seen in Fig. 7. Though the test was interrupted at  $1.4 \times 10^7$  revolutions, no sign of film rupture was found.

Fig. 8 indicates surface profiles of the shaft. As shown in Fig. 9, measurements were made at four points: virgin area(point A), near end point of operating region(point B), loaded side(point C) and unloaded side(point D) of operating region. By comparing to virgin area where Ra is 0.59  $\mu$ m and P-V(peak to valley) is 4.54, we find the loaded side of operating area

Figure 7 Variation of friction torque of specimen 003

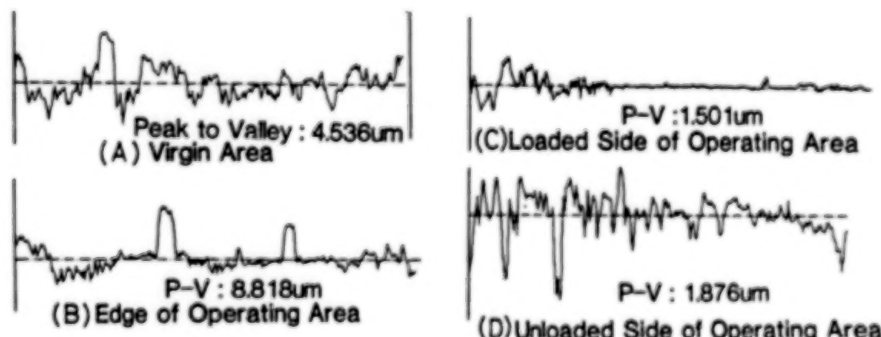
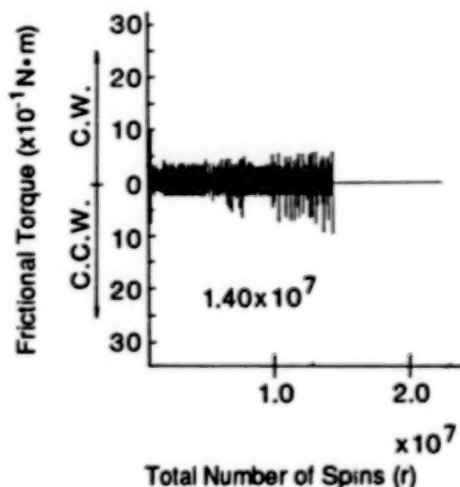
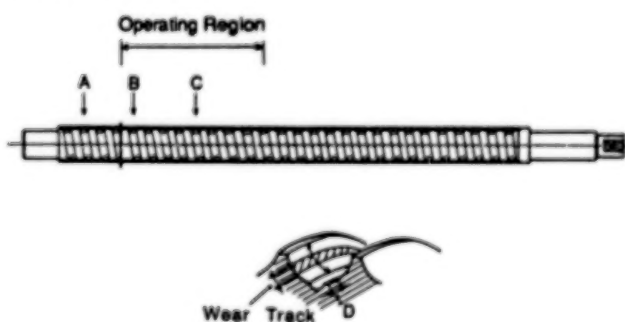


Figure 8 Surface profile of specimen 003 after test

Figure 9  
Surface profile  
test points



(point C) has the surface roughness Ra of 0.08 and P-V of 1.5. This shows the solid lubricant film is worn away almost to the substrate surface. However, EPMA analysis indicated the existence of solid lubricants.

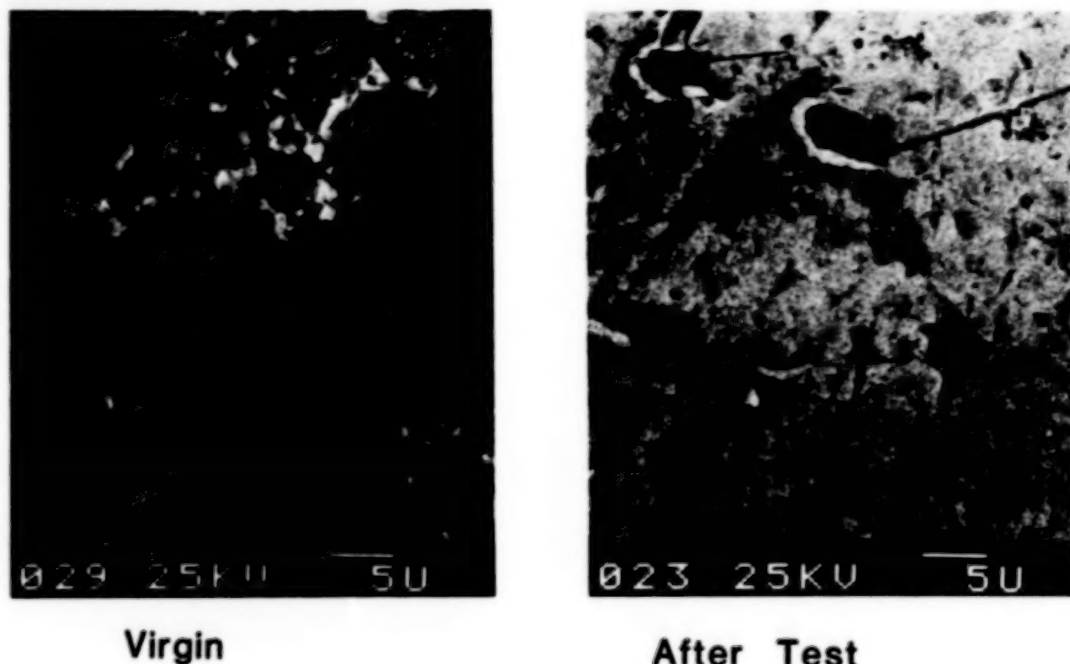


Figure 10 SEM picture of ball surface before and after test

Solid lubricants were found on loaded areas of the shaft but not on balls. Figure 10 compares a SEM picture of a virgin ball and that of a tested ball. The ball surface after test seems to have no lubricant film. This was confirmed by analysis using a Scanning Auger Microprobe Analyzer (Fig. 11 in the next page). Elements of solid lubricant films found on the ball before test (Mo, S, Ag and Sb) were lost on the tested ball. Operation of the ball-screw was not affected, as seen in Fig. 7. Thus, lubrication was maintained by films remaining on the shaft and nut after solid lubricants on balls were exhausted.

#### Ti-6Al-4V Ball-Screw

To reduce weight, a ball screw made of 6Al-4V-Ti alloy was developed. 40 % reduction in weight was achieved by changing material from stainless steel to titanium alloy.

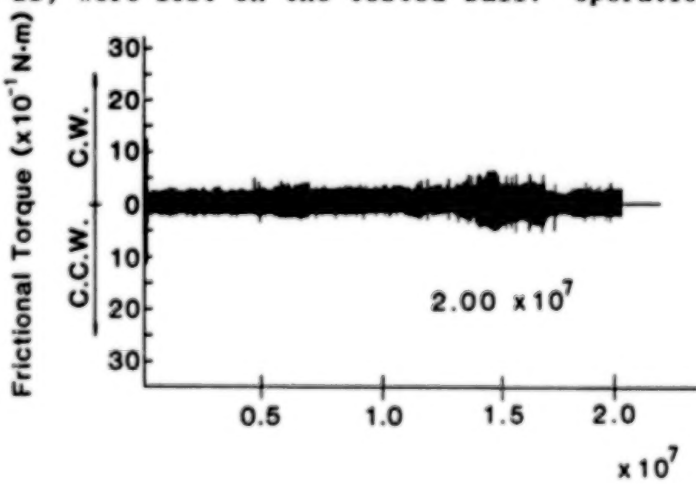
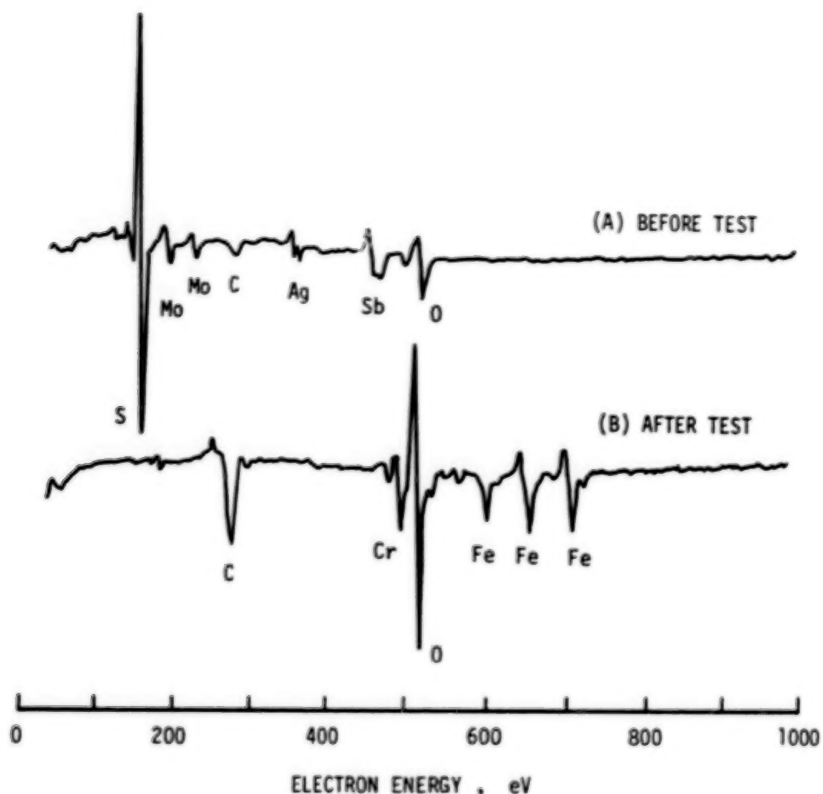


Figure 12 Variation of friction torque of 6Al-4V-Ti ball-screw

Figure 11 Auger spectrum of ball of specimen 003 before and after test



This Ti-6Al-4V ball screw was examined under the same conditions (157.7 MPa and 200 rpm) as the stainless-steel ball-screw 003. Variation of friction torque is given in Fig. 12. The specimen was successfully run to  $2.0 \times 10^7$  revolutions. It exhibited low friction and a friction pattern similar to the stainless-steel ball-screw.

Surface profiles of the shaft are shown in Fig. 13. Figure 14 presents pictures of the shaft surfaces. EPMA analysis revealed that again, no component of the film was found on the ball surface.

However, more solid lubricant seems to be left on the titanium alloy shaft than on the stainless-steel shaft. Considering the fact that the Ti shaft was operated  $6 \times 10^6$  revolutions more than the 440C shaft, we conclude that the newly-developed 6Al-4V-titanium ball-

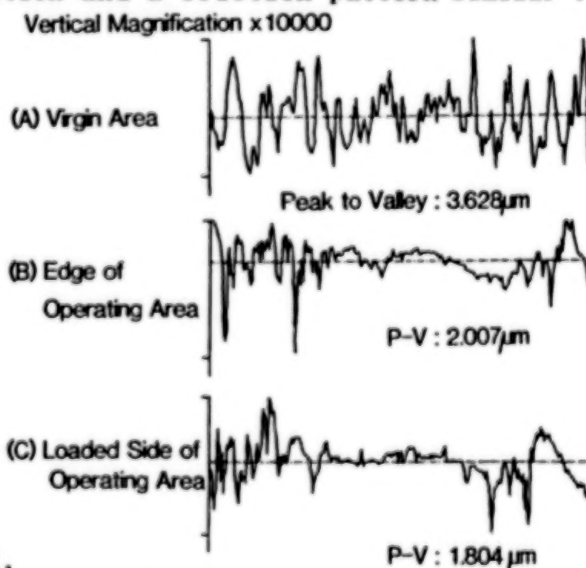
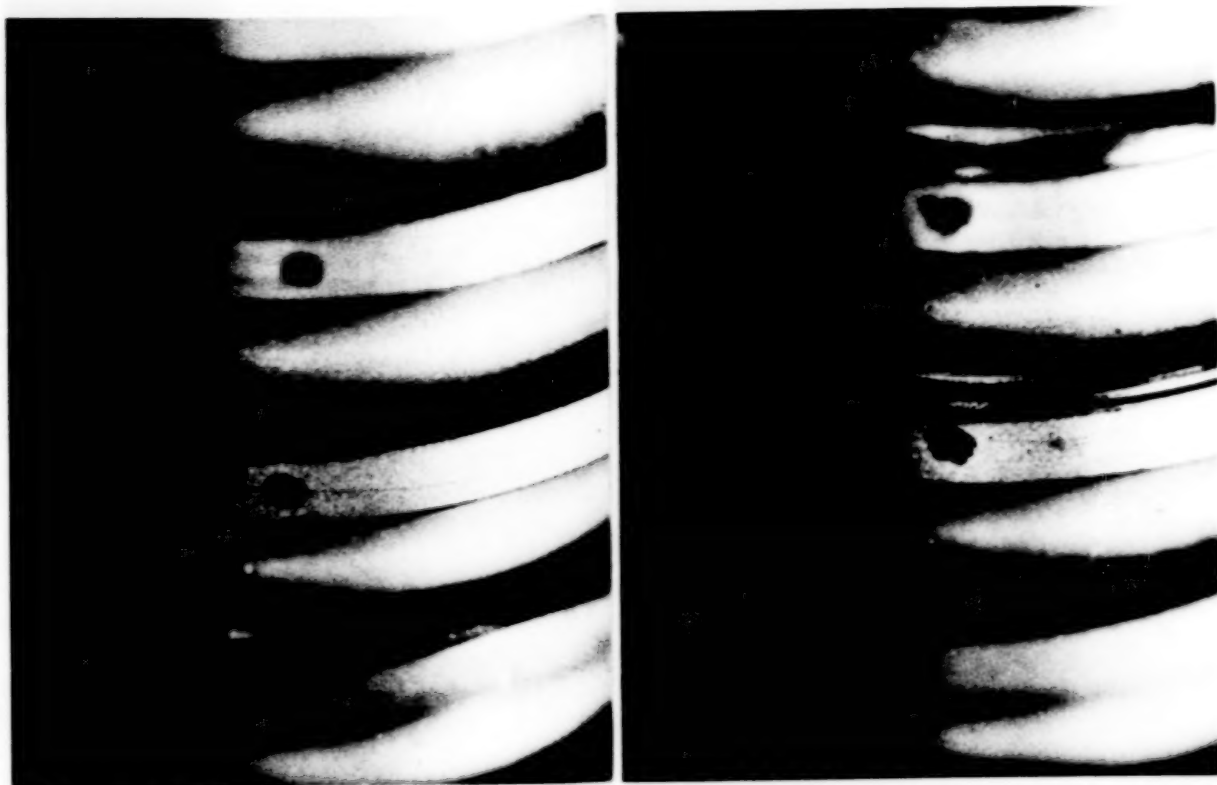


Figure 13 Surface profile of titanium alloy shaft

Figure 14 Surface of titanium shaft after test



**(A) Virgin Area**

screw possesses better performances than 440C ball-screw.

**(C) Loaded Side of  
Operating Area**

**Conclusion**

Solid lubricated ball-screws made of stainless steel and titanium alloy were tested in ultra-high vacuum and found to be applicable to space mechanisms. A 40 % reduction in weight was possible with a newly-developed 6Al-4V-Ti ball-screw compared to a stainless-steel one. The titanium alloy ball-screw demonstrated better lubricating ability than that of SUS 440C. Obtained results can be summarized as follows:

- (1) Long wear-life of more than  $1 \times 10^7$  revolutions was achieved with ball-screws lubricated by an inorganic-bonded film under a load of 157.7 MPa at 200 rpm at  $10^{-6}$  Pa.
- (2) A 6Al-4V-titanium ball-screw was developed and exhibited longer wear life than ones made of 440C.
- (3) The mechanical efficiency of the tested solid lubricated ball-screw reaches 0.95 under good lubricating conditions.

### References

- 1) Y. Fujimori, S. Kibe, et al. Deployable Truss Beam (DTB) Structural Models, Proc. 16th ISTS, pp. 431-436, ISTS, 1988
- 2) D.E. Stewart & R.H. Bentall, Procurement-Treatment and Evaluation of Recirculating Ball Screws for Use in Vacuum, ESA SP 111, pp. 267, ESA, 1975
- 3) K. Sunakoda & K. Akimoto, Development of Seismic Support Snubber Using Solid Lubricant, Proc. 1989 ASME Pressure Vessels and Piping Conference, ASME, 1989

# **TOPEX HIGH-GAIN ANTENNA SYSTEM DEPLOYMENT ACTUATOR MECHANISM**

Stephen R. Jones \*

## **ABSTRACT**

A deployment actuator mechanism has been developed to drive a two-axis gimbal assembly and a high-gain antenna to a deployed and locked position on the Jet Propulsion Laboratory Ocean Topography Experiment (TOPEX) satellite. The Deployment Actuator Mechanism requirements, design, test, and associated problems and their solutions are discussed in this paper.

## **INTRODUCTION**

A High-Gain Antenna System (HGAS) was developed, under contract to Fairchild Space Company, to provide a data link between the TOPEX satellite and the Tracking and Data Relay Satellite System (TDRSS). Figure 1 illustrates the deployed HGAS mounted on the TOPEX satellite. The major components of the HGAS include a Two-Axis Gimbal (TAG) assembly, a High-Gain Antenna (HGA), a cradle assembly, and a Deployment Actuator Mechanism with a 1.4-meter long, 0.15-meter diameter, thin-wall aluminum mast. A layout of the stowed HGAS is presented in Figure 2.

Due to constraints within the ARIANE launch vehicle shroud, the HGAS will be launched in a stowed configuration on the outside of the satellite instrument module and will deploy once the satellite is in orbit. During launch, the TAG assembly and the HGA are supported by the cradle assembly, using three pyrotechnically actuated separation bolts. Once in orbit, the separation bolts are fired, and the Deployment Actuator Mechanism drives the TAG assembly and the HGA to a fixed 90-degree position with respect to the spacecraft. As the deployment nears completion, a pair of lock pins engage to secure and align the system.

---

\* Honeywell Satellite Systems Operations, Glendale, Arizona

## **DESIGN REQUIREMENTS**

The Deployment Actuator Mechanism is required to deploy one time in orbit. Manual retraction capability is provided for ground-based testing. The system is required to utilize redundant drive motors, bearings, lock assemblies, and lock and position telemtries. The lock assembly must provide for proper alignment of the gimbals and antenna following deployment and must provide the stiffness necessary to meet the deployed first-mode frequency requirement. Full deployment must be complete in less than 1800 seconds following pyrotechnic release of antenna and gimbals from the cradle assembly. As a final requirement, the deployment actuator mechanism must be thermally isolated from the spacecraft on which it is mounted.

## **MECHANICAL DESIGN**

The Deployment Actuator Mechanism is a passive device that is driven by a pair of multileaf negator springs and is rate limited by a viscous fluid rotary damper. A pair of spring-driven, wedge-shaped lock pins align and secure the system as deployment is completed. The device utilizes a redundant bearing design featuring a lined spherical bearing and a dry lubricated journal bearing to provide two dissimilar rotating surfaces. A two-channel ganged potentiometer provides positional telemetry during deployment, while a pair of microswitches indicate lock position. The Deployment Actuator Mechanism is presented in Figure 3, and a layout of the device is shown in Figure 4. Design requirements and performance capabilities are presented in Table 1.

A passive system was traded off against an active system during the conceptual phase of the Deployment Actuator Mechanism design. Because the system is required to deploy once in orbit, and retraction capability is not required, a passive design offered advantages of less weight, higher reliability, and no power consumption. A redundant electromechanical actuator would be considerably more complex than a passive design, requiring redundant electric motors, gear trains, and clutches. Also, the drive electronics required to operate an electromechanical actuator could not be readily accommodated by the existing gimbal drive electronics boxes. Finally, initial weight estimates predicted that an active system would weigh approximately 65 percent more than a passive system.

A number of spring configurations were studied as a means of storing the energy required for deployment, including helical extension springs, helical torsion springs, and constant torque multileaf negator springs. In terms of package size and weight, the multileaf negator spring was the most attractive option. Additionally, this design has flight history in deployment applications, originating as a clock spring design on the Mariner Mars Spacecraft in 1971 and later modified to the present multileaf configuration for use on the Viking spacecraft in 1975 (Ref. 1). The spring layout is presented in Figure 5. The Deployment Mechanism utilizes a pair of 3.6-newton-meter six-leaf springs, each capable of deploying the system.

Crushable honeycomb, a viscous fluid rotary damper, and an eddy current damper were investigated as a means of controlling the rate of deployment and minimizing impact loads during lock-pin engagement. Crushable honeycomb was eliminated from consideration due to concerns regarding torque margin, repeatability, and ease of test. The eddy current rotary damper was given serious study; however, due to its complexity and lack of flight history, it was eliminated from consideration. A viscous fluid rotary damper was selected based on prior flight history, reliability, and cost.

The selected viscous fluid rotary damper is a small, light, limited-rotation device that produces approximately 452-newton-meter/(radian/second) damping at room temperature. Similar devices have flight history on commercial satellites as well as the Goddard COBE satellite. Damping is produced through viscous shear of 30,000-centistoke McGahn Nusil CV7300 silicon fluid between a rotating vane shaft and a stationary housing. A bypass valve provides adjustability of the damping rate by allowing fluid to be pumped from the high-pressure side of the vane shaft to the low-pressure side. The damper uses a reservoir with a flexible diaphragm to compensate for fluid volume changes with temperature. The reservoir interfaces with the damping chamber through a set of check ball valves that isolate the high-pressure side of the vane shaft from the reservoir during damper operation. A cross section is shown in Figure 6.

The bearing design must be capable of carrying launch and thermal-induced loads and must provide for a single, limited-rotation, low-speed deployment once in orbit. A number of redundant bearing configurations were considered, including a three-ring bearing design, a tapered roller bearing with a journal bearing interface, and a spherical

bearing with a journal bearing interface. A spherical bearing with a Teflon®-impregnated Nomex liner in conjunction with a dry lubricated journal bearing at the shaft-to-inner-race interface proved adequate, given the requirements. A layout of this configuration is presented in Figure 7. The spherical bearings are manufactured to MIL-B-81820 and feature a low no-load breakaway torque, a low coefficient of friction, tight radial clearance, and a high static load carrying capability. The dry lubricant meets the requirements of MIL-L-81329 and consists of molybdenum disulfide and graphite in a sodium silicate bonding agent.

The lock assembly must align and lock the Deployment Actuator Mechanism into the deployed position. The lock assembly consists of a pair of wedge-shaped, spring-loaded pins, which preload adjustment screws against a hard stop, as shown in Figure 8. The adjustment screws allow for precise alignment of the deployed system, and the preload provided by the wedge-shaped pins results in zero backlash, allowing the system to meet the deployed first-mode requirements. A tool allows the pins to be retracted for restowing during test.

The thermal design was approached from a number of directions. The thermal isolation requirement was met by installing NEMA FR4 epoxy laminate thermal isolating pads on each side of titanium mounting bolts at the spacecraft interface. The damper utilizes a heated cover and is thermally isolated from the surrounding structure to ensure that it is maintained above its minimum operating temperature. Additional thermal control measures consist of gold plating and thermal blankets.

Positional telemetry is provided during deployment by a redundant, single-shaft, wire-wound potentiometer that interfaces with the Deployment Actuator Mechanism shaft. A pair of microswitches indicate when the system is fully deployed and lock pins are engaged.

## **TEST**

An engineering Deployment Actuator Mechanism was assembled for development testing, including characterization of spring and damper operation, drag torque measurements, alignment repeatability measurements, three-axis vibration, and hot and cold thermal-vacuum deployments. The engineering Deployment Actuator Mechanism was

then integrated with other engineering components for system-level development testing, including three-axis vibration, stowed, and deployed first-mode frequency measurements and deployment testing in which thermal-induced loads were simulated and pyrotechnic separation bolts were fired.

Assembly of the flight Deployment Actuator Mechanism began with characterization of spring and damper operation. The springs and damper were tested using a fixture that utilizes a pulley and weights to produce an input torque. Leaf spring torque was found to be within 3 percent of the 3.6-newton-meter analytical prediction. The damper was found to produce damping rates of 1356 and 169 newton-meters/(radian/second) at temperatures of -20 and 75 degrees C, respectively. Damping was found to vary with input torque; however, because the spring torque is constant, this is not a concern in this application.

Room-temperature drag torque measurements were made without the damper and springs installed. Representative cables were installed across the joint to simulate the resistance torque that the TAG, coaxial, and pyrotechnic cables would produce. Although the dry lubricated journal bearings and the Teflon-lined spherical bearings each resulted in an average drag torque of 0.7 newton-meter, the journal bearings proved to be the primary rotating surface. With 7.0 newton-meters of available spring torque, the torque margin is 10.0. Based on engineering test data, the drag torque can be expected to increase by approximately 0.2 newton-meter at -20 degrees C, resulting in a torque margin of 7.8. The Deployment Actuator Mechanism drag torque was considerably less than the 1.7 newton-meters originally budgeted, resulting in a torque margin greater than the design requirement of 4.0.

Although alignment measurements were not made with the flight hardware, alignment repeatability measurements were made on the engineering hardware by using optical cubes and a theodolite. In five consecutive deployment tests, alignment was found to be repeatable to 0.02 degree, considerably better than the 0.05-degree requirement.

The Deployment Actuator Mechanism was subjected to 9.8g's rms random vibration as a workmanship test. Random vibration of the flight hardware was trouble free.

Deployment time was measured as a function of temperature in a thermal-vacuum chamber. The mechanism was deployed horizontally to minimize gravity effects. A short length of mast replaced the 1.4-meter flight mast. It was not necessary to simulate the inertia of the rotating load because the relatively high damping rate of the system in relation to the rotational inertia makes the rate of deployment essentially independent of inertia.

The time required for deployment varied between 45 seconds at 58 degrees C and 238 seconds at -8 degrees C. Room-temperature deployment time was approximately 85 seconds. The cold-temperature deployment time fell easily within the 1800-second requirement. Based on acceptable impact loads, the minimum acceptable deployment time is 45 seconds. Although the hot deployment did not violate the 45-second minimum deployment time, it did deploy somewhat faster than expected, due primarily to the low drag torque of the flight deployment actuator.

### **PROBLEMS RESOLVED**

Post vibration inspection of the engineering Deployment Actuator Mechanism revealed that the dry lubricant in the journal bearing was flaking, resulting in a measurable increase in drag torque. A number of possible causes were investigated including improper application and moisture contamination. Although the sodium silicate bonding agent used in the dry lubricant is impervious to many solvents, it can be dissolved by moisture. Improper application could include surface contamination, inadequate curing, or excess thickness. After considerable testing, the problem was found to be excessive lubricant thickness. The solution involved applying the lubricant to a single bearing surface, rather than both bearing surfaces, and burnishing the lubricant to reduce thickness. This solution resolved the problem and resulted in decreased drag torque during normal operation.

It was during thermal-vacuum testing of the flight hardware that the most serious problems arose. These problems involved the potentiometer and viscous damper.

During thermal-vacuum deployment testing, noise appeared on one channel of the redundant potentiometer. A failure analysis investigation revealed contamination on the windings. A review of the materials and processes used in the manufacture of the part showed

that the contamination is not an inherent problem and is probably an isolated incident. Five qualification parts are being tested for signs of contamination. In addition, the spare flight part is being screened to establish flight worthiness.

The most serious problem is related to thermal-vacuum operation of the viscous fluid rotary damper and is characterized by a region of undamped travel immediately after deployment has been initiated, followed by normal operation throughout the remainder of the travel. The phenomenon is random in nature and has occurred at hot and cold temperatures. The maximum undamped travel was 15 degrees, resulting in unacceptably high impact loads in the damper input shaft as damper operation returned to normal. Because a potentiometer was not installed to provide positional telemetry during engineering model thermal-vacuum testing, the problem did not become apparent until acceptance testing of the flight unit.

A review of the fill procedure revealed inadequacies that could result in air or a void within the damper. Although air was found in an engineering damper, there was no sign of air in the flight damper. A void could not be ruled out, however, so the damper was emptied and refilled using a fill fixture in which the device was evacuated and then filled with degassed fluid under pressure.

A second area of concern was the method used to compensate for changes in the damping fluid volume over temperature. The damper uses a reservoir with a flexible diaphragm to compensate for fluid volume changes. The reservoir interfaces with the damping chamber through a set of check ball valves that isolate the high-pressure side of the vane shaft from the reservoir during damper operation. In previous space applications, the external side of the diaphragm was pressurized at 1 atmosphere with a sealed cover on the rear of the damper. Positive pressure on the diaphragm appears to be critical to the operation of the device. Due to concerns that pressurization of the damper would increase the likelihood of a fluid leak developing at the shaft seal, the damper used on the Deployment Actuator Mechanism had a vented cover. The vented cover was eliminated in favor of a sealed cover.

Subsequent testing has shown that the anomaly still exists. Thermal-vacuum test results are presented in Table 2. The average

free travel was 3.8 degrees with a maximum of 10.1 degrees and a minimum of 1.8 degrees.

Because operation of the damper is not well understood, and a solution to the problem is not forthcoming, design changes are being implemented to replace the original damper with a customer-furnished damper. The customer-furnished damper was developed for use on the TOPEX solar array drive mechanism and has successfully completed extensive qualification and acceptance testing. Operation of the customer-furnished damper is similar to operation of the original damper. Additional testing following integration of the customer-furnished damper is expected to show that the Deployment Actuator Mechanism meets or exceeds all design requirements, with performance similar to that shown in Table 1.

### **CONCLUSION**

A Deployment Actuator Mechanism has been developed and is presently undergoing flight acceptance testing. The most challenging problem encountered during the development and test of the Deployment Actuator Mechanism was a viscous rotary damper anomaly. Although virtually identical dampers have flight heritage, the device proved unsuitable in this application, and design changes are being implemented to replace the device with a customer-furnished damper. With the exception of the damper anomaly, development has been essentially trouble free. The Deployment Actuator Mechanism is expected to meet or exceed all design requirements following integration of the customer-furnished damper. Although developed specifically for the TOPEX satellite, the Deployment Actuator Mechanism is a versatile design and may be adapted to a variety of other deployment applications.

### **REFERENCE**

- (1) "Viscous Rotary Vane Actuator/Damper," Jack D. Harper, 10th Aerospace Mechanisms Symposium, April 22-23, JPL Technical Memorandum 33-777, pp. 198-207.

**TABLE 1. REQUIREMENTS AND CAPABILITIES**

Parameter	Requirement	Capability
Mass (kg)	<18.1	12.6
Footprint (m x m)	0.40 x 0.29	0.40 x 0.29
Operating Temp (°C)		
Maximum	38.0	58.0
Minimum	11.5	-8.5
Non-operating Temp (°C)		
Maximum	63.0	83.0
Minimum	-7.5	-27.5
Deployment Time (s)		
58°C	=>45	45
-8.5°C	<1800	300
Spring Torque (N-m)	6.8	7.0
Drag Torque (N-m)	<1.7	0.9
Torque Margin	>4.0	7.8
Damping Rate (N-m/rad/s)		
58°C	>147	169 @ 75°C
-8.5°C	<4859	1356 @ -20°C
Alignment (deg)		
Initial	0.05	0.05
Repeatability	0.05	0.02
Deployed Stiffness (Hz)	>5.0	7.2

**TABLE 2. THERMAL-VACUUM DEPLOYMENT TEST RESULTS**

Test	Temperature (°C)	Deployment Time (s)	Average Damping (N-m/rad/s)	Undamped Travel (deg)
1	29.8	87	376	1.9
2	-8.8	220	943	2.2
3	-7.5	218	956	4.2
4	59.0	45	210	6.4
5	-6.8	214	917	1.9
6	-8.4	238	1022	1.8
7	58.3	48	1965	3.9
8	22.4	108	4166	2.1
9	58.5	46	1997	10.1

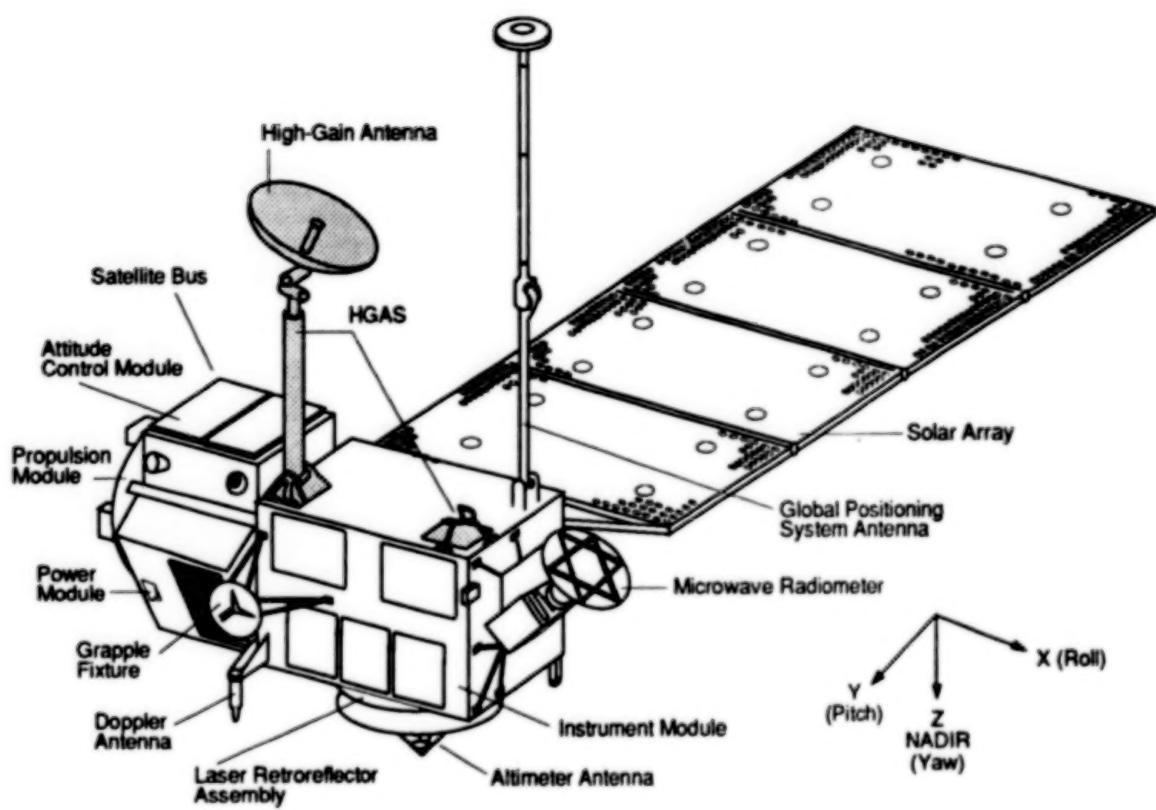


Figure 1. TOPEX Spacecraft/HGAS

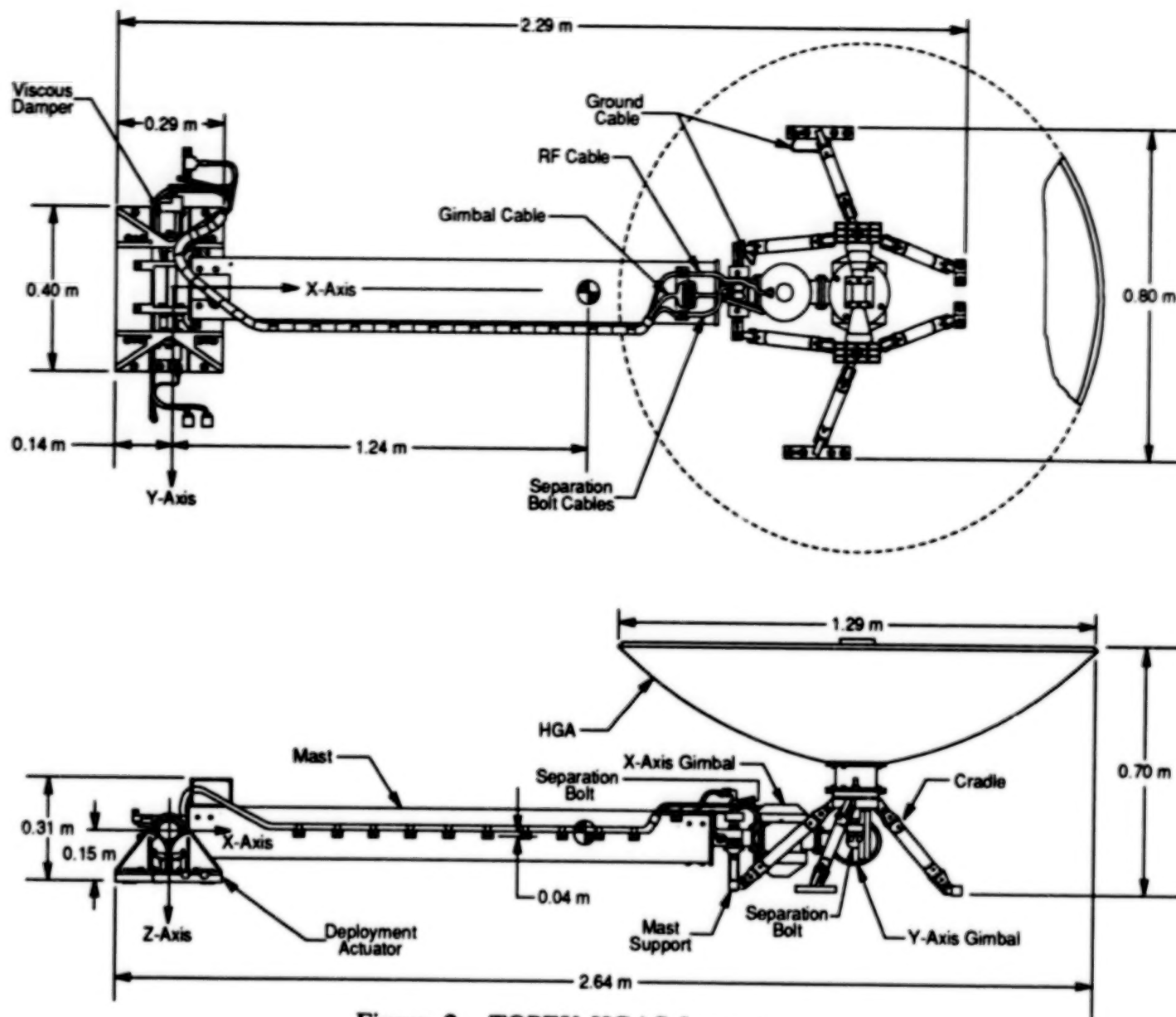
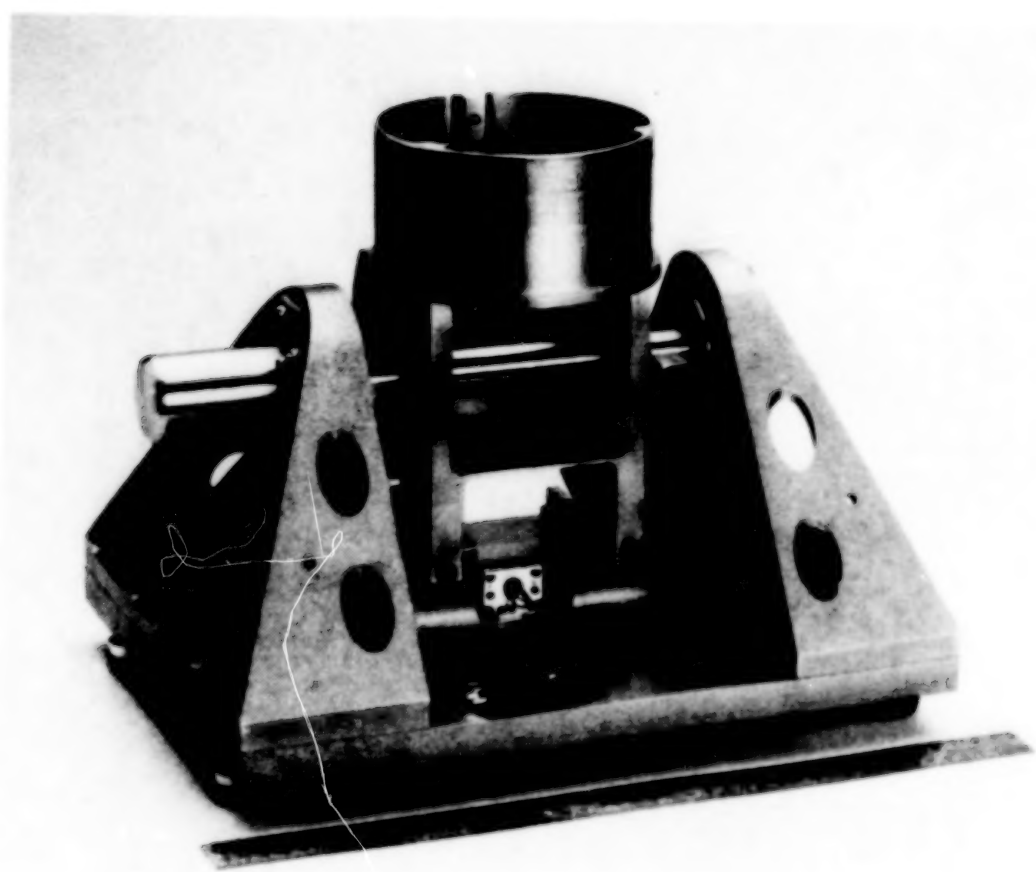


Figure 2. TOPEX HGAS Layout



**Figure 3. Deployment Actuator, Deployed Position**

**BLANK**

**PAGE**

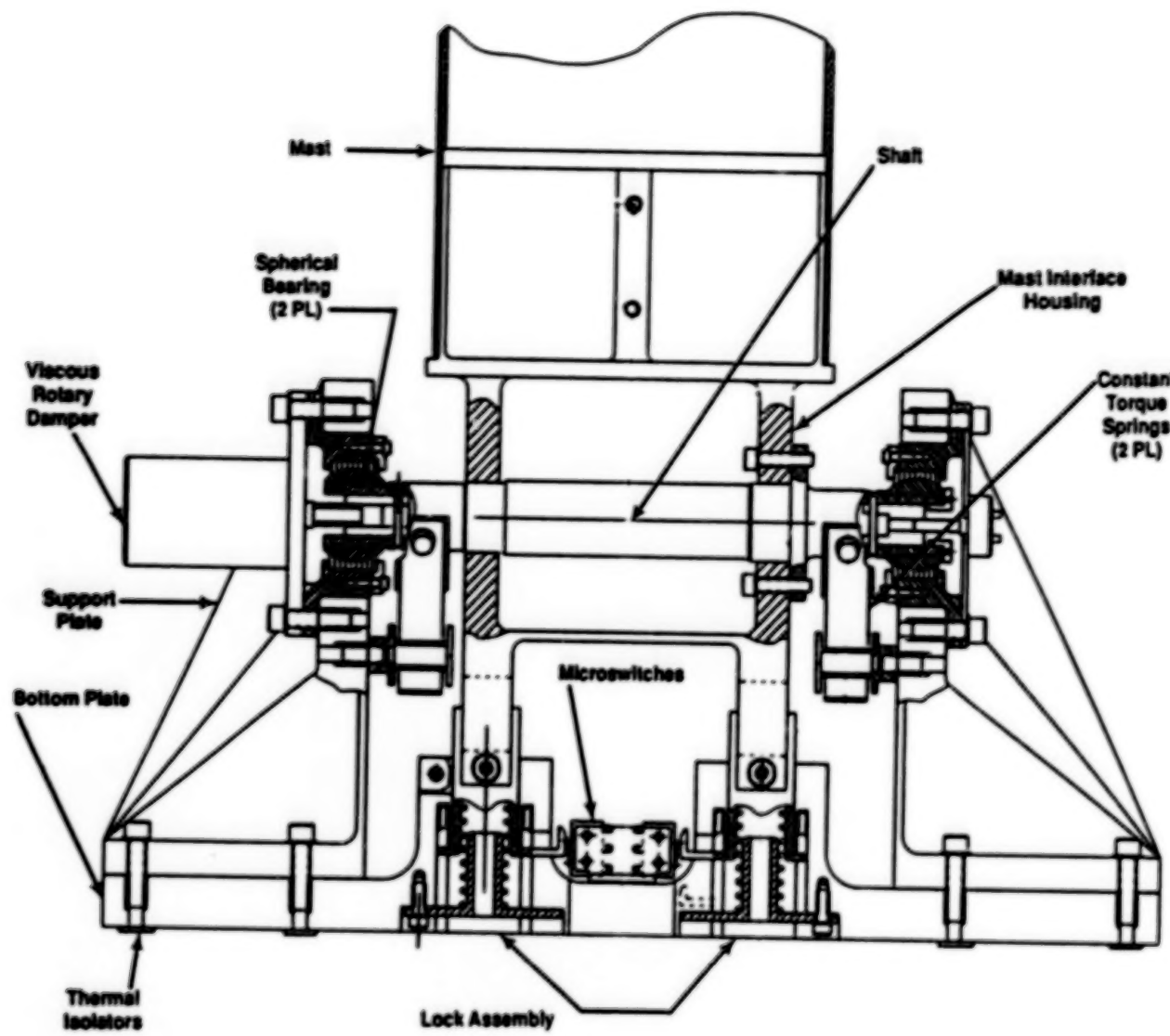


Figure 4. Deployment Actuator Layout

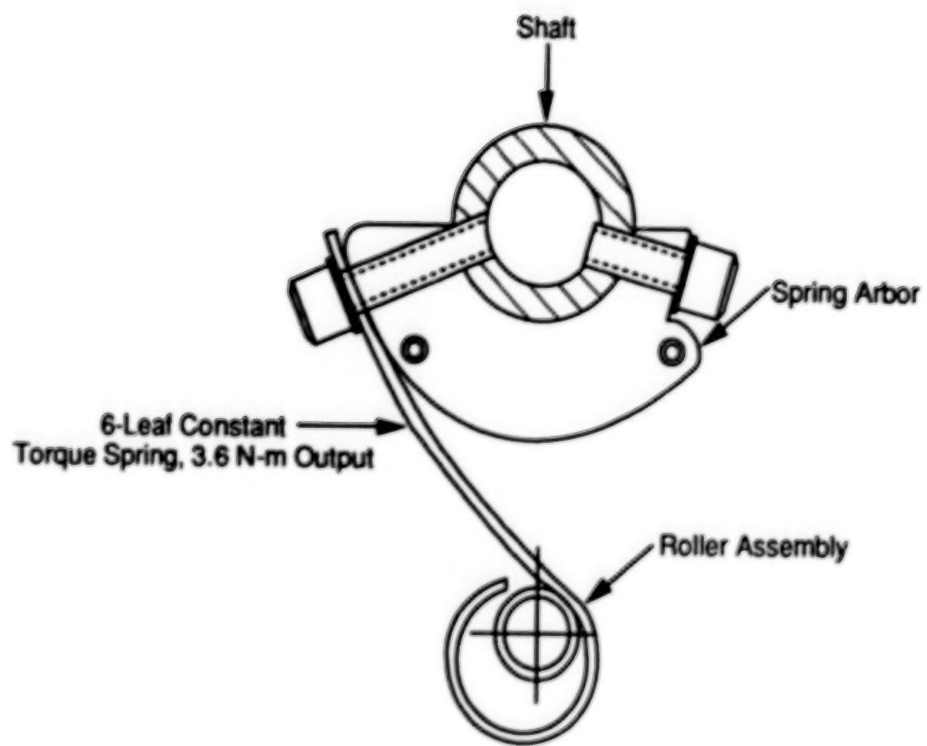


Figure 5. Constant Torque Spring Detail, Deployed Position

**BLANK**

**PAGE**

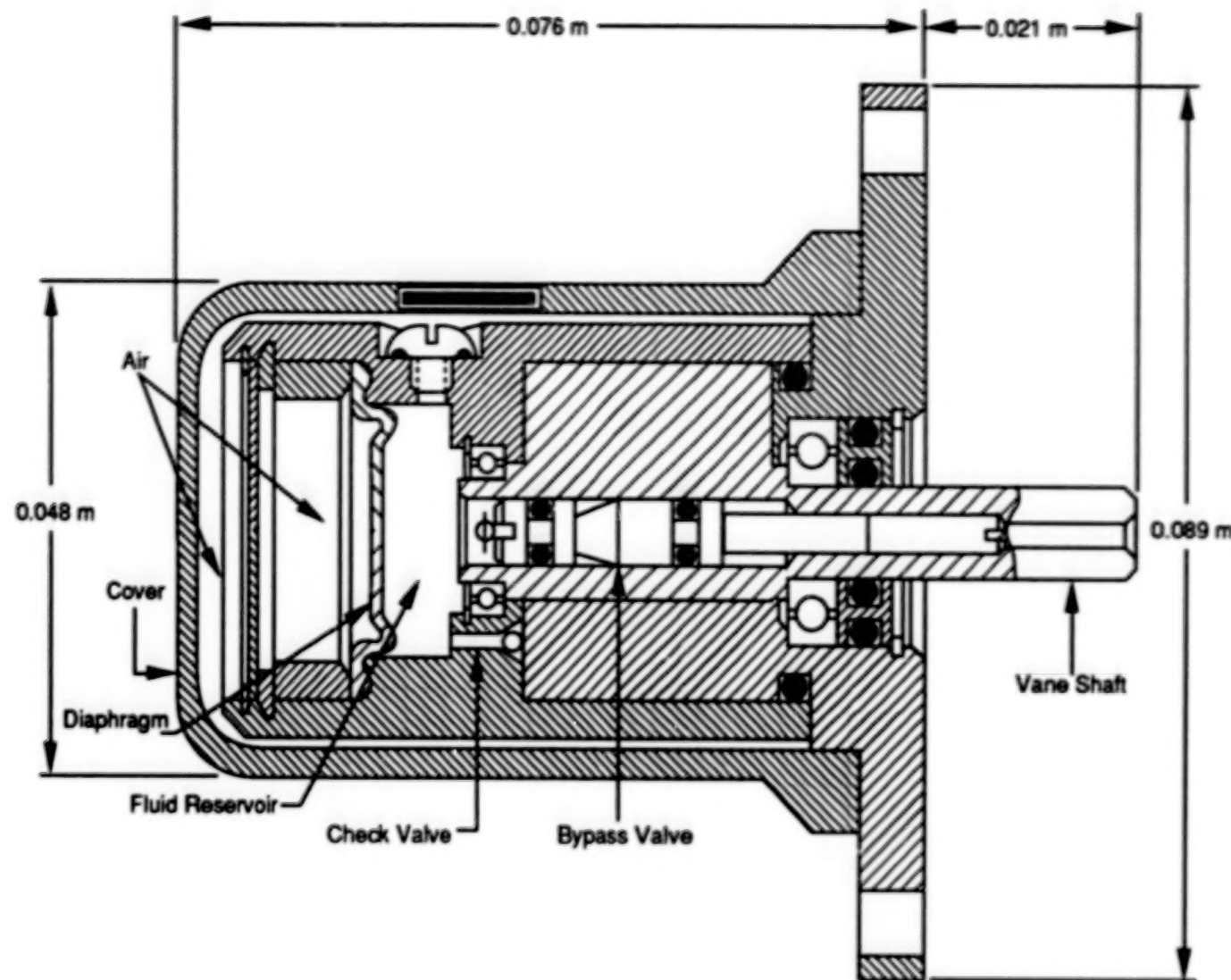


Figure 6. Rotary Damper Cross Section

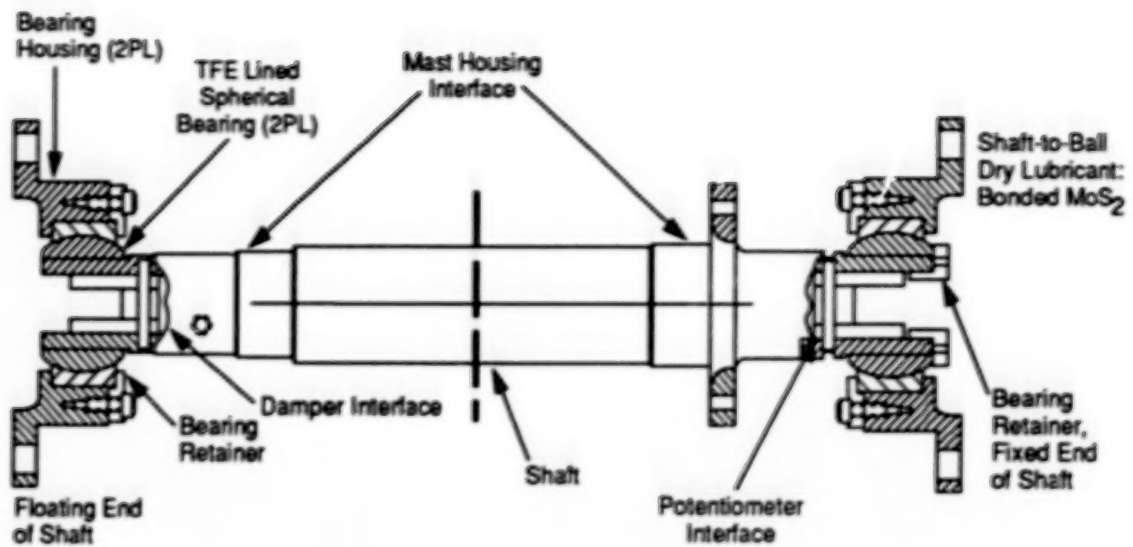


Figure 7. Bearing Detail

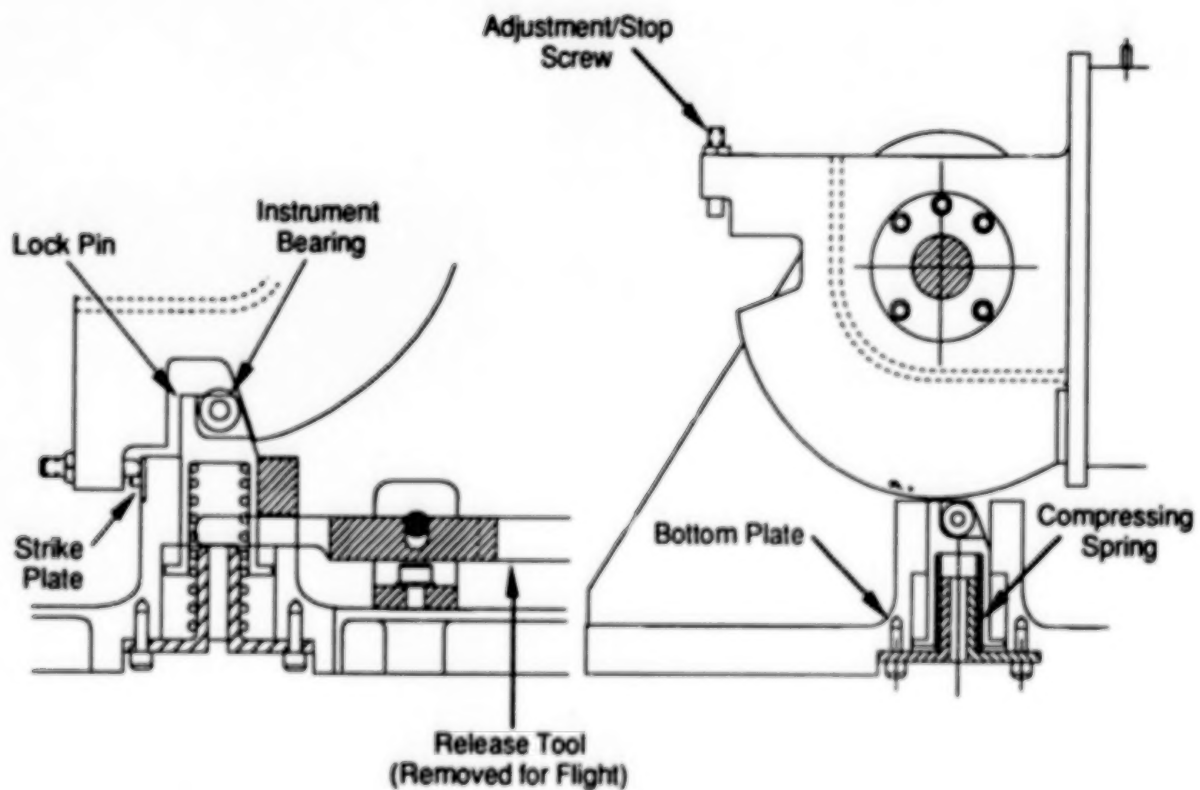


Figure 8. Lock Assembly Detail

## **RESETTABLE BINARY LATCH MECHANISM FOR USE WITH PARAFFIN LINEAR MOTORS**

Daryl Maus\* and Scott Tibbitts\*

### **ABSTRACT**

A new resettable Binary Latch Mechanism has been developed utilizing a paraffin actuator as the motor. This linear actuator alternately latches between extended and retracted positions, maintaining either position with zero power consumption. The design evolution and kinematics of the latch mechanism are presented, as well as development problems and lessons that were learned.

### **BACKGROUND**

The increasing use of resettable paraffin linear actuators on spacecraft as operators of covers, apertures, caging and other mechanisms has created a need for latches designed to utilize the unique characteristics of paraffin actuators. Of particular interest is a latch which can utilize the multiple-operation capability of the actuator and which allows the output from a single actuator to alternately latch between extended and retracted positions while maintaining either position with zero power consumption.

For mechanisms with multiple in-flight operation requirements, this would offer advantages in weight and size over the electric motor and gear drive systems currently used. For single release applications, such as caging devices, the resettability of the latch during preflight testing would offer advantages over pyrotechnic devices that require replacement, discharge material and deliver considerable shock to instruments.

This type of mechanism was developed as the aperture driver on the ISTP/Geotail Comprehensive Plasma Instrument, built by the University of Iowa. Their requirements for multiple operation, weight, force, stroke and power consumption fit the performance of the SRC IH-5055 actuator but included zero power latching in the extended position. The available physical envelope for a latching mechanism was small: about 2.3x4.2x3.2 cm (.90"x1.65"x1.25"), including a limit switch.

Marshall Space Flight Center concurrently had a similar requirement for the VIS instrument on the ISTP/Polar spacecraft. Their requirement allowed more space for the mechanism but included 2 limit switches. The mechanism described in this paper was developed for these and subsequent similar requirements.

---

\*Starsys Research Corporation, Boulder, Colorado

## LATCH REQUIREMENTS

The mission applications generated the following specific requirements:

- 1) Limit mass to a maximum of 95 grams with one switch, 120 grams with two switches.
- 2) Limit the single-switch latch dimensions to 2.3x4.2x3.2 cm (.90"x1.65"x1.25").
- 3) Provide dynamic load-moving capability of 23 kg (50 lbf).
- 4) Provide static or latched load-holding capability of 23 kg (50 lbf).
- 5) Operate with an overtravel of less than .19 cm (.075") (overtravel is the amount of additional stroke required to affect the change of latch state).
- 6) Provide a stroke between latched positions of at least 1.2 cm (.45").
- 7) Have a lifetime of more than 2,500 extended/retracted cycles.
- 8) Sustain launch vibrations of 20G in any direction.

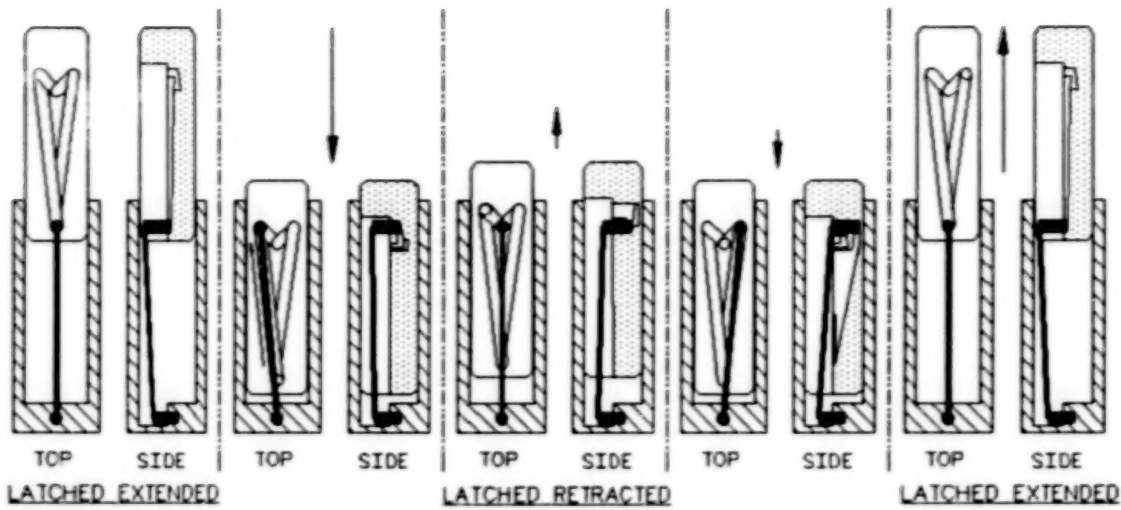
## DESIGN APPROACH

Binary mechanisms are devices that allow an output to latch alternately between two mechanical states, extended and retracted, when repeatedly actuated with the same input. An example in everyday life of such a mechanism is the ball-point pen. Repeated actuations cause the pen point to alternate between extended and retracted positions.

SRC research was unable to identify precedents for the use of binary mechanisms on spacecraft. To establish the state-of-the art in binary mechanisms, an extensive evaluation of commercial latches (including ball-point pen mechanisms) was performed.

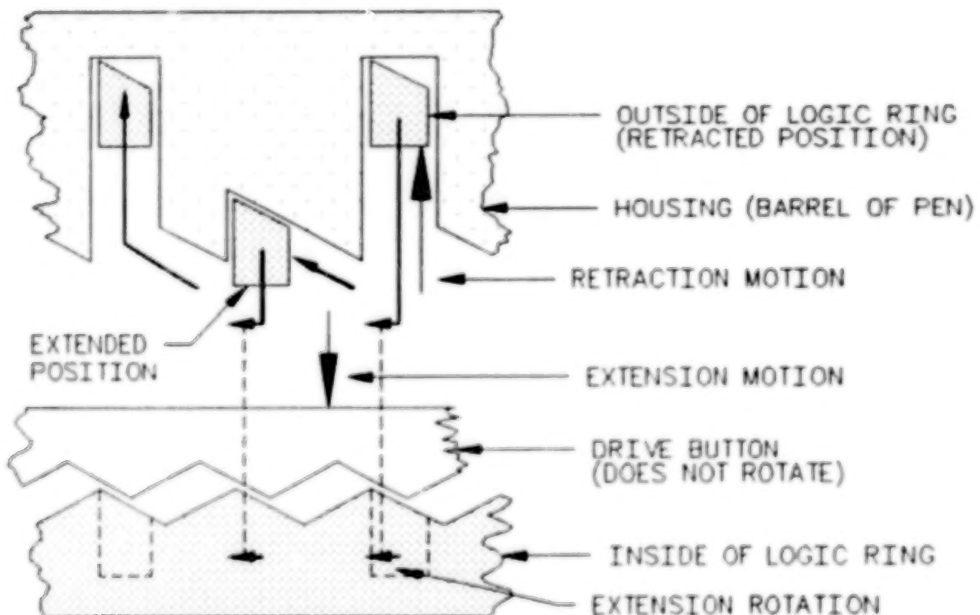
This evaluation included database and literature searches as well as a patent search and review. Commercial latches were acquired, disassembled, inspected, and analyzed.

The following diagrams of several common binary latch mechanisms illustrate their operation:



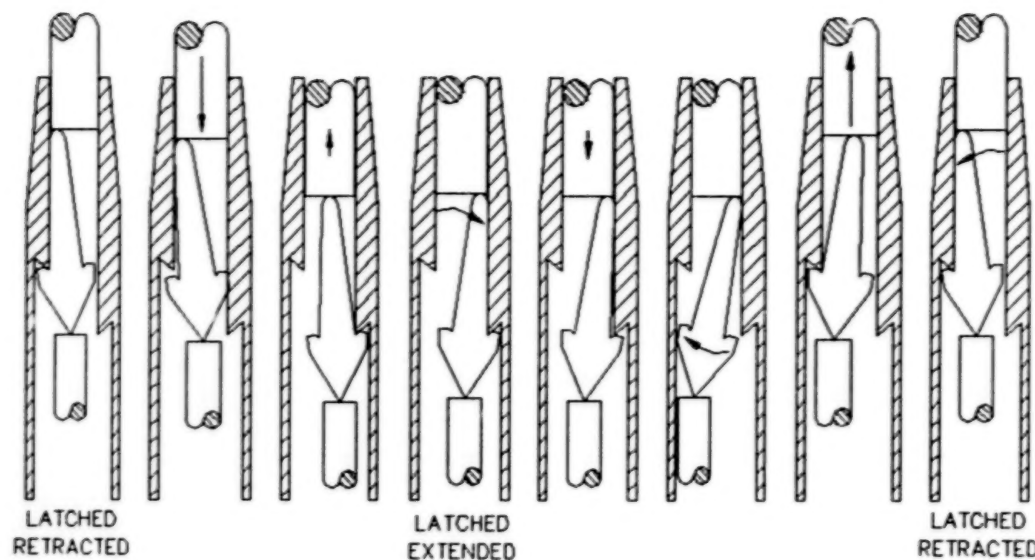
### Pin in track

The logic element, in this case a spring-loaded pin, is guided through a track that moves with the output shaft. Steps in the z-axis in the track create a non-reversible motion of the pin. The pin is moved alternately between the extended and retracted positions by the extension and retraction of the input. The size of the pin determines the load-carrying capability and the overtravel.



### Typical ball-point pen

The logic element, in this case a ring with ramps that interface with the drive button and the pen housing, is guided in a rotating pattern. The "out of phase" interaction of the ramps translates some of the axial movement of the drive button into rotation of the logic ring. The logic ring latches in extended and retracted positions in the housing. Contact surfaces are small and overtravel is large.



### Flipper ball-point pen

The output load is carried through the logic element, a flipper. The action of this load creates lateral forces that cause the flipper to flip or rotate about pivot points that engage features in the housing. The flipper thus moves through a non-reversible pattern of positions in response to the reciprocating input. The extended and retracted position latching is accomplished by engaging the flipper in the housing, thereby blocking the motion of the output shaft. Overtravel is very high and contact area small.

The following generalizations were made for the theory of operation underlying these binary mechanisms:

- 1) One part can always be identified as the logic element. When a reciprocating input is provided, the other components direct the motion of this element through a non-reversible pattern or series of positions.
- 2) The logic element locks up or latches the output in the extended and retracted positions.
- 3) The non-reversible pattern of movement of the logic element by the latch components translates the single input into two opposite movements, retraction and extension, and two latched positions - extended and retracted.
- 4) The latch component motion can usually be described as a 2-axis motion (x-y). Motion and force along another axis create non-reversibility.

It was determined that the existing latches reviewed were not suited for application to spacecraft mechanisms in general or the latch requirements in particular. Problems included:

- 1) None of the latches reviewed was designed to transmit high loads. They all carried the load through the latch components and many carried the load through the logic element. It was concluded that sizing the latch components to carry high loads would produce a bulky mechanism. In addition, high loading of the surfaces of the moving logic element would produce high wear and friction. Using self-lubricating polymeric materials for the latch components would further exacerbate the problem because of their lower compressive strengths and therefore larger size requirement.
- 2) Typical overtravel was high, usually greater than .4 cm (.15"). The overtravel was typically a function of latch component size and therefore would only become greater if the latch components were enlarged to handle high loads.

Evaluation of a prototype of a conventional ball-point pen mechanism modified to carry high loads and fabricated of metal components confirmed the preliminary assessments. High loading on the logic element created high wear and friction, which ultimately limited lifetime and decreased reliability.

After careful review, it was concluded that combining load-carrying structural and mechanical logic function into a single component created these problems. The opposite approach was explored as a possible solution. Function was separated and each component was optimized to function as either a structural or logic component. While this approach introduced more components, an improvement in reliability and lifetime was expected.

## DESIGN

A new approach for the mechanism was proposed, the mechanical analogue of a relay. A small, lightly loaded binary latch would control a larger latch transmitting high loads. The component geometries of the lightly loaded binary latch could then be optimized to minimize overtravel, and the load-carrying latch could be sized to handle the high throughput loads. This would allow the mechanism to carry high loads with minimal overtravel.

A series of mechanism concepts was developed and evaluated for concurrence with the design objectives and particularly for simplicity and low part count. The concepts evolved through several intuitive steps which were facilitated by the thorough understanding of binary latch principles gained from the previous state-of-the-art research.

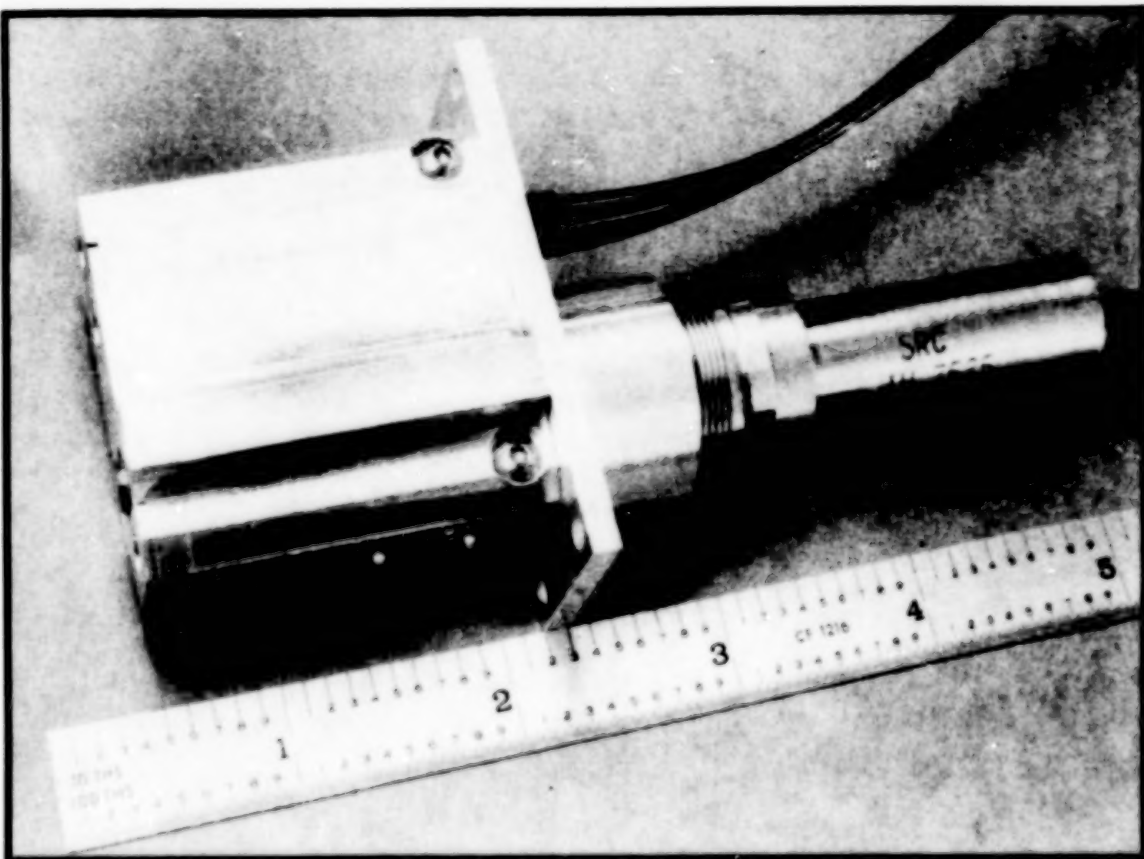
The final concept placed the binary latch inside the load-carrying components. The logic element of this latch would position itself to interfere with the movement of the load-carrying components relative to the housing when they were

in the extended position, thereby latching the mechanism. This arrangement simplified the design by having different parts of one component serve two functions, as a low-force logic element and as a high-force latch.

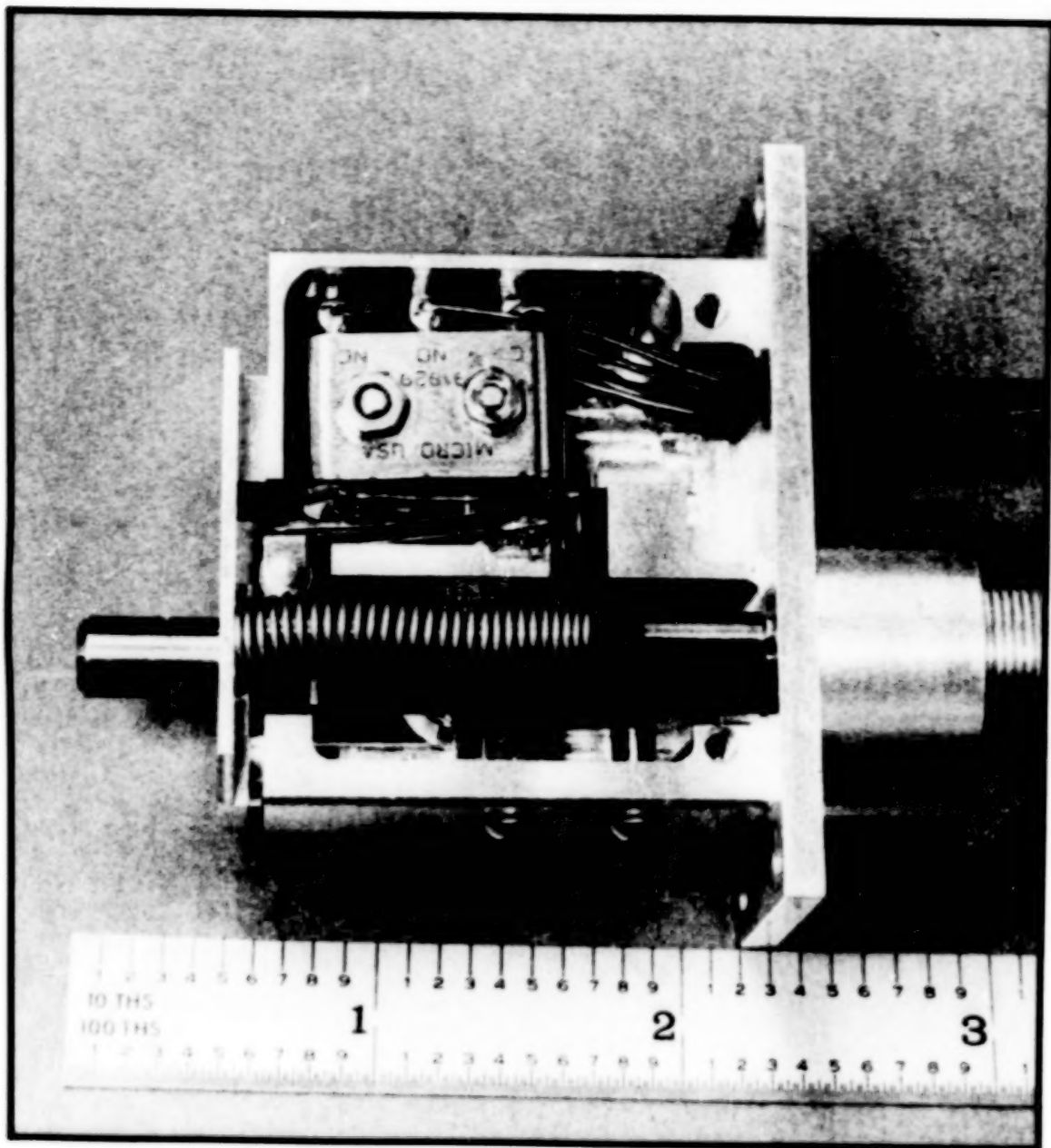
This final design has the following characteristics:

- 1) To latch and unlatch the mechanism, the logic element, called the "toggle," moves between a series of stable positions.
- 2) The toggle moves through the series of positions by pivoting about different features of the toggle. These movements are created by a separate low-force spring, the toggle spring, rather than by the throughput loads.
- 3) The toggle does not carry loads during actuator extension or retraction. It locks up the load-carrying components when in the latched position. No motion, and consequently no significant wear, can occur when the toggle is loaded.
- 4) The shapes of the toggle and latch components are optimized to minimize overtravel. Overtravel ideally can be limited to only what is required to accommodate tolerance stack-up.
- 5) None of the output loads is translated to sliding surfaces during extension or retraction, eliminating significant wear points in the mechanism.

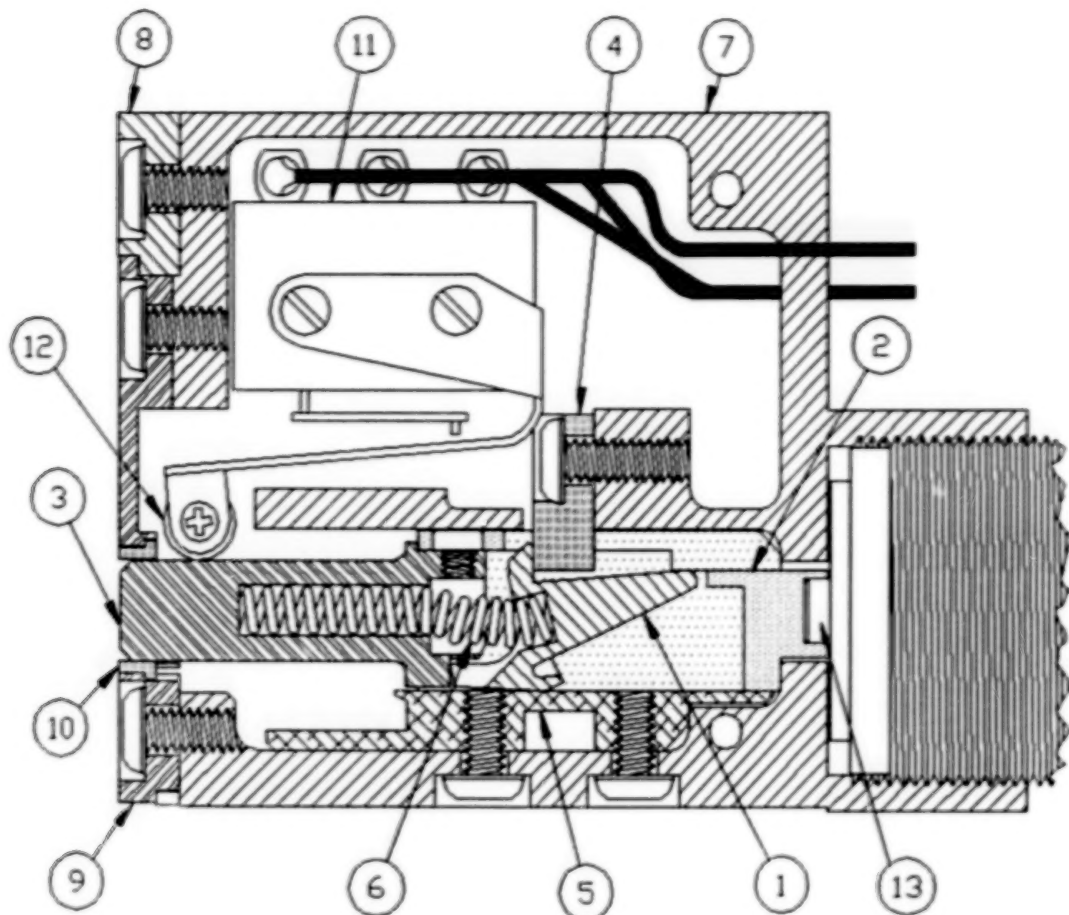
Operation of the mechanism is described in the following pictures and illustrations:



Latch mechanism (two switch version) with paraffin actuator

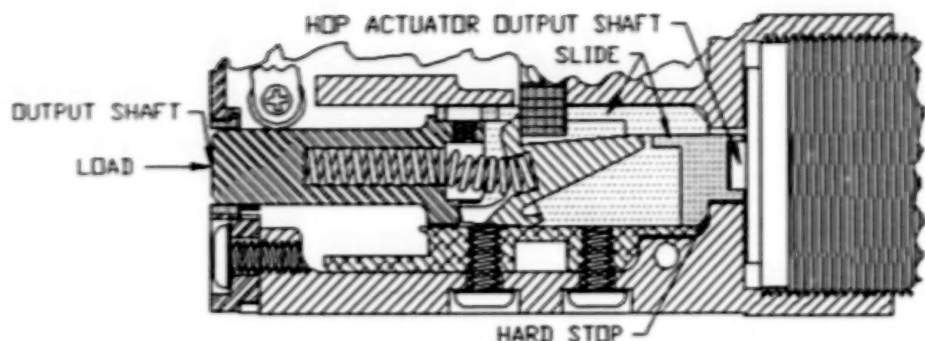


Latch mechanism with cover removed



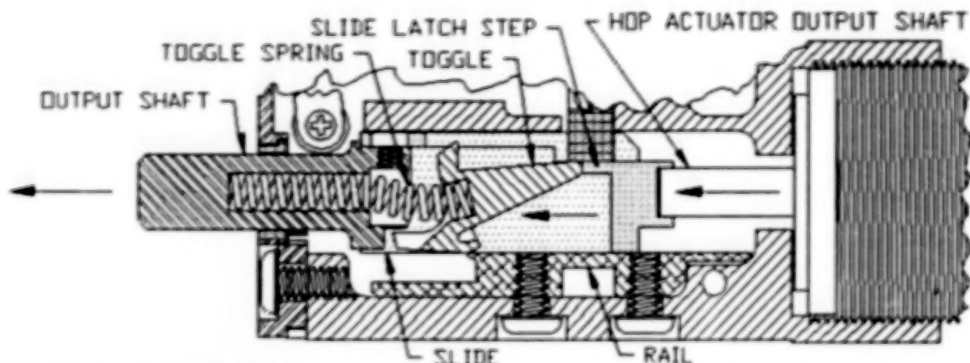
- 1) **Toggle** - The logic element of the mechanism. Moves inside the slide to latch the mechanism. (303 stainless steel)
- 2) **Slide** - Carries the throughput load from the output shaft around the toggle to the actuator shaft. (Envex 1115)
- 3) **Output shaft** - Carries the load to the slide and to the toggle in the latched position. Houses the toggle spring. (303 stainless steel)
- 4) **Reset Plate** - Resets toggle to its initial position. (Envex 1115)
- 5) **Rail** - End of the rail captures the toggle forcing it to pivot into the latched position. The toggle slides on the rail. (630 bronze)
- 6) **Toggle spring** - Applies an axial off-center load to the toggle, which forces the toggle to pivot through various overcenter positions. (18-8 stainless)
- 7) **Housing** - Houses components and mounts to spacecraft. Actuator mounts to housing. (6061-T6 Aluminum)
- 8) **Cover** - Encloses components after assembly and restrains bushing. (6061-T6 Aluminum)
- 9) **End Cap** - Captures bushing and supports output shaft. Allows visual access to components. (6061-T6 Aluminum)
- 10) **Bushing** - Guides the output shaft. (Envex 1115)
- 11) **Limit Switch** - Signals actuator extension. (Honeywell 9HM1)
- 12) **Switch Blade and roller assembly** - Interfaces with slide to actuate the limit switch. (Microswitch JS-151)
- 13) **Actuator output shaft** - Output of paraffin motor. (Nitronic 60)

## OPERATION



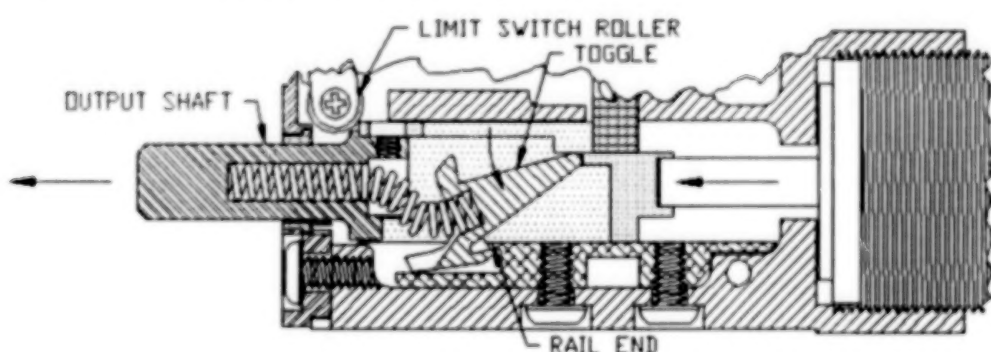
### 1) Initial position:

The actuator is fully retracted. Loads on the output shaft are carried by the slide around the toggle to an internal hard stop in the housing. The return springs (not shown) maintain this position during launch loads.



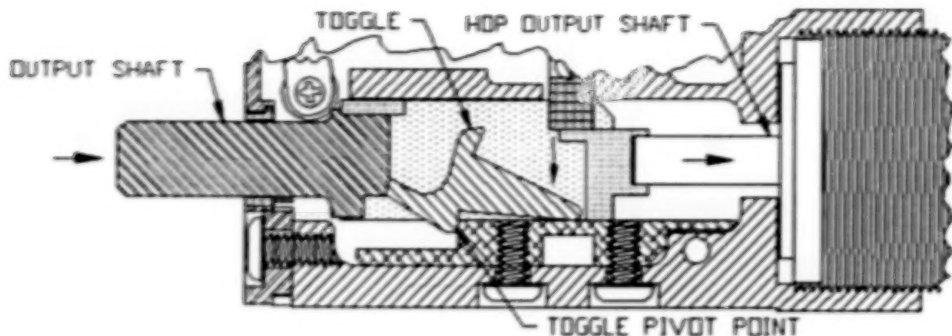
### 2) Actuator extending:

When power is supplied to the actuator, it slowly extends against a load carried axially from the output shaft through the slide to the actuator output shaft. The toggle spring establishes the position of the toggle and the direction in which it will rotate. It is held against the slide latch step and biased towards the rail during this phase.



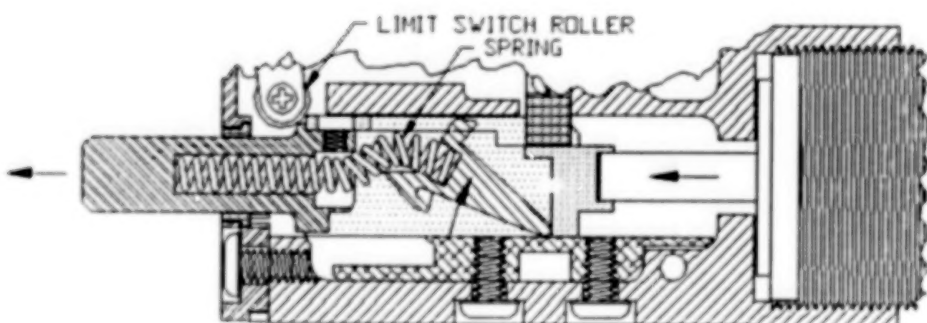
### 3) Prelatching:

The bias force on the toggle forces the toggle to pivot over the end of the rail. Actuator extension is signaled by the limit switches and the actuator is de-energized.



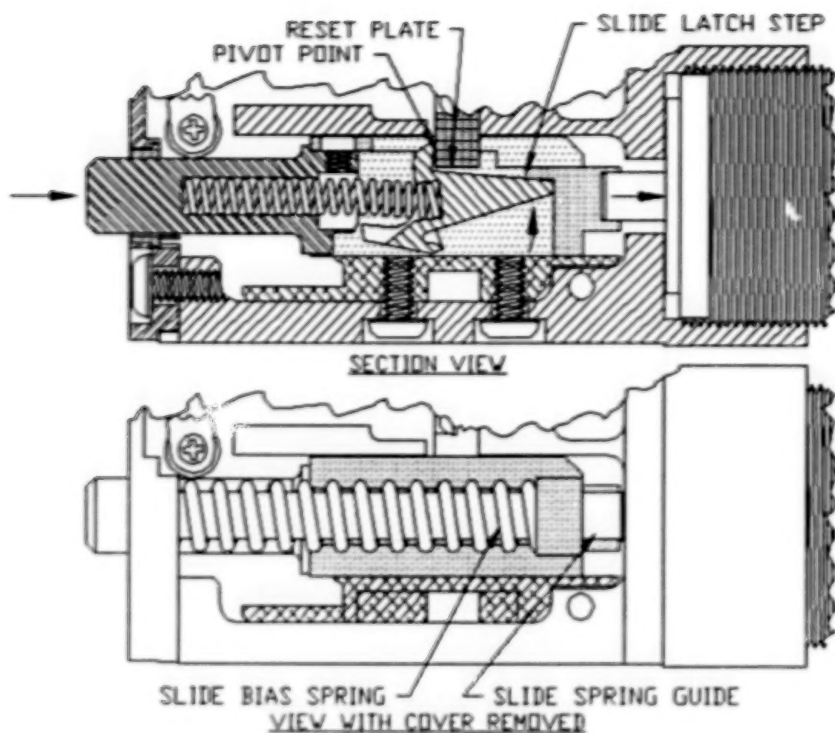
**4) Actuator retracting:**

The actuator begins to retract. Because the toggle is over the end of the rail points, it is captured and, under the action of the toggle spring, pivots about this point toward the rail. Friction forces alone are sufficient to maintain this position, however, .08 cm (.030") high points on the rail ensure that the toggle maintains this position under high vibration loads. As the output shaft continues to retract, loads are transferred from the output shaft through the latched toggle to the rail and retraction is halted. In this position, high loads are accommodated by this high-strength output shaft-toggle-rail load path. There is no wear because the load is applied to the toggle only after it is stationary. The pivoting of the toggle has shifted the direction of the toggle spring bias, preparing the toggle for the next step.



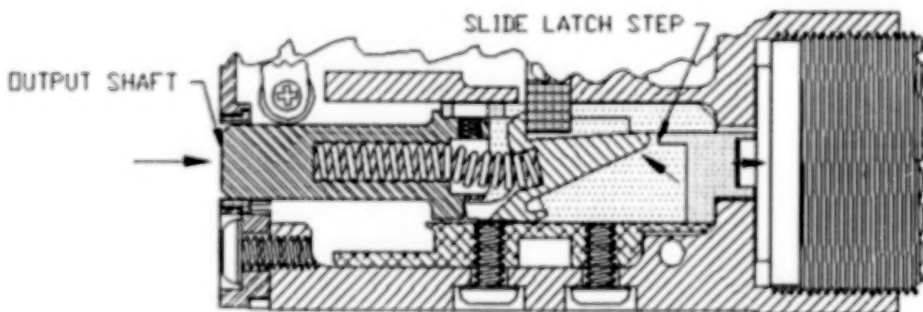
**5) Unlatching:**

When the mechanism is to be unlatched, the actuator is energized and begins to extend. Immediately the toggle is unloaded as loads are again transferred axially from the mechanism output shaft, through the slide, to the actuator output shaft. The toggle spring is now biasing the toggle away from the rail. As the slide advances, it moves the toggle forward, raising it above the rail points. Under the action of the toggle spring, the toggle pivots away from the rail to the far side of its housing in the slide. Actuator extension is again signaled by the limit switches and the actuator is de-energized.



**6) Retraction:**

The actuator retracts, allowing the mechanism, under the force of the slide bias springs, to retract at a slow, controlled rate. A tab on the toggle encounters the reset plate near the bottom of the stroke. Retraction past this point allows the toggle spring to rotate the toggle away from the rail toward the slide latch step, towards its original position.

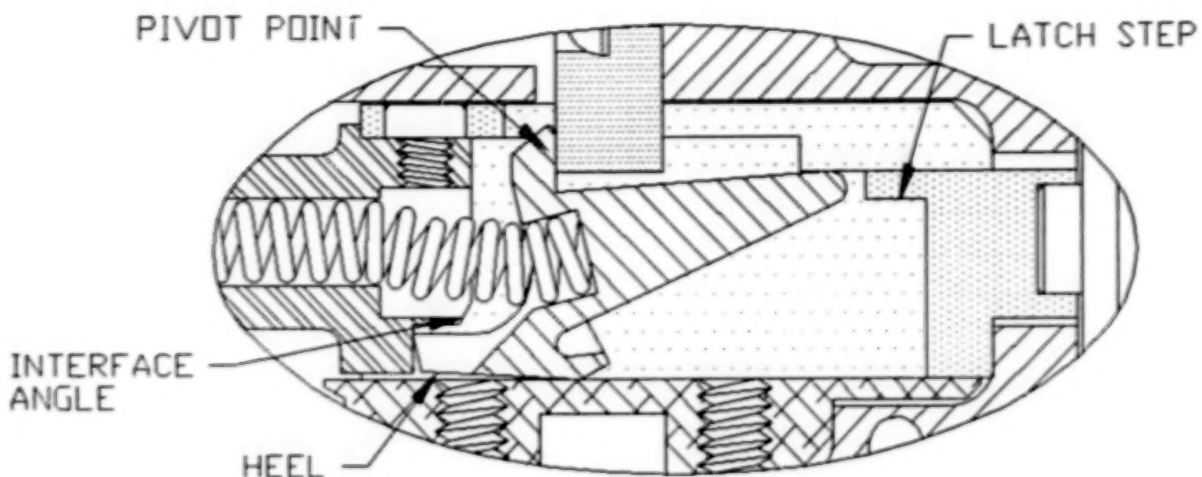


**7) Full retraction:**

As the mechanism fully retracts, the reset plate lifts the toggle onto the slide latch step, resetting all the components and completing the mechanism cycle.

## DESIGN REFINEMENT

Reducing the design from a concept to component parts required determining the optimal toggle length, width, length-to-width ratio, the toggle side travel, the pivot locations, the toggle "heel" length, the heel pivot point, output shaft interface angle, the toggle pivot angle, the toggle spring position, the latch step height, etc. All these attributes interact with one another to define the latch performance and, most importantly, to establish overtravel.



An analytical approach to optimizing these attributes was precluded by the complexity of the geometric solutions. In other words, there were more variables than equations. An interactive, iterative approach was used as an alternative to analysis to determine these attributes and generate the final component dimensions.

- 1) A first approximation of the component geometry was laid out on a CAD system. The mechanism was drawn in different positions.
- 2) Manipulation on the CAD system of the components in different positions provided a better understanding of the relationships between the parts and their attributes.
- 3) Iterative modifications to the component shapes provided approximate solutions to the component geometry.
- 4) The CAD output was translated to pasteboard prototypes which allowed more detailed evaluation of the kinematics throughout the latching cycle.
- 5) A final geometric solution and assembly drawing was completed by repeating the CAD/pasteboard prototype loop several times.
- 6) Individual part prints were completed and prototype hardware was fabricated. Some components were fabricated of clear polycarbonate to allow visual inspection of part movement and loading during operation.
- 7) The prototype was observed during operational testing and components were modified to optimize for function and overtravel.
- 8) Material selection was completed, component design finalized and test hardware was fabricated.

## RESULTS OF PROTOTYPE FABRICATION AND TESTING

As initially configured, all siding surfaces in the mechanism were metal on molydisulfide-impregnated polyimide (Vespel and Envex are trade names for Mil Spec versions of this material). This required the slide, rail and bushing to be made of polyimide. Fabricating these parts required developing machining expertise because of the brittleness of the material and its tendency to chip and split when in shear. Carbide tools, backing up edges, high tool speeds and high feed rates were necessary for fabricating the complex shapes required.

The polyimide rail failed during initial testing. The rail end points, around which the toggle pivots (see the Prelatching and Actuator retracting diagrams) fractured from unexpected high inertial loads. The toggle impacted the rail ends as it moved into the latched position and again when it rotated. Both motions and the associated impact led to a rapid brittle failure, breaking the ends off the rail. More tightly controlling the toggle movement might have eliminated this failure, but it was clear that a more durable material was required for this part to ensure reliability under all conditions.

Because limiting weight was important and because the rail experienced light loading from the toggle sliding along it, 6Al-4V titanium was initially substituted. Galling occurred within 100 cycles although contact surface loading was less than 25 psi against the stainless steel toggle. The galling produced progressively higher drag and could not be mitigated by smoother surface finishes. The titanium was therefore deemed unsuitable.

CDA 624 aluminum silicon bronze, CDA 655 silicon bronze and CDA 630 aluminum nickel bronze were tried next. After initial wear-in, approximately 50 cycles, the toggle was burnished from contact with the rail and neither part demonstrated significant wear during subsequent testing to 20,000 cycles. CDA 630 bronze was selected because of its resistance to corrosion and slightly better wear characteristics.

Thermal testing revealed interference between the output shaft and its bushing at low temperatures. The bushing, fabricated from polyimide, shrank onto the output shaft at -60°C and created friction. Enlarging the bushing bore corrected the problem.

Repeated latch operation at 80kg (150 lbf), greater than three times normal load, was performed. The mechanism functioned smoothly with no deformation or excessive component wear, confirming satisfactory strength margins for the latch and load-carrying components.

Standard mounting of the Honeywell Microswitch 9HM1 switch and its associated roller blade uses only the clamping friction created by torquing the switch mounting screws to 1728gm-cm (1.5 in-lb) to secure the blade in position. Because one of the mechanisms designed required stacking two 9HM1 switches on top of each other, there was a concern that the blades and therefore the switch

actuation point might shift from vibration. The mounting security was improved by assembling the switches with urethane between all the parts, effectively bonding the assembly.

The mechanism was subjected to vibration testing at 20, 30, and 50G rms. There was no change in mechanism function and the latch stayed in position during vibration. The Honeywell 9HM1 limit switch point of operation shifted by .025cm (.010") after 20G vibration. This shift was due to changes in the internal components of the switch and was expected. Mechanism tolerance was sufficient to accommodate this shift and no further shifts were noted at the 30G and 50G vibration levels.

After establishing satisfactory performance, the mechanism and its parts were reviewed for structural margin and optimized for such manufacturing issues as tolerance, ease of fabrication, assembly, fasteners, etc. The final design was used for fabrication of qualification and flight assemblies.

## FINAL CHARACTERISTICS OF THE LATCH MECHANISM

### Size/mass:

Final dimensions of the single switch version of the mechanism are 2.3x4.2x3.2 cm (.90"x1.65"x1.25") and mass is 86 grams. Dimensions of the 2-switch version are 2.5x4.3x4.5cm (1.0"x1.7"x1.75") and mass is 100 grams.

### Output loads:

During extension and retraction, output loads are carried axially from the actuator shaft to the mechanism output shaft. None of the output load is translated to normal forces on wearing or moving surfaces. 100kg (220lbf) static load testing and qualification testing at 80kg (175lbf) dynamic load for 15 cycles produced no wear or damage to latch components. This testing established a margin of greater than three above the nominal rated operating load of 23kg (50lbf).

### Overtravel/stroke:

As currently configured, .08cm (.030") of overtravel is required to operate the latch. An additional .08cm (.030") is required to operate the limit switches. A remaining .152cm (.060") of overtravel is used to ease part tolerance requirements, assembly tolerance, and to accommodate a large variation in environmental temperature. Total overtravel is .32cm (.125"). Overtravel was reduced to .19cm (.075") by utilizing a custom switch blade and by tightly controlling tolerances.

The use of an SRC IH 5055 actuator with 1.5cm (.575") of available stroke provided 1.1cm (.45") of stroke between the retracted and extended latched positions, even with the more generous .32cm (.125") of overtravel.

#### Reliability/lifetime/wear:

Outside of the output shaft assembly which transmits the throughput load, the actual latch mechanism contains one moving part, the toggle, which moves by the forces created by the toggle spring (approx. 1.5kg). The final mechanism configuration limits the sliding surfaces to four interfaces. The loadings listed are maximum limits that could occur with 23kg (50lbf) of throughput load:

#### Toggle/rail interface

303 stainless steel against 630 bronze with 2kg/sq.cm (25psi) loading.

#### Toggle/slide interface

303 stainless steel against molydisulfide-impregnated polyimide with 1kg/sq.cm (10psi) loading.

#### Slide/rail and housing interfaces

Molydisulfide-impregnated polyimide against 630 bronze and 6061-T6 aluminum with 2kg/sq.cm (20psi) loading.

#### Bushing/output shaft

Molydisulfide-impregnated polyimide against 303 stainless steel with 2kg/sq.cm (25psi) loading.

These surface loading levels are two-to-three orders of magnitude less than standard design limits for self-lubricated systems, therefore high-cycle lifetimes are expected. Lifetime testing for a total of 20,000 cycles was performed on the final prototype design at various temperatures and loads. The mechanism was disassembled, and the components were examined under a 20x microscope after initial wear-in and again after the test program. Mechanism wear was negligible after initial burnishing. The expected life of the device will exceed 100,000 cycles, based on testing and wear information. Testing to greater than 100,000 cycles will be completed this year.

Fatigue on all components is minimal. Strains on the toggle spring are well within design limits for infinite life. Strains on the internal bias springs used to reset the actuator and the slide are low and provide for a lifetime of  $10^7$  cycles.

#### Vibration:

All moving parts are retained in fixed positions by springs exerting forces approximately 100 times the component mass. Qualification testing at 50G rms random vibration along 3 axes has been performed with no change in mechanism performance.

#### Friction/lubrication/outgassing:

The normal loads on all sliding surface interfaces during operation are very low, less than 1kg (2lbf), therefore friction is negligible. No liquid lubricants are required because all sliding surfaces are self-lubricating and outgassing can be limited to negligible levels.

## **CONCLUSION**

The project was successful from a technical standpoint, with the flight unit assemblies meeting or exceeding all the original design requirements. As with most design efforts, there were some surprises. Lessons that were learned during this process included:

- 1) Leave room to maneuver. The initial design requirements were aggressive in all areas, such as mass, size, and performance. This allowed few opportunities to trade off less important features for more important ones.
- 2) Having a full background understanding of a mechanism is worth the effort. Thorough state-of-the-art research, including non-aerospace commercial mechanism designs, greatly supports a design effort. Besides the obvious advantages of not having to "reinvent the wheel" or avoiding possible patent infringement, thorough state-of-the-art research:
  - a) provides lateral leaps to new approaches.
  - b) affords a "heads up" to possible problems.
  - c) provides an broad-based understanding of a particular mechanism's design principles or philosophies and its suitability to the given requirements.
- 3) Iteratively designing a complex mechanism in CAD and using pasteboard mock-ups can be a more efficient process than detailed mathematical analysis of component geometries:
  - a) Components can be visualized throughout their range of motion.
  - b) Interferences can be identified and eliminated.
  - c) Kinematics and component shapes can be easily optimized by simultaneously seeing the effect of changes in all positions.

## **PROJECT STATUS**

Flight hardware was fabricated and delivered for the University of Iowa Comprehensive Plasma Instrument aperture cover driver in April 1990. The mechanism has successfully passed all qualification testing. The ISTP/Geotail spacecraft carrying the instrument is scheduled for launch in July, 1992.

Flight hardware is being fabricated and will be delivered in February 1991 to Marshall Space Flight Center for the Ultraviolet Instrument aperture cover and folding mirror driver to be flown on ISTP/Polar.

Flight hardware is being fabricated and will be delivered to Ball Aerospace for the caging mechanism and occulter for the Ultraviolet Coronagraph Spectrometer to be flown on ISTP/SOHO.

# HARMONIC DRIVE GEAR ERROR: CHARACTERIZATION AND COMPENSATION FOR PRECISION POINTING AND TRACKING

Ted W. Nye and Robert P. Kraml\*

## ABSTRACT

Imperfections and geometry effects in harmonic drive gear reducers cause a cyclic gear error, which at a systems level, results in high frequency torque fluctuations. To address this problem, gear error testing was performed on a wide variety of sizes and types of harmonic drives. We found that although all harmonic drives exhibit a significant first harmonic, higher harmonics varied greatly with each unit. From life tests, we found small changes in harmonic content, phase shift, and error magnitude (on the order of .008 degrees peak-to-peak maximum) occurred for drives with many millicns of degrees of output travel. Temperature variations also influenced gear error. Over a spread of approximately 56°C (100°F), the error varied in magnitude approximately 20 percent but changed in a repeatable and predictable manner. Concentricity and parallelness tests of harmonic drive parts resulted in showing alignments influence gear error amplitude. Tests on dedoidaled harmonic drives showed little effect on gear error; surprisingly, in one case for a small drive, gear error actually improved. Electronic compensation of gear error in harmonic drives was shown to be substantially effective for units that are first harmonic dominant.

## INTRODUCTION

Spacecraft mechanisms of the future are requiring more precise pointing and tracking features while maintaining simplicity, long life, and low weight. One key component that enables space mechanisms to meet these objectives are harmonic drive gear reducers. Shown in Figure 1, harmonic drives are well known for their high gear reduction ratios, low weight, small volume, zero backlash, and high efficiency. For the many beneficial features they possess, there are at least two undesirable characteristics, namely soft torsional stiffness and gear error. Soft torsional windup results in undesirable, low frequency vibration modes in appendages that are susceptible to excitations from gear error or motor ripple torque anomalies. At modal frequencies, the cyclic torque disturbances (or jitter) will resonate payloads and the spacecraft bus. In this article, we discuss gear error in the harmonic drive, what it is sensitive to, and what can be done about it.

---

\* TRW, Space & Technology Group, Redondo Beach, California

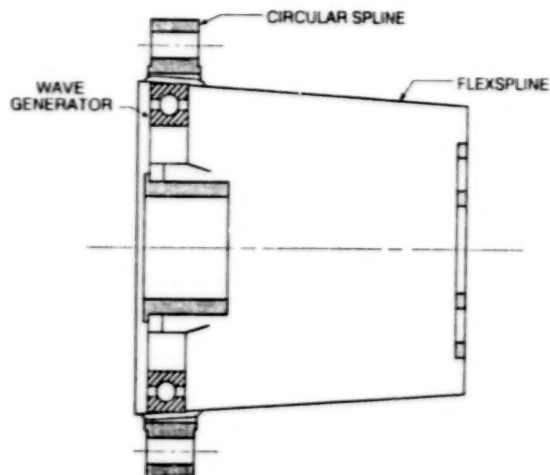


Figure 1 Harmonic Drive Section View

Gear error or positional accuracy is the difference between the theoretical and measured angular position of the input and output of a gear reducer. Typically, we see integer values for a gear ratio. What we actually measure is the integer value plus a small cyclic error imposed upon it. As mentioned previously, this small cyclic error can cause substantial disturbances in appendages.

Sasahara et al. in [1]\*\* documented vibrations in an industrial robot when driven near resonance. Accelerometer data presented showed a beating behavior where the amplitude was influenced by torsional stiffness and circular spline deformation. They concluded that radial tooth errors and tooth meshing composite errors are large contributors to positional accuracy problems. In [2], Ahmadian developed an expression for geometric error in harmonic drives by use of parametric curves to model flexspline deformation. He concluded with a theoretical model that captures the first order effects of gear error behavior due to geometry. A brief, applications oriented discussion on positional error is presented in [3]. Also included is a rough estimating relationship to quantify the error and figures that show the nominal behavior over one revolution of travel.

Harmonic drive gear error could be described in two categories - that caused by internal effects and that caused by external effects. Internal influences are due to geometry, tolerances, tooth shape, and material. The last item has an influence because of machining dimensional stability. External influences on gear error are due to usage and environment such as changes over life, temperature, mounting alignment, incorrect assembly such as dedoidal, over-load effects such as ratcheting, and how error changes with external load.

\*\* Numbers in square brackets refer to references.

## MEASUREMENT TECHNIQUES

Figure 2 shows our test setup used for determining positional error. Harmonic drives were mounted in assemblies (actuators) containing a stepper motor and support bearings. Both input and output shaft positions were measured with 19 bit optical encoders. The test was controlled by a PC/AT compatible computer via several interface cards to peripheral devices. Two encoder display readouts were used to visually compare input and output shaft positions. The stepper motor was controlled with an indexer/driver arrangement which allowed the motor to be operated at a selectable power supply voltage and command rate. For life tests, the actuator assembly was enclosed in a vacuum chamber to simulate a spacecraft environment. For thermal tests, the entire encoder/actuator assembly was enclosed in an oven. The majority of measurements were performed at room temperature in a laboratory environment.

Our test procedure involves these basic steps:

1. Zero out input and output encoders at the starting position.
2. Make sure fixture was stable.
3. Step the actuator to a new position by a pre-defined step size.
4. Compare the difference between output and scaled input, this is gear error.
5. Continue steps 3 and 4 for at least one output revolution.

Results were stored on a hard disk, then analyzed and plotted. This setup has proven to be accurate and repeatable for many tests involving harmonic drives.

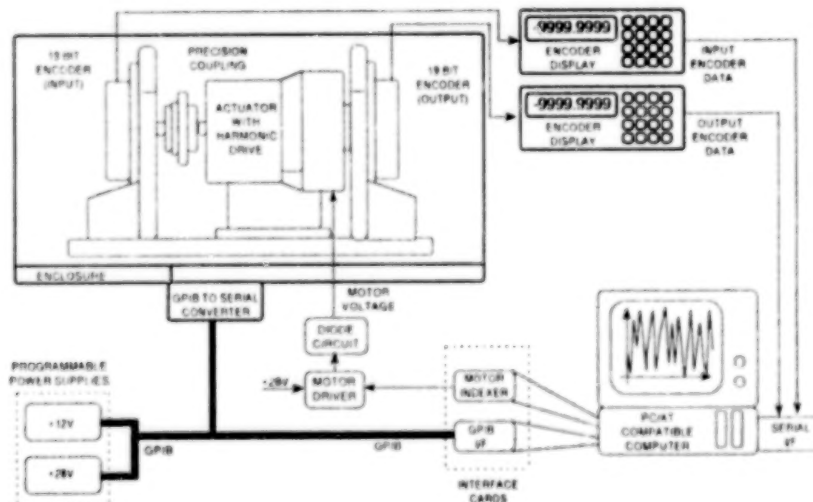


Figure 2 Gear Error Test Station

## GEAR ERROR CAUSES

Although a detailed analytical study was not performed with regard to the causes of positional accuracy variations, discussions with harmonic drive manufacturers have indicated some qualitative explanations. For the low cycle beating effect, maximum error is caused by the errors in two parts combining to produce the total error. As the components rotate relative to each other, some errors cancel, which produce the minimum error.

Most of the first through ninth harmonic effects are attributed to:

1. Tooth placement errors on the flexspline.
2. Tooth placement errors on the circular spline.
3. Out-of-roundness of the circular spline.
4. Variation in wall thickness between the flexspline pitch diameter and bore.
5. Flexspline out-of-roundness.
6. Bearing outer race out-of-roundness.
7. Variation in wall thickness between the outer race ball groove and the outside diameter.
8. Lack of concentricity between the flexspline and circular spline in the assembled position.
9. Lack of squareness between the flexspline and circular spline in the assembled position.
10. Fit-up between the flexspline and circular spline teeth in the assembly.

Gear error improves as the harmonic drive size increases. Smaller units become much more sensitive to dimensional tolerances, hence, they are also more likely to contain higher harmonics. A formula given in [3] for the upper bound of positional error is:

$$\epsilon = \frac{8}{d_m} \quad (1)$$

Where  $\epsilon$  is the peak-to-peak error in arcminutes and  $d_m$  is the pitch diameter in inches. This relationship provides a good estimate for a commercial unit but substantial improvement in performance over this has been demonstrated for flight hardware (typically less than half of the above prediction).

## GENERAL CHARACTERISTICS

Harmonic drive positional error is a frustrating phenomenon due to fact that two seemingly identical units may have completely different error signatures. Figures 3 and 4 show such behavior, where for similar units, the second contains harmonics approaching 55 percent of the fundamental. Without a positional accuracy test, one cannot, for example, make simple dimensional checks or get indications of error from other measurements such as friction or stiffness. The general full rotational behavior of gear error is shown in Figure 5. Typically, one sees a characteristic beating amplitude modulated twice per output rotation. There are sometimes exceptions however, as measured in one unit shown in Figure 6. Positional error seems to be independent of gear ratio, but for reference, all units tested in this report had 100:1 reductions. Materials used for the drives in these tests were primarily 304, 17-4, 15-5, or equivalent stainless steels.

"Well-behaved" gear error contains few or no higher harmonics where "poorly-behaved" contains many high frequency components (superimposed upon the fundamental). This qualitative label is given because of the ability to digitize and electronically compensate a given error signature. More discussion on compensation follows in a later section. The harmonic content of a typical gear error plot was analyzed with Fast Fourier Transform software and is shown in Figure 7.

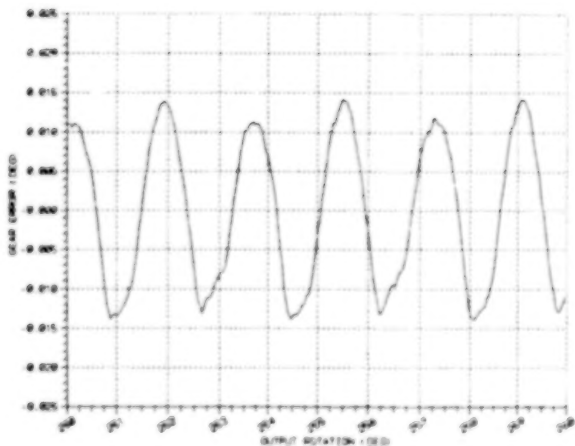


Figure 3 Well-Behaved Gear Error

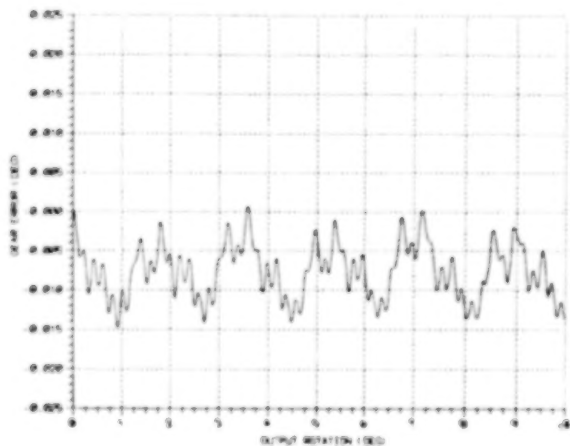
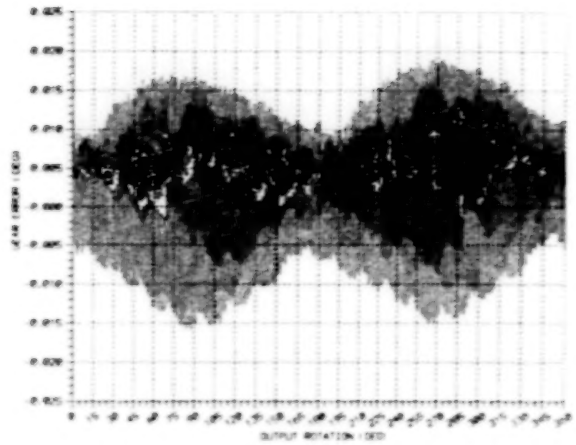
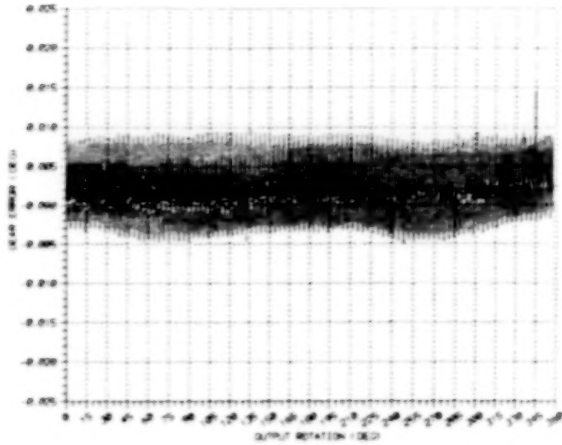


Figure 4 Poorly-Behaved Gear Error



**Figure 5 Typical Gear Error Over One Output Revolution**



**Figure 6 Exceptional Gear Error Over One Output Revolution**

Harmonic errors occur in factors of 2 of input rotations. For example in Figure 7, the largest harmonic corresponds to the first harmonic, occurring twice per input rotation. The second harmonic occurs every 4 cycles of input rotation. In many instances we observed a large ninth harmonic, occurring every 18 cycles per input rotation.

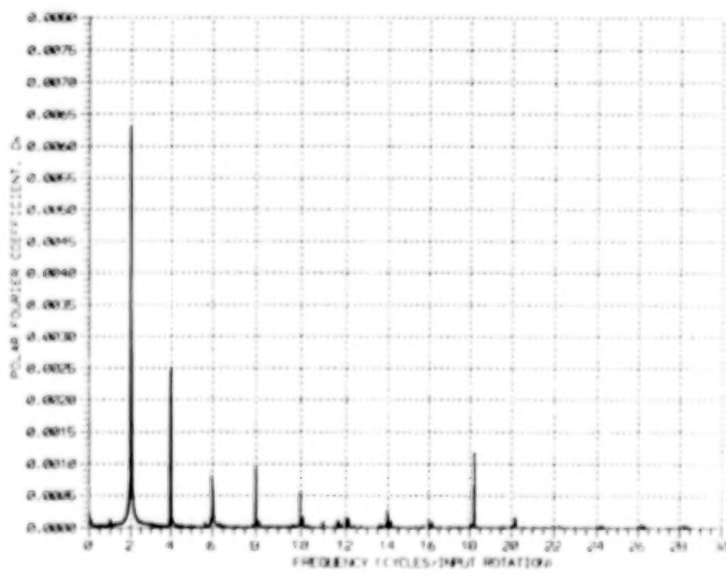


**Figure 7 Frequency Plot of Harmonic Drive Gear Error**

Recently there have been developments of a new (IH) tooth profile as discussed in [4]. The new tooth, shown in Figure 8, is used with a wave generator plug exhibiting a shape that allows for a higher quantity of teeth to be engaged without "ticking." Ticking is caused when gear teeth tips prematurely collide before engagement. The newer tooth profiles (and perhaps very precise machining) seem to have improved the variation and higher harmonics of gear error for these drives. Figures 9 and 10 show measurements on an IH tooth profile unit. Each IH tooth profile drive tested demonstrates well-behaved gear error. Higher harmonics were present but were observed at very high frequencies. The causes of the high frequency component may be tooth engagement related but are distinctly different from conventional tooth signatures.

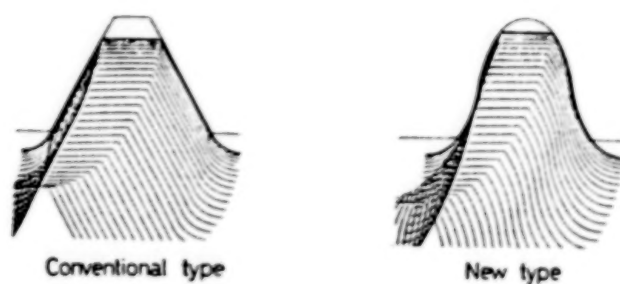


**Figure 8 Comparison of Harmonic Drive Tooth Profiles**

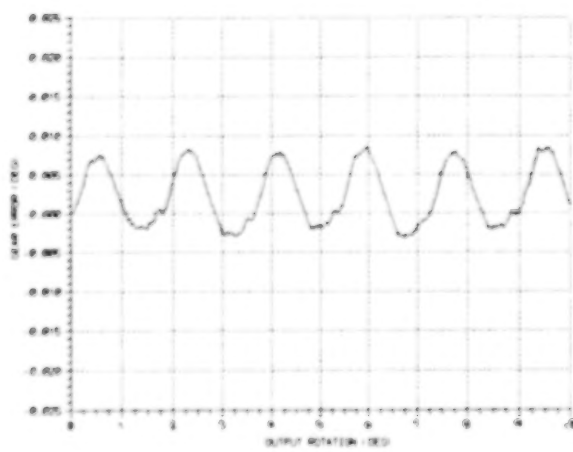


**Figure 9** IH Tooth Harmonic Drive Gear Error over One Output Revolution

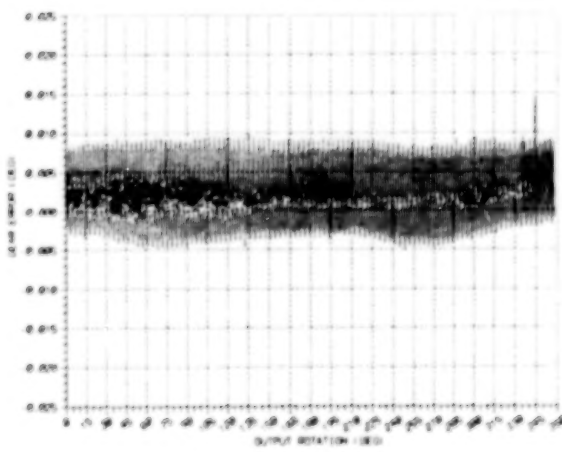


**Figure 10** Detailed View of IH Tooth Harmonic Drive Gear Error

## BEHAVIOR OVER LIFE

For an electronic compensation scheme to be effective, gear error must be stable in amplitude and phase over life. Several wear tests have shown this to be generally true. Figure 11 shows gear error before and after a life test of many million degrees of output travel.

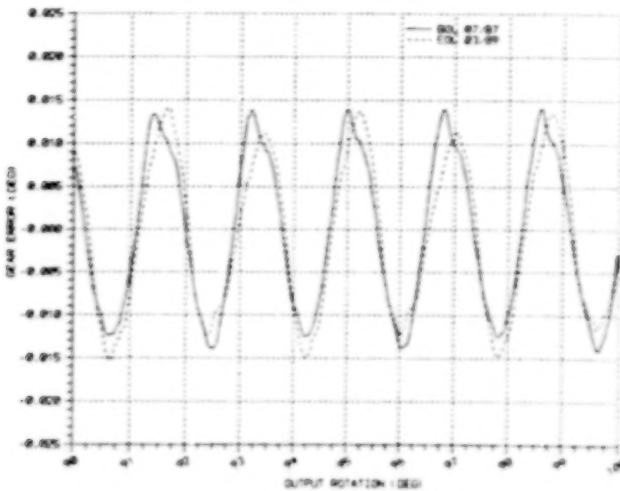


Figure 11 Gear Error Change with Life

Data in Table 1 shows the error measured from life tests. Note that the 8.1 cm (3.2 in) pitch diameter unit used for the life test turned out to have exceptionally small gear error. Very slight changes in the error wave forms did occur with negligible phase shift. Spectral plots shown in Figures 13 and 14 for the 10.2 cm (4.0 in) pitch diameter harmonic drive illustrated how the spectral components changed slightly over life. A slight increase in harmonic content was expected due to generation of wear debris. Wear particles get trapped in the gear teeth and wave generator, thus they affect concentricities and clearances. The counter to this effect is

Table 1 Gear Error Changes from Life Tests

Pitch Diameter	P-P Theoretical Gear Error	P-P Beginning of Life Gear Error	P-P End of Life Gear Error
8.1 cm (3.2 in)	.042 deg	.009 deg	.017 deg
10.2 cm (4.0 in)	.033 deg	.028 deg	.029 deg

removal of material from high and low spots on the gear teeth and interface surfaces. We could, on the other hand, expect this effect to smooth out and reduce the gear error. None-the-less, our only conclusion was that gear error is only slightly affected with life.

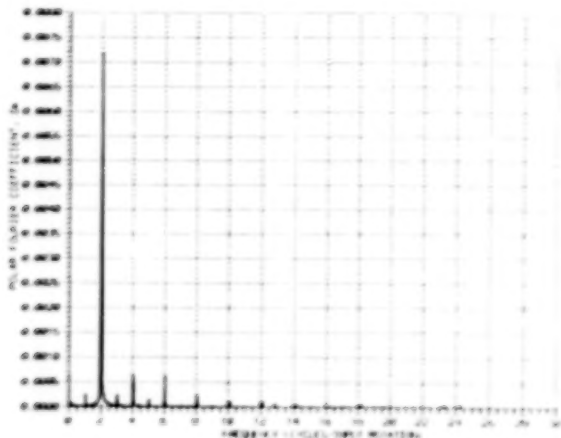


Figure 12 Beginning of Life Gear Error Spectral Content

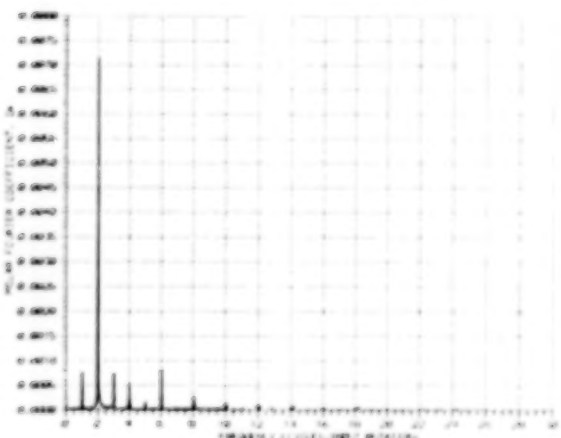
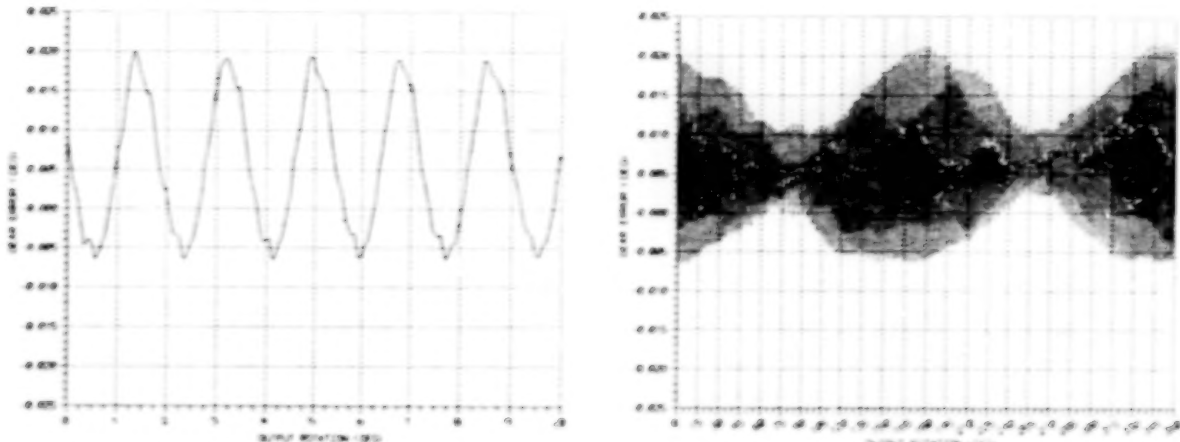


Figure 13 End of Life Gear Error Spectral Content

#### TEMPERATURE SENSITIVITY

Increasing temperature changes gear error with absolute shifts and small increases of peak-to-peak errors. Harmonic content appears to slightly increase with higher temperatures. Although most of these effects are small, Figures 14, 15, and 16 show the absolute shift and peak-to-peak growth with temperature. Table 2 shows numerically how these variations occurred for this 10.2 cm (4.0 in) pitch diameter test unit. The significance of the absolute error shifts are moot due to the fact that the peak-to-peak oscillations are primarily responsible for dynamic disturbances that concern us. The cause of the error change is unknown, however, similar tests on harmonic drives for stiffness show substantial reductions with increasing temperatures approaching 66°C (150°F).



**Figure 14** Gear Error Comparison at  $52^{\circ}\text{C}$  ( $125^{\circ}\text{F}$ )

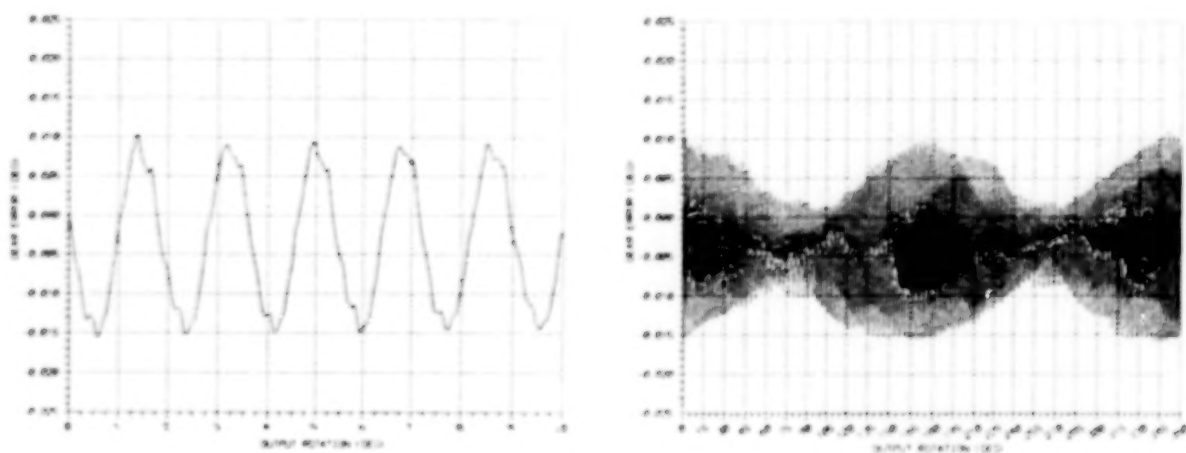


**Figure 15** Gear Error Comparison at  $24^{\circ}\text{C}$  ( $75^{\circ}\text{F}$ )

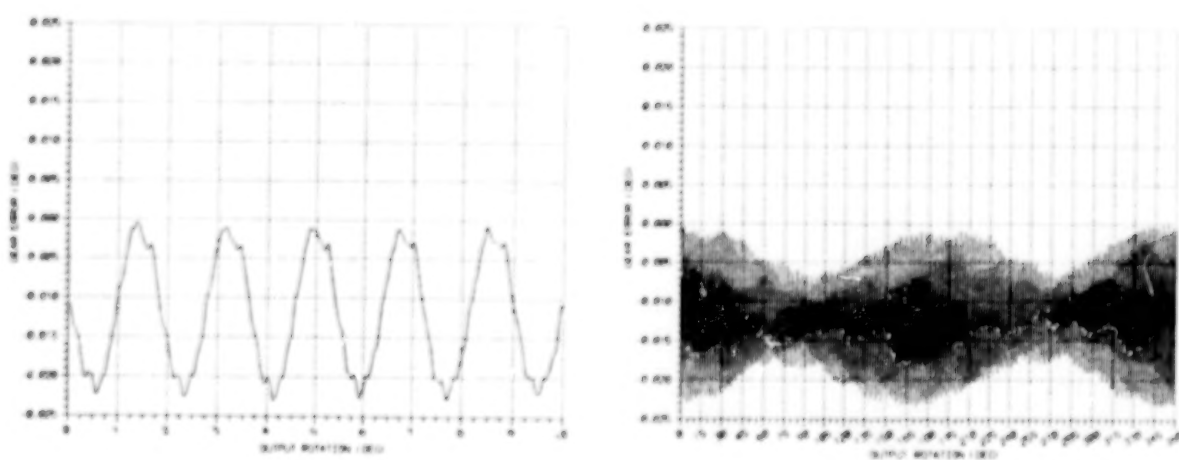


**Figure 16** Gear Error Comparison at  $-1^{\circ}$  ( $30^{\circ}\text{F}$ )

Table 2 Temperature Effects on Gear Error

Temperature	P-P Theoretical Gear Error	P-P Measured Gear Error	5th Harmonic Polar Fourier Coefficient
52°C (125°F)	.033 deg	.028 deg	.00040
24°C (75°F)	.033 deg	.026 deg	.00035
-1°C (30°F)	.033 deg	.023 deg	.00030

#### ALIGNMENT SENSITIVITY

Positional error tests were run on a 8.1 cm (3.2 in) pitch diameter unit to determine the importance of concentric and perpendicular mountings. In the first test, several flex spline mounting hubs were intentionally made off-center by a given displacement. Gear error results from this effect are shown in Figure 17. Sensitivity to concentric alignment appears to be relatively small for tolerances that are typical for aerospace assemblies. Commercial products with coarser tolerancing however, could be affected with this runout. The data supports using care in determining concentricity for mounting assemblies.

The second test involved modifying the perpendicularity of the circular spline with respect to the flex spline. Figure 18 shows how gear error increased with mounting angle error. The same conclusion can be drawn as previous, that perpendicularity must be carefully controlled.

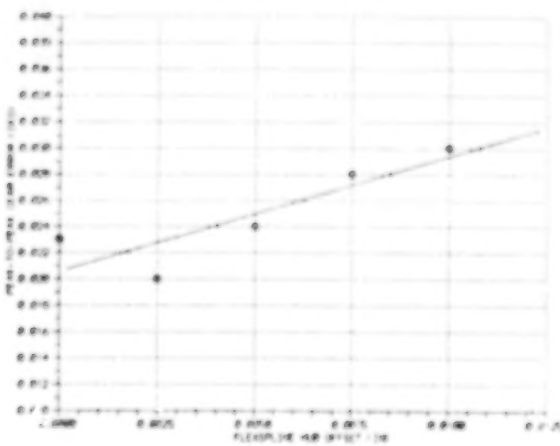


Figure 17 Flexspline and Circular Spline Offset

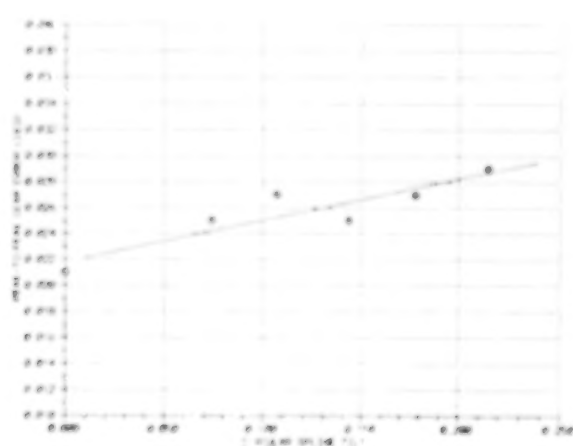


Figure 18 Flexspline and Circular Spline Perpendicularity

## EFFECTS OF RATCHET AND DEDOIDAL

Ratcheting is an over-load condition where, due to a high output load, the harmonic drive will slip one or more teeth. Many times this ratcheting will leave the harmonic drive in the dedoidaled condition. Dedoidal is commonly labeled to a harmonic drive where the wave generator and flex spline gears are no longer concentric with the circular spline. Rather than the oval wave generator and flex spline teeth being centered in the circular spline, they are slipped over to one side. This effect is more commonly encountered during incorrect assembly. Symptoms of dedoidal are large variations in starting friction torque and a significantly reduced wear life.

Tests of gear error changes after high loads and ratchet were performed on 3.6 cm (1.4 in) and 8.1 cm (3.2 in) pitch diameter harmonic drives. The smaller units had large gear error prior to testing and did not exhibit the typical modulated two lobed beating pattern as shown for one set of data in Figure 19. Dedoidal conditions did not significantly change the error signatures as seen in Figure 20, but surprisingly, slightly improved the error amplitude. To ratchet our units, the flex spline and circular spline were fixed, and the wave generator was turned until tooth skipping occurred. Each unit was ratcheted at least four times in separate tooth locations with each test resulting in a dedoidaled condition. After ratchet, the gear error again did not seem significantly affected. Figures 21 and 22 show the amplitude and characteristics were comparable, but the dedoidal caused an absolute shift. Tests on the larger units were done in the same manner as the smaller units, but were not torqued to a ratchet condition. Gear error changes were again small. We concluded that gear error is not an effective means to verify the load history of a harmonic drive, nor can it be used to determine dedoidaled conditions.

## GEAR ERROR COMPENSATION

Gear error compensation is accomplished by measuring the error of a given harmonic drive and then modifying an input motor voltage appropriately to effect an error cancellation. Figures 23 and 24 show the before and after result of compensation.

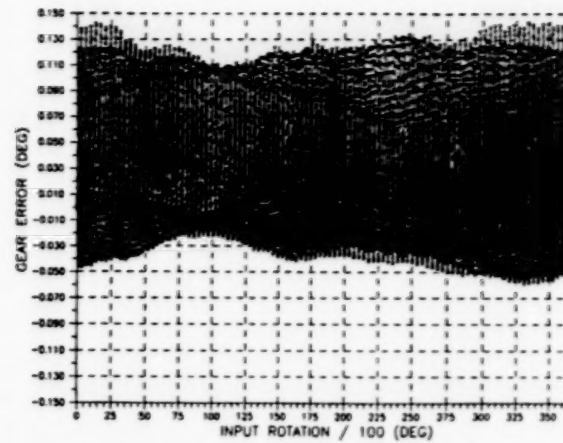


Figure 19 3.6 cm Pitch Diameter Unit,  
Gear Error Prior to Test

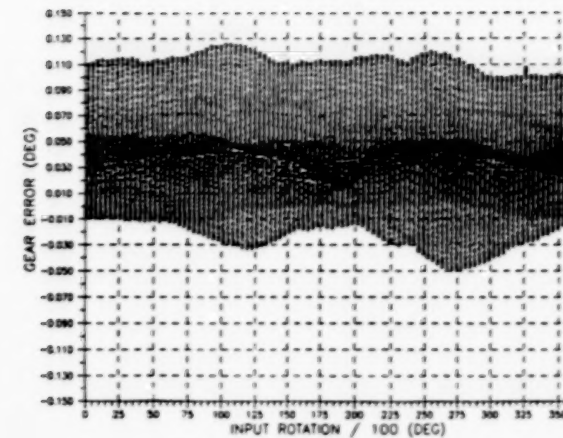


Figure 20 3.6 cm Pitch Diameter Unit  
Gear Error in Dedoidal  
Condition

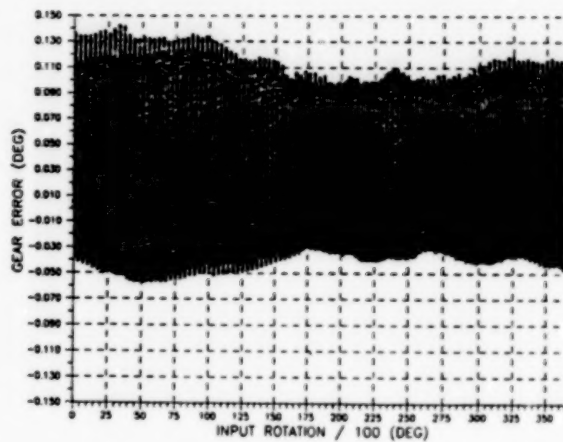


Figure 21 3.6 cm Pitch Diameter Unit  
Gear Error After Ratchet

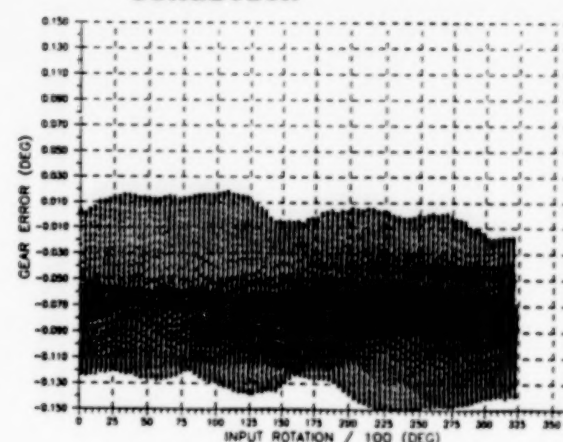
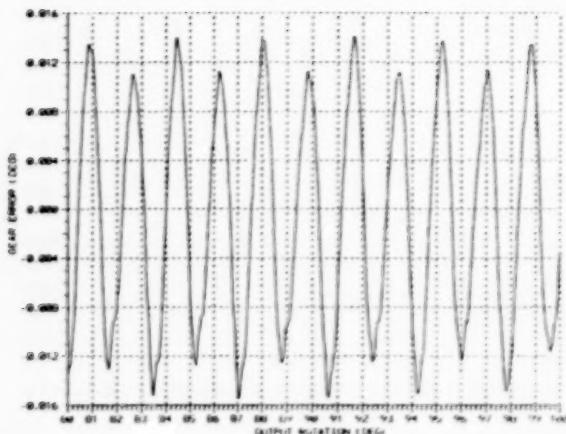
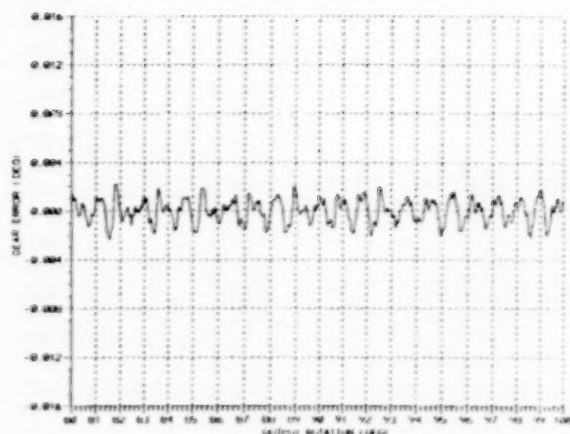


Figure 22 3.6 cm Pitch Diameter Unit,  
Gear Error After Ratchet in  
Dedoidal Condition

249



**Figure 23 Uncompensated Gear Error**



**Figure 24 Compensated Gear Error**

To implement this scheme, a sine wave excited stepper motor was driven in a variable frequency fashion. This means for one sine wave that would cause 15 degrees of motor output rotation for example, the voltage waveform was artificially shortened or lengthened to effect an output position compensation. Figures 25, 26 and 27 show graphically the compensation effect. Compensation is implemented with a look-up table (and linear interpolation algorithm) that contains sufficient entries to cancel as many higher harmonic terms as desired. For our  $15^\circ$  stepper system with 100:1 gear ratio, we chose one compensation voltage point for every 15 degrees of motor shaft rotation, or 24 entries per revolution. Thus, our compensation table contained 2400 entries.

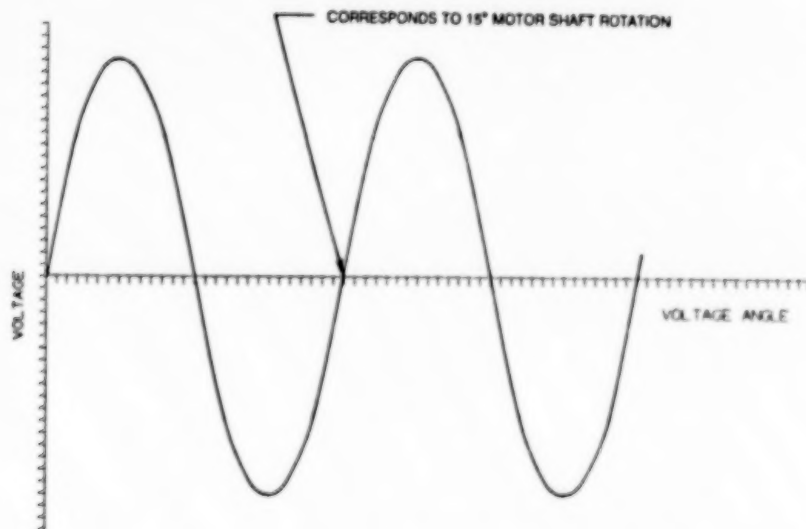


**Figure 25 Nominal Motor Input Voltage**

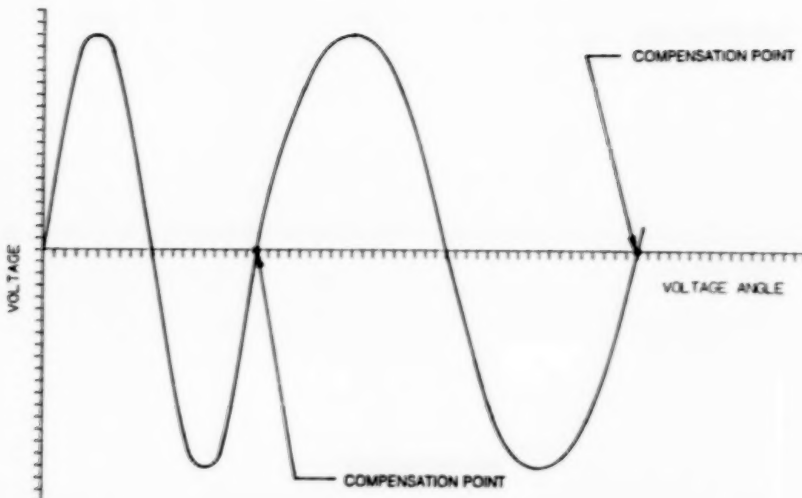


**Figure 26 Compensated Motor Input Voltage**

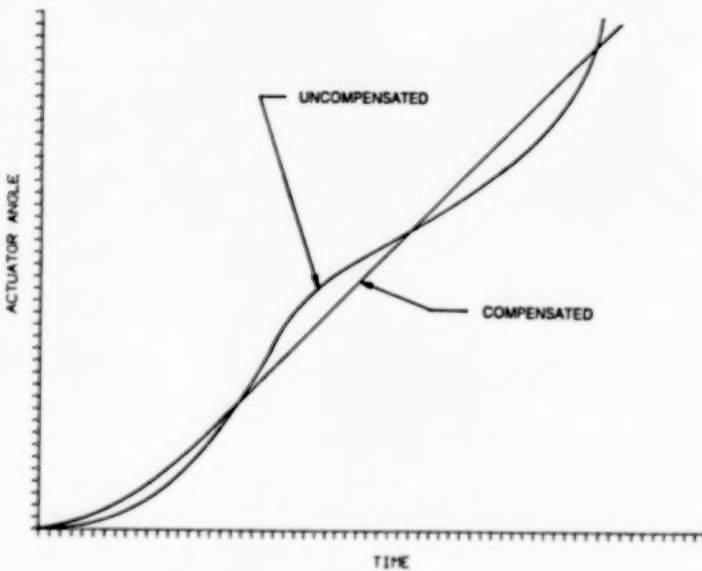


**Figure 27 Actuator Output Displacement with Time**

The need for "well-behaved" gear error that is first harmonic dominant is now evident. Canceling the higher harmonics is required above the Nyquist frequency. The alternative is a much larger compensation or look-up table. The Nyquist frequency of our system was 12 cycles per revolution of the input shaft, which meant we could cancel up to the sixth harmonic. Some harmonic drives contained a strong ninth harmonic that, with our chosen frequency, could "alias" to below the Nyquist frequency. Higher harmonics such as this were therefore filtered out from the compensation table.

This compensation scheme has worked well provided the harmonic content of gear error does not become too large. The total positional error, which translates into a torque ripple when gimballing a payload, can be typically reduced as much as 80 percent over a non-compensated system. The idea has been implemented on flight hardware to increase pointing/tracking accuracy and reduce on-orbit vibrational disturbances.

#### SUMMARY

Harmonic drive gear error was studied for the effects of unit size, tooth form, life, temperature, alignment and overload conditions. We verified that gear error decreases with larger size and always demonstrates a significant first harmonic. Life tests showed the error to be fairly stable in amplitude and phase for many million degrees of output travel. Our tests showed gear error increased slightly with temperature and misalignments between components. Overload conditions resulted in little change to gear error signatures, including tests run in the dedoidaled condition. Finally, a compensation scheme was presented that takes measured error anomalies for the gear reducers and electronically corrects for them via the motor driver.

#### REFERENCES

1. Sasahara, M., Zhang, Y., and Hidaka, T., "Vibration of a Strain Wave Gearing in an Industrial Robot," ASME Proceedings of the 1989 Power Transmission and Gearing Conference, 1989, pp. 789-794.
2. Ahmadian, M., "Kinematic Modeling and Positional Error Analysis of Flexible Gears," Clemson University research report under grant No. RI-A-86-8, 1987.
3. Harmonic Drive, Precision Reduction Gearing, Designer's Manual, Harmonic Drive Division, Quincy Technologies, Inc.
4. Harmonic Drive Gearing, S Series Design Brochure based on the IH Tooth Profile, No. HI-10-1988, HD Systems, Inc.

**PAYLOAD SPIN ASSEMBLY  
FOR THE  
COMMERCIAL TITAN LAUNCH VEHICLE**

Wilf Robinson,\* Greg Pech\*\*

**ABSTRACT**

Honeywell Inc., Satellite Systems Operations has completed a contract to design, build, and test a Payload Spin Assembly (PSA) for installation onto the Martin Marietta Titan III Commercial launch vehicle. This assembly provides launch support for satellite payloads up to 5783 kilograms (6.37 tons) and controls release, spin-up, and final separation of the satellite from the second stage. Once separated, the satellite's Perigee Kick Motor (PKM) boosts the satellite into its transfer orbit. The first successful flight occurred December 31, 1989. This paper discusses requirements, design, test, and problems associated with this unique mechanical assembly.

**INTRODUCTION**

Integration of satellite payloads onto launch vehicles always presents a challenging set of interface problems, but the challenges multiply when the launch vehicle must also spin the payload at rates up to 70 rpm before release. Spin stabilization of satellites destined for geostationary service (altitude 22,000 miles) is required in low earth orbit (altitude 100 miles) before ignition of the satellite's PKM to improve orbit insertion accuracy and thus extend the satellite's operational life. This is an adaptation of enhancing rifle accuracy with a spinning bullet.

The PSA has been designed and developed to provide structural and electrical interfaces between a satellite payload and the Titan III Expendable Launch Vehicle (ELV) and perform controlled satellite spin-up and release. In this capacity the PSA must allow communications between the satellite and the ELV in all phases of prelaunch and launch operations and support the satellite, while reacting to dynamic loads induced by ELV accelerations and acoustics. It must then perform a precision satellite spin-up and release, while exposed to mission temperature extremes. The PSA structural stiffnesses, weight, mass distribution, spin-up accelerations, interfaces, and self-generated shock loads must also be compatible with both the ELV and the satellite to ensure mission success.

Rigorous development and qualification testing performed on two PSAs contributed to a thorough understanding of system performance, successfully identified design weaknesses, and then verified the associated solutions. The result is a flight-qualified mechanism contained in a single compact package that

---

\* Honeywell Inc., Satellite Systems Operations, Glendale, Arizona

\*\* Martin Marietta, Denver, Colorado

meets all specification requirements. All functions are testable at the component and system levels, and many functions are redundant, providing a fully integrated, flexible, and reliable system.

The location of the PSA in its first launch application is shown in Figure 1. This configuration flew and performed flawlessly on the first Commercial Titan launch, December 31, 1989, when it spun the SKYNET 4A satellite to 60 rpm. The precise injection of this payload has extended the satellite's operational life well beyond the users' expectations.

## REQUIREMENTS

1. Provide interface with Titan III aft payload adapter and the upper payload PKM.
2. Provide a system that can support a range of payloads between 1814 kg (4000 lb),  $I_z = 868 \text{ kg-m}^2$  (640 slug-ft $^2$ ) and 5783 kg (12,750 lb),  $I_z = 5424 \text{ kg-m}^2$  (4000 slug-ft $^2$ ).
3. Accelerate selected payload from 0 rpm to desired speed (between 4 and 70 rpm) in 7 minutes while applying less than 13.8 kg-m (100 ft-lb) to Titan vehicle.
4. Separate the 5783-kg (12,750-lb) payload from a 12,247-kg (27,000-lb) mass at minimum velocity of 0.61 m/s (2 ft/s) with a tip-off rate not to exceed 0.10 deg/s.
5. Provide structural stiffnesses of: axial  $81.35 \times 10^5 \text{ N-m}$  ( $5 \times 10^5 \text{ lb/in.}$ ); torsional  $0.45 \times 10^8 \text{ N-m/rad}$  ( $4 \times 10^8 \text{ in.-lb/rad}$ ); moment  $0.11 \times 10^9 \text{ N-m/rad}$  ( $1 \times 10^9 \text{ in.-lb/rad}$ ).
6. PSA mass to be 195 kg (430 lb) maximum.
7. Provide redundant drive motors and electronics with bus current limited to 65 amperes per channel.
8. Environment:
  - Operational temperature of -23 to +60°C (-10 to +140°F)
  - Vacuum level of  $> 1 \times 10^{-5}$  torr
  - Random vibration at component level
  - Acoustic test at system level

An exploded view of the PSA is shown in Figure 2, and an operational mission time line is shown in Figure 3.

## DESIGN DESCRIPTION

The PSA has a basic inverted hollow cone configuration approximately 1.5 m (5 ft) in diameter and 1.22 m (4 ft) high, with flight weight just under 195 kg (430 lb). It comprises a primary and secondary structure, each with a stationary and

rotating component. This configuration meets the requirement to provide an upper interface with the PKM and a smaller diameter lower interface with the Titan III aft-payload adapter. Secondary structures are extended below this lower interface to provide internal clearance for the PKM nozzle. The PSA contains a redundant drive motor/electronics combination and a centrally mounted Slip-Ring Assembly (SRA) for signal transmission across the rotating interface. A pyrotechnically released spin V-band clamps the primary rotating structure to the stationary structure for launch. A separation V-band retains the payload to the PSA, clamping it through a Motor Adapter Ring (MAR).

Following release of the spin V-band, the rotating structure is spun for 7 minutes to the desired speed on the single "X" bearing, whose inner race housing is a ring gear to which both drive motor pinions mesh.

At operating speed, the separation V-band is released, freeing the spinning payload, which is injected into its transfer orbit with a velocity of 0.61 m/s ( $\frac{2}{3}$  ft/s) by the force exerted from four coil springs.

## **STRUCTURE**

The PSA structure consists of two main elements: rotating structure and stationary structure.

The MAR, which rotates, provides the interface with the payload PKM and a 1626-mm (64.0-in.) diameter separation V-band.

The primary rotating structure is a riveted monocoque construction comprising upper and lower rings connected by a four-piece skin.

This structure provides half the clamping interface for both the separation V-band and the spin-release V-band.

The secondary rotating structure (Figure 2) rotates with the spin bearing and provides support for payload harnesses between the rotating element of the SRA and the rotating primary structure.

The primary stationary structure provides half the interface for the spin release V-band and the bolt interface that attaches the complete PSA to the Titan Payload Adapter (PLA).

This structure also provides the outer mounting diameter for the 1181-mm (46.5-in.) diameter thin-section spin bearing.

The secondary stationary support structure (Figure 2) provides attachment for the two-brush DC Drive Motor Assemblies (DMA), the two Spin Electronics Assemblies (SEA), and the SRA.

## SPIN SYSTEM

The PSA spin system consists of the following major components: spin bearing, ring gear, two redundant DMAs, two redundant SEAs, off-load spring, and spin-release V-band (Figure 4).

This system provides all functions necessary to apply a controlled torque to the payload, which maintains constant acceleration for nearly 7 minutes, at which time operational spin rate has been achieved and stabilized. The operational sequence starts 1 hour and 4 minutes after launch. The Titan issues the command that pyrotechnically activates the two spin V-band separation bolts, releasing the band. This release allows the off-load spring to assume its natural uncompressed position, thereby elevating the primary rotating structure to provide a 2.54-mm (0.10-in.) clearance from the primary stationary structure. Two seconds after release, both DMAs are energized, allowing rotation of the structure, MAR, and payload. The SEAs control current going to each DMA such that a constant acceleration is maintained for 6 minutes and 55 seconds, at which time the command switches to a speed-control mode to stabilize rotational speed of the payload. At 7 minutes and 3 seconds, all power is removed from the system, and at 7 minutes and 4.5 seconds, the separation sequence is initiated by a command that pyrotechnically releases the separation V-band allowing the payload to be ejected.

The spin bearing is a 1181-mm (46.50-in.) Outside Diameter (OD) by 1143-mm (45.0-in.) Inside Diameter (ID) by 15.9-mm (0.625-in.) thin-section X configuration. It contains 192, 440C balls, which are separated by 16 segmented 6/6 nylon + 6% Teflon separators. Axial capacity of this bearing is 147 kN (33,000 lb). This bearing is lubricated with 3 grams of Bray® 815Z oil, which was selected primarily for its good boundary lubrication characteristics and low outgassing (less than 0.3%). The small quantity of lubricant reduced cold temperature viscous drag torque. This spin system is powered from Titan batteries that limit power to 65 amperes/channel. It was essential, therefore, as part of overall torque budget, to maintain control on bearing drag torque over the complete environmental range. A 40.7-N·m (30-ft-lb) max design goal was established.

The ring gear has a pitch diameter of 1092 mm (43.0 in.) with 215 teeth cut at a 5-Diametral Pitch (DP) and pressure angle of 20°. This gear is cut on the inner diameter of a 7075-T7351 aluminum ring forging whose outer diameter of 1143 mm (45.0 in.) provides the mounting face for the spin-bearing inner diameter. The gear is anodized, nonlubricated, and meshes with both DMA pinions to provide a 10:1 reduction in a lightweight package. No lubrication was required at the gear interface due to low contact stress (<20 ksi) and low number of cycles (<250K). Because the spin system is unidirectional, there was no backlash requirement, though backlash was measured at 0.38 mm (0.015 in.).

It was a major system requirement that the PSA contain a redundant spin-up system. Accordingly, two independent motor/electronics combinations were provided.

Each DMA is coupled into the spin system through its pinion, which meshes with the ring gear. Each DMA is independently capable of meeting mission spin requirements by applying a constant 14.37 N-m (10.6 ft-lb) of torque at a rated speed of 720 rpm at the pinion. The DMAs are 85% efficient, power being supplied from the vehicle's batteries and controlled through SEAs in the form of a high-current (up to 80 A) and a low-end voltage of 21 volts. The DMAs were designed, built, and qualified in 6 months.

Each DMA contains the following major components: roller clutch, planetary gear train, brushless dc motor, AC tachometer, and housing (Figure 5). The following paragraphs highlight the key features of each component.

The **roller clutch** is a unidirectional mechanical device capable of transmitting motor torque while decoupling the motor in the absence of torque. This decoupling allows independent operation of the redundant motors without complications and reliability problems associated with retraction/engagement devices. The clutch is a Honeywell-patented device that is designed to ensure that rollers share the load equally without producing a radial force on shaft bearings. It is designed for 827 MPa (120 ksi) Hertzian stress at a 20.3-N-m (15-ft-lb) torque load.

A highly reliable, compact 5:1 **planetary gear train** is employed for speed reduction between motor and pinion gear. The design, based on previous flight heritage, is capable of transmitting 8.12 N-m (6 ft-lb) at 3600 rpm input (sun gear). The gear train has a fixed ring gear and four planet gears connected on bearings to an output carrier. All gears are AGMA 10 quality and lubricated with Bray 601 grease.

The **brush-type DC motor** is a Honeywell-patented design employing an 8-pole, rare-earth, permanent magnet stator and wave-wound armature, commutated by eight brush pairs, connected to provide parallel paths. Winding and brush configurations are dictated by high-current power supply and provide sparkless commutation and a fault-tolerant design. The motor produces 3.5 N-m (2.6 ft-lb) of torque over the 0-3600 rpm speed range with less than 5% ripple. The limited-life application allows the use of simple and compact brush commutation. Carbon graphite brushes with molybdenum disulfide provide good performance and wear characteristics in both air and vacuum environments.

The **AC tachometer** consists of a 3-phase, 8-pole, calibrated permanent magnet generator. When combined with commutation electronics, a speed-dependent voltage is produced with <1% linearity error and <1% ripple over the -29° to +65°C (-20 to 150°F) temperature range and 0 to 3600 rpm speed range.

The two SEAs are identical and capable of meeting the PSA operational requirements independently (Figure 6); each dissipates 153 W, with a maximum input of 65 A at 28 ±3 VDC.

Each SEA provides speed control to its mating DMA, and a motor current in excess of 50 A, in order to meet worst-case mission requirements (largest payload at lowest operational temperature). Drive capability was achieved by paralleling 6 MOSFET transistors whose fast switching times minimized losses. The large voltage transients were controlled by a snubbing circuit and by adding inductance to the source lead of each transistor and referencing the gate drive to the low side of this added inductance. This arrangement provided the feedback needed to control transistor turn-off transient.

A mission profile card is used to select the desired spin rate and to establish overspeed protection as required by each payload. The SEA provides constant acceleration for nearly 7 minutes, up to any selectable speed between 4 and 70 rpm.

The SEA contains four Circuit Card Assemblies (CCA) packaged in an environmentally sealed aluminum chassis, which is 233 mm (9.2 in.) wide by 311 mm (12.25 in.) long by 107 mm (4.2 in.) high and weighs 6.6 kg (14.5 lb). The main chassis is a one-piece ribbed aluminum structure, with a pressure-relief valve activated at a differential of 24 kPa (3.5 psi).

Covers for the SEA are one-piece aluminum construction and ribbed for increased stiffness. The motor driver CCA, containing the power MOSFETs, has high thermal dissipation and is mounted directly to bottom cover for increased thermal conduction to the PSA structure.

The CCAs use multilayer Printed Wiring Boards (PWB) designed to MIL-STD-275E and fabricated from MIL-P-55110 polyimide material. Internal wiring to the MOSFETs is a challenge due to dense packaging and high currents and the use of 14-gauge MIL-W-22759/32 Tefzel®-coated wire.

The SEA operates at -23 to +60°C (-10 to +140°F) in a vacuum less than  $1 \times 10^{-5}$  torr and is packaged to withstand 20g rms random vibration and the shock environment resulting from firing the V-band pyrotechnic bolts.

A unique feature of the PSA is the offload spring. This item is a flat double-element diaphragm spring that, in its natural unclamped position, elevates the spinning portion of the PSA, and hence the payload, away from the stationary structure, providing the clearance necessary for the spin-up phase of the operation (Figures 4 and 7). For launch, this spring is deformed by the clamping action of the spin V-band, which forces primary rotating and stationary structures together. Relative structural stiffness between the offload spring and clamped primary structures also allows a major portion of launch loads to bypass the spin bearing. This offload spring connects to the rotating structure on one side and the ring gear on the other. Shims are used during assembly to set the 2.54-mm (0.1-in.) gap.

Axial stiffness of this 7075-T7351 forged offload spring was sufficient to elevate a 1814-kg (4000-lb) ground test payload without counter balancing and was designed to have moment stiffness and strength to resist payload pitching motions at 70 rpm, V-band clamping and launch loads.

Extensive analysis was completed on this vital component, which showed a worst-case safety margin of 0.02 at stress levels of 0.365 MPa (53 ksi).

The spin release V-band consists of 12 separate aluminum alloy retainers, each loosely clipped to a 2-segment titanium tension strap. It is nominally 1270 mm (50.0 in.) in diameter and weighs 21.3 kg (47.0 lb) (Figure 8).

The inner surface of each retainer is machined to a 30-degree cone angle that mates directly with each half of the spin release interface (Figure 4). The 30-degree cone angle resulted from a trade between stress levels and the need to totally preclude any self locking given the maximum coefficient of friction at this interface. Retainers were fabricated from 7075-T7351 forgings to give the strength necessary to meet the requirement that no gap ever exist at the spin interface, under worst-case combination limit loads, creep, tolerances, and environments.

The two-segment titanium strap holds the retainers in position with a 89-kN (20,000-lb) tension load derived from the two separation bolts acting through titanium trunnions, which are retained loosely in loops at the end of each strap segment. This tension load was derived from the no-gap requirement and was achieved by torquing the separation bolts alternately at increasing levels until the required load was achieved. This load was monitored by an in-series load cell, which also provided a means of monitoring load creep under all ground conditions.

Each separation bolt (Figure 9) is supplied with a screw-in power cartridge complete with electron-beam welded redundant NASA Standard Initiators (NSI). On command, the initiators fire the power cartridge, which drives an internal piston causing the bolt to fracture and the V-band to release. Each separation bolt is fabricated from 4340 steel providing the strength and no-particle generation characteristics. To ensure a smooth release, retainer clamping faces are treated with Tufran H® and the straps with Canadize® Teflon. Following release, the V-band is pulled away from the PSA with six torsion springs to prevent impact with the rotating structure and to retain the released band with the system.

One challenge associated with the sudden release of highly tensioned V-bands is dissipation of the strain energy. This was accomplished by energy absorbers that utilized compression of aluminum honeycomb as the absorbing media. Before-and-after release configurations of these devices are shown in Figures 10 and 11.

## SEPARATION SYSTEM

Following the 7-minute spin-up sequence, the PSA is required to separate the spinning payload and simultaneously inject it into its transfer orbit with a velocity of at least 0.61 m/s (2 ft/s).

Seven minutes and 4 seconds after spin-up initiation, the separation V-band is released by pyrotechnically fracturing both separation bolts. This release allows four symmetrically spaced separation springs to push the spinning payload away from the PSA and Titan III second stage. The separation spring configuration and its interface with the MAR are shown in Figures 2 and 12.

During the payload push-off maneuver, the four separation springs must impart the required velocity in a balanced manner to control tip-off rate. The four equally spaced titanium Beta C springs have a wire diameter of 10 mm (0.394 in.) and a mean diameter of 70 mm (2.75 in.). Each spring exerts an installed load of 354 kg (782 lb). To control tip-off rate, the four springs are selected for load at loaded length and then energy matched at the assembly level in a manner shown in Figure 13. All this matching would be useless, however, should one spring fail during its expected storage life. Tests were conducted on a sample set of springs, which established life-cycle margins far in excess of any projected operational use. For further security, all springs were shot-peened and dye-penetrant tested, and the open installation allowed complete visual inspection. The high installed load of these springs raised safety concerns, which were alleviated by use of spring compression tools that were always installed unless separation tests were being conducted.

The separation V-band is an identical assembly to the spin V-band except it has a larger nominal diameter of 1626 mm (64.0 in.). This separation band is closer to the payload Center of Mass (CM), used smaller retainers, and weighed 11.8 kg (26 lb). This band was tensioned by incrementally torquing its two separation bolts to achieve a measured load of 44.5 kN (10,000 lb). Load measurement, release, energy absorption, and retraction/retention were similar to that used on the spin-release V-band.

## TELEMETRY

The PSA provides the means of communication between the satellite and Titan throughout all mission phases: prelaunch to separation. The main items of interest are signals showing satellite status, connections to release the spinning separation V-band, verification of V-band release, and payload status information provided to the Titan Inadvertent Separation Destruct System (ISDS), part of the range safety requirements.

The main hardware item in this system is the SRA, which is mounted centrally in the secondary stationary support structure. Electrical harnesses from the Titan connect directly into six static connectors on the SRA, with the PSA harnesses connecting to the rotating side. These harnesses are supported by the

secondary rotating structure, travel across the primary rotating structure, and terminate in two groups of low-separation-force connectors at the PSA side of the structure/MAR interface. Harnesses from the satellite connect to the deployment side of each connector.

The SRA is a 170-channel, gold-on-gold, Bray NPT-4 lubricated unit that weighs 11.8 kg (26.0 lb) and is shown in Figure 14. Each channel has a 5-A capability, using four wipers per channel. This unit was a flight-qualified design with the exception of providing the no-interruption requirement during the launch phase, which was a flow-down requirement from the Titan ISDS system. There was no practical method of verifying such a requirement, so a specification was developed that gave any discontinuity a maximum value of 0.25 ohm with a duration of less than 100 ms and a repetition rate of greater than 1.0 ms.

The two groups of payload separation connectors are spring loaded to cancel the small pin-to-socket drag loads at separation. This was a direct result of the payload tip-off requirement. Two circuits were directly looped in those connectors to provide verification of payload separation. A single break wire was connected across each end of both V-bands to provide telemetry, which verified separation.

The tachometer in each DMA provided angular velocity information directly to each SEA to control the payload spin-up profile.

### **TEST PROGRAM**

Even though the PSA program was schedule driven, an extensive test program was planned from the beginning. The philosophy adopted called for thorough testing at component and subassembly levels, to be followed by a complete qualification and acceptance test program at the system level.

A completely functioning engineering model was designed and built in 8 months. Each component assembled into this model was thoroughly tested in its most extreme environments and then in the complete assembly. The object of this effort was to gain confidence in the design prior to the build of the qualification and flight units, to develop all assembly and test procedures, to design and build all test equipment early in the program, and to develop subcontractor capabilities in preparation for the flight build. After system testing, the engineering model was incorporated by Martin Marietta into the modal test structure.

A flight-worthy qualification model was built and subjected to the extensive test program shown in Table 1, again with each component/subassembly being qualified in its own environment prior to installation. All four flight units and their components were fabricated and tested to the acceptance test flow chart shown in Table 1. A summary of main component tests is shown in Table 2.

Test equipment for this program centered around the PSA safety fixture. All spin-up, separation, load, and (with the addition of side panels) thermal cycle

testing was conducted in this fixture. It was designed to support axial loads of up to 453,500 kg (1 million pounds), which is the theoretical buckling load of the PSA structure, as well as contain the largest spinning payload in the event of a major failure. (No such event occurred.) Pneumatic cylinders were used to axially decelerate the off-loaded or counterbalanced simulated payloads during separation testing, and a radial roller system centrally constrained the single-point suspended spinning payload during the deceleration stage. The simulated payloads were configured from a steel Center of Gravity (CG) offset drum, 1.5 m (5 ft.) in diameter and weighing 907 kg (2000 lb), to which was added a series of 2.4-m (8 ft)-diameter steel plates to attain correct mass and inertia.

Load testing used a series of hydraulic cylinders and calibrated load cells to simultaneously apply axial, shear, torsion, and moment loads. Structural stresses were converted directly from 44 strain gages, and deflections were monitored with a series of dial indicators (Figure 15). The PSA performed flawlessly after ultimate load application.

All operational testing of the PSA was performed with an automated test set using an 8088 PC system. All data was recorded on a separate disk for each test, which proved invaluable in performance diagnosis. Speed, time, acceleration, voltages, DMA current, and temperatures were routinely recorded. SRA continuity was measured during every spin-up test. During V-band releases, 500 frames/s high-speed photography was used. This initially showed some surprising motions, which caused redesigns in the energy absorber links (to prevent structural contact) and the addition of cleats to hold trunnions and V-band loops together. Damage to clips holding V-band retainers to the tension strap was a recurring problem because the V-band release dynamics were not fully understood. Replacing the light aluminum alloy clips with heavier steel clips solved the problem. Four equally spaced high-speed cameras were used to monitor separation velocity and tip-off rate.

Component testing was, for the most part, trouble free, except for the failure of the qualification unit DMA to pass insulation testing. This failure was caused by a combination of brush wear debris and wire insulation cracking. The problem was solved by adding a coat of Chemglaze® to motor windings. A failure occurred with the separation bolts when test samples did not fracture after pyrotechnic ignition; a combination of powder charge, its mix, and undercutting of the bolt caused this problem. Problems in establishment of the SRA no-interrupt requirement were extensive, as well as the equipment needed for verification; once resolved, the unit performed well.

The major difficulty during component testing was associated with the spin-bearing drag torque measurement, particularly at -23°C (-10°F). A torque budget of 41 N·m (30 ft-lb) had been established, and drag numbers as high as 136 N·m (100 ft-lb) were initially measured. The problem was due to mismatch in coefficient of thermal expansion of aluminum housings and steel bearing races. To better control these interfaces, steel races were interference fitted into their respective housings, and final grinding of the bearing raceways was completed at this

subassembly level. The heavy interference fit was set to cancel any subsequent thermal effects, thus maintaining bearing preload and its internal configuration.

Testing of the Engineering Model (EM) was trouble free, except for problems debugging test equipment and procedures (exactly the role of the EM). When qualification testing started, a major failure occurred during the third spin-up: the SEA totally failed 3 minutes after test start. All six MOSFET transistors failed due to thermal overload, which was a surprise in view of successful testing of the EM. After a lengthy investigation, it was found that during rapid switching, the MOSFETs had become unstable because the designed-in snubber circuit could not control the speed of these S-level components. The EM components were of lesser quality and therefore slower, well within the snubber circuit capabilities. This circuit was changed, and additional inductance was added in the transistor source lead. This cured the problem but showed that building EMs even with small differences can lead to surprises.

During subsequent spin-ups, problems arose with the slow, or in some cases, total lack of engagement of the DMA clutch. An analysis of the clutch geometry indicated that if all possible tolerances occurred in one direction, this problem could happen. It happened that one of the qualification unit DMAs had this combination. All clutches were disassembled, larger diameter engagement rollers were installed, and a limited Acceptance Test Procedure (ATP) was performed to get the motors back on line. The lesson here is: if it can happen, it will.

Analysis of high-speed V-band separation films showed that the energy absorbers were not being activated and were, in fact, going over center and impacting the structure. The links to these absorbers were shortened and a mechanical stop included; lighter-weight honeycomb was also used. All these measures cured this impact problem, which arose through lack of understanding the fine details of V-band dynamics. The PSA failed to attain full 70 rpm during testing in the thermal cycle environment, the problem being that six of the spin-bearing separators displaced from the bearing and wedged together. This displacement occurred because incorrect bearing retainers had been installed, which stemmed from the need to thermal fit the bearing prior to final race grind. Machine access for this grinding had made a reconfiguration of the bearing installation necessary, part of which was redesigned retainers. These were not available at assembly time, so the obsolete configuration was used against the advice of the bearing manufacturer. Schedule pressure is never a reason to ignore sound advice.

In thermal-vacuum testing, the PSA again failed to spin up during the second cold cycle after having shown nominal performance during the first cycle; however, during the first cycle, the PSA had been clamped together with the spin V-band, which, after the 1-hour soak, had been released. The second cycle configuration was, therefore, entirely different thermally and allowed a major thermal mismatch to occur. The problem should never have occurred because the unit, at that time, was in a nonoperational configuration.

The Electromagnetic Interference/Electromagnetic Compatibility (EMI/EMC) demands on the PSA were extensive, and testing was a lengthy affair. A total of 80 complete spin-ups were required to cover the entire spectrum and stay within the DMA's thermal limits. The test equipment was more of a problem than the unit.

After these major problems during qualification, all the flight units, particularly Flight No.1, were failure free. With hardware of this size, any problem consumes considerable time, and it is essential to carefully design the test equipment and overlook nothing. Problems erode schedule to a much greater extent than with smaller sized hardware, and safety is always an issue. Observing a 5783-kg (12,750-lb) simulated payload with a spin-axis inertia of  $5424 \text{ kg-m}^2$  ( $4000 \text{ slug-ft}^2$ ) spinning at 70 rpm demands respect.

### **ACKNOWLEDGEMENTS**

The authors would like to recognize the help and advice given in the preparation of this paper by the entire PSA team at Martin Marietta and Honeywell Inc. Particular thanks is given to Dianne Lindquist and Fae Weaver for their patience and efforts with the typing and publication of this paper.

TABLE 1. SYSTEM TEST

Test Requirement	Parameters	
Physical Inspection	Configuration verification	
Mass Properties	Weight and CG in three axes	
Interfaces	Verified by use of master gages	
Functional Test	Spin up to 70 rpm with 4,000-lb payload in 7 minutes; both motors nominal voltage	
Thermal Cycle	8 cycles; 0 to +130°F functional test at each temperature extreme; release of spin V-band at first low and high temperatures	Accept.
Functional Test	As above	
Performance Test	Simulated flight payload, stalled motor, release spin V-band, spin-up, release separation V-band, measure separation velocity; five additional spin-ups at maximum and minimum voltages, one or two motors	
Alignment & Balance	Measure axial and radial runouts, verify balance is within 100 oz-in.	
Functional Test	As above	
Thermal Cycle	12 cycles -10 to +140°F, otherwise as above	Qual
Functional Test	As above	
Thermal Vacuum Test	3 cycles -10 to +140°F; 10 <sup>-5</sup> torr; spin-up at each extreme; minimum payload; Release spin V-band at first low temperature	
Functional Test	As above	
Acoustic Test	Exposure to 148 OASPL	
Performance Test	As above	
Alignment and Balance	As above	
EMI/EMC	MIL-STD-1541 and MIL-STD-461C radiated/conducted emissions and radiated/conducted susceptibility	
Limit Load Test	Measure stress and stiffness at combination of axial load (76,500 lb), shear (31,900 lb), moment (1.6M in.-lb) and torsion (382,000 in.-lb.)	
Alignment & Balance	As above	
Service Life	5 spin V-band releases and spin up to 70 rpm; 3 separation releases	
Ultimate Load Test	As limit load, except applied loads were increased by 25%	
Functional Test	As above	

**TABLE 2. COMPONENT TEST**

Item	Test Summary
V-Bands	Samples of the looped ends were vibrated under tension to verify fatigue characteristics of the design as caused by the overhang of the energy absorbers. Samples were pull tested to destruction to verify design margins and manufacturing processes, particularly riveted joints.
SEA	All flight components were S-level or up-screened and certified. All boards were tested at the assembly level prior to conformal coating. Full-box environmental performance testing with health checks after each environment. The SEAs were tested to 20g rms random vibration, in thermal vac, thermal cycle, and the V-band release shock environment.
SRA	Full environmental testing under vibration, thermal vac, thermal cycle, and shock. Special monitoring to establish the no-interrupt requirement during vibration.
DMA	Insulation, full performance at worst-case voltages after vibration, thermal vac, thermal cycle, and shock as well as operation in explosive atmosphere.
Separation Bolts	Sample tested at lowest load, lowest current and lowest powder charge. All-fire/no-fire current testing.
Spin Bearing	Drag torque measured at low, ambient, and high temperatures at 70 rpm. Externally driven by a motor acting through a calibrated torque transducer.

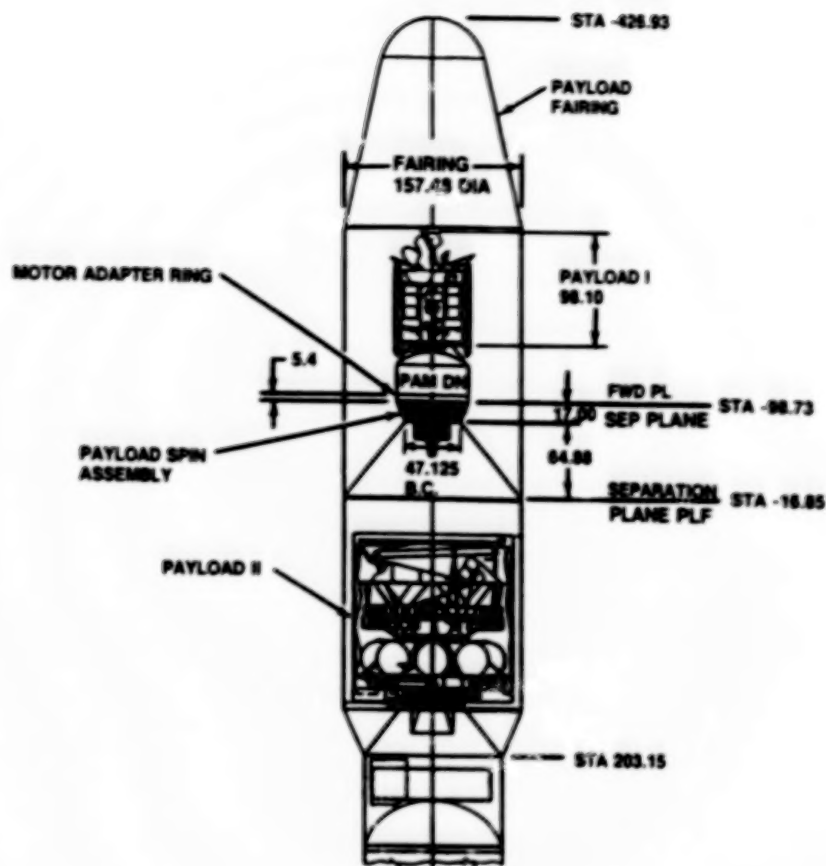


Figure 1. Commercial Titan JC SAT/Skynet Mission

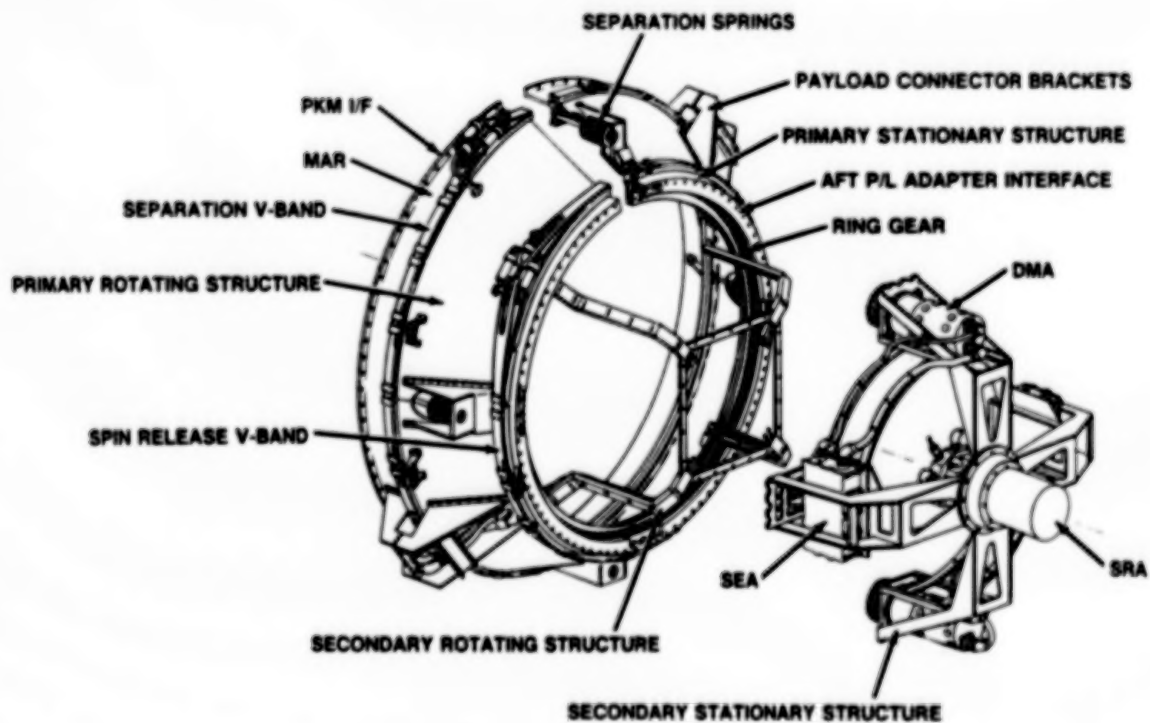


Figure 2. PSA

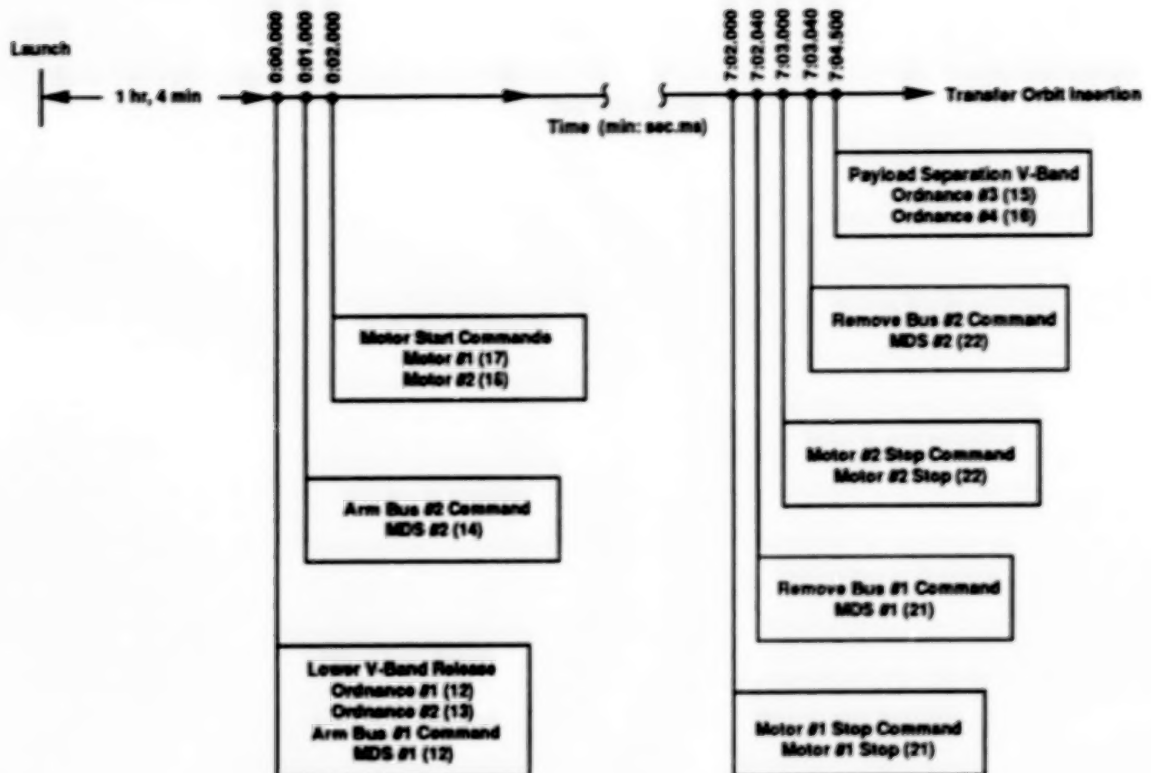


Figure 3. PSA Operation Sequence

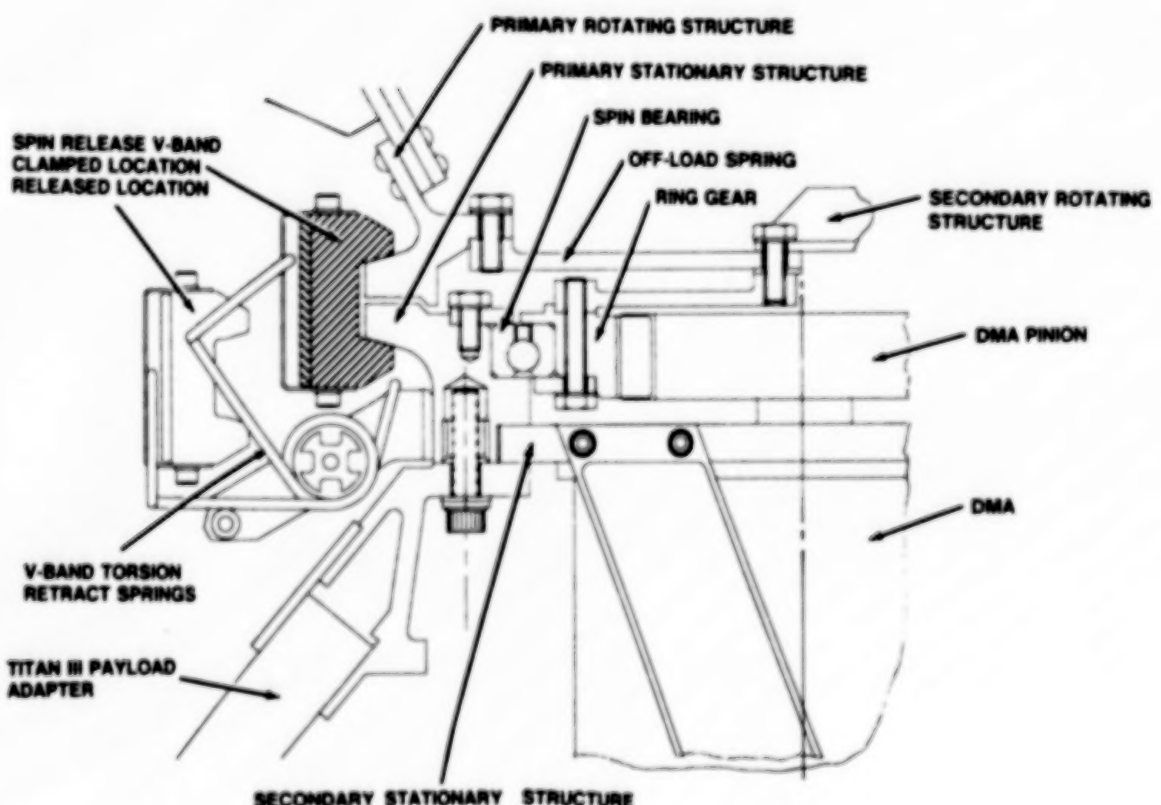


Figure 4. Spin System

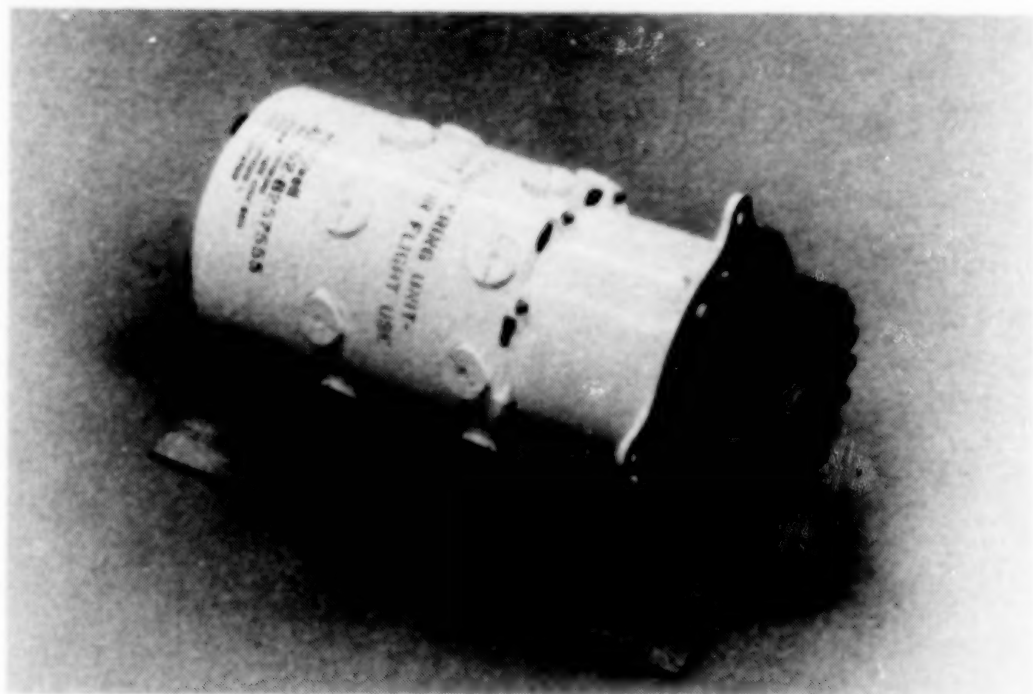
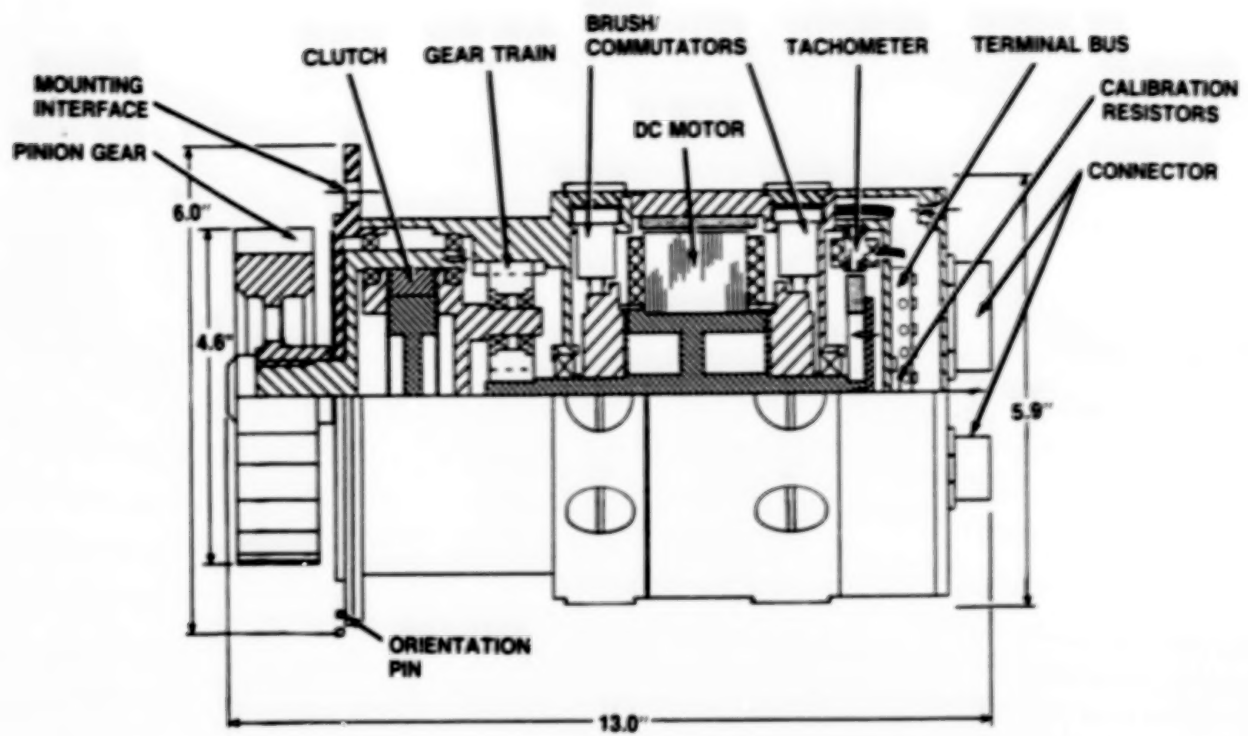


Figure 5. DMA

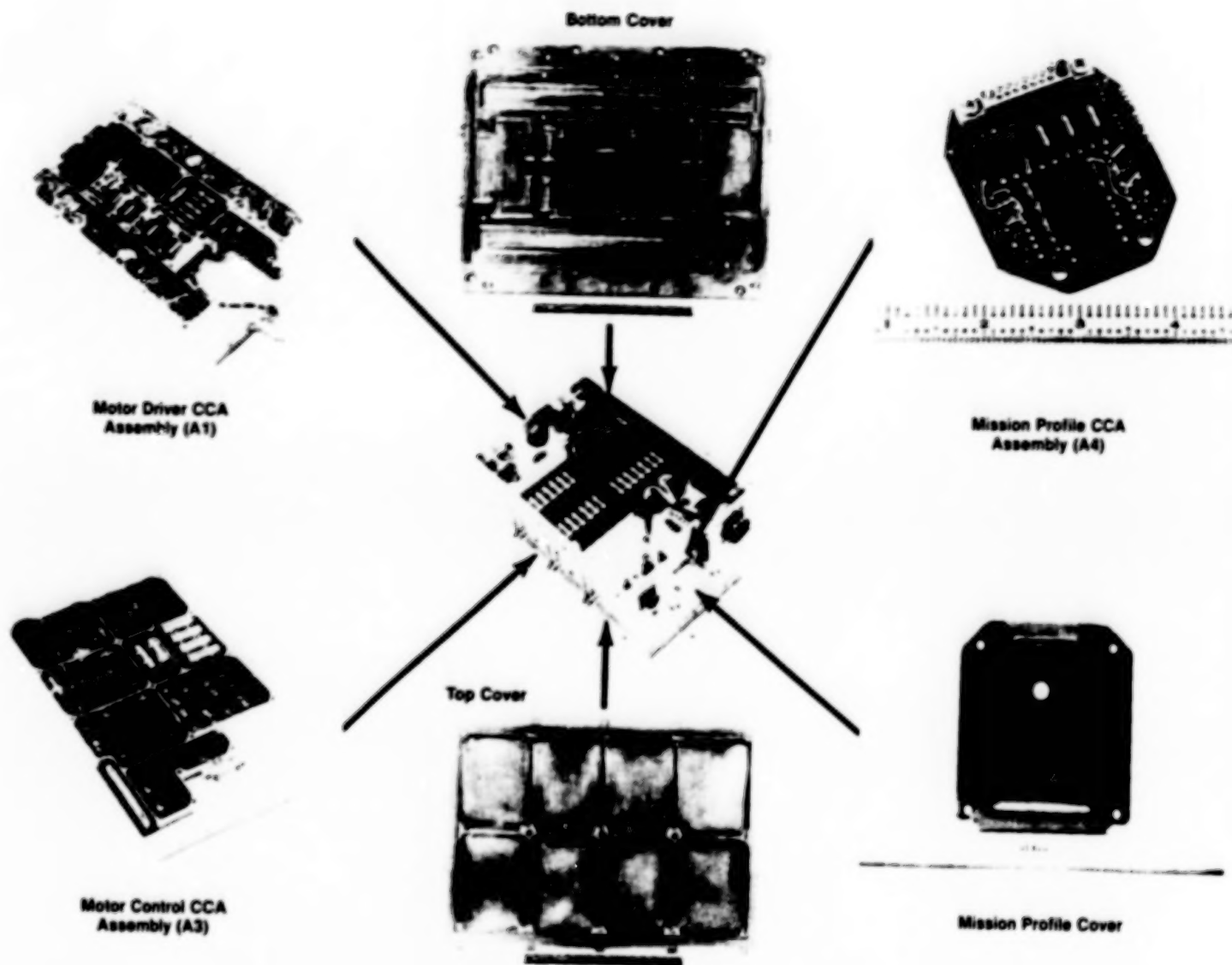


Figure 6. SEA

270

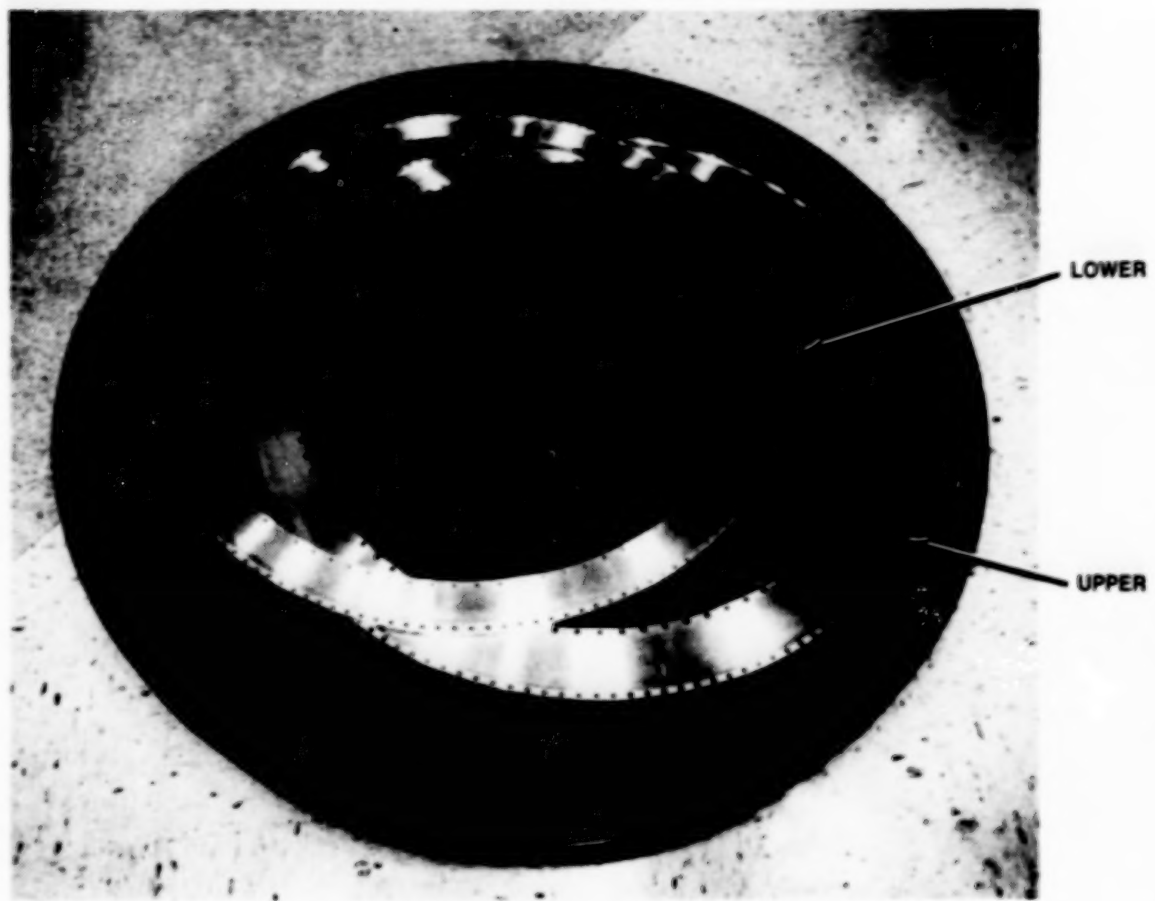


Figure 7. Off-Load Spring

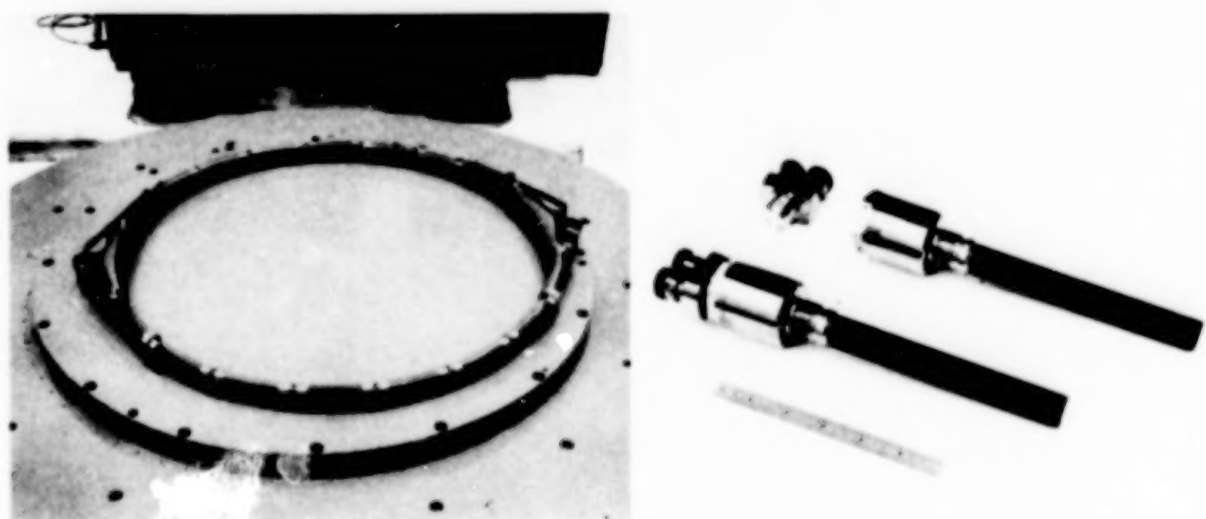


Figure 8. Spin Release V-Band

Figure 9. Separation Bolt and Pressure Cartridge

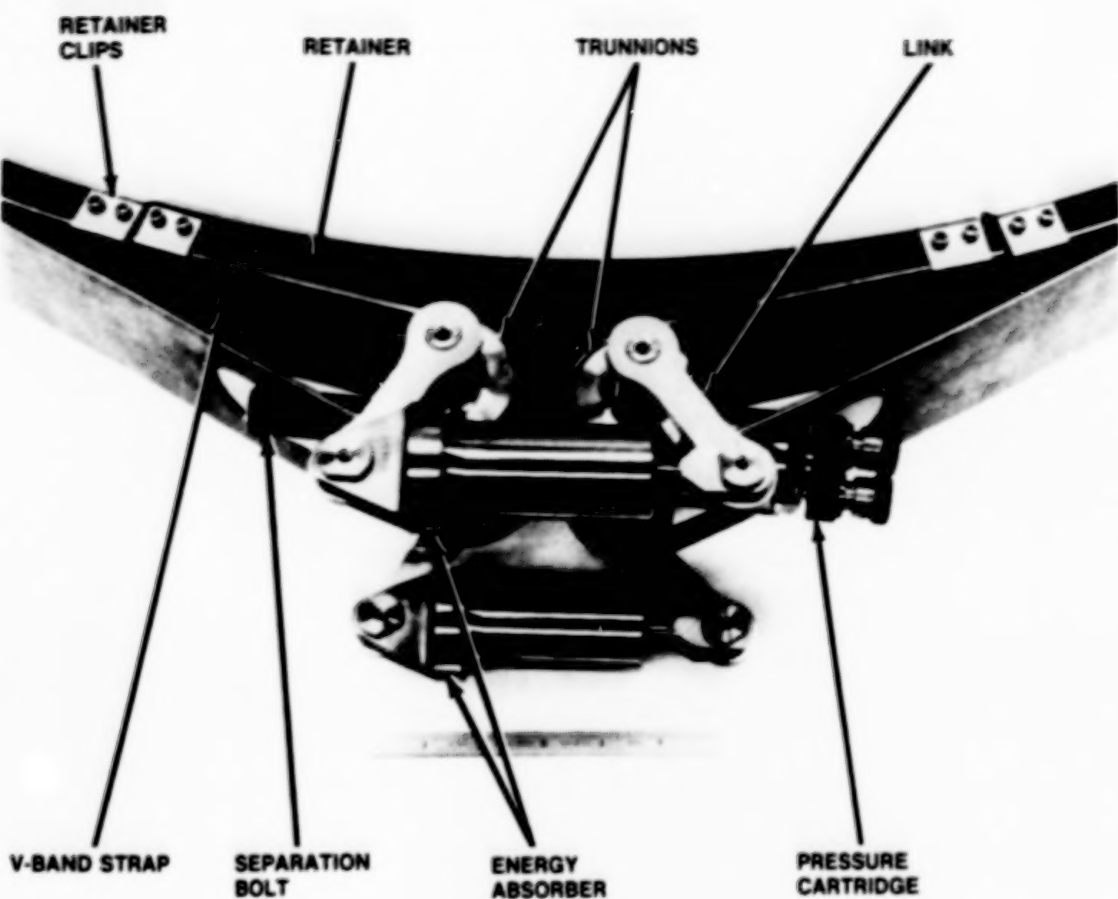


Figure 10. V-Band Energy Absorber Before Release

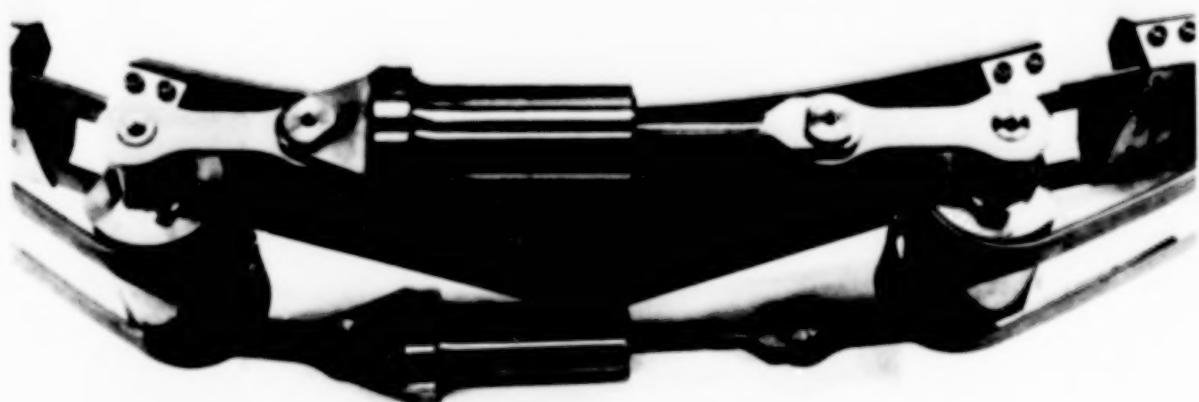


Figure 11. V-Band Energy Absorber After Release

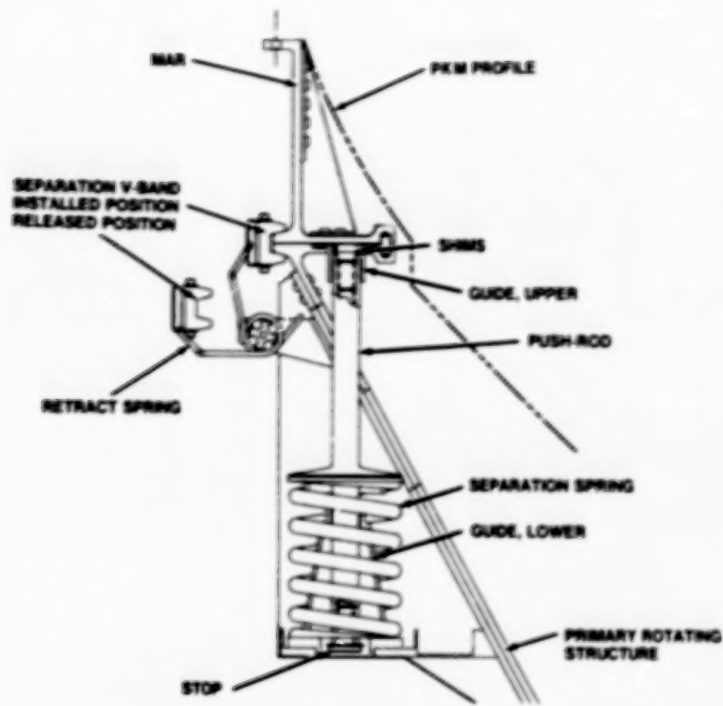


Figure 12. Separation Spring

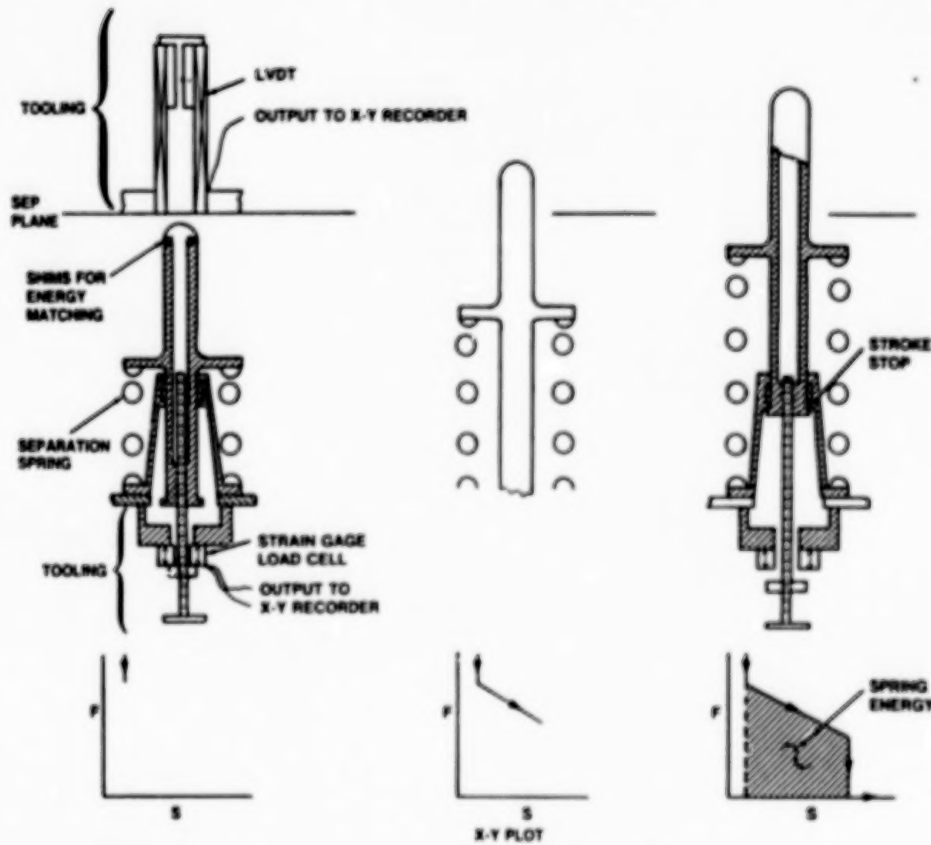


Figure 13. Separation Spring Energy Measurement

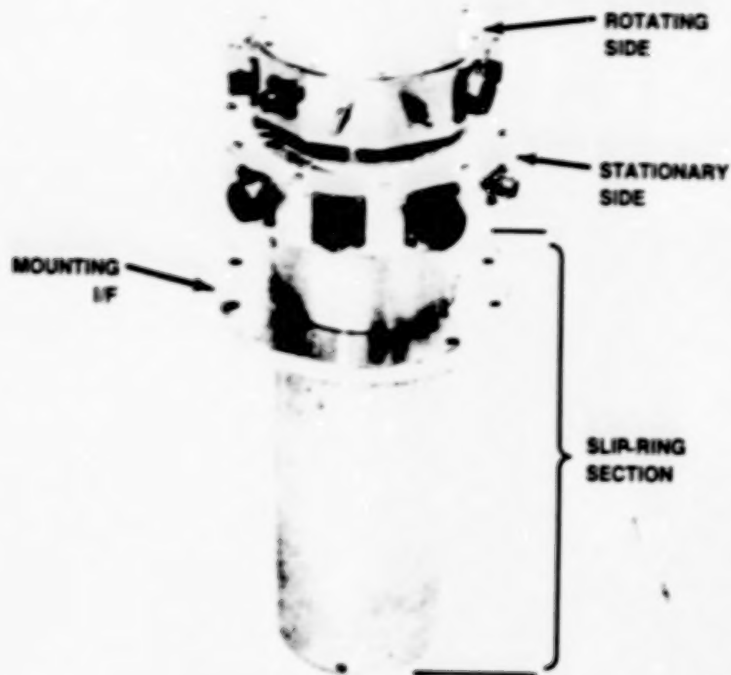


Figure 14. Slip-Ring Assembly

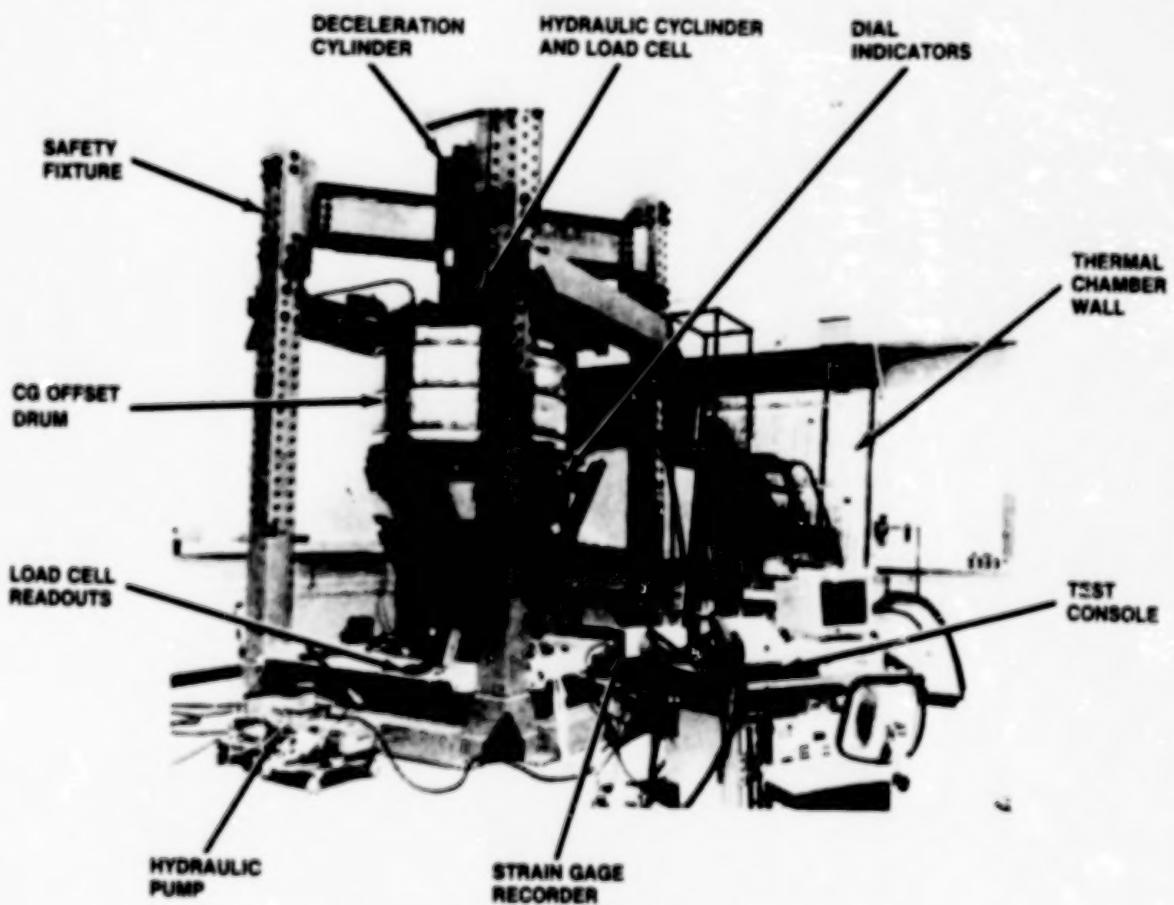


Figure 15. Test Equipment

## SMA APPLICATIONS IN AN INNOVATIVE MULTISHOT DEPLOYMENT MECHANISM

D. Stella, G. Pedrazzoli, G. Secci\*  
C. Portelli\*\*

### ABSTRACT

This paper deals with an innovative Deployment and Retraction hinge Mechanism (DARM), developed by CONTRAVES ITALIANA in the frame of a technological program which has been funded by Italian Space Agency (A.S.I.). The mechanism includes two restraint/release devices, which enable it to be stable in its stowed or deployed position while sustaining all associated loads, and to carry its payload by remote command.

The main characteristics of the DARM are as follows:

- deployment and retraction movements are spring actuated
- the available amount of functional sequences is almost unlimited
- no use of electrical motors is made.

These features were accomplished by:

- the application of a special kinematic scheme to the mechanical connection between the spring motor and the swivel head arm;
- the use of Shape Memory Alloys (SMA) actuators for both release and spring recharge functions.

DARM is thus a mechanism which can find many applications in the general space scenario of in-orbit maintenance and servicing. In such a frame, the DARM typical concept, which has a design close to very simple one-shot deployment mechanisms, has a good chance to replace existing analog "machines."

Potential items that could be "moved" by DARM are:

- booms for satellite instruments
- antenna reflector tips
- entire antenna reflectors
- solar panels.

---

\* CONTRAVES Italiana S.p.A. - Rome, Italy

\*\* Agenzia Spaziale Italiana (A.S.I.) - Rome, Italy

## INTRODUCTION

The DARM concept was established at the end of a "general purpose" Phase "A" of the ASI/CONTRAVES Italiana program. The objective of the program was to define and develop an innovative space mechanism which could have concrete applications in both the actual and future space scenario. After the general feasibility "A" phase, a Predevelopment B1 phase started where the main objective was mechanism functional concept validation. A functional model was built and successfully tested. At the end of this phase it was demonstrated that:

- a spring-actuated hinge deployment mechanism could also perform retraction movements without any configuration change, and that the high accuracy of both movements and final positions could be achieved;
- that two complete operative sequences (each including one deployment and one retraction) could be accomplished and guaranteed;
- two open points did still exist and had to be solved in the development phase in order to make the mechanism a real autonomous and high performance device:
  - to remotely actuate release of mechanisms movements
  - to increase the available amount of functional sequences.

Thus, the subsequent B2 phase – the real development one – was initiated with the final objective of closing such open points and completing design activities, up to manufacturing and testing of an Engineering Model. To this aim, a specific application of the mechanism was found, and the associated technical specifications were taken into account: the Engineering Model was designed as the Antenna Deployment Mechanism of T.L.C. antenna reflectors of ITALSAT 2 satellite.

As far as DARM peculiarities are concerned, the following can be said.

- The spiral spring motor turns a crank by applying a torque at its spin axis. The crank is connected by a sliding surface coupling to a gliph element, and causes the element to oscillate within a specific angular range. The swivel arm is coupled by a gear to the gliph. The arm's stowed and deployed positions correspond to the angular positions where the gliph inverts its angular speed. At that point, the latches of the restraint/release devices lock the arm.
- SMA actuators allow remote actuation of two important functions of the mechanism:
  - releasing of the swivel arm to let it pass from stowed to deployed position and vice versa by direct action on the latches;
  - recharging of the spiral spring motor during non-active periods, such as after any deployment when the mechanism is not required to move.

For both the above cases, SMAs were used in the design of linear actuators. These actuators are equipped with local heaters in order to perform their functions. The use of SMAs was decided as an alternative to other traditional electrical actuators after a trade-off study, and the final choice was justified by consistent mass, reliability, and low complexity advantages. SMAs are conveniently used in a wide range of civil and industrial applications (thermal valves,

heat sensitive links, wire detection systems, control systems, connectors, etc.), but recently, European and non-European symposia on the subject of mechanisms have demonstrated the increasing interest also of the Space Community for such innovative and versatile materials.

A short technical description of the DARM Engineering Model, with special emphasis on SMA actuators, and a synthesis of development tests is presented, where the features of those innovative elements are well highlighted.

## TECHNICAL DESCRIPTION

The DARM Engineering Model is shown in Fig. 1. Its assembly drawings, as well as its main subdevices, are shown in Fig. 2.

The mechanism is constituted by:

- a Main Structure (M.S.) (see Fig. 3), which includes external mechanical interfaces to the satellite support wall, and which supports all other elements;
- a Swivel Head Arm (S.H.A.), which includes external mechanical interfaces to the payload (antenna reflector arm) and is pivoted to the M.S.;
- Functional Elements.

DARM can be considered as a modular mechanism, where the main functions are accomplished by means of physically separable elements, or elements groups, even though the Engineering Model has a particular compact integrated configuration.

The principal modules are:

- Hinge Trunnions (M.S. and S.H.A.)
- Spring Motor (for deployment and retraction) (S.M.)
- Motion Inversion Device (including giph and crank) (M.I.D.)
- Spiral Spring Recharge Device (S.S.R.D.)
- Two Restraint/Release Devices (R./R.D.)

The first four modules constitute the mechanism Main Body, while the two R./R.D.s perform an independent function and would be capable of doing so even if they were mounted far from the Main Body itself. For instance, the Main Structure could be "split" in three parts with minor design changes (see dotted lines in Fig. 2), and the R./R.D.s could be accommodated according to a different layout (the Probe Section of these should be mounted on the payload structure in this case).

### Spring Motor and Motion Inversion Device

Only a few words will be said about this traditional part of the mechanism.

Energy for both deployment and retraction movements is stored in a preloaded (Teflon coated) spiral spring. The spring torque is transmitted to the S.H.A. by means of a kinematic

chain, which is capable of inverting the arm rotational movement every 90 degrees. The kinematic chain is inspired by a classical mechanical system: the Fairbairn's Guide. The minor changes which were introduced in such a basic system are described in Fig. 4.

The S.M. and M.I.D. are supported by a separate lightweight structure which is fixed sideways to the M.S. Minor changes to this separate structure enable the S.M. and the arm hinge axis to be directly connected. In this case, the M.I.D. cannot be integrated, and the mechanism would become a "one shot" machine.

### Spiral Spring Recharge Device

Figure 5 shows in detail all the parts that constitute the device. The S.S.R.D. is the device that eliminates almost entirely the problem of the limited number of maneuvers of DARM by recharging the spiral spring during idle times. By taking advantage of the SMA's characteristics, two linear actuators can be created which allow both the translation along its own axis and the rotation of a front-toothed wheel. The synchronization and composition of the two movements can be exploited to produce the rotation of the wheel driven by the front-toothed wheel. This wheel, which is connected mechanically with the spiral spring, can therefore cause the spring to recharge partially. The S.S.R.D. can guarantee a recharge movement of 80 degrees per cycle. Since, in the case of the DARM, the spiral spring has a preloading of 1400 degrees, i.e., about four complete rotations on the axle, obviously it will be necessary to put the S.S.R.D. into motion several times in order to achieve complete recharge. The spiral spring does not have to be completely unwound in order to be recharged. In fact, it can be recharged in any position between 0 (zero) and 1400 degrees, and in this way, the consecutive sequence of the number of cycles to be carried out with the recharge mechanisms can be reduced. The elements created from the SMA operate by means of heating, obtained by electrical resistances in contact by conduction with the elements.

This device was conceived as an option, to a certain extent. The DARM technical requirements included a minimum capability of two deployments and two retractions as the functional performance. The DARM S.S.R.D. can be thus considered as a Functional Model (not yet optimized) to be used for concept validation aims (which were successfully achieved). For this reason, such a device was not included in the mechanism test configuration during environmental tests.

### Restraint / Release Devices

The two R./R.D.s perform the following functions:

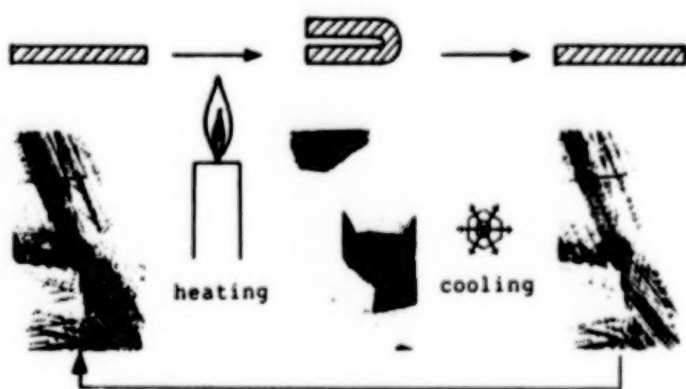
- carry end stops for deployment and retraction of the Arm and/or the associated payload
- carry latches to restrain the Arm and/or the associated payload during launch and in orbit
- sustain launch and operative loads
- release the Arm, allowing it to deploy or to retract

Each R./R.D. includes two fixed subdevices, which can be fully integrated in the M.S., or separately mounted. Two "travelling" subdevices, which carry the probes and must engage in the fixed subdevices at the end of deployment or retraction, can be fixed to the Arm or to an appropriate region of payload structure. Each fixed subdevice includes a reusable release actuator. Several kinds of such actuators are known, and most of them are based on electric motors or magnetic devices. These known actuators have several drawbacks especially related to their excessive mass and size, which are very important parameters in space applications. The known actuators have also shown poor performance when a relatively high force is required to actuate the R./R.D. The S.M.A.-based DARM release actuator overcomes these problems, with its lightweight and small size characteristics and its good performance over repeated operations.

A complete R./R.D. is shown in Fig. 6. With reference to the figure, the operation of the actuator is described. When desired, the power source powers the resistance member (12), which heats the metal strip (10). When the metal strip reaches a selected temperature, it bends, as schematically shown by dashed lines in the drawing, and the pusher member (13) pushes the cam member (7) rotating the lever (5). The ledge (8) is thus disengaged from the hook (4), and the latch moves to the release position, allowing the moving arm to rotate to deploy the structure. When the metal strip (10) cools off, and the electrical resistance is not being powered anymore, the strip returns to the substantially straight position. The strip (10) can repeat this operation several times without any degradation of its physical and geometrical characteristics.

### SMA ACTUATORS

The Shape Memory Alloys are able to carry out complicated and versatile motions, achieved only by heating and cooling, without application of any external stress. It is important to know that no lubrication is necessary to obtain an SMA actuator movement, i.e., friction and wear are absent. The shape memory effect has its origin inside the alloy itself. It is caused by a "martensitic" phase transformation occurring at fixed temperatures. Three different characteristics of shape memory behavior are known, whereby the so-called "two way effect" has to be used for actuators. The effect can be represented as in the scheme here below.



Two-Way SMA Effect

The two-way effect is imparted by plastic deformation of the element at low temperature. When subsequently heated above the transformation temperature, the element returns almost completely to its initial shape. All kinds of motion can be achieved: bending or torsion, expansion or contraction. During motion, the element is capable of exerting a force (or torque). Both force and stroke are controlled by the dimensions of the element. The trigger temperature can be adjusted by the manufacturer quite accurately by controlling the percentage of the alloy constituents. The effect can be repeated many times. Two different linear SMA actuators are present in the DARM: the first one is a strip, and is used in the R/R.D.; the second one is a helical spring and is used in the S.S.R.D.

## TESTS AND RESULTS

The test plan to which the DARM Engineering Model was submitted included both functional/performance and environmental tests. Besides the above tests, an additional set of tests was specifically addressed to investigate the SMA actuator behavior. In particular, it was decided to submit the release actuator (SMA strip) to the following tests:

- life cycle test,
- functionality at extremely low temperature tests,
- limit performance test.

### Test on the Mechanism

All test results are presented below, in the same sequence in which they were carried out.

#### MOTOR SPRING TORQUE

- MAXIMUM WINDING ANGLE : 1548°
- SPRING TORQUE : 0.48 Nm
- SPRING STIFFNESS :  $K = 0.0177 \text{ Nm / rad}$

#### TORQUE MARGIN ( T.M. )

- 1st PHASE - MINIMUM T.M. : + 280%
- 2nd PHASE - MINIMUM T.M. : + 80%
- 3rd PHASE - MINIMUM T.M. : + 205%
- 4th PHASE - MINIMUM T.M. : + 35%

#### KINEMATIC PARAMETERS

	DEPLOYMENT/ RETRACTION DURATION TIME	MAXIMUM ANGULAR SPEED	MAX MOMENTUM	FINAL SPEED
1st PHASE	11 s	0.25 rad / s	5.5 Nms	0.14 rad / s
2nd PHASE	19.5 s	0.11 rad / s	2.42 Nms	0.05 rad / s
3rd PHASE	12.5 s	0.20 rad / s	4.4 Nms	0.13 rad / s
4th PHASE	25 s	0.08 rad / s	1.76 Nms	0.04 rad / s

MOMENT OF INERTIA  $I = 22 \text{ Kg m}^2$

**ACCURACY AND REPEATABILITY  
OF DEPLOYMENT ANGLE**

REQUIREMENT	MEASURED VALUES	
	1st DEPLOYMENT	2nd DEPLOYMENT
ACCURACY	$\leq \pm 54''$	+7.95''      +12.4''
REPEATABILITY	$\leq \pm 36''$	-16.45''      -17.4''

**FUNCTIONAL TESTS IN VARIOUS THERMAL/PRESSURE CONDITIONS**

ENVIRONM. CONDITIONS	POWER SUPPLY	CURRENT ("MINCO" HEATERS)	CONSUMED POWER	ACTUATION TIMES	CONSUMED ENERGY
T = +20°C P = 1 bar	30V	1.8A	54W	20 s	1080 J
T = +50°C P = 1 bar	30V	1.8A	54W	17 s	918 J
T = +50°C P = 10 <sup>-6</sup> bar	30V	1.8A	54W	14 s	756 J
T = -50°C P = 1 bar	30V	1.8A	54W	75 s	4050 J
T = -54°C P = 10 <sup>-6</sup> bar	30V	1.8A	54W	40 s	2160 J

**RANDOM VIBRATIONS**

	G RMS
"X" AXIS	22.03
"Y" AXIS	23.4
"Z" AXIS	25.62

DURATION : 2 MINUTES  
RESULT : NO DAMAGES AT ALL

**STIFFNESS**

STIFFNESS :	MEASURED VALUE
RADIAL	$0.26 \times 10^8 \text{ N/m}$
AXIAL	$0.19 \times 10^7 \text{ N/m}$
ON STATION : AGAINST "LATCH"	$0.18 \times 10^6 \text{ Nm/rad}$
ON STATION : AGAINST "STOP"	$0.39 \times 10^5 \text{ Nm/rad}$

**LATCH-UP SHOCKS AT INTERFACE ( AVERAGE VALUES )**



	SHOCK IN "X" DIRECTION (g)	SHOCK IN "Y" DIRECTION (g)
1st PHASE	3.86	3.45
2nd PHASE	1.24	1.38
3rd PHASE	3.29	2.59
4th PHASE	1.03	1.16

**STATIC LOADS**

- 1) 1200 N RADIAL
  - 2) 1500 N AXIAL + 1000 N RADIAL  
( SIMULTANEOUSLY )
- RESULTS : NO DAMAGE AT ALL

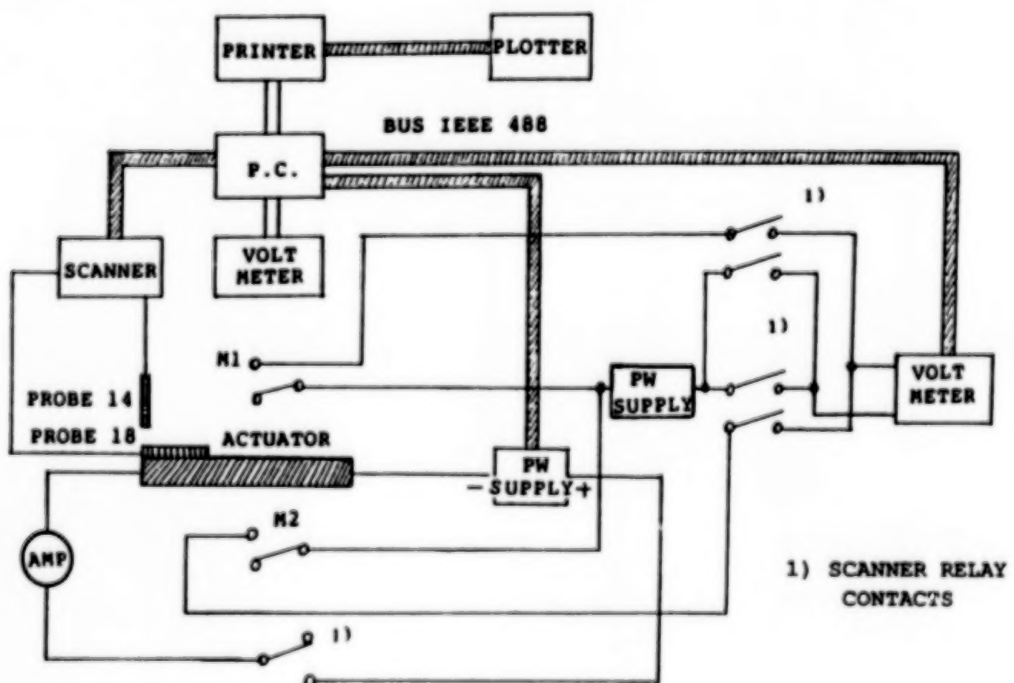
## Tests on SMA Actuators

The SMA strip underwent all the functional and environmental tests to which the whole DARM was subjected. After successful completion of such tests, two strips underwent additional tests with the following results.

### Life-Cycle Test

- Number of cycles: 400
- Every single cycle had the following sequence:
  - 1: external temperature stabilization
  - 2: heating up to stroke completion (indicated by a position sensor)
  - 3: stop heating
  - 4: natural cooling down to reverse stroke completion (indicated by position sensor)
- Configuration: actuator without any significant load
- Monitoring and commands:
  - active and reverse stroke associated duration
  - strip external surface temperature (with maximum temperature limitation)
  - ambient temperature.

The test scheme is shown below:



Note: The test setup is shown in Fig. 7, and the test results are shown in Fig. 8.

### Low Temperature Test

- Ambient temperature stabilization at -150 C degrees.
- Heating up to active stroke completion (visually checked by means of a millimetric reference).
- Monitoring of the strip external surface temperature.
- Natural cooling down.

The test setup is shown in Fig. 9, and the test result is shown in Fig. 10.

### Maximum Load Test

Many functional tests were performed on the test item after completion of the Life Cycle and Low Temperature tests using increasing loads in order to verify the SMA strip function capability and to find its "ultimate load." The test setup is shown in Fig. 11. The test results are summarized in the table here below.

Test Label	Load [N]	Displ. [mm]	T <sub>amb.</sub> [°C]	Stroke Duration Rot. Rev.	Voltage [V]	Current [A]
1	0	7	20	34	270	24
2	5	"	"	"	"	"
3	10	"	"	"	"	"
4	15	"	"	"	"	"
5	20	"	"	"	"	"
6	25	"	"	"	"	"
7	30	"	"	"	"	"
8	35	"	"	"	"	"
9	40	"	"	"	"	"
10	45	"	"	"	"	"
11	50	"	"	"	"	"
12	55	6.9	"	"	"	"
13	60	6.8	21	"	"	"

### CONCLUSIONS

The DARM Engineering Model has successfully passed a severe test program, which has demonstrated the mechanism concept and functional capability to fulfill a spread set of technical requirements. It can be considered as a reference point in the general scenario where deployment and retraction capabilities are required to a hinge mechanism, and when such a mechanism must have a simple and reliable configuration and must not necessarily require electrical power to perform its main functions.

DARM includes innovative SMA actuators for its release and self-recharge functions. The specific tests which have been performed on such extremely simple actuators have highlighted their high reliability and their capability to perform their function with:

- very good repeatability during their expectable life (i.e., one hundred cycles),
- acceptable performance variations at the end of very long life (four hundred cycles),
- peculiar advantages (with respect to other actuators) at very low temperatures (no friction),
- high adaptability to mechanical overloading (about ten times the nominal load without any permanent damage).

#### REFERENCES

1. R. G. Hostenkamp, "Features of the Solar Array Drive Mechanism for the Space Telescope." Dornier System GmbH. II European Space Mechanism & Tribology Symposium, Meersburg, FR Germany, 1985.
2. D. Stella, M. Simonelli and C. Piredda, "DARM: a new Deployment and Retraction Mechanism which doesn't need electric power." Contraves Italiana S.p.A. III European Space Mechanisms & Tribology Symposium, Madrid, Spain, 1987.
3. K. Escher and E. Hornbogen, "Shape Memory Alloys for robot grippers and mechanical hands." Ruhr-Universitaet Bochum. IV European Symposium of Space Mechanisms & Tribology, Cannes, France, 1989.

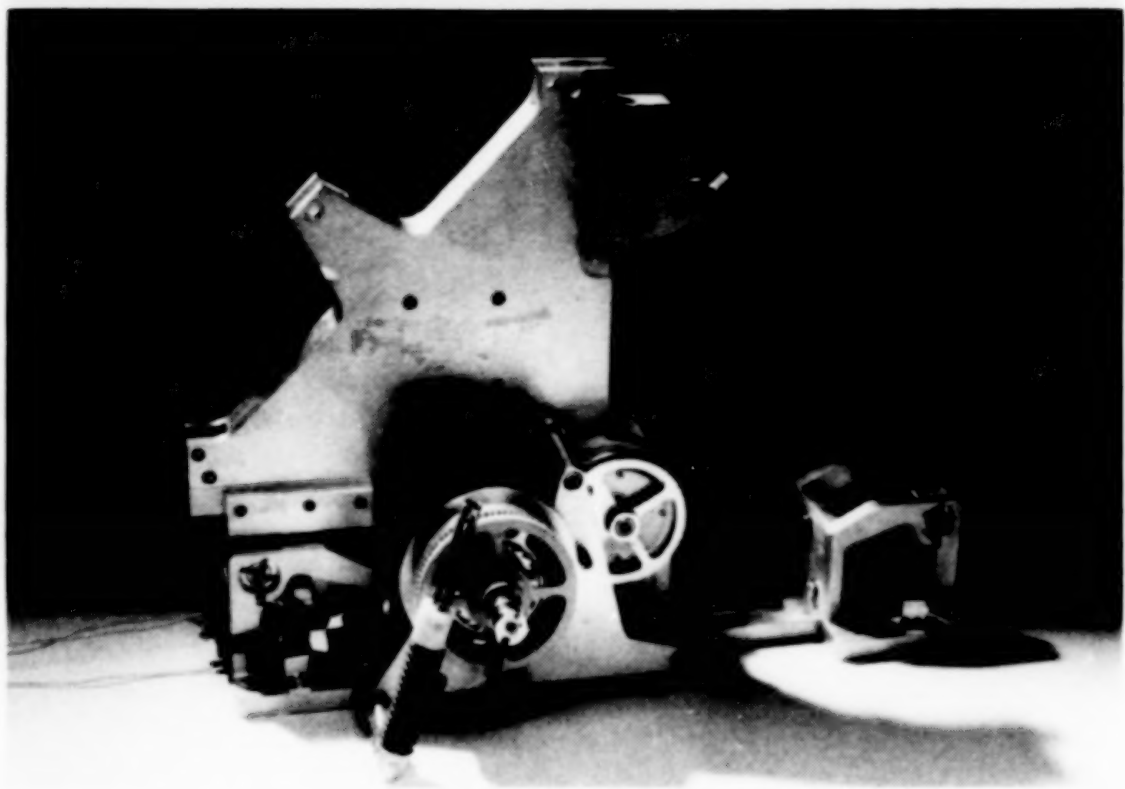


Fig.1 - DARM Engineering Model

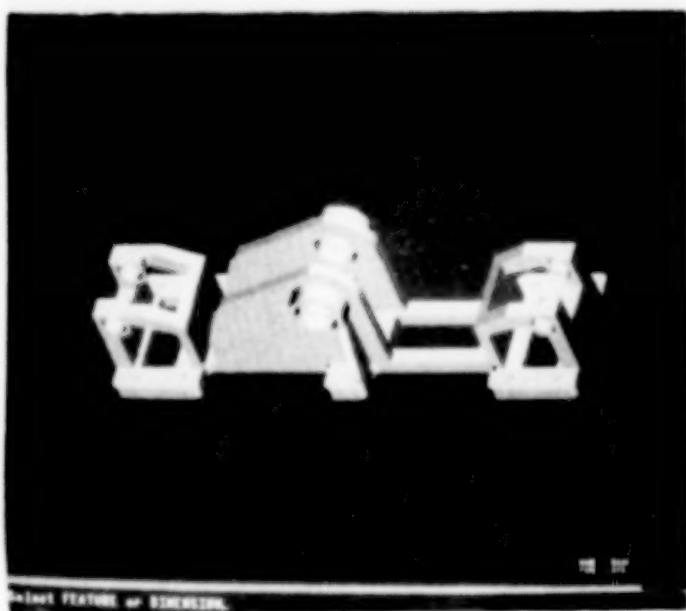


Fig.3  
Computer generated  
image of Main  
Structure (M.S.)

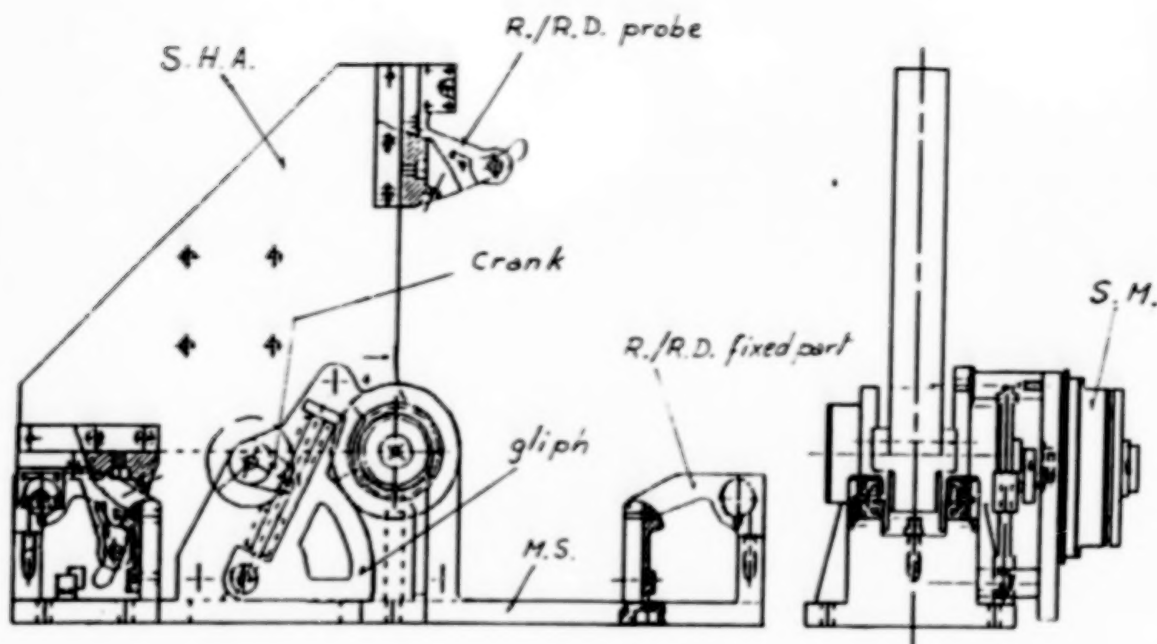


Fig.2  
DARM Ass.y  
drawings

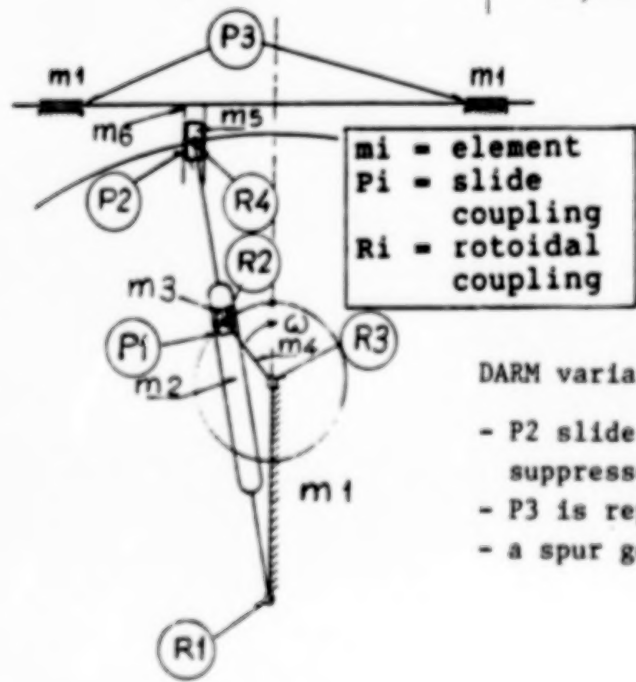
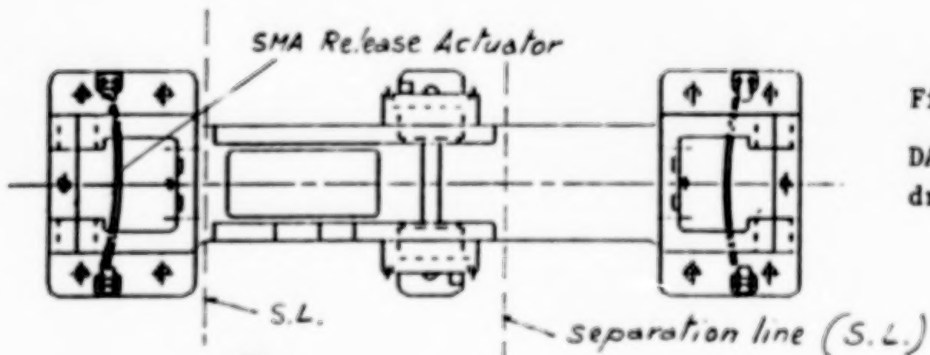
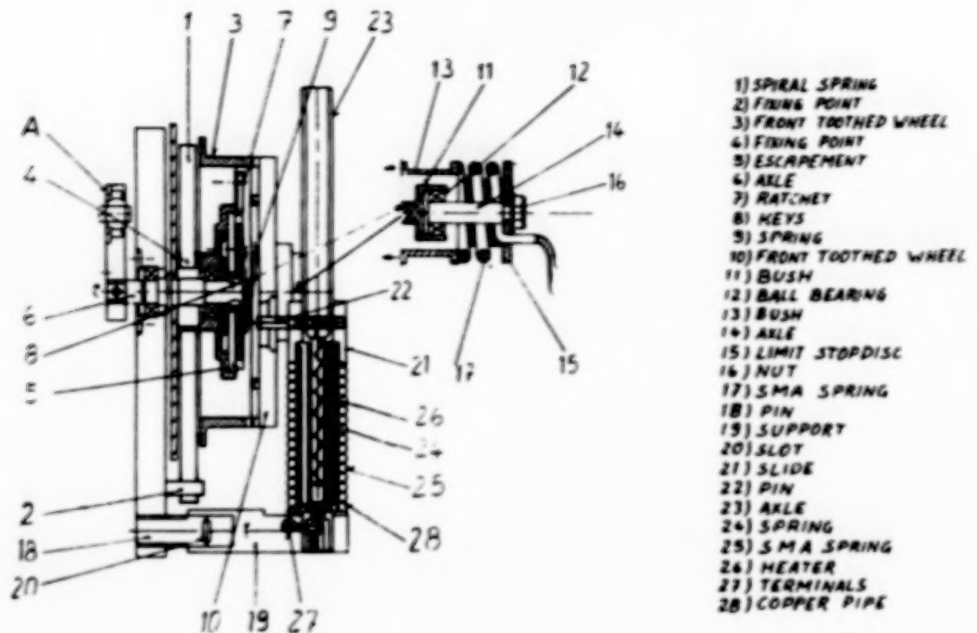
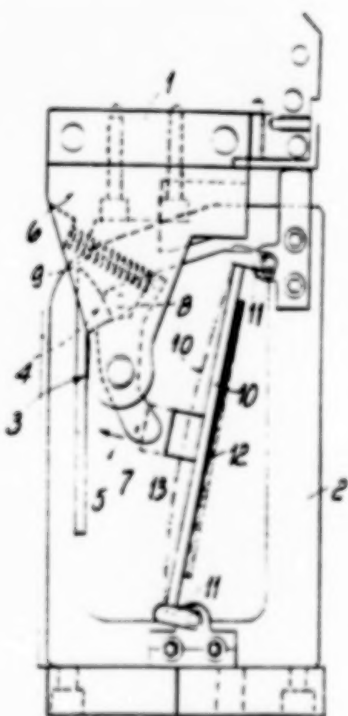


Fig.4  
The Fairbairn's Guide



**Fig.5**  
Spiral Spring Recharge Device (S.S.R.D.)



**Fig.6**  
Restraint/Release Device (R./R.D.)

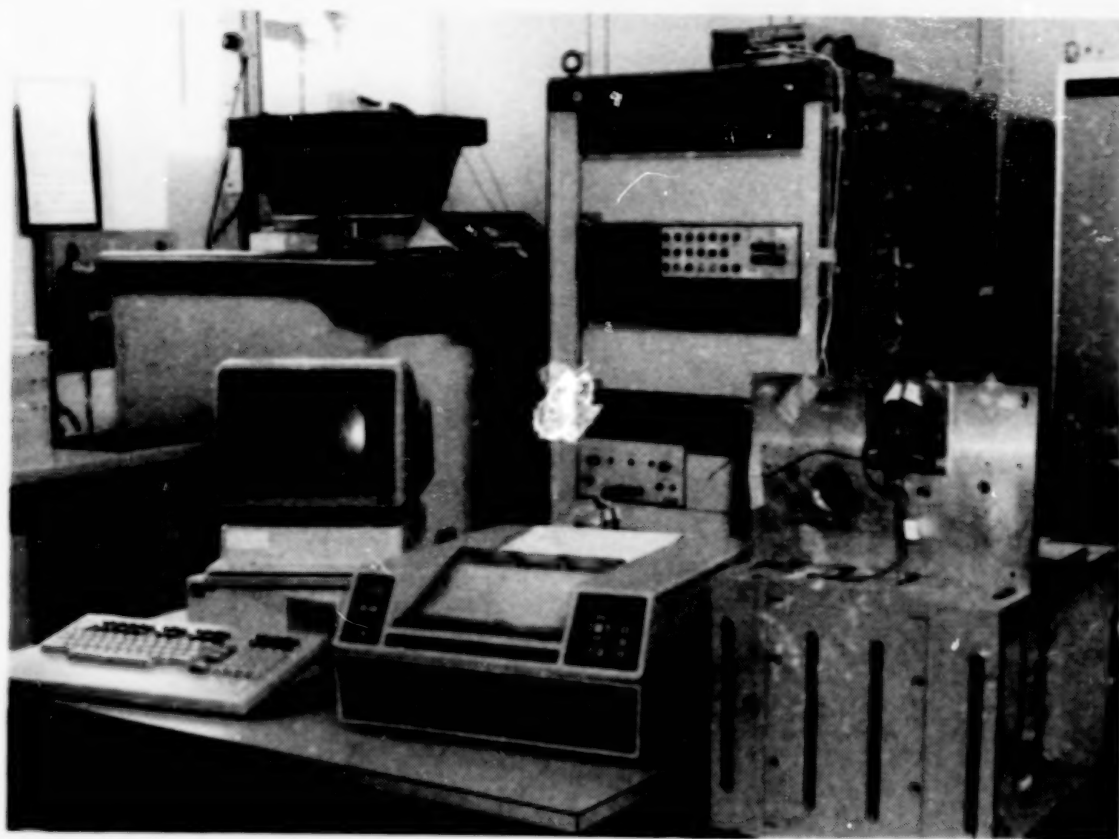


Fig.7 - Life Cycle Test set-up

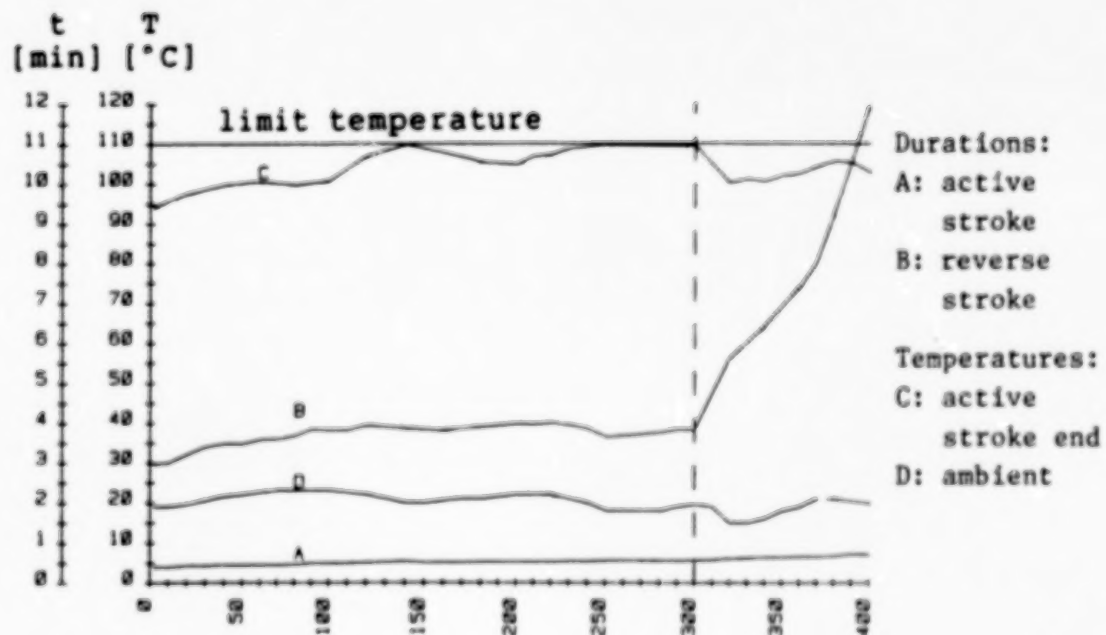


Fig.8 - Life Cycle Test results

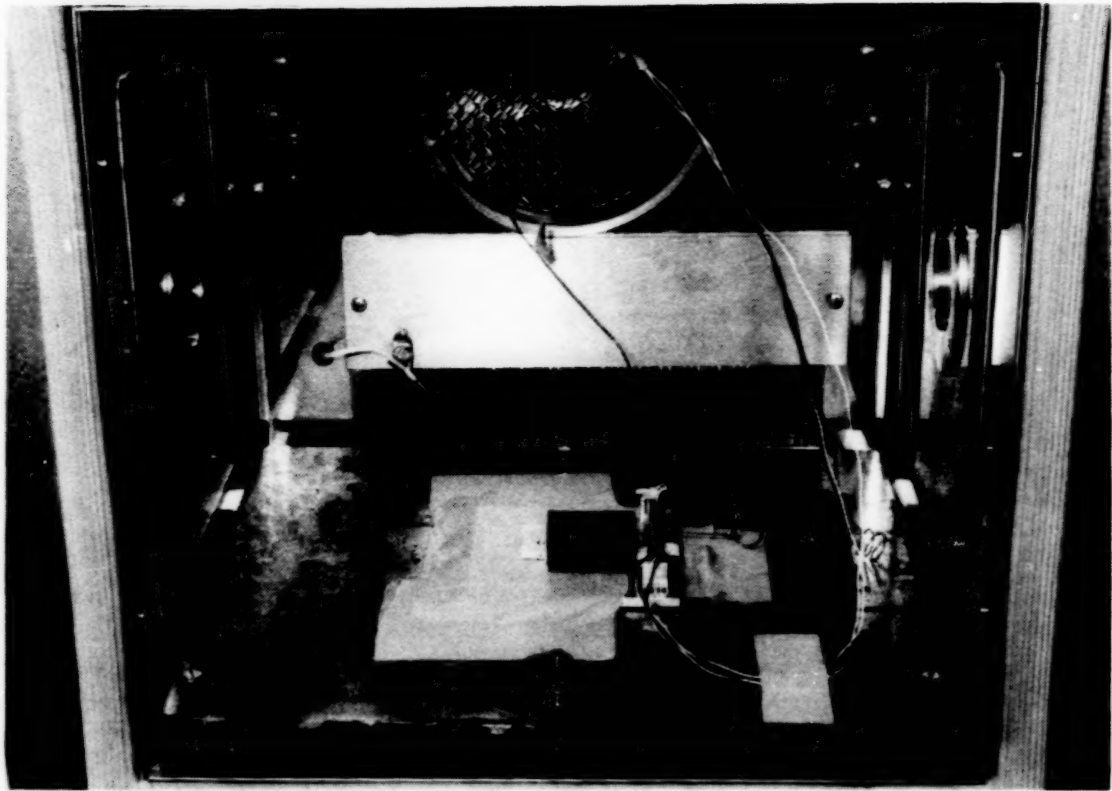


Fig.9 - Low Temperature Test set-up

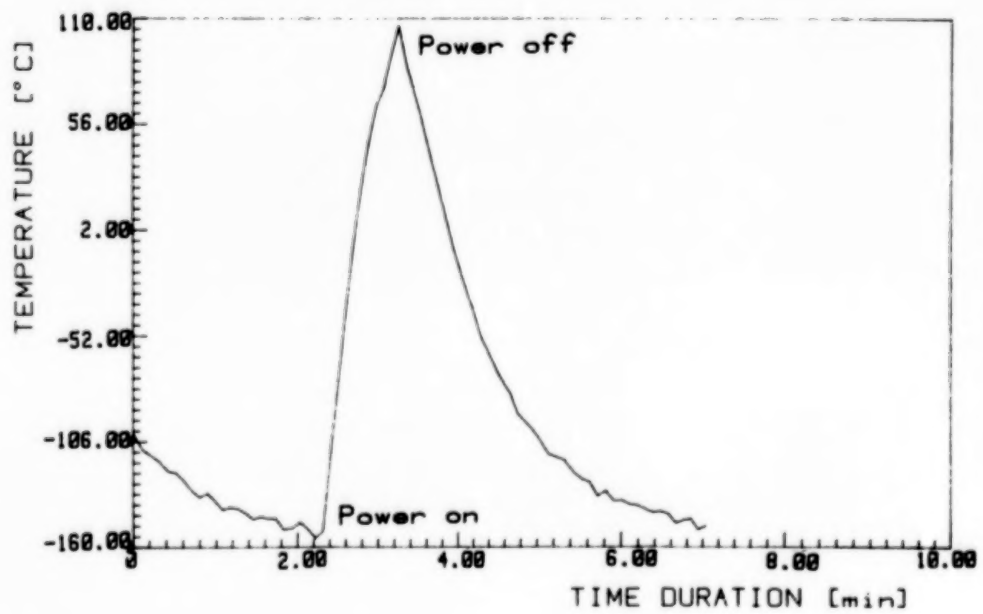


Fig.10  
Low Temperature Test results (strip temp.)

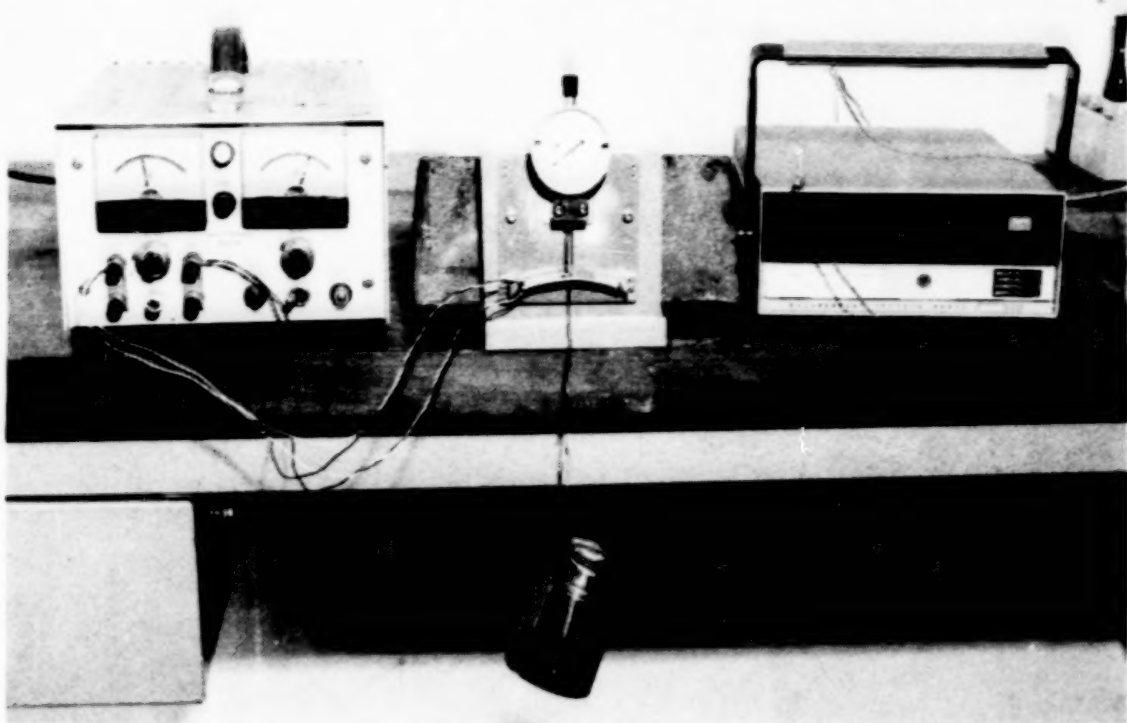


Fig.11 - Maximum Load Test set-up

# SPACE SHUTTLE HOLDDOWN POST BLAST SHIELD

F. B. Larracas\*

## ABSTRACT

This paper describes the original and subsequent designs of the Solid Rocket Booster/Holddown Post blast shield assemblies and their associated hardware. It presents the major problems encountered during their early use in the Space Shuttle Program, during the Return-to-Flight Modification Phase, and during their fabrication and validation testing phases.

The actions taken to correct the problems are discussed, along with the various concepts now being considered to increase the useful life of the blast shield.

## INTRODUCTION

The exhaust plume of the SRB's used during Space Shuttle launches consists of hot gases and aluminum oxide particles and has the effect of a huge sandblaster. Launch hardware such as the Holddown Post System, which serves as a support stand and restrains the Space Shuttle System during Space Shuttle main engine thrust buildup, sustains extensive damage during launch. If unprotected, the Solid Rocket Booster (SRB) aft skirt shoes and their mating spherical bearings are rendered useless after each launch and must be scrapped. Then there were blast shields....

The blast shield was conceived to prevent loss of launch hardware. In fact, current launch hardware cost comparisons estimate that the use of at least four blast shields saves the program approximately \$250,000 per launch.

The blast shield is a mechanism that is attached to the holddown post with mount brackets which also act as hinges (see figure 1). The shield rests against the fragment catcher of the frangible nut prior to launch. It is spring loaded, and during lift-off of the Space Shuttle, the front edge (skid plate) "cams off" the fragment catcher. This action increases the spring tension which causes the blast shields to close after separation from the SRB aft skirt. As its name implies, it shields the shoe, the top of the holddown post, and the spherical bearing from the hostile environment of the SRB's exhaust plume.

Because of the northerly drift angle of the Space Shuttle during lift-off, the north holddown posts (numbers 3, 4, 7, and 8) sustain the majority of the blast damage. Consequently, blast shields are installed only on these posts (see figure 2).

## ORIGINAL DESIGN

The original design of the blast shield consists of the following major components:

---

\* Lockheed Space Operations Company, John F. Kennedy Space Center, Florida

- a. Hood. The hood is of hip-roof-shaped construction and is made of ASTM A36 steel plates. It has longitudinal and lateral stiffeners. The hood also has two hinge clevis mounts incorporated with the longitudinal stiffeners. The plates are pre-drilled for the hinge shaft. The hood of the blast shield closes over the holdown post to protect it and its associated hardware from launch blast.
- b. Latch. Latch assemblies are located inside the clevis mounts and above the hinge shaft (left and right side). They prevent the hood from reopening due to back pressure of the exhaust blast. The latches are spring loaded so that pressure is applied towards the hinge brackets as the hood closes.
- c. Hinge Shaft. The hinge shaft is made from ASTM A490 bolt material and supports the hood and the main torsion springs that close the hood. Spring stops are installed on both ends of the shaft.
- d. Shaft Locking Pins. The shaft locking pins (two per blast shield) are made of drill rod material. These pins lock the shaft to the mount brackets after the springs have been armed. The pins are inserted through holes in the mount brackets, which are positioned at 45 degrees. The top ends of the pins protrude out of the mount brackets by 25 millimeters (1 inch) and are held in place by cotter pins.
- e. Mount Brackets. The mount brackets are weldments (two per blast shield) made from ASTM A514 steel that are bolted to the holdown post on the side away from the SRB's. They are used to attach the blast shield to the holdown post, and also serve as hinges.
- f. Main Torsion Springs. The torsion springs (two each) are made from ASTM A229 music wire and provide the energy to close the blast shield. One leg is longer than the other. The longer leg is turned 10 degrees from the parallel axis.
- g. Skid Plate. The skid plate is mounted on the front edge of the blast shield with three hex head cap screws and contacts both the fragment catcher and the SRB aft skirt, which are made of Inconel and aluminum, respectively. It serves as a buffer between the fragment catcher and the SRB aft skirt and, to prevent contact damage, is made of 5086-H32 aluminum plate.
- h. Spring Stops. The spring stops are made of ASTM A36 steel and are located near the ends of the hinge shaft. They are L-shaped and are held in position by flats on the shaft ends and by spring pins.
- i. Shaft Support Lugs. The shaft support lugs are located on each side of the blast shield near the shaft ends. They support the shaft in case of excessive bending loads and provide an attachment point for the spring arming tool and shaft blast covers.

The lugs are made of ASTM A36 steel plate which is welded to the side of the blast shield in the vertical position. A hole at the bottom

accommodates the shaft ends. Two tapped holes located just above the shaft hole serve as attachment points for the arming tool and the shaft blast covers.

- j. **Shaft Blast Covers.** Also made from ASTM A36 steel, the shaft blast covers protect the shaft ends. They are attached to the shaft support lugs with two self-locking screws.

#### PROBLEMS ASSOCIATED WITH THE ORIGINAL DESIGN

The early versions of the blast shields failed to close during two launches prior to Space Transportation System (STS) mission 33 (51-L) (Challenger). These failures resulted in debris and raised concerns that the debris could become projectiles and damage flight hardware. For example:

- a. On STS-26, launched July 29, 1985, post-launch inspection revealed "all blast shields came down; Blast shield on post #3 was slow in closing; skid plate missing; spherical bearing and shoe damaged; underside of blast shield has bad erosion damage...."
- b. On STS-31, launched November 26, 1985, "Blast shields on post #'s 4 and 8 did not close. They were standing open at approximately 80 deg. after launch. All hardware was intact with no missing debris (parts). Shoes and bearings were eroded...."

The used blast shields were stored in several areas at the John F. Kennedy Space Center (KSC) and photographed for record purposes. Using these photos and reports published by blast shield inspection teams, areas of debris concern were identified. Specifically, in the failed-open blast shield condition, the following components are exposed to direct blast impingement with the following observed effects:

- a. **Shaft Locking Pins.** The protruding part of the shaft locking pin was exposed to direct blast impingement. The cotter pins could not be located and are suspected of being vaporized or pulverized. The pins can easily slide back out of the mounting brackets and become projectiles.
- b. **Main Torsion Springs.** The sandblasting effect of the SRB's has been observed to ablate the exposed (top) portion of the springs by more than 13 millimeters (0.50 inch), leaving 28 partial (horseshoe shaped) rings hanging on the main shaft.
- c. **Skid Plate.** The aluminum skid plate could not be located and is suspected of being vaporized or possibly pulverized by the sandblasting effect of the SRB exhaust.
- d. **Spring Stops.** The spring stops became debris.
- e. **Shaft Support Lugs.** None of the lugs ever detached from the blast shield during launch. However, in at least one post-launch inspection, some lugs were reported to be "barely hanging on to the blast shield."

Further, some of them could be detached manually from the blast shield without any effort.

- f. **Shaft Blast Covers.** Although the shaft blast covers adequately protect the shaft ends, and have not been observed to sustain launch damage, they could become launch debris for the following reasons:
  - (1) They are attached to the shaft support lugs.
  - (2) They are outside the blast shield's envelope; therefore, they are fully exposed to the exhaust blast.

#### PRE STS-33 (51-L) MODIFICATION PHASE

Prior to the STS-33 mission, launched January 28, 1986, the blast shields were modified to ensure proper closure during launch, thereby reducing the possibility of blast shield parts becoming debris.

The major problems associated with the original design were weak main springs due to a low factor of safety on yield strength and the relaxation of the main springs, probably due to heat soak. In December 1985, the NASA KSC Design Support Contractor was directed to design a "kick spring" mechanism to aid the blast shield in closing during launch. The mechanism's design consisted primarily of a plunger, a compression spring, a housing, and 6-millimeter (0.25-inch) diameter retaining cables. The assembly was mounted between the mounting brackets behind the blast shield. The working principle was as follows: At some point during lift-off, the blast shield is intended to engage the plunger, which compresses the spring. As the aft skirt leaves the blast shield, the plunger provides the "extra kick" to close the blast shield. The rationale: The faster the blast shield closes, the less chance that debris will be generated.

#### POST STS-33 (51-L) FINDINGS

The post-launch report of STS-33 revealed that all blast shields closed normally with no damage to shoes and bearings. But the newly installed kick springs did not fare so well: The plungers, the springs, and their restraint cables were missing on all four holdown posts. One kick spring was found on the flat haunch of holdown post number 1, which is on the opposite side of holdown post number 3 (see figure 2). Two plungers were found at the north perimeter fence, approximately 400 meters (1/4 mile) away from the holdown post site! The cables were never found. These discoveries led to speculation that the kick springs may have contributed to the Challenger tragedy.

In a National Aeronautics and Space Administration (NASA) investigation report submitted in February 1986, the following facts were considered:

- o The SRB plume flame is approximately 178 meters (600 feet) long.
- o Two plungers were found at the north perimeter fence.
- o The end cap was in place on one of the plungers, permitting metallurgical analysis. Analysis of an end cap indicated 0.30-millimeter (0.012-inch) buildup of aluminum oxide around the sides.

- A full-duration exposure to flame will deposit approximately 0.74 mm (0.029 in.) coating.
- Therefore, 0.30 millimeter (0.012 inch)/0.74 millimeter (0.029 inch) = 41-percent exposure.
- o Estimated height,  $h = 0.41 \times 178$  meters (600 feet) = 73 meters (246 feet).
- o A preliminary assessment stated that the plungers came off after the vehicle was 200 to 300 feet up. Plungers were blown into the SRB flame trench and out to the perimeter fence.

A Film Analysis Report dated March 10, 1986, stated that, "The relatively short dwell time and rapid closure rate observed on all four blast shields suggests that the kick springs were in place and working until sometime after closure. However this cannot be confirmed by direct observation." Closures could not be determined due to flame obscuration. The report further stated that no direct impingement of SRB flame was evident in the vicinity of the kick springs throughout the observational interval (approximately 1.120 seconds), indicating that the cable restraints were still intact.

On the other hand, based on the known drift characteristics of the launch vehicle, it is probable that direct SRB flame impingement was of sufficient magnitude to burn off the cables after 1.120 seconds.

Both reports concluded that the kick spring assembly did not contribute to the Challenger tragedy. The incident did, however, increase concerns regarding holdown post and blast shield debris.

#### POST 51-L MODIFICATION (RETURN-TO-FLIGHT) PHASE

Between January 1987 and September 1988, the blast shield underwent an extensive modification program. Once again, the primary concern was strengthening the areas of the design contributing to the release of debris. Thus, redesign efforts focused on ensuring proper closure of the blast shields, eliminating the kick spring/plunger mechanism that proved so susceptible to launch blast, and modifying the design wherever possible to minimize blast impingement.

Accordingly, the blast shields were modified as follows (see figure 3):

a. Hood.

- (1) The hinge clevises were opened up to prevent the hood from binding with the mounting brackets.
- (2) The clevis hole diameter was increased and bored to allow more clearance between the shaft and the holes.
- (3) The latch shaft holes were enlarged to ensure proper operation of the latches and to preclude binding.

- (4) The spring stop plates welded to the blast shield were properly located from the centerline of the main shaft to ensure that the springs engage the blast shield at the proper angles given the allowable tolerances.
- b. Shaft Locking Pins. To eliminate the exposed cotter pins that held the locking pins in place, a new shaft locking pin was designed with a threaded end at the bottom. It was also shortened so that no part would be exposed to the exhaust blast.
- c. Mount Bracket. The hinge holes in the original brackets did not align properly when mounted on the holdown post. This anomaly was concluded to be a contributing factor to blast shield failures because the shaft was binding with the hinge holes. Also, the addition of the spring blast covers reduced the clearance between the SRB shoes and the blast shield. Using the old brackets would have required the addition of shim plates between the holdown post and the brackets.

New one-piece bracket weldments made of AISI 4140 and heat treated to 1,034,000 kPa (150 ksi) to 1,241,000 kPa (180 ksi) were fabricated. The shim plate thickness was incorporated into the baseplate. The hinge holes on the vertical mounts were line bored.

- d. Main Torsion Springs. To minimize debris, the main torsion spring envelope was reduced to allow full enclosure of the springs. Specifically, the mean outside coil diameter of the main torsion spring was reduced along with the number of coils.

Since the main torsion springs were suspected to be the major contributor to the blast shield's failure to close, they were modified further. The rationale for failure: Their constant exposure to high temperatures coupled with their prolonged pre-armed condition weakens them. Consequently, the main torsion springs were redesigned using ASTM A407 spring wire and increasing the wire diameter. The ASTM A407 spring wire has a higher tensile strength than the original ASTM A229 music wire: 1,550,000 kPa (225 ksi) versus 1,350,000 kPa (196 ksi), resulting in a higher factor of safety on yield, namely, 1.70 versus 1.01.

However, several concerns are inherent with the use of the new material. For example, KSC design specifications require a minimum factor of safety of 2 to 1. They further specify that no material used in Ground Support Equipment (GSE) shall have an ultimate tensile strength exceeding 1,241,000 kPa (180 ksi). The new material violated both specifications.

The concerns here were very real. The high tensile strength results in susceptibility to Stress Corrosion Cracking (SCC). These springs can stay on the launch pads for weeks in the armed (pre-loaded) position. The humid, salty atmosphere at KSC coupled with the loaded condition of the springs can hasten the effects of stress corrosion cracking.

On the other hand, the original springs had a very low factor of safety on yield (1.01) and were clearly inadequate for use on the blast shields, as evidenced by their failures. Designing springs with a factor of safety on yield of 2 would have required a bigger spring or the use of a higher strength material. Due to the limitations of the existing spring envelope, a bigger spring would have required a total redesign of the blast shields. Increasing the ultimate strength was equally unacceptable due to the increased chance of failure due to SCC.

Consequently, a waiver was obtained to allow the use of the new spring design with a factor of safety on yield of less than 2 and an ultimate tensile strength exceeding 1,241,000 kPa (180 ksi).

Interestingly, the use of square wire springs was considered. The section properties of a square wire spring increase the factor of safety and the strength, which would have eliminated the use of kick springs and/or additional springs while allowing a smaller spring envelope. Because it is not available as an off-the-shelf item and because of its relatively high cost, however, the use of square wire springs was rejected.

Therefore, the round wire springs were selected for use with the provision that they only be used for one launch. This policy was implemented to avoid failure due to heat soak or SCC caused by repeated use.

- e. **Center Torsion Springs**. The kick spring assembly was replaced with center torsion springs made from AISI 5160 steel. Although the preferred choice was ASTM A401 steel wire, it was not available in 17.5 millimeters (0.69 inch) diameter. Two springs were installed in the middle section of the hinge or main shaft between the mounting clevises. The initial blast shield position is at 47 degrees; it engages the center torsion springs at approximately 67 to 70 degrees during lift-off.

The advantages of this design over the original design are that it consists of one-piece construction, it is easier to install, and it has a higher factor of safety (greater than 2 to 1 on yield).

- f. **Spring Blast Cover Plates**. ASTM A36 steel plate spring blast covers were added for both the outboard and center torsion springs to prevent blast impingement. The blast cover plates were welded to the blast shield weldment. The outboard springs (or main springs) were fully encased while the center springs were provided with a bent plate for exhaust blast protection in case of blast shield failure in the open position. The center springs could not be fully enclosed due to the design of the spring stop.

- g. **Skid Plate**. The basic profile of the skid plate was retained; however, the method of mounting changed. The original aluminum skid plate was mounted with three hex head bolts located on the front edge of the blast shield and was directly exposed to the exhaust blast. Two mounting plates were added to the modified skid plates to allow them to be bolted from the sides of the two longitudinal stiffeners, affording protection from direct exhaust blast impingement.

Although aluminum was used in the original design, post-launch inspections of blast shields soon revealed that aluminum components become debris. If the blast shields were to fail in the open position, the retaining bolts and the skid plate itself could be eroded and blasted away during launch. The concerns of skid plate damage to the SRB aft skirt and the fragment catcher, when weighed against the debris concerns associated with aluminum, left only one choice: The aluminum skid plates were replaced with steel skid plates.

- h. **Spring Stops.** Because of the increased loads and change in dimensions of the new main springs, the spring stops were changed to AISI 4140. They were also tapered to provide clearance for the spring legs.
- i. **Shaft Support Lugs and Shaft End Blast Covers.** The designs of the shaft support lugs and shaft end blast covers were simplified. The lugs were replaced with a spacer plate welded to the blast shield roof just above the shaft ends. The end cover plates were fabricated from steel plate and mounted with five socket head screws, the heads of which are recessed into the plate. These modifications streamlined the design of the blast shield by enclosing the end cover plates within the blast shield envelope.

## VALIDATION TESTING

The exhaust plume of the SRB strikes the holdown post at T+1.6 seconds from SRB ignition. Consequently, one of the design requirements of the blast shield is that it must be in the closed position before the exhaust plume strikes the holdown post. Analysis predicted that, based on the center of gravity location, the drift angle of the Shuttle lift-off, the spring torque, and the surrounding pressure [1,034 kPa (150 psi)], the blast shield should close in 950 milliseconds. Because of recent modifications, and to verify analysis, testing and qualification were required for each blast shield.

Testing was conducted at KSC's Launch Equipment Test Facility (LETF) and consisted primarily of mounting the blast shield on a holdown post with the SRB shoe and spherical bearing installed. The blast shield was initially opened to a 47-degree angle, then wire rope cables and drop weights were attached to the blast shield. The weights were released using gaseous nitrogen (GN2) nuts. Release of the drop weights pulls the blast shield to its maximum opening angle (80 to 81 degrees) thereby simulating SRB lift-off (see figure 4). At the full-open point, the blast shield is released from the drop weight to close back onto the SRB shoe. Time is measured from the moment the drop weight is released to the moment the blast shield closes, resting on the SRB shoe.

This method of testing, however, did not accurately depict Shuttle lift-off. The release timing of the GN2 nuts varied somewhat, and the wire rope cables had a tendency to snag in the sheaves/pulleys during the closing cycle, thus delaying closure time.

Therefore, a Lift Off Simulator (LOS) Test Fixture was designed and built to more accurately simulate that period of time during lift-off when the blast shields are in contact with the SRB aft skirts (see figure 5). The fixture consists of the following major components/assemblies:

- a. **Winch and Cable System**. A dropweight-operated winch-and-cable system is used to lift the aft skirt assembly, thereby simulating lift-off.
- b. **Holddown Post Assembly**. The original LOS used an actual holddown post assembly, shoe, and spherical bearings. Although actual shoes and spherical bearings are still used, because of its relative scarcity, the holddown post has since been replaced with a facsimile.
- c. **Drop Weights**. The drop weights and aft skirt assembly weight are set at a ratio to simulate 0.55 g lift-off acceleration.
- d. **GN2 Release Nuts**. The drop weights are released by GN2 nuts.
- e. **Aft Skirt Assembly**. In the aft skirt assembly, an actual support column and, because of its relatively high cost, a facsimile of the fragment catcher are used. The aft skirt assembly guide rails were set at 17 degrees from the vertical to simulate the drift angle during Shuttle lift-off. Since then, the drift angle has been revised to 13.5 degrees.
- f. **Instrumentation**. The instrumentation system consists of the following components:
  - (1) An accelerometer mounted on the blast shield for event tracking.
  - (2) An electrical break switch mounted on the simulator guide panels for start time event signal.
  - (3) An electrical crush switch mounted on the shoe for blast shield closure event signal.
  - (4) A Linear Voltage Displacement Transducer (LVDT) or fishreel for data plots of displacement versus time.
  - (5) Three high-speed cameras (located at the front, back, and side of the LOS).
- g. **Blast Shield**. The actual blast shield being tested is mounted on the holddown post to rest on the aft skirt section.

The LOS was first used to validate the blast shields used in the STS-26R (Return-To-Flight) mission. The Interactive Laboratory System (ILS) indicated, in its observation of the LOS performance, that the LOS was rising at 0.60 g, faster than the 0.55-g acceleration indicated by camera data. The discrepancy was attributed to errors in reading the defined start times - the time is read from the ILS plots (instrumentation errors) then compared with camera data (viewing angle errors). However, since the discrepancy was negligible, data collected from blast shield drops were considered acceptable.

The first set of blast shields was then tested on the newly designed and built LOS. The results verified analysis data; specifically, the closure times averaged about 800 milliseconds and no interferences were encountered.

## RETURN-TO-FLIGHT MODIFICATION PHASE COMPLICATIONS

Several problems were encountered during the Return-to-Flight blast shield modification program. For example:

- a. **Blast Shield Fabrication.** The ten blast shields being modified were existing blast shields that had never been used for launch. These blast shields were measured and compared with the existing drawings, with an alarming discovery: No two blast shields were built the same, not one of the blast shields was built per the drawings, and the measurements taken exceeded allowable tolerances! Thus, the factor of quality control during fabrication entered the picture.

Not much could be done about the differences in the dimensions of these blast shields, and few avenues existed to reduce the possibility of binding. Specifically:

- (1) The hinge shaft holes were line bored to a larger diameter.
  - (2) Bushings then were press fitted in the enlarged holes then the bushings were line bored to the proper diameter with the correct amount of tolerance.
  - (3) The clevis areas were widened by milling off about 1/8 inch from each side. The smallest gap allowed between the mount bracket and the clevis was 4.3 millimeters (0.17 inch).
- b. **Mount Brackets.** The vertical portion of the mounting brackets interfered with the mating blast shields. Opening up the clevis mount of the blast shield eliminated the interference. This problem was just one of many which have resulted in the trial-and-error evolution of the mount brackets (see figure 6). Specifically, the brackets used during the 60-percent and 90-percent design phase were weldments. A fillet weld at the lower baseplate of the brackets was ground to provide room for the mounting bolts.

The blast shield then underwent validation testing at KSC's Launch Equipment Test Facility (LETF). After testing, the blast shield was removed from the holdown post that was used as a test stand. One of the bottom base plates fell off . . . under a no-load condition! The cause was determined to be lack of weld fusion: a fillet weld was used instead of a bevel weld, as called for in the drawings. Grinding the fillet weld left about a 1.5-millimeter (0.06-inch) weld holding the foot to the vertical bracket. Additionally, several problems were associated with the use of welded 4140 parts, including a lack of established procedures and a lack of welders experienced in welding 4140 steel.

As a result, the mount brackets were made out of a one-piece AISI 4140 steel billet. The billet was rough cut to a basic shape then machined to its final form in the annealed condition. Heat treatment and magnetic particle inspection followed machining.

More recently, the use of casting was adopted to reduce fabrication costs. The first article casting was made and passed X-ray and magnetic particle testing. A second batch of four was then poured at the foundry. During the machining phase, the machinists observed that the second batch machined harder than the first article. After machining, the brackets were sent out for heat treatment. The brackets came back from heat treatment with large cracks, typically near the heavy sections of the brackets.

An analysis performed by the KSC Analysis Laboratory revealed that the cracks were caused by a higher than allowable carbon and manganese content in the alloy. The foundry's computer printout indicated otherwise. A second analysis performed by the foundry, however, confirmed the KSC findings.

A subsequent investigation revealed that quality control personnel had not taken samples of the second pour. Later, they took samples from another pour which happened to have the proper alloy composition required for the brackets. Unfortunately, the alloy used for the unsampled pour, the alloy that was used for the brackets, was not the correct composition.

Again, the design process had been complicated by inadequate quality control during fabrication and manufacturing.

- c. Skid Plate. The skid plate could not be mounted because of interference with mounting lugs. Moreover, the mounting holes did not line up. As a result, each skid plate was individually modified to fit its corresponding blast shield.
- d. Shaft Interference. The main shafts interfered with the end cover plates in some blast shields. The shafts were not made to print; they were longer than what was called for in the drawings. Consequently, the shafts had to be remachined to proper dimensions and the end cover plates had to be shimmed. The ends of the shafts were also heavily lubricated prior to installation.
- e. Main and Center Torsion Springs. The springs were cold formed and heat treated as specified. One of the main problems encountered in the manufacturing process was maintaining the required spring leg angles. The allowable tolerance for the leg angles is  $\pm 1$  degree. The spring manufacturer normally holds a  $\pm 5$  degree tolerance. However, due to the criticality of the engagement angle between the blast shield and springs, a  $\pm 5$  degree tolerance was not acceptable. To compensate, the test conductor determines how many shims are required so that the springs engage the blast shield at the proper angles during validation and acceptance testing.

## CURRENT PROBLEMS

Since STS-26R, no failures have occurred: As of this writing, all the blast shields used have closed. Debris is negligible. However, several problems still must be addressed:

- a. The blast shield survives only two launches. After the second launch, the hood's top surface is badly eroded. In several cases, burnthrough has been observed requiring that these blast shield assemblies be scrapped and replaced with new ones.
- b. The provision that the springs must be replaced after each launch has proven costly.
- c. The addition of 19-millimeter (0.75-inch) shims to the baseplate of the mount bracket moved the blast shield hood, slightly exposing the front edge of the SRB shoe to exhaust blast. This exposure results in SRB shoe erosion during some launches.
- d. A lack of quality control is still evident in the fabrication process of the blast shields; specifically, fabricators are unable to hold the required dimensional tolerances.

## CONCLUSION

Several improvements are still required to optimize blast shield operation. Some of them, being implemented as of this writing, are:

- a. Scrapping the entire blast shield assembly after the second use is not economical. Some parts of the assembly, including the mounting brackets, the main shaft, the spring stops, the latches, and the shaft end cover plates are not directly exposed to the SRB exhaust plume and can still be used for at least four or five launches. Basically, only the hood and the springs require replacement. However, cannibalization of Ground Support Equipment designated as scrap is not allowed at KSC.

The economics of cannibalization has been presented to Logistics engineers at KSC, resulting in the implementation of a new procedure allowing cannibalization for the refurbishment of blast shields that have been used for two launches. To date, the savings realized in the cost of refurbishing versus fabricating new blast shield assemblies has been approximately 35 to 40 percent.

- b. The cost of machining the bracket from a steel billet is expensive. Economically, a casting is a less expensive approach. Less machining is involved and, consequently, a reduced possibility of failure due to human error in machining.
- c. Further analysis and testing are required to determine if the springs can be used for more than one launch.
- d. A redesign of the hood is being considered, including possible replacement of the welded hood with a casting and thickening of the top plates to allow more use out of each assembly. Another alternative

is the use of a bolt-on-type sacrificial plate. The plate would allow easy replacement after burnthrough has occurred.

- e. Quality control is being strongly emphasized. Space Shuttle flights involve human lives and expensive hardware and payloads. A blast shield failure could be catastrophic. Quality control, particularly during the fabrication process, must be emphasized. Engineers and designers can incorporate numerous factors of safety within their designs, but if they begin with defective products, the efforts of the design process can be negated.

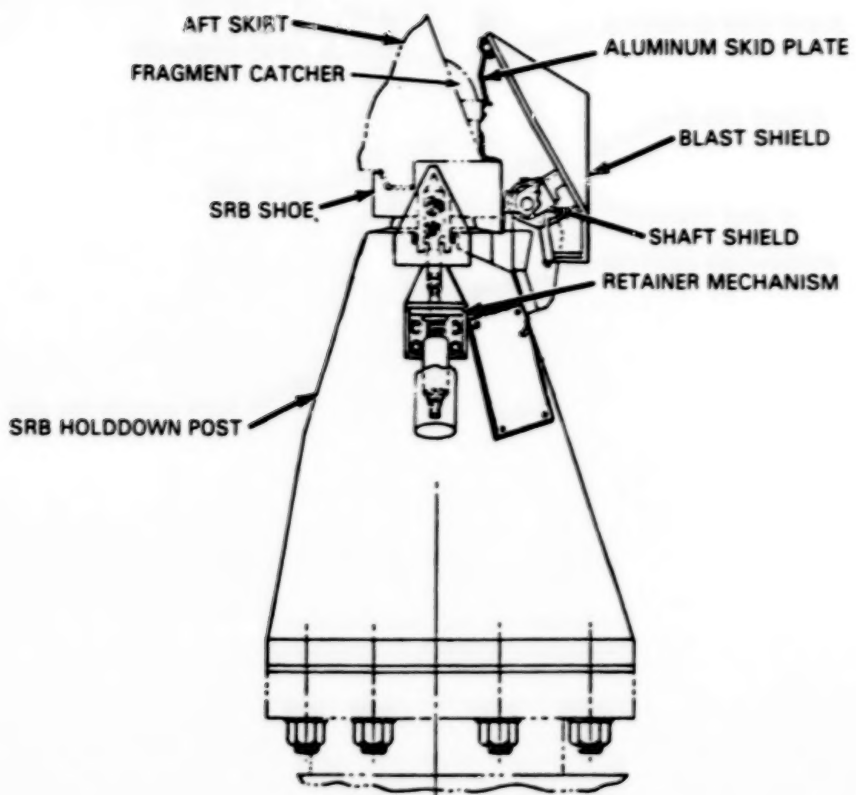


Figure 1. Hooldown Post Blast Shield Installation (Original Design)

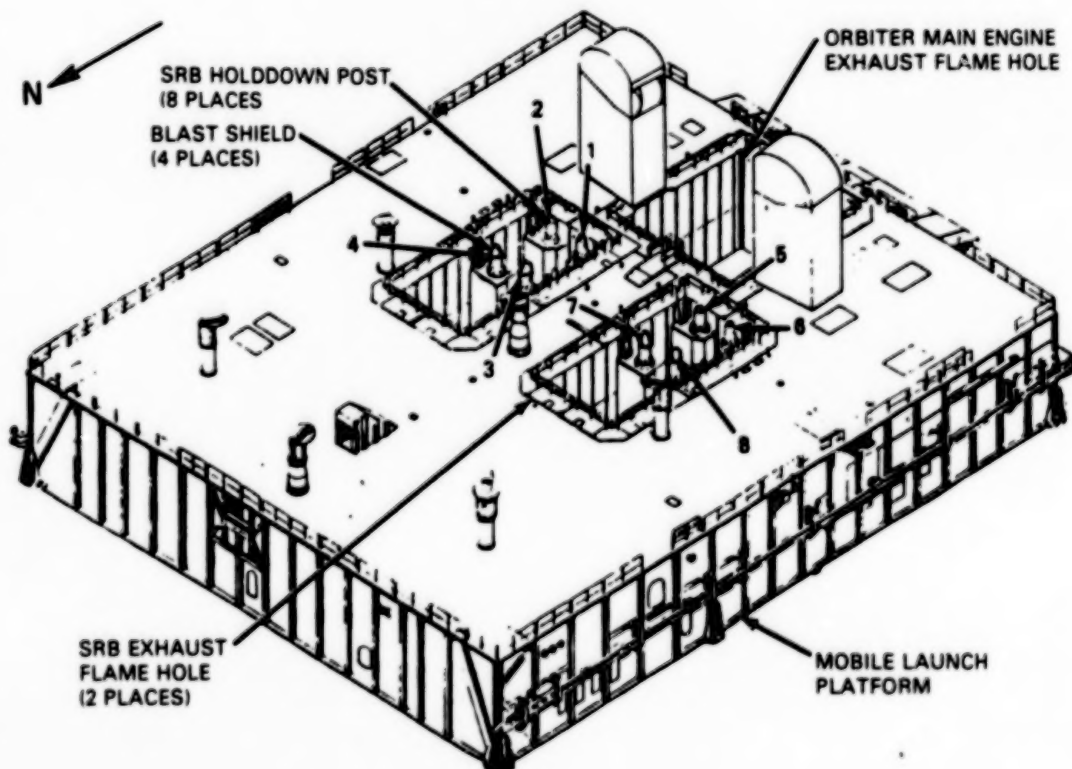


Figure 2. Blast Shield Locations on the Mobile Launch Platform

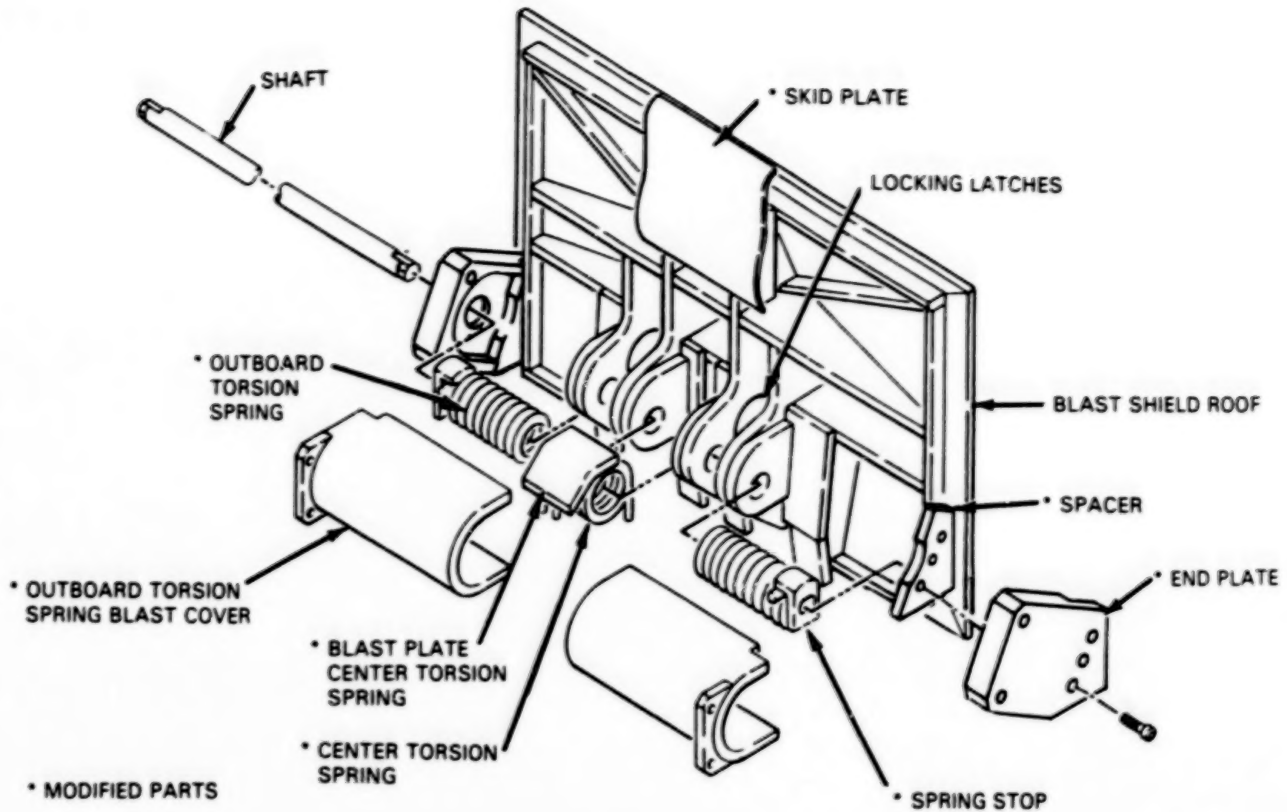


Figure 3. Blast Shield Modification and Installation

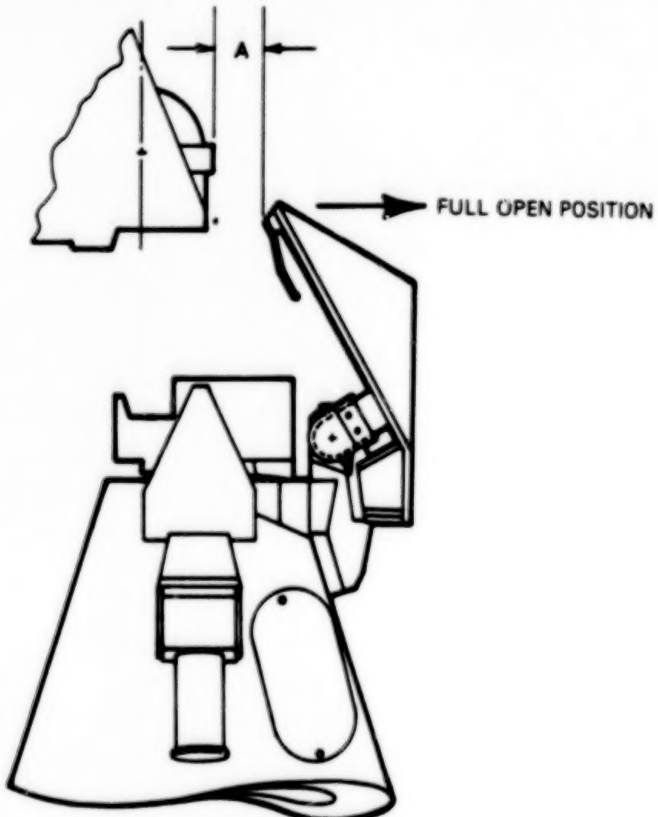


Figure 4. Blast Shield Full-Open Position

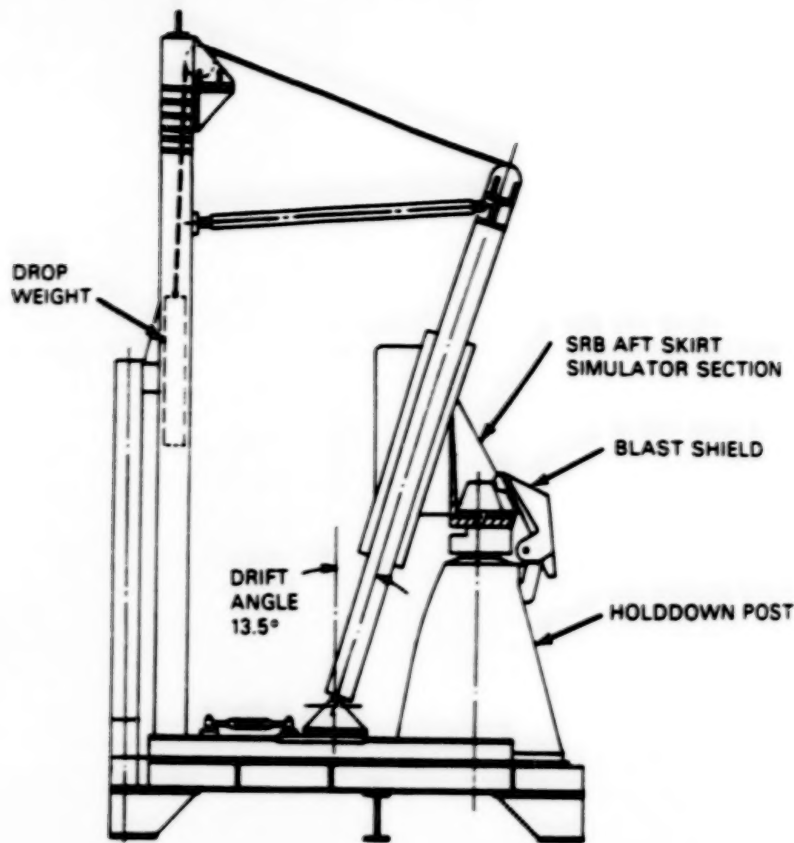


Figure 5. Lift-Off Simulator (LOS) Test Fixture

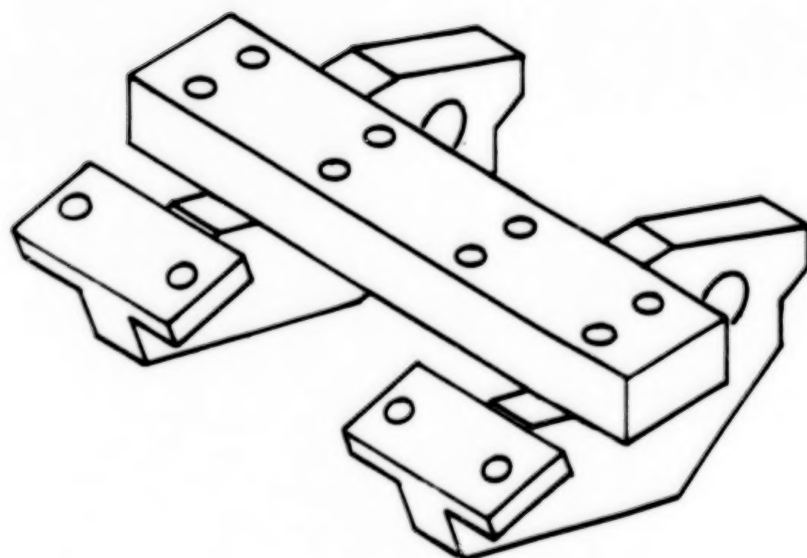


Figure 6. Mount Bracket (Current Design)

**THE DYNAMIC TORQUE CALIBRATION UNIT:  
AN INSTRUMENT FOR THE CHARACTERIZATION OF BEARINGS  
USED IN GIMBAL APPLICATIONS**

Louise Jandura\*

**ABSTRACT**

The Dynamic Torque Calibration Unit (DTCU), an instrument for the characterization of duplex ball bearing pairs used in gimbal applications, has been designed and built. The design and operation of the unit are described. Preliminary data from the instrument are presented to illustrate the kinds of experiments that can be performed with the DTCU.

**INTRODUCTION**

The Strategic Defense Initiative Organization (SDIO)-sponsored Tribomaterials Precision Gimbal Demonstration Program is an effort to develop technology for precision gimbals to support SDIO's pointing and tracking applications. The program's objective is the demonstration of enhanced performance of gimbal systems through the use of advanced tribomaterials in ball bearings. This approach recognizes that gimbal-bearing capabilities often drive the systems' conceptual-design requirements so that improvement in the bearings would lead to improved system performance.

Work funded through this program encompasses the range from development of new tribomaterial coatings to gimbal design. The Jet Propulsion Laboratory's (JPL's) role in the Tribomaterials Program is the evaluation of bearings, drawing upon the laboratory's experience as a designer and builder of precision-pointing systems. In contrast to many other members of the program whose primary role and interest are in developing new dry lubricants and in understanding the material properties of these films, JPL's contribution is in the evaluation and characterization of the coated bearings from a bearing user's point of view.

In keeping with its role as an evaluator of bearings, JPL has built a precision instrument designed to characterize a pair of test bearings in a single-axis test under carefully controlled conditions. This instrument is called the Dynamic Torque Calibration Unit (DTCU).

---

\* Member of Technical Staff, Guidance and Control Section, Jet Propulsion Laboratory, California Institute of Technology, Pasadena, California.

## BACKGROUND

Other researchers have developed instruments to test bearings or bearing pairs under conditions appropriate for evaluating bearings for gimbal systems. These conditions include slow-speed operation and oscillatory operation, among others. Some of the instruments described in the literature are summarized below.

Greer and Mack [1] describe an instrument that tests a pair of angular contact ball bearings mounted back-to-back with a constant preload. A velocity servo drives the inner races of the pair at a constant speed while a position servo acts in a torque-rebalance servo loop to maintain the outer races at a null position. Torque measurements are made from the torque-balance servo loop. Results are presented on the spectral distribution of torque noise from the bearings as a function of various bearing parameters.

Leveille [2] describes tests performed in a slow-speed device that uses a single test bearing under a load. In this case, the test bearing's outer race is rotated at a constant speed while torque is measured by a strain-gage transducer mounted to the inner race.

In many papers [e.g., 3, 4] by researchers from the European Space Tribology Laboratory (ESTL), data are included from instruments capable of measuring bearing torque under both continuous and oscillatory motion. At ESTL, the test article is a preloaded duplex pair. The outer races of the test pair are driven and torque is measured at the inner races using an inductive torque transducer. These tests can be conducted in a vacuum.

Phinney et al. [5] conducted oscillatory life tests in a vacuum on lightly preloaded, face-to-face bearing pairs. The instrument accepts up to five bearing pairs at a time. The inner races are oscillated while torque is measured on the outer races through a strain gauge attached to a cantilever beam. Each bearing pair is instrumented separately.

The researchers listed above performed a variety of both performance and life tests. JPL set out to design an instrument specifically for performance testing (e.g., Dahl parameters [6], running torque, torque noise) of bearings coated with a dry lubricant and intended for use in a gimbal platform. The goal is to take very precise torque data while driving the test bearings with the same precision as that required in a gimbal application. This instrument's unique capability is in the precise position and rate control of the drive system. The torque-sensing capability, while significantly precise, is not unique. The desired test-item configuration is two angular contact bearings mounted back-to-back to form a duplex pair, because that is a common gimbal-bearing design.

## DESIGN REQUIREMENTS

Given the scenario described above, the following design requirements for the DTCU were established:

- RATE TABLE:
  - Rate: 698 mrad/s ( $40^\circ/\text{s}$ ) maximum
  - Rate Error: < 3.5 mrad/s
  - Position Resolution: 12  $\mu\text{rad}$  (19 bits)
  - Absolute Position Error: < 96  $\mu\text{rad}$
  - Modes of Operation: 1) continuous rotation in either direction,  
2) oscillatory
- TORQUE SENSOR:
  - Torque Range: 0 to 2 N·m
  - Bandwidth: 0 to 100 Hz
  - Resolution: < 0.001 N·m
  - Accuracy: <  $\pm$  0.001 N·m

In addition to the specifications listed above, there were a few more requirements on the design task. The unit was required to operate in a vacuum. By necessity, the testing must be done in a dry environment (vacuum or nitrogen) to protect the integrity of the film. The instrument must be able to accept bearings of many different sizes that support a range of applications. The bearing test pair must be removed as a unit so it can be inserted into other test equipment as desired without disturbing the preload. The schedule was tight. All design, procurement, fabrication, and assembly was to be completed in six months.

The requirements on the drive system come directly from the sponsor's requirement to support a wide range of SDIO pointing and tracking applications. The desire is to exercise the test item with the same class of precision encountered in a gimbal application. The torque-sensor requirements flow directly from the drive-system requirements. Given the maximum drive system rate of 698 mrad/s or 0.11 Hz, the 100-Hz bandwidth of the torque sensor provides more than adequate frequency content. Moreover, we are most concerned with disturbances at frequencies within the typical gimbal-controller bandwidth, and this is

at least an order of magnitude less than 100 Hz. The high end of the torque range requirement is set about an order of magnitude higher than that required for the kind of precision bearings used in gimbals. Further, the tribomaterial coatings are expected to produce lower levels of friction than typical liquid-lubricated bearings. This high-end requirement was maintained to give maximum flexibility in the types of bearings that can be tested.

## DESIGN

The DTCU is composed of three major portions: a torque sensor or torque-rebalance loop, a drive system or rate table, and the bearing pair under test. It is similar to the instrument described by Greer and Mack [1]. DTCU operation is depicted in Figures 1 and 2.

A pair of test bearings is mounted back-to-back in a bearing cartridge under a known preload. The cartridge is then mounted on the DTCU shaft. The inner races of the bearing pair are precisely driven by the DTCU rate-table motor and its controller. The torque transmitted via the balls to the outer races of the bearing pair is measured by the torque-rebalance loop.

The operation of the torque-rebalance loop is shown in more detail in Figure 2. Two electrodynamic or voice-coil actuators are positioned to exert a pure torque couple to the outer races of the bearing pair. Two eddy-current differential position sensors mounted  $\pi/2$  rad (90°) apart monitor the position of the outer races of the bearing pair. The advantage of this sensor configuration over a single sensor is that it reduces the effects of bearing runout and other drive eccentricities to an acceptable level. Three sensors mounted  $2\pi/3$  rad (120°) apart would be immune to these effects but that option was too expensive. A torque-rebalance control loop drives the voice-coil actuators using the eddy-current sensors for feedback. This keeps the outer races of the bearing pair at a null position while the inner races of the bearing pair are driven by the rate table. The current developed in the voice coils to hold the outer race at a null position is proportional to the torque transmitted through the bearing pair.

Both the voice-coil actuators and the eddy-current sensors operate through an air gap; therefore, there is no direct mechanical contact between the test bearings and the measurement system. When properly aligned, this noncontacting system allows measurement without stray loads.

### Rate Table

The mechanical rate-table design uses a 16-pole, brushless dc motor, an Inductosyn, two liquid-lubricated ABEC class 7 bearings, a flywheel, and a magnetic shield. An Inductosyn is a printed-winding pancake

resolver. The magnetic shield prevents motor electromagnetic emissions from disturbing the Inductosyn operation. The flywheel was added after analysis revealed that more inertia would provide better rate stability. Tight tolerances are maintained on both the bearing mounting surfaces and the Inductosyn mounting surfaces in keeping with the desire for precise control of the position and rate of the shaft. The Inductosyn is mounted near the top of the shaft to provide more accurate knowledge of the portion of the shaft near the test-bearing pair. This lessens the effect of windup between the motor and the top of the shaft. Static o-ring and labyrinth seals are used to minimize contamination of the test article by the lubricants of the rate-table bearings.

### Torque Sensor

The mechanical design of the torque-rebalance loop portion of the DTCU is intended to maintain the positions of the two linear voice-coil actuators and the two eddy-current sensors. The magnet portion of both voice-coil actuators and the sensor heads of both eddy-current sensors are positioned from a plate mounted on the top of the DTCU housing. The coil portion of the two voice-coil actuators and the targets for the two eddy-current sensors are mounted on the bearing cartridge and their weight is supported through the outer races of the bearing pair. This weight was designed to be minimal (less than 2.3 kg (5 lb)) and is statically balanced by appropriate counterweights to prevent the introduction of a moment load on the test article.

### Bearing Cartridge

Although the bearing-cartridge design is not yet complete, it is being designed with the following features in mind. The cartridge will provide the preload for the bearing. Both hard and soft preloads can be accommodated. Once installed in its cartridge, the bearing pair can be removed from the DTCU so that it may be installed in other test equipment as necessary without disturbing the preload. The cartridge also aligns the bearing pair with the shaft. Finally, the cartridge will align and support the torque measurement equipment that is attached on the outer race of the bearing pair.

Figure 3 is a schematic diagram of the bearing-cartridge design. The two main challenges in this design are fixing the cartridge to the rate-table shaft and establishing the preload. Our interim design addresses the first problem, but does not yet completely answer the preload question. This will be resolved in the final version of the design.

The schematic shown in Figure 3 illustrates the means of attaching the bearing cartridge to the shaft. The split hub on the bottom of the bearing cartridge fits over the rate-table shaft and is clamped to the shaft. The tolerance and the fit of the split hub keep the bearing cartridge and

therefore the test article concentric with the shaft. It is then ready to be mounted in other test equipment. Also shown in the figure are labyrinth seals on both the top and bottom of the test article. These are included to further minimize contamination of the test bearings by any outgassed lubricant that escapes from the labyrinth seal of the rate table.

### Control Law Design

The electrical design of the DTCU consists of two major parts: a rate-table motor controller and a torque-rebalance loop controller. The rate-table motor controller is represented in Figure 4. To accomplish the required rate control, we have implemented what is fundamentally a precision position controller. The controller is not simple and is intended to give a class of performance similar to an actual spacecraft pointing platform. Although this is not completely possible without expensive inertial sensors, this performance is being approached by the use of a 12  $\mu$ rad (19-bit) resolution Inductosyn position sensor. With this controller, difficult torque measurements, such as those associated with precision staring and controlled rate reversal, are possible.

The design challenge is to obtain 14.5  $\mu$ rad pointing with this sensor. Conventional proportional-integral-derivative (P-I-D) compensation is inadequate to achieve this pointing stability, so a 3-state sequential least-squares estimator was created to obtain the necessary rate feedback. In Figure 4, the entire estimator is represented in the  $K_r s$  block. The controller is a digital/analog hybrid design that performs all precision functions digitally (950  $\mu$ s sampling time) and provides digital outputs for data logging. Both analog and digital input command signals are accommodated.

Figure 5 is a block diagram of the torque-rebalance loop controller. This is a standard P-I-D controller. No complications, as in the rate table controller, were necessary to obtain a tight 100-Hz bandwidth (-3 dB point) loop with current to the voice coils as the measure of torque. In this manner, the voice coils become the reference for torque and the eddy-current sensors serve only to close the loop.

### ASSEMBLY

The most critical part of the DTCU rate-table assembly is the mounting of the Inductosyn. The positioning of this sensor is important in both the commutation of the motor and the precise control of the shaft. Tight specifications exist for parallelism, concentricity, and the gap between the rotor and stator pieces of the Inductosyn. Shims and spacers are used to create the correct gap and to level out the parts. The Inductosyn spacing was measured as shown in Figure 6. In this assembly, the top plate of the rate table is mounted on four posts designed specifically to allow access for measuring the Inductosyn gap. The entire

assembly is fastened to a milling machine table where radial alignment of the top plate and the shaft to the bottom plate is established. This is necessary because the four posts provide only accurate axial spacing, not radial alignment. In the final assembly, the housing provides the radial alignment. The final gap was measured at 0.2 mm (0.007 in) and was uniform all around. Inductosyn rotor radial runout was measured as no more than 0.008 mm (0.0003 in) total indicator readout.

Accurate positioning of the torque-sensor mechanical assembly is necessary to achieve the desired sensor performance. This is done using a milling machine for measurements. The torque sensor is assembled with alignment rods to accurately position the magnet support, the voice-coil actuator, and the coil bracket. The voice-coil magnets are centered on the shaft center in two directions as described in Figure 7. The coil brackets are adjusted until the coils are concentric with the magnets. Finally, the position-sensor supports are shimmed so that the position-sensor targets are approximately centered in the position-sensor supports when the coils of the voice-coil actuators are centered in their magnets.

Figures 8, 9, and 10 show the DTCU completely assembled and integrated with the electronics. Figure 8 is an overview of the rack of electronics and the DTCU. Figure 9 is a view of only the DTCU. The connectors and sensor preamps mounted on the top plate of the instrument are visible. Also shown in Figure 9 and shown in closeup in Figure 10 is the torque sensor. The test-article mounting plate supports both the coils of the voice-coil actuator and the eddy-current sensor targets. Only one sensor pair and one actuator are visible in Figure 10. The voice-coil magnet and the position-sensor supports are attached to the torque-sensor base plate. One of the eddy-current sensor heads is seen between the sensor target and the right position-sensor support. The black box in the foreground is the eddy-current-sensor electronics for the sensor in the picture.

## TEST RESULTS

Since the bearing-cartridge design is not yet complete, a substitute bearing was configured so that the DTCU could be tested. Figure 11 shows a schematic of the DTCU test setup using this substitute bearing. The bearing consists of a metal disk covered on its top surface with a 2-mm-thick disk of teflon. In this configuration, the substitute bearing is clamped to the shaft and the test-article mounting plate is placed on the teflon surface. Note that this is different than the mounting configuration used with a bearing pair in the cartridge. In the latter case, the bearing pair is mounted to the shaft as shown in Figure 3, and the test-article mounting plate is attached to the outer races of the bearing pair below the test article. However, for purposes of testing the operation of the DTCU, the substitute bearing configuration is functionally equivalent to

the final mounting configuration. The rate-table shaft turns the substitute bearing, while the torque-rebalance loop maintains a null position against the friction torque transmitted through the teflon surface.

Figures 12 and 13 contain data taken with the DTCU using the substitute bearing. These experiments are meant to illustrate only the kinds of data that can be taken with the DTCU and to demonstrate its complete operation. The test conditions and data-collection parameters were chosen arbitrarily to illustrate the DTCU capabilities in both its higher and lower speed ranges. Different test profiles and higher rate sampling are possible. The values for torque presented in the figures are only an approximate calibration of the torque sensor. The final calibration has not yet been done.

Figure 12 is a plot of running torque taken with the substitute bearing running at 800 mrad/s in the counterclockwise direction. This rate is half the maximum rate of the DTCU and a little faster than the sponsor's specification for the maximum gimbal-slew rate. For this experiment, sampling was set for once every 17.5 mrad (1°) of position or approximately 46 Hz at this rate.

Figure 13 illustrates data from an experiment to measure Dahl friction parameters. The bearing was oscillated through about 1.75 mrad (0.1°) with a sine function of 0.1 Hz. Sampling was done at 10 Hz. The figure illustrates the hysteretic behavior found in this regime from which the bearing's Dahl parameters may be derived.

#### FUTURE WORK

The next steps in the DTCU development are to carefully validate the DTCU operation, to precisely calibrate the instrument and to complete the bearing-cartridge design. The evaluation of bearings can begin after these three steps are completed.

Another related area of DTCU development is adapting it for the torque characterization of other mechanical components such as motors, slip rings, and gear trains. The biggest technical challenge here is developing a scheme for mounting components other than bearing pairs.

#### CONCLUSIONS

The DTCU has been designed, fabricated, assembled, and tested. Experiments for running torque and Dahl parameters were performed using a substitute bearing. The initial testing indicates that the design requirements have been met or exceeded. The DTCU has the ability to test bearings under conditions similar to those of an actual spacecraft pointing platform. This test capability provides for precise torque characterization of duplex ball bearing pairs.

## REFERENCES

- [1] Greer, H., and Mack, R. A.: "Experimental Investigation of Torque Noise in Satellite Bearings," Journal of Spacecraft and Rockets, Vol. 12, No. 3, March 1975, pp. 146 - 150.
- [2] Leveille, A. R.: "Slow Speed Torque Variation," presented at Thayer School of Engineering -- AOA, Bearings Conference, Dartmouth College, September 1968.
- [3] Todd, M. J.: "Solid Lubrication of Ball Bearings for Spacecraft Mechanisms," Tribology International, Vol. 15, No. 6, December 1982.
- [4] Stevens, K. T.: "Experiments on the Torque of Ball Bearings over Small Angles of Movement," ESA/TRIB 1, 1980.
- [5] Phinney, D. D., et al.: "Experience with Duplex Pairs in Narrow Angle Oscillating Applications," Proceedings of the 22nd Aerospace Mechanisms Symposium, 1988, pp. 211 - 226.
- [6] Dahl, P. R.: "Measurement of Solid Friction Parameters of Ball Bearings," SAMSO TR-77-132, The Aerospace Corporation, 1977.

## ACKNOWLEDGMENTS

The DTCU mechanical design is the work of Bob Summers and Louise Jandura. The electrical design was done by Ted Kopf and Russ Allen. The author would also like to thank Mike Agronin, Ken Holmes, Carl Marchetto, and Ray Schliesmann for substantial contributions to the DTCU development.

This work was performed at the Jet Propulsion Laboratory, California Institute of Technology, and was sponsored by the United States Air Force, Wright Research and Development Center through an agreement with the National Aeronautics and Space Administration.

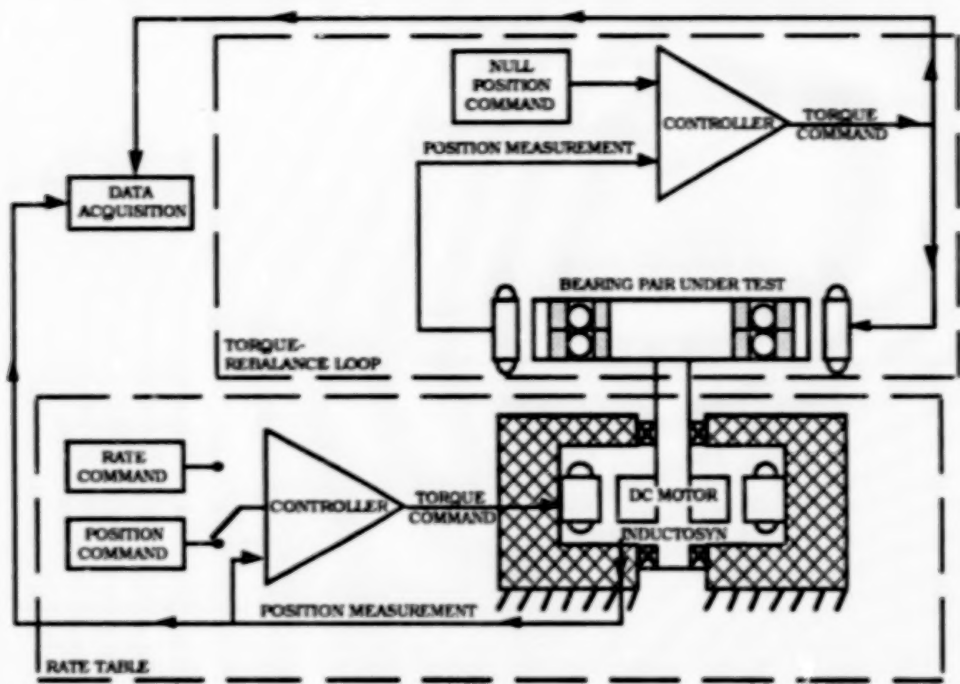


Figure 1. Schematic of the Dynamic Torque Calibration Unit (DTCU).

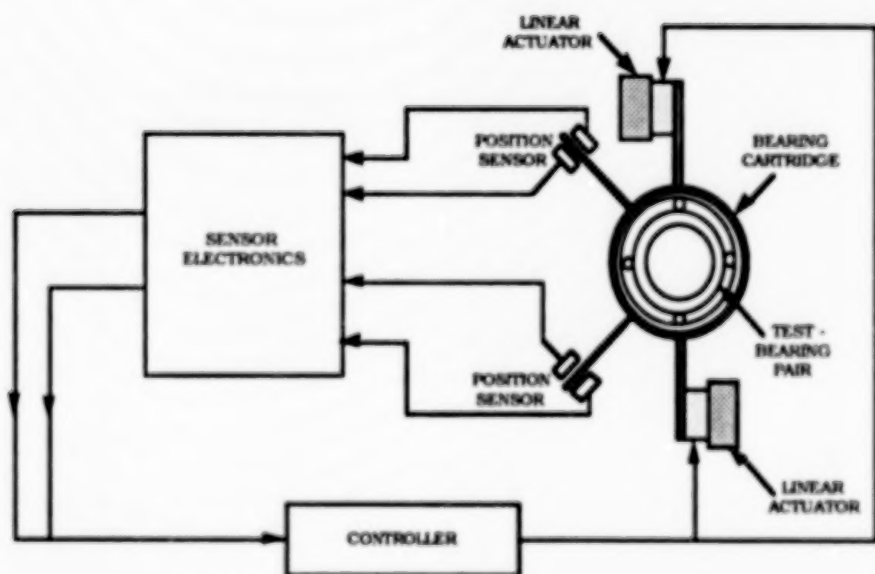


Figure 2. DTCU torque-rebalance loop operation.

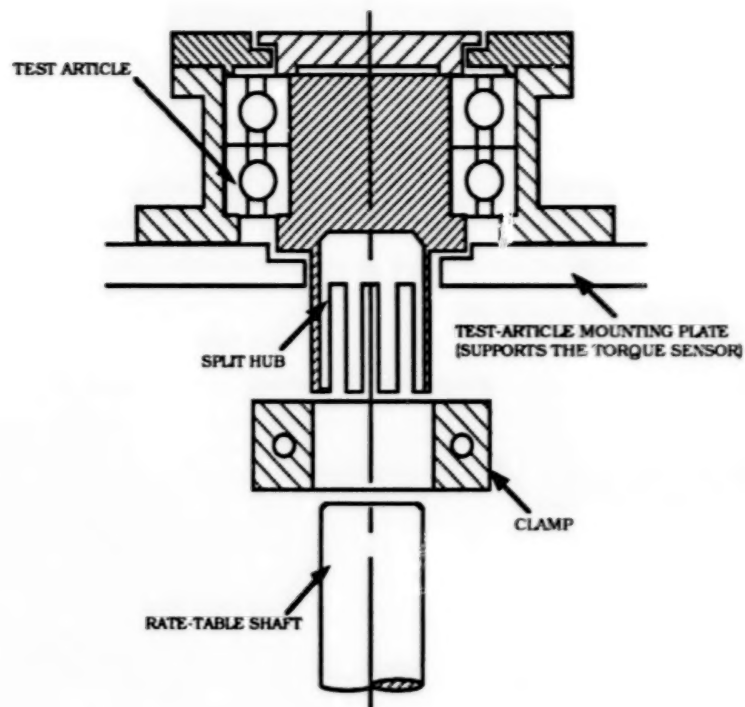


Figure 3. Bearing-cartridge design.

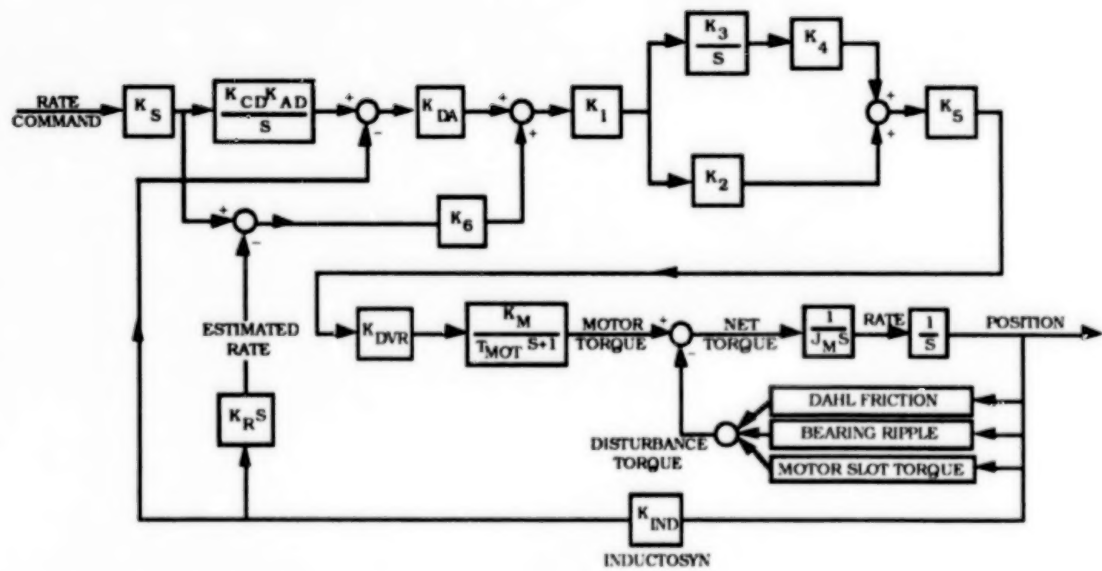


Figure 4. Rate-table controller.

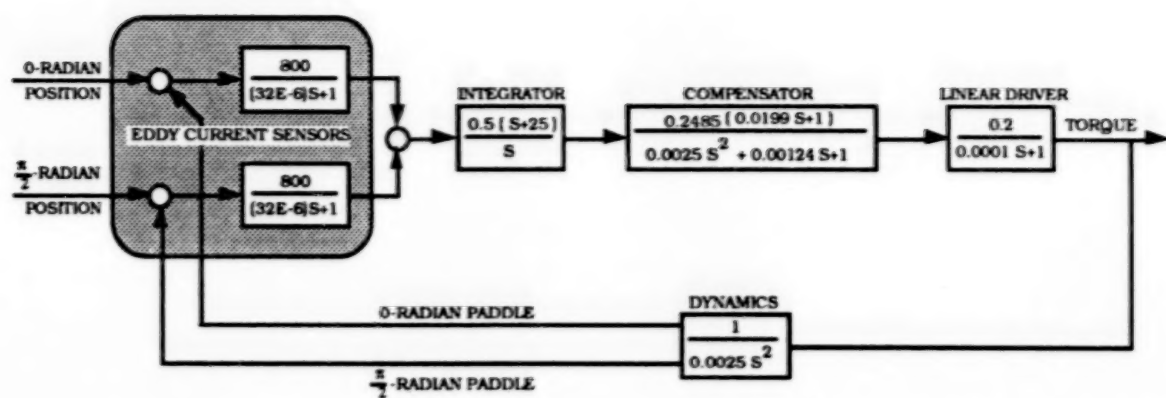


Figure 5. Torque-rebalance loop controller.

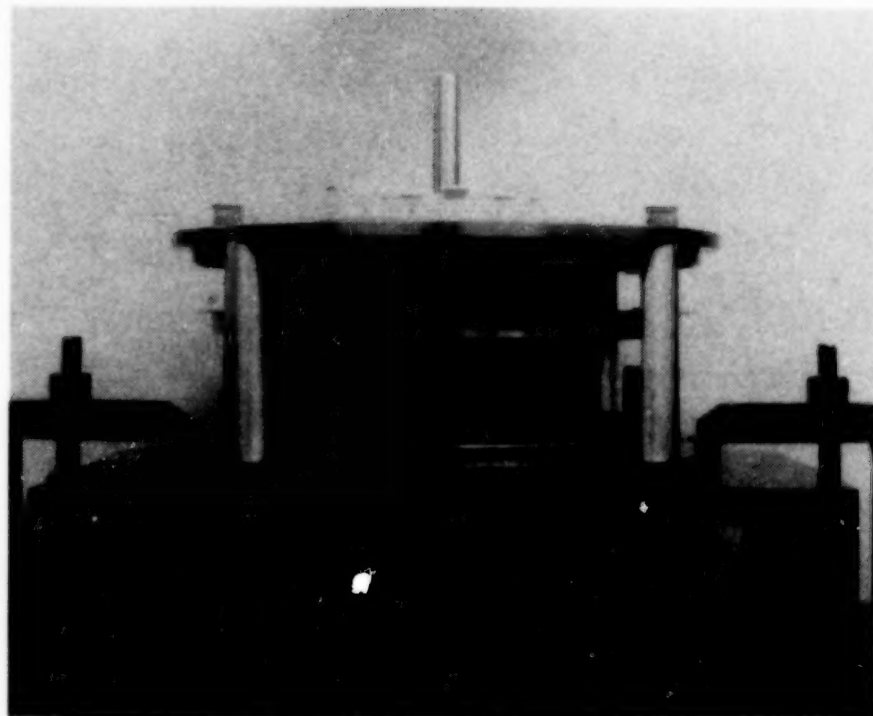


Figure 6. DTCU preliminary assembly mounted on a mill table.

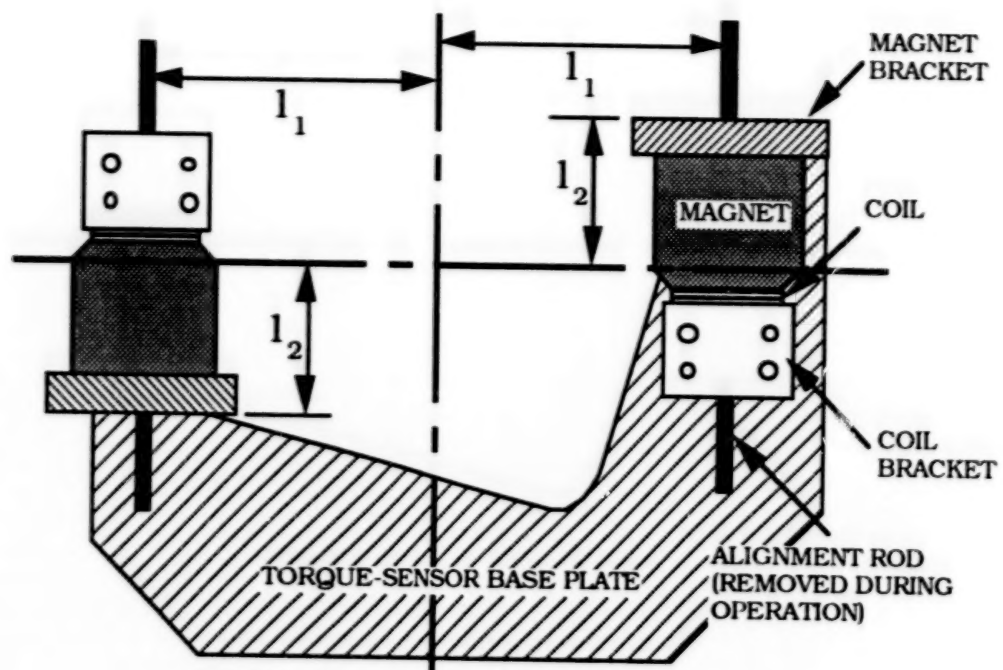


Figure 7. Torque-sensor alignment.



Figure 8. The DTCU and its electronics.

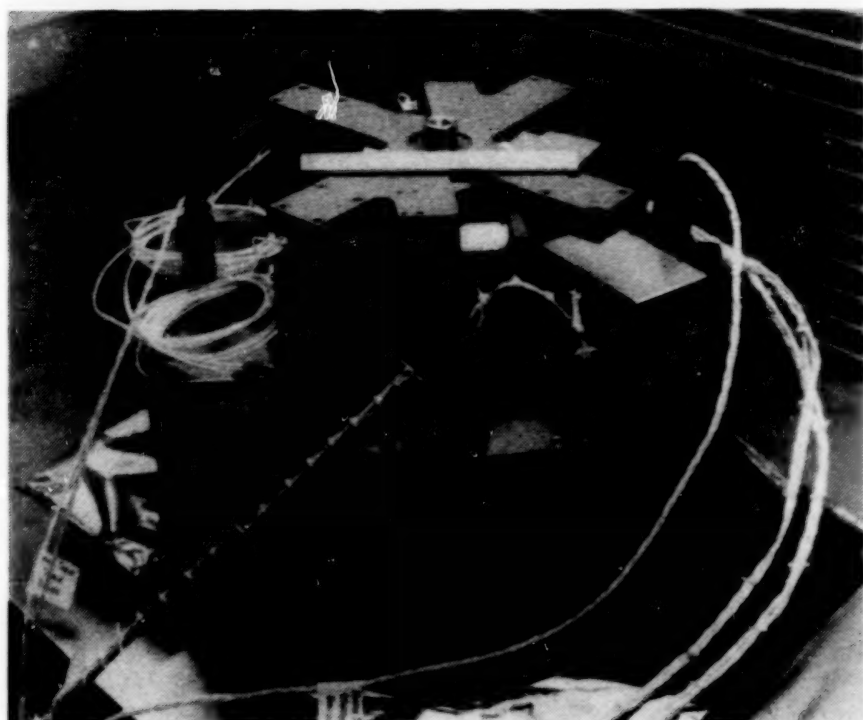


Figure 9. The DTCU.

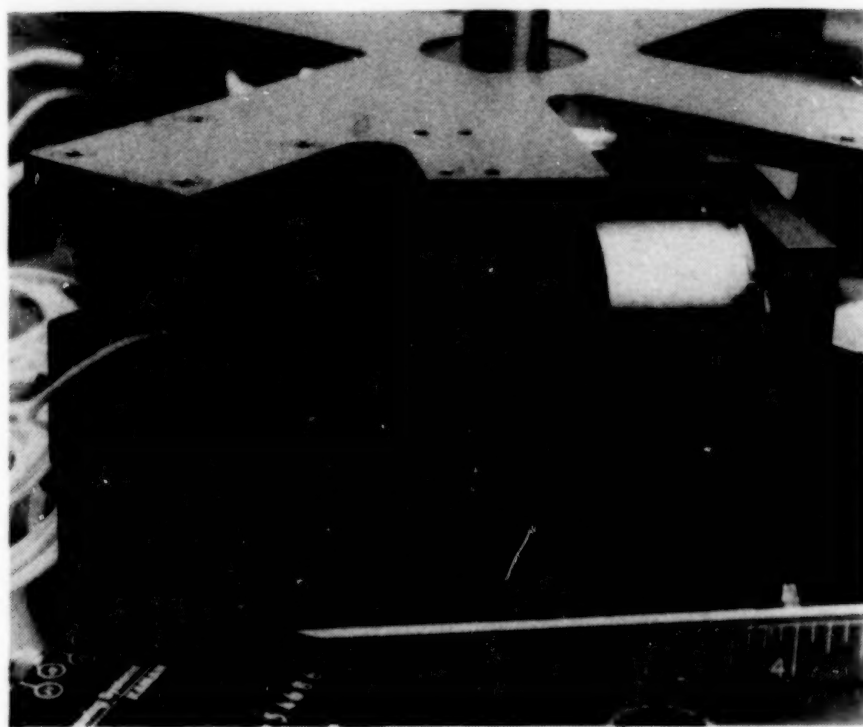


Figure 10. Closeup of the DTCU's torque sensor.

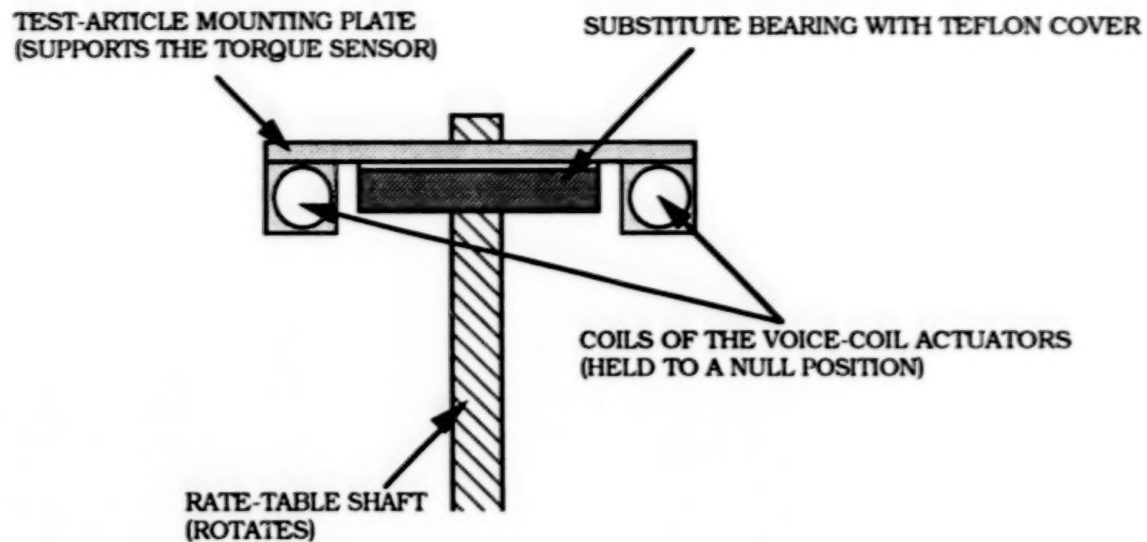


Figure 11. Test setup using a substitute bearing.

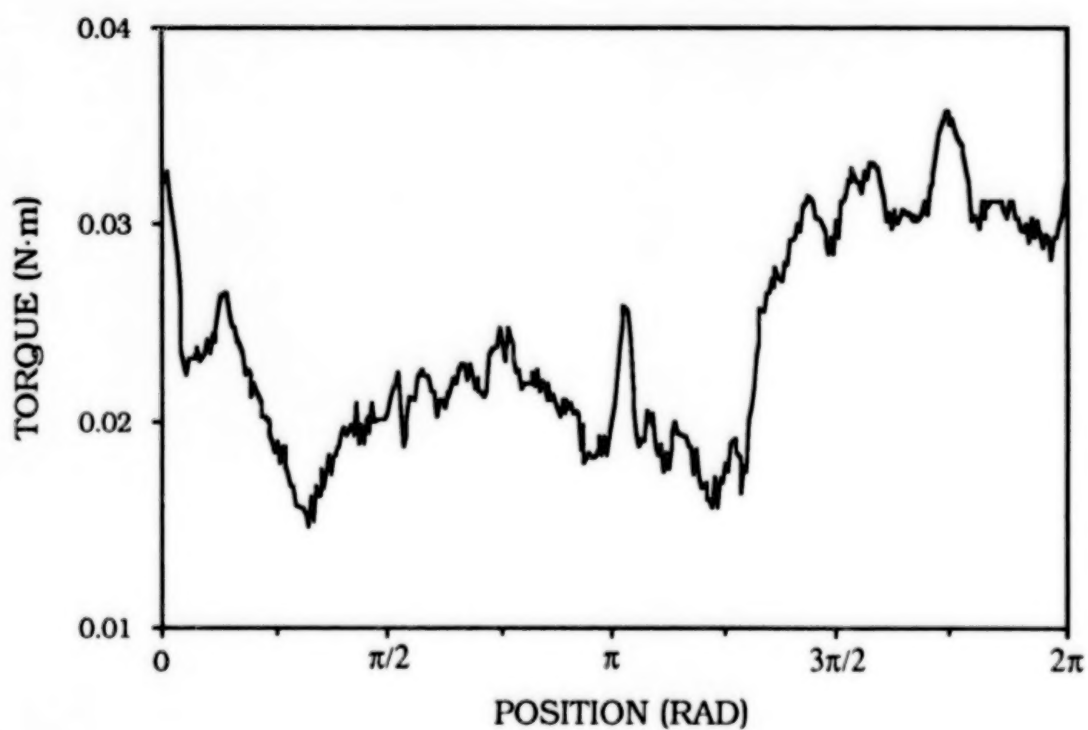


Figure 12. Running torque experiment using the substitute bearing.

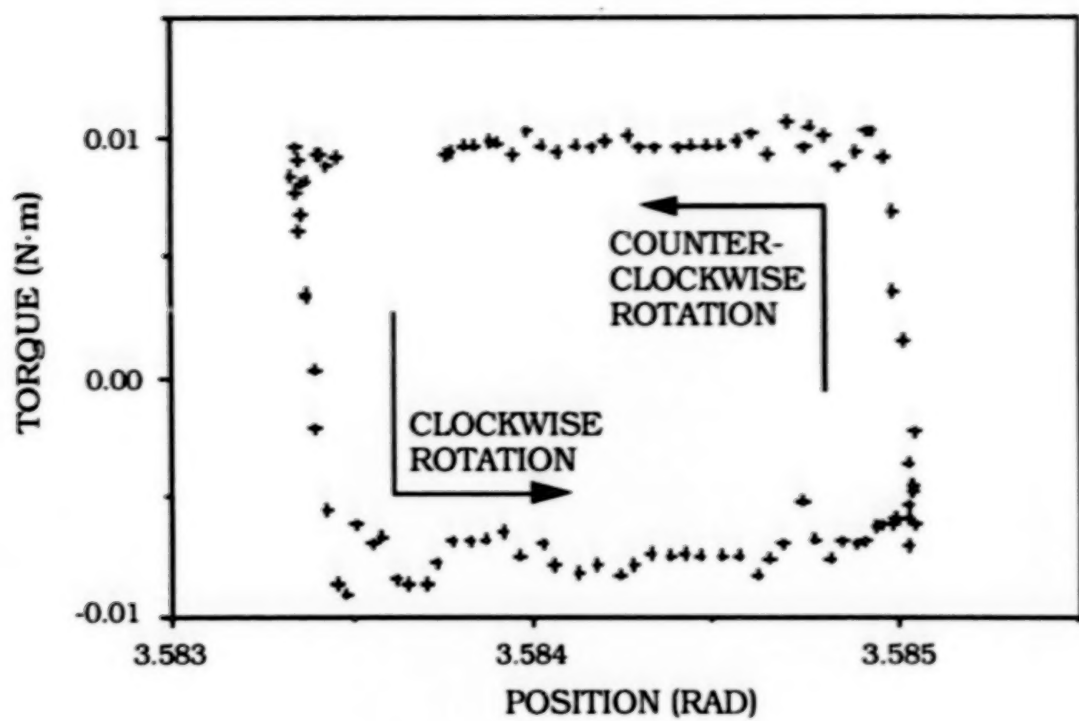


Figure 13. Dahl friction experiment using the substitute bearing.

# **A New Active Virtual Pivot Six-Degree-of-Freedom Hand Controller for Aerospace Applications**

**William C. Marshall, Kathleen M. Radke, Robert E. DeMers,  
David J. Lowry, and Lee Levitan**

**Systems and Control Sciences Department  
Systems and Research Center  
Honeywell Inc.  
3660 Technology Drive  
Minneapolis, MN 55418**

## **Abstract**

During 1989 a new six-degree-of-freedom (6-DOF) active hand controller concept was designed and constructed based on the concept of a "virtual pivot." This concept, labeled VPHC, was first demonstrated in a 1985 study by a member of the design team, and a patent was issued in 1990. Operator control input occurs via a force/torque sensor rigidly mounted to the handgrip. Sensed force/torque signals are used by microprocessors to generate motor drive control for each of six independently controlled motors mounted on the three-legged mechanism. The control microprocessor uses input biasing and rate-feedback motor controllers to generate the sensed feel of virtual springs and deadbands found in more conventional designs.

An important advantage of this design is that the location of the virtual pivots, reflective forces and torques, breakout force levels, sensed spring rates, operating modes, etc., can be changed simply by changing the software. This approach yields an autonomous VPHC that can easily adapt itself to an individual operator (by software extension). A proof-of-concept version has been demonstrated, and further improvements are currently being studied and implemented.

## **Introduction**

In the space-based platforms planned for the Space Station and Lunar-Mars initiative, a significant range of activities will have to be performed using hand controls. These include:

- Telerobotics using crane-type arms, which have relatively crude end-effectors.
- Telerobotics using dexterous manipulators, which have end-effectors with more degrees of freedom.
- Remotely piloted vehicles.
- Coordinated control of two robot arms simultaneously.

Given that the task demands for these activities are quite different, it is appropriate to provide several kinds of hand controllers; however, space constraints and the need for commonality (to reduce training/retraining time and increase generalization) have led us to examine the feasibility of using a single controller for all tasks. Such a controller will have to be flexible and easy to reprogram as the task demands dictate, accommodate the needs of a diverse user population, and require minimal space. In addition, it will have to be reliable and provide for graceful degradation. Our design is a unique invention embodying the virtual pivot concept first shown by us in 1985. Our 1989 initiative work resulted in a successful demonstration of this concept expanded to six degrees of freedom.

## **General Design Goals**

Our 1989 goals were to construct an effective and efficient 6-DOF hand controller that incorporates system engineering principles, including human factors requirements, and that has broad applicability for both space-based and ground/air-based activities. We intended to use the virtual pivot concept invented during our 1985 research initiative. The design approach required us to:

- Implement the virtual pivot concept expanded to a 6-DOF capability.

- Achieve unconstrained 6-DOF motion with  $\pm 3.8$  cm ( $\pm 1.5$ -in.) translations and  $\pm 350$  mr ( $\pm 15$  deg) angular displacements.
- Provide both rate and position mode operations.
- Allow reasonable task performance under degraded conditions (i.e., use a force/torque sensor as a force stick if the virtual pivot hand controller [VPHC] motors fail).

### **General Design Implementation**

The VPHC (see Figure 1) is intended to serve as a general-purpose, adaptable force feedback 6-DOF hand controller for a variety of space applications. System equations were developed that relate potentiometer measurements to the inferred position and attitude and implement feel dynamics to the human operator in response to translation or rotation of the hand grip. The VPHC uses input biasing to generate the sensed feel of springs and mechanical deadbands (see Figure 2). Operator control input occurs via a force/torque sensor rigidly mounted under the handgrip. This sensor responds to 6-DOF linear forces and moments (applied to the handgrip by the operator) and in turn supplies six signals representing Cartesian force and moment vectors. This force/torque sensor also provides backup capability to the VPHC as a force stick if the motor drives fail.

The VPHC system equations were derived to convert the measurements of three leg lengths and six angles into grip platform attitude Euler angles and position from the origin of the platform coordinate system. An initial analysis of the force/moment equations showed that mechanical lockup cannot occur over the allowed range of motion. Relationships between desired angular and linear velocities of the platform and measurements of leg extension and leg angles were also derived (solving the reverse kinematics problem). These straightforward algorithms efficiently generate the command inputs to a closed-loop control system in the real-time mechanization.

## Basic Design Features

Figure 3 is a sketch of the hand control mechanical design. There are three ball joints at the top of telescoping legs. Leg lengths are measured by linear potentiometers. Also shown are three linear screw drive motors in the legs and three motors and shaft angle pickoffs used to determine the spherical coordinates for each leg. In addition, there is a 6-DOF force/torque sensor mounted under the platform to measure operator input for 6-DOF rate control. The handgrip is mounted on the force/torque sensor. During system calibration, the fixed displacement vector (from the origin of the platform coordinate frame) of the operator's wrist joint is to be estimated. Figure 4 shows the vector relationships between the base and platform coordinate frames.

**Processor Interface**—The signal interface required to determine platform orientation and translation in six degrees of freedom consists of nine potentiometer measurements (three per leg) that define the three position vectors of the platform's three fixed ball joints with respect to the three base leg pivot points. The processor must then return the three Euler angles and the three linear translations from nominal platform origin. In addition, the force/torque sensor inputs are used in either position or rate mode to command a 6-DOF velocity that the motorized legs and shaft drives are to deliver. Hence, the processor must first solve the geometric task of computing orientation and translation and then compute the requisite leg rotational and linear velocities that result in the commanded system state.

**Kinematic Equations**—Kinematic solutions to the handgrip platform Euler angles (defining attitude angles) and linear displacements from the center of the coordinate frame are uniquely obtained by using nine potentiometers rather than a smaller number (theoretically possible). The telescoping legs (whose lengths are actuator driven) are attached to the platform by ball joints and to the base by double-gimbaled motorized joints. The outer gimbals are rigidly attached to the base, are motor driven, and cause a roll motion about the leg's motor axis of rotation. The outer gimbal axis defines the leg coordinate frame x axis for each of the three legs. These three axes are each oriented along the radial directions with respect to the center of the base. This results in the forward base point having its motor axis along the x axis of the base coordinate frame. The azimuth angles to the other two base points have constant values of  $\frac{2}{3}\pi$  and  $\frac{4}{3}\pi$  radians (120 and 240 deg). Inner gimbals

allow rotation about the respective leg pitch axes. Letting the lengths of the three legs  $d_i$ , where  $i = 1, 2, 3$ , be defined by  $0 < d_{i\min} < d_i < d_{i\max}$ , then the position vectors of the platform's ball joints with respect to the base frame  $S_B$  are

$$\vec{P}_i = E_i(\psi_0)E(\theta_i, \phi_i) \begin{bmatrix} 0 \\ 0 \\ d_i \end{bmatrix} + \vec{P}_{B_i}; i = 1, 2, 3 \quad (1)$$

where

$$E(\theta_i, \phi_i) = \begin{bmatrix} \cos\theta_i & 0 & \sin\theta_i \\ \sin\theta_i \sin\phi_i & \cos\phi_i & -\cos\theta_i \sin\phi_i \\ -\sin\theta_i \cos\phi_i & \sin\phi_i & \cos\theta_i \cos\phi_i \end{bmatrix} \quad (2)$$

and

$$E_i(\psi_0) = \begin{bmatrix} \cos\psi_0 & -\sin\psi_0 & 0 \\ \sin\psi_0 & \cos\psi_0 & 0 \\ 0 & 0 & 1 \end{bmatrix}; \psi_0 = 0, 120, 240 \text{ deg for } i = 1, 2, 3 \quad (3)$$

**Processor Overview**—The processor is a Motorola VMEbus 68020 single-board microcomputer housed in a standard Motorola chassis with several analog-to-digital interface cards. Six tachometers on the three legs measure motor speeds of shaft and leg-extending motors (two per leg). Potentiometers measure leg extension and the two shaft angles of each leg (nine potentiometers in all). Rate and position control modes differ. In the position mode, removal of grip force/torque commands from the operator causes the VPHC to remain at its latest attained attitude and linear displacement. Removal of input in the rate mode will cause a return to the initial displacement origin. Any of the six degrees of freedom may be locked out if desired. Software stops are provided to prevent the system from running into hard stops, which might cause damage. Figure 5 is an overview diagram of the control channels. The reverse kinematics and platform Euler angle computations are discussed in the next two subsections.

**Geometric Relationships**—Defining the position vectors of the pivots by  $\bar{R}_{Bi}$  and  $\bar{R}_{Pi}$ , where  $i = 1, 2, 3$ , in the two separate frames  $S_B$  (the base frame) and  $S_P$  (the platform frame) results in

$$\begin{aligned}\bar{R}_{B1} &= \begin{bmatrix} r_B \\ 0 \\ 0 \end{bmatrix}; \bar{R}_{B2} = \begin{bmatrix} -r_B/2 \\ (\sqrt{3}/2)r_B \\ 0 \end{bmatrix}; \bar{R}_{B3} = \begin{bmatrix} -r_B/2 \\ -(\sqrt{3}/2)r_B \\ 0 \end{bmatrix} \\ \bar{R}_{P1} &= \begin{bmatrix} r_P \\ 0 \\ 0 \end{bmatrix}; \bar{R}_{P2} = \begin{bmatrix} -r_P/2 \\ (\sqrt{3}/2)r_P \\ 0 \end{bmatrix}; \bar{R}_{P3} = \begin{bmatrix} -r_P/2 \\ -(\sqrt{3}/2)r_P \\ 0 \end{bmatrix}\end{aligned}\quad (4)$$

The vector  $\bar{R}_C$  defines the origin of the  $S_P$  frame and is given by

$$\bar{R}_C = \frac{1}{3} \sum_{i=1}^3 (\bar{R}_i + \bar{R}_{Bi}) \quad (5)$$

or

$$\bar{R}_C = \frac{1}{3} \sum_{i=1}^3 E_i(\Psi_0) \begin{bmatrix} -d_i \sin \theta_i \\ d_i \cos \theta_i \sin \phi_i \\ -d_i \cos \theta_i \cos \phi_i \end{bmatrix} = \frac{1}{3} \sum_{i=1}^3 \bar{R}_i \quad (6)$$

since the sum  $\sum \bar{R}_{Bi} = 0$

Referring to Figure 4, the platform  $\hat{X}_P$  unit vector is directed from the center toward  $P_1$ . The  $\hat{Y}_P$  unit vector is parallel to the line from  $P_3$  to  $P_2$ . Then

$$\begin{aligned}\hat{X}_P &= \left( \frac{1}{r_P} \right) [\bar{R}_1 - \bar{R}_C] = \left( \frac{2}{3} \bar{R}_1 - \frac{1}{3} (\bar{R}_2 + \bar{R}_3) \right) \\ \hat{Y}_P &= \left( \frac{1}{\sqrt{3} r_P} \right) [\bar{R}_2 - \bar{R}_3] \\ \hat{Z}_P &= \hat{X}_P \times \hat{Y}_P = \left( \frac{2\sqrt{3}}{9 r_P^2} \right) [\bar{R}_1 \times \bar{R}_2 + \bar{R}_2 \times \bar{R}_3 + \bar{R}_3 \times \bar{R}_1]\end{aligned}\quad (7)$$

The direction cosines of the  $X_p$ ,  $Y_p$ , and  $Z_p$  unit vectors are the components of the preceding vector equations. The Euler rotation matrix from  $S_B$  to  $S_p$  is then

$$E_{P/B} \equiv \begin{bmatrix} \hat{X}_p \cdot \hat{X}_B & \hat{Y}_p \cdot \hat{X}_B & \hat{Z}_p \cdot \hat{X}_B \\ \hat{X}_p \cdot \hat{Y}_B & \hat{Y}_p \cdot \hat{Y}_B & \hat{Z}_p \cdot \hat{Y}_B \\ \hat{X}_p \cdot \hat{Z}_B & \hat{Y}_p \cdot \hat{Z}_B & \hat{Z}_p \cdot \hat{Z}_B \end{bmatrix} = \{e_{ij}\} \quad (8)$$

All information concerning the relative attitude orientation between the VPHC base and platform frames is contained in the Euler matrix  $E_{P/B}$ . Euler angles can be defined in 24 different ways depending on the sequence of rotations (in a positive sense about each of three axes). There are 12 permutations starting with either frame  $S_p$  or  $S_B$ , or 24 total. Each set of three angles is not interchangeable (except for very small rotations). Each set does, however, result in the same rotation of one frame to another when applied in its specific sequence.

The following set arises from a yaw rotation about the  $S_B$  z axis followed by a pitch rotation about the y axis and a final roll about the x axis:

$$\begin{aligned} \psi_p &= \tan^{-1}(e_{12}/e_{11}) = \text{Yaw} \\ \theta_p &= \sin^{-1}(-e_{13}) = \text{Pitch} \\ \phi_p &= \tan^{-1}(e_{23}/e_{33}) = \text{Roll} \end{aligned} \quad (9)$$

Each rotation assumes the right-hand rule for positive sense. The inverse transformation performs a roll-pitch-yaw transformation (in that order) and is not uncommon in the aircraft industry.

**Platform Velocity Equations**—Tachometers mounted on the VPHC legs and roll axis shafts are used in a velocity feedback controller that drives each motorized leg to null a separate commanded velocity. These six velocities are in turn computed according to the six signals from the Lord force/torque sensor (after biasing to provide reflected force or torque dynamics for the operator).

At present, handgrip force signals are interpreted as referenced to the base coordinate frame as a linear velocity command. The torque

moments, however, are presently interpreted as referenced to the platform coordinate frame as an angular velocity command. The coordinate system used is arbitrary and can be easily redefined in processor code and provided later as an optional VPHC operating mode if desired.

The inertial velocity of each leg is composed of the linear velocity of the platform's center summed with the rotational velocity about the center, that is

$$\vec{V}_i = \frac{d}{dt} \vec{R}_i = \vec{V}_C + \vec{\omega}_P (\vec{R}_i - \vec{R}_C); i = 1, 2, 3 \quad (10)$$

where all quantities are assumed to be expressed in the same coordinate system. Differentiating the left side (using the previous equation for  $\vec{R}_i$ ) results in

$$\vec{V}_i = \frac{d}{dt} \vec{R}_i = E_i(\psi_0) \left\{ \frac{d}{dt} \left[ E_i(\theta_i, \phi_i) \begin{bmatrix} 0 \\ 0 \\ -d_i \end{bmatrix} \right] \right\} = \vec{V}_C + \vec{\omega}_P (\vec{R}_i - \vec{R}_C); i = 1, 2, 3 \quad (11)$$

or

$$\vec{V}_i = \Omega_i(\psi_0, \theta_i, d_i) \begin{bmatrix} \dot{\theta}_i \\ \dot{\phi}_i \\ \dot{d}_i \end{bmatrix} = \vec{V}_C + \vec{\omega}_P (\vec{R}_i - \vec{R}_C); i = 1, 2, 3 \quad (12)$$

Then

$$\begin{bmatrix} \dot{\theta}_i \\ \dot{\phi}_i \\ \dot{d}_i \end{bmatrix} = \Omega_i^{-1} [\vec{V}_C + \vec{\omega}_P (\vec{R}_i - \vec{R}_C)]; i = 1, 2, 3 \quad (13)$$

In the above equation, only the expressions for leg roll and length rates are of interest as the VPHC leg pitching rates are automatically driven by mechanical constraints. This solution requires inversion of a 3 by 3 matrix, where

$$\Omega_i(\psi_0, \theta_i, \phi_i, d_i) = E_i(\psi_0) \begin{bmatrix} 0 & -d_i \cos \theta_i & -\sin \theta_i \\ d_i \cos \theta_i \cos \phi_i & -d_i \sin \theta_i \sin \phi_i & \cos \theta_i \cos \phi_i \\ d_i \cos \theta_i \sin \phi_i & d_i \sin \theta_i \cos \phi_i & -\cos \theta_i \sin \phi_i \end{bmatrix}; i=1,2,3 \quad (14)$$

The above platform angular velocity vector input commands,  $\vec{\omega}_P$ , are referenced to  $S_B$ ; if they are referenced to  $S_P$  instead, they are simply converted by the inverse Euler transformation as follows:

$$\vec{\omega}_P = \begin{bmatrix} \omega_X \\ \omega_Y \\ \omega_Z \end{bmatrix}_B = E_{P/B}^{-1} \begin{bmatrix} \omega_{X_c} \\ \omega_{Y_c} \\ \omega_{Z_c} \end{bmatrix}_P \quad (15)$$

The inverse Euler matrix is simply the transpose of the matrix since the coordinate frame is orthogonal and Cartesian.

## Conclusions

The unique demonstrable feature of the VPHC is that the sensed location of the pivot point can be set arbitrarily. It can be set through the center of the grip, above or below it, or centered inside the operator's wrist. For example, with a pivot point below the grip, it would act like a conventional military aircraft hand controller, with the pivot point where the stick attaches to the floor. However, with the pivot point above the grip, the top of the grip seemingly would be attached to a point above it, and the entire device would be swinging freely below it. This programmable pivot point allows maximum flexibility and adaptability. These changes can be made simply by entering the appropriate software commands.

The VPHC is an active device, using motors to control forces and torques. (A passive controller uses springs instead of motors.) This offers two additional features that are important for a hand controller that must be used in a variety of situations:

- The operating characteristics can be changed simply by changing the software. Thus, breakout forces, the degrees of freedom available, and spring rates, etc., can be modified without changing any hardware.

- Based on information from the object being controlled, the operator can be given feedback through the grip. This capability is called force reflection and usually involves providing tactile feedback through the grip when the controlled object (e.g., a robot arm) contacts the target (or other) object.

The combination of a programmable virtual pivot point with an active hand controller offers the unique capability to configure the hand controller to match the demands of the current task and to satisfy the wishes of a particular user.

## Summary

In 1989, we extended the 1985 passive single-axis concept and invented a 6-DOF orthogonal-axis active hand controller. Figure 1 illustrates the change. The enhanced design has two key features:

- A motor-driven mechanical configuration that allows independent 6-DOF motions consisting of three linear translations and three angular rotations referred to Cartesian orthogonal axes. Motion is constrained to  $\pm 3.8$  cm ( $\pm 1.5$  in.) and/or  $\pm 350$  mr ( $\pm 20$  deg) about the origin of the virtual pivot coordinate frame.
- Motor-driven force feedback (microprocessor controlled) that replaces spring centering. Gradients of forces or torques vs. displacements (in each of six axes; see Figure 2) are stored as parameters that can be modified by keyboard input. This modification provides adaptability or programmability of key hand controller operating characteristics: (1) sensed (virtual) pivot axis locations and range of motion in each axis; (2) sensed spring force reflection or the feel of the instrument (force/displacement gradients); (3) the capability, if desired, to implement bilateral force feedback from the system being controlled (via motor control feedback) to the human operator; and (4) the capability of operator-mode control to introduce menu-driven commands (via the VMEbus single-board computer).

Many other uses for an adaptable hand controller exist, such as control of fixed-wing aircraft (e.g., the National Aerospace Plane) and rotary-wing aircraft (e.g., the Advanced Apache), telerobotics for a variety of applications (e.g., radiation cleanup sites), and underwater applications both for vehicle maneuvering and robotic manipulation.

## Bibliography

DeMaio, J., and Radke, K.M., *Development of the Virtual Pivot Hand Controller*, Honeywell Final Report, December 1986.

DeMaio, J., Radke, K.M., and Tauer, J., "Virtual Pivot Hand Controller," U.S. Patent Application a47111721-US, September 30, 1988.

Honeywell Space Systems Group, *Hand Controller Commonality Study*, Report No. 289-16007, February 27, 1989.

Honeywell SRC, "Crew Systems Technology Development," in 1990 Honeywell IR&D Program Report, Vol. 2.

Radke, K.M., Lowry, D., Marshall, W., DeMers, R., and Blomberg, J., "Adaptable Six-Degree-of-Freedom Virtual Pivot Hand Controller," Honeywell Invention Disclosure, October 1989.

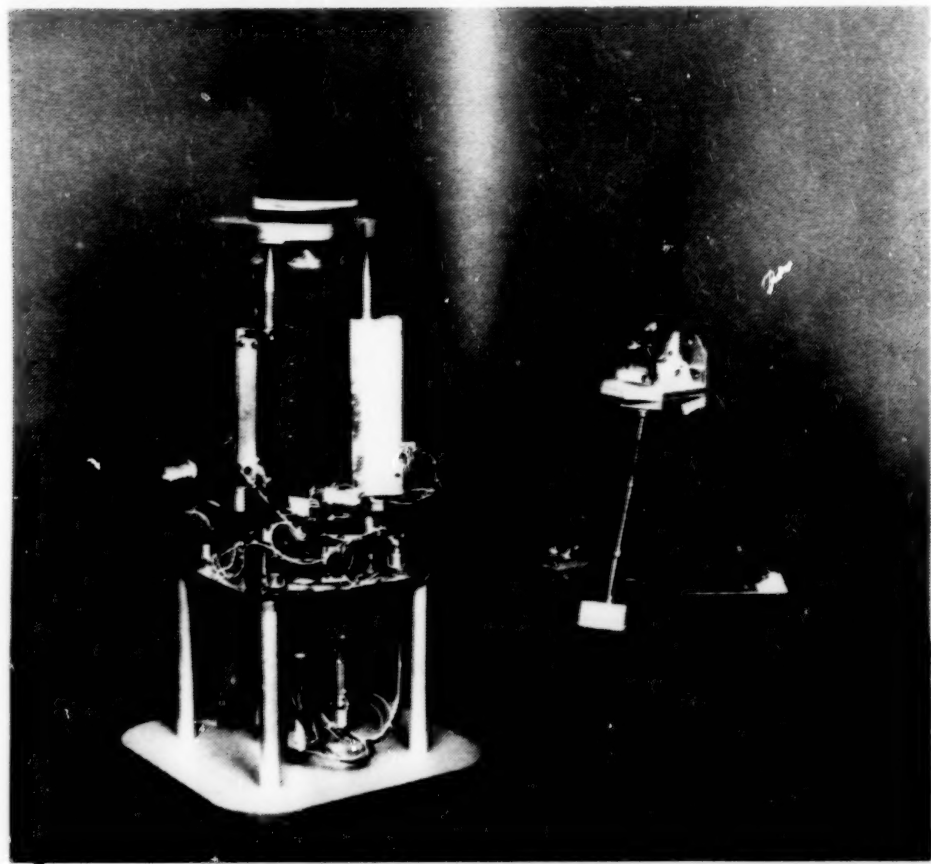


Figure 1. 1989 6-DOF VPHC Design (left) and Original 1985 Single-DOF VPHC Design (right)

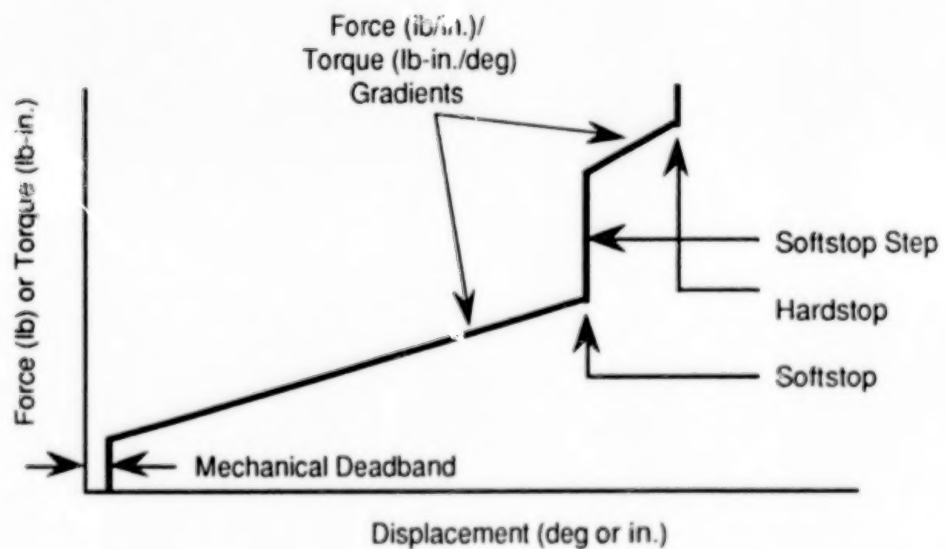


Figure 2. Handgrip-Applied Force/Torque vs. Displacement Profiles

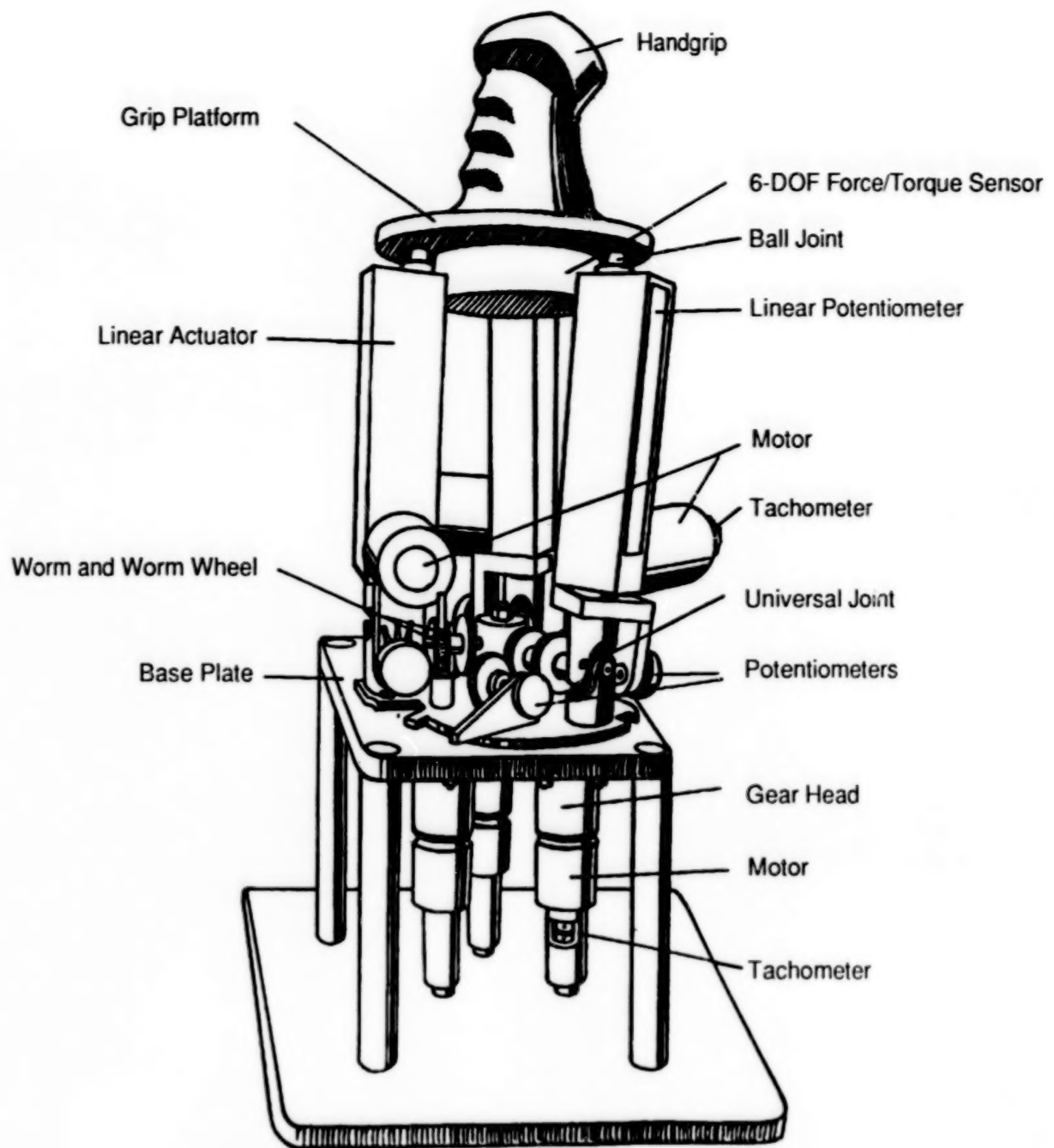


Figure 3. Hand Controller Mechanical Design

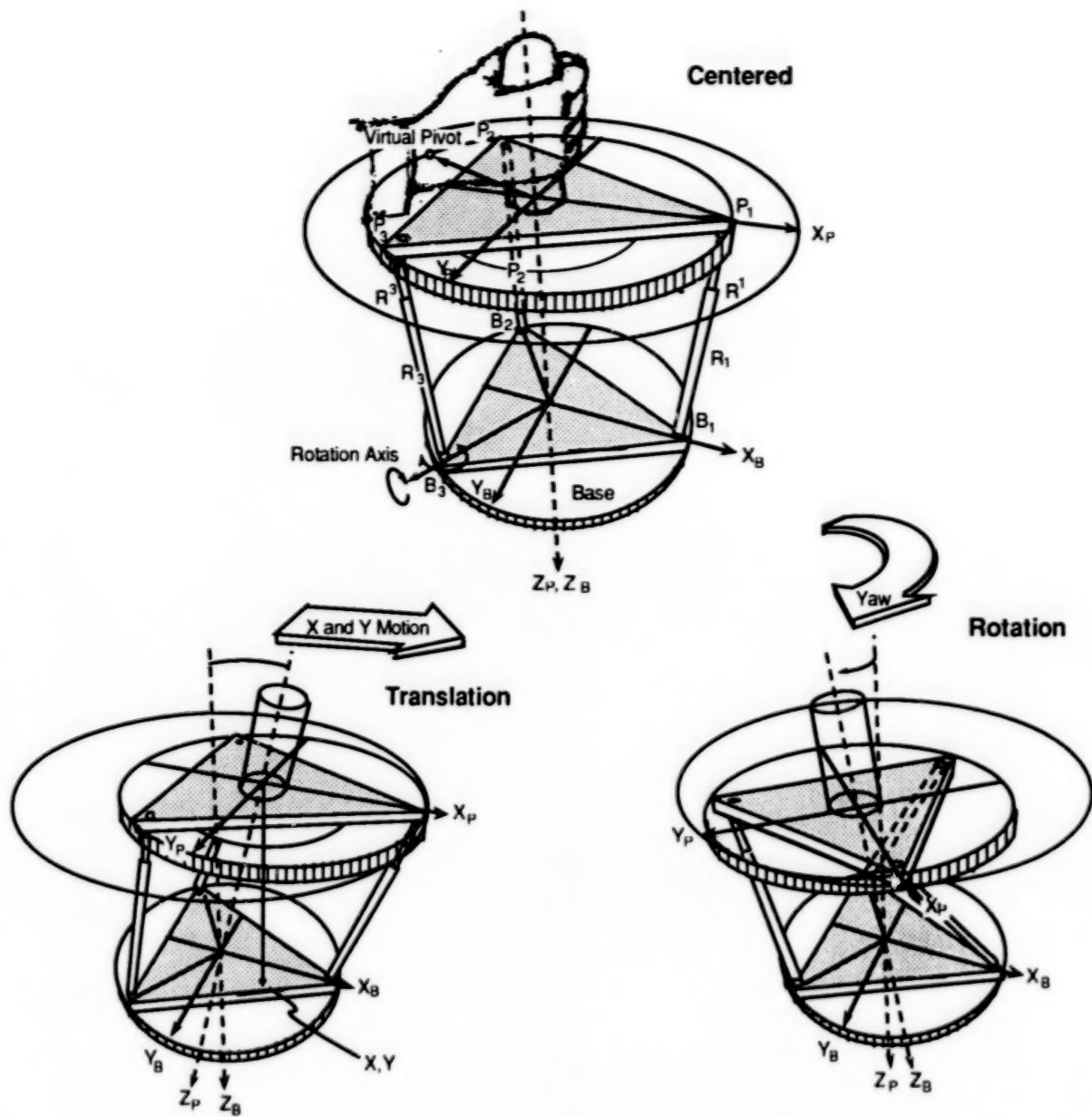


Figure 4. Vector Relationships between Base and Platform Coordinate Frames

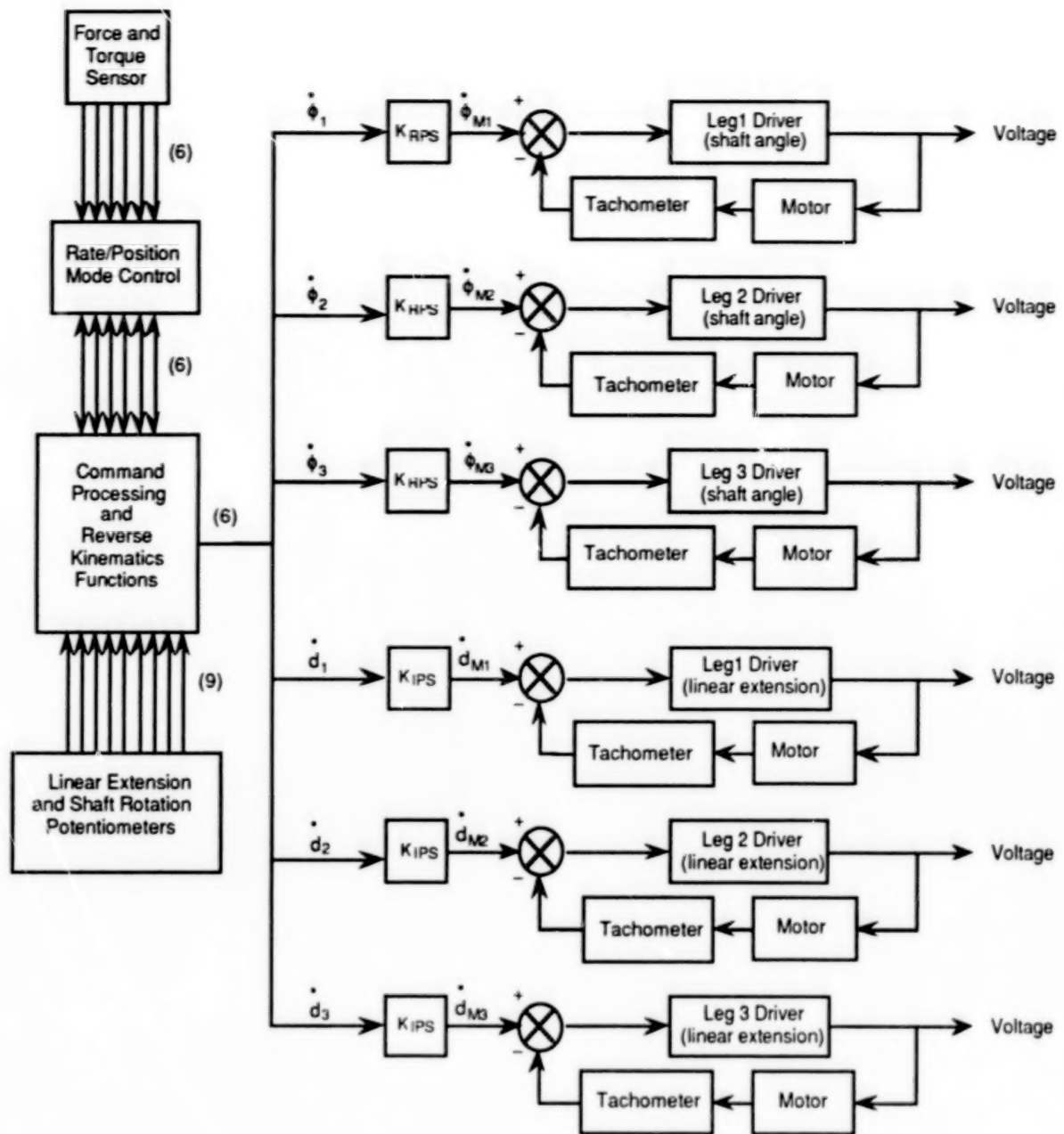


Figure 5. VPHC Motor Control Channels

## TECHNICAL REPORT STANDARD TITLE PAGE

1. Report No. NASA CP-3113	2. Government Accession No.	3. Recipient's Catalog No.	
4. Title and Subtitle 25th Aerospace Mechanisms Symposium		5. Report Date May 1991	
		6. Performing Organization Code	
7. Author(s)	8. Performing Organization Report No.		
9. Performing Organization Name and Address  JET PROPULSION LABORATORY California Institute of Technology 4800 Oak Grove Drive Pasadena, California 91109		10. Work Unit No.	
		11. Contract or Grant No. NAS7-918	
		13. Type of Report and Period Covered Conference Publication	
12. Sponsoring Agency Name and Address National Aeronautics and Space Administration, Washington, D.C., 20546; California Institute of Technology, Pasadena, CA, 91109; Lockheed Missiles & Space Co., Inc., Sunnyvale, CA, 94088		14. Sponsoring Agency Code	
15. Supplementary Notes			
16. Abstract			
<p>The Proceedings of the 25th Aerospace Mechanisms Symposium held at the Jet Propulsion Laboratory, Pasadena, California on May 8-10, 1991 are reported in this NASA Conference Publication. Twenty-two papers are documented regarding aeronautical and spacecraft hardware. Technological areas include actuators, latches, cryogenic mechanisms, vacuum tribology, bearings, robotics, ground support equipment for aerospace applications and other mechanisms.</p>			
17. Key Words (Selected by Author(s))  Space Station      Paraffin Actuator Gimbals            Harmonic Gear Momentum Damper    Bearings Cryogenic Mechanisms    Blast Shield Tribology           Hand Controller		18. Distribution Statement  Unclassified - Unlimited  Subject Category 39	
19. Security Classif. (of this report) Unclassified	20. Security Classif. (of this page) Unclassified	21. No. of Pages 340	22. Price A15

338

**END**

**7 - 08 - 91**

